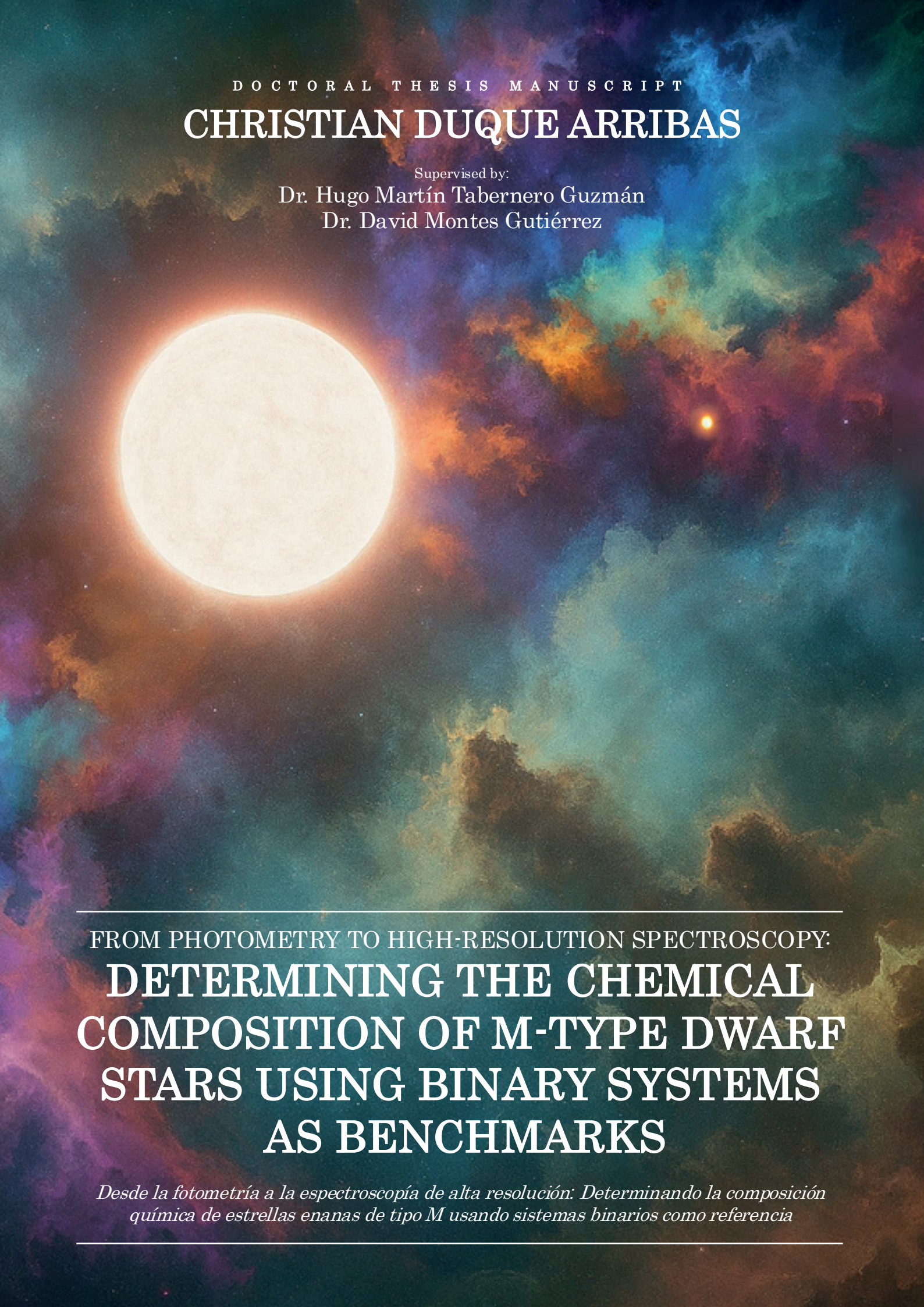

DOCTORAL THESIS MANUSCRIPT

CHRISTIAN DUQUE ARRIBAS

Supervised by:

Dr. Hugo Martín Tabernero Guzmán

Dr. David Montes Gutiérrez

FROM PHOTOMETRY TO HIGH-RESOLUTION SPECTROSCOPY:

DETERMINING THE CHEMICAL COMPOSITION OF M-TYPE DWARF STARS USING BINARY SYSTEMS AS BENCHMARKS

Desde la fotometría a la espectroscopía de alta resolución: Determinando la composición química de estrellas enanas de tipo M usando sistemas binarios como referencia

Ph.D. Thesis
Doctor in Astrophysics

Universidad Complutense de Madrid
Departamento de Física de la Tierra y Astrofísica, Facultad de Ciencias Físicas
iparcos–ucm (Instituto de Física de Partículas y del Cosmos de la UCM)

— Programa de Doctorado en Astrofísica —

From photometry to high-resolution spectroscopy: Determining the chemical composition of M-type dwarf stars using binary systems as benchmarks

Desde la fotometría a la espectroscopía de alta resolución: Determinando la composición química de estrellas enanas de tipo M usando sistemas binarios como referencia

Christian Duque–Arribas

Supervisors:
Dr. Hugo Martín Tabernero Guzmán
Dr. David Montes Gutiérrez

Madrid, September 2025

Facultad de Ciencias Físicas
Universidad Complutense de Madrid

Plaza de Ciencias, 1
Ciudad Universitaria
28040 – Madrid
https://fisicas.ucm.es

Some of the figures and material included in this work have already been published in the journals *Astronomy & Astrophysics* (ISSN 0004-6361), *Monthly Notices of the Royal Astronomical Society* (ISSN 0035-8711), and *The Astrophysical Journal* (ISSN 1538-4357).

"The reward of the young scientist is the emotional thrill of being the first person in the history of the world to see something or to understand something. Nothing can compare with that experience. The reward of the old scientist is the sense of having seen a vague sketch grow into a masterly landscape."

— Cecilia Payne-Gaposchkin,
the astrophysicist who discovered what stars are made of

UNIVERSIDAD COMPLUTENSE MADRID

DECLARACIÓN DE AUTORÍA Y ORIGINALIDAD DE LA TESIS PRESENTADA PARA OBTENER EL TÍTULO DE DOCTOR.

D. Christian Duque Arribas, estudiante en el Programa de Doctorado en Astrofísica de la Facultad de Ciencias Físicas de la Universidad Complutense de Madrid, como autor de la tesis presentada para la obtención del título de Doctor y titulada:
Desde la fotometría a la espectroscopía de alta resolución: Determinando la composición química de estrellas enanas de tipo M usando sistemas binarios como referencia (From photometry to high-resolution spectroscopy: Determining the chemical composition of M-type dwarf stars using binary systems as benchmarks) y dirigida por Dr. Hugo Martín Tabernero Guzmán y Dr. David Montes Gutiérrez,

DECLARO QUE:

La tesis es una obra original que no infringe los derechos de propiedad intelectual ni los derechos de propiedad industrial u otros, de acuerdo con el ordenamiento jurídico vigente, en particular, la Ley de Propiedad Intelectual (R.D. legislativo 1/1996, de 12 de abril, por el que se aprueba el texto refundido de la Ley de Propiedad Intelectual, modificado por la Ley 2/2019, de 1 de marzo, regularizando, aclarando y armonizando las disposiciones legales vigentes sobre la materia), en particular, las disposiciones referidas al derecho de cita.

Del mismo modo, asumo frente a la Universidad cualquier responsabilidad que pudiera derivarse de la autoría o falta de originalidad del contenido de la tesis presentada de conformidad con el ordenamiento jurídico vigente.

En Madrid, a 11 de septiembre de 2025

Contents

Agradecimientos

Este trabajo es el resultado de cinco años de esfuerzos, dudas y aprendizajes, tanto en lo académico como en lo personal. No es solo una tesis doctoral, sino también el reflejo de todas las personas que han estado a mi lado en este proceso. A todos vosotros, gracias:

A **Hugo y David**, mis directores,
por brindarme esta oportunidad y por su dedicación todos estos años.

A **Jose**, centro de gravedad de CARMENES,
por su constante ayuda y sabios consejos.

Al Departamento de Física de la Tierra y Astrofísica, por su cercanía,
y en especial a los **astrojóvenes**, por todos los momentos compartidos.

A **Vardan y Elisa**, por recibirme con los brazos abiertos en Porto,
y a todos los que dejaron huella en la ciudad y en mí.

A **mis amigos**, los de siempre y los que se han ido sumando en el camino,
por acompañarme en cada victoria y también en cada tropiezo.

A **mi familia**,
por su apoyo incondicional.

A todas las personas que, de una forma u otra,
habéis estado ahí en algún momento de este viaje.

Y a ti, lector,
por detenerte en estas páginas.

A todos, **GRACIAS**,
porque en cada paso de este camino hay algo de vosotros.

Summary

Introduction

M-type dwarf stars constitute the most numerous stellar population in the Milky Way and are central to contemporary astrophysics. Their ubiquity, longevity, and prevalence in the solar neighbourhood make them key targets in studies of star formation, Galactic chemical evolution, and exoplanet detection. However, their low effective temperatures give rise to spectra dominated by molecular bands, which complicates the use of standard spectroscopic techniques traditionally applied to solar-type stars.

In this context, the present doctoral thesis aims to improve our ability to estimate the chemical properties of M-dwarf stars by developing and validating alternative methods based on photometry, low- and high-resolution spectroscopy, and modern statistical approaches. A central pillar of this work is the use of wide binary systems composed of an F-, G-, or K-type star and an M-dwarf companion. Assuming a common origin and therefore a shared chemical composition, these systems act as empirical benchmarks that allow the calibration of methods applied to the cooler M components based on the well-characterised properties of their primaries.

Aims and results

This thesis addresses the challenge of determining metallicities and elemental abundances in M dwarfs by employing different approaches. We begin by exploring the potential of photometric data to infer metallicity. Using broadband magnitudes from *Gaia*, 2MASS, and CatWISE, we construct empirical calibrations within a Bayesian linear regression framework. These models, trained on M dwarfs with spectroscopic metallicities from APOGEE, are validated using a sample of wide binaries, confirming their predictive accuracy.

To capture more complex, non-linear relationships between photometry and metallicity, we explore a complementary approach based on artificial neural networks (ANNs). Trained on the same calibration sample, the network slightly outperforms the polynomial models. We included an uncertainty estimation via Monte Carlo dropout. This method balances flexibility and scalability and highlights the value of machine learning for stellar parameter inference.

Recognising that the accuracy of any calibration depends on the reliability of its reference data, we conduct a detailed abundance analysis of the FGK-type primaries in the benchmark binaries. Based on a previous study that derived stellar parameters and elemental abundances for 13 atomic species (Na, Mg, Al, Si, Ca, Sc, Ti, V, Cr, Mn, Fe, Co, and Ni) using the equivalent width method and high-resolution HERMES spectra, we extend the analysis by deriving, for the first time, the abundances of carbon and oxygen. In addition, we update the abundances of odd-Z iron-peak elements (Sc, V, Mn, and Co), incorporating hyperfine structure and non-LTE corrections where appropriate. The results follow established Galactic chemical trends, reinforcing the validity of the FGK stars as reference standards.

Building on this foundation, we present a new empirical method to determine elemental abundances in M dwarfs from low-resolution CAFOS spectra. By measuring spectral indices sensitive to different elements and calibrating them via projection predictive variable selection in a Bayesian framework using FGK+M wide binaries as chemical benchmarks, we derive [X/H] values for multiple elements across a sample of over 770 M dwarfs. Our abundance estimates show consistency with high-resolution studies and Galactic chemical trends, demonstrating that low-resolution spectroscopy, when combined with robust empirical calibrations, enables reliable chemical characterisation of cool stars.

Finally, we present new high-resolution spectroscopic observations of M-dwarf secondaries in wide binaries, obtained with the CARMENES spectrograph at the Calar Alto Observatory. Using the StePar Syn code, a Bayesian spectral synthesis tool, we derive $T_{\rm eff}$, $\log g$, and [Fe/H] for each star. The derived metallicities agree well with those of the corresponding FGK primaries, validating the spectroscopic analysis. Building on the groundwork laid by previous studies within the CARMENES consortium, this sample will contribute to advancing the chemical characterisation of M dwarfs using CARMENES spectra.

Conclusions

The methodologies developed in this thesis represent significant advances in the chemical characterisation of M-type dwarf stars. Photometric calibrations offer fast and scalable metallicity estimates across large stellar samples down to M5 V, with typical deviations below 0.1 dex. Neural networks introduce a flexible, data-driven alternative capable of modelling complex, non-linear patterns in photometric data, providing similar results that the Bayesian calibrations. Low-resolution spectroscopic indices extend abundance determinations to large and faint samples, specially for the early-type M dwarfs; and high-resolution spectra enable precise parameter determinations and form the basis for detailed chemical analyses.

The use of wide binary systems as empirical calibrators has proven to be a powerful strategy. By anchoring the analysis of M dwarfs to the well-characterised FGK-type companions, we overcome key limitations in direct spectral modelling of cool stars and enhance the precision and reliability of chemical measurements. Comparisons with independent high-resolution studies and established Galactic chemical trends further corroborated the reliability of the results.

These results are particularly relevant in light of upcoming large-scale surveys and space missions such as Ariel, PLATO or the Habitable Worlds Observatory, which will observe thousands of M dwarfs and require efficient, accurate tools for their characterisation. The approaches developed here are well suited to meet that challenge, contributing to studies of stellar populations, Galactic evolution, and the architecture of planetary systems around low-mass stars.

Keywords: binaries: general — methods: data analysis — techniques: photometric — techniques: spectroscopic — stars: abundances — stars: fundamental parameters — stars: late-type

Resumen

Introducción

Las estrellas enanas de tipo M constituyen la población estelar más numerosa de la Vía Láctea y ocupan una posición central en la astrofísica contemporánea. Su ubicuidad, longevidad y prevalencia en el vecindario solar las convierten en objetivos clave en estudios sobre formación estelar, evolución química galáctica y detección de exoplanetas. Sin embargo, sus bajas temperaturas efectivas dan lugar a espectros dominados por bandas moleculares, lo que dificulta la aplicación de técnicas espectroscópicas tradicionalmente empleadas en estrellas de tipo solar.

En este contexto, la presente tesis doctoral tiene como objetivo mejorar nuestra capacidad para estimar las propiedades químicas de las estrellas enanas M mediante el desarrollo y validación de métodos alternativos basados en datos fotométricos, espectroscopía de baja y alta resolución, y herramientas estadísticas modernas. Un pilar fundamental de este trabajo es el uso de sistemas binarios formados por una estrella de tipo F, G o K y una compañera enana M. Asumiendo un origen común y, por tanto, una composición química compartida, estos sistemas actúan como referencias empíricas que permiten calibrar métodos aplicados a las componentes M más frías a partir de las propiedades bien caracterizadas de sus compañeras primarias.

Objetivos y resultados

Esta tesis aborda el reto de determinar las metalicidades y abundancias elementales en enanas M mediante diferentes enfoques. Comenzamos explorando el potencial de los datos fotométricos para inferir la metalicidad. Utilizando magnitudes en banda ancha procedentes de *Gaia*, 2MASS y CatWISE, construimos calibraciones empíricas en un marco de regresión lineal Bayesiana. Estos modelos, entrenados con enanas M que cuentan con metalicidades espectroscópicas de APOGEE, se validan utilizando una muestra de sistemas binarios, confirmando su precisión predictiva.

Para capturar relaciones no lineales más complejas entre la fotometría y la metalicidad, exploramos un enfoque complementario basado en redes neuronales artificiales (ANNs). Entrenado con la misma muestra de calibración, el modelo neuronal supera ligeramente a los modelos polinómicos. Incorporamos una estimación de incertidumbre mediante la técnica de Monte Carlo dropout. Este enfoque ofrece un equilibrio entre flexibilidad y escalabilidad, y demuestra el valor del aprendizaje automático en la inferencia de parámetros estelares.

Reconociendo que la precisión de cualquier calibración depende de la fiabilidad de los datos de referencia, llevamos a cabo un análisis detallado de abundancias de las estrellas primarias de tipo FGK en los sistemas binarios de referencia. Basándonos en un estudio previo que derivó los parámetros estelares y abundancias de 13 elementos (Na, Mg, Al, Si, Ca, Sc, Ti, V, Cr, Mn, Fe, Co, y Ni) usando el método de las anchuras equivalentes y espectros de alta resolución obtenidos con el espectrógrafo HERMES, extendemos el análisis derivando, por primera vez, las abundancias de carbono y oxígeno. Además, actualizamos las abundancias de elementos del pico de hierro (Sc, V, Mn, y Co), incorporando correcciones por estructura hiperfina y efectos fuera del equilibrio

termodinámico local (no-ETL) cuando es necesario. Los resultados siguen las tendencias químicas galácticas establecidas, reforzando la validez de las estrellas FGK como estándares químicos.

Sobre esta base, presentamos un nuevo método empírico para determinar abundancias elementales en enanas M a partir de espectros de baja resolución obtenidos con CAFOS. Mediante la medición de índices espectrales sensibles a distintos elementos y su calibración vía selección de variables mediante proyección predictiva en un marco Bayesiano, utilizando sistemas binarios FGK+M como referencia, derivamos valores de [X/H] para múltiples elementos en una muestra de más de 770 enanas M. Nuestras estimaciones de abundancias muestran una buena concordancia con estudios de alta resolución y con las tendencias químicas galácticas, demostrando que la espectroscopía de baja resolución, combinada con calibraciones empíricas robustas, permite una caracterización química fiable de estrellas frías.

Finalmente, presentamos nuevas observaciones espectroscópicas de alta resolución de enanas M secundarias en sistemas binarios, obtenidas con el espectrógrafo CARMENES en el Observatorio de Calar Alto. Utilizando el código StePar Syn, una herramienta de síntesis espectral en un marco Bayesiano, derivamos los parámetros atmosféricos $T_{\rm eff}$, $\log g$ y [Fe/H] para cada estrella. Las metalicidades obtenidas coinciden con las de las estrellas primarias correspondientes, lo que valida el análisis espectroscópico. Sobre la base establecida por estudios previos del consorcio CARMENES, esta muestra contribuirá a profundizar en la caracterización química de las enanas M mediante el uso de espectros de CARMENES.

Conclusiones

Las metodologías desarrolladas en esta tesis representan avances significativos en la caracterización química de las estrellas enanas de tipo M. Las calibraciones fotométricas permiten estimaciones de metalicidad rápidas y escalables a grandes muestras estelares hasta M5 V, con dispersiones por debajo de 0.1 dex. Las redes neuronales introducen una alternativa flexible y basada en datos, capaz de modelar relaciones no lineales complejas, ofreciendo resultados similares a las calibraciones Bayesianas. Los índices espectroscópicos de baja resolución extienden la determinación de abundancias a grandes muestras, especialmente para las enanas M tempranas; y los espectros de alta resolución permiten la determinación de parámetros precisos, sentando las bases de análisis detallados de la composición química.

El uso de sistemas binarios como calibradores empíricos ha demostrado ser una estrategia muy eficaz. Ligando el análisis de las enanas M a las propiedades químicas bien conocidas de sus compañeras de tipo FGK, superamos limitaciones clave en la modelización espectral directa de estrellas frías y mejoramos la precisión y fiabilidad de las mediciones químicas. Las comparaciones con estudios independientes de alta resolución y las tendencias químicas Galácticas también corroboraron la fiabilidad de los resultados.

Estos resultados adquieren especial relevancia en el contexto de futuras misiones espaciales y grandes cartografiados estelares, como Ariel, PLATO o el Habitable Worlds Observatory, que observarán miles de enanas M y requerirán herramientas eficientes y precisas para su caracterización. Los enfoques desarrollados en este trabajo están bien posicionados para contribuir a ese esfuerzo, facilitando estudios de poblaciones estelares, evolución química galáctica y caracterización de sistemas planetarios alrededor de estrellas de baja masa.

Palabras clave: binarias: general — métodos: análisis de datos — técnicas: fotometría — técnicas: espectroscopía — estrellas: abundancias — estrellas: parámetros fundamentales — estrellas: últimos tipos

CHAPTER 1

Introduction

"Non est ad astra mollis e terris via (there is no easy way from the earth to the stars)."
— Seneca

1.1 The chemical composition of the sky above

Humanity has been captivated by the celestial bodies and their nature since the very beginning. In On the Heavens (350 BC), Aristotle introduced the concept of a fifth element, known as aether or quintessence, arguing that while the four elements (fire, earth, air, and water) were corruptible and terrestrial, the stars, showing no signs of change, must be composed of a distinct, eternal, and celestial substance. The astronomers of ancient Mesopotamia were the first to draw a link between astronomy and chemistry, associating the seven classical metals with the brightest celestial bodies, as follows:

- Gold, corresponding with the Sun ☉
- Silver, corresponding with the Moon ☽
- Quicksilver or Mercury, corresponding with Mercury ☿
- Copper, corresponding with Venus ♀
- Iron, corresponding with Mars ♂
- Tin, corresponding with Jupiter ♃
- Lead, corresponding with Saturn ♄

During the 17th century, alchemists would typically refer to metals by their planetary names, using 'Saturn' for lead and 'Mars' for iron, while compounds of tin, iron, and silver were still known as 'jovial', 'martial', and 'lunar', respectively. Although only the element Mercury has retained its ancient designation, the notion of linking chemical elements to the cosmos has persisted throughout history. In 1789, the newly discovered element uranium was named after the planet Uranus; tellurium (discovered in 1782 and named in 1798) was derived from the Latin word for Earth, 'tellus'; while elements such as cerium and palladium (1803) were named after the asteroids Ceres and Pallas, which were discovered just a couple of years before. Later discoveries followed this trend: selenium (1817) and helium (1895) were named after the Greek words for Moon and Sun, respectively. During the last century, a pair of synthetic elements were named neptunium and plutonium (1940) in honor of the outermost planets in the Solar System at that time. Although subsequent discoveries led to the reclassification of Ceres and Pluto as dwarf planets, and Pallas as an asteroid, the legacy of naming elements after celestial bodies endures, reflecting humanity's timeless aspiration to bridge the terrestrial and the celestial.

Today, thanks to many contributions over the years, the realms of astronomy and chemistry are intertwined in a more rigorous and objective manner. Isaac Newton's foundational work on the nature of light, along with the pioneering observations of the solar spectrum by William Herschel and Joseph von Fraunhofer, marked significant early developments. The analysis of stellar spectra

led to the emergence of astrophysics as a scientific discipline during the 19th century. The efforts of women such as Williamina Fleming, Annie Jump Cannon, and Cecilia Payne-Gaposchkin, who worked as calculators at the Harvard Observatory during the late 19th and early 20th centuries, played a crucial role in establishing the contemporary stellar classification system (see Sobel 2016). These and other contributions led to a deeper and more accurate understanding of the cosmos. Yet, it was not until a mere century ago that the actual chemical composition of stars began to be understood. At the beginning of the 20th century, the prevailing scientific consensus was that there were no significant elemental distinctions between the Sun and our planet. In 1914, the astronomer Henry Norris Russell stated that *'If the Earth's crust should be raised to the temperature of the Sun's atmosphere, it would give a very similar absorption spectrum. The spectra of the Sun and other stars were similar, so it appeared that the relative abundance of elements in the universe was like that in Earth's crust.'* (Russell, 1914b). It was Cecilia Payne-Gaposchkin (1900 – 1979) who proposed in her doctoral dissertation that stars are composed primarily of hydrogen and helium (Payne, 1925). Through the application of Saha's ionization theory (Saha, 1920, 1921), Payne accurately correlated the spectral classification of stars to their actual temperatures. She discovered that silicon, carbon, and other common metals present in the solar spectrum were present in roughly the same relative amounts as on Earth, aligned with the prevailing viewpoint of the time. However, Payne found that hydrogen and helium were vastly more abundant than any other element, making them the predominant building blocks of stars. Despite the initial skepticism and rejection of her conclusion, subsequent independent observations eventually confirmed its accuracy, marking a turning point in our understanding of stellar chemistry.

Early studies on the chemical composition of the Sun can be found in the literature during the last century (Russell, 1929; Unsöld, 1948; Goldberg et al., 1960; Anders & Grevesse, 1989; Grevesse & Sauval, 1998; Grevesse et al., 2007; Asplund et al., 2009, among others). According to current data, the mass fractions of H, He and metals in the present-day solar photosphere are $X = 0.7438$, $Y = 0.2423$, and $Z = 0.0139$ (Asplund et al., 2021). The elements heavier than helium are commonly referred to as "metals" and produce the majority of absorption lines in the stellar spectra. The metallicity of a star is defined relative to the Sun as

$$[\mathrm{M/H}] = \log_{10}(N_\mathrm{M}/N_\mathrm{H}) - \log_{10}(N_\mathrm{M}/N_\mathrm{H})_\odot \tag{1.1}$$

where $N_\mathrm{M}/N_\mathrm{H}$ is the relative abundance by number of all metals to hydrogen. Usually the iron abundance, [Fe/H], is used as a proxy of the overall metallicity in stellar astrophysics. The abundance of a given element X is reported with respect to the abundance of either hidrogen,

$$[\mathrm{X/H}] = \log_{10}(N_\mathrm{X}/N_\mathrm{H}) - \log_{10}(N_\mathrm{X}/N_\mathrm{H})_\odot, \tag{1.2}$$

or iron,

$$[\mathrm{X/Fe}] = \log_{10}(N_\mathrm{X}/N_\mathrm{Fe}) - \log_{10}(N_\mathrm{X}/N_\mathrm{Fe})_\odot. \tag{1.3}$$

Sometimes absolute abundances, not relative to the Sun, are given as

$$A_\mathrm{X} = \log_{10}(N_\mathrm{X}/N_\mathrm{H}) + 12, \tag{1.4}$$

hence $A_\mathrm{H} = 12.00$ by definition (Gray, 2022). We show the present-day solar abundances as a function of atomic number in Fig. 1.1. Significant peaks are observed around O, Fe, Ba, and Pb, while Li, F, and Sc exhibit notably low abundances compared to nearby elements, as they are not major products of the nucleosynthesis processes in stars. Additionally, elements with even atomic numbers exhibit higher abundances compared to their odd-numbered neighbours, a phenomenon known as the odd-even effect, which arises due to stellar evolution and nuclear physics principles.

Over the last century, studies have focused on the chemical composition of the Sun and F-, G-, and K-type stars, which present a well-defined spectral continuum along with several absorption lines suitable for analysis (Jofré et al., 2019). Nonetheless, the coolest stars have been generally overlooked until the past two decades.

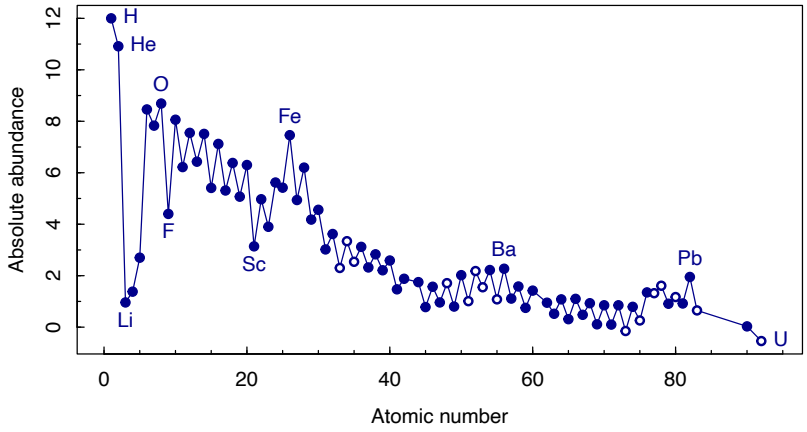

Figure 1.1: Present-day solar photospheric abundances as a function of atomic number. For elements for which no photospheric determination has been possible, CI chondritic abundances are represented as open circles. Data taken from Asplund et al. (2021).

1.2 The cool red dwarf stars

The predominant stellar population in the solar neighbourhood remains imperceptible to the naked eye due to its subtle brightness, less than 10% of the solar luminosity (Croswell, 2002). M-type dwarf stars, also known as red dwarfs, are the coolest, smallest, and most abundant main-sequence stars in the Galaxy (Henry & Jao, 2024). The peak of emission of these stars is shifted to longer, redder wavelengths in comparison to solar-type stars due to their lower effective temperatures. These stars, which become fully convective below $0.35\,\mathcal{M}_{\odot}$, are also characterised by very active chromospheres and coronae, particularly in the case of younger, lower-mass objects (West et al., 2008; Jeffers et al., 2018; Kiman et al., 2021). Table 1.1 lists representative average astrophysical parameters of M dwarfs, based on the sample by Cifuentes et al. (2020), and the different spectral type dwarf stars are represented in Fig. 1.2.

These stars hold a distinctive position of interest across multiple branches of astrophysics. They have main-sequence lifetimes that exceed the current age of the universe, result from slow fusion processes within predominantly convective interiors (Adams & Laughlin, 1997). Moreover, they constitute the most prevalent main-sequence stars in the Milky Way, accounting for more than 75% of them (Henry et al., 2006; Winters et al., 2015; Reylé et al., 2021; Kirkpatrick et al., 2024). Consequently, M dwarfs stand as excellent probes for exploring the chemical and dynamical evolution of our Galaxy (Bahcall & Soneira, 1980; Reid et al., 1997; Chabrier, 2003; Ferguson et al., 2017).

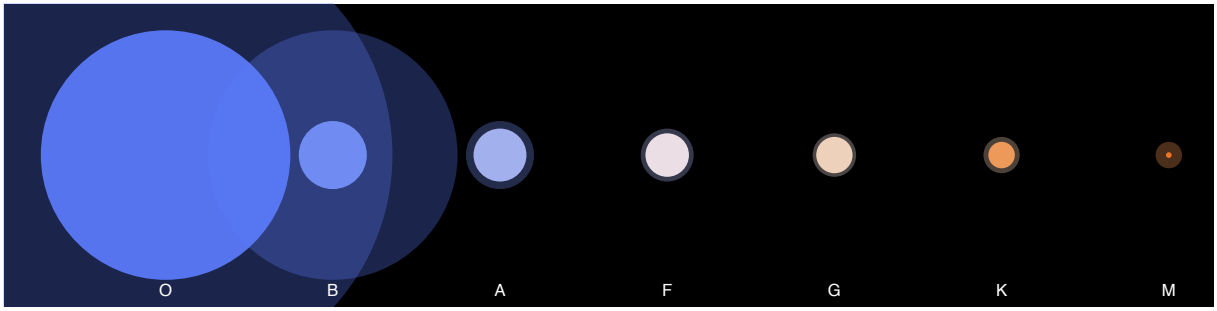

Figure 1.2: Representation of dwarf stars from each spectral type to scale, showing their true colours given by Harre & Heller (2021).

Table 1.1: Average astrophysical parameters for M-type dwarf stars divided by spectral subtype, taken from Cifuentes et al. (2020).

Spectral type	$T_{\rm eff}$ (K)	L ($10^{-4}\,L_\odot$)	$\mathcal{R}$ ($\mathcal{R}_\odot$)	$\mathcal{M}$ ($\mathcal{M}_\odot$)
M0.0 V	3900 ± 140	757 ± 230	0.613 ± 0.060	0.622 ± 0.063
M0.5 V	3800 ± 110	585 ± 210	0.571 ± 0.076	0.578 ± 0.080
M1.0 V	3700 ± 85	496 ± 150	0.550 ± 0.075	0.556 ± 0.079
M1.5 V	3600 ± 90	409 ± 160	0.519 ± 0.082	0.524 ± 0.086
M2.0 V	3500 ± 105	306 ± 130	0.473 ± 0.088	0.475 ± 0.093
M2.5 V	3400 ± 97	228 ± 96	0.433 ± 0.086	0.432 ± 0.090
M3.0 V	3300 ± 87	161 ± 74	0.389 ± 0.085	0.386 ± 0.090
M3.5 V	3300 ± 92	111 ± 57	0.343 ± 0.082	0.338 ± 0.087
M4.0 V	3200 ± 88	87 ± 47	0.309 ± 0.079	0.302 ± 0.083
M4.5 V	3100 ± 88	50 ± 27	0.263 ± 0.069	0.253 ± 0.073
M5.0 V	3100 ± 58	28 ± 13	0.207 ± 0.041	0.195 ± 0.043
M5.5 V	3000 ± 85	20.1 ± 8.3	0.173 ± 0.032	0.159 ± 0.034
M6.0 V	2900 ± 108	11.1 ± 3.9	0.138 ± 0.020	0.121 ± 0.021
M6.5 V	2750 ± 124	7.2 ± 1.7	0.123 ± 0.011	0.106 ± 0.011
M7.0 V	2700 ± 94	6.3 ± 1.1	0.119 ± 0.009	0.101 ± 0.010
M7.5 V	2500 ± 82	5.8 ± 1.2	0.121 ± 0.008	0.104 ± 0.009
M8.0 V	2500 ± 91	5.1 ± 1.6	0.121 ± 0.014	0.104 ± 0.014
M8.5 V	2400 ± 88	3.4 ± 1.5	0.107 ± 0.015	0.088 ± 0.016
M9.0 V	2350 ± 86	2.69 ± 0.35	0.096 ± 0.013	0.077 ± 0.014
M9.5 V	2300 ± 45	2.35 ± 0.43	0.096 ± 0.007	0.077 ± 0.008

Despite significant advancements in modelling stellar spectra over the last decades, discrepancies persist between the observational characteristics of M dwarfs and the values predicted by synthetic spectra. For instance, effective temperatures can deviate by as much as 200–300 K, while radii predictions can differ from interferometric measurements by up to 25% (Jones et al., 2005; Boyajian et al., 2012; Sarmento et al., 2020). These variations may stem from factors such as the level of activity and the presence of starspots (López-Morales & Ribas, 2005; Silverstein, 2019; Somers et al., 2020; Wanderley et al., 2023), distinctions in metallicity (Berger et al., 2006; López-Morales, 2007), or the synthetic gap, i.e. the differences in feature distributions between synthetic and observed data (Fabbro et al., 2018; Passegger et al., 2020, 2022; Bello-García et al., 2023). Furthermore, the modelling of atmospheres in late-type stars presents several intricate challenges. The presence of stellar convection in M dwarfs can challenge certain underlying physical assumptions related to radiative transfer (Bergemann et al., 2017; Olander et al., 2021). Additionally, the incompleteness of line lists and atomic parameters employed in these models further complicates the situation (Shetrone et al., 2015).

Over the past decades, M dwarfs have gained increasing importance, largely due to their role in exoplanet research. An exoplanet, also referred to as an extrasolar planet, is a planetary body that orbits a star beyond the boundaries of our Solar System. When it comes to detecting exoplanets, the two most effective techniques, namely the radial velocity and transit methods, are favoured in the case of M dwarfs (Nutzman & Charbonneau, 2008; Engle & Guinan, 2011; Shields et al., 2016; Reiners et al., 2018). The lower masses of these stars facilitate the detection of exoplanets by analyzing their radial velocity curves. On top of that, due to the faintness of M dwarfs, their habitable zone, the distance interval from a star where conditions are suitable for the presence of liquid water (Kasting et al., 1993), is located much closer to the star compared to solar-type stars (Tarter et al., 2007; Kopparapu et al., 2014; Martínez-Rodríguez et al., 2019). This closeness translates into shorter orbital periods for exoplanets within the habitable zone,

which makes their detection by the transit method much easier. Moreover, the likelihood of detecting small planets around M dwarfs is high, with an occurrence rate of $0.90^{+0.04}_{-0.03}$ per star for planets between 0.5 and 4 $R_\oplus$, and an occurrence of $0.51^{+0.06}_{-0.05}$ per star for Earth-sized planets, up to 1.4 $R_\oplus$ (Dressing & Charbonneau, 2013; Sabotta et al., 2021; Ribas et al., 2023; Kaminski et al., 2025). Furthermore, the exoplanets orbiting M dwarfs span a large range of masses, from 0.066 $M_\oplus$ (Kepler-138 b; Jontof-Hutter et al. 2015) to 1841 $M_\oplus$ ($\sim$ 5.79 $M_{\rm Jup}$; GJ 676 A b; Feng et al. 2022), and some potentially habitable planets have been discovered around M dwarfs, including Proxima Centauri (Ribas et al., 2016; Faria et al., 2022) and TRAPPIST-1 (Gillon et al., 2017; Grimm et al., 2018). However, to accurately determine the planetary parameters, it is essential first to obtain precise measurements of the host star's parameters. On top of that, M dwarfs are the bridge between the hydrogen burning stars and the domain of substellar objects (Kirkpatrick et al., 1999; Burgasser et al., 2006; Cushing et al., 2011).

There are several programs focused on finding exoplanets around M dwarfs using ground-based radial velocity instruments such as ESPRESSO (Pepe et al., 2010, 2021), HARPS (Mayor et al., 2003), HARPS-N (Cosentino et al., 2012), or MAROON-X (Seifahrt et al., 2020) in the optical range, HPF (Mahadevan et al., 2012), GIANO-B (Origlia et al., 2014), IRD (Kotani et al., 2018), NIRPS (Wildi et al., 2017) or SPIRou (Donati et al., 2020; Moutou et al., 2023) in the near-infrared, and CARMENES (Quirrenbach et al., 2020; Ribas et al., 2023; Caballero et al., 2025), GIARPS (Claudi et al., 2018), NIRPS+HARPS (Bouchy et al., 2017), or the future HIRES@ELT (Marconi et al., 2020) covering both wavelenth regimes.

All in all, M-type dwarf stars stand as pivotal objects in astrophysics, from the Galactic to the exoplanetary level. This has led the astrophysical community to direct its attention toward characterizing these cool stars, with a primary challenge being the determination of their chemical composition, or metallicity. Stars are formed through the gravitational collapse of molecular clouds comprised of gas and dust. During their lifetimes, stars synthesize many elements heavier than helium and eventually release some of them back into the interstellar medium, from which new stars are born. Consequently, the chemical makeup of stars evolves from one stellar generation to the next, providing a record of the prevailing gas conditions at the time and location of the formation of a star. The origin of the chemical elements is shown in Fig. 1.3.

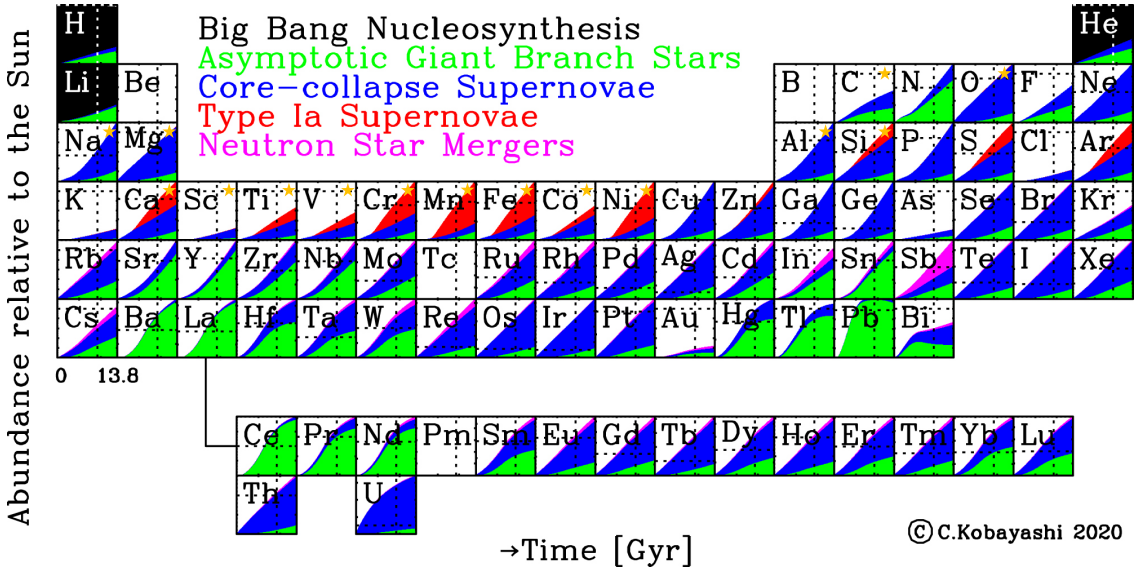

Figure 1.3: Time evolution of the origin of elements in the periodic table, taken from Kobayashi et al. (2020). The elements analysed in this thesis are marked with an orange star.

Stellar metallicity is defined as the relative abundance of elements heavier than helium, and the iron abundance ratio [Fe/H] usually serves as a proxy for the overall metallicity. In cool stars, metals play a crucial role in shaping both spectral line strengths and continuum opacity by regulating the abundance of H^- ions, which depend on electron donation from metallic elements. Determining the metallicity of M dwarfs presents a formidable challenge. The measurement of abundances in these cool stars has been constrained by the intricacies involved in the analysis of their spectra, which are notably more complex than those of solar-type stars. This difficulty arises from the lower atmospheric temperatures of M dwarfs, resulting in a profusion of lines caused by numerous molecular species, including TiO, VO, ZrO, FeH, and CaH in the optical range, as well as H_2O and CO in the near-infrared regime (e.g. Kirkpatrick et al., 1991; Allard et al., 1997; de Laverny et al., 2012; Van Eck et al., 2017; Passegger et al., 2018; Marfil et al., 2021; Heiter et al., 2021). This forest of lines and molecular features dominate the spectrum, making it difficult to accurately determine their atmospheric parameters.

For the case of FGK-type stars, it has been observed that the frequency of gas giant planets increases with stellar metallicity, which is known as the planet-metallicity correlation (Gonzalez, 1997; Fischer & Valenti, 2005; Brewer et al., 2016). However, this correlation remains unclear for lower-mass planets, with clues that terrestrial planet can be formed without any preferance on the metal content of the star (Sousa et al., 2008, 2011; Buchhave et al., 2012). It has been proposed that M dwarfs follow the same tendency: the higher the metallicity, the higher the probability of having icy and gaseous giant planets orbiting around them (Johnson & Apps, 2009; Rojas-Ayala et al., 2010; Terrien et al., 2012; Hobson et al., 2018). However, M dwarfs are less likely to harbour giant planets (Endl et al., 2006; Johnson et al., 2007). In addition, understanding a star's chemical composition helps us infer the attributes of its respective exoplanets. For instance, the carbon-to-oxygen and magnesium-to-silicon ratios (C/O and Mg/Si) provide information about the structure and composition of exoplanets; the C/O ratio controls the distribution of carbonaceous compounds, while Mg/Si determines the composition of an exoplanet's core and mantle (Larimer, 1975; Bond et al., 2010; Santos et al., 2015, 2017; Brewer et al., 2016; Suárez-Andrés et al., 2018; Maldonado et al., 2020; Tabernero et al., 2024). How these elements are distributed within an exoplanet impacts not only its internal structure and density, but also its potential to sustain life as we know it on Earth. Therefore, studying the correlations between stellar properties, and in particular the chemical composition, and the presence of exoplanets can be useful in selecting targets for future exoplanet surveys and in understanding planetary formation mechanisms (Santos et al., 2017; Adibekyan et al., 2021, 2024; Behmard et al., 2025a).

For optimal reliability, the spectroscopic parameters should be cross-validated against values derived from independent techniques. For example, effective temperatures can be obtained from photometry or interferometric angular diameter measurements, while surface gravity is often constrained through asteroseismology. However, interferometry presents some challenges for the faintest M dwarfs (López-Morales & Ribas, 2005; Irwin et al., 2011; Boyajian et al., 2012), and asteroseismology is currently not applicable to M dwarfs due to limitations in detecting their oscillations (see Rodríguez-López, 2019, and references therein). Regarding the main focus of this thesis, binary systems serve as excellent benchmarks for verifying metallicities and chemical abundances.

1.3 Not all the stars are single

Located 4.25 light-years (or 1.30 pc) away from our Sun lies our closest neighbour, the red dwarf Proxima Centaury. However, this star is not alone in the sky, but it revolves around a pair of solar-type stars, forming a triple system known as α Centauri (Richaud, 1689; Innes, 1915;

Beech 2015). A binary or multiple stellar system is defined as one comprising two or more stars that follow closed orbits around their common center of mass, that is, the stars are gravitationally bound. In a binary system, the brighter star is referred to as the primary, while the dimmer companion is designated as the secondary. Reylé et al. (2021) compiled a volume-complete sample of stars, brown dwarfs and exoplanets within 10 pc from the Sun. Their findings revealed the presence of 246 single, 69 double, 19 triple, three quadruple, and two quintuple systems, resulting in a multiplicity frequency of 27.4% (see Fig. 1.4). The likelihood of encountering multiple stellar systems rises with the mass of the primary star (Lada, 2006; Parker & Meyer, 2014), spanning from 10–30% for very low-mass stars and brown dwarfs (Burgasser et al., 2003, 2007; Fontanive et al., 2018) to surpassing 70–80% for OBA stars (Shatsky & Tokovinin, 2002; Mason et al., 2009; Sana et al., 2012). Several recent studies indicated a multiplicity fraction of $\sim 27\%$ for the case of M dwarfs (Cortés-Contreras et al., 2017; Winters et al., 2019; Clark et al., 2024; Cifuentes et al., 2025), while the later work suggested that this value could reach 40% if new unresolved binary candidates are taken into account. M dwarfs predominantly form binary systems with low-mass stars. In contrast, systems containing both an O-, B-, or A-type star and an M dwarf are extremely rare. This absence arises from the initial mass function and the brief main-sequence lifetimes of massive stars, which evolve too quickly for such pairings to be commonly observed. The largest database of double and multiple systems used in contemporary astronomical research is the Washington Double Star catalogue[1] (WDS; Mason et al., 2001), collecting more than 157 000 systems to date.

Binary stars serve as invaluable resources for numerous scientific endeavors. They provide a unique opportunity to acquire the most precise measurements of stellar masses and radii, crucial for calibrating stellar evolutionary models and establishing fundamental relationships such as mass-luminosity or mass-radius for main-sequence stars (Popper, 1980; Torres et al., 2010; Boyajian et al., 2012; Eker et al., 2018; Schweitzer et al., 2019). Additionally, the study of multiple

[1] http://www.astro.gsu.edu/wds/

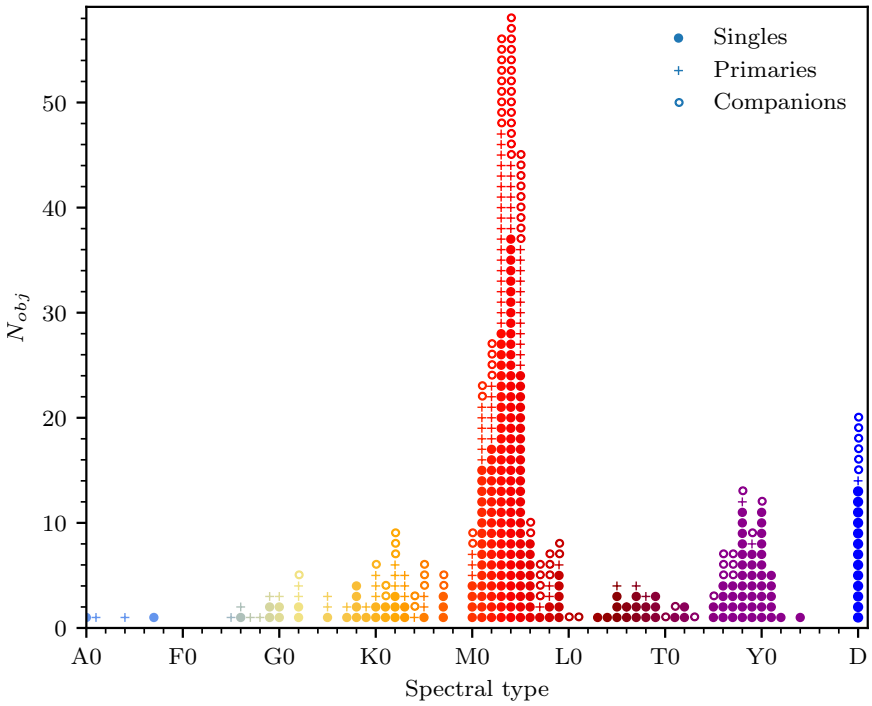

Figure 1.4: Spectral type distribution of the 10 pc sample indicating multiplicity, taken from Reylé et al. (2021).

systems allow us to understand and constrain the models of stellar formation and evolution. Particularly pertinent to the focus of this thesis is the assumption that binary systems, originating from the same molecular cloud and at the same time, should exhibit shared chemical compositions. Nevertheless, in certain scenarios, minor disparities in composition between components may emerge from factors such as non-simultaneous formation despite being in close proximity, initial chemical heterogeneity within the molecular cloud, the accretion of planetary material by some components post-formation, or the process of atomic diffusion, i.e. gravitational settling and radiative levitation (Desidera et al., 2004, 2006; Michaud et al., 2015; Brewer et al., 2016; Dotter et al., 2017; Andrews et al., 2018; Moedas et al., 2022).

Since M-dwarf spectra are complex and notoriously difficult to model due to the presence of prominent molecular features, in comparison to those of solar-type stars (e.g. Allard et al., 2000; Passegger et al., 2018; Marfil et al., 2021), several studies have investigated M-dwarf metallicities using wide physical binary systems formed by a F-, G-, or K-primary star and a M-dwarf companion (e.g. Woolf & Wallerstein, 2006; Bean et al., 2006; Rojas-Ayala et al., 2010; Terrien et al., 2012; Mann et al., 2013, 2014; Newton et al., 2014; Montes et al., 2018; Ishikawa et al., 2020; Souto et al., 2020, 2022; Qiu et al., 2024; Duque-Arribas et al., 2024; Behmard et al., 2025b). These binary systems provide an excellent opportunity to test not only the metallicities of the M dwarfs with those for their warmer primaries, but also the chemical abundances for individual atomic species. Consequently, we will utilise these binary systems throughout the thesis to conduct our analyses.

1.4 How we study the stellar light

The stellar atmosphere is the outer layer of a star from which the energy generated within the star is emitted. However, this region is not completely transparent to all wavelengths of light, and part of it is absorbed or scattered, depending on the stellar parameters (such as the effective temperature, the surface gravity, or the chemical composition). Hence starlight reveals the intrinsic characteristics of stars, and we have some essential keys to decode it (see Gray, 2022, and references therein).

1.4.1 Photometry and the Hertzsprung–Russell diagram

Multi-colour photometry measures the energy output of a star across several wavebands. This energy distribution provides critical insights into the star's physical parameters including the effective temperature, spectral type, luminosity class, photospheric chemical abundances, surface gravity, and the effects of interstellar reddening. In Fig. 1.5 we show several photometric filters, retrieved from the SVO Filter Profile Service[2] (Rodrigo et al., 2012), compared to some typical synthetic stellar spectra from the BT-Settl models (Allard, 2014).

In the visible part of the spectrum, the third Gaia data release (Gaia DR3; Gaia Collaboration et al., 2023) provides the position and apparent magnitude in the G band (330–1050 nm) for 1.8 billion sources. For 1.5 billion of them, parallax and proper motion data are also available. In addition, photometry in the $G_{\rm BP}$ (330–680 nm) and $G_{\rm RP}$ (630–1050 nm) bands is offered for another 1.5 billion sources (Gaia Collaboration et al., 2016, 2021a; Riello et al., 2021). Since the M-dwarf spectral emission peak is between 900 and 1500 nm (Cifuentes et al., 2020), we will need photometric measurements not only in the visible, but also in the infrared wavelength

[2] https://svo2.cab.inta-csic.es/theory/fps/

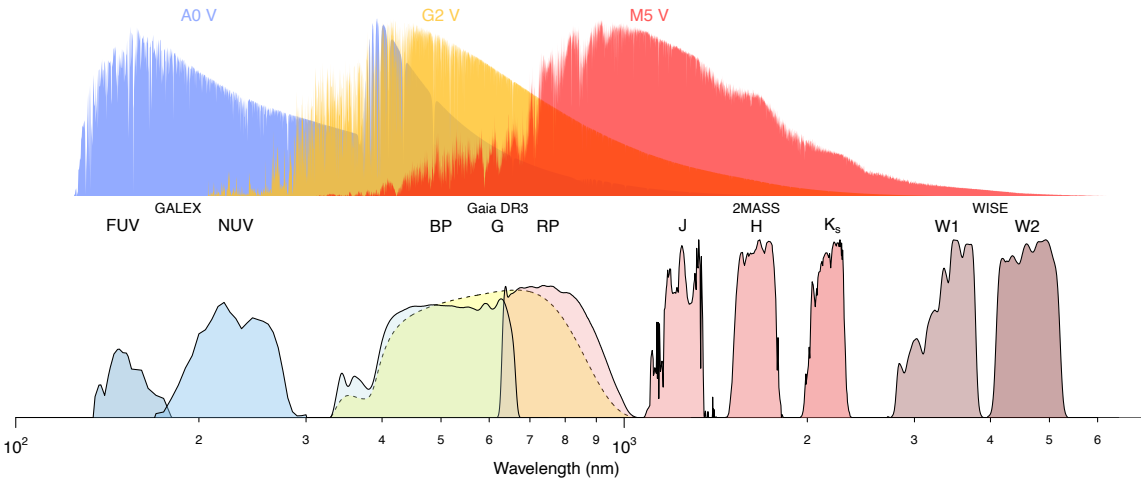

Figure 1.5: Several photometric filters covering from the UV to the mid-IR regimen compared with synthetic spectra of an A0 V, a G2 V, and a M5 V star.

range. Of particular utility is the Two Micron All Sky Survey (2MASS; Skrutskie et al. 2006), a ground-based photometric survey that provided magnitudes in the near-IR J (1229 nm), H (1639 nm) and K_s (2152 nm) bands for over 500 million point sources. For larger wavelengths, space-based telescopes are crucial since mid- and far-IR observations are strongly affected by thermal emission and telluric absorption bands. The Wide-field Infrared Survey Explorer (WISE; Wright et al. 2010) offers data in the mid-IR bands $W1$, $W2$, $W3$, and $W4$, centred at 3316 nm, 4564 nm, 10 787 nm, and 21 915 nm, respectively.

Rosenberg (1910), Hertzsprung (1911) and Russell (1914a) independently discovered that, when plotting the absolute magnitude of the stars as a function of their spectral type (or colour index), the majority of stars align along a well-defined, nearly continuous branch, now known as the main sequence. This finding reveals that stellar luminosity is intrinsically linked to temperature. Given that the Stefan–Boltzmann law,

$$L = 4\pi R^2 \sigma_B T_{\rm eff}^4 \,, \tag{1.5}$$

where $\sigma_B \approx 5.670 \cdot 10^{-8}\,\mathrm{W\,m^{-2}\,K^{-4}}$, also depends on the stellar radius, it follows that main-sequence stars must exhibit a constrained range of radii. The few stars positioned above the main sequence, being significantly more luminous than their main-sequence counterparts at similar temperatures, must therefore have larger radii. This plot, which represents the luminosity or absolute magnitude of stars versus their spectral type, effective temperature or colour index is known as colour–magnitude diagram, Hertzsprung–Russel diagram, or simply HR diagram. This discovery represented a significant milestone in our understanding of stellar evolution. Today, we know that the main sequence is fundamentally a mass sequence, with the lower-mass stars lying at the cooler end. The prevalence of stars along the main sequence is because this hydrogen-burning phase represents the longest and most stable stage of their lifetimes. In contrast, stars above the main sequence are either in their early formation phases or late evolutionary stages, both of which are relatively brief compared to their main-sequence lifespan. We show in Fig. 1.6 the first 'colour–magnitude' diagram[3], published by Rosenberg (1910), and a modern version based on *Gaia* data published by Reylé et al. (2021).

[3]Rosenberg actually represented the apparent magnitude of stars in the Pleiades cluster against the strengths of the calcium K line and two hydrogen Balmer lines, which serve as a proxy for the temperature of the star. Since the stars in the same cluster are located at the same distance, their apparent magnitudes directly correlate with their absolute magnitudes, so this early diagram was effectively a plot of luminosity against temperature.

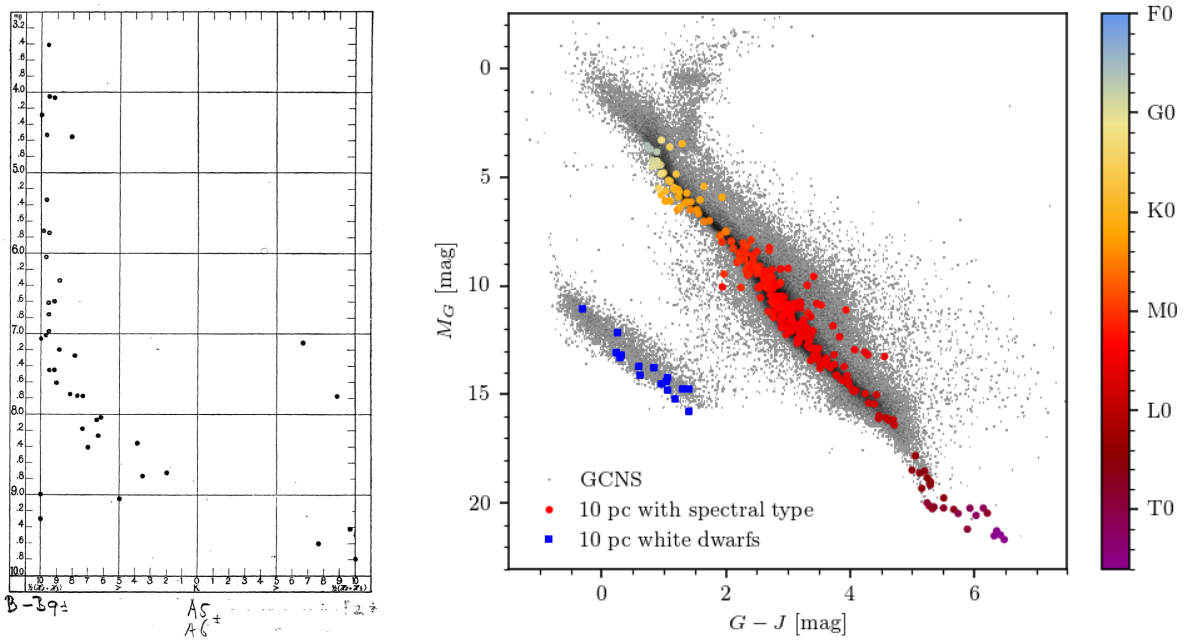

Figure 1.6: Left panel: First 'colour–magnitude'' diagram of the history, published by Rosenberg (1910). Right panel: Colour–magnitude diagram of the 10 pc sample, published by Reylé et al. (2021), overimposed on the Gaia Catalogue of Nearby Stars (grey dots; Gaia Collaboration et al. 2021b). The colour bar indicates the spectral type, and white dwarfs are in dark blue.

Stellar metallicity influences the position of stars in both colour–colour and colour–magnitude diagrams. In cool stars such as M dwarfs, continuum opacity is dominated by molecular sources and the H^- ion, whose formation is highly sensitive to the abundance of free electrons, largely supplied by metals. Therefore, higher metallicities increase the opacity, altering the radiative transfer in the stellar atmosphere and affecting the stellar structure, making metal-rich dwarfs slightly cooler and less luminous at a given mass. These effects are especially pronounced in M dwarfs, where molecular absorption bands further amplify the metallicity dependence of broadband colours (John, 1988; Ferguson et al., 2005; Casagrande & VandenBerg, 2014; Gray, 2022). Consequently, metallicity variations introduce a measurable spread in the lower main sequence. Since the effective temperature and stellar luminosity are directly correlated with the colour indices and absolute magnitudes (Cifuentes et al., 2020), colour–colour and colour–magnitude diagrams constitute useful tools for indirect metallicity estimation.

Although the photometric data can be used to derive some parameters of a vast number of stars, we should keep in mind that their accuracy is limited compared to spectroscopic methods.

1.4.2 Spectroscopy: the equivalent width and the spectral synthesis methods

The spectral analysis of a star yields all the essential information necessary for its characterisation. In particular, we can derive its chemical composition by analysing the spectral lines produced by the atoms and molecules in its outer layers. Each element or molecule produces a unique set of spectral lines that serve to quantify its abundance. Nonetheless, the significant observational time required and the complexity of their spectra have impeded extensive radial-velocity surveys using high-resolution spectroscopy, particularly for the latest spectral types, until the last decades. The spectral classification of M-type stars has relied over the years on low-resolution spectroscopy using their molecular bands such as TiO, VO and CaOH (Morgan, 1938; Boeshaar, 1976; Boeshaar

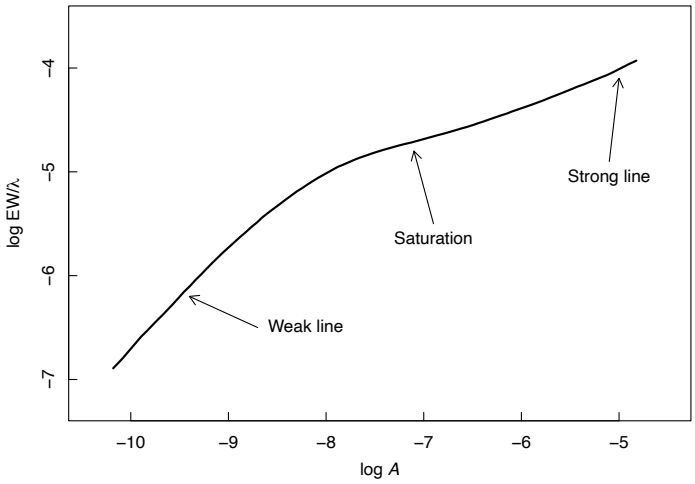

Figure 1.7: Curve of growth of the Fe I λ6065 line from a stellar model. Data taken from Gray (2022).

& Tyson, 1985; Kirkpatrick et al., 1991). Additionally, low-resolution spectra of M dwarfs enable the study of stellar activity by examining certain chromospheric activity indicators, such as the well-studied pseudo-equivalent width of Hα along with the Balmer lines in the visible regime, and the He I D_3, Na I D doublet, Ca II H&K, Ca II IRT lines and Paschen series in the near infrared (Montes et al., 2000; Schöfer et al., 2019).

One of the most commonly employed techniques in the spectral analysis of stars is the equivalent width (EW) method. The EW provides a measure of the strength of an absorption line and is influenced by the star's atmospheric parameters. Mathematically, the EW is defined as the integral of the absorption line profile, representing the area of the line as a rectangle whose height corresponds to the normalized continuum flux and whose width equals the EW value:

$$EW = \int \frac{F_c - F(\lambda)}{F_c} \mathrm{d}\lambda \tag{1.6}$$

The integration is performed over a narrow window surrounding the spectral line. In practice, absorption lines are fitted using Gaussian curves to estimate their areas. These EW values can then be employed to estimate the abundance of a specific element relying on the ionisation and excitation balance, if the stellar parameters are known. All stellar atmospheric parameters influence the EW to varying degrees. In particular, an increase in the abundance of an element results in more photons being absorbed, thereby enhancing the line strength. However, the relationship between EW and abundance is generally not linear; instead, it follows a pattern known as the curve of growth. In Fig. 1.7 we represent the curve of growth of the Fe I λ6065 line derived from a model photosphere, where the reduced EW is used to normalise Doppler-dependent effects such as microturbulence or thermal broadening.

The determination of the stellar atmospheric parameters using the EW method follows the next steps:

1. The EW measurements of the Fe I and Fe II lines can be executed manually, for example using the `splot` task of the Image Reduction and Analysis Facility[4] (`IRAF`, Tody 1986), or automatically with tools designed for this task, such as ARES[5] (Sousa et al., 2007, 2015), TAME[6] (Kang & Lee, 2012), or the `EWComputation`[7] python module (Souto et al., 2020).

[4] https://iraf-community.github.io
[5] https://github.com/sousasag/ARES
[6] http://astro.snu.ac.kr/~wskang/tame/
[7] https://github.com/msotov/EWComputation

2. Using some initial input values, generally the solar parameters, a stellar atmosphere model is computed. The leading atmospheric models for cool stars are PHOENIX (Hauschildt et al., 1997; Husser et al., 2013), ATLAS9 (Castelli & Kurucz, 2003), MARCS (Gustafsson et al., 2008), BT-Settl (Allard, 2014), and the NewEra model grid (Hauschildt et al., 2025).
3. Then, the *EWs* and the stellar model are employed, along with a radiative transfer code, for example MOOG[8] (Sneden, 1973) or *turbospectrum* (Alvarez & Plez, 1998), to determine the iron abundance for each individual spectral line. For the $T_{\rm eff}$, the excitation equilibrium imposes no correlation between the abundance and the excitation potential χ_l of the lines. Simultaneously, to determine the $\log g$, ionisation equilibrium requires the same abundance to be retrieved from the neutral and ionised lines. Therefore, if the slope of the abundances versus χ_l is not zero, or the abundances from lines of different ionisation stages are not the same, the process starts iterating again from step 2 adjusting the model parameters to achieve equilibrium. Once both excitation and ionisation equilibria conditions are met, the iron abundance has already converged too.

The *EW* method is implemented in various publicly available codes, such as FAMA[9] (Magrini et al., 2013), GALA[10] (Mucciarelli et al., 2013), SPECIES[11] (Soto & Jenkins, 2018), and StePar[12] (Tabernero et al., 2019). This strategy can achieve high precision when applied to high-resolution spectra with well-defined continua, as is often the case for FGK stars. Nevertheless, these conditions are not met for the M dwarfs, whose spectra exhibit blended lines and prominent molecular features.

An alternative approach for determining spectroscopic stellar parameters, more suitable for M dwarfs, is the spectral synthesis method. This technique involves comparing the observed spectrum against theoretical spectra, which are synthesised on-the-fly or interpolated from pre-computed grids, to find the best match. A subset of spectral features is often chosen over the entire spectrum to minimise computational time and focus on the most informative regions. The outcomes of spectral synthesis are influenced by various factors, including the specific approaches employed, the choice of atmospheric models, the radiative transfer code used to calculate the synthetic spectra, the atomic data, and the methods applied during the minimisation process. Consequently, and given the complexity of M-dwarf spectra, the results reported in the literature are less consistent for M dwarfs compared to those for FGK stars (see Passegger et al. 2022). As an example, Fig. 1.8 shows the sensitivity to variations in stellar atmospheric parameters in the synthetic spectra when fitting an observed spectrum.

Since this thesis focuses on M dwarfs on the main sequence, their surface gravities are confined to a relatively narrow range, between approximately 4.5 and 5.0 dex. Consequently, the effects of gravity on their spectral lines are far less pronounced than in giant stars. As noted by Gray (2022), pressure effects in stellar spectra, controlled by surface gravity, are much weaker than temperature effects: comparable changes in the line profile can result from variations of several hundred per cent in $\log g$, or from temperature changes of only a few tens of per cent.

Several implementations of the spectral synthesis method have been published and are freely accessible, including the APOGEE Stellar Parameter and Chemical Abundance Pipeline[13] (ASPCAP, García Pérez et al. 2016), Spectroscopy Made Easy[14] (SME, Valenti & Piskunov 1996; Piskunov & Valenti 2017), iSpec[15] (Blanco-Cuaresma et al., 2014; Blanco-Cuaresma, 2019), Fast

[8] http://www.as.utexas.edu/~chris/moog.html
[9] http://cdsarc.u-strasbg.fr/viz-bin/qcat?J/A+A/558/A38
[10] http://www.cosmic-lab.eu/gala/gala.php
[11] https://github.com/msotov/SPECIES
[12] https://github.com/hmtabernero/StePar
[13] https://www.sdss4.org/dr17/irspec/aspcap/
[14] https://www.stsci.edu/~valenti/sme.html
[15] https://www.blancocuaresma.com/s/iSpec

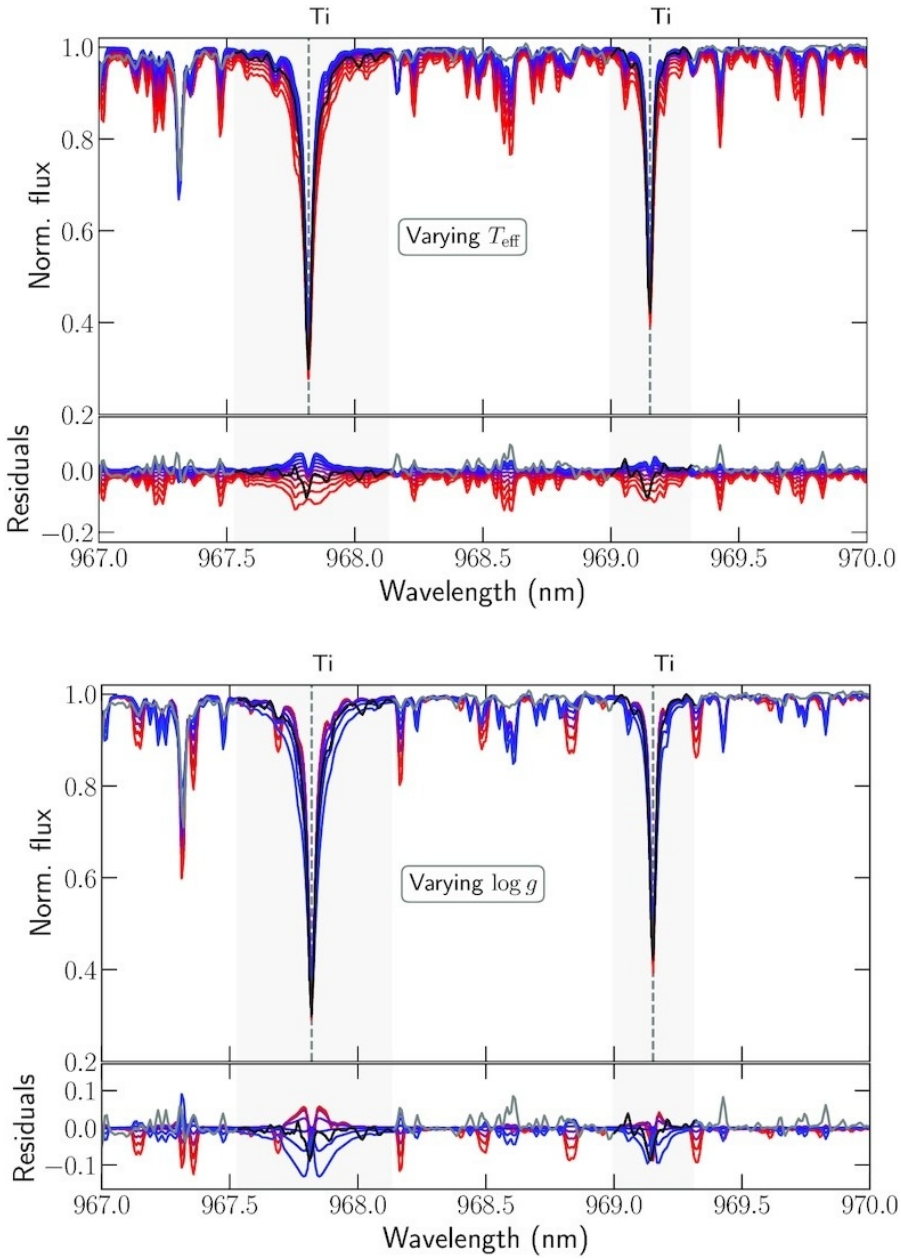

Figure 1.8: Example of the spectral synthesis method, comparing the spectrum of Gl 15A (in grey and black) and PHOENIX synthetic spectra, coloured for different values of the parameters, with red being the lowest and blue the highest. The associated parameters vary from 3000 K to 4000 K in steps of 100 K in $T_{\rm eff}$ (top panel), and from 3.0 to 6.0 dex in steps of 0.5 dex in $\log g$ (bottom panel). The bottom plots show the residuals. Image taken from Cristofari et al. (2022).

Analysis of Spectra Made Automatically[16] (FASMA, Andreasen et al. 2017; Tsantaki et al. 2020), or StePar Syn[17] (Tabernero et al., 2022), among others.

In the literature, several studies have applied the spectral synthesis method not only to determine stellar atmospheric parameters but also to derive chemical abundances in M dwarfs. Souto et al. (2017, 2018) used APOGEE spectra to derive the abundances of several elements of

[16] https://github.com/MariaTsantaki/FASMA-synthesis
[17] https://github.com/hmtabernero/SteParSyn

three exoplanet-hosting M dwarfs. For the GTO sample of the CARMENES consortium, Abia et al. (2020) derived the Rb, Sr, and Zr abundances, while Shan et al. (2021) and Tabernero et al. (2024) focused on the V abundances, affected by HFS effects, and on Mg and Si abundances, respectively. Furthermore, Souto et al. (2022) derived abundances for 14 elements from APOGEE spectra for a sample of 11 M dwarfs in binary systems with FGK stars, and Hejazi et al. (2024) determined the abundances of 10 elements for a M2.5 V star hosting a sub-Neptune exoplanet in its habitable zone, targeted by several JWST programs.

The equivalent width and the spectral synthesis methods continue to be the prevailing approaches for stellar characterisation and abundance analysis. However, machine-learning approaches have been recently introduced and increasingly applied to large stellar surveys, offering the capability of processing large, multidimensional data efficiently. These data-driven methods rely on training sets of stars with well-known parameters, which are typically derived using traditional *EW* or spectral synthesis techniques. During recent years, several authors have applied machine-learning algorithms to characterise M dwarfs (e.g. Sarro et al., 2018; Antoniadis-Karnavas et al., 2020; Birky et al., 2020; Passegger et al., 2020; Bello-García et al., 2023; Mas-Buitrago et al., 2024, and references therein).

1.5 Aims and scope of the PhD thesis

The core focus of this PhD thesis is to investigate and improve the determination of the chemical composition of M-type dwarf stars. These cool, low-mass stars, though the most numerous in the Galaxy, present notable observational and analytical challenges due to the complexity of their spectra, which are dominated by molecular bands and require specialised techniques for robust chemical analysis.

To address these challenges, the thesis explores a multi-faceted strategy combining photometric, low-resolution, and high-resolution spectroscopic methods. The thesis is organised into a series of investigations, each corresponding to one of the following chapters:

- **Chapter 2** explores large-scale photometric surveys, such as Gaia, 2MASS, and CatWISE, as a means to estimate the metallicity of M dwarfs based solely on broad-band photometry. Using a carefully curated calibration sample of M dwarfs with known spectroscopic metallicities, Bayesian regression models are constructed to map metallicity as a function of optical–infrared colour and absolute magnitude combinations. The derived calibrations outperform previous empirical relations in precision and are validated against independent samples of M dwarfs in wide binaries with FGK-type primaries. This methodology provides an efficient and easy way to infer M-dwarf metallicities for a vast number of stars while circumventing the challenges associated with their complex spectra. The results of this chapter are published by Duque-Arribas et al. (2023).
- Extending the work of Chapter 2, **Chapter 3** develops and applies a machine-learning approach to infer metallicity from broad-band photometry using artificial neural networks (ANNs). The model architecture is optimised via hyperparameter tuning, and Monte Carlo dropout is employed to estimate predictive uncertainties. The trained ANN reaches comparable/improved accuracy relative to Bayesian regression. The results are validated on the sample of M dwarfs in wide binaries, confirming generalisability. This chapter highlights the increasing role of data-driven models in stellar parameter inference and demonstrates the potential of ANNs for efficient, non-spectroscopic metallicity estimation. The results of this chapter are published by Duque-Arribas et al. (2025).

- Recognising that M-dwarf spectra are often too complex for detailed abundance analysis, **Chapter 4** focusses on the hotter F-, G-, and K-type primary stars with M-dwarf companions introduced by Montes et al. (2018), who derived precise stellar atmospheric parameters of the primary stars, including the chemical abundances for 13 atomic species (Na, Mg, Al, Si, Ca, Sc, Ti, V, Cr, Mn, Fe, Co, Ni), using high-resolution spectra and the StePar implementation of the *EW* method (Tabernero et al., 2019). Relying on the same data and methodology, we compute precise abundances of carbon and oxygen, and refine previous determinations of the odd-Z iron-peak elements, i.e. scandium, vanadium, manganese, and cobalt, incorporating hyperfine structure effects and correcting for non-local thermodynamic equilibrium. The derived abundances align with the Galactic trends found in the literature. Moreover, we investigate potential correlations between the stellar abundances and the presence of exoplanets. This study provides reference abundances for calibrating and testing M-dwarf chemical analyses. The results of this chapter are published by Duque-Arribas et al. (2024).
- **Chapter 5** explores the potential of low-resolution spectroscopy to derive elemental abundances of M dwarfs. By assuming chemical homogeneity in wide binaries, we calibrate the abundances of M-dwarf secondaries by statistically linking their low-resolution spectral features (Alonso-Floriano et al., 2015) to the well-determined compositions of their FGK primaries. We introduce a novel calibration method to derive M-dwarf abundances using low-resolution CAFOS spectra. The methodology incorporates projection predictive feature selection to identify the most informative indices, and Bayesian inference for abundance prediction and uncertainty quantification. Separate calibrations are derived for early- and late-type M dwarfs. The calibrations are applied to a large sample of more than 770 M dwarfs, delivering individual abundances for up to 15 elements (C, O, Na, Mg, Al, Si, Ca, Sc, Ti, V, Cr, Mn, Fe, Co, Ni). These results are consistent with photometric metallicity estimates and the well-known Galactic trends for FGK stars. We also compare our results with high-resolution determinations from the literature and find good agreement in most cases. The results of this chapter are part of a publication currently in preparation.
- **Chapter 6** describes the open-time observations of the M-dwarf secondaries in FGK+M wide binary systems, obtained with the CARMENES high-resolution spectrograph. These observations aim to expand the limited number of M-dwarf companions in the original CARMENES GTO sample, thereby increasing the availability of high-resolution data for chemical benchmark studies. These spectra allow us to determine the stellar atmospheric parameters (effective temperature, surface gravity, and metallicity) using StePar Syn (Tabernero et al., 2022), a Bayesian implementation of the spectral synthesis method. The derived parameters provide a homogeneous and reliable characterisation of the M-dwarf companions, which serve as valuable benchmarks for ongoing and future analyses of the chemical composition of cool stars.
- **Chapter 7** comprises the main conclusions of this thesis and outlines potential directions for future research on the chemical composition of M-type dwarf stars.

This comprehensive, multi-technique approach demonstrates that, despite their complexity, M dwarfs can be chemically characterised with high precision. The methodologies developed in this thesis lay the groundwork for future studies of M-dwarf populations in the Milky Way and for exoplanet host characterisation.

CHAPTER 2

Photometric metallicities of M dwarfs: a Bayesian approach

"It often seems to me that the night is even more richly coloured than the day; having hues of the most intense violets, blues and greens. Certain stars are lemon-yellow, others have a pink, green, forget-me-not blue glow. It is obvious that putting little white dots on the blue-black surface is not enough to paint a starry sky."
— Vincent van Gogh

The content of this chapter has been adapted from the article *Photometric calibrations of M-dwarf metallicity with Markov chain Monte Carlo and Bayesian inference*, published in The Astrophysical Journal (C. Duque-Arribas, D. Montes, H. M. Tabernero, et al. 2023, ApJ, 944, 106).

2.1 Introduction

Due to the intricate nature of the cooler atmospheres of M-type dwarf stars, the determination of their metallicity requires observationally expensive data, such as high-resolution spectra, and a complicated subsequent analysis. For this reason, several studies have focused on photometric calibrations of the metallicity using several sky surveys, such as Gaia (Gaia Collaboration et al., 2016), Two Micron All Sky Survey (2MASS; Skrutskie et al. 2006), Wide-field Infrared Survey Explorer (WISE; Wright et al. 2010), or Sloan Digital Sky Survey (SDSS; Alam et al. 2015), among others.

Initially, Stauffer & Hartmann (1986) used broadband photometry to identify nearby M dwarfs with metallicities significantly different from that of the Sun. Bonfils et al. (2005) proposed an empirical calibration to derive the metallicity of M-dwarf components in wide visual binaries using the $V - K_s$ versus M_{K_s} colour–magnitude diagram, obtaining a precision of 0.20 dex and demonstrating that metallicity explains the dispersion in the empirical V-band mass–luminosity relation. Later, Johnson & Apps (2009), Schlaufman & Laughlin (2010), and Neves et al. (2012) updated the photometric calibration based on the same colour–magnitude diagram. Johnson et al. (2012) and Mann et al. (2013) estimated the metallicity of M dwarfs using the $J - K_s$ versus $V - K_s$ colour–colour diagram. Hejazi et al. (2015) used SDSS and 2MASS photometry to derive metallicity from the $g - K_s$ versus $J - K_s$ colour–colour diagram, while Dittmann et al. (2016) exploited 2MASS and MEarth passband in a color–magnitude for this purpose. Schmidt et al. (2016) explored the $r' - z'$ versus W1−W2 colour–colour diagram, combining SDSS and WISE photometry, to derive new calibrations for late K- and early M-dwarf metallicities. They explored the sensitivity of colour indices to metallicity, illustrating the importance of the W1−W2 color index as a metallicity indicator. Davenport & Dorn-Wallenstein (2019) presented `ingot`, a k-nearest neighbours regressor to estimate [Fe/H] of low-mass stars using Gaia, 2MASS, and WISE photometry (and Gaia astrometry). Medan et al. (2021) trained a Gaussian process

regressor to calibrate two photometric metallicity relationships: for K- and early M dwarfs ($3500\,\mathrm{K} < T_{\mathrm{eff}} < 5280\,\mathrm{K}$), and for intermediate M dwarfs ($2850\,\mathrm{K} < T_{\mathrm{eff}} < 3500\,\mathrm{K}$), combining SDSS and WISE photometry. Rains et al. (2021) followed again the approach of Bonfils et al. (2005), although using $G_{\mathrm{BP}} - K_s$ instead of $V - K_s$.

The aim of the work presented in this chapter is to extend these previous studies and perform different photometric calibrations based on colour–colour and colour–magnitude diagrams applying Bayesian statistics and Markov Chain Monte Carlo (MCMC), and compare them with the "Leave One Out–Cross Validation" criterion (LOO-CV; Vehtari et al. 2017).

2.2 Analysis

2.2.1 Star samples

Birky et al. (2020, hereafter B20) presented a sample of 5875 early- and intermediate-type M dwarfs (down to M6 V) in the Apache Point Observatory Galactic Evolution Experiment (APOGEE; Majewski et al. 2017, Abolfathi et al. 2018) and Gaia DR2 (Gaia Collaboration et al., 2018b) surveys. Stellar parameters were inferred for these stars using `The Cannon` (Ness et al., 2015), a fully empirical model that, beyond the reference labels, employs no line lists or radiative transfer models, transferring labels from high-resolution spectra for which we know parameters to those for which we do not, and circumventing the difficulties of modelling the stellar atmospheres and common issues associated such as incomplete line lists. We used the B20 sample to train our calibrations and check their accuracy (Sect. 2.3). The coverage, distribution, and biases of this star sample are displayed in Fig. 2.1. The B20 sample does not cover the T_{eff} vs. [Fe/H] space

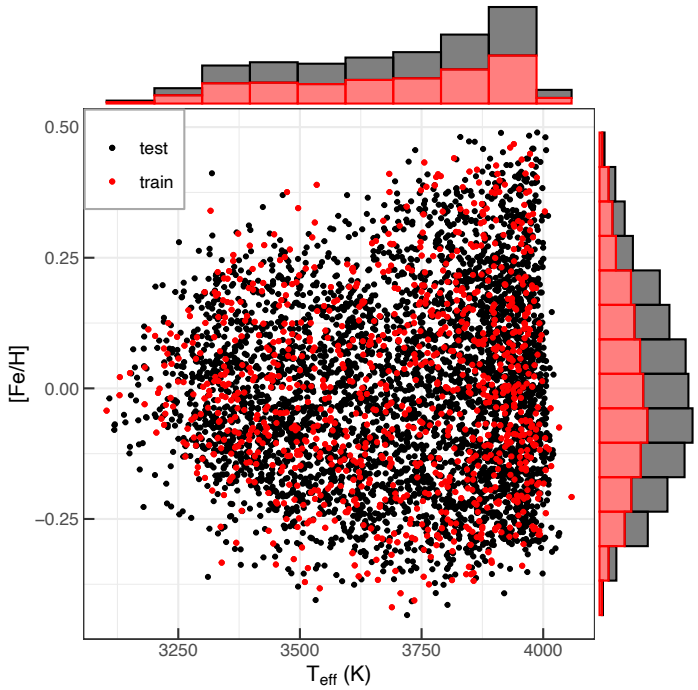

Figure 2.1: T_{eff} vs. [Fe/H] diagram for the training (red) and test (black) subsamples from B20, showing the histograms for both variables.

homogeneously, since only early M dwarfs have the highest metallicity values and in the coolest range the sample is biased to solar-metallicity stars.

Moreover, we tested the predictive performance of the calibrations with the sample presented by Montes et al. (2018), who studied 192 binary systems made of late F, G, or early K primaries and late K- or M-dwarf companion candidates. The authors carried out observations with the HERMES spectrograph at the 1.2 m Mercator telescope (Raskin et al., 2011) and obtained high-resolution spectra for the 192 primaries and five secondaries. These spectra were analysed with the automatic code StePar (Tabernero et al., 2019), based on the equivalent width method, to derive precise stellar atmospheric parameters (effective temperature $T_{\rm eff}$, surface gravity $\log g$, and metallicity [Fe/H]). Since binaries are assumed to be born at the same time and from the same molecular cloud, the composition and age of the FGK-type primary star can be extrapolated to its secondary M dwarf (Desidera et al., 2006; Andrews et al., 2018). Next we checked our calibrations for these stars and compared them to other photometric estimations found in the literature.

2.2.2 Photometry and data filtering

The third Gaia data release (Gaia DR3; Gaia Collaboration et al., 2023) provides the position and apparent magnitude in the G band (330–1050 nm) for 1.8 billion sources. For 1.5 billion of them, parallax and proper motion data are also available. In addition, photometry in the $G_{\rm BP}$ (330–680 nm) and $G_{\rm RP}$ (630–1050 nm) bands is offered for another 1.5 billion sources (Gaia Collaboration et al., 2016, 2021a; Riello et al., 2021). To study M dwarfs, which have the peak of the emission beyond 1000 nm (Cifuentes et al., 2020), we also used information in the infrared (IR) wavelength range: 2MASS provides magnitudes in the near-IR J (1229 nm), H (1639 nm) and K_s bands (2152 nm), while *WISE* offers data in the mid-IR bands $W1$, $W2$, $W3$, and $W4$, centered at 3316 nm, 4564 nm, 10 787 nm, and 21 915 nm, respectively. In particular, we used the data from the updated version CatWISE2020 (Marocco et al., 2021), which has enhanced sensitivity and accuracy. Initially, the analysis was performed with the AllWISE version (Cutri et al., 2021), but the uncertainties in the $W1-W2$ colour index were a factor of ~ 2 larger than those of CatWISE2020.

First, we crossmatched the star samples described above with the Gaia DR3, 2MASS, and CatWISE2020 catalogs. For that, we used the Tool for OPerations on Catalogues And Tables (`TOPCAT`; Taylor 2005). In particular, we used the automatic positional crossmatch tool of the Centre de Données astronomiques de Strasbourg, CDS `X-match`, with a search radius of 5 arcsec and the "All" find option. Next, we used the `Aladin` sky atlas (Bonnarel et al., 2000) to inspect and correct the possibly mismatched cases.

These data do not have homogeneous quality. Consequently, we applied the data filtering indicated by Gaia Collaboration et al. (2018a). In particular, for colour–magnitude diagrams, we made use of the absolute magnitude calculated using the Gaia parallax and selected only stars that fulfill the 10 % relative precision criterion, which corresponds to an uncertainty in M_G lower than 0.22 mag. Similarly, we applied filters to the relative flux error on the G, $G_{\rm BP}$, and $G_{\rm RP}$ magnitudes, which led to uncertainties of 0.022 mag, 0.054 mag, and 0.054 mag, respectively. To discard close unresolved or partially resolved binaries, we also applied a conservative filter in the astrometric quality indicator RUWE (renormalised unit weight error) as indicated by Lindegren et al. (2021), retaining those stars with RUWE values < 1.4. For sources where the single-star model provides a good fit to the astrometric observations, the RUWE value is expected to be around 1.0, and value significantly greater (> 1.4) could indicate that the source is nonsingle or problematic for the astrometric solution.

Table 2.1: Data filtering criteria applied to astrophotometric data

Survey	Filter

Gaia EDR3	`parallax_over_error > 10`
	`ruwe < 1.4`
	`photo_g_mean_flux_over_error > 50`
	`photo_bp_mean_flux_over_error > 20`
	`photo_rp_mean_flux_over_error > 20`

2MASS[a]	`Qfl = AAA`
CatWISE2020[b]	`qph = AA**`

[a] `Qfl` is the quality flag in 2MASS JHK_s bands.
[b] `qph` is the quality flag in WISE $W1W2W3W4$ bands.

In addition, we selected the stars with an "A" quality flag in the J, H, K_s, $W1$, and $W2$ bands, which corresponds to an approximate signal-to-noise ratio higher than 10. We discarded the $W3$ and $W4$ bands from our analysis, as they tend to present a lower photometric quality, and they may be contaminated by the emission of the interstellar dust. All these criteria are compiled in Table 2.1. Applying these criteria to the 5875 stars presented by B20, we ended up with a sample of 5453 M dwarfs.

Finally, we removed young objects and evolved stars, i.e. stars arriving or leaving the main sequence, since for those cases the age plays an important role in the position of the star in the colour–colour and colour–magnitude diagrams. To do this, we estimated the radii and masses of the stars with the M_{K_s} absolute magnitude using the calibrations given by Mann et al. (2015) [Eq. 5] and Mann et al. (2019) [Eq. 5], respectively. With these two properties, we calculated the surface gravity $\log g$. The pre-main-sequence and the evolved stars are expected to have inflated radii, and thus lower surface gravities. Therefore, we calibrated the surface gravity using the effective temperature and metallicity and removed these lower surface gravity stars, those with a difference between the photometric and fitted surface gravities larger than 0.03 dex. Hence we obtained a final sample of 4919 M dwarfs. We show in Fig. 2.2 the Kiel diagram ($T_{\rm eff}$ vs. $\log g$) before and after having removed the lower $\log g$ stars. Note the gradient of metallicity present in the main sequence of the Kiel diagram, having decreasing $\log g$ with increasing metallicity for a given effective temperature.

After removing the age dependence by excluding stars outside the main sequence, and considering that M dwarfs evolve extremely slowly along it, the remaining variations observed in the Kiel, colour–colour, and colour–magnitude diagrams can be attributed primarily to differences in stellar metallicity: A higher metal content increases the number of free electrons in the stellar atmosphere, enhancing the continuum opacity of molecular species and the H^- ion, and thereby decreasing the luminosity and effective temperature of the star (see Sect. 1.4.1). As these stellar parameters are directly correlated with the absolute magnitudes and colour indices respectively, we are able to identify and quantify metallicity variations using photometric data.

The crossmatch between Montes et al. (2018), Gaia DR3, and CatWISE2020 catalogs resulted in a subsample of 115 M dwarfs among the 192 systems after having eliminated nonphysical pairs (Espada, 2019) or systems with double-lined spectroscopic binaries. Then, we applied the data filtering mentioned above and constrained to identical values as in B20, that is, early and mid M dwarfs between M0 V and M5 V, and having $1.85\,{\rm mag} \leq G - J \leq 3.10\,{\rm mag}$, $-0.10\,{\rm mag} \leq W1 - W2 \leq 0.24\,{\rm mag}$, and $-0.5 \leq {\rm [Fe/H]} \leq 0.5\,{\rm dex}$, and retrieved a final sample of 46 FGK+M systems to test the calibration.

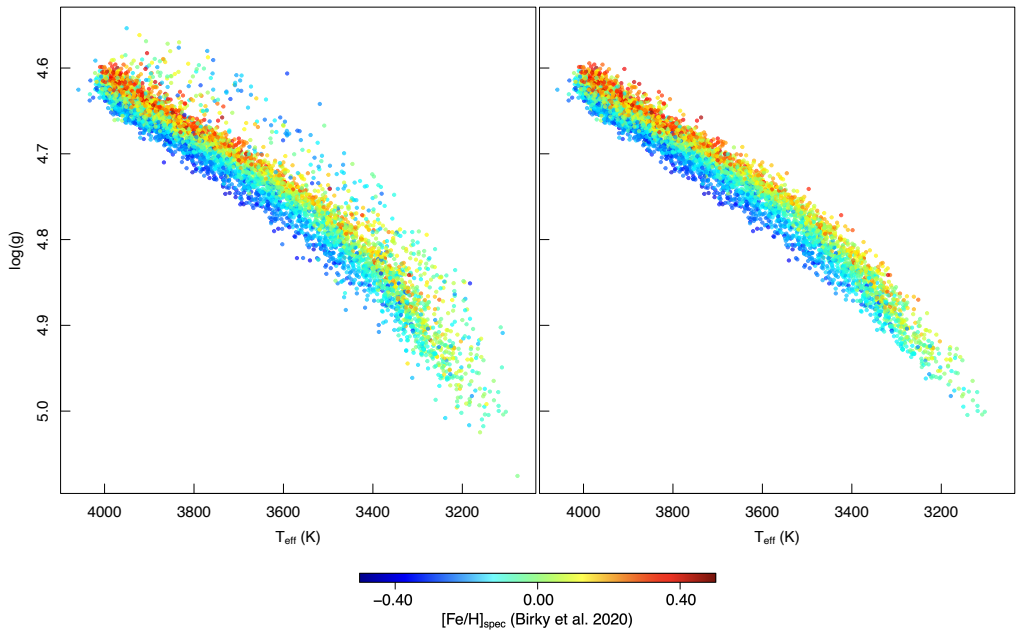

Figure 2.2: Kiel diagram of the B20 sample, before (left panel) and after (right panel) having removed the stars with lower surface gravity, i.e. not in the main sequence.

2.2.3 Calibrations, statistical analysis, and model selection

We divided the 4919 crossmatched, filtered M dwarfs from B20 into two subsamples: 1000 stars constitute the calibration or training sample, and the remaining 3919 stars are the test sample to check the accuracy of the calibrations. The $T_{\rm eff}$–[Fe/H] space and their corresponding histograms for both subsamples are shown in Fig. 2.1.

The calibrations were derived with MCMC using `Stan` (Carpenter et al., 2017; Stan Development Team, 2022) through its R interface, namely `RStan`. `Stan` is a C++ library for Bayesian modelling and inference that incorporates, among other components, the Hamiltonian Monte Carlo no-U-turn sampler (HMC+NUTS) algorithm. After deriving different calibrations, we compared them with the LOO-CV criterion, which allowed us to choose the calibration that best reproduces the metallicity values by penalising the more complicated models (i.e. with more free parameters) with respect to the simplest ones. The LOO-CV criterion defines the expected log-pointwise predictive density as:

$$\mathrm{elppd}_{\rm LOO} = \sum_{i=1}^{N} \log(P(x_i|\boldsymbol{x_{-i}})) \tag{2.1}$$

where $P(x_i|\boldsymbol{x_{-i}})$ denotes the probability of predicting x_i using the data without the ith observation (Gelman et al., 2014; Vehtari et al., 2017). The value of $\mathrm{elppd}_{\rm LOO}$ can be either positive or negative since it uses the probability density, not the probability itself. The model with the largest $\mathrm{elppd}_{\rm LOO}$ presents the best predictive accuracy. The computed $\mathrm{elppd}_{\rm LOO}$ is defined as the sum of N independent components, so its standard error can be computed as the standard deviation of the N components divided by $\sqrt{N}$. We used the R package `loo` for implementing the necessary functions and for estimating $\mathrm{elppd}_{\rm LOO}$ with the Pareto smoothed importance sampling method (Vehtari et al., 2015).

In order to derive the best calibration using the LOO-CV criterion, we tried different calibrations, starting with a linear model and increasingly adding more terms following a stepwise

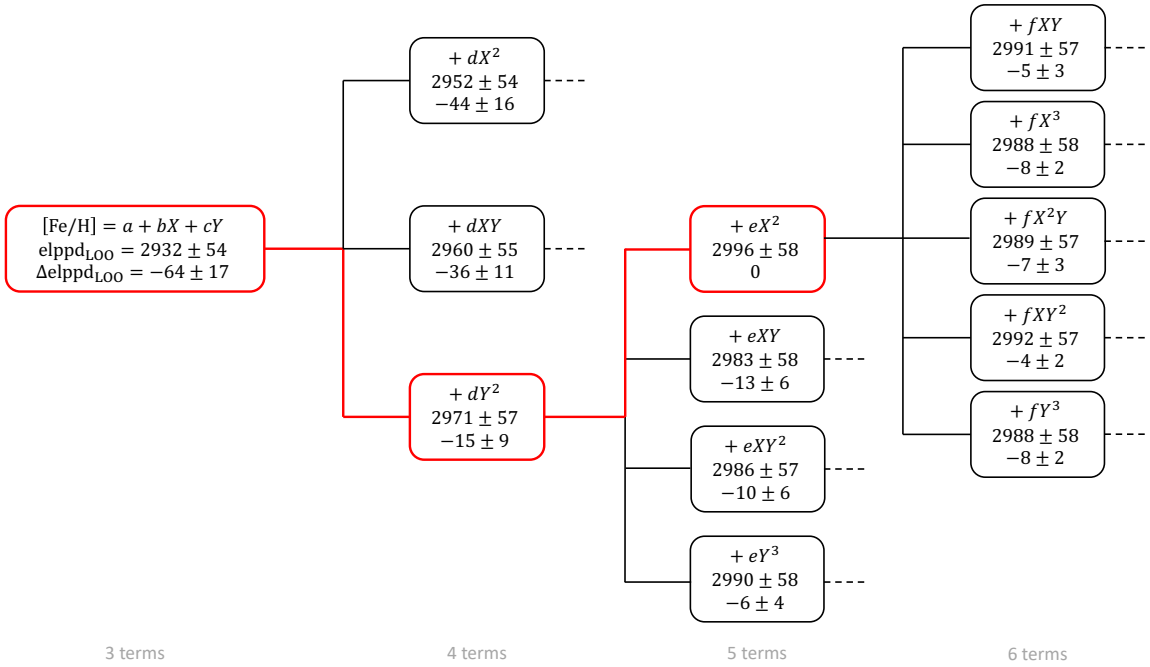

Figure 2.3: Comparison of different metallicity photometric calibrations with LOO-CV following a stepwise regression (forward selection) procedure, where $X = W1 - W2$, $Y = G_{\rm BP} - G_{\rm RP}$, $\mathrm{elppd_{LOO}}$ is the expected log-pointwise predictive density given by Eq. 2.1, and $\Delta\mathrm{elppd_{LOO}}$ is the difference with respect to the model with the largest $\mathrm{elppd_{LOO}}$, given by Eq. 2.2 and marked in red.

regression procedure (forward selection), shown in Fig. 2.3 for the $W1 - W2$ vs. $G_{\rm BP} - G_{\rm RP}$ diagram as an example. For this case, we performed the stepwise regression including up to six terms and found that the model with the best predictive performance (i.e., the largest $\mathrm{elppd_{LOO\text{-}CV}}$) is given by:

$$[\mathrm{Fe/H}] = a + bX + cY + dY^2 + eX^2 \tag{2.2}$$

The distribution of the residuals of the calibrations exhibited extended wings and could not be fitted by a Gaussian distribution. As a result, we used a generalised linear model with a t-distribution instead of a Gaussian one to model the corresponding likelihood. Furthermore, this robust regression (with t-distribution instead of the Gaussian likelihood) significantly increased the $\mathrm{elppd_{LOO\text{-}CV}}$. For the robust regression, we used weakly informative priors for the coefficients, that is, $a, b, c, d, e \sim \mathit{normal}(0{,}10)$. The likelihood is given by $[\mathrm{Fe/H}] \sim \mathit{t\text{-}Student}(\mu, \nu, \sigma)$, where μ is the expression in Eq. 2.2, and the priors for the scale parameter and degrees of freedom are $\sigma \sim \mathit{half\text{-}Cauchy}(0{,}1)$ and $\nu \sim \mathit{exponential}(1/30)$, respectively. These are suitable priors for σ and ν since the *half-Cauchy* distribution is a less informative prior than the normal distribution, with heavier tails, and the $\mathit{exponential}(1/30)$ distribution captures the behavior of the degrees of freedom in the t-distribution, that is, nearly all the variation in the family of t-distribution happens when ν is fairly small and for $\nu > 30$ the t-distribution is essentially normal. Therefore, since $\nu = 30$ is the mean of the $\mathit{exponential}(1/30)$ distribution, with this prior we give the same weights to the low and high regimes of ν. We provide a graphical representation of the model in Fig. 2.4 (see Kruschke 2014).

A Bayesian approach to error measurement can be formulated by treating the true quantities being measured as missing data or latent variables, needing a model of how the measurements are derived from the true values. We can suppose that the 'true' values of a predictor A_i, for example the magnitude in a given photometric band, are not known, but for each i star, a measurement $A_i^{\rm obs}$ of A_i is available. Then the approach is to assume that the measured values arise from a

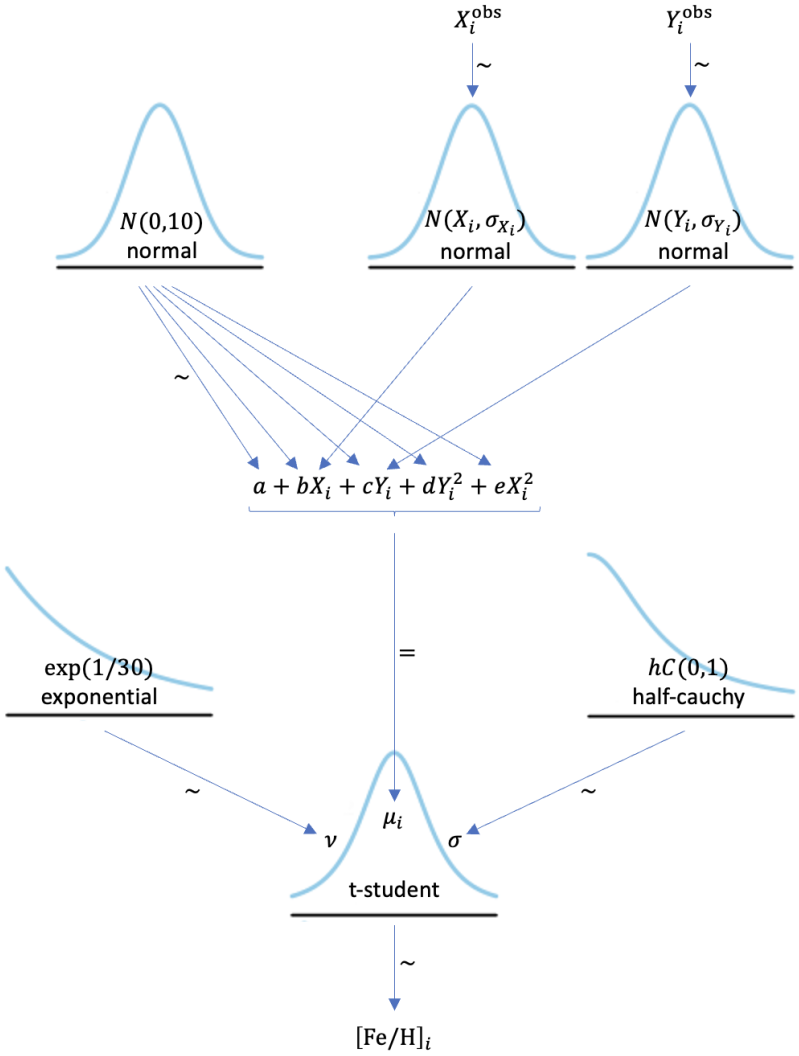

Figure 2.4: Summary of the distributions used in the Stan model for the robust regression, where $X_i^{\rm obs}$ and $Y_i^{\rm obs}$ indicate the observed values of the predictors, with their observational errors σ_{X_i} and σ_{Y_i}, respectively. Therefore the observed values of the predictors come from a normal distribution (with standard deviations equal to the observed errors) around the 'true' values X_i and Y_i. In the same way, μ is the predicted value of the metallicity, which relates to the observed metallicity through a t-distribution with parameters ν (degrees of freedom) and σ (scale parameter). For the coefficients we assumed normal priors, while an exponential distribution and a half-Cauchy distribution are used as priors for ν and σ, respectively. See Kruschke (2014) for more details on the interpretation of this kind of graph.

normal distribution with a mean equal to the true value and some measurement error σ_{A_i}, that is, $A_i^{\rm obs} \sim normal(A_i, \sigma_{A_i})$. Therefore, the regression is not performed with the measured values $A_i^{\rm obs}$ but with the true ones A_i (see Fig. 2.4).

Finally, to ensure the convergence of the MCMC chains we applied the Gelman–Rubin diagnostic or shrink factor $\hat{R}$ (Gelman & Rubin, 1992; Brooks & Gelman, 1998), which analyzes the difference between multiple Markov chains. The convergence is assessed by comparing the estimated between-chains and within-chain variances for each model parameter. If $\hat{R} < 1.1$ for all parameters, one can be confident that convergence has been reached. In our case, we obtained a shrink factor of $\hat{R} = 1.0$ for all parameters. We typically run three simultaneous chains with 3000 steps in each of them and 500 warm-up iterations.

2.3 Results and discussion

2.3.1 Colour–colour diagrams

Colour–colour diagrams allow us to compare apparent magnitudes at different wavelengths. In these diagrams the chemical composition plays a fundamental role, showing a gradient of metallicity that is more noticeable for cool stars (Gaia Collaboration et al., 2018a). In particular, the $W1-W2$ colour index constitutes an appropriate metallicity indicator (Schmidt et al., 2016).

In Table 2.2 we present the posterior mean and standard deviation of the coefficients of the calibration given by Eq. 2.2 for different colour–colour combinations, the scale parameter and degrees of freedom of the Student's t-distribution, and their comparison with LOO-CV, sorted from the best to the worst combination according to their elppd value. The posterior distributions of the coefficients are Gaussian. All these calibrations fit the observed metallicities with a residual standard deviation of 0.08–0.09 dex, of the same order as the [Fe/H] uncertainty provided by B20, which means we are performing our regression until the observational limit. An example of colour–colour diagram is shown in the top left panel of Fig. 2.5. The remaining colour–colour diagram combinations are available in Fig. A.1.

In the top right panels of Fig. 2.5 we also represent the [Fe/H] values reported by B20 versus the estimated values using the $W1-W2$ vs. $G_{\rm BP}-G_{\rm RP}$ colour–colour diagram, and the corresponding residuals, for the 3919 stars from the test subsample, colour-coded by $G_{\rm BP}-G_{\rm RP}$ color index. We conclude that most of the estimated metallicities follow the one-to-one relationship and that there is no correlation between them and $T_{\rm eff}$, as expected. Some photometric metallicities are more than 2σ above or below the spectroscopic value given by B20, but they are just 112 stars, 2.9 % of the test sample.

2.3.2 Colour–magnitude diagrams

Colour–magnitude or Hertzsprung–Russell diagrams represent the absolute magnitude or luminosity versus the colour index, spectral type, or $T_{\rm eff}$. The position of a star in these diagrams is mainly given by its initial mass, chemical composition, and age, but other effects such as rotation, stellar winds, or magnetic fields also play a role (Gaia Collaboration et al., 2018a). Similar to what is observed in our colour–colour diagrams, colour–magnitude diagrams also present a metallicity gradient.

We proceeded with the analysis as in the previous section. In Table 2.3 we present the coefficients of the calibration given by Eq. 2.2 for different colour–magnitude combinations and their comparison using the LOO-CV criterion.

Table 2.2: Fit parameters of colour–colour diagram calibrations[a]

X (mag)	Y (mag)	a (dex)	b ($\rm mag^{-1}$)	c ($\rm mag^{-1}$)	d ($\rm mag^{-2}$)	e ($\rm mag^{-2}$)	σ (dex)	ν	$\rm elppd_{LOO}$	$\Delta\rm elppd_{LOO}$
$W1-W2$	$G_{\rm BP}-G_{\rm RP}$	-2.72 ± 0.18	-3.96 ± 0.13	1.91 ± 0.16	-0.253 ± 0.036	0.65 ± 0.90	0.0960 ± 0.0049	22.32 ± 19.58	2996 ± 58	0
$W1-W2$	$G-H$	-4.92 ± 0.47	-3.54 ± 0.11	2.49 ± 0.30	-0.266 ± 0.049	2.07 ± 0.79	0.0875 ± 0.0050	8.27 ± 4.13	2974 ± 61	-21 ± 26
$W1-W2$	$G-K_s$	-4.39 ± 0.43	-3.71 ± 0.12	2.03 ± 0.26	-0.189 ± 0.040	2.45 ± 0.80	0.0875 ± 0.0048	8.62 ± 4.81	2965 ± 62	-31 ± 25
$W1-W2$	$G-J$	-3.32 ± 0.29	-3.87 ± 0.13	2.06 ± 0.24	-0.243 ± 0.049	1.11 ± 0.88	0.0953 ± 0.0052	15.77 ± 13.79	2891 ± 59	-105 ± 20
$W1-W2$	$G_{\rm RP}-K_s$	-4.93 ± 0.43	-3.52 ± 0.12	3.50 ± 0.38	-0.536 ± 0.085	3.05 ± 0.79	0.0863 ± 0.0048	7.19 ± 2.81	2882 ± 64	-113 ± 33
$W1-W2$	$G_{\rm RP}-H$	-5.70 ± 0.49	-3.20 ± 0.11	4.60 ± 0.48	-0.83 ± 0.12	2.34 ± 0.80	0.0878 ± 0.0049	7.35 ± 2.80	2873 ± 62	-123 ± 36
$W1-W2$	$G_{\rm RP}-J$	-2.87 ± 0.22	-3.70 ± 0.13	3.23 ± 0.32	-0.70 ± 0.11	1.21 ± 0.90	0.0995 ± 0.0052	19.36 ± 17.28	2765 ± 59	-231 ± 29
$W1-W2$	$G-W1$	-3.59 ± 0.44	-3.43 ± 0.14	1.56 ± 0.26	-0.131 ± 0.037	2.06 ± 0.87	0.1024 ± 0.0055	13.12 ± 10.73	2720 ± 58	-276 ± 18
$W1-W2$	$G-W2$	-3.14 ± 0.37	-4.14 ± 0.16	1.28 ± 0.21	-0.089 ± 0.030	2.52 ± 0.93	0.1001 ± 0.0059	13.44 ± 11.48	2696 ± 60	-300 ± 19
$W1-W2$	$G_{\rm RP}-W1$	-3.72 ± 0.43	-3.20 ± 0.14	2.44 ± 0.36	-0.327 ± 0.076	2.46 ± 0.91	0.1061 ± 0.0056	11.97 ± 8.70	2603 ± 57	-393 ± 23
$W1-W2$	$G_{\rm RP}-W2$	-3.00 ± 0.35	-4.15 ± 0.17	1.80 ± 0.29	-0.188 ± 0.059	3.16 ± 0.96	0.1036 ± 0.0060	12.48 ± 10.09	2568 ± 59	-428 ± 24

[a] The polynomial fits the expression $\rm[Fe/H]=a+bX+cY+dY^2+eX^2$.

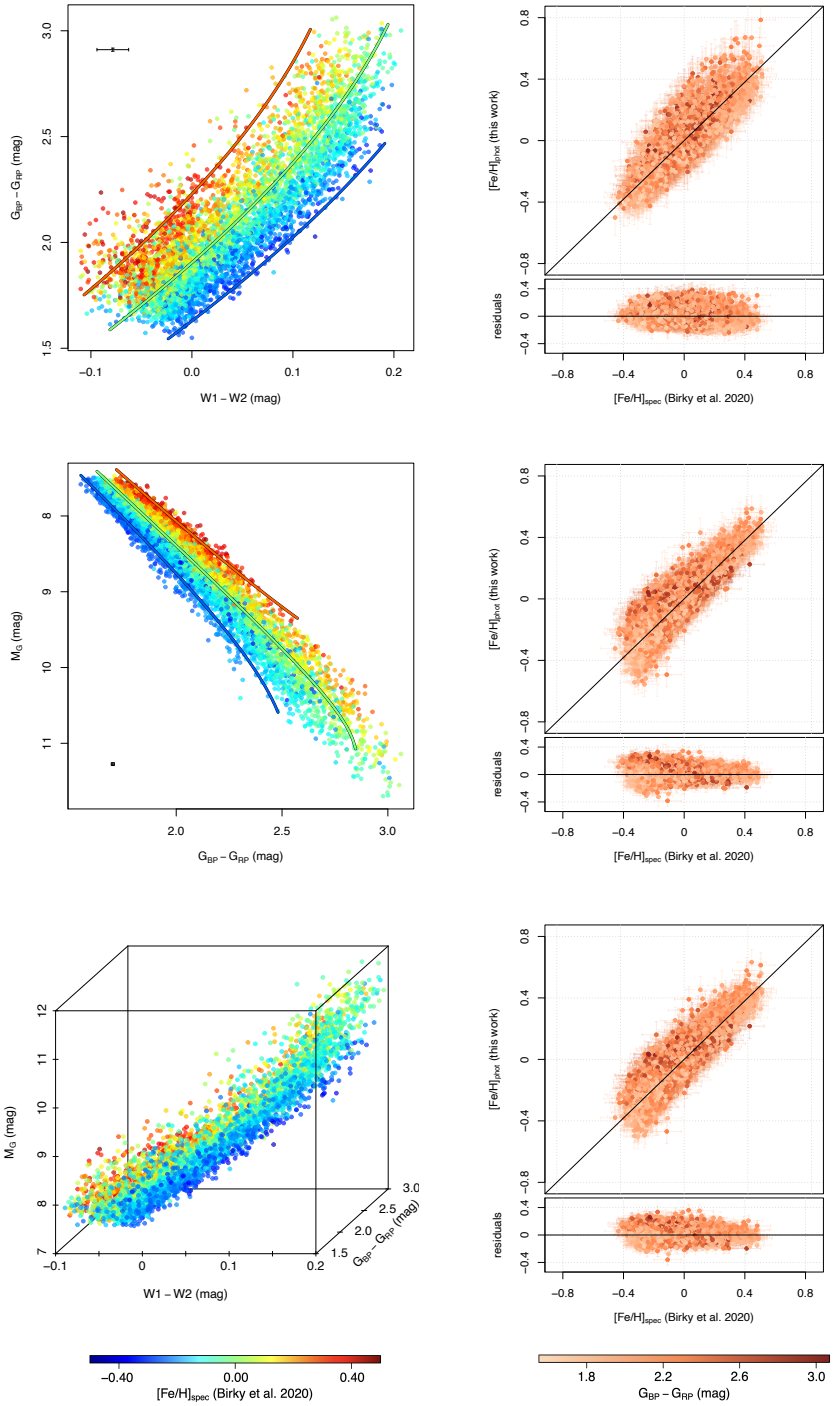

Figure 2.5: *Left panels*: from top to bottom, representative examples of color–color, color–magnitude, and color–color–magnitude diagrams of the stars from B20, color-coded by $[\mathrm{Fe/H}]_{\mathrm{spec}}$, with the respective calibrations given by this work (red: $[\mathrm{Fe/H}] = 0.3$ dex, green: $[\mathrm{Fe/H}] = 0.0$ dex, blue: $[\mathrm{Fe/H}] = -0.3$ dex). The mean uncertainties of the color indices and absolute magnitudes involved are also shown with a black dot. *Right panels*: comparison between the spectroscopic metallicity values reported by B20 and the photometric estimations with the corresponding diagrams in the left for the 3919 stars from the test subsample, and respective residuals, color-coded by $G_{\mathrm{BP}} - G_{\mathrm{RP}}$ color index (darker symbols: cooler stars; lighter symbols: warmer stars). The solid lines denote the 1:1 relationship and the residuals = 0.

Table 2.3: Fit parameters of colour–magnitude diagram calibrations[a]

X (mag)	Y (mag)	a (dex)	b (mag^{-1})	c (mag^{-1})	d (mag^{-2})	e (mag^{-2})	σ (dex)	ν	$\mathrm{elppd}_{\mathrm{LOO}}$	$\Delta\mathrm{elppd}_{\mathrm{LOO}}$
$G_{\mathrm{BP}} - G_{\mathrm{RP}}$	M_G	8.89 ± 0.36	5.89 ± 0.24	-3.22 ± 0.13	0.1432 ± 0.0068	-0.933 ± 0.054	0.0706 ± 0.0033	4.20 ± 0.71	3611 ± 61	0
$G_{\mathrm{BP}} - G_{\mathrm{RP}}$	M_{K_s}	4.75 ± 0.22	2.93 ± 0.16	-2.63 ± 0.11	0.1790 ± 0.0090	-0.416 ± 0.036	0.0718 ± 0.0034	4.43 ± 0.79	3519 ± 62	-92 ± 24
$G_{\mathrm{BP}} - G_{\mathrm{RP}}$	M_H	4.44 ± 0.22	3.19 ± 0.17	-2.54 ± 0.10	0.1660 ± 0.0083	-0.468 ± 0.037	0.0710 ± 0.0035	4.08 ± 0.70	3491 ± 62	-120 ± 22
$G_{\mathrm{BP}} - G_{\mathrm{RP}}$	M_J	7.34 ± 0.31	3.49 ± 0.17	-3.19 ± 0.13	0.1953 ± 0.0094	-0.525 ± 0.039	0.0725 ± 0.0035	4.25 ± 0.75	3460 ± 62	-151 ± 18
$G - W1$	M_{K_s}	2.25 ± 0.32	2.39 ± 0.23	-2.29 ± 0.10	0.1559 ± 0.0084	-0.209 ± 0.034	0.0761 ± 0.0034	4.32 ± 0.70	3399 ± 63	-212 ± 50
$G - W1$	M_H	1.63 ± 0.32	2.70 ± 0.24	-2.19 ± 0.10	0.1430 ± 0.0081	-0.250 ± 0.036	0.0766 ± 0.0035	4.25 ± 0.68	3372 ± 63	-239 ± 49
$G - W1$	M_J	3.91 ± 0.34	2.94 ± 0.25	-2.72 ± 0.12	0.1665 ± 0.0089	-0.279 ± 0.037	0.0773 ± 0.0035	4.38 ± 0.74	3367 ± 62	-244 ± 47
$G - K_s$	M_H	1.16 ± 0.35	2.84 ± 0.27	-2.072 ± 0.098	0.1356 ± 0.0079	-0.276 ± 0.041	0.0773 ± 0.0037	4.66 ± 0.85	3351 ± 63	-260 ± 46
$G - K_s$	M_J	3.24 ± 0.38	3.05 ± 0.28	-2.55 ± 0.12	0.1556 ± 0.0089	-0.303 ± 0.043	0.0797 ± 0.0038	5.26 ± 1.11	3323 ± 62	-288 ± 44
$G - H$	M_{K_s}	0.65 ± 0.40	3.09 ± 0.30	-2.009 ± 0.099	0.1366 ± 0.0082	-0.331 ± 0.049	0.0768 ± 0.0038	4.30 ± 0.78	3311 ± 63	-300 ± 45
$G - W1$	M_G	2.64 ± 0.34	4.73 ± 0.34	-2.42 ± 0.12	0.1064 ± 0.0063	-0.486 ± 0.049	0.0807 ± 0.0035	4.57 ± 0.74	3270 ± 61	-341 ± 52
$G - K_s$	M_{K_s}	1.80 ± 0.37	2.39 ± 0.27	-2.10 ± 0.10	0.1427 ± 0.0087	-0.215 ± 0.042	0.0817 ± 0.0038	5.39 ± 1.14	3268 ± 62	-343 ± 48
$G - K_s$	M_G	1.69 ± 0.37	4.93 ± 0.36	-2.24 ± 0.11	0.0984 ± 0.0059	-0.530 ± 0.054	0.0796 ± 0.0039	5.38 ± 1.20	3256 ± 63	-355 ± 48
$G - H$	M_J	1.89 ± 0.41	3.66 ± 0.31	-2.35 ± 0.12	0.1431 ± 0.0086	-0.413 ± 0.051	0.0785 ± 0.0040	4.43 ± 0.86	3252 ± 63	-360 ± 42
$G - J$	M_{K_s}	3.42 ± 0.27	2.84 ± 0.25	-2.36 ± 0.11	0.1600 ± 0.0092	-0.351 ± 0.052	0.0825 ± 0.0041	5.33 ± 1.22	3245 ± 62	-366 ± 40
$G - W2$	M_{K_s}	4.43 ± 0.29	1.95 ± 0.21	-2.72 ± 0.12	0.185 ± 0.010	-0.143 ± 0.031	0.0797 ± 0.0037	4.20 ± 0.69	3241 ± 63	-370 ± 46
$G_{\mathrm{RP}} - W1$	M_{K_s}	1.49 ± 0.33	3.82 ± 0.33	-2.16 ± 0.10	0.1481 ± 0.0085	-0.531 ± 0.070	0.0785 ± 0.0034	4.19 ± 0.63	3223 ± 64	-388 ± 59
$G - W2$	M_H	3.86 ± 0.28	2.30 ± 0.22	-2.65 ± 0.12	0.1733 ± 0.0095	-0.189 ± 0.032	0.0794 ± 0.0037	3.93 ± 0.61	3205 ± 63	-406 ± 45
$G - J$	M_H	2.97 ± 0.26	3.18 ± 0.25	-2.27 ± 0.11	0.1481 ± 0.0087	-0.414 ± 0.052	0.0821 ± 0.0042	4.91 ± 1.08	3203 ± 62	-408 ± 39
$G_{\mathrm{RP}} - W1$	M_H	0.91 ± 0.32	4.20 ± 0.34	-2.057 ± 0.099	0.1352 ± 0.0080	-0.607 ± 0.071	0.0792 ± 0.0035	4.15 ± 0.63	3193 ± 64	-418 ± 58
$G_{\mathrm{RP}} - W1$	M_J	3.04 ± 0.36	4.51 ± 0.36	-2.55 ± 0.12	0.1566 ± 0.0089	-0.661 ± 0.077	0.0797 ± 0.0035	4.25 ± 0.65	3186 ± 63	-426 ± 56
$G - H$	M_H	0.13 ± 0.40	3.26 ± 0.31	-1.862 ± 0.095	0.1212 ± 0.0077	-0.358 ± 0.051	0.0804 ± 0.0040	4.45 ± 0.83	3167 ± 62	-445 ± 46
$G - W2$	M_J	6.75 ± 0.35	2.57 ± 0.23	-3.32 ± 0.15	0.203 ± 0.011	-0.221 ± 0.034	0.0816 ± 0.0039	4.17 ± 0.71	3158 ± 62	-453 ± 42
$G - H$	M_G	-0.02 ± 0.41	5.52 ± 0.40	-1.97 ± 0.10	0.0857 ± 0.0055	-0.656 ± 0.064	0.0788 ± 0.0042	4.45 ± 0.87	3154 ± 63	-457 ± 46
$G_{\mathrm{RP}} - K_s$	M_H	0.16 ± 0.38	4.53 ± 0.41	-1.873 ± 0.097	0.1228 ± 0.0078	-0.699 ± 0.090	0.0785 ± 0.0039	4.49 ± 0.80	3137 ± 65	-474 ± 54
$G_{\mathrm{RP}} - K_s$	M_J	2.00 ± 0.40	4.80 ± 0.42	-2.29 ± 0.12	0.1398 ± 0.0087	-0.749 ± 0.094	0.0810 ± 0.0040	5.07 ± 1.06	3104 ± 64	-507 ± 53
$G_{\mathrm{RP}} - K_s$	M_{K_s}	0.79 ± 0.39	3.87 ± 0.40	-1.89 ± 0.10	0.1289 ± 0.0086	-0.568 ± 0.090	0.0834 ± 0.0039	5.11 ± 0.99	3055 ± 63	-556 ± 56
$G_{\mathrm{RP}} - W2$	M_{K_s}	4.68 ± 0.28	2.80 ± 0.29	-2.77 ± 0.13	0.189 ± 0.011	-0.306 ± 0.060	0.0824 ± 0.0037	3.99 ± 0.60	3047 ± 64	-564 ± 53
$G_{\mathrm{RP}} - H$	M_{K_s}	-0.86 ± 0.43	5.28 ± 0.47	-1.705 ± 0.096	0.1156 ± 0.0080	-0.94 ± 0.12	0.0793 ± 0.0041	4.23 ± 0.77	3046 ± 64	-565 ± 53
$G - J$	M_J	5.22 ± 0.33	3.27 ± 0.27	-2.70 ± 0.13	0.1646 ± 0.0099	-0.433 ± 0.056	0.0905 ± 0.0045	6.29 ± 1.83	3035 ± 60	-576 ± 40
$G - J$	M_G	5.12 ± 0.33	5.59 ± 0.37	-2.57 ± 0.13	0.1131 ± 0.0069	-0.797 ± 0.074	0.0879 ± 0.0047	6.03 ± 2.06	3024 ± 61	-587 ± 40
$G - W2$	M_G	6.96 ± 0.37	4.76 ± 0.34	-3.32 ± 0.16	0.1469 ± 0.0084	-0.457 ± 0.049	0.0859 ± 0.0039	4.10 ± 0.64	3012 ± 60	-599 ± 46
$G_{\mathrm{RP}} - W2$	M_H	4.16 ± 0.28	3.27 ± 0.30	-2.70 ± 0.13	0.177 ± 0.010	-0.395 ± 0.061	0.0825 ± 0.0039	3.80 ± 0.57	3005 ± 64	-606 ± 52
$G_{\mathrm{RP}} - W1$	M_G	1.49 ± 0.34	6.74 ± 0.46	-2.13 ± 0.11	0.0939 ± 0.0061	-1.042 ± 0.096	0.0845 ± 0.0036	4.24 ± 0.63	2985 ± 62	-626 ± 63
$G_{\mathrm{RP}} - H$	M_J	0.13 ± 0.45	5.92 ± 0.50	-1.94 ± 0.11	0.1177 ± 0.0082	-1.08 ± 0.12	0.0815 ± 0.0044	4.44 ± 0.87	2977 ± 64	-634 ± 51
$G_{\mathrm{RP}} - W2$	M_J	7.13 ± 0.35	3.59 ± 0.32	-3.37 ± 0.16	0.207 ± 0.012	-0.448 ± 0.066	0.0850 ± 0.0040	4.04 ± 0.65	2947 ± 63	-664 ± 49
$G_{\mathrm{RP}} - J$	M_{K_s}	3.58 ± 0.26	4.23 ± 0.35	-2.17 ± 0.12	0.1468 ± 0.0097	-0.94 ± 0.13	0.0895 ± 0.0046	6.22 ± 1.81	2935 ± 62	-676 ± 47
$G_{\mathrm{RP}} - K_s$	M_G	0.15 ± 0.39	7.11 ± 0.51	-1.87 ± 0.11	0.0816 ± 0.0056	-1.17 ± 0.11	0.0806 ± 0.0042	4.78 ± 0.95	2917 ± 65	-695 ± 59
$G_{\mathrm{RP}} - H$	M_H	-1.25 ± 0.45	5.36 ± 0.50	-1.547 ± 0.095	0.1001 ± 0.0077	-0.96 ± 0.12	0.0841 ± 0.0044	4.53 ± 0.89	2901 ± 63	-710 ± 54
$G_{\mathrm{RP}} - J$	M_H	3.23 ± 0.26	4.57 ± 0.37	-2.06 ± 0.11	0.1338 ± 0.0091	-1.05 ± 0.13	0.0903 ± 0.0048	6.02 ± 1.78	2884 ± 62	-727 ± 47
$G_{\mathrm{RP}} - H$	M_G	-1.98 ± 0.46	8.06 ± 0.62	-1.467 ± 0.096	0.0628 ± 0.0051	-1.51 ± 0.15	0.0828 ± 0.0047	4.40 ± 0.88	2778 ± 65	-833 ± 56
$G_{\mathrm{RP}} - J$	M_J	5.20 ± 0.36	4.48 ± 0.40	-2.38 ± 0.14	0.144 ± 0.011	-1.03 ± 0.14	0.1007 ± 0.0051	8.68 ± 4.77	2701 ± 59	-910 ± 47
$G_{\mathrm{RP}} - W2$	M_G	7.32 ± 0.41	6.36 ± 0.49	-3.24 ± 0.18	0.1430 ± 0.0093	-0.877 ± 0.098	0.0928 ± 0.0041	3.94 ± 0.57	2643 ± 61	-968 ± 56
$G_{\mathrm{RP}} - J$	M_G	5.03 ± 0.39	7.00 ± 0.54	-2.08 ± 0.14	0.0897 ± 0.0074	-1.70 ± 0.19	0.1019 ± 0.0058	9.45 ± 6.34	2530 ± 60	-1082 ± 50

[a] The polynomial fits follow the expression $[\mathrm{Fe/H}] = a + bX + cY + dY^2 + eX^2$.

In the central panels of Fig. 2.5, we represent the colour–magnitude diagram $G_{\rm BP} - G_{\rm RP}$ vs. M_G of the 4919 stars from B20 (left) and the comparison between the spectroscopic [Fe/H] values and the corresponding estimated values for the 3 919 stars from the test subsample (right). Again, the rest of colour–magnitude diagrams can be found in Fig. A.2. In the case of the $G_{\rm BP} - G_{\rm RP}$ vs. M_G colour–magnitude diagram, 237 stars (6.0 %) are more than 2σ above or below the spectroscopic value.

2.3.3 Colour–colour–magnitude diagrams

Some authors, such as Davenport & Dorn-Wallenstein (2019), added an absolute magnitude as a third variable in their calibrations in order to improve their estimations, which we refer to as colour–colour–magnitude diagrams. Thus, we performed a stepwise regression using three variables, finding that the model with the best predictive performance is given by:

$$[\mathrm{Fe/H}] = a + bX + cY + dZ + eY^2 + fZ^2, \tag{2.3}$$

where, as an example, $X = W1 - W2$ and $Y = G_{\rm BP} - G_{\rm RP}$ are two colour indices, and the absolute magnitude $Z = M_G$ is added as a third variable. We display the coefficients of the calibration given by Eq. 2.3 in Table 2.4. As Davenport & Dorn-Wallenstein (2019), we found an improvement by adding M_G to the $W1 - W2$ vs. $G_{\rm BP} - G_{\rm RP}$ diagram, having that the residual dispersion σ and the $\mathrm{elppd_{LOO}}$ improve with the addition of this third independent variable. The three-dimensional colour–colour–magnitude $W1 - W2$ vs. $G_{\rm BP} - G_{\rm RP}$ vs. M_G and the comparison between the spectroscopic and estimated [Fe/H] values for the 3919 test stars are plotted in Fig. 2.5 (bottom panels) and the pairs plot of the coefficients regarding this model is shown in Fig. 2.6. For this colour–colour–magnitude diagram, 201 stars (5.1 %) are more than 2σ above or below the spectroscopic value. The statistics of the residuals regarding the three calibrations displayed in Fig. 2.5 are shown in Table 2.5.

2.3.4 Comparison with previous photometric estimations

We compared our results with previous photometric estimates from the literature (B05: Bonfils et al. 2005 [Eq. 1], JA09: Johnson & Apps 2009 [Eq. 1], N12: Neves et al. 2012 [Eq. 3], M13: Mann et al. 2013 [Eq. 29], DD19: Davenport & Dorn-Wallenstein 2019 [`ingot`], R21: Rains et al. 2021 [Eq. 2]). To do this, we used the stellar sample of FGK+M binary systems presented by Montes et al. (2018). We did not compare with Schlaufman & Laughlin (2010) and Johnson et al. (2012) because updated versions of their calibrations are in N12 and M13, respectively. We did not compare either with Schmidt et al. (2016), Hejazi et al. (2015) and Medan et al. (2021) since less than the 50 % of the M companions presented in Montes et al. (2018) have a counterpart in the SDSS catalog, nor with Dittmann et al. (2016) which requires the MEarth photometry.

Table 2.4: Fit parameters of colour–colour–magnitude diagram calibrations[a]

Z (mag)	a (dex)	b ($\mathrm{mag^{-1}}$)	c ($\mathrm{mag^{-1}}$)	d ($\mathrm{mag^{-1}}$)	e ($\mathrm{mag^{-2}}$)	f ($\mathrm{mag^{-2}}$)	σ (dex)	ν	$\mathrm{elppd_{LOO\text{-}CV}}$	$\Delta\mathrm{elppd_{LOO\text{-}CV}}$
M_G	5.87 ± 0.44	-1.40 ± 0.12	5.08 ± 0.24	-2.45 ± 0.14	-0.788 ± 0.052	0.1094 ± 0.0071	0.0691 ± 0.0032	5.43 ± 1.19	3961 ± 59	0
M_{K_s}	2.70 ± 0.27	-1.39 ± 0.12	2.82 ± 0.15	-1.99 ± 0.11	-0.392 ± 0.034	0.1355 ± 0.0090	0.0677 ± 0.0032	4.82 ± 0.93	3864 ± 61	-97 ± 20
M_J	4.42 ± 0.37	-1.54 ± 0.12	3.23 ± 0.17	-2.34 ± 0.14	-0.472 ± 0.037	0.1442 ± 0.0097	0.0697 ± 0.0034	5.37 ± 1.19	3859 ± 60	-102 ± 15
M_H	2.42 ± 0.27	-1.42 ± 0.13	3.01 ± 0.16	-1.90 ± 0.11	-0.430 ± 0.036	0.1248 ± 0.0087	0.0686 ± 0.0033	4.86 ± 0.95	3839 ± 60	-121 ± 18

[a] The polynomial fits follow the expression $[\mathrm{Fe/H}] = a + bX + cY + dZ + eY^2 + fZ^2$, where $X = W1 - W2$, $Y = G_{\rm BP} - G_{\rm RP}$, and Z is the corresponding absolute magnitude.

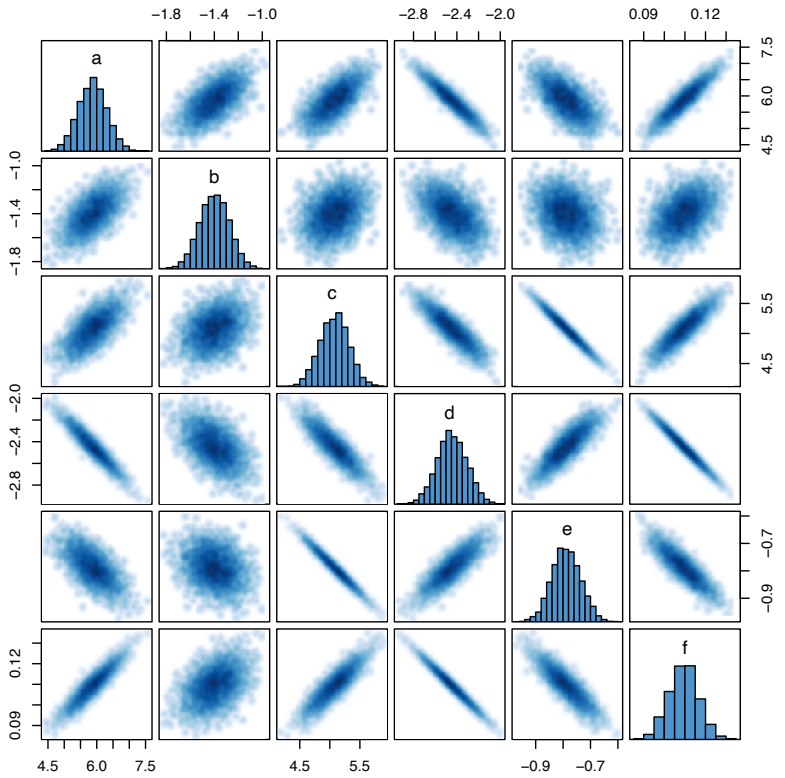

Figure 2.6: Pairs plot of the coefficients of our best model: $W1 - W2$ vs. $G_{\rm BP} - G_{\rm RP}$ vs. M_G.

Table 2.5: Statistics[a] of the residuals of the best colour–colour, colour–magnitude, and colour–colour–magnitude calibrations

	$\overline{x}$	$\tilde{x}$	σ_x	MAD(x)
$W1 - W2$ vs. $G_{\rm BP} - G_{\rm RP}$	0.003	−0.004	0.112	0.103
$G_{\rm BP} - G_{\rm RP}$ vs. M_G	0.012	−0.006	0.095	0.072
$W1 - W2$ vs. $G_{\rm BP} - G_{\rm RP}$ vs. M_G	0.009	−0.006	0.089	0.075

[a] Mean ($\overline{x}$), median ($\tilde{x}$), standard deviation (σ_x), and median absolute deviation (MAD(x)).

In Fig. 2.7 we represent the spectroscopic metallicity values of the primary stars reported by Montes et al. (2018) versus the photometric estimates for the M-dwarf companions using the best accurate colour–colour–magnitude calibration. The open circles represent the 115 stars and the filled circles the 46 stars that remain after applying the criteria described in Sect. 2.2 (i.e. stars with good-quality data). Qualitatively, our estimations and the ones from R21 for the 46 stars follow the 1:1 relationship with less dispersion than the estimated values from previous studies.

For a more quantitative comparison, we studied the distributions of the differences between the primary's $[{\rm Fe/H}]_{\rm spec}$ and the secondary's $[{\rm Fe/H}]_{\rm phot}$. The histograms of these distributions are plotted in Fig. 2.8, while some statistics are compiled in Table 2.6, along with the Pearson's and Spearman's correlation coefficients for the spectroscopic and photometric metallicity values. Our metallicity estimations and their uncertainties, shown for the 46 M dwarfs in Table A.1, are quantitatively less biased and have less dispersion and a greater correlation than those from previous studies. Our calibration can also be used even when some of the filtering criteria are not met, obtaining a distribution that, despite having outliers, is not biased and reproduces reasonably well the metallicity values.

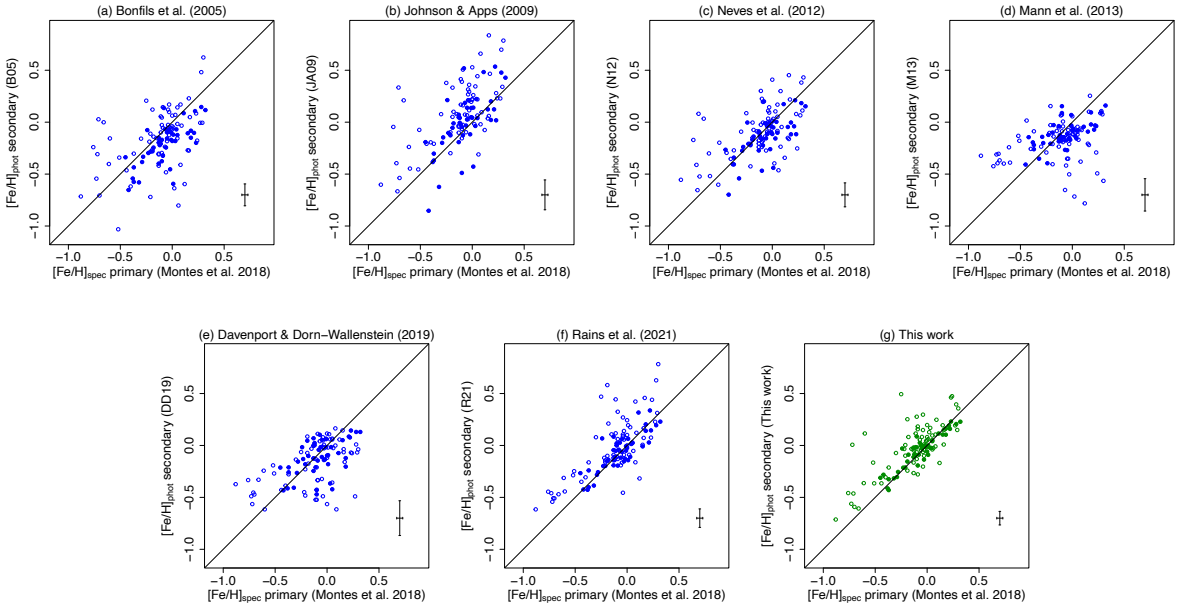

Figure 2.7: Comparison between the spectroscopic metallicity of the the FGK-type primary stars measured by Montes et al. (2018) and the photometric metallicity estimated by B05, JA09, N12, M13, DD19, R21 (blue), and by us (green) using the best accurate colour–colour–magnitude calibration from Table 2.4 of the 46 secondary M dwarfs of Sect. 2.2. The open circles represent the 115 stars and the filled circles the 46 stars with good photometric and astrometric data. The solid line denotes the 1:1 relationship. The error bars show the mean spectroscopic uncertainty and the MAD of the differences between the metallicities of each of the literature methods and the spectroscopic values.

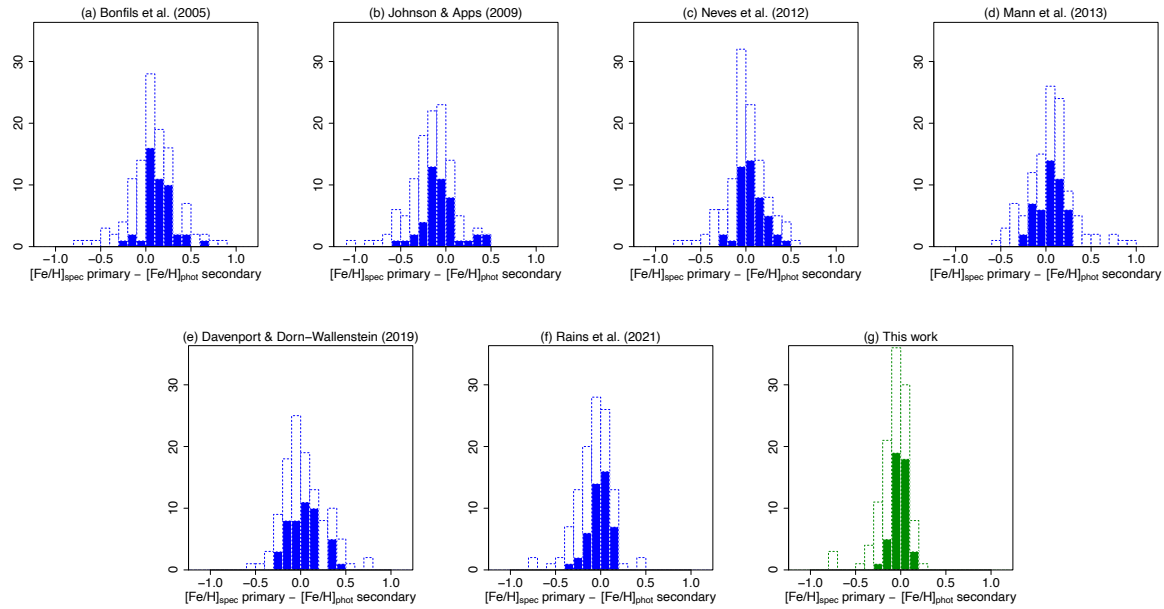

Figure 2.8: Same as Fig. 2.7 but for the distributions of the difference between primary's $[Fe/H]_{spec}$ and solid and dashed histograms instead of solid and open circles.

Table 2.6: Statistics[a] of the differences between primary's $[Fe/H]_{spec}$ and secondary's $[Fe/H]_{phot}$

	$\overline{x}$	$\tilde{x}$	σ_x	MAD(x)	r	r_S
B05	0.144	0.111	0.147	0.105	0.71	0.67
JA09	−0.064	−0.086	0.206	0.144	0.69	0.66
N12	0.071	0.039	0.149	0.115	0.69	0.66
M13	0.043	0.063	0.144	0.156	0.65	0.64
DD19	0.047	0.056	0.176	0.167	0.53	0.52
R21	−0.007	0.001	0.105	0.089	0.84	0.78
This work	−0.012	−0.004	0.087	0.081	0.90	0.83

[a] Mean ($\overline{x}$), median ($\tilde{x}$), standard deviation (σ_x), median absolute deviation (MAD(x)), and Pearson 's (r) and Spearman's (r_S) correlation coefficients.

In Fig. 2.9 we compared all the photometric estimations for the metallicity of M-dwarf companions. We found that the calibrations by B05, JA09 and N12 are highly correlated, since they are based on the same color–magnitude diagram. We also noted that our estimations show a good consistency with the ones by R21.

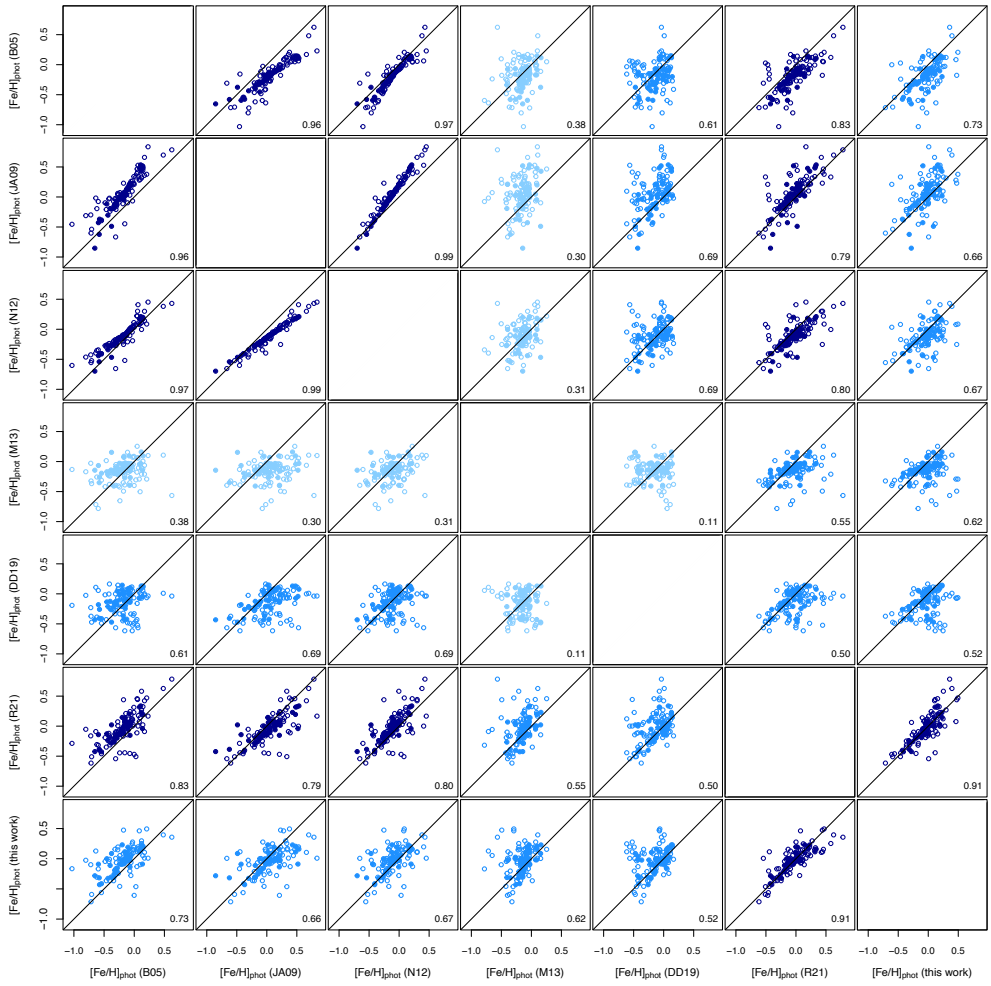

Figure 2.9: Comparison between the different photometric estimations for the metallicity of the M-dwarf companions. The panels are colour-coded by the correlation coefficient r given in the bottom right corner (dark blue: $r \geq 0.75$; blue: $0.50 \leq r < 0.75$; light blue: $r < 0.50$).

2.4 Summary

In the work presented in this chapter, we studied the photometric estimations of metallicity for M dwarfs. The precision, accuracy, and homogeneity of both astrometry and photometry from Gaia DR3, complemented by near- and mid-IR photometry from 2MASS and CatWISE2020, allowed us to study different calibrations based on colour–colour and colour–magnitude diagrams. In order to obtain the best quality for calibrations, we filtered our data and removed multiple stars, lower surface gravity stars or with low photometric or astrometric quality.

Using the sample presented by B20, we derived several photometric calibrations using MCMC methods with `Stan`. We studied the metallicity gradient shown in colour–colour and colour–magnitude diagrams in order to estimate the metallicity of early and mid M dwarfs (down to M5.0 V). We compared the predictive performance of the different calibrations with the LOO-CV criterion, and combined the information in a three-dimensional colour–colour–magnitude diagram. We obtained an improvement when adding an absolute magnitude as a third variable to the optical-IR colour–colour diagrams.

Finally, we compared our most accurate calibration with other photometric metallicity estimations found in the literature (B05, JA09, N12, M13, DD19, and R21) for an additional sample of M-dwarf common proper motion companions to FGK-type primary stars with well-defined spectroscopic metallicities (Montes et al., 2018). Our metallicity estimations are not significantly biased and have a lower dispersion than those of previous photometric studies. Our most accurate calibration is given by:

$$[\mathrm{Fe/H}] = a + bX + cY + dZ + eY^2 + fZ^2, \tag{2.4}$$

where $X = W1 - W2$, $Y = G_{\mathrm{BP}} - G_{\mathrm{RP}}$, $Z = M_G$, and a, b, c, d, e, and f are the parameters provided in the first row of Table 2.4. A code in GitHub[1] and a shinyapp[2] are provided to facilitate the calculation of the metallicity estimations and their uncertainties (Duque-Arribas, 2022).

The Bayesian approach leads to an improvement due to several factors, among which are the objective determination of the terms to be included in the calibrations based on the application of an information criterion such as the LOO-CV, the inclusion of errors in the variables, and the implementation of a robust approach adopting a t-Student likelihood instead of the Gaussian one used in the frequentist analysis. Furthermore, the improvement of our calibration may also be due to the use of the colour index $W1 - W2$. Some of the previous calibrations did not include this colour index, but relied on indices that included instead the visual magnitude V, which has been shown to perform poorly in M-dwarf analyses (see Cifuentes et al. 2020).

This work can be extended in several ways. More passbands from different surveys can be used, mainly in the optical and near-IR, such as SDSS, J-PLUS, and J-PAS (Cenarro et al., 2019) from the ground or EUCLID (Laureijs et al., 2011) from space. Furthermore, the calibrations can be extended to late M dwarfs using other star samples, which would allow the obtaining of a complete understanding of the photometric estimations of metallicity for these cool stars.

In the next chapter, we explore another state-of-the-art methodology to extract the metallicity of M dwarfs from photometric data.

[1] `https://github.com/chrduque/metamorphosis.git`
[2] `https://chrduque.shinyapps.io/metamorphosis`

CHAPTER 3

Photometric metallicities of M dwarfs: a neural network approach

"With four parameters I can fit an elephant and with five I can make him wiggle his trunk."
— John von Neumann, cited by Enrico Fermi

The content of this chapter has been adapted from the article *A neural network approach to determining photometric metallicities of M-type dwarf stars*, published in Astronomy & Astrophysics (C. Duque-Arribas, H. M. Tabernero, D. Montes, et al. 2025, A&A, 698, L12).

3.1 Introduction

In the previous chapter, we demonstrated the potential of photometric surveys for estimating the metallicity of M-type dwarf stars using a Bayesian linear regression framework.

We now introduce a novel method for estimating photometric metallicities of M dwarfs using artificial neural networks (ANNs). The literature knows several ANNs that were applied to astrophysical studies, including the determination of stellar parameters from the Sloan Digital Sky Survey–III APOGEE spectra (Fabbro et al., 2018), from CARMENES spectra (Passegger et al., 2020; Bello-García et al., 2023; Mas-Buitrago et al., 2024), or from the *Gaia* Radial Velocity Spectrograph (RVS) data from DR3 (Manteiga et al., 2025), evolutionary states of red giants from asteroseismology (Hon et al., 2017), star-galaxy classification (Kim & Brunner, 2017), and a stellar spectral classification (Kheirdastan & Bazarghan, 2016). Relatively few studies have explored the use of ANNs for deriving photometric metallicities, however. Whitten et al. (2019) estimated effective temperatures and metallicities for stars hotter than $T_{\rm eff} > 4500\,\mathrm{K}$ using J-PLUS photometry (Javalambre-Photometric Local Universe Survey; Cenarro et al. 2019). Fallows & Sanders (2022) estimated metallicities of red giant stars from *Gaia* EDR3 (Gaia Collaboration et al., 2016, 2021a) and the 2MASS (Skrutskie et al., 2006) and WISE (Wright et al., 2010) surveys, and Molina-Jorquera et al. (2024) relied on S-PLUS photometry (Southern Photometric Local Universe Survey; Mendes de Oliveira et al. 2019) to classify giant and dwarf stars and to determine the metallicity of red giants. Finally, Ferreira Lopes et al. (2025) estimated the stellar parameters for about five million stars from S-PLUS multiband photometry, although the authors indicated that the results for stars with $T_{\rm eff} < 4000\,\mathrm{K}$ should be interpreted with caution.

Despite these advancements, no study to date has specifically focused on applying ANNs to estimate photometric metallicities for M dwarfs as a standalone population. We present an ANN that we used to estimate the metallicity of M-type dwarf stars based on their visible and infrared photometry.

3.2 Methodology

3.2.1 Data and preprocessing

The proposed approach was carried out on the same stellar sample used in Chapter 2. This is, we made use of the final sample of 4919 M dwarfs described in Section 2.2.2.

This sample was then randomly divided into three subsets: 60% for training, 20% for validation, and 20% for testing, that is, 2951, 984 and 984 stars, respectively. The first subset was used to train the ANN, the second subset to estimate its accuracy and tune the hyperparameters, and the third subset to test the ANN.

Following the same approach of the previous chapter, we evaluated the predictive performance of the ANN using a separate dataset of FGK+M binary systems from Montes et al. (2018). The primary stars have well-determined stellar atmospheric parameters derived from high-resolution spectroscopy with the equivalent width method (Tabernero et al., 2019), and it is reasonable to assume that the M-dwarf companions share the same chemical composition (Desidera et al., 2006; Andrews et al., 2018). In this case we had 115 stars, 46 of them with good-quality data.

3.2.2 ANN architecture

We employed the `Keras`[1] API, which operates on the `TensorFlow`[2] framework, to build our model. Hyperparameter optimization, in our case, for the number of hidden layers, the number of neurons per layer, and the learning rate, was performed using the `RandomizedSearchCV` class from the `scikit-learn`[3] library. This approach efficiently explores the hyperparameter space by sampling it randomly, allowing for the identification of near-optimal configurations in less time compared to exhaustive methods, such as the grid search. The optimization process used a k-fold cross-validation, with four folds in our implementation, and it evaluated the model based on a modified mean squared error (MSE) as the loss metric.

The modification of the MSE was included to mitigate the overabundance of solar-metallicity stars in the sample, as noted by Fallows & Sanders (2022). Otherwise, the ANN might inadvertently interpret this imbalance as a trend in the data, which would lead to biased predictions. To counteract this, we included a weighting factor $W = 4 \times |[\mathrm{Fe/H}]| + 0.5$ as a linear multiplier on the MSE. This weighting reduced the influence of the stars with $[\mathrm{Fe/H}] \approx 0$ while it linearly increased the effect for objects with higher or lower metallicities. This ensured a more balanced contribution throughout the entire metallicity range. We tested alternative weighting strategies, including quadratic and exponential functions, but found that they did not improve the results. The linear form was chosen for its simplicity and effectiveness. The specific coefficients were determined empirically: The slope ensured a gradual yet sufficient increase in weight as the metallicity deviated from solar, while the intercept of 0.5 prevented complete suppression of the most abundant metallicities. This balance was found to stabilize training and improve model generalization, in particular, for stars at the extremes of our metallicity range.

The architecture of the neural network was chosen based on the empirical performance during the hyperparameter tuning. We explored a range of configurations that are summarised in Table 3.1. Our final architecture, with two hidden layers of 64 neurons each, consistently achieved the lowest validation loss without signs of overfitting. Simpler architectures showed higher

[1] https://keras.io/about/
[2] https://www.tensorflow.org/
[3] https://scikit-learn.org/stable/

Table 3.1: Summary of the tested ANN hyperparameters.

Hyperparameter	Explored values
Number of hidden layers	1, 2, 3, 4, 5
Neurons per layer	8, 16, 32, 64, 128, 256
Learning rate	reciprocal($1{\cdot}10^{-4}$, $1{\cdot}10^{-2}$)
Dropout rate	0.1, 0.2, 0.3, 0.4, 0.5

validation errors, while more complex architectures offered no additional performance gain and occasionally led to overfitting.

The input layer incorporated eight features, each corresponding to an absolute magnitude using the *Gaia* parallaxes: $M_{G_{\rm BP}}$, M_G, and $M_{G_{\rm RP}}$ from *Gaia*, M_J, M_H, and $M_{K_{\rm S}}$ from 2MASS, and M_{W1}, and M_{W2} from CatWISE2020. The hidden layers, fully connected, contained 64 neurons per layer. The output layer consisted of a single neuron for regression. The network was trained using the Adam optimizer (a stochastic gradient descent method; Kingma & Ba 2017) with a learning rate of $2 \cdot 10^{-4}$. For the learning rate, we sampled values from a reciprocal (log-uniform) distribution in the range $[1{\cdot}10^{-4}, 1{\cdot}10^{-2}]$, as this approach gives greater weight to lower values, which are more likely to yield stable convergence during training. A schematic representation of the neural network is displayed in Fig. 3.1.

The neurons in the input and hidden layers incorporated linear activation functions, whereas the output layer adopted a hyperbolic tangent (tanh) activation function. This choice constrained the predictions to the range $(-1, +1)$ dex. Because the training sample spans a narrower metallicity range (-0.45 to $+0.45$) dex, this activation ensured that predictions remained bounded within a safe interval during training. It also implies a limitation, however: The model is not suited for extrapolating beyond the training range. For stars with true metallicities outside this domain, the output will saturate toward ± 1, reflecting the asymptotic behaviour of the tanh function.

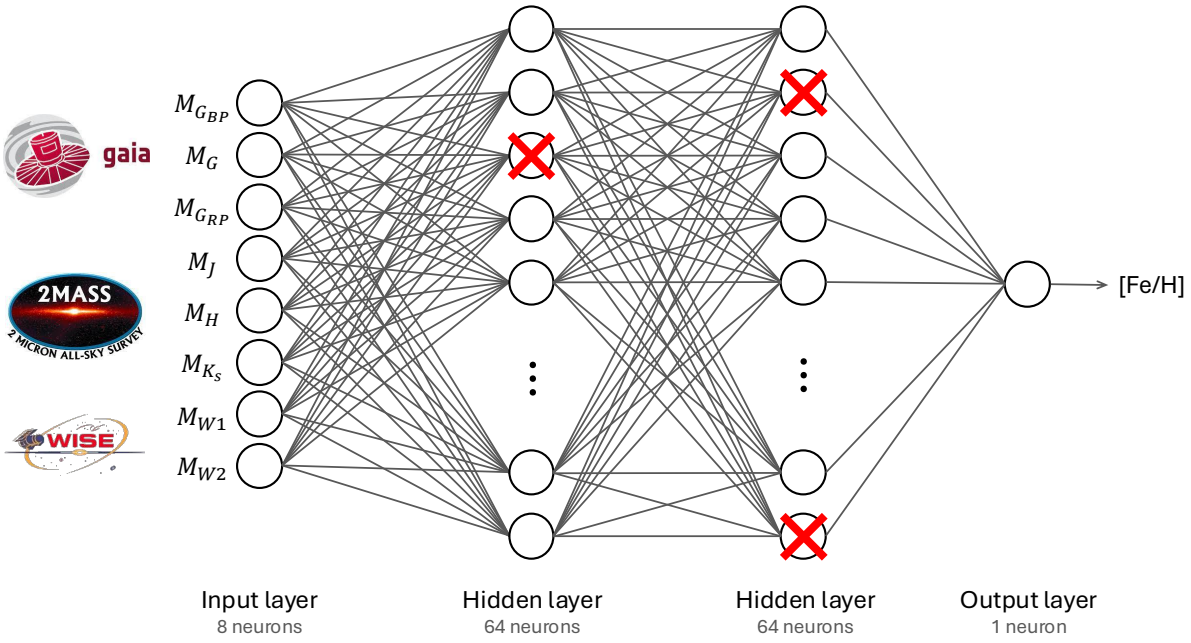

Figure 3.1: Schematic representation of our ANN architecture. The red crosses indicate dropout neurons.

These predictions should not be interpreted as accurate estimates, but rather as an indication that the input is outside the reliable operating range of the model.

We also incorporated batch normalisation after the input and hidden layers. This technique normalises activations during training, stabilising and accelerating convergence by mitigating internal covariate shifts (Ioffe & Szegedy, 2015). Additionally, dropout was implemented after the hidden layers, with the dropout rate included as a tunable hyperparameter. This technique is discussed in greater detail in the following subsection.

3.2.3 Monte Carlo dropout

Dropout is one of the most popular regularisation techniques for neural networks that aims at mitigating overfitting during the training stage by randomly dropping a fraction of the neurons (Hinton et al., 2012; Srivastava et al., 2014). During every training step, each neuron has a certain probability that is included as a tuneable hyperparameter of being ignored but being active during the next step. By applying this technique, the ANN learns as a cohesive unit and avoids over-reliance on any particular neuron. We applied dropout to the layers of our neural network and set the dropout rate at 20%.

In the classical dropout, neurons are no longer dropped after the training stage. Gal & Ghahramani (2016) introduced a technique called Monte Carlo (MC) dropout, however, which enhances the performance of a trained dropout model and provides a more accurate measure of the model uncertainty. This is achieved by ensuring that the dropout layers remain active after the training, which produces a distribution of predictions instead of a single estimate. Averaging over these multiple predictions with dropout provides a Monte Carlo estimate that is more reliable than a single prediction. Gal & Ghahramani (2016) also established a deep connection between dropout networks and the approximate Bayesian inference.

3.3 Results and discussion

After training the ANN and optimising its hyperparameters using the training and validation datasets, we evaluated its performance on the test sample. As outlined in the previous section, we applied MC dropout to generate 100 stochastic forward passes per star. This provided more robust estimates and an uncertainty measure for these predictions. We also generated 500 samples, but the predictions did not change.

In Fig. 3.2 we compare the spectroscopic metallicity values reported by Birky et al. (2020) and the photometric metallicity predictions generated by our ANN for the test subsample, colour-coded by $G_{\mathrm{BP}} - G_{\mathrm{RP}}$, which is a proxy for the stellar effective temperature (Cifuentes et al., 2020). Most of the estimated metallicities closely align with the one-to-one relation. This indicates the reliability of the model. Furthermore, as expected, no significant correlation is observed between the predicted metallicities and effective temperature. The prediction residuals exhibit a standard deviation of 0.08 dex, which is compatible with the values reported in Chapter 2 using a Bayesian approach.

In Fig. 3.3 we present the colour–magnitude diagram for the test subsample, colour-coded by metallicity estimates from our ANN. The diagram shows the clear recovery of the expected metallicity gradient along the main sequence. This alignment underscores the ability of the ANN to capture and reproduce well-known trends in stellar populations. For a detailed discussion of metallicity gradients in the colour–colour and colour–magnitude diagrams, we refer to Chapter 2.

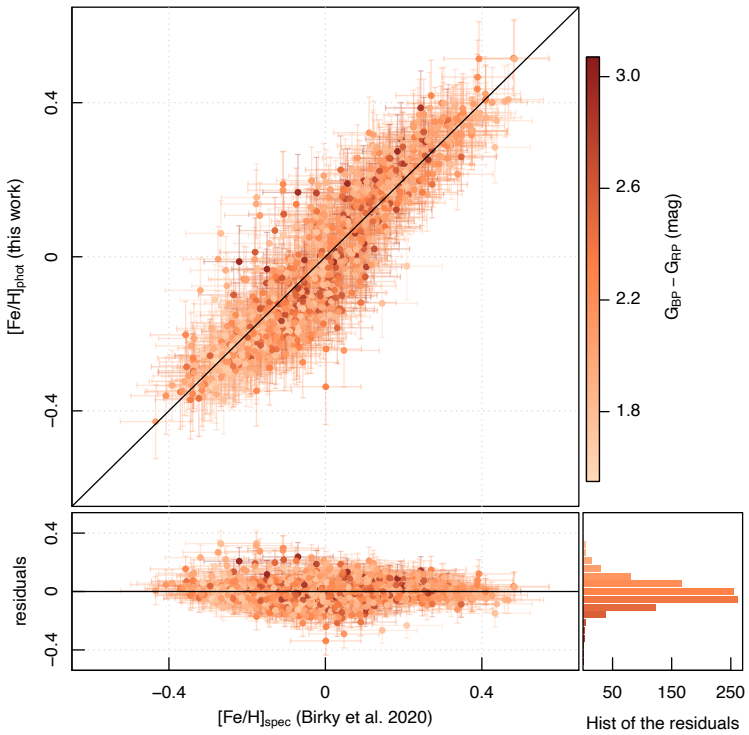

Figure 3.2: Comparison between spectroscopic metallicities reported by Birky et al. (2020) and photometric estimates by our ANN. The 984 stars from the test sample and their corresponding residuals are color-coded by $G_{\rm BP} - G_{\rm RP}$ color (darker symbols show cooler stars, and lighter symbols show warmer stars). The solid lines denote the 1:1 relation, and the residuals are zero. In the bottom right corner we represent the histogram of the residuals.

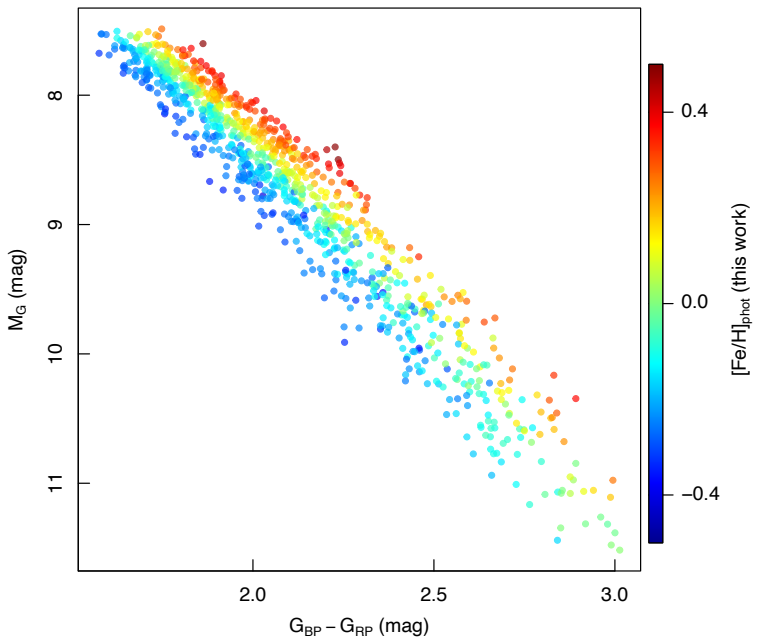

Figure 3.3: Color-magnitude diagram of the 984 stars from the test sample, color-coded by the metallicity estimates provided by our ANN.

Finally, as an additional test, we applied our ANN to the M-dwarf secondaries in wide binary systems reported by Montes et al. (2018). In Fig. 3.4 we compare the spectroscopic metallicities of the primary stars reported by Montes et al. (2018) and the photometrically estimated values for the M-dwarf companions using our ANN. The statistics of the residuals between the spectroscopic and photometric metallicities for the 46 stars with good-quality data, obtained with previous photometric studies found in the literature and with our ANN, are reported in Table 3.2. We achieved a strong correlation between photometric and spectroscopic metallicities of the M dwarfs compared with these previous results, as illustrated by Fig. 3.5.

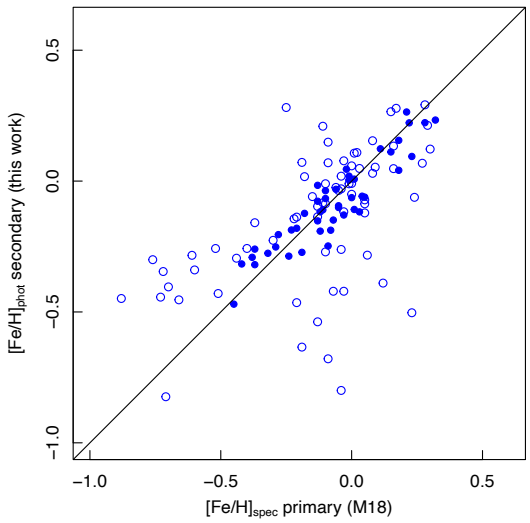

Figure 3.4: Comparison between spectroscopic metallicity of the FGK-type primary stars measured by Montes et al. (2018) and the photometric metallicity estimated for the M-dwarf companions by this work using an ANN. The filled circles represent the 46 good-quality subsample.

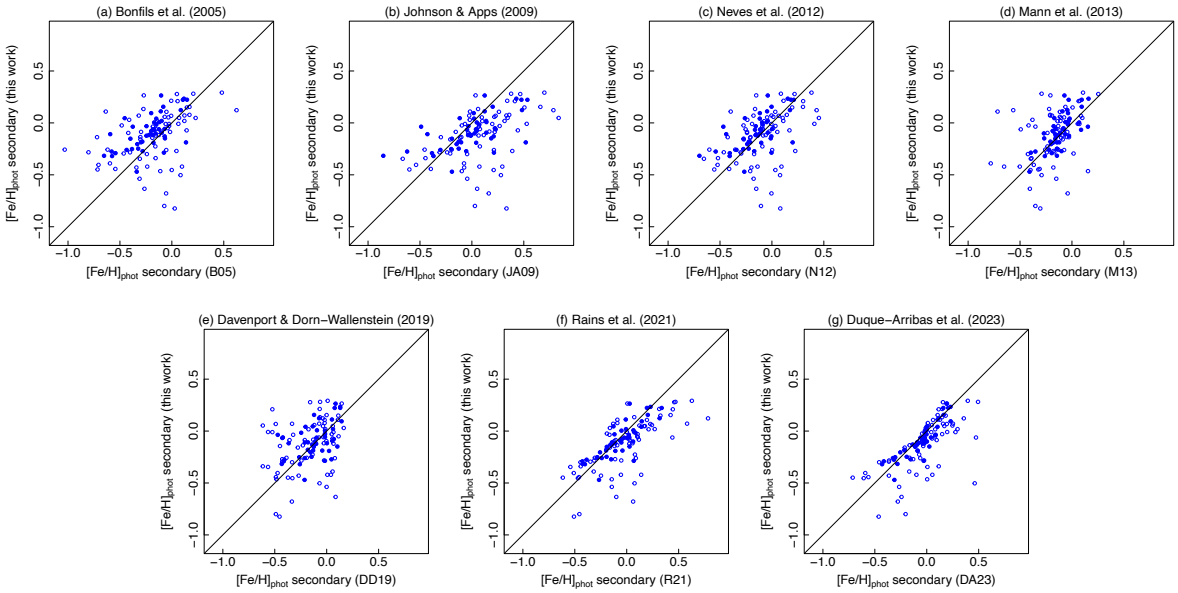

Figure 3.5: Same as Fig. 3.4, but for the photometric metallicities estimated by Bonfils et al. (2005), Johnson & Apps (2009), Neves et al. (2012), Mann et al. (2013), Davenport & Dorn-Wallenstein (2019), Rains et al. (2021), and Duque-Arribas et al. (2023).

Table 3.2: Statistics[a] of the differences between the primary $[Fe/H]_{spec}$ and the secondary $[Fe/H]_{phot}$.

	$\overline{x}$	$\tilde{x}$	σ_x	MAD(x)	r	r_S
B05	+0.144	+0.111	0.147	0.105	0.71	0.67
JA09	−0.064	−0.086	0.206	0.144	0.69	0.66
N12	+0.071	+0.039	0.149	0.115	0.69	0.66
M13	+0.043	+0.063	0.144	0.156	0.65	0.64
DD19	+0.047	+0.056	0.176	0.167	0.53	0.52
R21	−0.007	+0.001	0.105	0.089	0.84	0.78
DA23	−0.012	−0.004	0.087	0.081	0.90	0.83
This work	+0.015	+0.001	0.082	0.075	0.92	0.88

[a] Mean ($\overline{x}$), median ($\tilde{x}$), standard deviation (σ_x), median absolute deviation (MAD(x)), and Pearson 's (r) and Spearman's (r_S) correlation coefficients, where $x = [Fe/H]_{spec} - [Fe/H]_{phot}$ in dex.

Among the most recent studies, both Rains et al. (2021) and Duque-Arribas et al. (2023), i.e. the results from Chapter 2, employed polynomial fits to the main sequence to estimate the photometric metallicities of M dwarfs. The model by Rains et al. (2021) relied on *Gaia* and 2MASS photometry alone and omitted the W1−W2 colour index, which is a known metallicity-sensitive feature (Schmidt et al., 2016). This omission likely contributes to its slightly larger dispersion compared to our Bayesian model in Chapter 2 and the present work. The results of this chapter are similar to those presented in the previous chapter, as expected because both studies used the same underlying dataset. The modest improvement achieved here can probably be attributed to the greater flexibility of the ANN relative to the polynomial fitting approach.

3.4 Comparison of Bayesian and neural network approaches

The methodologies presented in Chapters 2 and 3 both aim to estimate the metallicity of M-type dwarf stars using photometric data from large-scale surveys. However, they represent fundamentally different paradigms in statistical modelling, each with distinct advantages and limitations.

The Bayesian regression approach of Chapter 2 relies on physically interpretable, low-order polynomial relationships between photometry and [Fe/H]. It allows for a transparent treatment of uncertainty and facilitates model comparison through the leave-one-out cross-validation (LOO-CV) score. The posterior distributions over model parameters offer insight into the influence of individual features, and the analytical structure of the model makes it suitable for applications where interpretability and uncertainty quantification are critical.

In contrast, the neural network model presented in Chapter 3 offers superior flexibility, capable of capturing nonlinear and higher-order interactions that are difficult to model analytically with polynomials. Although it lacks the interpretability of traditional regression models, the network demonstrates slightly improved predictive performance on both the training and validation samples. Moreover, the use of Monte Carlo dropout allows for a Bayesian-like approximation to the posterior predictive distribution, enabling uncertainty estimates even within a deep learning framework.

Despite their differences, both models demonstrate strong agreement when tested on an independent sample of M dwarfs in wide binaries. The residuals with respect to the metallicities inferred from the FGK primaries remain low, and no significant systematic offsets are observed

(see Fig. 3.5 and Table 3.2). This consistency suggests that both techniques are viable for studies of M-dwarf metallicities, especially in the absence of high-resolution spectroscopic data.

Looking ahead, a promising avenue would be to unify the strengths of both approaches through Bayesian neural networks. These models place distributions over the weights of the network and provide a fully probabilistic treatment of uncertainty. While computationally more demanding, recent advances in variational inference and scalable approximate Bayesian methods make Bayesian neural networks increasingly practical (see e.g. Blundell et al., 2015; Wang & Yeung, 2016; Maddox et al., 2019; Goan & Fookes, 2020). Such models could deliver the expressive power of deep learning together with the rigorous uncertainty quantification characteristic of Bayesian methods, representing a compelling direction for future research in photometric stellar parameter estimation.

3.5 Summary

We presented a machine-learning framework for estimating the photometric metallicities of M dwarfs, for which we exploited the capabilities of ANNs combined with the accuracy and homogeneity of the visible and infrared photometry from the *Gaia* DR3, 2MASS, and CatWISE surveys. By employing robust techniques such as weighting adjustments in the loss function to mitigate the effects of sample imbalances, MC dropout for the uncertainty estimation, and hyperparameter optimisation, we demonstrated that our ANN with two hidden layers can achieve highly accurate and reliable predictions.

We trained the model with the sample presented by Birky et al. (2020). Its performance on the test sample showed a mean residual of 0.00 ± 0.08 dex. Additionally, the results confirmed that the predicted metallicities closely match spectroscopic values and exhibit no correlation with the effective temperature. This validated the ability of the model to generalise without introducing biases. The validation on an independent dataset of 46 M dwarfs in FGK+M binary systems from Montes et al. (2018) further reinforced the predictive accuracy of the ANN and underscored its versatility when applied to new data. These results agree well with those presented in Chapter 2 using a Bayesian linear regression approach.

This ANN-based approach provides a scalable and efficient alternative for processing large photometric datasets. Its ability to infer stellar metallicities using only broadband photometry significantly reduces the reliance on time-intensive spectroscopic observations. This framework can be extended to incorporate additional features or input data to enhance the accuracy and applicability of the predictions. Furthermore, the model could be adapted to other stellar types or parameter determinations, which would broaden its applicability in stellar astrophysics. The Python code is publicly available at GitHub[4].

In summary, this work highlights the potential of machine learning, particularly ANNs, in advancing our ability to determine the stellar metallicity efficiently and accurately. It paves the way for transformative applications in the era of large-scale astronomical surveys.

[4] https://github.com/chrduque/metamorphosis-NN.git

CHAPTER 4

Carbon, oxygen, and odd-Z iron-peak abundances of F-, G-, and K-primaries in wide binary systems

"The cosmos is within us. We are made of star-stuff. We are a way for the universe to know itself."
— Carl Sagan

The content of this chapter has been adapted from the article *Calibrating the metallicity of M dwarfs in wide physical binaries with F-, G-, and K-primaries – II: Carbon, oxygen, and odd-Z iron-peak abundances of the primary stars*, published in Monthly Notices of the Royal Astronomical Society (C. Duque-Arribas, H. M. Tabernero, D. Montes, et al. 2024, MNRAS, 528, 3028).

4.1 Introduction

In Chapters 2 and 3 we introduced a first approximation to the metallicities of M dwarfs based on photometric data. However, spectroscopy remains the most powerful technique for studying stellar properties in greater detail. Since M-dwarf spectra are complex and notoriously difficult to model due to the presence of prominent molecular features, in comparison to those of solar-type stars (e.g. Allard et al., 2000; Passegger et al., 2018; Marfil et al., 2021), several studies have investigated M-dwarf metallicities using wide physical binary systems formed by a F-, G-, or K-primary star and a M-dwarf companion (e.g. Woolf & Wallerstein, 2006; Bean et al., 2006; Rojas-Ayala et al., 2010; Terrien et al., 2012; Mann et al., 2013, 2014; Newton et al., 2014; Montes et al., 2018; Ishikawa et al., 2020; Souto et al., 2020, 2022; Qiu et al., 2024; Behmard et al., 2025b). These binary systems provide an excellent opportunity to test not only the metallicities of the M dwarfs with those for their warmer primaries, but also the chemical abundances for individual atomic species.

In the first paper of the series *Calibrating the metallicity of M dwarfs in wide physical binaries with F-, G-, and K-primaries* (Montes et al., 2018), we established a sample of 192 wide physically-bound systems, derived precise stellar atmospheric parameters ($T_{\rm eff}$, $\log g$, ξ, and chemical abundances for 13 atomic species) for the primary stars using the equivalent width (EW) method and high-resolution spectra, under the local thermodynamic equilibrium (LTE) assumption, and performed a kinematic analysis, classifying the stars in different Galactic populations and stellar kinematic groups. In the work presented in this chapter, we update the abundances of scandium (Sc), vanadium (V), manganese (Mn) and cobalt (Co) taking into account hyperfine structure (HFS) and non-local thermodynamic equilibrium (NLTE) effects, and determine new abundances for carbon (C) and oxygen (O). The LTE approximation simplifies

energy distribution through particle collisions, but it becomes less accurate close to the stellar surface, where the radiation field deviates from being local, isotropic, and Planckian (Steenbock & Holweger, 1984; Rutten, 1988; Thévenin & Idiart, 1999). Additionally, interactions between electron and nuclear spins of species with non-zero nuclear spin cause energy states to split, resulting in multiple components in the absorption line of the corresponding transition (Abt, 1952; Kurucz, 1993; Jofré et al., 2017; Heiter et al., 2021).

Oxygen and carbon are, after H and He, the most abundant chemical elements in the Universe. Carbon plays a role in dust formation processes in the interstellar medium (Leger & Puget, 1984; Weingartner & Draine, 2001; Draine & Li, 2007), contributes significantly to the stellar interior and atmospheric opacity (Burrows et al., 1997; Baraffe et al., 1998; Meynet & Maeder, 2002), and it is an essential element for life as we know it, being important in searching for biomarkers in habitable exoplanets (Des Marais et al., 2002; Scalo et al., 2007; Seager & Deming, 2010). Furthermore, the oxygen abundance is used to map the chemical enrichment and star formation history of stellar populations in the Milky Way and to infer the metallicities from the H II regions (Tolstoy et al., 2009; Moustakas et al., 2010). The studies of C and O abundances have become more and more popular in recent years in the context of determining the composition of terrestrial exoplanets. Theoretical models predict that carbon-to-oxygen and magnesium-to-silicon ratios (C/O and Mg/Si) may provide information about the structure and composition of planets; the C/O ratio controls the distribution of Si among carbide and oxide species, while Mg/Si determines the silicate mineralogy (Larimer, 1975; Bond et al., 2010; Suárez-Andrés et al., 2018; Tabernero et al., 2024). Recent studies suggest that elemental abundance ratios may differ when studied in host stars and in planetary atmospheres: some ratios such as Mg/Si and Fe/Si show similar values, but larger differences are found for C/O due to the dependence of the distance for volatile elements (Carter-Bond et al., 2012; Marboeuf et al., 2014; Thiabaud et al., 2015).

On the other hand, iron-peak elements, i.e. elements in the periodic table from Sc to Ge, are synthesised in thermonuclear explosions of supernovae and in Si-burning during explosive burning of core-collapse supernovae (Kobayashi, 2016). However, the stellar yields of these elements are under debate (Kobayashi et al., 2020). In particular, the accurate determination of the abundances for odd-Z iron peak elements (Sc, V, Mn, and Co) require non-local thermodynamic equilibrium modelling of spectral lines taking into account the hyperfine structure splitting. These elements are relevant in several astrophysical analysis. For instance, manganese is fundamental in stellar population and nucleosynthesis studies to constrain the physics of SNe Ia (Seitenzahl et al., 2013). Cobalt is an interesting element in regard to the galactic chemical evolution, but there are disagreements about the overall abundance trend of Co in the halo and disc and about its nucleosynthesis production (Bergemann et al., 2010). Additionally, scandium holds significance in comprehending Am and Fm stars, which exhibit an overabundance of iron-peak elements but a deficiency in scandium and calcium.

4.2 Analysis

4.2.1 Stellar sample

The sample used in this work was presented in Montes et al. (2018) and consists of 192 binary systems made of late-F, G-, or early-K primaries and late-K or M dwarf companion candidates. We carried out observations with the HERMES spectrograph (Raskin et al., 2011) at the 1.2 m Mercator Telescope at the Observatorio del Roque de los Muchachos (La Palma, Spain) and obtained high-resolution spectra for 196 FGK-type stars. These spectra were analysed with the

automatic code StePar[1] (Tabernero et al., 2019), which relies on the equivalent width method, to derive precise stellar atmospheric parameters (effective temperature $T_{\rm eff}$, surface gravity $\log g$, microturbulence velocity ξ and iron abundance [Fe/H]) for 179 stars. However, we were not able to determine the stellar parameters of the rest stars due to factors such as double-line spectroscopic binaries, fast-rotating stars, too hot stars ($T_{\rm eff} > 6700\,{\rm K}$) for not having enough iron lines, and too cool stars ($T_{\rm eff} < 4500\,{\rm K}$) with too many overlapping iron lines.

We re-analised the proper motions and parallaxes of these systems using *Gaia* DR3 (Gaia Collaboration et al., 2023) in order to discard optical (non-physical) pairs. We cross-matched our primary stars (observed with HERMES) and our M-dwarf companions (observed with CAFOS) with the latest Gaia data release, obtaining accurate parallaxes and proper motions. With these data, we apply the same criteria as in Montes et al. (2018) to distinguish between physical (bound) and optical (unbound) systems (see Fig. 4.1). To do that, we computed two parameters for each pair of stars: the μ ratio, defined as:

$$(\mu \text{ ratio})^2 = \frac{(\mu_\alpha \cos\delta_1 - \mu_\alpha \cos\delta_2)^2 + (\mu_{\delta_1} + \mu_{\delta_2})^2}{(\mu_\alpha \cos\delta_1)^2 + (\mu_{\delta_1})^2} \tag{4.1}$$

and the proper motion position angle difference:

$$\Delta{\rm PA} = |{\rm PA}_1 - {\rm PA}_2|, \tag{4.2}$$

where ${\rm PA}_i$ is the angle between $\mu_\alpha \cos\delta_i$ and μ_{δ_i}, being $i = 1$ for the primary star and $i = 2$ for the companion candidate. As in Montes et al. (2018), we established the limits in the pairs that have μ ratio > 0.15 and/or proper motion position angle difference $\Delta{\rm PA} > 15\,{\rm deg}$. The systems that do not fulfill these requirements are plotted in red in Fig. 4.1 and compiled in Table 4.1. The system WDS 15282-0921 (G9 V + K2 V + M4.5) presents a $\Delta{\rm PA} < 15\,{\rm deg}$ and $0.15 < \mu$ ratio < 0.25. As discussed in Montes et al. (2018), it is a very wide pair ($\rho > 1200$ arcsec) affected by high proper motion projection effect; see Caballero (2009) for a discussion on

[1] https://github.com/hmtabernero/StePar

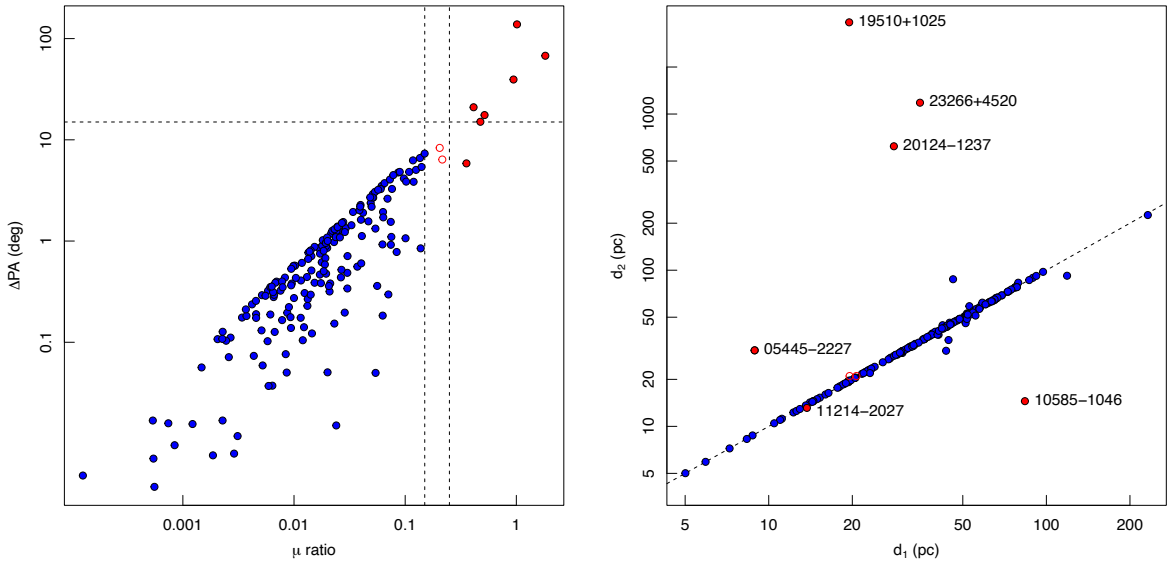

Figure 4.1: Left panel: ΔPA vs. μ ratio diagram, indicating the physical (blue), doubtful (red open circles), and optical (red filled circles) systems attending to the criteria of Montes et al. (2018). Dashed vertical and horizontal lines denote the 0.15 and 0.25 *mu* ratio and 15 deg ΔPA. Right panel: heliocentric distances for primary and secondary stars, indicating the 1:1 relationship.

Table 4.1: Binary systems with non-physical M-dwarf companions.

WDS	Name	SpT	Obs.[a]	$\mu_\alpha \cos\delta$ (mas yr^{-1})	μ_δ (mas yr^{-1})	d (pc)	Remarks
05445-2227	γ Lep	F6 V	H	-291.757 ± 0.087	-368.52 ± 0.13	8.905 ± 0.012	
	AK Lep	K2 V	H	-304.905 ± 0.013	-352.606 ± 0.019	8.8916 ± 0.0018	physical pair
	vB 1	M3.5 V	C	-253.353 ± 0.010	-588.407 ± 0.016	30.677 ± 0.014	no common μ, d
10585-1046	BD-10 3166	K0 V	H	-184.695 ± 0.019	-8.175 ± 0.016	83.70 ± 0.12	
	LP 731-76	M5.0V	C	-192.999 ± 0.041	-83.965 ± 0.033	14.5007 ± 0.0079	no common μ, d
11214-2027	SZ Crt	K7 V	H	174.02 ± 0.35	-79.43 ± 0.25	13.724 ± 0.061	RUWE = 18.145
	HD 98712 B	M2.5 V	C	220.400 ± 0.030	-129.231 ± 0.019	13.1248 ± 0.0046	no common μ
15282-0921	HD 137763	G9 V	H	73.58 ± 1.15	-475.35 ± 1.01	19.55 ± 0.28	
	HD 137778	K2 V	H	82.532 ± 0.028	-356.698 ± 0.022	20.685 ± 0.012	high μ projection effect
	GJ 586 C	M4.5	C	25.376 ± 0.032	-308.377 ± 0.024	21.005 ± 0.014	high μ projection effect
19510+1025	o Aql A	F8 V	H	241.713 ± 0.087	-136.695 ± 0.064	19.488 ± 0.034	
	'o Aql B'	M0.0 V	C	-0.633 ± 0.019	-5.032 ± 0.016	3865 ± 294	no common μ, d
	o Aql C	M3.5 V	C	263.941 ± 0.041	-116.171 ± 0.032	19.465 ± 0.015	physical pair
20124-1237	ξ Cap	F7 V	H	193.111 ± 0.039	-195.622 ± 0.023	28.234 ± 0.028	
	BD-13 5608B	K5 V	C	1.874 ± 0.014	-20.577 ± 0.010	621.7 ± 5.5	no common μ, d
	LP 754-50	M0 V	···	192.657 ± 0.017	-194.040 ± 0.012	28.222 ± 0.015	physical pair
23266+4520	HD 220821	G0 V+	H	437.963 ± 0.053	107.188 ± 0.051	35.060 ± 0.090	
	J23263798+4521054	M III	C	-4.630 ± 0.019	-6.759 ± 0.018	1182 ± 37	no common μ, d
	BD+44 4419B	M4.5	···	432.28 ± 0.37	115.93 ± 0.38	35.63 ± 0.64	physical pair

[a] Stars observed with HERMES (H) or CAFOS (C).

very wide physical pairs. We also compared the distances of primaries and companions using the parallaxes given by Gaia DR3 (right panel of Fig. 4.1).

The system WDS 05445-2227 comprises two physical components, but the M dwarf is just an optical unbound companion. The system WDS 10585-1046 is not a physical pair. Regarding the primary star in the WDS 11214-2027 system, there is a slight difference in proper motion between Gaia DR2 and DR3, and a significantly larger RUWE value of 18.15, which could suggest that the source is either nonsingle or problematic for the astrometric solution. Moreover, this is a near system ($d \sim 13.4$ pc) with small separation ($\rho = 4$ arcsec), which may impact the final proper motion values. As for the systems WDS 19510+1025, 20124-1237, and 23266+4520, they have M-dwarf companions observed with CAFOS, but none of them are physical pairs. However, there are other M-dwarf physical companions in those systems, with the first one already observed with CAFOS and the latter two remaining unobserved.

Therefore, we derived reliable spectroscopic stellar parameters for 174 primaries and 5 companions. For additional details on the basic properties of the studied systems and stellar parameters, please see Appendix B in Montes et al. (2018). In Fig. 4.2 we show a colour–magnitude diagram of the primary and secondary stars in our sample.

4.2.2 Abundances, HFS effects, and NLTE corrections

To derive the carbon and oxygen abundances, we use the same line list as Tabernero et al. (2021b), that is, C I lines at 5052.17, 5380.34, and 6587.61 Å and the O I infrared triplet lines at 7771.9, 7774.2 and 7775.4 Å. These C I lines can be perfectly described in LTE. On the other hand, the O I triplet, typically strong in solar-type stars and located in a spectral region free from other blending lines, is significantly affected by NLTE (Kiselman, 1993; Asplund et al., 2009; Amarsi et al., 2015). In Fig. 4.3 we show these C I and O I spectral lines in five representative primaries, all of them with solar metallicity but covering different spectral types. We can see that the lines become very weak for the cooler stars, and the C I λ5380 Å line may present an unknown blend for $T_{\rm eff} < 5200$ K (Delgado Mena et al., 2021).

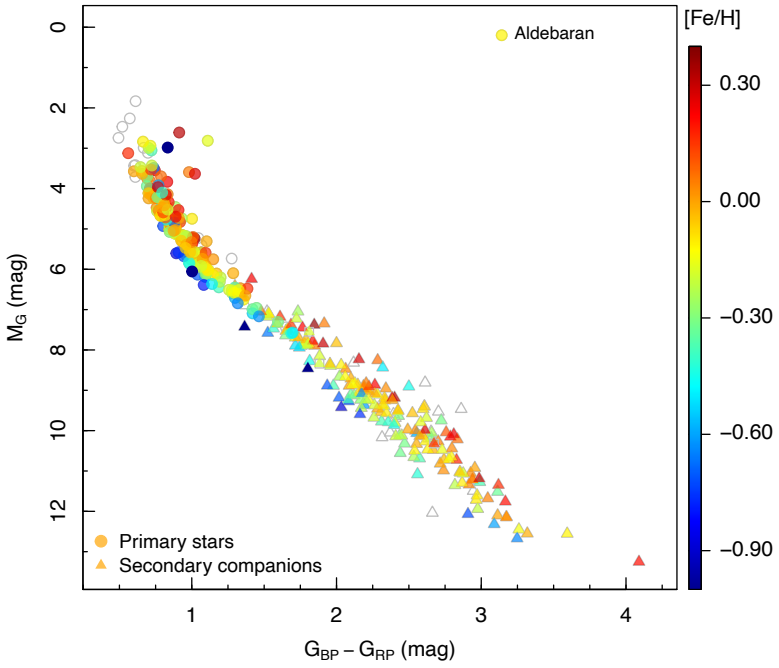

Figure 4.2: Colour–magnitude diagram of the primary and secondary stars in our sample using *Gaia* DR3 data, colour-coded by primaries' [Fe/H]. Open data symbols are stars in systems whose primary is without derived stellar parameters.

The line list used for the Sc, V, Mn, and Co abundances is the same as in Montes et al. (2018). Table 4.2 lists the atomic data for the lines analysed, retrieved from the Vienna Atomic Line Database (VALD3, Ryabchikova et al. 2015).

In order to calculate the required abundances, we assumed the stellar parameters derived with StePar in Montes et al. (2018) and used the *EW* method, a grid of MARCS stellar atmospheric models (Gustafsson et al., 2008), and the 2019 version of the code MOOG[2] (Sneden, 1973). The *EW* were computed using ARES[3] (Sousa et al., 2015). The final abundances were computed in a differential manner, in a line-by-line basis, with respect to our solar spectrum (using the asteroid Vesta) as in Montes et al. (2018), minimising systematic uncertainties that may arise due to the analysis method and atomic data used. Out of 179 stars with available stellar parameters, we measured C abundances for 161 stars, O abundances for 173 stars, Sc abundances for all 179 stars, V abundances for 176 stars, Mn abundances for all 179 stars, and Co abundances for 178 stars. Since the C I line at 5380.34 Å presents an unkown blend, it was not considered for the final carbon abundance for stars with $T_{\rm eff} < 5200$ K. The solar abundances for each line are listed in Table 4.2.

The odd-Z iron-peak elements Sc, V, Mn, and Co suffer from hyperfine structure, which splits their absorption lines into multiple components (Jofré et al., 2017; Heiter et al., 2021). Shan et al. (2021) showed that the impact of hyperfine structure on certain absorption lines in cool photospheres can be more pronounced compared to Sun-like stars. Therefore, it must be considered in order to derive precise abundances with the *EW* method. In our analysis, we used the 'abfind' driver within MOOG to derive carbon and oxygen abundances. However, to account for the HFS components of Sc, V, Mn, and Co, we used the 'blends' driver, as in several previous studies (see e.g. da Silva et al., 2015; Maldonado et al., 2015, 2020; Biazzo et al., 2015, 2022).

[2] https://www.as.utexas.edu/~chris/moog.html
[3] https://github.com/sousasag/ARES

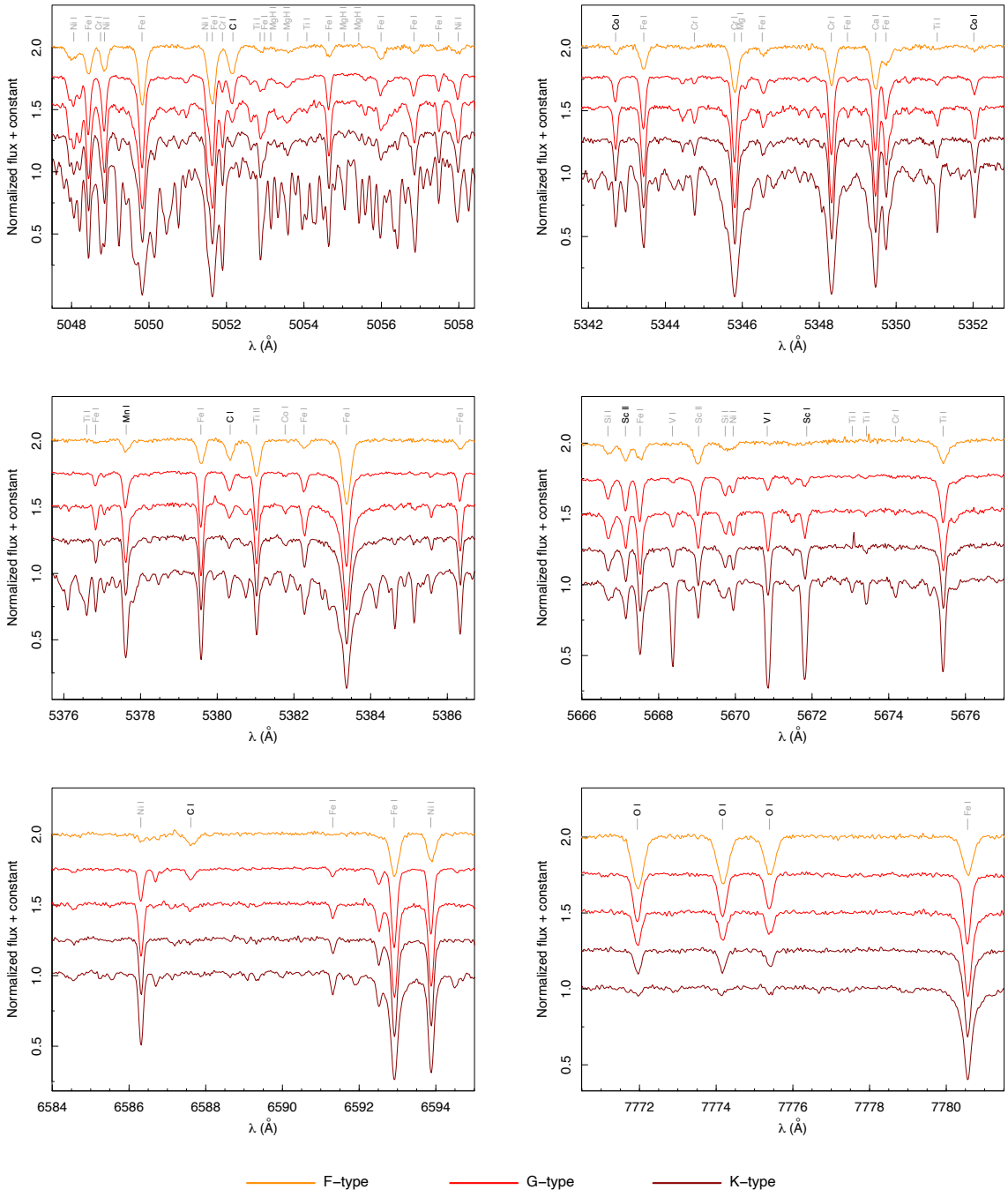

Figure 4.3: High-resolution spectra of five representative primaries from our sample of solar metallicity and different spectral types (*from top to bottom*): HD 35638 (F5 V), HD 43587 (G0 V), HD 82939 (G5 V), BD+68 1345 A (K0 V), and HD 6660 A (K4 V). Each panel shows zoomed ranges near some of the lines investigated.

Table 4.2: Atomic parameters for the lines used with the corresponding solar abundances in LTE, NLTE corrections, and number of HFS components.

Element	λ (Å)	$\log(gf)$	χ_l (eV)	$A(\mathrm{X})^{\mathrm{LTE}}_{\odot}$	NLTE corr.	# HFS comp.
C I	5052.17	−1.304	7.68	8.359	···	···
C I	5380.34	−1.615	7.68	8.429	···	···
C I	6587.61	−1.021	8.54	8.327	···	···
O I	7771.944	0.369	9.15	8.779	−0.081	···
O I	7774.166	0.223	9.15	8.789	−0.070	···
O I	7775.388	0.002	9.15	8.769	−0.052	···
Sc I	5520.519	0.290	1.865	3.321	···	4
Sc I	5671.860	0.500	1.4478	3.037	···	21
Sc II	5526.789	−0.010	1.7682	3.207	···	20
Sc II	5657.886	−0.540	1.5070	3.265	···	13
Sc II	5667.135	−1.210	1.5004	3.248	···	7
Sc II	5684.190	−1.030	1.5070	3.116	···	9
Sc II	6245.621	−1.022	1.5070	3.011	···	15
Sc II	6320.832	−1.816	1.5004	3.059	···	7
V I	5670.831	−0.430	1.0806	4.002	···	21
V I	5737.027	−0.740	1.0636	3.906	···	16
V I	6081.461	−0.610	1.0509	3.901	···	10
V I	6224.520	−2.010	0.2866	4.074	···	21
V I	6251.802	−1.370	0.2866	3.895	···	21
V I	6274.659	−1.700	0.2670	4.005	···	6
V I	6285.162	−1.540	0.2753	3.971	···	12
Mn I	4502.204	−0.345	2.9197	5.347	+0.026	15
Mn I	4671.647	−1.675	2.8884	5.508	+0.030	15
Mn I	4739.072	−0.607	2.9408	5.402	+0.032	10
Mn I	5377.626	−0.166	3.8437	5.344	+0.042	12
Mn I	5399.500	−0.345	3.8530	5.481	+0.039	10
Mn I	5413.697	−0.647	3.8590	5.480	+0.036	6
Co I	4594.669	−0.042	3.6320	4.604	···	21
Co I	4792.854	0.001	3.2524	4.800	+0.111	18
Co I	4813.471	0.120	3.2158	4.849	+0.116	21
Co I	5301.017	−2.000	1.7104	4.953	+0.099	16
Co I	5342.706	0.741	4.0208	4.769	···	21
Co I	5352.020	0.060	3.5764	4.790	···	20
Co I	5359.188	0.244	4.1494	4.736	···	21
Co I	5647.207	−1.560	2.2800	4.883	+0.102	12
Co I	6814.958	−1.900	1.9557	4.774	+0.087	10

Stellar parameters for the Sun are $T_{\mathrm{eff}} = 5777 \pm 18$ K, $\log g = 4.41 \pm 0.05$, and [Fe/H] = 0.0 dex (A(Fe) = 7.48 ± 0.01 dex). References for the NLTE corrections: O – Bergemann et al. (2021); Mn – Bergemann et al. (2019); Co – Bergemann et al. (2010) and Voronov et al. (2022).

Furthermore, some of the O, Mn and Co lines used in the abundance determination are affected by NLTE. Since the MARCS models are based on a standard LTE approximation, the O abundances were later corrected for NLTE effects with the corrections given by Bergemann et al. (2021), the Mn abundances with corrections by Bergemann et al. (2019), and the Co abundances with corrections by Bergemann et al. (2010) and collisional data from Voronov et al. (2022), using the web interface at `http://nlte.mpia.de/`. These corrections are based on the plane-parallel 1D `MAFAGS-OS` model atmosphere code (Grupp, 2004). We display the NLTE corrections against

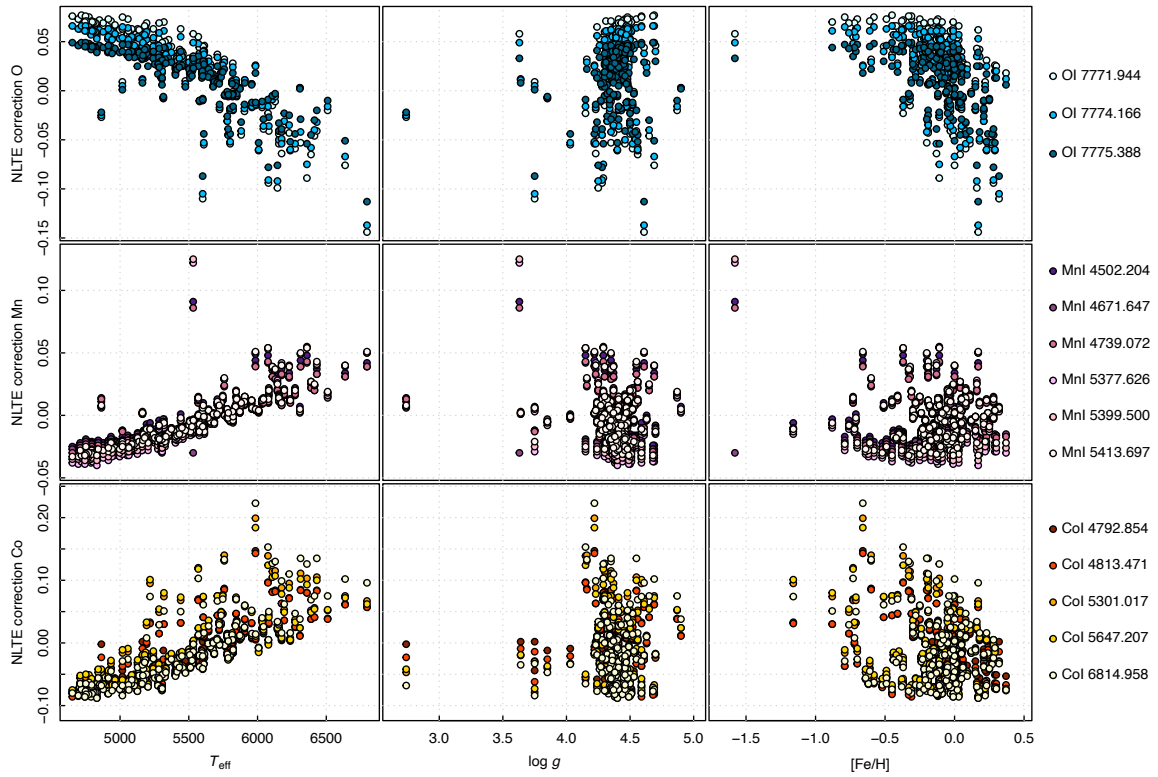

Figure 4.4: NLTE corrections for the O, Mn and Co lines versus de stellar parameters ($T_{\rm eff}$, $\log g$, and [Fe/H]).

the stellar parameters in Fig. 4.4. We found a significant trend with $T_{\rm eff}$, which is positive for Mn and Co NLTE corrections but negative for O NLTE corrections. According to Zhao et al. (2016), Sc only presents large NLTE corrections in the low-metallicity regime ([Fe/H] < -1.5). We also compile the number of HFS components and the NLTE corrections in Table 4.2. The atomic data of the HFS components are compiled in Tables B.2–B.5.

4.2.3 Abundance uncertainties

In Montes et al. (2018), the abundance uncertainties were computed as the scatter of the abundances obtained from each line for the same atomic species. In this work, we proceeded as in Battistini & Bensby (2015) (hereafter BB15), Delgado Mena et al. (2021) (hereafter DM21), and others, taking the uncertainties in the stellar parameters ($T_{\rm eff}$, $\log g$, ξ, and [Fe/H]) also into consideration. The abundance uncertainty due to the errors on stellar parameters were estimated by calculating the abundance differences when one of each of the stellar parameters was modified by its individual error given in Table B.3 of Montes et al. (2018). The final abundance errors are given by the quadratic sum of these individual errors and the line-to-line scatter. The average of these contributions to the total uncertainty for each abundance and spectral type is given in Table 4.3. As the analysis is differential relative to the Sun in a line-by-line basis, systematic errors should be minimised.

Oxygen and carbon can form several molecules, such as the CO, in the atmospheres of late-type stars. Therefore, abundances of O and C are bound via chemical equilibrium. As demonstrated by Pavlenko et al. (2019), the interdependence of these abundances in solar-type stars is negligible, within the errorbars.

Table 4.3: Average of the different contributions to the total abundance uncertainties, analysing the abundance sensitivies to changes of each stellar parameter.

Abundance	Stars	Line-to-line scatter (dex)	$\Delta T_{\rm eff}$ (dex)	Δ[Fe/H] (dex)	$\Delta \log g$ (dex)	$\Delta\xi$ (dex)	Total error (dex)
[C/H]	F-type stars	±0.034	±0.018	±0.001	∓0.026	±0.001	±0.048
	G-type stars	±0.081	±0.023	±0.001	∓0.027	±0.001	±0.092
	K-type stars	±0.111	±0.062	±0.002	∓0.066	±0.001	±0.143
[O/H]	F-type stars	±0.060	±0.024	±0.001	∓0.015	±0.005	±0.073
	G-type stars	±0.073	±0.034	±0.001	∓0.016	±0.003	±0.098
	K-type stars	±0.094	±0.099	±0.001	∓0.056	±0.004	±0.144
[Sc/H]	F-type stars	±0.083	±0.009	±0.004	∓0.023	±0.006	±0.098
	G-type stars	±0.075	±0.008	±0.004	∓0.022	±0.006	±0.089
	K-type stars	±0.133	±0.023	±0.008	∓0.042	±0.018	±0.153
[V/H]	F-type stars	±0.163	±0.031	±0.001	∓0.003	±0.001	±0.173
	G-type stars	±0.065	±0.036	±0.000	∓0.000	±0.002	±0.079
	K-type stars	±0.057	±0.098	±0.001	∓0.010	±0.027	±0.126
[Mn/H]	F-type stars	±0.113	±0.020	±0.001	∓0.001	±0.002	±0.116
	G-type stars	±0.089	±0.020	±0.001	∓0.001	±0.006	±0.095
	K-type stars	±0.097	±0.034	±0.006	∓0.006	±0.018	±0.107
[Co/H]	F-type stars	±0.066	±0.023	±0.001	∓0.000	±0.001	±0.077
	G-type stars	±0.056	±0.016	±0.002	∓0.009	±0.003	±0.061
	K-type stars	±0.074	±0.012	±0.008	∓0.038	±0.011	±0.087

4.2.4 Solar abundances

Since our analysis is differential relative to the Sun in a line-by-line basis, we also derived the abundances for the Sun, obtaining $A(\mathrm{C})_\odot = 8.372 \pm 0.052$ dex, $A(\mathrm{O})_\odot = 8.711 \pm 0.012$ dex, $A(\mathrm{Sc})_\odot = 3.158 \pm 0.118$ dex, $A(\mathrm{V})_\odot = 3.965 \pm 0.070$ dex, $A(\mathrm{Mn})_\odot = 5.427 \pm 0.073$ dex, and $A(\mathrm{Co})_\odot = 4.795 \pm 0.099$ dex. The comparison between our solar abundances and the ones from the literature is shown in Fig. 4.5. The differences may be due to the use of different line lists, and the assumptions made, such us LTE, 1D models, etc.

4.3 Results and discussion

4.3.1 Carbon and oxygen abundances

We display the distributions of [C/Fe], [O/Fe], and [C/O] as a function of metallicity in left panels of Fig. 4.6. Previous papers (e.g. Bertran de Lis et al. 2015, DM21) have set the limit for reliable abundances of C and O at 5200 K; for stars below this effective temperature, abundances provided by different lines start to disagree. In Fig. 4.6 we distinguish stars with $T_{\rm eff} < 5200$ K as open circles, and note that most of the outliers belong to this category. Our analysis revealed increasing [C/Fe] and [O/Fe] ratios with decreasing [Fe/H], while the [C/O] ratio increase towards higher metallicities. Moreover, adopting the Galactic populations derived in Montes et al. (2018) from the Galactocentric space velocities (see Montes et al. 2001; Bensby et al. 2003, 2005), namely halo, thick disc, thick-to-thin transition disc, and thin disc, we observed that thick disc stars present higher [C/Fe] and [O/Fe] values than thin disc stars in the common metallicity interval. Furthermore, we overplot (with orange lines) the GCE models from Kobayashi et al. (2020) (hereafter K20 model), which assumed failed supernovae (SNe) for stars with initial masses higher

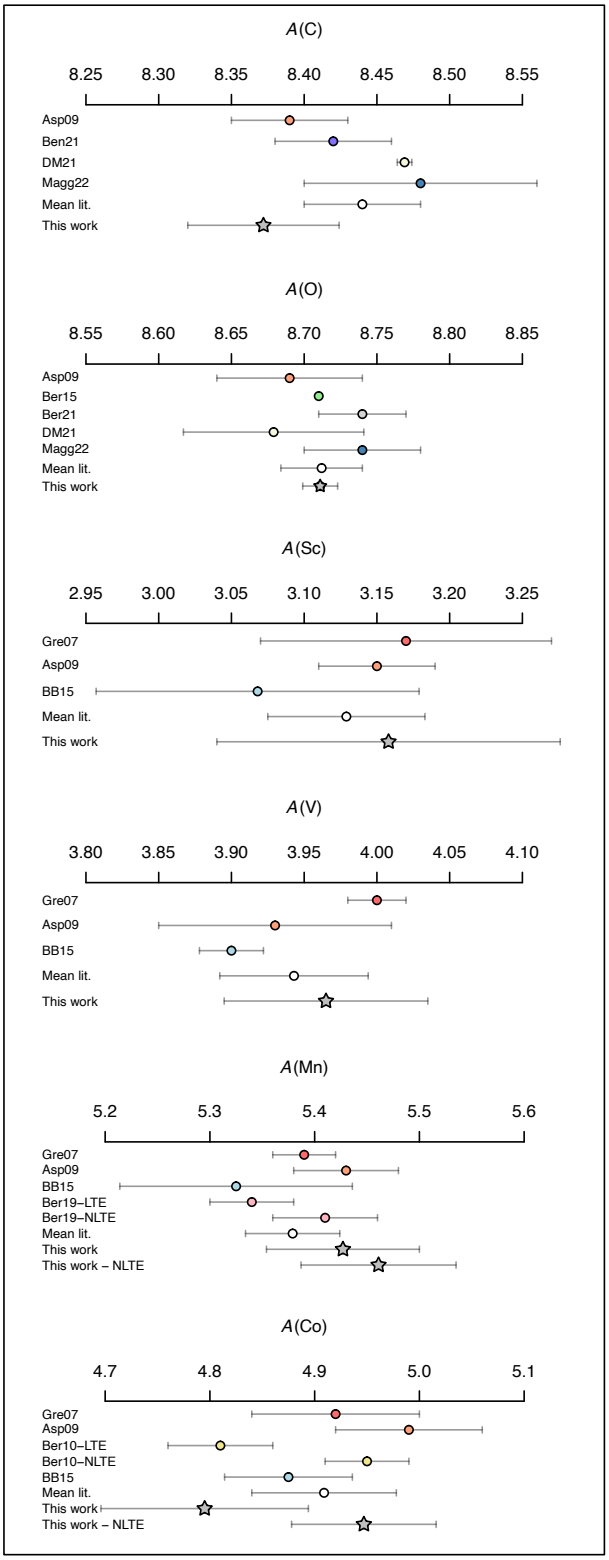

Figure 4.5: Comparison for our solar abundances (gray stars) with the literature: Grevesse et al. (2007) (Gre07 – red), Asplund et al. (2009) (Asp09 – orange), Bergemann et al. (2010) (Ber10 – yellow), Bertran de Lis et al. (2015) (Ber15 – green), Battistini & Bensby (2015) (BB15 – blue), Bergemann et al. (2019) (Ber19 – pink), Bensby et al. (2021) (Ben21 – purple), Bergemann et al. (2021) (Ber21 – light gray), Delgado Mena et al. (2021) (DM21 – beige), Magg et al. (2022) (Magg22 – dark blue), and the mean value from the literature (Mean lit. – white).

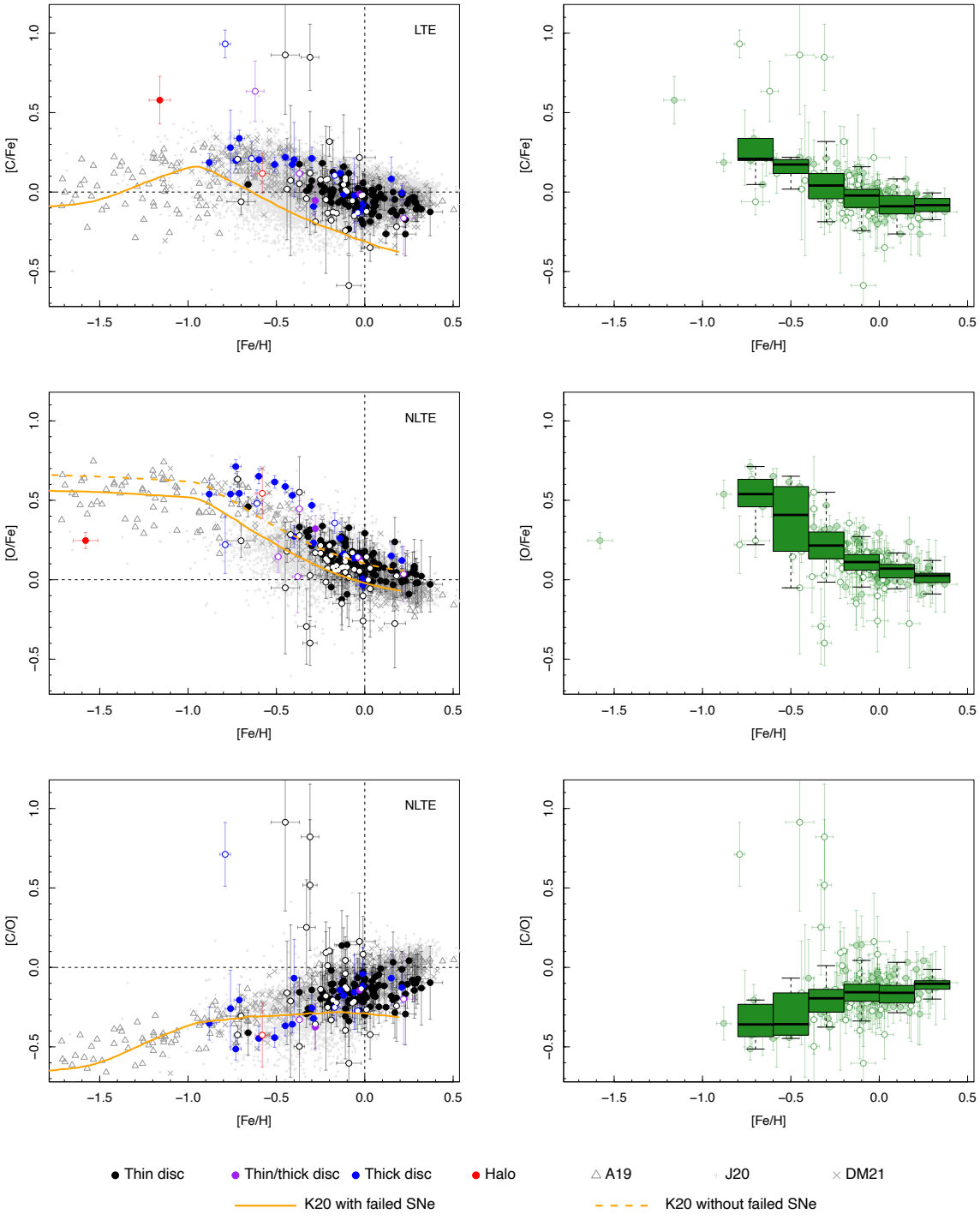

Figure 4.6: Left panels: Abundance ratios of [C/Fe], [O/Fe], and [C/O] versus [Fe/H], in comparison with Amarsi et al. (2019) (A19) using the 1D/NLTE results, Jönsson et al. (2020) (J20), and DM21. Colours for different populations: black – thin disc, blue – thick disc, purple – thin/thick disc, red – halo. Open circles: stars with $T_{\rm eff} < 5200\,$K; filled circles: stars with $T_{\rm eff} \geq 5200\,$K. Models of GCE from Kobayashi et al. (2020) with failed SNe at $> 30 M_{\odot}$ (solid orange line) and without failed SNe (dotted orange line) are overplotted. Right panels: Box and whisker plots of [C/Fe], [O/Fe], and [C/O] versus [Fe/H].

than $30 M_{\odot}$. For the [O/Fe] abundance we also included a K20 model without failed SNe. To better examine the trends of these ratios with increasing metallicity, we show box and whisker plots in right panels of Fig. 4.6.

Our findings on the [C/Fe] trend are consistent with previous studies by Delgado Mena et al. (2010, 2021) and Amarsi et al. (2019). Other authors reported similar results (e.g. Takeda & Honda, 2005; Reddy et al., 2006; González Hernández et al., 2010, 2013; Nissen et al., 2014; Buder et al., 2019; Franchini et al., 2020; Stonkutė et al., 2020), showing increasing [C/Fe] ratios with decreasing metallicity down to [Fe/H] ~ -0.8 dex, after which the trend flattens and then decreases for halo stars. Notably, the halo star HD 149414 Aa,Ab exhibits a higher carbon abundance than expected based on the general trend. This overabundance could be attributed to the fact that this star is a single-lined spectroscopic binary (SB1; Latham et al. 2002) with $T_{\rm eff} = 5217 \pm 57$ K, in close proximity to the 5200 K limit.

Several studies have examined the distribution of [O/Fe] over [Fe/H], and found that the [O/Fe] ratio rises with decreasing metallicity, albeit with varying slopes, and reaches a plateau around [Fe/H] $= -0.8$ dex. While some of them found just a shallow decline in the [O/Fe] trend at high metallicities (e.g. Bensby et al., 2004, 2014; Takeda & Honda, 2005; Ramírez et al., 2007; Petigura & Marcy, 2011; Franchini et al., 2021), other studies suggested a flattening at solar or super-solar metallicities (e.g. Bensby et al. 2004; Ramírez et al. 2013; Bertran de Lis et al. 2015, DM21). These differences could be attributed to the use of different oxygen indicators or whether the author included or neglected NLTE effects, inelastic collisions with hydrogen, etc. In this case, the red giant branch star BD+80 245 ([Fe/H] $= -1.58 \pm 0.07$ dex) shows a low O abundance when compared to the Galactic trend. The low metallicity, which implies weak lines, and low signal-to-noise ratio of this star (S/N ~ 60) could explain the underabundance obtained with the EW method. Moreover, we note that the thick-disc stars present higher C and O abundances than the thin-disc stars at equivalent [Fe/H] values.

These results for the [C/Fe] and [O/Fe] trends discussed above are consistent with what it is expected from Galactic chemical evolution. Both [C/Fe] and [O/Fe] decrease with increasing [Fe/H], which reflects the increasing relevance of SNe Ia with time, fueling the increase in iron, relative to SNe II. However, the slopes of both trends are different, with the carbon following iron more closely than oxygen, due to their different production sites. Oxygen is produced by SNe II from massive progenitors (Woosley & Weaver, 1995). Carbon, on the other hand, is produced by synthesis in stellar interiors, then dredged up from cores and released into the interstellar medium by massive stellar winds and radiation pressure (Gustafsson et al., 1999). However, the lower-mass post-AGB stars contribute as well, and their relative importance is still a matter of debate (see Franchini et al., 2020, and references therein). Therefore, the enrichment of carbon is delayed in time with respect to oxygen, explaining the different slopes. As can be seen in Fig. 4.6, our results follow the general trend of the K20 models but, as stated by Kobayashi et al. (2020), the predicted [C/Fe] is ~ 0.1–0.2 dex lower than the observational data, with a steeper decrease for [Fe/H] > -1. However, as shown by Delgado Mena et al. (2021) in their Fig. 3, including the contribution of Wolf–Rayet stars to the carbon production can increase the [C/Fe] abundance (Kobayashi et al. in prep.). In the case of [O/Fe], the model follows the general trend of the observations, but with lower abundances for [Fe/H] > -1 dex. In this case, we also added a K20 model without failed SNe (dashed orange line), which seems to better reproduce our results for [Fe/H] > -1 dex.

In the left panel of Fig. 4.7 we compare the [C/H] and [O/H] ratios for the five stars in common with DM21. DM21 provide the abundances of the O I 6158 and 6300 Å lines independently, hence we represent our O abundances (using the O I infrared triplet) against both results. The abundances of these stars closely correspond to those provided by DM21, especially in the case of carbon abundances, which exhibit a low scatter.

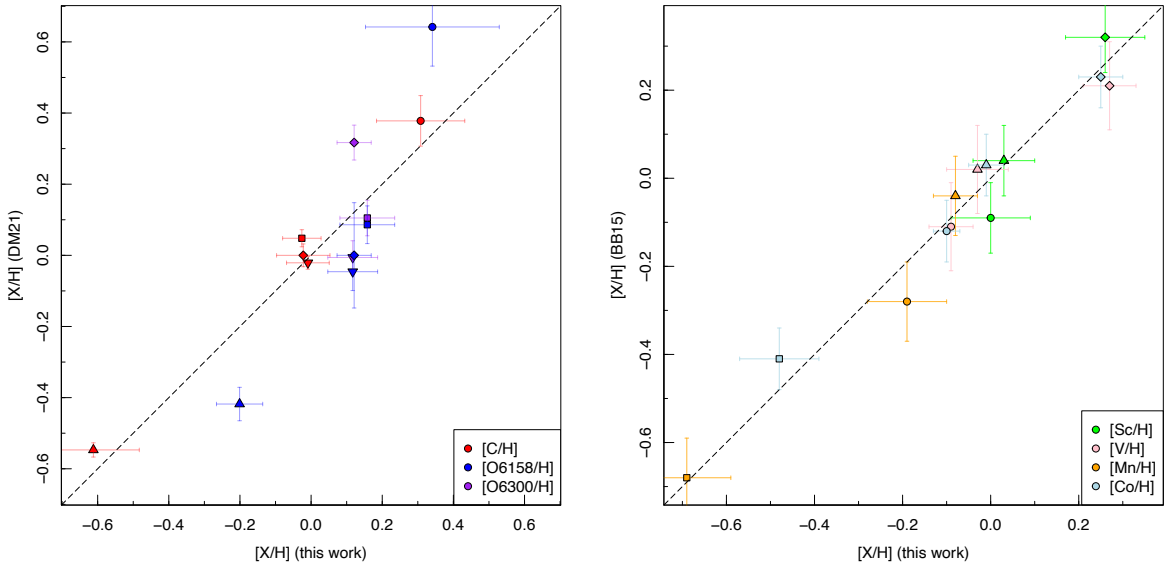

Figure 4.7: Left panel: Comparison between the C and O abundances obtained by DM21 (who reported the O I 6158 and 6300 Å abundances independently), and by this work for the stars in common: HD 8389 A (circle), HD 11964 A (square), HD 40397 A (diamond), HD 59984 (point-up triangle), and HD 222582 A (point-down triangle). Right panel: Comparison between the Sc, V, Mn, and Co abundances by BB15 and by this work, only in LTE, for the stars in common: HD 40397 A (circle), HD 114606 A (square), HD 190360 A (diamond), and HD 222582 A (point-up triangle).

4.3.2 Odd-Z iron-peak abundances

We show the distribution of [X/Fe] ratios for the odd-Z iron-peak elements versus the metallicity in Fig. 4.8, in comparison with the results of BB15. We also overplot in orange a modification of the GCE models from Kobayashi et al. (2011) that includes a hypernova jet effect (dashed line; hereafter K15, see Sneden et al. 2016; Zhao et al. 2016; Kobayashi et al. 2020), and the K20 models (solid line). The [Sc/Fe] vs. [Fe/H] trend behaves like the α-elements, which suggests a common production site, and it is in good agreement with the results by Nissen et al. (2000), Brewer & Carney (2006), Neves et al. (2009), Adibekyan et al. (2012b), Tabernero et al. (2012), and BB15. We observe higher abundances for the thick disc stars in contrast to the thin disc. The K20 model predicts [Sc/Fe] ~ -1 dex for our metallicity range, not visible in our panel. The K15 model provides a better fit to the observations, though it does not show the weak decrease of [Sc/Fe] with increasing metallicity for [Fe/H] > -1 dex. In theoretical models, both Sc and V are consistently found to be underproduced across all metallicity ranges compared to observational data. The abundances of both elements could potentially be influenced by the neutrino process, a factor not accounted for in these GCE models.

The [V/Fe] vs. [Fe/H] trend also emulates an α-element, with solar abundance at [Fe/H] $= 0$ and a rise towards lower metallicities, but with significantly more scatter than the other elements when including the stars with $T_{\rm eff} < 5200$ K. Vanadium is an intricate element that presents biases and higher dispersion for the cooler objects. For this reason, some studies established a cutoff limit around 5300 K (for example, see Neves et al. 2009 and Adibekyan et al. 2012b). The general trend is consistent with Brewer & Carney (2006), Neves et al. (2009), Adibekyan et al. (2012b), Tabernero et al. (2012), and BB15. As in the case of Sc, V is underproduced by the GCE models. The K20 model shows a plateau and a weak decrease toward higher metallicities for [Fe/H] > -1 dex, a similar behaviour that the observations, despite the 0.4–0.5 dex bias.

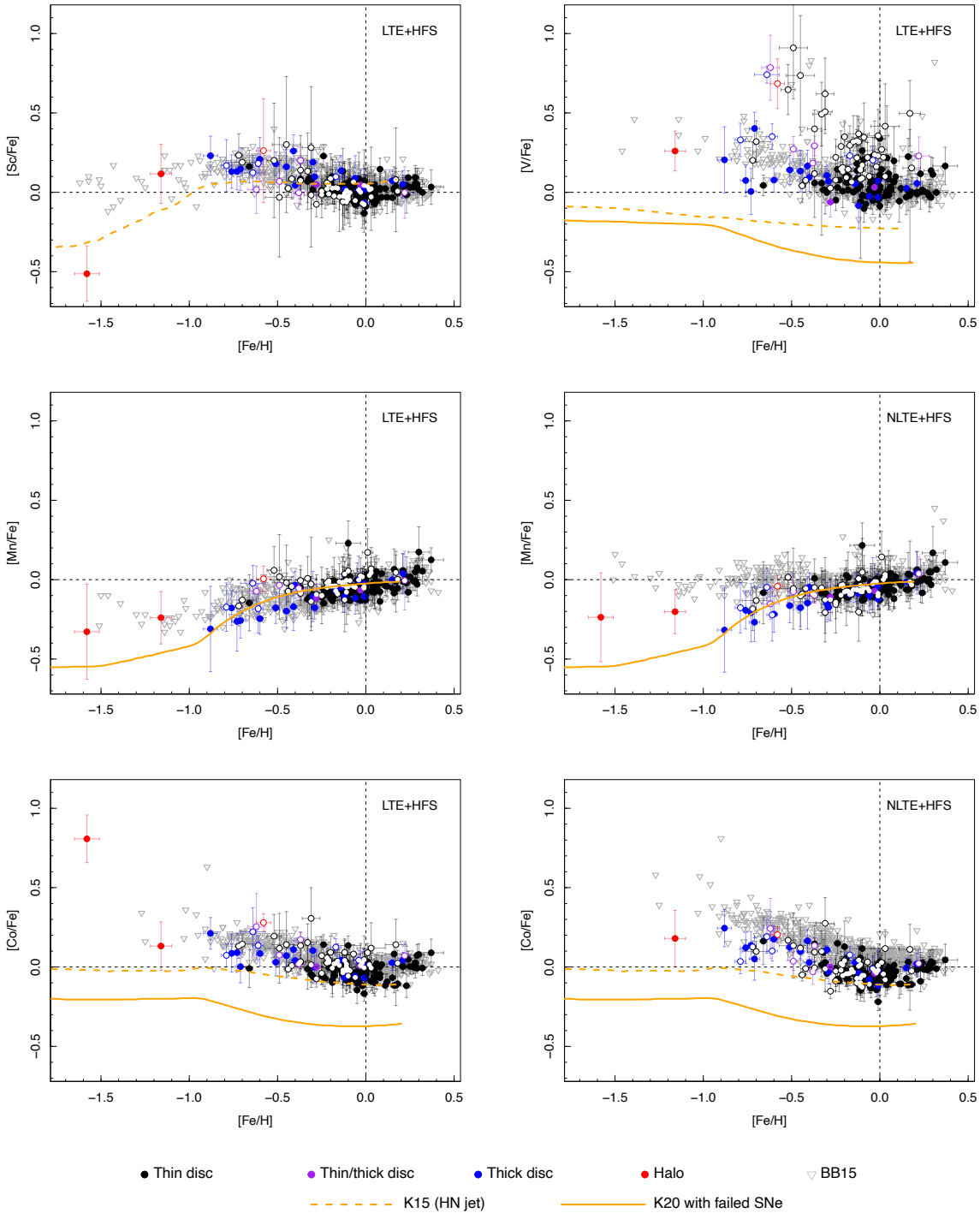

Figure 4.8: Abundance ratios of [Sc/Fe], [V/Fe], [Mn/Fe] (LTE and NLTE), and [Co/Fe] (LTE and NLTE) versus [Fe/H], in comparison with BB15. Colours for different populations: black – thin disc, blue – thick disc, cyan – thin/thick disc, red – halo. Open circles: stars with $T_{\rm eff} < 5200\,{\rm K}$; filled circles: stars with $T_{\rm eff} \geq 5200\,{\rm K}$. Models of GCE from Kobayashi et al. (2011), modified to include a hypernova jet effect (dotted orange line), and from Kobayashi et al. (2020) with failed SNe at $> 30 M_{\odot}$ (solid orange line) are overplotted.

The [Mn/Fe] vs. [Fe/H] trend, assuming LTE, seems to work opposite to an α-element (Gratton, 1989), i.e. it decreases steadily towards lower metallicities and shows sub-solar abundances for all metallicities up to [Fe/H] = 0. This trend can be explained by models in which Mn is produced in SNII at metallicities below [Fe/H] < -1 (Tsujimoto & Shigeyama, 1998), while at [Fe/H] > -1 the increasing [Mn/Fe] ratio with increasing [Fe/H] is due to a contribution from SNIa (Kobayashi, 2016). This trend is in good agreement with the results by Nissen et al. (2000), Brewer & Carney (2006), Feltzing et al. (2007), Neves et al. (2009), Adibekyan et al. (2012b), Tabernero et al. (2012), and BB15. Nonetheless, when taking into account NLTE corrections, our trend presents a different behaviour compared to the one by BB15, whose trend becomes virtually flat over the metallicity range studied. As the authors discussed, no models have been able to explain this flattening. The K20 model predicts a plateau around [Mn/Fe] ~ 0.55 dex for the low-metallicity regime, and then an increase above [Fe/H] > -1 dex.

Co shows a trend similar to α-elements, with over-abundant [Co/Fe] at low metallicities. The halo star BD+80 245 (G0 IV) seems to be Co-rich. Assuming LTE, this trend is in agreement with Brewer & Carney (2006), Neves et al. (2009), Adibekyan et al. (2012b), Tabernero et al. (2012), and BB15. However, we find some differences when considering NLTE corrections in comparison with BB15, who reported higher Co abundances for a given metallicity. The K20 model reproduces the α-element trend, but provides values ~ 0.3 dex lower than the observations. However, when including the hypernova jet effects (K15 model), the prediction is closer to the data.

Since our results for Mn and Co abundances assuming LTE are in good agreement with those by BB15, the differences when considering NLTE seem to be due to the use of different NLTE corrections. We compared our results of the [Sc/H], [V/H], [Mn/H], and [Co/H] ratios for the four stars in common with BB15 in the right panel of Fig. 4.7, finding similar values.

Finally we compared these results with the ones obtained in Montes et al. (2018) in Fig. 4.9. We found that the outliers with [Sc/Fe] > 0.5 disappear and the stars now follow the general Galactic trend, but the halo star BD+80 245 (G0 IV), which presents a lower Sc abundance. Regarding the V abundances, the new results exhibit reduced scatter, with the persistent outliers attributed to lower effective temperatures, below 5200 K. When accounting for HFS and NLTE, we generally observed slightly higher Mn abundances and some diminished Co abundances, while maintaining the same overall trend.

4.3.3 Exoplanets

Analysing the correlations between stellar properties, such as metallicity and chemical abundances, and the occurrence of exoplanets can provide valuable insights for the selection of targets in forthcoming exoplanet surveys and for comprehending the mechanisms behind planetary formation. In particular, it has been extensively reported that the stars that host giant planets present higher metallicities than the stars without detected planets (e.g. Gonzalez, 1997; Fischer & Valenti, 2005; Brewer et al., 2016). This giant planet – stellar metallicity correlation supports the core-accretion scenario as the basis for planet formation (e.g. Ida & Lin, 2004; Ercolano & Clarke, 2010). The main goal of this section is to examine potential notable distinctions between the sample of stars hosting planets and the sample of stars lacking known planets, specifically regarding metals aside from iron.

We conducted a search for confirmed exoplanets around the primary stars of our sample in the literature using The Extrasolar Planets Encyclopaedia[4]. In Montes et al. (2018), 21 exoplanets in 14 planetary systems were found in the literature; now we have 24 exoplanets in 17 planetary

[4] http://exoplanet.eu

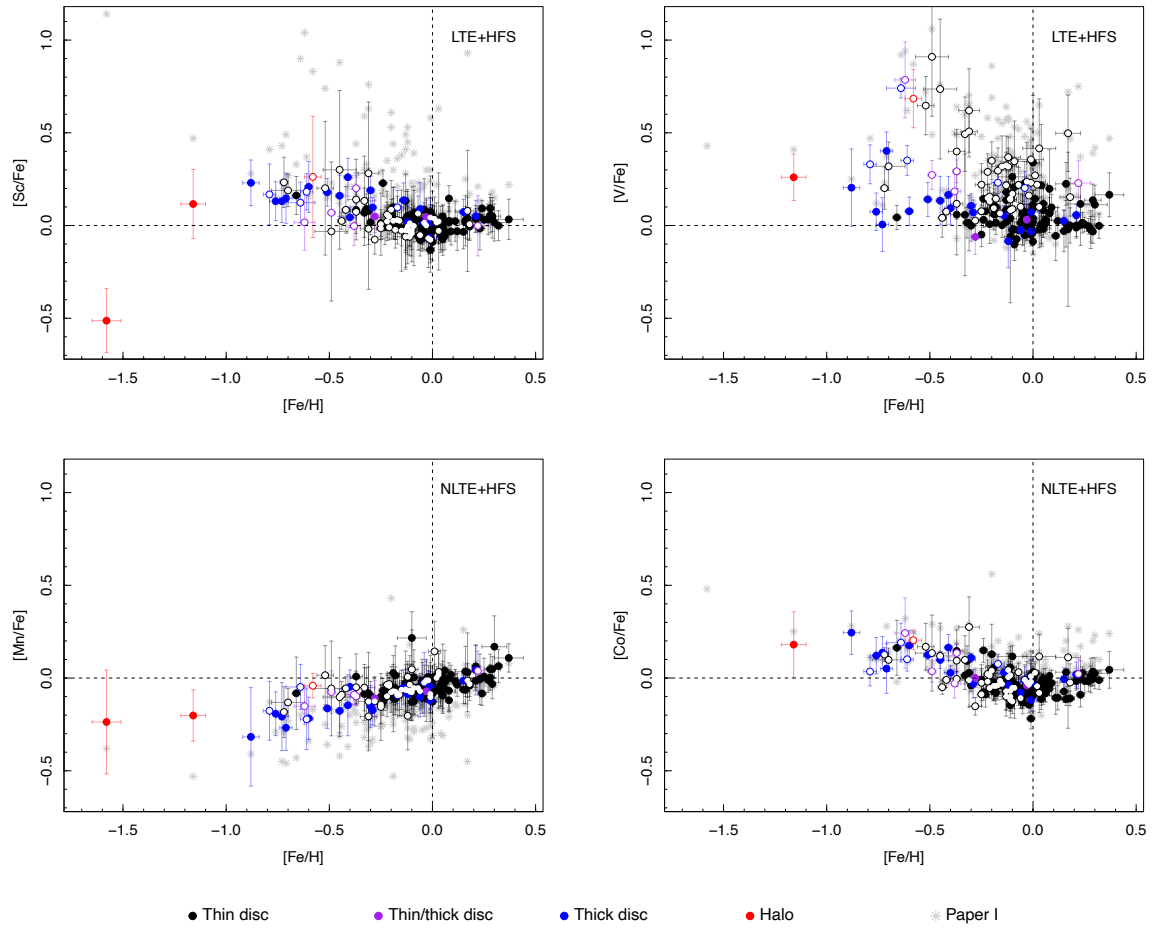

Figure 4.9: Abundance ratios of [Sc/Fe], [V/Fe], [Mn/Fe], and [Co/Fe] versus [Fe/H], including HFS splitting and NLTE effects when necessary, in comparison with Montes et al. (2018) (gray asterisks). Colours for different populations: black – thin disc, blue – thick disc, cyan – thin/thick disc, red – halo. Open circles: stars with $T_{\rm eff} < 5200$ K; filled circles: stars with $T_{\rm eff} \geq 5200$ K.

systems. Two exoplanets were originally listed for the star HD 38529 A in Montes et al. (2018), but it has since been determined that one of them is a substellar companion of $23.7^{+4.1}_{-3.1}\,M_{\rm Jup}$. As a result, we now recognise only one exoplanet orbiting this star. Moreover, none of the M-dwarf companions in our sample present confirmed exoplanets. We plot in Fig. 4.10 the galactic trends for [C/Fe], [O/Fe], and [C/O], indicating the stars with confirmed exoplanets with $m \sin i$ greater or less than 30 Earth masses ($\sim 0.094\,M_{\rm Jup}$), in comparison to single stars. As discussed in Montes et al. (2018), the exoplanet host stars tend to be metal-rich. Given the small number of exoplanet host stars in our sample, we do not see any difference between the stars harboring exoplanets with $m \sin i$ greater or less than 30 Earth masses.

In Montes et al. (2018) we performed a Kolmogorov-Smirnoff (K-S) test to evaluate the disparity between the stars in our sample with and without planets, independently of their mass, safely concluding that both metallicity distributions were significantly different. Now we repeated the K-S test for the [Fe/H], since the number of known exoplanet has increased, but we obtain the same results. The probability that both samples follow the same distribution is just of 0.0004. We compile the K-S statistics and p-values in Table 4.4, and plot the corresponding cumulative distribution function in Fig. 4.11. The p-value represents the significance level of the K-S test, i.e. the probability that the two groups belong to the same population.

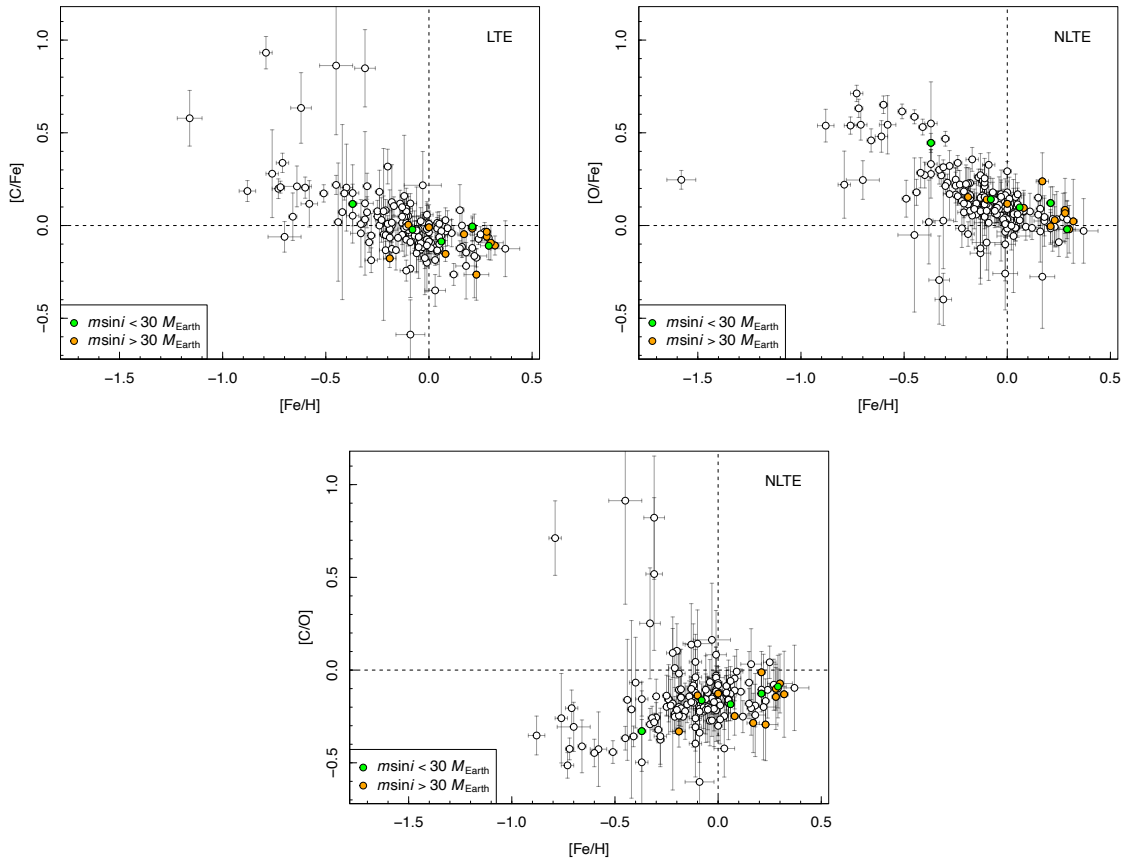

Figure 4.10: Abundance ratios of [C/Fe], [O/Fe], and [C/O] versus [Fe/H], indicating the stars with exoplanets, and colour-coded by $M \sin i$.

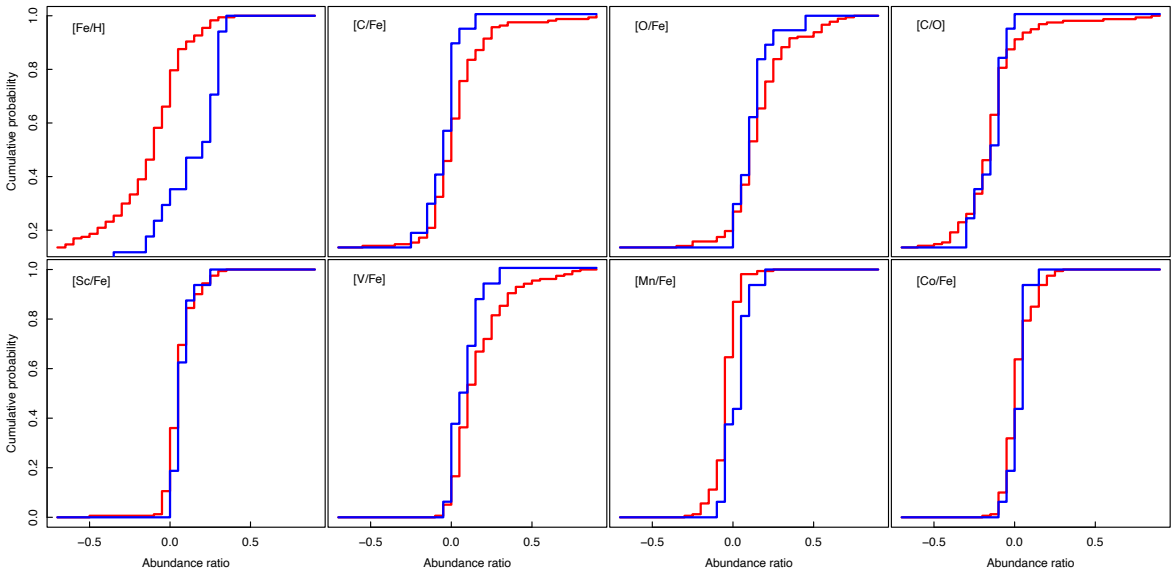

Figure 4.11: Normalised cumulative distribution function of the abundance ratios of several elements of the stars in our sample with (blue) and without (red) detected exoplanets.

Table 4.4: Kolmogorov-Smirnoff test results

Abundance	D	p–value
[Fe/H]	0.5228	0.0004
[C/Fe]	0.3781	0.0242
[O/Fe]	0.2557	0.2496
[C/O]	0.1452	0.8763
[Sc/Fe]	0.2966	0.1545
[V/Fe]	0.2785	0.2098
[Mn/Fe]	0.4635	0.0023
[Co/Fe]	0.2313	0.3727

Preceding studies indicated that planet hosts and single stars seem to be evenly distributed for solar metallicity, and the presence of planets does not lead to differences in the carbon abundances. However, for sub-solar metallicities, planet hosts present an enhancement of C (see Nissen et al., 2014; Delgado Mena et al., 2021). We applied the K-S test for the [C/Fe], [O/Fe], and [C/O] ratios, finding that only for the [C/Fe] ratio, the distributions of host and single stars are different, with only a probability of 0.0242 that both populations have the same [C/Fe] distribution. These results are in agreement with da Silva et al. (2015) and Delgado Mena et al. (2021), who showed a significant difference in carbon abundance between host and singles stars, but no difference, or not so strong, in the case of oxygen.

Repeating the analysis for the [X/Fe] ratios of the odd-Z iron-peak elements, we obtained that only for the [Mn/Fe] ratio, both distributions are significantly different, with just a probability of 0.0023 for the planet hosts and single stars of coming from the same distribution. Previous studies reported overabundances of [Mn/Fe] of planet hosts in comparison to single stars (Zhao et al., 2002; Bodaghee et al., 2003; Kang et al., 2011; da Silva et al., 2015). Nevertheless, Adibekyan et al. (2012a) did not find that diference for the [Mn/Fe] ratio.

Our findings might indicate that other species than iron also play an important role in the planet formation mechanisms; for example, carbon is a pivotal element in the formation of ices within a protoplanetary disc. The overabundance of Mn could be explained by its lower condensation temperature in comparison to the other investigated elements. Notwithstanding, these results should be revised in the future with a larger sample of exoplanet hosts.

4.4 Summary

In the work presented in this chapter, we took a break on the direct study of the M dwarfs. We have extended the analysis of the chemical composition of FGK stars in wide binary systems with M-dwarf companions, started by Montes et al. (2018), by deriving abundances of carbon and oxygen, and updating previous determinations of scandium, vanadium, manganese, and cobalt taking into account hyperfine structure effects and correcting for non-local thermodynamic equilibrium. For that, we made use of the equivalent width method (StePar; Tabernero et al. 2019) and high-resolution spectra. We compared our results with previous abundance determinations of F-, G-, and K-dwarfs found in the literature, finding a good agreement in the Galactic trends of the investigated abundances. As in previous studies, we noticed that some of the obtained abundances are not reliable for stars with $T_{\rm eff} < 5200\,$K, especially C, O, and V.

Furthermore, we explored the relationship between stellar chemical composition and the presence of exoplanets. Our analysis, which includes a sample of 24 exoplanets orbiting 17

of the primary stars, reveals statistically significant differences in the distribution of iron, the carbon-to-iron ratio, and the manganese-to-iron ratio between stars hosting exoplanets and those without detected planets. These findings suggest that, beyond iron, carbon and manganese may also play a significant role in the processes of planet formation.

This work delivers a homogeneous and robust set of chemical abundance measurements for a large sample of FGK-type primary stars, establishing a reliable reference framework for studies of both stellar populations and exoplanet hosts. In the following chapters of this thesis, we will build upon this foundation by calibrating spectral indices in low-resolution CAFOS spectra of the M-dwarf companions and deriving their stellar atmospheric parameters through spectral synthesis using high-resolution CARMENES observations.

CHAPTER 5

Elemental abundances of M dwarfs from low-resolution spectral indices

"If you just focus on the smallest details, you never get the big picture right."
— Leroy Hood

The content of this chapter has been adapted from the article *Calibrating the metallicity of M dwarfs in wide physical binaries with F-, G-, and K-primaries – III: Low-resolution spectral indices for the M-dwarf abundances using projection predictive feature selection*, currently in preparation.

5.1 Introduction

In the previous chapter, we extended the chemical analysis of F-, G-, and K-type primaries in wide binary systems. We now turn our attention to their M-dwarf companions. The goal of this chapter is to calibrate the abundances of 15 atomic species in M dwarfs using spectral indices and features extracted from low-resolution optical spectra.

The low luminosity of M dwarfs poses a great challenge for high-resolution spectroscopy, which require large-aperture telescopes and long integration times to achieve sufficiently high signal-to-noise ratios. In contrast, low-resolution spectra can be obtained more efficiently using several spectrographs, such as the Baryon Oscillation Spectroscopic Survey of the Sloan Digital Sky Survey (SDSS/BOSS; Dawson et al. 2013), the Large Sky Area Multi-Object Fiber Spectroscopic Telescope (LAMOST; Cui et al. 2012), or the Calar Alto Faint Object Spectrograph[1] (CAFOS).

Spectral indices derived from low-resolution spectra have traditionally been used for spectral typing of cool stars (see Alonso-Floriano et al., 2015, and references therein). Moreover, several studies have used low-resolution spectral indices to estimate the metallicity of M dwarfs by calibrating with binary systems. For instance, Rojas-Ayala et al. (2010, 2012) demonstrated that M-dwarf metallicities could be inferred from low-resolution K-band spectra using the Na I doublet and Ca I triplet, while Terrien et al. (2012) achieved similar results with H-band spectra. However, these studies were based on a limited number of binary systems (~ 20) for calibration. In contrast, Mann et al. (2013) analysed a sample of 112 FGK+M binary systems to empirically identify 120 low-resolution spectral indicators that correlate with [Fe/H].

Building upon this idea, this chapter extends the use of low-resolution spectral indices to derive empirical calibrations for 15 atomic species in M dwarfs, using the chemical compositions of their FGK-type primaries as references.

[1] https://www.caha.es/telescope-2-2m/cafos

5.2 Analysis

5.2.1 Sample

The stellar sample analysed in this chapter was originally introduced by Alonso-Floriano et al. (2015), who obtained low-resolution spectra with CAFOS at the 2.2 m Calar Alto telescope for 967 stars between March 2011 and February 2016. Some of these stars are part of the binary systems presented by Montes et al. (2018) and analysed in the previous chapter of this thesis. For the purpose of this work, we focused on the 162 companions observed with CAFOS and whose primary stars present stellar parameters and abundances (see Montes et al. 2018 and Duque-Arribas et al. 2024) derived with the *EW* method using the StePar code (Tabernero et al., 2017, 2019, 2021b). Figure 5.1 shows the spectral type distribution of the selected M dwarfs as a function of the metallicity of their corresponding primaries, assumed to represent their intrinsic chemical composition. The abundance coverage for the M-dwarf companions is as follows: all 162 stars have [Fe/H], [Na/H], [Mg/H], [Si/H], [Ti/H], [Ni/H], [Sc/H], and [Mn/H]; 161 have [Ca/H], [Cr/H], and [Co/H]; 160 have [Al/H]; 159 have [V/H]; 158 have [O/H]; and 145 have [C/H].

CAFOS at the 2.2 m Calar Alto telescope provides a wavelength coverage between 4200 and 8300 Å with a resolution of ∼1500. All the spectra used in this work have signal-to-noise ratios higher than 50, ensuring reliable measurements of spectral features. At this resolution, we rely

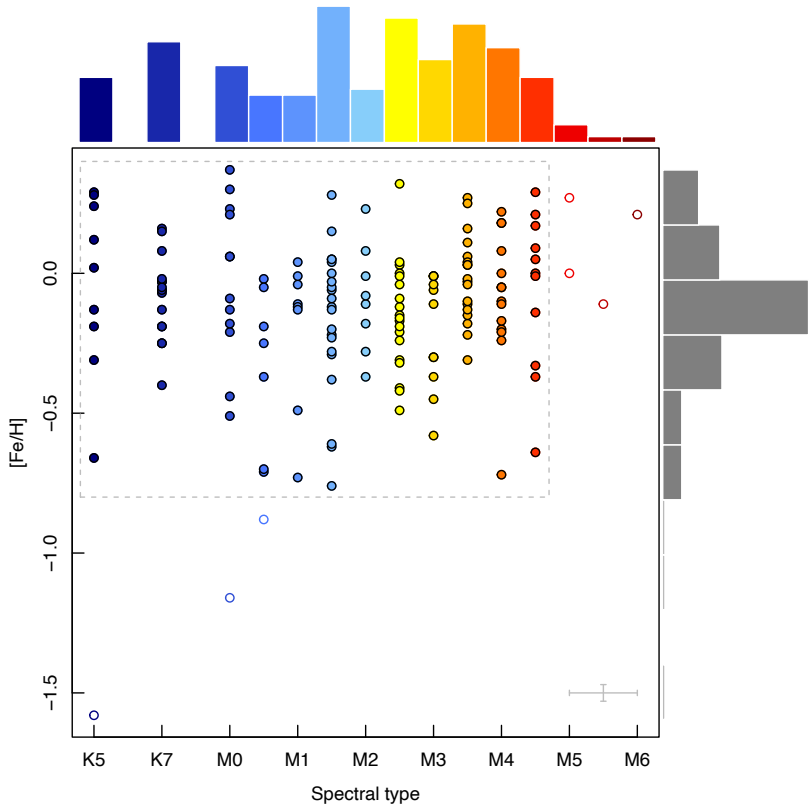

Figure 5.1: Spectral types of the 162 M-dwarf companions observed with CAFOS versus the corresponding primaries' [Fe/H]. The gray rectangle delimits the range of application of the calibrations, and stars outside this area are plotted as open circles. The average uncertainties of the spectral types and [Fe/H] are shown in the bottom right corner.

on spectral indices, defined as flux ratios measured over specific wavelength intervals, to extract information about the stellar photosphere. Alonso-Floriano et al. (2015) compiled a list of 31 spectral indices defined in the literature (Kirkpatrick et al., 1991, 1995, 1999; Reid et al., 1995; Martín & Kun, 1996; Martin et al., 1996; Martín et al., 1999; Hawley et al., 2002; Lépine et al., 2003; Wilking et al., 2005; Shkolnik et al., 2009). Among them, nine are associated with TiO features, seven to VO, six to CaH, three to the pseudo-continuum, and the remaining ones to H and neutral metallic lines. Additionally, we included seven metal-sensitive features defined by Mann et al. (2013) within the CAFOS spectral range. The full list of $31 + 7$ indicators is compiled in Table 5.1.

Our goal is then to predict the abundances of the M-dwarf companions using these spectral indices and features. The question that arises is which subset of variables should be used to best predict each given abundance.

5.2.2 Methodology

This problem is known as predictive inference and feature selection with scarce but high-dimensional data. In our case, to predict a target variable (a given abundance), we have $N = 162$ stars and $p = 38$ predictors (the spectral indices and features). The idea is to find a linear model that predicts data well but utilises only a small subset of features. The problem is then twofold: feature selection and prediction. Although several techniques attempt to approach these two problems simultaneously, Piironen et al. (2018) proposed a two-stage strategy: first, construct the best predictive model using as much information as you can, known as the reference model; and then find a minimal subset of predictors that provides predictions similar to the reference model, so the predictive performance is not significantly enhanced by the addition of extra predictors. This is referred to as projection predictive feature selection, and it shows a good trade-off between sparsity and predictive accuracy. This technique, based on the ideas of Goutis & Robert (1998) and Dupuis & Robert (2003), is available through the R package `projpred`[2].

A Gaussian linear regression model is given by

$$y_i = \beta \mathbf{x}_i + \epsilon_i, \qquad \epsilon_i \sim \mathrm{N}(0, \sigma^2), \qquad i = 1, ..., N \tag{5.1}$$

where $\mathbf{x}$ is the p-dimensional vector of predictors, β the corresponding regression coefficients, ϵ_i the residual error term, and σ^2 the noise variance. To evaluate the relevance of the predictors, a widely used Bayesian method involves applying a sparsifying prior to each coefficient β_i. In our case, we incorporated a weakly informative regularised horseshoe prior to account for the potential irrelevance of certain predictors. The general idea of this prior is that it drives all the coefficients towards zero, while some of them are allowed to escape the shrinkage. Moreover, regularisation of this prior has been shown to frequently enhance the robustness and accelerate the MCMC posterior inference process. For more information on the regularised horseshoe prior, we refer to Piironen & Vehtari (2017) and Piironen et al. (2018).

To fit the reference models we used `Stan` (Carpenter et al., 2017; Stan Development Team, 2022) with the R package `brms`[3] (Bürkner, 2017). We run 4 MCMC chains, each of them with 2000 iterations and 1000 of warmup, and assigned a regularised horseshoe prior on each coefficient. For the reference models, we considered two cases: a linear model comprising only the predictors, and a quadratic model which also incorporates the quadratic terms of the predictors. We compared these two cases with the Leave One Out – Cross Validation criterion (LOO-CV; Vehtari et al. 2017). See Section 2.2.3 for more details. Given the expected log-pointwise predictive density ($\mathrm{elppd}_{\mathrm{LOO}}$) values for the models concerning [Fe/H], which are 60.4 ± 8.7 and 59.5 ± 8.6 respectively,

[2] https://github.com/stan-dev/projpred
[3] https://github.com/paul-buerkner/brms

Table 5.1: Spectral indices and metal-sensitive features used in this work.

Spectral indices				Metal-sensitive features			
Index	$\Delta\lambda_{num}$ [Å]	$\Delta\lambda_{den}$ [Å]	Reference	Feature	λ centre [Å]	λ width [Å]	Reference
CaOH	6230:6240	6345:6354	Reid et al. (1995)	F01	4648	23	Mann et al. (2013)
CaH 1	6380:6390	$\sum$ 6345:6355, 6410:6420	Reid et al. (1995)	F02	5608	20	Mann et al. (2013)
I2 (CaH)	6510:6540	6370:6400	Martín & Kun (1996)	F03	6118	20	Mann et al. (2013)
I3 (TiO)	6510:6540	6660:6690	Martín & Kun (1996)	F04	6232	20	Mann et al. (2013)
Hα	6560:6566	6545:6555	Reid et al. (1995)	F05	6416	41	Mann et al. (2013)
TiO 1	6718:6723	6703:6708	Reid et al. (1995)	F06	7540	20	Mann et al. (2013)
CaH 2	6814:6846	7042:7046	Reid et al. (1995)	F07	8208	35	Mann et al. (2013)
CaH 3	6960:6990	7042:7046	Reid et al. (1995)				
TiO-7053	7000:7040	7060:7100	Martín et al. (1999)				
Ratio A (CaH)	7020:7050	6960:6990	Kirkpatrick et al. (1991)				
TiO-7140	7015:7045	7125:7155	Wilking et al. (2005)				
PC1	7030:7050	6525:6550	Martin et al. (1996)				
CaH Narr	7044:7049	6972.5:6977.5	Shkolnik et al. (2009)				
TiO 2	7058:7061	7043:7046	Reid et al. (1995)				
TiO 3	7092:7097	7079:7084	Reid et al. (1995)				
TiO 5	7126:7135	7042:7046	Reid et al. (1995)				
TiO 4	7130:7135	7115:7120	Reid et al. (1995)				
VO-a	$\sum$7350:7370, 7550:7570	7430:7470	Kirkpatrick et al. (1999)				
VO	$\sum \alpha$7350:7400, β7510:7560[a]	7420:7470	Kirkpatrick et al. (1995)				
Ratio B (Ti I)	7375:7385	7353:7363	Kirkpatrick et al. (1991)				
VO-7434	7430:7470	7550:7570	Hawley et al. (2002)				
PC2	7540:7580	7030:7050	Martin et al. (1996)				
VO 1	7540:7580	7420:7460	Martín et al. (1999)				
TiO 6	7550:7570	7745:7765	Lépine et al. (2003)				
VO-b	$\sum$7860:7880, 8080:8100	7960:8000	Kirkpatrick et al. (1999)				
VO 2	7920:7960	8130:8150	Lépine et al. (2003)				
VO-7912	7990:8030	7900:7940	Martín et al. (1999)				
Ratio C (Na I)	8100:8130	8174:8204	Kirkpatrick et al. (1991)				
Color-M	8105:8155	6510:6560	Lépine et al. (2003)				
Na-8190	8140:8165	8173:8210	Hawley et al. (2002)				
PC3	8235:8265	7540:7580	Martin et al. (1996)				

[a] $\alpha = 0.5625$, $\beta = 0.4375$

it is evident that the quadratic model, despite its incorporation of second-order terms and double the number of predictors, fails to enhance the predictive performance of the linear model. Hence, the linear model suffices for the analysis.

Next, we perform the projection predictive variable selection using the R package `projpred`. It determines the best submodel for each submodel size, where size refers to the number of predictor terms, evaluating their predictive performance. The order in which `projpred` adds the predictors is known as the solution path. We analyse several performance statistics, for example $\mathrm{elppd}_{\mathrm{LOO}}$ and the root mean square error (RMSE), as a function of the submodel size to determine the size where the performance measures stabilise and are sufficiently close to the performance of the reference model. Once the selection is made, we can project the reference model onto the final submodel. The MCMC procedures yield draws that represent the projected posterior distribution that arises from projecting the posterior distribution of the reference model onto the parameter space of the final submodel. It must be mentioned that projected regression coefficients do not solely represent the individual effects of the corresponding predictors, but they may incorporate the influences of excluded predictors in the projection, particularly when dealing with strongly correlated predictors. Finally, we can generate draws from the predictive distributions using the final submodel. These draws consider both the uncertainty resulting from parameter estimation and the uncertainty originating from the observation (or sampling) model for the response.

Briefly, the process could be resumed as follows:

- Fit a reference model, i.e., the best predictive model using as much information as possible.
- Apply `projpred` to determine the solution path, that is, the best submodel for each size.
- Analyse performance as a function of the submodel size to choose the final submodel size.
- Project the reference model onto the final submodel.
- Generate predictions from the final submodel.

An illustrative example of the projective inference using the Stefan-Boltzmann law is shown in Appendix C.

Since the predictors, i.e. the spectral indices and features, also depend on the effective temperature of the star, some of them may be more useful for some spectral types. For this reason, we divided the general sample in two: the early-type subsample, down to M2.0, and the late-type subsample, for M2.5-type stars and cooler, as Mann et al. (2013). This way the early and late subsamples have nearly the same number of stars (84 and 78, respectively). Given the correlation of some of the spectral indices and the effective temperature (see Alonso-Floriano et al. 2015), this dependence is also included in the models. Then, for each abundance we performed the projection predictive feature selection process thrice: one for the whole sample, one for the early sample, and one for the late sample, obtaining then 3 models for each abundance. As seen in Fig. 5.1, the range of application for the [Fe/H] calibrations is K5 V $\leq$ SpT $\leq$ M4.5 V and $-0.8 \lesssim$ [Fe/H] $\lesssim +0.4$ dex, and the calibrations will just extrapolate for values outside this region, so their predictions should be treated with caution. The distributions and range of application for each abundance are given in Fig. 5.2.

One potential limitation of the approach presented here is the lack of direct spectral features for some elements within the low-resolution CAFOS spectral indices. However, our method does not rely on individual, unblended features attributable solely to the target element. Instead, the data-driven empirical models exploit statistical correlations between the spectral indices and the chemical composition of the stars: relationships that arise both from astrophysical co-production channels (e.g., shared nucleosynthetic origins; Kobayashi et al. 2020) and from blended molecular features in low-resolution spectra that are sensitive to overall atmospheric parameters. In stars, the abundances of several elements are often tightly correlated (e.g. Nissen & Schuster, 2010), enabling the inference of one abundance from the imprint of others.

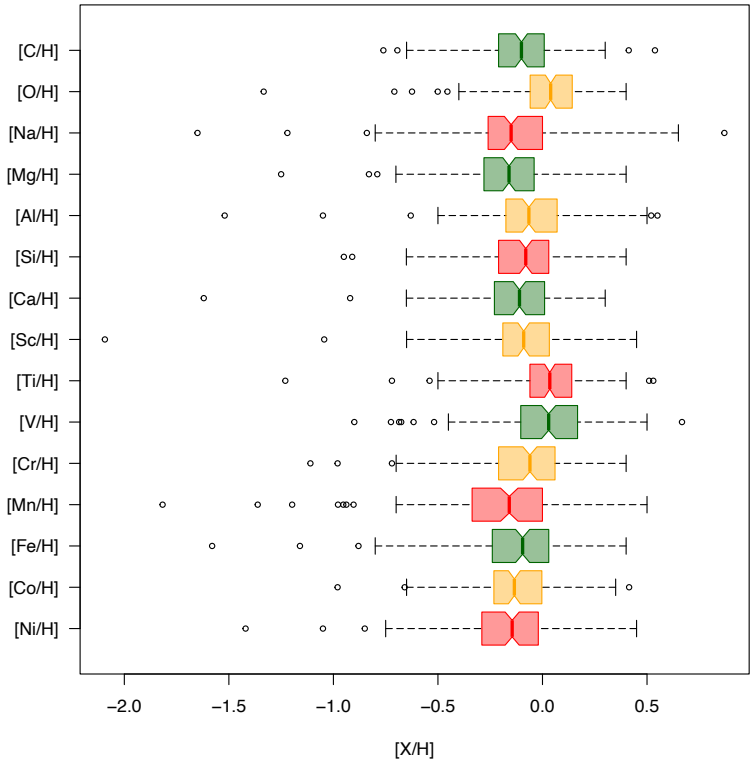

Figure 5.2: Boxplot of the abundances distributions, indicating the first quartile, the median (with its 95% confidence intervals), and the third quartile as the box, and the range of aplication of the calibrations is given by the whiskers. Stars outside this range are plotted as open circles.

5.3 Results and discussion

5.3.1 Calibrating with the FGK+M binary systems

We calibrated empirical relations between low-resolution spectral indices and chemical abundances for M-dwarf secondaries, using the compositions of their FGK-type primaries as reference. For each element, we constructed three different models: one trained on the full sample (the 'general' model), and two tailored to early- and late-type M dwarfs separately. To fully assess the performance of each model, we evaluated five test cases:

- the general model applied to the full sample,
- the general model applied only to early-type stars,
- the general model applied only to late-type stars,
- the early model applied to early-type stars, and
- the late model applied to late-type stars.

This approach allows us to determine whether specific calibrations are preferable to a single global model, and whether early/late-specific models offer improved predictive performance or reduced model complexity.

Fig. 5.3 shows the model size selection curves for [Fe/H] based on the $\mathrm{elppd}_{\mathrm{LOO}}$ and the RMSE metrics, while Figs. 5.4 and 5.5 compare the predicted abundances using the best submodel for the M-dwarf secondaries with the reference abundances of their FGK primaries. The full set of selected predictors, that is, the solution path for these models along with their corresponding coefficients,

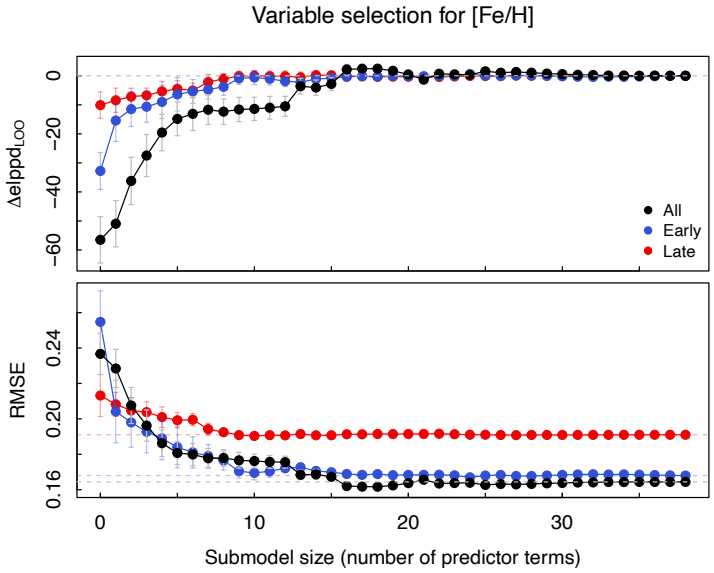

Figure 5.3: $\mathrm{elppd_{LOO}}$ and RMSE as a function of the submodel size for [Fe/H]. The different samples are plotted in different colors: black, blue, and red for the whole, early, and late samples, respectively.

is presented in Table C.2. Summary statistics of the residuals (mean, median, standard deviation, median absolute deviation, and Pearson's and Spearman's correlation coefficients) are listed in Table 5.2, and the corresponding residual distributions are illustrated in Fig. 5.6.

Iron abundance

Iron serves as the reference element for calibrating chemical abundance. The general and early models (black and blue curves in Figure 5.3) stabilised at 16 and 9 predictors, respectively, and both performed well on the early-type subsample. Larger models do not significantly perform better, i.e. they do not provide larger $\mathrm{elppd_{LOO}}$ values or lower RMSE. The dedicated early model, with fewer predictors, obtained similar scatter compared to the general one. For the late model, the solution path shows flatter curves, so the submodel size chosen is 7. That indicates that the predictors do not provide enough information for this subsample to estimate correctly [Fe/H], and the late model failed to improve over the global fit. Thus, for late-type stars, the general model performs better than the dedicated fit.

These three models systematically overestimate metallicities for $[\mathrm{Fe/H}] < 0$, and the late-type model underestimates for $[\mathrm{Fe/H}] > 0$. This is a well-known issue in Machine Learning models, which tend to regress extreme values toward the mean (Ting, 2024).

We report a residual scatter of ~ 0.14 dex between the primaries' [Fe/H] and the predicted values for the secondaries, which is lower than the 0.19 dex scatter found by Qiu et al. (2024) for a similar analysis, using FGK+M binary systems and LAMOST low-resolution spectra.

Carbon and oxygen abundances

The carbon abundance is reasonably well recovered using early-type M dwarfs. The dedicated early model required only six predictors and slightly outperformed the general model in terms of dispersion. For late-type stars, however, carbon predictions are poor, and the late model, with just one predictor, lacks predictive power.

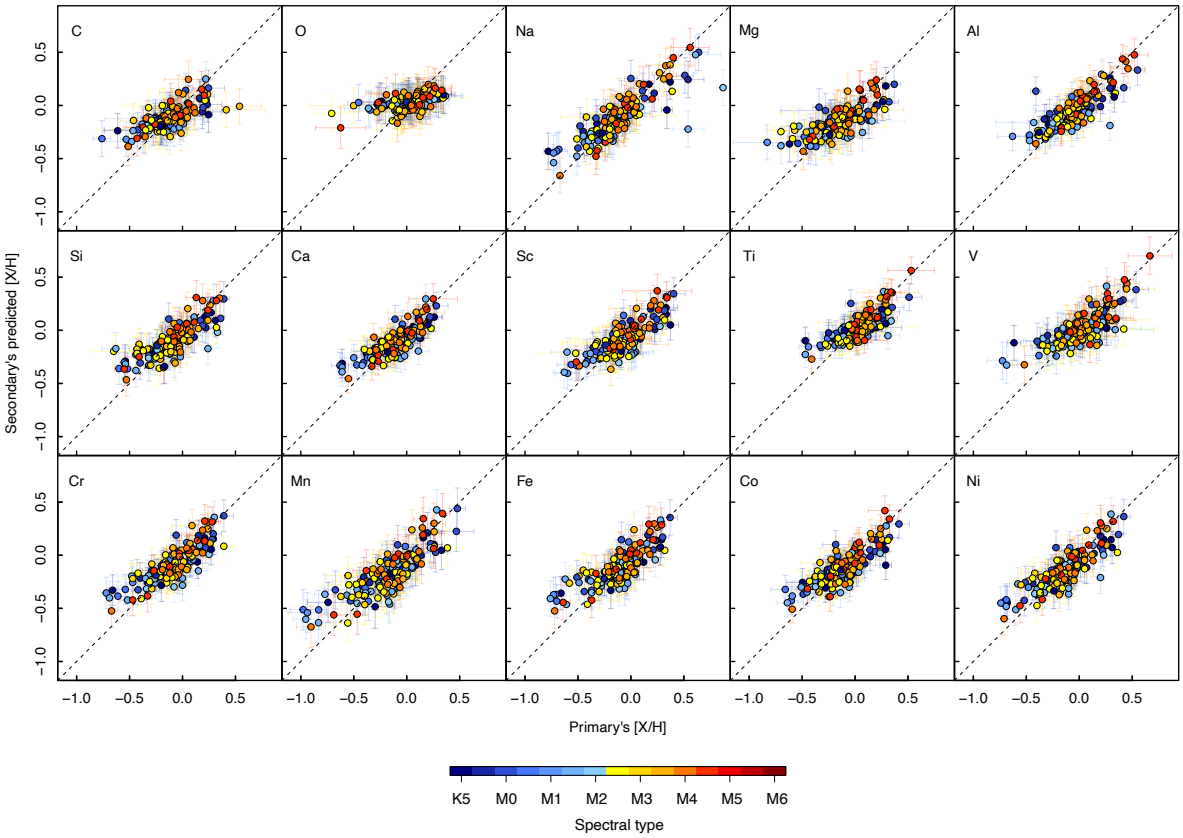

Figure 5.4: Predicted abundances using the general model for the full sample of M-dwarf companions versus the primaries' abundances. The stars are color-coded by spectral type.

Oxygen shows similar behaviour: the early model with nine predictors notably improves the accuracy over the general model, while the late-type model does not reproduce the oxygen abundance.

Light odd-Z elements: Na and Al

Both sodium and aluminium are well modelled using dedicated early- and late-type fits. While the general models require 19 predictors, the tailored versions achieve similar or even improved accuracy with significantly fewer terms: eight for Na, and four to five for Al. This makes the simplified models preferable for practical use without sacrificing performance.

α-elements: Mg, Si, Ca, and Ti

Magnesium, silicon, calcium, and titanium are best recovered in early-type stars using tailored models. In all these cases, the early fits reduce the number of predictors by nearly half while preserving or slightly improving the accuracy of the predictions.

For Mg and Si, late-type models perform worse than the general fit, likely due to limited sensitivity of spectral indices at later subtypes for these abundances. Although the general model for Ca presents slightly better results for the late-type stars using 19 predictors, the simpler late model, with only 5, achieves similar results. Ti shows robust behaviour in the late model, improving accuracy with a small model size (5 predictors), making [Ti/H] a well-behaved calibration across all spectral subtypes.

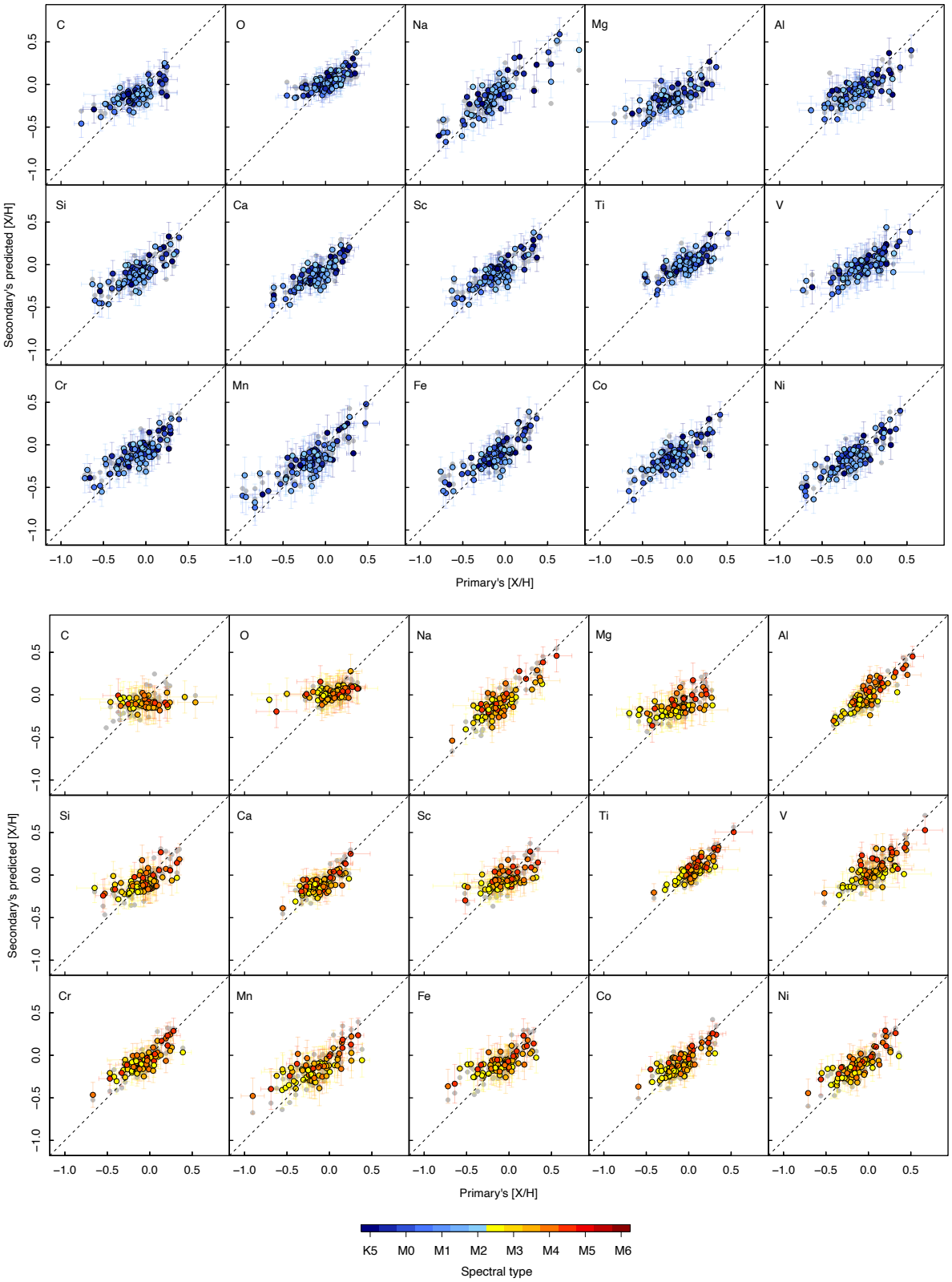

Figure 5.5: Predicted abundances for the M-dwarf companions versus the primary abundances fitting independently the early-type (upper panels) and the late-type (lower panels) subsamples. The stars are color-coded by spectral type. In gray we show the predictions using the general model for the same stars.

Table 5.2: Statistics of the differences between primaries' and secondaries' abundances.

Abundance	Sample	$N_{\text{predictors}}$	$\bar{x}$	$\tilde{x}$	σ_x	MAD(x)	r	r_S	Rec.
	all	9	−0.001	−0.002	0.143	0.130	0.72	0.74	
	all-early		−0.006	0.008	0.138	0.136	0.78	0.78	
[C/H]	all-late		0.004	−0.006	0.150	0.121	0.65	0.69	✓
	early	6	0.000	0.007	0.136	0.143	0.76	0.69	✓
	late	1	0.034	0.006	0.199	0.180	−0.02	−0.09	×
	all	8	−0.001	0.017	0.156	0.128	0.52	0.50	
	all-early		−0.005	0.007	0.150	0.132	0.59	0.54	
[O/H]	all-late		0.004	0.034	0.164	0.100	0.54	0.54	✓
	early	9	0.000	0.015	0.112	0.104	0.76	0.72	✓
	late	2	−0.001	0.030	0.169	0.125	0.51	0.49	×
	all	19	0.000	−0.004	0.145	0.121	0.85	0.85	
	all-early		0.002	−0.010	0.174	0.122	0.85	0.87	
[Na/H]	all-late		−0.002	0.002	0.105	0.120	0.89	0.82	
	early	8	−0.001	−0.008	0.155	0.150	0.87	0.82	✓
	late	8	−0.005	−0.007	0.122	0.147	0.84	0.74	✓
	all	19	0.000	0.006	0.149	0.129	0.75	0.74	
	all-early		0.008	0.009	0.155	0.125	0.76	0.71	
[Mg/H]	all-late		−0.008	0.000	0.141	0.137	0.74	0.77	✓
	early	7	−0.001	0.006	0.155	0.134	0.75	0.67	✓
	late	1	−0.008	−0.010	0.178	0.151	0.55	0.59	
	all	19	0.000	0.002	0.118	0.087	0.83	0.81	
	all-early		−0.002	−0.005	0.145	0.116	0.79	0.78	
[Al/H]	all-late		0.002	0.009	0.082	0.076	0.90	0.84	
	early	4	0.000	0.001	0.152	0.130	0.76	0.69	✓
	late	5	−0.003	−0.017	0.099	0.100	0.85	0.77	✓
	all	15	0.000	0.008	0.134	0.123	0.79	0.80	
	all-early		0.005	0.000	0.140	0.117	0.81	0.81	
[Si/H]	all-late		−0.005	0.014	0.127	0.121	0.78	0.80	✓
	early	7	0.001	0.001	0.134	0.127	0.81	0.77	✓
	late	2	−0.003	0.018	0.164	0.151	0.59	0.59	
	all	19	0.001	−0.002	0.110	0.116	0.81	0.79	
	all-early		0.002	0.020	0.123	0.116	0.82	0.81	
[Ca/H]	all-late		−0.001	−0.008	0.093	0.102	0.81	0.76	
	early	8	−0.001	0.001	0.121	0.106	0.82	0.76	✓
	late	5	0.001	−0.006	0.110	0.113	0.74	0.62	✓
	all	13	0.001	−0.003	0.126	0.121	0.81	0.77	
	all-early		0.003	−0.005	0.137	0.130	0.83	0.76	
[Sc/H]	all-late		−0.001	0.001	0.113	0.110	0.79	0.78	✓
	early	13	0.000	−0.013	0.133	0.127	0.83	0.74	✓
	late	1	−0.003	−0.013	0.145	0.130	0.61	0.61	
	all	16	0.000	−0.004	0.111	0.105	0.79	0.76	
	all-early		−0.007	−0.004	0.135	0.140	0.75	0.74	
[Ti/H]	all-late		0.007	0.000	0.077	0.082	0.87	0.81	
	early	5	0.000	0.010	0.123	0.119	0.79	0.76	✓
	late	5	0.001	0.004	0.080	0.087	0.85	0.80	✓
	all	12	0.001	0.005	0.145	0.132	0.79	0.77	
	all-early		−0.010	0.008	0.163	0.173	0.78	0.79	
[V/H]	all-late		0.012	0.005	0.122	0.112	0.81	0.73	
	early	9	−0.001	0.016	0.160	0.152	0.78	0.76	✓
	late	4	0.003	0.014	0.141	0.130	0.73	0.65	✓
	all	17	0.000	0.001	0.125	0.110	0.83	0.82	
	all-early		−0.001	0.003	0.141	0.132	0.83	0.81	
[Cr/H]	all-late		0.001	−0.001	0.104	0.100	0.85	0.83	
	early	8	0.001	−0.006	0.142	0.129	0.82	0.78	✓
	late	9	−0.002	−0.004	0.118	0.104	0.81	0.77	✓
	all	18	0.000	0.007	0.157	0.173	0.84	0.82	
	all-early		−0.001	0.004	0.166	0.157	0.86	0.86	
[Mn/H]	all-late		0.001	0.008	0.148	0.182	0.81	0.78	
	early	9	−0.001	−0.001	0.171	0.151	0.84	0.79	✓
	late	8	−0.008	0.010	0.177	0.150	0.73	0.71	✓
	all	16	−0.001	−0.004	0.141	0.133	0.81	0.80	
	all-early		0.000	0.011	0.150	0.135	0.83	0.82	
[Fe/H]	all-late		−0.001	−0.009	0.131	0.130	0.80	0.77	✓
	early	9	0.001	0.001	0.142	0.140	0.84	0.78	✓
	late	7	−0.006	0.032	0.159	0.136	0.70	0.65	
	all	9	0.001	−0.010	0.121	0.127	0.82	0.78	
	all-early		0.001	−0.022	0.135	0.142	0.83	0.78	
[Co/H]	all-late		0.001	−0.002	0.103	0.113	0.83	0.79	
	early	5	0.000	−0.013	0.135	0.109	0.81	0.73	✓
	late	5	−0.003	−0.003	0.114	0.100	0.79	0.74	✓
	all	21	0.000	−0.006	0.129	0.120	0.84	0.82	
	all-early		0.001	−0.014	0.140	0.125	0.86	0.83	
[Ni/H]	all-late		−0.001	−0.005	0.115	0.117	0.84	0.82	
	early	9	0.000	−0.010	0.136	0.148	0.86	0.79	✓
	late	12	−0.005	−0.009	0.131	0.101	0.79	0.80	✓

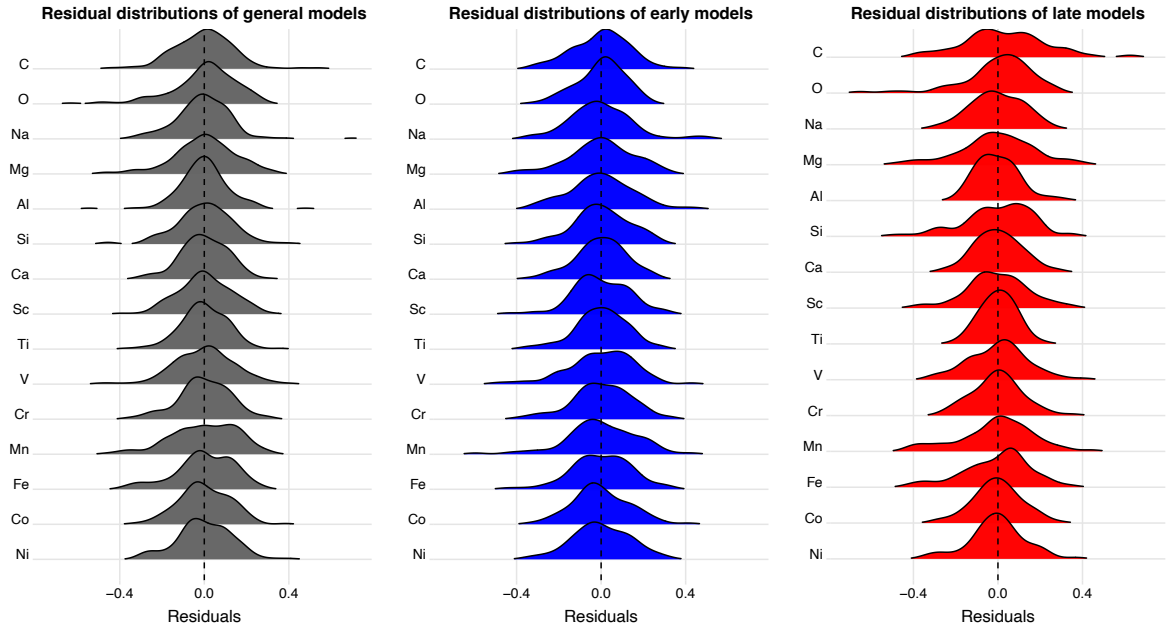

Figure 5.6: Distributions of the differences between primaries' and secondaries' abundances using the general, early and late models in black, blue, and red, respectively.

Iron-peak elements: Sc, V, Cr, Mn, Co, and Ni

For scandium, the general and early models yield similar performance with the same number of predictors for the early-type stars, but the late-type calibration, with just one predictor, fails to predict the abundance in the cooler stars.

For vanadium, chromium, manganese, cobalt, and nikel, the early and late models yield similar performance to the general model, while using approximately half the number of predictors.

Summary of calibration performance

In summary, early-type M dwarfs consistently benefit from dedicated calibrations that reduce model complexity while preserving or even improving accuracy. Late-type M dwarfs pose greater challenges: models trained only on them often underperform or fail to reproduce the abundances, and the general model remains the best option in most cases.

Sodium, aluminium, calcium, titanium, vanadium, chromium, manganese, cobalt, and nikel stand out as elements where both early and late models are viable, showing good results with fewer predictors. In contrast, elements such as carbon, oxygen, magnesium, silicon, scandium, and iron are best modelled using only the early-type stars, and the general calibrations are needed for the cooler stars.

Interpretation of the spectral indices and features

To further interpret the empirical models, we analysed the relative importance of the spectral indices used as predictors, listed in Table C.2. A few indices clearly dominate the top positions of the calibrations, reflecting consistent empirical patterns across the different stellar subsamples.

The F07 feature stands out as the most consistently selected predictor for all abundances in the general and early-type models, whereas the F05 feature becomes dominant in the late-type

stars. This behaviour agrees with the results of Mann et al. (2013), who originally defined both indices as metallicity indicators.

Several calibrations also rely on CaH molecular bands, particularly the CaH 1 index, which is systematically used in the whole and early-type samples for nearly all elements. For the early-type M dwarfs, the CaH 3 index appears to be most relevant for Cr, Mn, Fe, and Ni, while CaH Narr contributes significantly to the calibration of Ca, Sc, Cr, Fe, Co, and Ni. These indices trace the CaH absorption bands between 6000 and 7000,Å, which, although they vary with effective temperature, are relatively weak in M dwarfs for spectral classification. However, the bandstrengths of the hybride features (such us FeH, MgH, and CaH) are also correlated with abundance, increasing in strength with decreasing abundance. These CaH bands appear to be more sensitive to abundance variations among early-type M dwarfs, with the CaH 1 index saturating near spectral type M3 V due to a TiO absorption Reid et al. (1995), which is consistent with the observed behaviour in our calibrations.

From the viewpoint of nucleosynthesis origins, we note that the CaH 1 index (associated with the λ6380,Å CaH band) is applied across all elemental calibrations, whereas the CaH 3 and CaH Narr indices (tracing the λ6880,Å CaH band) are selected for elements predominantly produced in Type Ia supernovae, as illustrated in Fig. 1.3.

Another index of interest is Ratio B (Ti I), which encodes the atomic titanium line at 7358 Å. This index is frequently selected for the general and early models when deriving the abundances of C, Na, Mg, Al, Si, Ca, Ti, and V, but not for O, Sc, Cr, Mn, Fe, Co, or Ni. The first group corresponds to elements mainly or partially synthesised in core-collapse supernovae (Types Ib, Ic, and II), while the latter, but oxygen, are primarily associated with Type Ia supernovae.

As emphasised previously, these data-driven empirical calibrations explore statistical correlations between spectral features and chemical abundances, which may reflect shared nucleosynthetic origins or blended spectral features sensitive to overall composition. However, they do not try to explain or model the underlying astrophysical processes explicitly, and their purpose is therefore to complement, but not replace, more physically-motivated approaches.

5.3.2 Prediction of abundances for the CAFOS sample

We used the empirical calibrations presented by Alonso-Floriano et al. (2015) to derive the spectral types for the rest of CAFOS targets using least-squares fitting and the TiO 2, TiO 5, PC1, VO-7912 and Color-M spectral indices. Alonso-Floriano et al. (2015) published the spectral types of 753 of these stars based on the low-resolution spectral indices, and 41 more were added in Montes et al. (2018). We report here, for the first time, the spectral types for the remaining 173 stars. The full CAFOS sample with spectral classifications is presented in Table C.3. We also applied our calibrations to the full CAFOS sample to derive the abundances of 15 atomic species.

Comparison with photometric [Fe/H]

To test the reliability of our [Fe/H] predictions from low-resolution spectral indices, we compared them against photometric metallicities derived from the Bayesian calibrations presented in Chapter 2 (Duque-Arribas et al., 2023). This comparison required crossmatching the CAFOS sample with the *Gaia* DR3 and CatWISE2020 catalogues using the CDS X-match service within TOPCAT (Taylor, 2005), with a search radius of 15" and the "All" find option. Then we visually inspected and corrected mismatches using Aladin (Bonnarel et al., 2000). Of the 967 CAFOS stars, 783 were successfully matched to both catalogues. Finally, applying quality cuts and

excluding giant stars following the criteria from Section 2.2.2, we obtained a final comparison sample of 265 dwarf stars. The corresponding color–magnitude diagram is shown in Fig. 5.7.

After recovering the metallicity gradient in the main sequence for the subset of high-quality stars, we deduced that our predicted [Fe/H] values obtained from the low-resolution indices hold qualitative reliability. To further validate our findings quantitatively, we conducted a comparison between the photometric and low-resolution [Fe/H], as illustrated in Fig. 5.8. This analysis revealed a commendable predictive performance, with a residual scatter of ~ 0.13 dex, supporting the overall reliability of the low-resolution [Fe/H] predictions.

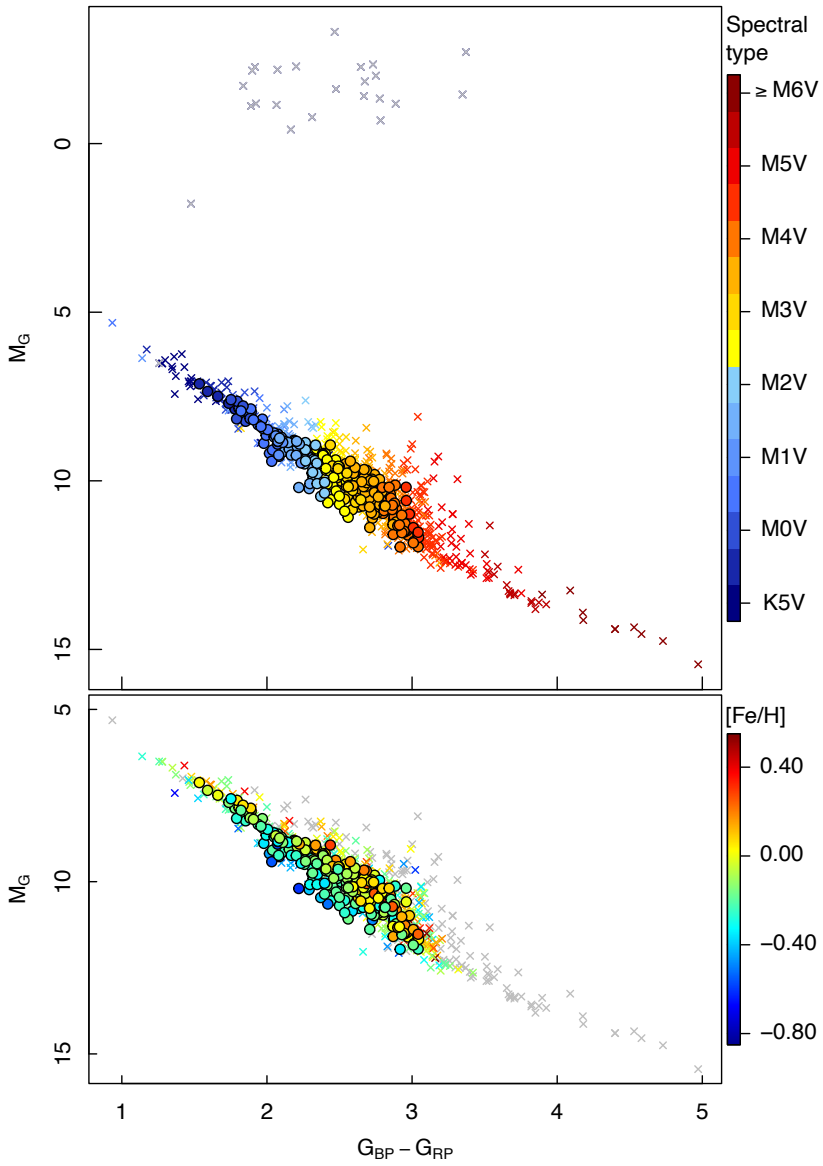

Figure 5.7: Upper panel: Color-magnitude diagram of the CAFOS sample, color-coded by spectral type. Giant stars appear in gray. Filled circles represent the stars with good astrophotometric data. Lower panel: Same main sequence, color-coded by the predicted [Fe/H] using the low-resolution indices. Stars outside the range of application are represented in gray.

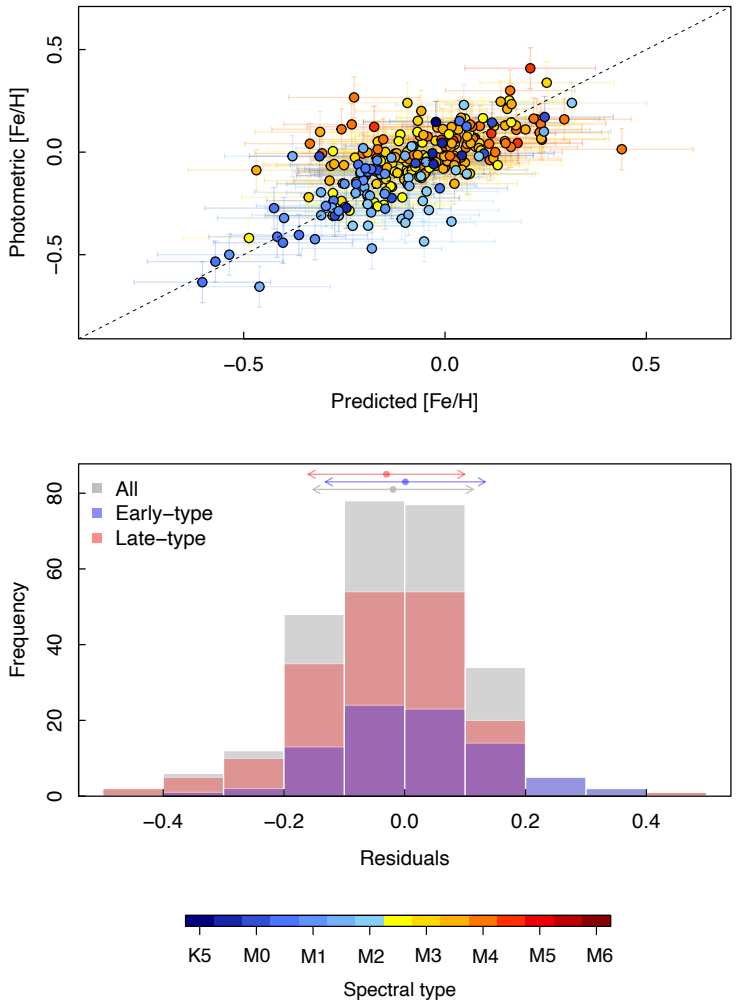

Figure 5.8: Upper panel: Comparison between our predicted [Fe/H] using the CAFOS low-resolution indices and the photometric [Fe/H] using the relations by Duque-Arribas et al. (2023) for the good-quality CAFOS subsample, color-coded by spectral types. Lower panel: Distributions of the residuals. The arrows at the top indicate the mean and standard deviation of each distribution.

Expected trends of [X/Fe] versus [Fe/H]

Given this consistency, we proceeded with confidence to estimate abundances for the full CAFOS sample, applying the calibration relations derived in this work. We excluded 25 giant stars, 74 dwarfs cooler than M4.5 V (outside our calibration domain), 64 reported young stars, 15 eruptive variables, and 24 known spectroscopic multiple systems, resulting in 774 stars suitable for abundance estimation. These predictions are compiled in Table C.4.

We explored the abundance trends by plotting the predicted [X/Fe] ratios versus [Fe/H] in Fig. 5.9. For comparison, we used the trends reported for solar-type stars by Mészáros et al. (2025), based on abundances derived from APOGEE spectra with the APOGEE Stellar Parameter and Chemical Abundances Pipeline (ASPCAP; García Pérez et al. 2016). These data were produced within the Milky Way Mapper programme (Johnson et al., in prep.), one of the three surveys of SDSS-V (Kollmeier et al., 2017, 2025). Importantly, Mészáros et al. (2025) do not report Sc abundances, and V and Co abundances are not reliable for dwarf stars, as indicated by the applicability regions in their Table 6. We also compared with the abundances for the

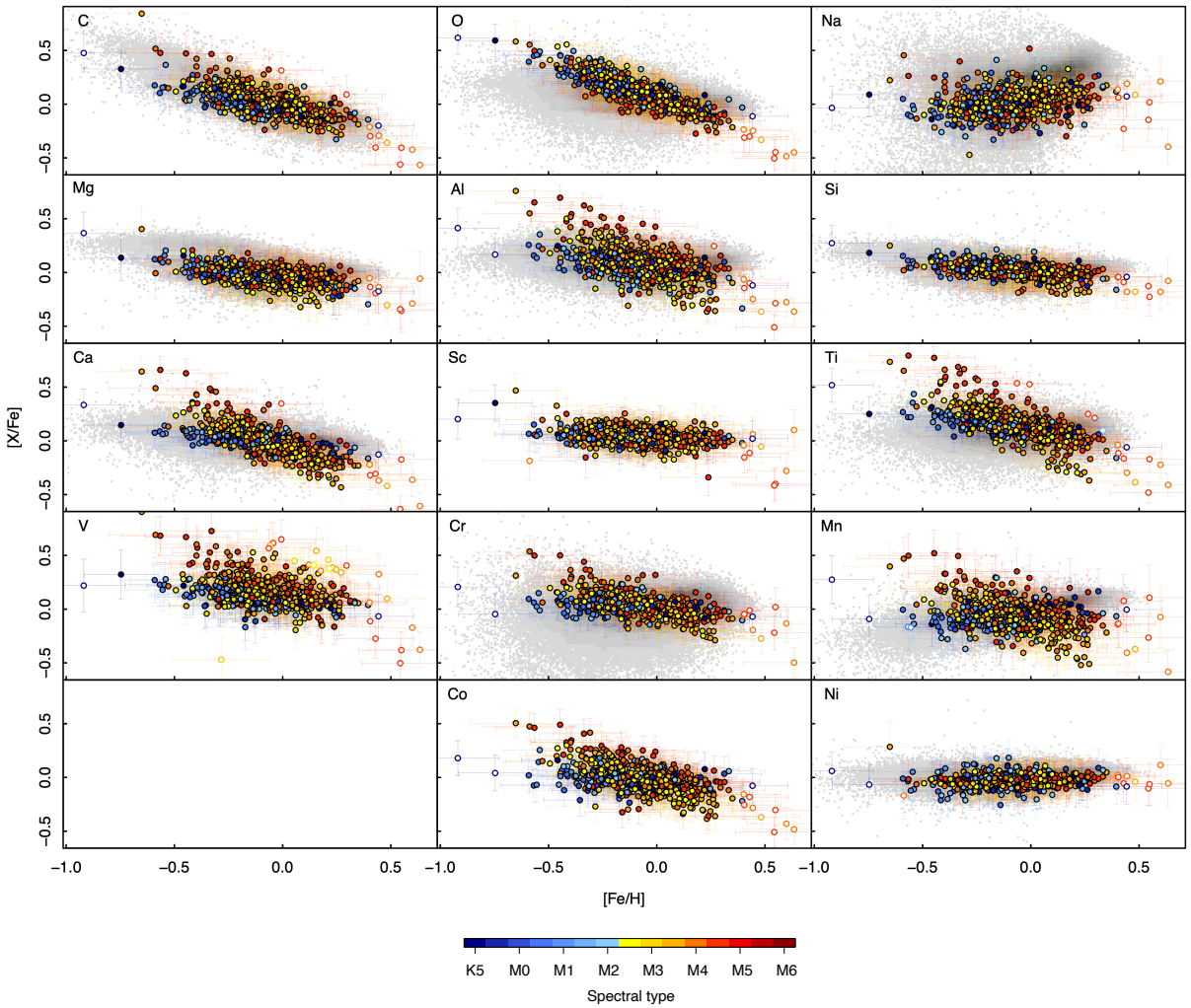

Figure 5.9: Abundance ratios [X/Fe] versus [Fe/H] for the CAFOS sample using our predicted values, color-coded by spectral type. Open circles denote stars with predictions outside the range of application of the calibrations. In gray we represent the trends for solar-type stars from Mészáros et al. (2025). See also Figs. C.4 and C.5.

FGK primaries from Montes et al. (2018) and Duque-Arribas et al. (2024) in Figs. C.4 and C.5. In general, we found that the global trends agree well with those from Mészáros et al. (2025), with particularly good consistency for C, Mg, Si, and Ni. For Al and Ca, the later-type M dwarfs showed slightly larger scatter, which may reflect intrinsic measurement challenges at cooler temperatures. For O and Ti, we obtained steeper trends than Mészáros et al. (2025), although our results remain compatible with those of Duque-Arribas et al. (2024) and Montes et al. (2018). Na and Cr exhibit similar trends, though the ASPCAP values show substantial scatter. Finally, Mn abundances in later-type M dwarfs fail to reproduce the expected behaviour.

Comparison with the literature

To further validate our results, we compared them against abundances derived from high-resolution spectroscopy found in the literature.

Maldonado et al. (2020) derived abundances of elements beyond iron for M-dwarf stars using high-resolution optical spectra obtained with HARPS (Mayor et al., 2003) and HARPS-N

(Cosentino et al., 2012). Their analysis combined principal component analysis with sparse Bayesian methods, calibrated with a sample of FGK+M binary systems. After carefully cross-matching with our CAFOS sample, we found 52 stars in common. Fig. 5.10 shows a comparison of our low-resolution abundance estimates against the results of Maldonado et al. (2020), and the statistics of the residuals are summarised in Table 5.3. Metrics are reported separately for early- and late-type M dwarfs.

We found a heterogeneous level of agreement across elements and spectral types. Carbon shows good correlations (~ 0.7) in both early- and late-type M dwarfs. Silicon and nickel also display consistent results, particularly in late-type stars, where the correlations tend to be stronger. Aluminium shows moderate correlations and relatively low scatter in both subsamples.

In contrast, some elements exhibit weaker agreement. Vanadium shows poor correlations ($r < 0.2$) and large dispersion in both early- and late-type stars, which may stem from the known challenges in measuring [V/H] reliably even in high-resolution data or due to the strong NLTE effects in the M dwarfs (see Shan et al. 2021). The [V/H] values reported by Maldonado et al. (2020) are clustered near solar and appear flatter than expected, with large internal scatter, and the authors themselves noted a discrepancy between M dwarfs and FGK-type stars. These issues suggest the [V/H] measurements in their sample may not be reliable. The iron abundances from Maldonado et al. (2020) appear systematically higher than ours by ~ 0.08 dex, with lower correlations for late types. The observed dispersions in [Fe/H] (~ 0.20–0.28 dex) are comparable to those reported by Maldonado et al. (2020) when comparing their results to Passegger et al. (2019) (~ 0.23–0.28 dex). Similarly, cobalt shows consistent negative offsets of ~ 0.20 dex, while

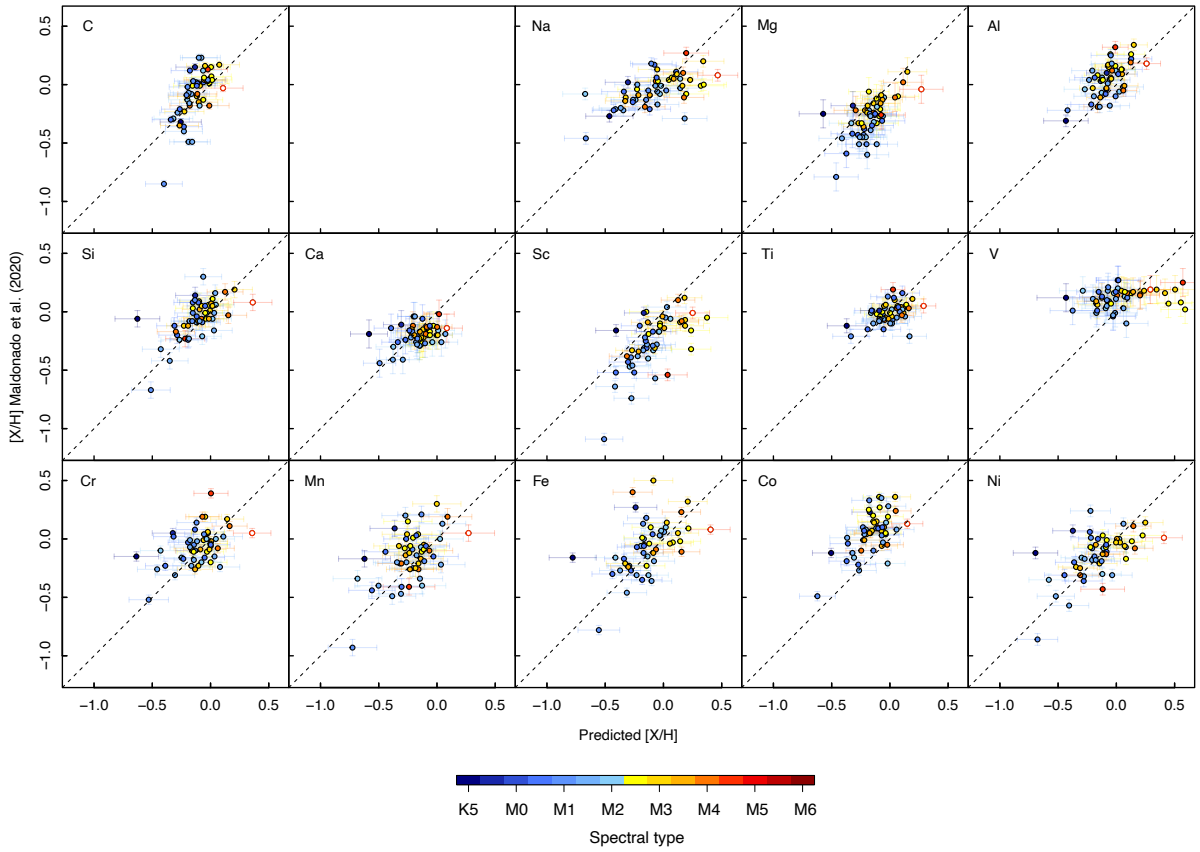

Figure 5.10: Comparison between the predicted abundances using our calibrations and values derived by Maldonado et al. (2020). Stars are color-coded by spectral type.

Table 5.3: Statistics of the differences with Maldonado et al. (2020).

Abundance	Sample	$\bar{x}$	$\tilde{x}$	σ_x	MAD(x)	r	r_S
[C/H]	Early	−0.049	−0.080	0.187	0.095	0.74	0.75
	Late	−0.040	−0.054	0.094	0.082	0.71	0.67
[Na/H]	Early	−0.090	−0.113	0.194	0.166	0.51	0.48
	Late	0.049	0.025	0.186	0.219	0.54	0.50
[Mg/H]	Early	0.152	0.182	0.148	0.094	0.42	0.44
	Late	0.082	0.080	0.097	0.095	0.74	0.70
[Al/H]	Early	−0.108	−0.098	0.119	0.126	0.60	0.49
	Late	−0.119	−0.133	0.121	0.119	0.53	0.54
[Si/H]	Early	−0.075	−0.077	0.161	0.160	0.60	0.59
	Late	−0.035	−0.036	0.105	0.077	0.70	0.72
[Ca/H]	Early	0.020	0.041	0.159	0.157	0.38	0.27
	Late	0.077	0.085	0.079	0.081	0.39	0.39
[Sc/H]	Early	0.156	0.145	0.171	0.097	0.70	0.61
	Late	0.181	0.128	0.182	0.156	0.44	0.42
[Ti/H]	Early	0.000	−0.013	0.123	0.130	0.40	0.42
	Late	0.015	0.026	0.101	0.103	0.37	0.44
[V/H]	Early	−0.179	−0.176	0.154	0.115	0.04	0.13
	Late	0.054	−0.026	0.233	0.163	0.15	0.27
[Cr/H]	Early	−0.079	−0.089	0.178	0.185	0.41	0.32
	Late	−0.004	0.002	0.152	0.114	0.37	0.45
[Mn/H]	Early	−0.075	−0.068	0.216	0.257	0.54	0.45
	Late	−0.082	−0.095	0.160	0.182	0.44	0.29
[Fe/H]	Early	−0.084	−0.080	0.199	0.130	0.50	0.49
	Late	−0.083	−0.062	0.279	0.202	0.17	0.36
[Co/H]	Early	−0.202	−0.202	0.152	0.150	0.61	0.55
	Late	−0.215	−0.217	0.126	0.105	0.36	0.33
[Ni/H]	Early	−0.072	−0.037	0.199	0.150	0.56	0.48
	Late	0.059	0.036	0.148	0.144	0.63	0.68

magnesium and scandium have positive offsets of ~ 0.15 dex. These offsets are in line with the biases already reported by Maldonado et al. (2020), whose results for the M dwarfs tend to show higher [Co/H] and lower [Mg/H] and [Sc/H] when compared to FGK dwarfs, potentially explaining the observed discrepancies.

We also found five stars in common with Ishikawa et al. (2020), who derived elemental abundances using high-resolution near-infrared spectra from CARMENES. In a follow-up study, Ishikawa et al. (2022) extended their analysis using observations from the InfraRed Doppler instrument (IRD; Tamura et al. 2012; Kotani et al. 2018) on the Subaru Telescope, focussing on mid- to late-type M dwarfs. In this case, we identified seven stars in common with our CAFOS sample. A comparison between our low-resolution abundance predictions and those from both studies is presented in Fig. 5.11, and the residual metrics are summarised in Table 5.4. We do not tabulate the statistics for [Si/H] and [V/H], as Ishikawa et al. (2022) derived these abundances only for GJ 436, the hottest star in their sample.

Despite the limited number of stars in common, the comparison reveals remarkably good agreement for most elements. Iron abundances show strong consistency, with a mean offset of only -0.015 dex, a standard deviation of 0.14 dex, and high correlation coefficients (~ 0.8). Sodium and calcium also exhibit excellent agreement, with dispersions below 0.15 dex and correlation coefficients exceeding 0.85. Chromium and manganese show slightly larger scatter (~ 0.17–0.22 dex) but still maintain strong correlations (~ 0.8). Magnesium and titanium display

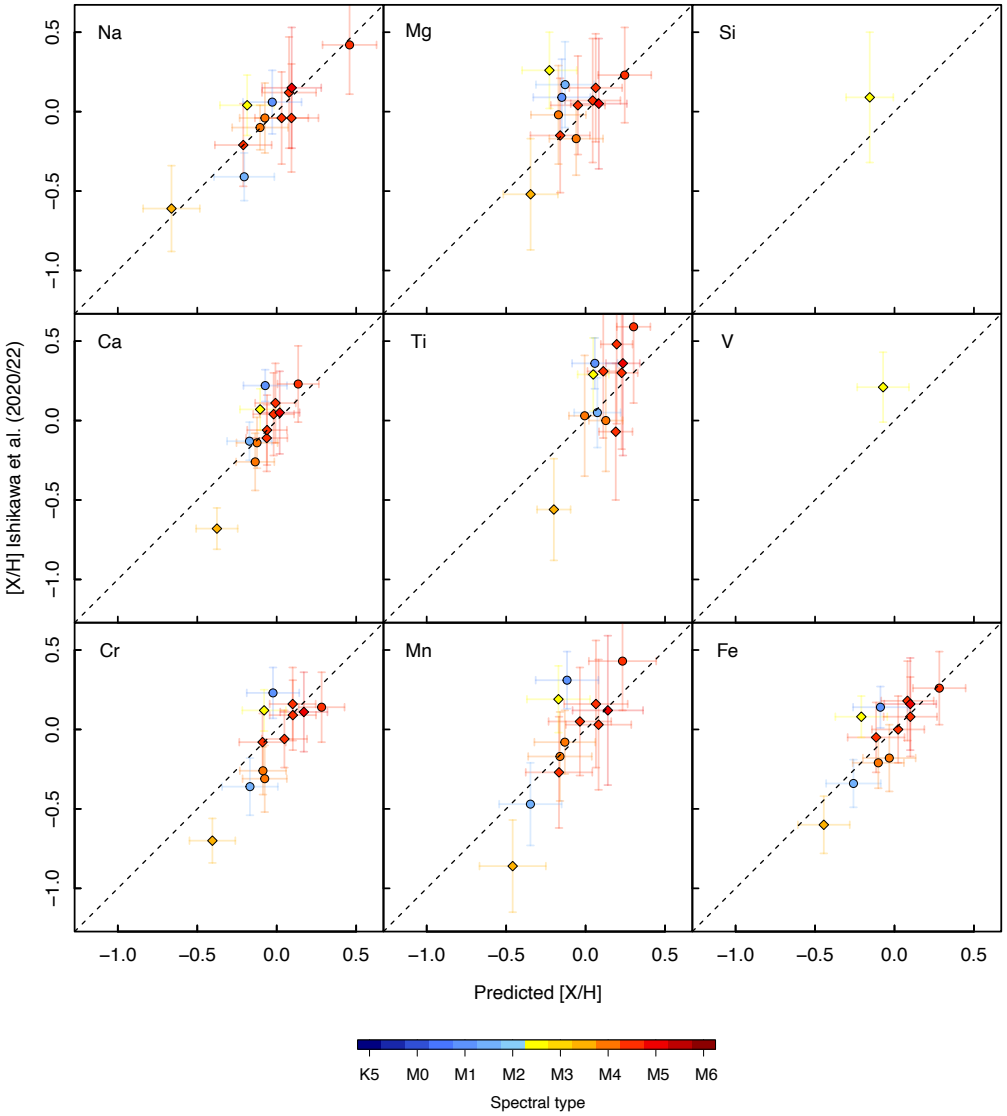

Figure 5.11: Comparison between our predicted abundances and values derived by Ishikawa et al. (2020) (circles) and Ishikawa et al. (2022) (diamonds). Stars are color-coded by spectral type.

somewhat lower correlations, especially in the case of Mg. Ishikawa et al. (2022) noted that their Mg abundance was derived from a single spectral line, potentially increasing the dispersion, while their [Ti/Fe] values for the M dwarfs showed a large scatter and did not follow the expected trend for FGK-type stars. Overall, these results confirm that our low-resolution predictions are in good agreement with independent high-resolution measurements, even for the latest spectral types.

Furthermore, the CARMENES consortium has extensively investigated the chemical composition of M dwarfs using high-resolution spectra obtained with the CARMENES spectrograph (Quirrenbach et al., 2020; Ribas et al., 2023). Notably, Passegger et al. (2019) and Marfil et al. (2021) provided detailed stellar parameters, including [Fe/H], for the CARMENES sample using both the visible and the near infrared regimes. Additionally, Shan et al. (2021) determined vanadium abundances accounting for hyperfine splitting, Tabernero et al. (2024) derived magnesium and silicon abundances, and Mas-Buitrago et al. (2024) followed a machine-learning approach to derive the stellar parameters, including [Fe/H]. Since a subset of these stars overlaps with our CAFOS sample, we performed a comparative analysis between their high-resolution abundances

Table 5.4: Statistics of the differences with Ishikawa et al. (2020, 2022).

Abundance	$\bar{x}$	$\tilde{x}$	σ_x	MAD(x)	r	r_S
[Na/H]	−0.004	−0.020	0.110	0.070	0.91	0.85
[Mg/H]	−0.088	−0.056	0.184	0.136	0.55	0.33
[Ca/H]	−0.027	−0.036	0.150	0.104	0.88	0.76
[Ti/H]	−0.065	−0.099	0.221	0.234	0.78	0.60
[Cr/H]	0.058	0.085	0.168	0.149	0.82	0.71
[Mn/H]	−0.043	−0.021	0.221	0.146	0.83	0.67
[Fe/H]	−0.015	0.019	0.140	0.129	0.83	0.78

and our low-resolution predictions. The outcomes of this comparison are illustrated in Fig. 5.12 and the corresponding residual metrics are summarised in Table 5.5, with early- and late-type subsamples analysed separately due to sufficient numbers in each group.

Overall, the comparison reveals moderate agreement, with some variation across elements and spectral subtypes. For iron, we observe noticeable differences depending on the literature source. For iron, our predictions show the best consistency with the machine-learning results of Mas-Buitrago et al. (2024), which exhibit small offsets and minimal dispersions below 0.17 dex across both early and late M dwarfs. The abundances by Marfil et al. (2021) show a better agreement for early-type M dwarfs. In contrast, the [Fe/H] values from Passegger et al. (2019) tend to be systematically higher than our predictions for early M dwarfs, with a mean offset

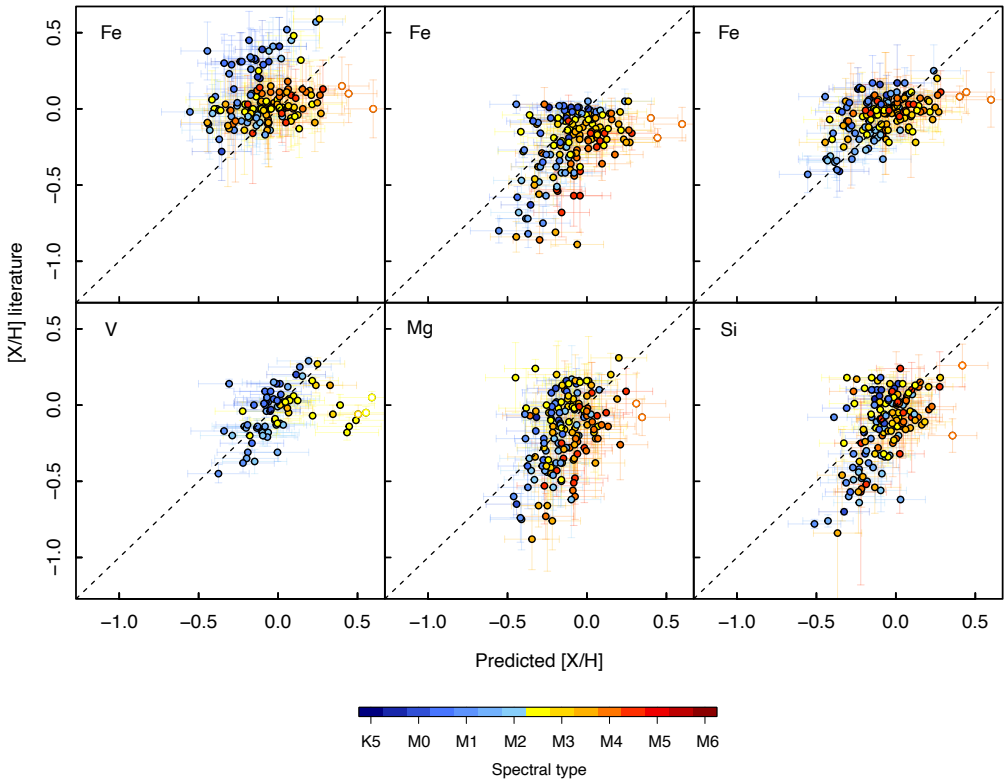

Figure 5.12: Comparison between the predicted abundances using our calibrations and literature values derived from CARMENES spectra for M dwarfs in common with previous studies: [Fe/H] from Passegger et al. (2019), Marfil et al. (2021), and Mas-Buitrago et al. (2024); [V/H] from Shan et al. (2021); and [Mg/H] and [Si/H] from Tabernero et al. (2024). Stars are color-coded by spectral type.

Table 5.5: Statistics of the differences with the CARMENES papers.

Abundance	Reference	Sample	$\bar{x}$	$\tilde{x}$	σ_x	MAD(x)	r	r_S
[Fe/H]	Passegger et al. (2019)	Early	−0.324	−0.350	0.199	0.186	0.48	0.40
		Late	−0.047	−0.055	0.181	0.151	0.33	0.33
[Fe/H]	Marfil et al. (2021)	Early	0.061	0.071	0.196	0.209	0.65	0.62
		Late	0.198	0.195	0.206	0.177	0.41	0.36
[Fe/H]	Mas-Buitrago et al. (2024)	Early	−0.103	−0.103	0.149	0.160	0.62	0.56
		Late	0.001	−0.022	0.166	0.158	0.46	0.41
[V/H]	Shan et al. (2021)	Early	−0.013	−0.033	0.128	0.119	0.67	0.68
		Late	0.157	0.079	0.211	0.082	0.11	0.13
[Mg/H]	Tabernero et al. (2024)	Early	0.007	0.020	0.198	0.225	0.61	0.58
		Late	0.067	0.082	0.241	0.252	0.30	0.27
[Si/H]	Tabernero et al. (2024)	Early	0.058	0.033	0.186	0.177	0.60	0.56
		Late	0.091	0.097	0.214	0.249	0.46	0.35

of −0.32 dex. This discrepancy with the Passegger et al. (2019) results for early M dwarfs was previously noticed by Marfil et al. (2021) as well.

The vanadium abundances from Shan et al. (2021) show good agreement for early-type M dwarfs, with a dispersion below 0.13 dex, but poorer performance for late types. This may suggest that our low-resolution features retain predictive power for V only in warmer stars. For magnesium and silicon, we find moderate correlations ($r \sim 0.60$ for early types) and small offsets ($\lesssim 0.1$ dex), though scatter remains non-negligible. As with vanadium, performance degrades in the late-type subsample for both Mg and Si, consistent with our earlier findings that abundance predictions from low-resolution spectra are more robust for early M dwarfs than for later subtypes.

Last but not least, we compared our abundance predictions to those from Mészáros et al. (2025) using ASPCAP for the Milky Way Mapper. Mészáros et al. (2025) said that, given the observed offsets in surface gravity and metallicity, abundances of stars with $T_{\rm eff} < 4500$ K and $\log g > 4.0$ dex should be used with caution. We carefully crossmatched the CAFOS sample with the Milky Way Mapper sample, obtaining 314 coincidences. Only 65 of these stars are not flagged as bad (`bad_flag` column). Finally, following the applicability regions indicated in Table 6 of Mészáros et al. (2025), we removed the stars cooler than $T_{\rm eff} < 3500$ K (with spectral types later than M2.0 V), obtaining a final sample of 24 stars for comparison.

In Fig. 5.13, we present a comparison of our low-resolution predictions versus the abundances by Mészáros et al. (2025) for C, O, Mg, Si, Ca, Fe, and Ni, whose values are reliable for dwarf stars above 3500 K. The residual statistics are summarised in Table 5.6. We excluded elements such as Na, Al, Ti, Cr, and Mn, which are only reliable for hotter dwarfs ($T_{\rm eff} > 4250$ K), as well as V and Co, which lack robust abundance determinations for dwarfs of any spectral type (Mészáros et al., 2025). ASPCAP does not report Sc abundances. In general, we found strong correlations for most elements, with dispersions between 0.10–0.18 dex and correlations as high as $r \sim 0.80$. Si shows a clear offset of ~ 0.15 dex, but with low dispersion and strong correlation. Magnesium, on the other hand, exhibits a larger scatter and the lowest correlation ($r = 0.57$). Oxygen appears to be the main outlier in the comparison, with a noticeable offset of 0.25 dex, possibly reflecting challenges in oxygen abundance determinations for cool dwarfs in both approaches.

Overall, our low-resolution abundance predictions show encouraging levels of agreement with independent high-resolution studies. The strongest correlations and smallest dispersions are observed when comparing with the SDSS-V Milky Way Mapper sample (Mészáros et al., 2025) and the results of Ishikawa et al. (2020, 2022), particularly for elements like Na, Ca, Cr, and Fe, where typical dispersions are below 0.15 dex and correlations reach $r \sim 0.8$–0.9. The comparison with

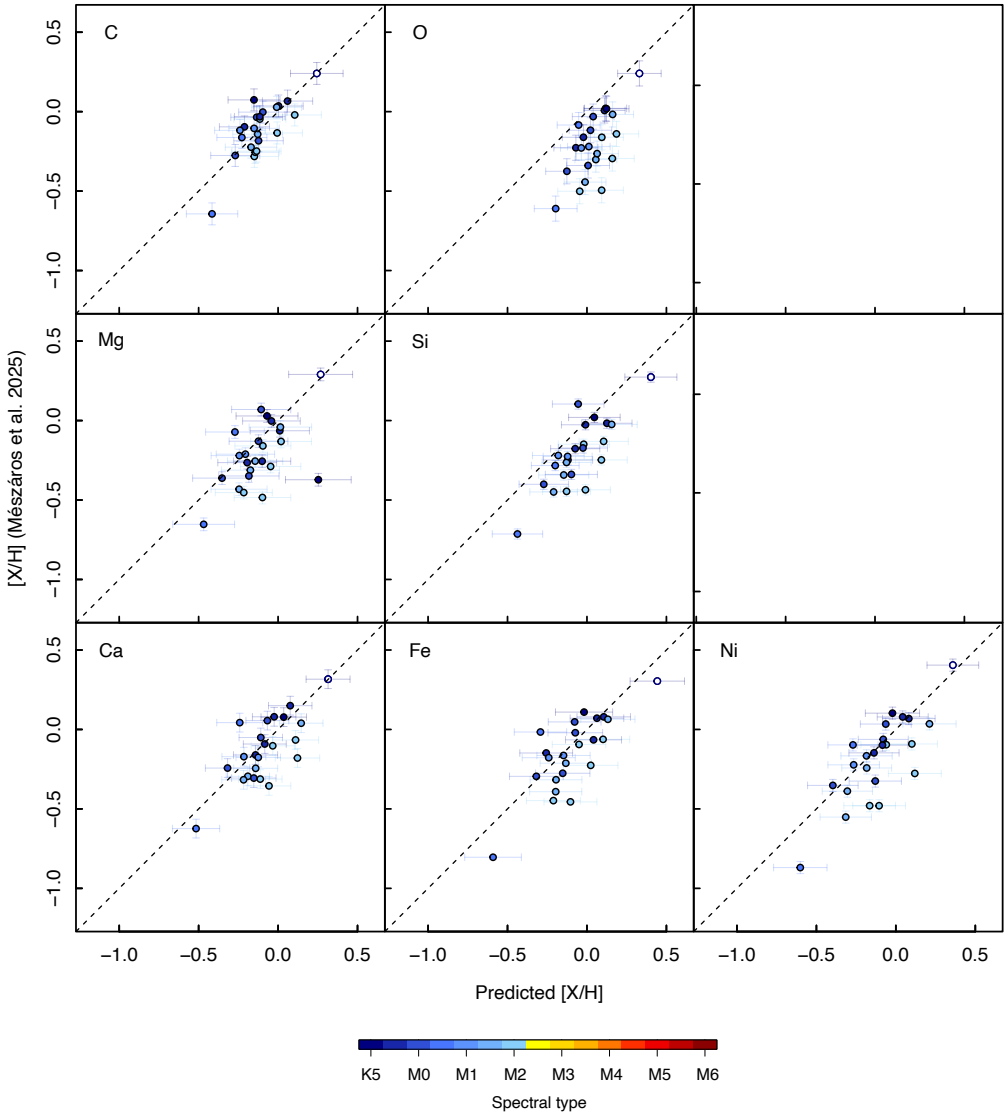

Figure 5.13: Comparison between the predicted abundances using our calibrations and the abundances by Mészáros et al. (2025). Stars are color-coded by spectral type.

the CARMENES consortium reveals more variable results, with the best performance found for Fe (from Mas-Buitrago et al. 2024) and V (in early-type stars). The agreement with Maldonado et al. (2020) is more heterogeneous, with consistent trends for several elements, but also systematic offsets for Mg, Sc, Fe, and Co.

In order to contextualise the observed discrepancies, we also compared the [Fe/H] determinations from the different literature sources among themselves. Figure 5.14 shows pairwise comparisons for [Fe/H] for the stars in common, without including our low-resolution results. The figure reveals non-negligible offsets and scatter between independent studies, even when similar instruments or analysis techniques were used. These systematic differences highlight the intrinsic challenges of abundance determinations in M dwarfs, which are subject to varying choices in atmospheric models, line lists, spectral regions, and assumptions about stellar parameters. This reinforces the importance of using homogeneous training samples and consistent methodologies when developing empirical calibrations.

Table 5.6: Statistics of the differences with Mészáros et al. (2025).

Abundance	$\bar{x}$	$\tilde{x}$	σ_x	MAD(x)	r	r_S
[C/H]	−0.001	−0.007	0.107	0.113	0.79	0.66
[O/H]	0.249	0.232	0.151	0.186	0.67	0.58
[Mg/H]	0.096	0.073	0.176	0.139	0.57	0.50
[Si/H]	0.157	0.135	0.123	0.091	0.82	0.77
[Ca/H]	0.043	0.051	0.138	0.141	0.75	0.60
[Fe/H]	0.058	0.068	0.147	0.142	0.79	0.69
[Ni/H]	0.077	0.014	0.161	0.101	0.80	0.75

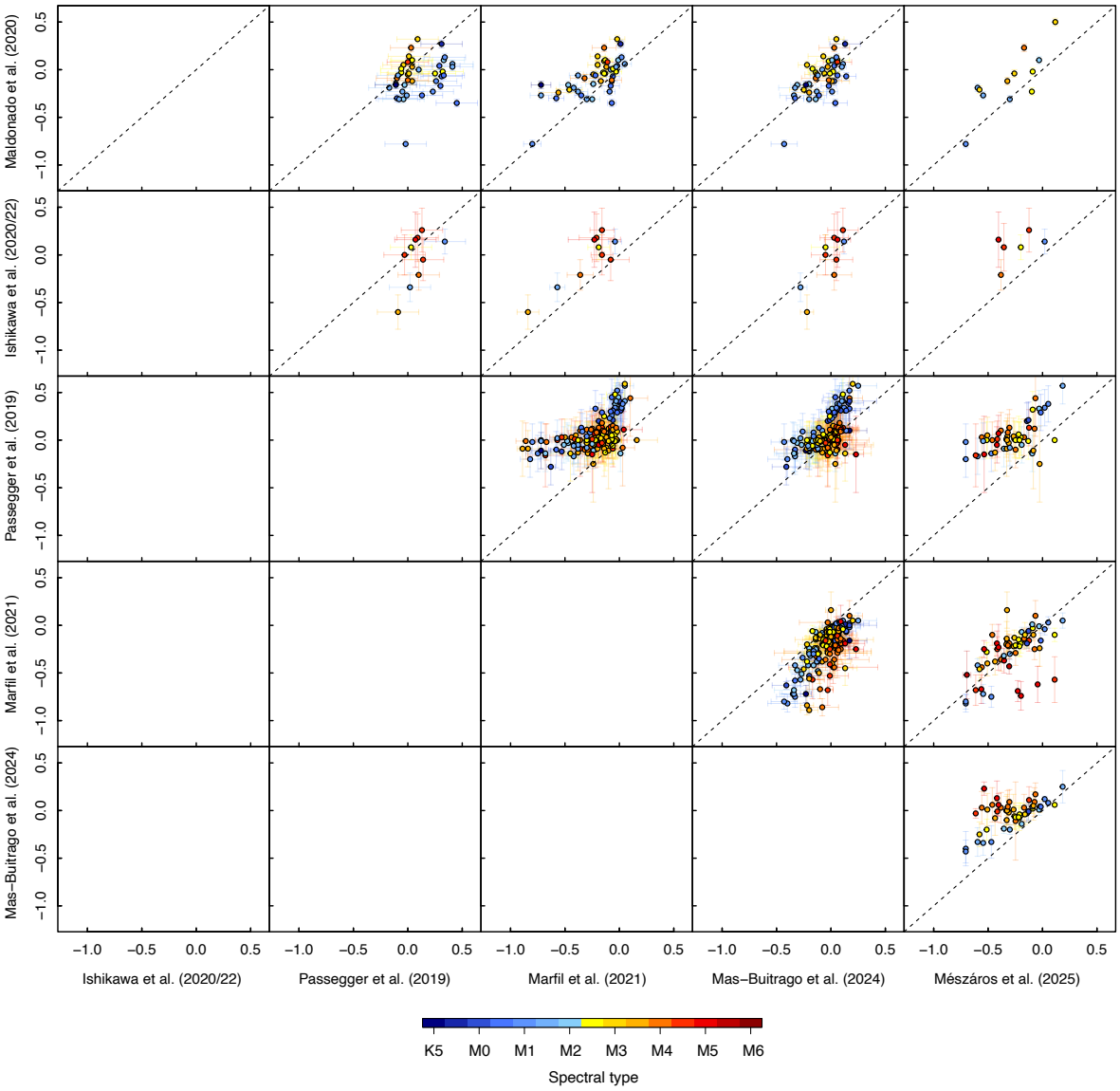

Figure 5.14: Pairwise comparison of [Fe/H] values from different literature sources (Maldonado et al., 2020; Ishikawa et al., 2020, 2022; Passegger et al., 2019; Marfil et al., 2021; Mas-Buitrago et al., 2024; Mészáros et al., 2025) for M dwarfs in common. Stars are color-coded by spectral type.

These results demonstrate that, despite the limitations of low-resolution data, carefully constructed empirical calibrations can recover reliable chemical abundances for M dwarfs, particularly in the early-type regime, thus enabling large-scale chemical studies of these stars with modest observational resources.

5.4 Summary

This chapter reinforces the value of wide binary systems with FGK primaries and M-dwarf companions as critical benchmarks for calibrating the fundamental properties of M-type stars. Because both components of these systems are coeval and chemically homogeneous, they offer a unique opportunity to test and refine empirical calibrations.

We demonstrated that low-resolution spectra, when carefully analysed, can recover chemical abundances for up to 15 atomic species in M dwarfs. By training empirical models on a sample of 162 FGK+M binaries, we derived abundance calibrations that are not only statistically robust but also practical in terms of required data quality and model complexity. To this end, we used the `projpred` package, which performs projection predictive variable selection for regression models. We found that separate calibrations for early- and late-type M dwarfs improve predictive performance in many cases, though the late-type stars remain more challenging.

The final application to nearly 800 stars in the CAFOS sample illustrates the scalability of the method. We recover the metallicity gradient in the colour–magnitude diagram, and our [Fe/H] estimates aligned well with those derived photometrically. The [X/Fe] vs. [Fe/H] trends we obtained are broadly consistent with those observed for FGK-type stars. Finally, our results show good agreement with independent high-resolution studies in the literature. This validates our methodology and highlights the potential of combining benchmark binaries with statistical learning techniques to study the chemical properties of cool dwarfs.

This work also underscores the need to explore advanced, data-driven methodologies to fully exploit the available data. Looking forward, the integration of machine learning and other statistical approaches, together with larger samples of benchmark stars and more homogeneous data, could help address the limitations of current methods and improve the precision of abundance estimates.

CHAPTER 6

CARMENES high-resolution spectroscopy of the M-dwarf secondaries

"Starlight tells us about the nature of stars. Spectroscopy is the key by which the starlight is decoded."
— David F. Gray

6.1 Introduction

Throughout this thesis, we have explored the chemical composition of M-type dwarf stars from multiple perspectives. We have employed various techniques to estimate their metallicities using photometric data, extracted information from low-resolution spectra, and characterised their hotter companions in wide binary systems. As the saying goes, "all roads lead to Rome", and in our case, these diverse approaches have all converged toward a common goal: it is now time to investigate M dwarfs using high-resolution spectroscopy.

Installed at the 3.5 m telescope at the Calar Alto Observatory (Almería, Spain), the CARMENES[1] instrument (Quirrenbach et al., 2020) is a state-of-the-art spectrograph designed to detect Earth-mass exoplanets around M dwarfs by means of the radial velocity (RV) technique. It delivers high-accuracy RV measurements with long-term stability across a broad wavelength range where M-dwarf stars have the peak of their spectral energy distribution. The instrument consists of optical (VIS) and near-infrared (NIR) channels covering the 5200–9600 Å and 9600–17100 Å wavelength regions with spectral resolutions of R = 94 600 and R = 80 400, respectively. This wide wavelength coverage provides a range of stellar activity indicators and valuable spectral information for stellar characterisation.

Between 2016 and 2020, as part of the guaranteed time observations (GTO) programme for the CARMENES consortium, a total of 19 633 spectra were collected for a sample of 362 targets (Ribas et al., 2023). This sample was selected from the CARMENES input catalogue, known as Carmencita (CARMENES Cool dwarf Information and daTa Archive; Alonso-Floriano et al. 2015), which currently contains approximately 2200 M dwarfs in the solar neighbourhood. The selection focused on the brightest M dwarfs ($J < 11.5$ mag) observable from Calar Alto ($\delta > -23°$) across all spectral subtypes. These stars were chosen independently of their multiplicity, age, or metallicity. The Carmencita targets have been extensively studied in numerous publications, which provide detailed insights into their spectral types, kinematics, multiplicity, photometry, rotational velocities, and activity indicators (Alonso-Floriano et al., 2015; Cortés-Contreras et al., 2017; Jeffers et al., 2018; Díez Alonso et al., 2019; Cifuentes et al., 2020; Perdelwitz et al., 2021; Shan et al., 2024; Cortés-Contreras et al., 2024; Cifuentes et al., 2025).

Regarding the topic of this thesis, the CARMENES GTO sample has been the subject of several analyses aimed at deriving atmospheric parameters through various methods (Passegger et al., 2018, 2019, 2020; Marfil et al., 2021), and some chemical abundances (Abia et al., 2020; Shan

[1] Calar Alto high-Resolution search for M dwarfs with Exoearths with Near-infrared and optical Échelle Spectrographs; https://carmenes.caha.es

et al., 2021; Tabernero et al., 2024). However, only seven M dwarfs within the CARMENES GTO sample are known to be bound in wide physical binaries with an FGK-type primaries (Montes et al., 2018): J02362+068 (M4.0 V), J04153-076 (M4.5 V), J05415+534 (M1.0 V), J07361-031 (M1.0 V), J08526+283 (M4.5 V), J14251+518 (M2.5 V), and J17052-050 (M1.5 V). This limited number of known M-dwarf secondaries in wide binaries with well-characterised solar-type primaries motivates the primary objective of this chapter: to expand the sample of such benchmark systems and to explore their potential for high-resolution spectroscopic analysis using the CARMENES instrument.

6.2 Analysis

6.2.1 Observations and reduction

Between January 2023 and December 2024, we obtained over 200 individual spectra of 44 M-dwarf secondaries from the sample of Montes et al. (2018), which had not previously been observed with CARMENES. These observations were carried out under a series of open-time proposals using the CARMENES instrument, led by C. Duque-Arribas, and with the collaboration of H. M. Tabernero, D. Montes, J. A. Caballero, C. Cifuentes, E. Marfil, E. Nagel, V. M. Passegger, A. Reiners, A. Schweitzer, and Y. Shan. The observing campaings and the corresponding time allocations were as follows: 23A-3.5-010 (36h), 23B-3.5-009 (22.5h), 24A-3.5-007 (20h), and 24B-3.5-008 (29h). The observed stars were selected from among the brightest M-dwarf secondaries in our list, with the aim of maximising coverage in the spectral type versus [Fe/H] parameter space, as shown in Fig. 6.1.

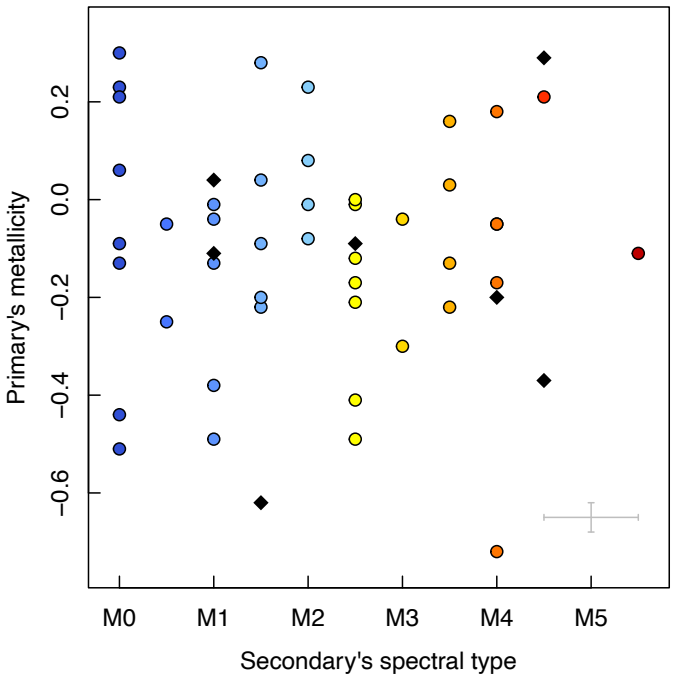

Figure 6.1: Spectral types of the M-dwarf companions observed with CARMENES versus the corresponding primaries' [Fe/H]. The seven GTO targets are marked as black diamonds. Average uncertainties are shown in the bottom right corner.

For each star, the individual spectra were corrected of telluric absorption using the software package `molecfit`[2] (Smette et al., 2015; Kausch et al., 2015), following the methodology described by Nagel et al. (2023). After telluric correction, the spectra were co-added to create high signal-to-noise (S/N) template spectra for each target (E. Nagel priv. comm.). The projected rotational velocities ($v \sin i$) were estimated using the cross-correlation technique described in Reiners et al. 2018 (A. Reiners priv. comm.). Table 6.1 summarises the basic properties of the observed M-dwarf secondaries, including both the newly observed stars and those previously observed in the CARMENES GTO programme. In particular, we provide the Washington Double Star catalogue identifier for each binary system, the target names, coordinates, J-band magnitude, spectral type, projected rotational velocity, signal-to-noise ratio, and number of individual observations for the M-dwarf secondaries. The table also includes the name and spectral type of the corresponding FGK-primaries.

Since CARMENES operates in vacuum, we applied a vacuum-to-air conversion following the International Astronomical Union standard (Morton, 2000):

$$\lambda_{\rm air} = \frac{\lambda_{\rm vacuum}}{n}, \tag{6.1}$$

where the refraction index n is given by:

$$n = 1 + 8.34254 \cdot 10^{-5} + \frac{2.406147 \cdot 10^{-2}}{130 - s^2} + \frac{1.5998 \cdot 10^{-4}}{38.9 - s^2} \tag{6.2}$$

and $s = 10^4/\lambda_{\rm vacuum}$, with $\lambda_{\rm vacuum}$ expressed in Å. Finally, we applied Doppler corrections to shift the spectra into the laboratory rest frame using the measured radial velocities of the targets.

6.2.2 Stellar parameters using StePar Syn

Stellar atmospheric parameters (effective temperature, surface gravity, and metallicity) were determined using the StePar Syn[3] code (Tabernero et al., 2022), a Python 3 Bayesian implementation of the spectral synthesis method. StePar Syn relies on a Markov chain Monte Carlo (MCMC) sampler to map the parameter space by comparing synthetic model spectra with observed data. The code has been successfully applied in several astrophysical studies, including analyses of stars in young open clusters (Lohr et al., 2018; Negueruela et al., 2018, 2021; Alonso-Santiago et al., 2019, 2020), red supergiants in the Magellanic clouds (Tabernero et al., 2018), the first super-AGB candidate in the Milky Way (Tabernero et al., 2021a), the CARMENES GTO sample (Marfil et al., 2021), and exoplanet host stars observed by ESPRESSO and CARMENES (e.g. Borsa et al., 2021; Demangeon et al., 2021; Lillo-Box et al., 2021; Mallorquín et al., 2023; Murgas et al., 2024; Goffo et al., 2024; González Hernández et al., 2024; Geraldía-González et al., 2025).

To compute the stellar parameters of our sample using StePar Syn, we used the line list and model grid described by Marfil et al. (2021). The line list consists of 75 Fe I and Ti I atomic lines, carefully selected from the CARMENES template spectra of three representative early-, mid-, and late-type M dwarfs, and the TiO γ and ϵ molecular bands, known for their high sensitivity to $T_{\rm eff}$ (Rajpurohit et al., 2014; Passegger et al., 2016). The spectral ranges synthesised around these features are shown in Fig. 6.2. The synthetic spectra were computed from a grid of BT-Settl model atmospheres (Allard, 2014) and the radiative transfer code `turbospectrum` (Plez, 2012). For further details on the StePar Syn code and the adopted methodology, we refer to Tabernero et al. (2022) and Marfil et al. (2021).

To mitigate degeneracies in the parameter space, particularly between $\log g$ and [Fe/H], we adopted Gaussian priors for $T_{\rm eff}$ and $\log g$. The priors were centered on the values of $T_{\rm eff}$ and

[2] http://www.eso.org/sci/software/pipelines/skytools/molecfit
[3] https://github.com/hmtabernero/StePar Syn/

Table 6.1: Sample of the M dwarfs in wide physical binaries with FGK-type primaries analysed in this work.

	M-dwarf secondaries									FGK primaries	
WDS	Karmn	Name	RA	DEC	Jmag	SpT	$v \sin i$	S/N	# obs.	Name	SpT
01076+2257	J01076+229	HD 6660 B	01:07:38	+22:57:22	9.53	M3.5 V	···	···	2	HD 6660 A	K4 V
01572-1015	J01571-102	HD 11964 B	01:57:11	-10:14:53	8.41	M0.0 V	···	···	5	HD 11964 A	G8 IV
02361+0653	J02362+068	BX Cet	02:36:15	+06:52:19	7.33	M4.0 V	≤ 2	···	···	HD 16160 A	K3 V
02442+4914	J02441+492	θ Per B	02:44:10	+49:13:54	6.69	M1.5 V	≤ 2	112	5	θ Per A	F7 V
02556+2652	J02555+268	HD 18143 C	02:55:36	+26:52:21	9.56	M4.0 V	···	···	5	HD 18143 A	K2 IV
03042+6142	J03047+617	vMa 2-4	03:04:43	+61:44:10	8.88	M3.0 V	···	···	4	HD 18757	G4 V
03332+4615	J03332+462	HD 21845 B	03:33:14	+46:15:19	8.38	M0.0 V	···	···	4	V577 Per	G5 V
03480+4032	J03480+405	J03480588+4032226	03:48:06	+40:32:23	9.35	M1.5 V	···	···	5	HD 23596	F8 V
03520+3947	J03519+397	TYC 2868-639-1	03:51:58	+39:46:57	8.28	M0.0 V	≤ 3	103	6	HD 275867	K2 V
03575-0110	J03574-011	HD 24916 B	03:57:29	-01:09:23	7.77	M2.5 V	···	···	4	HD 24916 A	K4 V
04153-0739	J04153-076	o^{02} Eri C	04:15:22	-07:39:17	6.75	M4.5 V	2.1 ± 1.5	···	···	o^{02} Eri A	K0.5 V
04559+0440	J04559+046	HD 31412 B	04:55:55	+04:40:16	8.50	M2.0 V	···	···	5	HD 31412	F9.5 V+
05003+2508	J05003+251	HD 31867 B	05:00:19	+25:07:51	9.41	M1.0 V	···	···	2	HD 31867 A	G2 V
05289+1233	J05289+125	G 102-4	05:28:56	+12:31:54	9.65	M4.0 V	···	···	6	HD 35956 Aa,Ab	G0 V
05413+5329	J05415+534	HD 233153	05:41:31	+53:29:23	6.59	M1.0 V	≤ 2	···	···	V538 Aur	K1 V
05427+0241	J05427+026	G 99-27	05:42:45	+02:41:42	9.45	M3.0 V	≤ 2	48	4	HD 38014	K1 V
06332+0528	J06332+054	HD 46375 B	06:33:12	+05:27:53	8.70	M2.0 V	≤ 2	60	5	HD 46375 A	K1 V
06461+3233	J06461+325	HD 263175 B	06:46:07	+32:33:15	8.99	M1.0 V	···	···	3	HD 263175 A	K3 V
07191+6644	J07191+667	HD 55745 B	07:19:09	+66:44:30	8.88	M0.0 V	···	···	3	HD 55745 A	F8 V
07400-0336	J07361-031	BD-02 2198	07:36:07	-03:06:39	6.79	M1.0 V	3.1 ± 1.5	···	···	V869 Mon	K2 V
08138+6306	J08143+630	NLTT 19115	08:14:19	+63:04:40	9.91	M1.5 V	···	···	2	HD 67850	G0 V
08526+2820	J08526+283	ρ Cnc B	08:52:41	+28:18:59	8.56	M4.5 V	≤ 2	···	···	ρ Cnc A	G8 V
09152+2323	J09151+233	BD+23 2063B	09:15:10	+23:21:33	9.14	M0.0 V	≤ 2	94	6	HD 79498	G5 V
09211+6024	J09212+603	LP 91-22	09:21:18	+60:21:47	9.13	M1.5 V	≤ 2	64	7	BD+61 1116	K0 V
09327+2659	J09328+269	HD 82443 B	09:32:48	+26:59:44	10.36	M5.5 V	···	···	9	DX Leo	G9 V
11152+7329	J11151+734	HD 97584 B	11:15:11	+73:28:36	7.88	M2.5 V	≤ 2	55	4	HD 97584 A	K4 V
11218+1811	J11218+181	BD+19 2443B	11:21:49	+18:11:28	7.65	M0.0 V	≤ 2	84	4	HD 98736	K0 V
13114+0938	J13113+096	HD 114606 B	13:11:22	+09:36:13	9.68	M0.0 V	≤ 2	96	4	HD 114606 A	G1 V
13169+1701	J13168+170	HD 115404 B	13:16:51	+17:01:00	6.53	M0.5 V	···	···	6	HD 115404 A	K2 V
14245+6015	J14244+602	LP 97-826	14:24:27	+60:15:17	9.73	M2.0 V	≤ 2	60	5	BD+60 1536	K5 V
14252+5151	J14251+518	θ Boo B	14:25:12	+51:49:54	7.88	M2.5 V	≤ 2	···	···	θ Boo A	F7 V
15123+3939	J15118+395	LP 222-50	15:11:51	+39:33:02	9.87	M2.5 V	≤ 2	54	5	HD 135144	K3 V
15204+0015	J15204+001	Ross 1050	15:20:28	+00:11:27	9.45	M0.0 V	≤ 2	71	5	HD 136378	K1 V
15289+5727	J15291+574	G 224-69	15:29:09	+57:24:42	8.83	M1.0 V	···	···	4	HD 138367	F7 V
15353+6005	J15354+600	LP 99-392	15:35:26	+60:05:08	9.27	M3.5 V	···	···	5	HD 139477	K3 V
15482+0134	J15481+015	HD 141272 B	15:48:09	+01:34:36	9.30	M2.5 V	···	···	5	V382 Ser	G8 V
16048+3910	J16048+391	HD 144579 B	16:04:51	+39:09:36	9.90	M4.0 V	···	···	5	HD 144579 A	G8 V
17050-0504	J17052-050	HD 154363 B	17:05:14	-05:05:39	6.78	M1.5 V	≤ 2	···	···	HD 154363 A	K5 V
17178+5227	J17176+524	LP 138-36	17:17:39	+52:24:22	9.77	M3.5 V	···	···	7	HD 156985	K2 V
18006+2934	J18007+295	HD 164595 B	18:00:45	+29:33:57	9.06	M2.0 V	≤ 2	67	4	HD 164595 A	G2 V
18090+2409	J18090+241	PM J18090+2409	18:09:02	+24:09:04	9.30	M1.0 V	···	···	5	HD 166301	G0 V
18409+3132	J18409+315	BD+31 3330B	18:40:55	+31:31:52	8.21	M1.0 V	≤ 2	89	5	BD+31 3330A	K2.5 V
19510+1025	J19510+104	o Aql C	19:51:01	+10:24:40	8.89	M3.5 V	···	···	6	o Aql A	F8 V
20036+2954	J20034+298	HD 190360 B	20:03:26	+29:52:00	9.55	M4.5 V	···	···	1	HD 190360 A	G7 V
20111+1611	J20112+161	GJ 783.2 B	20:11:13	+16:11:07	9.63	M4.0 V	···	···	3	HD 191785	K0 V
20169+5017	J20167+502	BD+49 3245G	20:16:44	+50:17:14	9.41	M2.5 V	···	···	6	HD 193216 Aa,Ab	G5 V
21519+4221	J21518+423	HD 207966 B	21:51:54	+42:20:39	8.51	M0.5 V	≤ 2	70	5	HD 207966 A	G8 V
22159+5440	J22160+546	HD 211472 B	22:16:03	+54:40:00	9.72	M4.0 V	···	···	3	V447 Lac	K1 V
22467+1210	J22467+121	ξ Peg B	22:46:42	+12:10:21	7.94	M1.5 V	≤ 3	50	4	ξ Peg A	F6 V
23355+3101	J23354+310	HD 221830 B	23:35:30	+31:00:59	9.48	M2.5 V	···	···	3	HD 221830 A	F9 V
23536+1207	J23535+121	PM J23535+1206S	23:53:36	+12:06:17	8.67	M2.5 V	···	···	7	MCC 870	K4 V

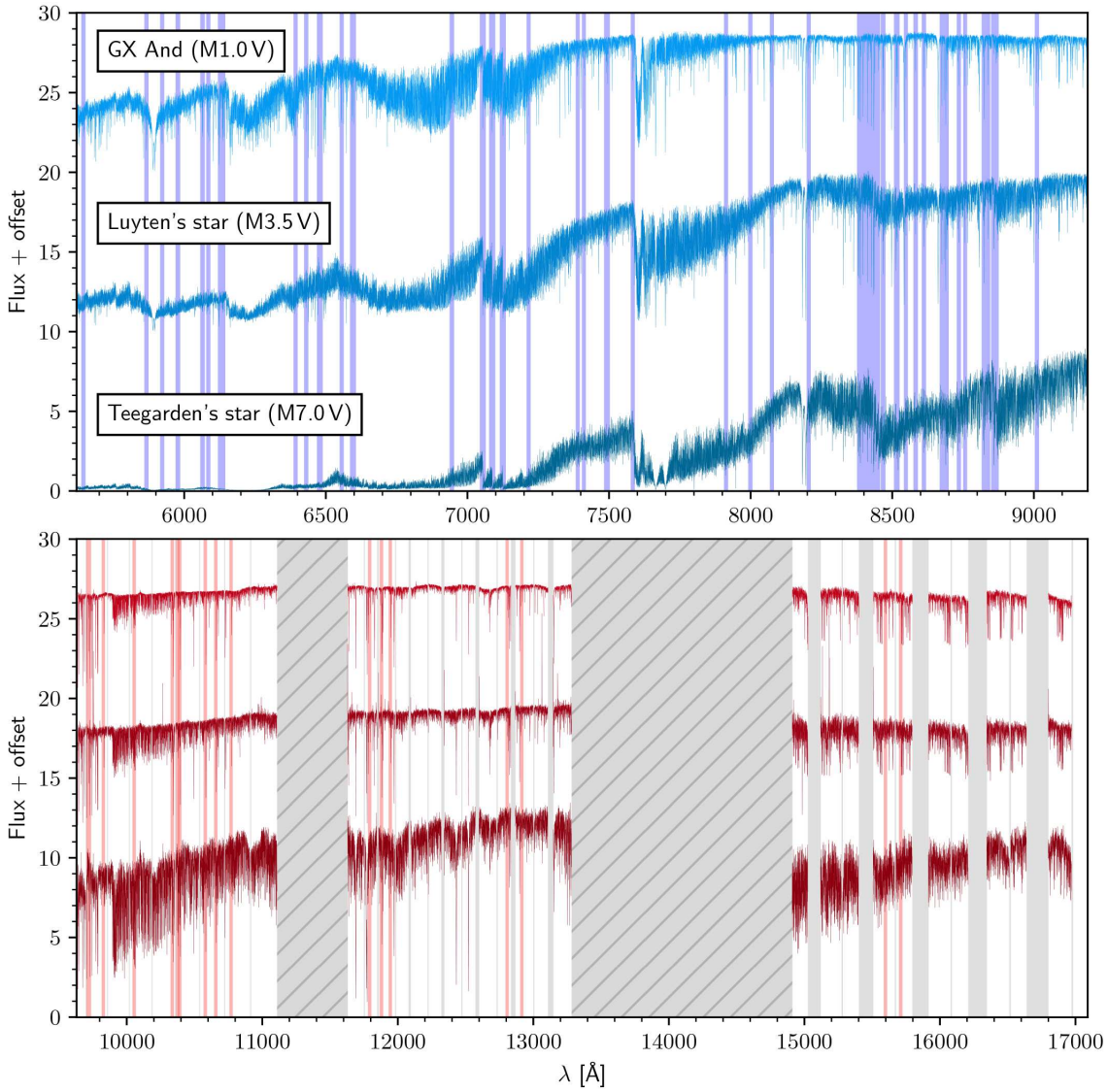

Figure 6.2: CARMENES template spectra of GX And (M1.0 V, J00183+440), Luyten's star (M3.5 V, J07274+052), and Teegarden's star (M7.0 V, J02530+168) in the VIS channel (top panel) and the NIR channel (bottom panel). Blue and red shaded regions denote the ranges synthesised. The two wide spectral gaps in the NIR channel shown as hatched rectangles correspond to regions severely affected by telluric absorption (Reiners et al., 2018). Inter- and intra-order gaps in the NIR channel are also shown, as grey shaded regions. Image taken from Marfil et al. (2021).

$\log g$ computed following the procedure described by Cifuentes et al. 2020 (C. Cifuentes priv. comm.), this is, the $T_{\rm eff}$ values were derived through a multi-band photometric analysis using the Virtual Observatory Spectral energy distribution Analyser[4] (VOSA; Bayo et al. 2008), while stellar radii and masses to compute the $\log g$ were determined using the Stefan-Boltzmann law and the empirical mass-radius relationship,

$$\frac{\mathcal{M}}{\mathcal{M}_\odot} = (-0.0240 \pm 0.0076) + (1.055 \pm 0.017)\frac{\mathcal{R}}{\mathcal{R}_\odot}, \tag{6.3}$$

given by Schweitzer et al. (2019). The standard deviations of the priors were set to 200 K for $T_{\rm eff}$ and 0.2 dex for $\log g$.

[4] https://svo2.cab.inta-csic.es/theory/vosa/

6.3 Results and discussion

At the time of writing this thesis, we successfully computed telluric-corrected, high signal-to-noise template spectra and derived stellar atmospheric parameters for a total of 16 M-dwarf secondaries out of the 44 stars in our observational sample. Combined with the seven additional M dwarfs from the CARMENES GTO programme previously analysed by Marfil et al. (2021), we now have homogeneous stellar parameters for a sample of 23 benchmark M dwarfs in wide binary systems.

The atmospheric parameters derived using the StePar Syn code are summarised in Table 6.2. The metallicities of the FGK-type primaries were taken from Montes et al. (2018), who derived them using the StePar code (Tabernero et al., 2019). In the case of the fast-rotating F7 V star θ Boo A ($v \sin i = 30.4\,\mathrm{km\,s^{-1}}$; Luck 2017), we adopted the metallicity value reported by Tabernero et al. (2022) using spectral synthesis. The corresponding Gaussian priors adopted for T_eff and $\log g$, derived using photometric SED fitting and empirical mass-radius relations, are listed in Table 6.3. We were not able to derive prior values for the star LP 91-22 (J09212+603) due to photometric contamination from the companion, so we use the average parameters for that spectral type as priors. A representative example of the StePar Syn output is shown in Fig. 6.3, illustrating the posterior distributions and parameter covariances for one of our targets.

To assess the consistency of the derived effective temperatures, we plot them against the corresponding stellar luminosities in Fig. 6.4. The resulting distribution aligns well with the expected values of main-sequence M dwarfs, providing additional confidence in the accuracy of our parameter determinations.

To validate our metallicity determinations, we compared the [Fe/H] values obtained for the M-dwarf secondaries with those of their FGK-type primaries derived by Montes et al. (2018). The results are displayed in Fig. 6.5, where we find good overall agreement between the two components of each binary system. This consistency supports the assumption of chemical homogeneity in

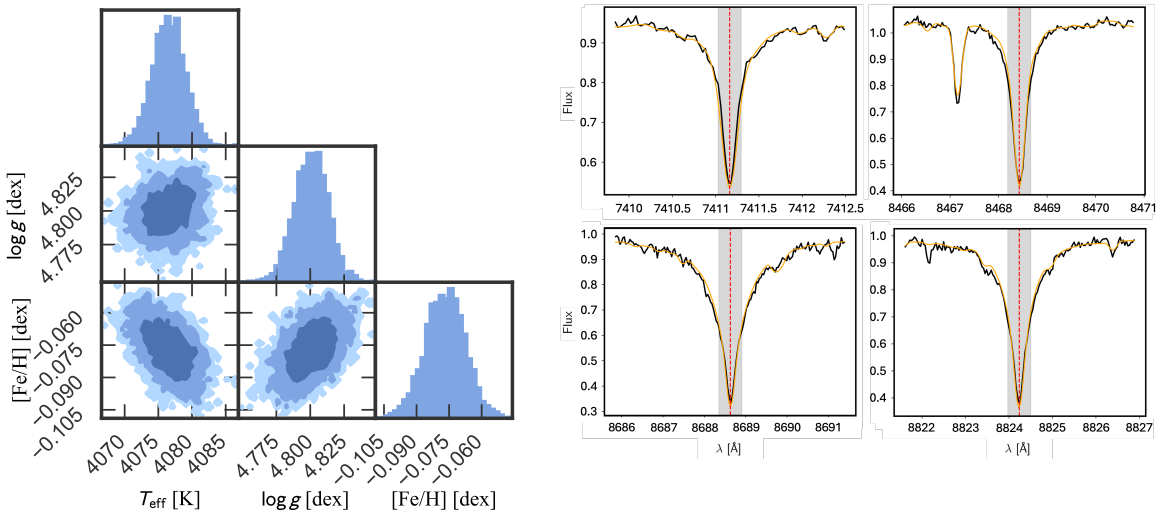

Figure 6.3: Left panel: Corner plot showing the marginal posterior distributions of T_eff, $\log g$, and [Fe/H] derived with StePar Syn for the M0.0 V star TYC 2868-639-1 (J03519+397). The shaded regions represent the 1σ, 2σ, and 3σ confidence intervals. Right panel: Examples of selected spectral lines for the same star, showing the observed spectrum (black) and the corresponding synthetic fit (orange). Vertical lines indicate the line centres, and shaded regions denote the wavelength intervals used for the comparison between observed and synthetic spectra.

Table 6.2: Stellar atmospheric parameters ($T_{\rm eff}$, $\log g$, and [Fe/H]) derived using the StePar Syn code for the M-dwarf secondaries.

FGK primaries			M-dwarf secondaries						
Name	SpT	[Fe/H]	Karmn	Name	SpT	$T_{\rm eff}$ (K)	$\log g$ (dex)	[Fe/H] (dex)	Reference
HD 16160	K3 V	-0.20 ± 0.02	J02362+068	BX Cet	M4.0 V	3335 ± 45	4.91 ± 0.10	-0.24 ± 0.12	M21
θ Per A	F7 V	0.04 ± 0.03	J02441+492	θ Per B	M1.5 V	3707 ± 3	4.79 ± 0.03	-0.20 ± 0.02	This work
HD 275867	K2 V	-0.13 ± 0.05	J03519+397	TYC 2868-639-1	M0.0 V	4077 ± 2	4.80 ± 0.01	-0.08 ± 0.01	This work
o^{02} Eri A	K0.5 V	-0.37 ± 0.02	J04153-076	o^{02} Eri C	M4.5 V	3179 ± 61	5.00 ± 0.18	-0.30 ± 0.17	M21
V538 Aur	K1 V	0.04 ± 0.02	J05415+534	HD 233153	M1.0 V	3825 ± 14	4.94 ± 0.10	-0.02 ± 0.06	M21
HD 38014	K1 V	-0.04 ± 0.03	J05427+026	G 99-27	M3.0 V	3378 ± 13	4.72 ± 0.06	-0.11 ± 0.04	This work
HD 46375 A	K1 V	0.23 ± 0.06	J06332+054	HD 46375 B	M2.0 V	3642 ± 7	5.21 ± 0.04	0.01 ± 0.02	This work
V869 Mon	K2 V	-0.11 ± 0.03	J07361-031	GJ 282 C	M1.0 V	3825 ± 12	5.06 ± 0.08	-0.04 ± 0.06	M21
ρ Cnc	G8 V	0.29 ± 0.04	J08526+283	ρ Cnc B	M4.5 V	3321 ± 37	4.87 ± 0.08	-0.10 ± 0.11	M21
HD 79498	G5 V	0.21 ± 0.02	J09151+233	BD+23 2063 B	M0.0 V	4077 ± 3	5.00 ± 0.03	0.16 ± 0.02	This work
BD+61 1116	K0 V	-0.22 ± 0.02	J09212+603	LP 91-22	M1.5 V	3715 ± 4	4.74 ± 0.03	-0.26 ± 0.02	This work
HD 97584 A	K4 V	-0.17 ± 0.04	J11151+734	HD 97584 B	M2.5 V	3520 ± 6	4.90 ± 0.04	-0.09 ± 0.03	This work
HD 98736	K0 V	0.30 ± 0.06	J11218+181	BD+19 2443 B	M0.0 V	4099 ± 3	4.64 ± 0.03	0.37 ± 0.02	This work
HD 114606 A	G1 V	-0.51 ± 0.02	J13113+096	HD 114606 B	M0.0 V	3921 ± 3	4.78 ± 0.01	-0.50 ± 0.01	This work
BD+60 1536	K5 V	-0.01 ± 0.05	J14244+602	LP 97-826	M2.0 V	3682 ± 6	4.43 ± 0.03	-0.14 ± 0.02	This work
θ Boo A	F7 V	-0.09 ± 0.01	J14251+518	θ Boo B	M2.5 V	3551 ± 22	4.90 ± 0.10	-0.14 ± 0.06	M21
HD 135144	K3 V	-0.21 ± 0.03	J15118+395	LP 222-50	M2.5 V	3447 ± 5	4.74 ± 0.03	-0.30 ± 0.04	This work
HD 136378	K1 V	-0.44 ± 0.02	J15204+001	Ross 1050	M0.0 V	3965 ± 4	4.90 ± 0.03	-0.51 ± 0.01	This work
HD 154363	K5 V	-0.62 ± 0.05	J17052-050	HD 154363 B	M1.5 V	3587 ± 14	4.89 ± 0.10	-0.39 ± 0.07	M21
HD 164595 A	G2 V	-0.08 ± 0.01	J18007+295	HD 164595 B	M2.0 V	3548 ± 4	4.77 ± 0.03	-0.25 ± 0.02	This work
BD+31 3330 A	K2.5 V	-0.49 ± 0.02	J18409+315	BD+31 3330 B	M1.0 V	3700 ± 1	4.78 ± 0.02	-0.51 ± 0.01	This work
HD 207966 A	G8 V	-0.05 ± 0.02	J21518+423	HD 207966 B	M0.5 V	3854 ± 3	4.62 ± 0.03	-0.27 ± 0.01	This work
ξ Peg A	F6 V	-0.20 ± 0.02	J22467+121	ξ Peg B	M1.5 V	3571 ± 5	4.70 ± 0.04	-0.37 ± 0.03	This work

Table 6.3: Stellar luminosities, masses, and radii, along with the Gaussian priors adopted for $T_{\rm eff}$ and $\log g$, computed following the methodology of Cifuentes et al. (2020).

Karmn	Name	SpT	L ($10^{-4}\,L_\odot$)	$\mathcal{M}$ ($\mathcal{M}_\odot$)	$\mathcal{R}$ ($\mathcal{R}_\odot$)	Prior $T_{\rm eff}$ (K)	Prior $\log g$ (dex)
J02362+068	BX Cet	M4.0 V	80.5 ± 0.5	0.260 ± 0.012	0.269 ± 0.007	3200 ± 200	4.96 ± 0.20
J02441+492	θ Per B	M1.5 V	419.5 ± 2.1	0.532 ± 0.020	0.527 ± 0.015	3600 ± 200	4.69 ± 0.20
J03519+397	TYC 2868-639-1	M0.0 V	863.5 ± 5.8	0.655 ± 0.022	0.644 ± 0.017	3900 ± 200	4.61 ± 0.20
J04153-076	o^{02} Eri C	M4.5 V	63.6 ± 0.4	0.254 ± 0.014	0.263 ± 0.010	3100 ± 200	4.98 ± 0.20
J05415+534	HD 233153	M1.0 V	570.6 ± 3.0	0.550 ± 0.013	0.544 ± 0.004	3800 ± 200	4.71 ± 0.20
J05427+026	G 99-27	M3.0 V	261.3 ± 1.4	0.468 ± 0.014	0.466 ± 0.014	3400 ± 200	4.74 ± 0.20
J06332+054	HD 46375 B	M2.0 V	436.0 ± 3.3	0.575 ± 0.021	0.568 ± 0.016	3500 ± 200	4.66 ± 0.20
J07361-031	GJ 282 C	M1.0 V	614.4 ± 6.6	0.572 ± 0.013	0.564 ± 0.005	3700 ± 200	4.70 ± 0.20
J08526+283	ρ Cnc B	M4.5 V	79.6 ± 0.6	0.260 ± 0.011	0.269 ± 0.006	3100 ± 200	4.94 ± 0.20
J09151+233	BD+23 2063 B	M0.0 V	920.3 ± 5.2	0.677 ± 0.023	0.665 ± 0.017	3900 ± 200	4.60 ± 0.20
J11151+734	HD 97584 B	M2.5 V	209.6 ± 0.9	0.416 ± 0.017	0.417 ± 0.012	3400 ± 200	4.79 ± 0.20
J11218+181	BD+19 2443 B	M0.0 V	931.9 ± 6.7	0.719 ± 0.024	0.704 ± 0.019	3800 ± 200	4.57 ± 0.20
J13113+096	HD 114606 B	M0.0 V	788.8 ± 2.3	0.593 ± 0.020	0.585 ± 0.015	4000 ± 200	4.65 ± 0.20
J14244+602	LP 97-826	M2.0 V	361.2 ± 1.1	0.521 ± 0.019	0.517 ± 0.015	3500 ± 200	4.70 ± 0.20
J14251+518	θ Boo B	M2.5 V	224.4 ± 1.1	0.394 ± 0.011	0.396 ± 0.005	3400 ± 200	4.80 ± 0.20
J15118+395	LP 222-50	M2.5 V	151.8 ± 0.4	0.351 ± 0.015	0.355 ± 0.010	3400 ± 200	4.85 ± 0.20
J15204+001	Ross 1050	M0.0 V	576.0 ± 2.1	0.531 ± 0.018	0.526 ± 0.014	3900 ± 200	4.69 ± 0.20
J17052-050	HD 154363 B	M1.5 V	337.6 ± 1.6	0.478 ± 0.012	0.476 ± 0.004	3500 ± 200	4.74 ± 0.20
J18007+295	HD 164595 B	M2.0 V	285.0 ± 1.3	0.460 ± 0.018	0.459 ± 0.013	3500 ± 200	4.75 ± 0.20
J18409+315	BD+31 3330 B	M1.0 V	395.6 ± 2.1	0.460 ± 0.017	0.459 ± 0.021	3800 ± 200	4.75 ± 0.20
J21518+423	HD 207966 B	M0.5 V	602.5 ± 4.0	0.606 ± 0.021	0.597 ± 0.016	3700 ± 200	4.64 ± 0.20
J22467+121	ξ Peg B	M1.5 V	218.1 ± 0.7	0.400 ± 0.016	0.402 ± 0.012	3500 ± 200	4.80 ± 0.20

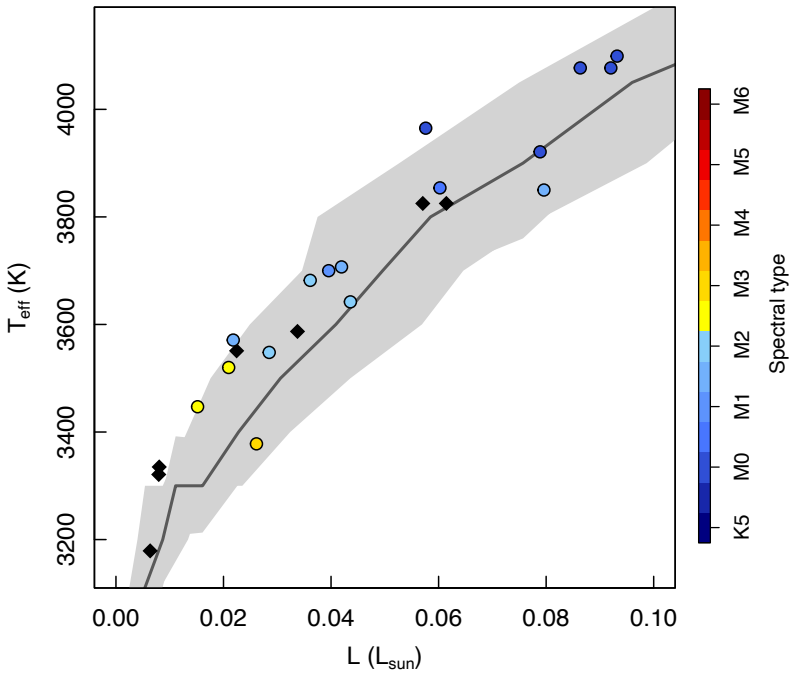

Figure 6.4: Stellar luminosities retrieved with VOSA versus the effective temperatures derived using StePar Syn (Tabernero et al., 2022) by Marfil et al. (2021) (black diamonds) and in this work (colour-coded by spectral subtype). The line and shadow region represent the average parameters given by Cifuentes et al. (2020).

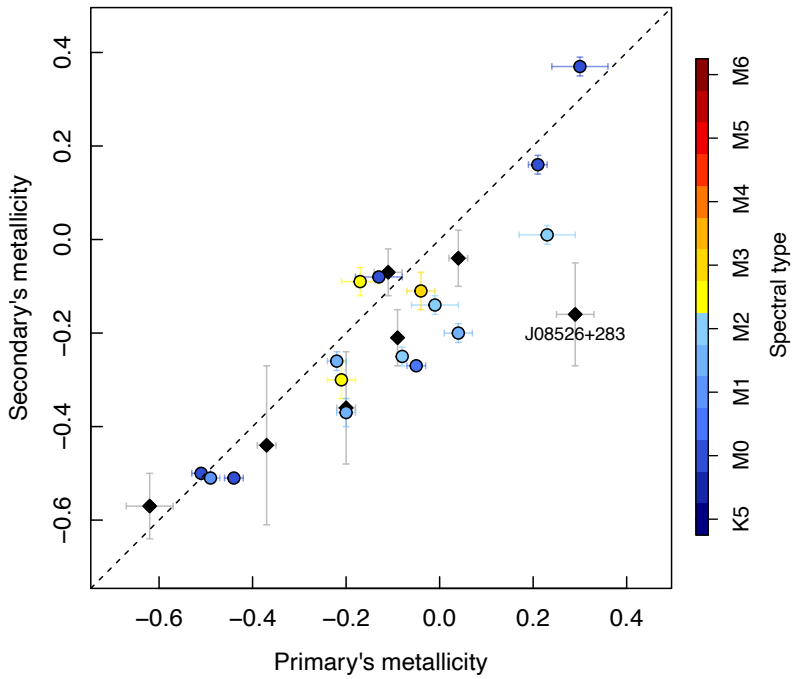

Figure 6.5: Comparison between the metallicities reported by Montes et al. (2018) for the FGK-type primaries and those derived for the corresponding M-dwarf secondaries using StePar Syn (Tabernero et al., 2022) by Marfil et al. (2021) (black diamonds) and in this work (colour-coded by spectral subtype).

wide binaries and reinforces the reliability of our spectroscopic analysis. The largest discrepancy in our sample corresponds to ρ Cnc B (J08526+283), a case already noted by Marfil et al. (2021), who suggested that the high C/O ratio, observed in the primary, could affect the metallicity determination of the M-dwarf companion, since the pseudo-continuum is very sensitive to C/O (Tsuji & Nakajima, 2014; Abia et al., 2020).

6.4 Future work: abundance determination of Al, Ca, Sc, and Ti

Once the stellar atmospheric parameters for our sample of M-dwarf secondaries are determined, the next natural step is a detailed chemical abundance analysis. Previous studies within the CARMENES Consortium have focused on various elements, including neutron-capture species such as Rb, Sr, and Zr (Abia et al., 2020); vanadium, whose line profiles are strongly affected by hyperfine structure (Shan et al., 2021); and Mg and Si, which are essential for understanding the formation and composition of rocky exoplanets (Tabernero et al., 2024). Moreover, Ishikawa et al. (2020) also derived Na, Mg, Ca, Ti, Cr, Mn, and Fe abundances for a small sample of M dwarfs from CARMENES near-infrared spectra.

Our future work will focus on determining the abundances of four additional elements of astrophysical interest: aluminium (Al), calcium (Ca), scandium (Sc), and titanium (Ti). These elements play important roles in several stellar contexts. For example, Ti lines contribute to the determination of stellar atmospheric parameters (Marfil et al., 2021), and Al is a well-known tracer of Galactic chemical evolution; the [Al/Fe] ratio, along with [α/Fe], serves as a useful diagnostic for distinguishing between thin and thick disc populations (e.g. Bensby et al., 2014).

This follow-up analysis will complement the parameter determinations presented here and contribute to a more complete chemical characterisation of M dwarfs, enhancing the value of wide binary systems as empirical benchmarks in stellar astrophysics.

6.5 Summary

In this chapter, we presented a new set of high-resolution spectroscopic observations of M-dwarf secondaries in wide binaries with FGK-type primaries, obtained with the CARMENES instrument at the Calar Alto Observatory. We computed and analysed telluric-corrected, high signal-to-noise co-added template spectra for 16 new targets, and combined them with previously studied GTO stars to build a homogeneous benchmark sample of 23 M dwarfs, and counting. Using the StePar Syn code, a Bayesian implementation of the spectral synthesis method, we derived their stellar atmospheric parameters (effective temperature, surface gravity, and metallicity). A comparison with the metallicities of the corresponding primaries confirmed the expected chemical consistency of these wide systems, further validating our methodology.

This benchmark sample provides an incredible opportunity for future abundance analyses in M dwarfs, enabling robust calibration of empirical techniques and comparisons across spectral types. The high-resolution CARMENES spectra will allow us to extend this work to include key elements such as Al, Ca, Sc, and Ti, contributing to the different goals of Galactic chemical evolution studies and the characterisation of cool stars as hosts of planetary systems.

CHAPTER 7

Conclusions and future work

"To finish a work? To finish a picture? What nonsense! To finish it means to be through with it, to kill it, to rid it of its soul, to give it its final blow, the coup of grace, for the painter as well as for the picture."
— Pablo Picasso

This thesis addresses one of the enduring challenges in stellar astrophysics: the chemical characterisation of M-type dwarf stars. These low-mass stars are not only the most abundant stellar population in the Milky Way but also key objects in studies of Galactic chemical evolution and exoplanet demographics. However, their cool temperatures and molecule-rich spectra make them notoriously difficult to analyse using traditional high-resolution spectroscopic techniques.

To overcome these challenges, the thesis integrates a set of complementary methodologies spanning photometric calibrations, low- and high-resolution spectroscopy, and modern statistical approaches, including Bayesian inference, artificial neural networks, and spectral synthesis. A unifying strategy throughout this work is the use of wide binary systems, in which M dwarfs are paired with warmer FGK-type stars. Assuming a common origin and thus a shared chemical composition, these systems provide robust empirical benchmarks for calibrating and validating the metallicity of M dwarfs.

Using the benchmark framework offered by wide binaries, the methodologies developed in this thesis can be extended to large M-dwarf populations observed in current and future photometric and spectroscopic surveys, without relying exclusively on time-intensive high-resolution observations. What follows is a summary of the main contributions of each chapter, culminating in a set of general conclusions that highlight the impact and future potential of the work.

Chapter 2 – Photometric metallicities of M dwarfs: a Bayesian approach

This chapter demonstrated that accurate metallicity estimates for M dwarfs can be obtained from the metallicity gradient seen in colour–colour and colour–magnitude diagrams using optical and infrared photometry from large surveys such as *Gaia*, 2MASS, and CatWISE. We constructed a set of Bayesian linear regression models using a sample of nearly 5000 M dwarfs with spectroscopic metallicities from APOGEE (Birky et al., 2020), using colour indices and absolute magnitudes as predictors. The models were optimised via Markov Chain Monte Carlo (MCMC) sampling with `Stan`, ensuring a fully probabilistic treatment of uncertainties. Model selection relied on leave-one-out cross-validation (LOO-CV), which provided a robust comparison of predictive performance.

Our metallicity estimates are valid for M dwarfs in the range of $-0.45 \leq [\mathrm{Fe/H}] \leq +0.45$ dex and spectral types down to M5.0 V, with deviations below the 0.10 dex level. External validation on a sample of FGK+M wide binaries from Montes et al. (2018) confirmed that the photometric metallicities agreed well with those of the primaries derived spectroscopically, with no significant systematic offsets.

This work provides a scalable and interpretable method for estimating metallicities using broad-band photometry, offering a powerful tool for characterising large M-dwarf samples in ongoing and future surveys. Our calibrations are available for the community via GitHub[1] and a shinyapp[2], providing accessible tools for stellar characterisation. The results of this chapter are published by Duque-Arribas et al. (2023).

Chapter 3 – Photometric metallicities of M dwarfs: A neural network approach

We introduced a complementary machine-learning strategy based on artificial neural networks (ANNs) to model the complex, non-linear relationships between photometry and metallicity. Trained on the same sample as the Bayesian regression models, the ANN demonstrated slightly improved predictive performance, with a mean residual of 0.00 ± 0.08 dex, particularly in capturing subtle non-linear effects.

To quantify uncertainties in the predictions of the network, a Monte Carlo dropout approach was used, providing a Bayesian-like estimate of predictive intervals. Although less interpretable than the polynomial models, the ANN offers greater flexibility and adaptability, making it especially suitable for application to very large photometric samples from ongoing and upcoming surveys.

The model is publicly available at GitHub[3], providing the community with a ready-to-use tool for population-scale studies of M dwarfs. Nevertheless, as with other data-driven approaches, its performance remains tied to the parameter space of the training sample, and extrapolation to poorly represented metallicity or spectral-type regimes should be treated with caution. The results of this chapter are published by Duque-Arribas et al. (2025).

Chapter 4 – Carbon, oxygen, and odd-Z iron-peak abundances of F-, G-, and K-primaries in wide binary systems

This chapter focused on a detailed abundance analysis of the FGK-type primaries in the benchmark binaries presented by Montes et al. (2018). We analysed high-resolution spectra obtained with the HERMES spectrograph using the StePar code (Tabernero et al., 2019), which implements the equivalent width method. Corrections for hyperfine structure and non-local thermodynamic equilibrium (non-LTE) effects were included where appropriate to ensure accurate abundance determinations.

The analysis yielded abundances for carbon, oxygen, and several odd-Z iron-peak elements (Sc, V, Mn, Co). These values align with the established Galactic chemical evolution trends, thereby confirming the reliability of the reference sample. We also confirmed, in agreement with previous works, that abundance determinations for C, O, and V become increasingly uncertain for stars cooler than $T_{\rm eff} < 5200$ K. Preliminary evidence of abundance differences between stars with and without detected exoplanets was noted for [C/Fe] and [Mn/Fe], though further investigation with larger samples is needed to draw firm conclusions. The results of this chapter are published by Duque-Arribas et al. (2024).

This chapter completes the detailed characterisation of the chemical abundances of the FGK-type primaries, including C, O, Na, Mg, Al, Si, Ca, Sc, Ti, V, Cr, Mn, Fe, Co, and Ni. These results provide a robust reference framework for calibrating and validating the abundances of the M-dwarf companions in the binary systems.

[1] https://github.com/chrduque/metamorphosis.git
[2] https://chrduque.shinyapps.io/metamorphosis
[3] https://github.com/chrduque/metamorphosis-NN.git

Chapter 5 – Elemental abundances of M dwarfs from low-resolution spectral indices

To extend chemical analyses to larger and fainter samples, this chapter developed a method to infer chemical abundances in M dwarfs using CAFOS low-resolution spectra. Assuming chemical homogeneity within the binary systems, we statistically linked spectral indices measured in the M-dwarf secondaries (Alonso-Floriano et al., 2015) to the detailed abundances of their FGK primaries (Montes et al., 2018; Duque-Arribas et al., 2024) through projection predictive feature selection and Bayesian regression. The resulting calibrations reproduce abundances for 15 atomic species in M dwarfs, with improved predictive performance when treating early- and late-type subsamples separately. The range of application for these calibrations is K5 V $\leq$ SpT $\leq$ M4.5 V and $-0.8 \lesssim$ [Fe/H] $\lesssim +0.4$ dex.

Applying this framework to a sample of more than 770 M dwarfs, we obtained abundance estimates that proved robust across different validation tests. The resulting abundance estimates were consistent with those obtained from photometric calibrations and followed the [X/Fe] vs. [Fe/H] trends that are well-known for FGK-type stars. Moreover, our results showed good agreement with independent high-resolution studies found in the literature. This method significantly expands the scope of chemical analysis for M dwarfs using accessible, low-cost data, enabling studies that would be infeasible with high-resolution spectroscopy alone.

Chapter 6 – CARMENES high-resolution spectroscopy of the M-dwarf secondaries

The final chapter focused on high-resolution spectroscopy of the M-dwarf secondaries in wide binary systems. New observations were acquired with the CARMENES spectrograph through open-time proposals, complementing the limited number of M dwarfs included in the CARMENES GTO sample. The spectra were analysed with the StePar Syn code (Tabernero et al., 2022), a spectral synthesis tool that employs Bayesian inference to derive effective temperatures, surface gravities, and metallicities.

The preliminary stellar parameters showed good agreement with those of the FGK primaries. These high-quality data establish a benchmark sample of M dwarfs that will enable future detailed abundance determinations.

General conclusions

This thesis developed and validated a set of complementary methodologies for estimating the metallicity and elemental abundances of M-type dwarf stars across various observational regimes. By combining photometric, low-resolution, and high-resolution spectroscopic data with both classical and machine learning techniques, the work addresses long-standing challenges in the chemical characterisation of cool stars.

A consistent feature throughout the thesis is the strategic use of wide binary systems as chemical benchmarks. These systems enable the transfer of chemical information from the well-understood FGK primaries to their M-dwarf companions, facilitating both calibration and validation of indirect methods. This framework provides a robust alternative to traditional analyses and enhances the reliability of abundance determinations.

The integration of Bayesian inference, machine learning, and spectral synthesis illustrates the strength of hybrid methodological frameworks in modern astrophysics. Bayesian models offer

interpretability and rigorous uncertainty quantification; neural networks contribute flexibility and predictive power; low-resolution spectroscopy enables the scalable chemical characterisation of large, faint stellar samples; and spectral synthesis delivers detailed atmospheric characterisation grounded in physical modelling.

We must emphasise that, although the empirical methodologies and correlations developed in this thesis have demonstrated strong predictive performance and practical utility, they do not by themselves constitute direct evidence of the physical mechanisms operating in stellar atmospheres. Rather, these results should be viewed as data-driven relationships that complement, but do not replace, physically-motivated models. Their interpretation therefore relies on complementary theoretical frameworks and future modelling efforts to fully connect the empirical trends with the underlying stellar physics.

Taken together, the results of this thesis contribute significantly to our understanding of chemical composition of M-type dwarf stars and establish a foundation for their inclusion in large-scale studies of Galactic archaeology and exoplanet host characterisation. The methodologies developed here are well suited to the challenges posed by current and upcoming stellar surveys, offering scalable and precise tools for the next generation of astrophysical research.

Future work

The results and methods developed in this thesis open several avenues for future research:

- Extension to later-type M dwarfs: While this thesis has primarily focused on early- to mid-type M dwarfs, a natural progression involves extending the analysis to later subtypes. These cooler stars are more challenging due to increasingly complex molecular absorption and lower luminosities, but they represent a significant fraction of the stellar population. Adapting photometric and spectroscopic techniques to this regimen will be essential to achieving a more complete chemical census of the M-dwarf population.
- Bayesian machine learning: One exciting avenue is the integration of probabilistic inference with the modelling flexibility of machine learning, through Bayesian neural networks (BNNs). Unlike traditional ANNs, BNNs place probability distributions over network weights, allowing for rigorous uncertainty estimation and improved generalisation. Their application to photometric or spectroscopic inference in stellar astrophysics remains unexplored and could yield both predictive accuracy and robust error estimates in parameter estimation.
- Elemental abundance analysis with CARMENES spectra: The high-resolution spectra acquired with CARMENES for a benchmark sample of M-dwarf secondaries provide an ideal dataset for detailed abundance studies. A next step will be to derive abundances for astrophysically relevant elements such as titanium, calcium, scandium, and aluminium. These elements are important for tracing nucleosynthetic processes, discriminating Galactic stellar populations, and understanding planet formation environments, particularly in the context of rocky exoplanet hosts. Additionally, previous abundances within the CARMENES consortium could be tested with the binary sample, in particular V from Shan et al. (2021) and Mg and Si from Tabernero et al. (2024).
- Application to upcoming surveys: The methodologies developed in this thesis are well suited to exploitation of data from future missions and surveys such as Ariel, PLATO and the Habitable Worlds Observatory. These facilities will observe large numbers of M dwarfs and will require efficient, scalable tools for stellar characterisation.

Pursuing these directions will strengthen the role of M dwarfs in the domain of Galactic archaeology, stellar evolution studies, and the broader search for habitable exoplanetary systems.

Acknowledgments

We would like to thank Dra. Bárbara Rojas-Ayala and Dra. Yutong Shan for their insightful comments on the thesis, which greatly enriched the manuscript. We also thank the anonymous referees for their valuable feedback, which helped improve the quality of the published papers.

This work was supported by a predoctoral contract funded through the 2020 call of the 'Contratos predoctorales de personal investigador en formación' programme (CT82/20–CT83/20) at the Universidad Complutense de Madrid (UCM). Additional financial support was provided by UCM and the Agencia Estatal de Investigación (AEI/10.13039/501100011033) of the Ministerio de Ciencia e Innovación, and by the European Regional Development Fund (ERDF) 'A way of making Europe', through projects AYA2016-79425-C3-1-P, PID2019-109522GB-C5[1,4], PID2019-107427GB-I00, and PID2022-137241NB-C4[2,4]. This research also received support from the "María de Maeztu" Centre of Excellence award to Centro de Astrobiología (MDM-2017-0737), and from the European Research Council (ERC) under the European Union's Horizon Europe programme (ERC Advanced Grant SPOTLESS, no. 101140786).

International research stays were partially funded by the Universidad Complutense de Madrid and the ERASMUS+ mobility programme through the calls EB14/23, EB33/24, and Erasmus+ KA131/2023.

This work has used the NASA's Astrophysics Data System; the SIMBAD database, operated at CDS, Strasbourg, France; the Washington Double Star catalogue maintained at the U.S. Naval Observatory; the VALD data base, operated at Uppsala University, the Institute of Astronomy RAS in Moscow, and the University of Vienna; the portal `exoplanet.eu` of The Extrasolar Planets Encyclopaedia. This work has made use of data from the European Space Agency (ESA) mission *Gaia* (`https://www.cosmos.esa.int/gaia`), processed by the *Gaia* Data Processing and Analysis Consortium (DPAC, `https://www.cosmos.esa.int/web/gaia/dpac/consortium`). Funding for the DPAC has been provided by national institutions, in particular the institutions participating in the *Gaia* Multilateral Agreement. This publication makes use of data products from the Two Micron All Sky Survey, which is a joint project of the University of Massachusetts and the Infrared Processing and Analysis Center/California Institute of Technology, funded by the National Aeronautics and Space Administration and the National Science Foundation. This publication makes use of data products from the Wide-field Infrared Survey Explorer, which is a joint project of the University of California, Los Angeles, and the Jet Propulsion Laboratory/California Institute of Technology, funded by the National Aeronautics and Space Administration. The first author used ChatGPT (OpenAI) in the final version of the manuscript to check for typographical errors.

Based on observations collected at the Centro Astronómico Hispano en Andalucía (CAHA) at Calar Alto, proposals 23A-3.5-010, 23B-3.5-009, 24A-3.5-007, and 24B-3.5-008, operated jointly by Junta de Andalucía and Consejo Superior de Investigaciones Científicas (IAA-CSIC).

List of publications

Peer-reviewed publications

First-author articles presented in this thesis are marked with a red star (⋆).

2025

11. **Discovery of a transiting hot water world candidate orbiting Ross 176 with TESS and CARMENES**
S. Geraldía-González, J. Orell-Miquel, E. Pallé, et al. (including **C. Duque-Arribas**)
Astronomy & Astrophysics, 700, A216. August 2025.

⋆ 10. **A neural network approach to determining photometric metallicities of M-type dwarf stars**
C. Duque-Arribas, H. M. Tabernero, D. Montes, et al.
Astronomy & Astropysics, 698, L12. June 2025.

2024

9. **The CARMENES search for exoplanets around M dwarfs: Magnesium and silicon abundances of K7-M5.5 stars**
H. M. Tabernero, Y. Shan, J. A. Caballero, et al. (including **C. Duque-Arribas**)
Astronomy & Astrophysics, 689, A223. September 2024.

8. **TOI-4438 b: a transiting mini-Neptune amenable to atmospheric characterization**
E. Goffo, P. Chaturvedi, F. Murgas, et al. (including **C. Duque-Arribas**)
Astronomy & Astrophysics, 685, A147. May 2024.

7. **Wolf 327b: A new member of the pack of ultra-short-period super-Earths around M dwarfs**
Murgas, F., Pallé, E., Orell-Miquel, J., et al. (including **C. Duque-Arribas**)
Astronomy & Astrophysics, 684, A83. April 2024.

⋆ 6. **Calibrating the metallicity of M dwarfs in wide physical binaries with F-, G-, and K-primaries – II: Carbon, oxygen, and odd-Z iron-peak abundances of the primary stars**
C. Duque-Arribas, H. M. Tabernero, D. Montes, et al.
Monthly Notices of the Royal Astronomical Society, 528, 3028. February 2024.

2023

5. **TOI-1801 b: A temperate mini-Neptune around a young M0.5 dwarf**
M. Mallorquín, E. Goffo, E. Pallé, et al. (including **C. Duque-Arribas**)
Astronomy & Astrophysics, 680, A76. December 2023.

4. **The CARMENES search for exoplanets around M dwarfs: Guaranteed Time Observations Data Release 1 (2016-2020)**
I. Ribas, A. Reiners, M. Zechmeister, et al. (including **C. Duque-Arribas**)
Astronomy & Astrophysics, 670, A139. February 2023.

⋆ 3. **Photometric calibrations of M-dwarf metallicity with Markov chain Monte Carlo and Bayesian inference**
C. Duque-Arribas, D. Montes, H. M. Tabernero, et al.
The Astrophysical Journal, 944, 106. February 2023.

2022

2. **Metallicities in M dwarfs: Investigating different determination techniques**
V. M. Passegger, A. Bello-García, J. Ordieres-Meré, et al. (including **C. Duque-Arribas**)
Astronomy & Astrophysics, 658, A194. February 2022.

2021

1. **The CARMENES search for exoplanets around M dwarfs: Stellar atmospheric parameters of target stars with StePar Syn**
E. Marfil, H. M. Tabernero, D. Montes, et al. (including **C. Duque-Arribas**)
Astronomy & Astrophysics, 656, A162. December 2021.

Non-refereed publications

2. **Las estrellas más frías del universo**
C. Duque-Arribas
Astronomía Nº 263. May 2021.
1. **The CARMENES M-dwarf planet survey**
A. Quirrenbach, CARMENES Consortium, P. J. Amado, et al. (including **C. Duque-Arribas**)
Society of Photo-Optical Instrumentation Engineers Conference Series 114472. December 2020.

Conference proceedings

12. **Low-resolution spectral indices to derive M-dwarf abundances using wide binary systems**
C. Duque-Arribas, H. M. Tabernero, D. Montes, et al.
Highlights of Spanish Astrophysics XI, Proceedings of the XVI Scientific Meeting of the Spanish Astronomical Society. Granada, Spain; July 2024.
11. **Determining Magnesium and Silicon Abundances from CARMENES Spectra**
H. M. Tabernero, Y. Shan, J. A. Caballero, et al. (including **C. Duque-Arribas**)
Highlights of Spanish Astrophysics XI, Proceedings of the XVI Scientific Meeting of the Spanish Astronomical Society. Granada, Spain; July 2024.
10. **Low-resolution spectral indices to derive M-dwarf abundances using wide binary systems**
C. Duque-Arribas, H. M. Tabernero, D. Montes, et al.
The 22nd Cambridge Workshop on Cool Stars, Stellar Systems, and the Sun (CS22). San Diego, USA; June 2024.
9. **Detailed chemical composition of wide FGK+M binary systems**
C. Duque-Arribas, H. M. Tabernero, D. Montes, et al.
Towards Other Earths III: The Planet-Star connection. Porto, Portugal; July 2023.
8. **Carbon, oxygen, and odd-Z iron-peak abundances in wide FGK+M binary systems**
C. Duque-Arribas, H. M. Tabernero, D. Montes, et al.
European Astronomical Society 2023 Annual Meeting. Kraków, Poland; July 2023.

7. **Photometric calibration of M-dwarf metallicity using Bayesian inference**
   C. Duque-Arribas, D. Montes, H. M. Tabernero, et al.
   Highlights of Spanish Astrophysics XI, Proceedings of the XV Scientific Meeting of the Spanish Astronomical Society. La Laguna, Spain; September 2022.
6. **Analysis of chromospheric flux-flux relationships of M Dwarfs using visible and near-infrared CARMENES spectra**
   F. Labarga, D. Montes, **C. Duque-Arribas**, et al.
   Highlights of Spanish Astrophysics XI, Proceedings of the XV Scientific Meeting of the Spanish Astronomical Society. La Laguna, Spain; September 2022.
5. **Chromospheric flux-flux relationships of Cool Dwarfs using VIS and NIR CARMENES spectra. Analysis of different emitters populations.**
   F. Labarga, D. Montes, **C. Duque-Arribas**, et al.
   The 21st Cambridge Workshop on Cool Stars, Stellar Systems, and the Sun (CS21). Toulouse, France; July 2022.
4. **Detailed chemical composition of wide FGK+M binary systems**
   C. Duque-Arribas, H. M. Tabernero, D. Montes, et al.
   The 21st Cambridge Workshop on Cool Stars, Stellar Systems, and the Sun (CS21). Toulouse, France; July 2022.
3. **Photometric calibrations of M dwarf metallicity using Bayesian inference**
   C. Duque-Arribas, D. Montes, H. M. Tabernero, et al.
   European Astronomical Society 2022 Annual Meeting. Valencia, Spain; June 2022.
2. **The metallicity of M dwarfs: photometric calibrations with Markov Chain Monte Carlo and Bayesian inference**
   C. Duque-Arribas, D. Montes, H. M. Tabernero, et al.
   The 20.5th Cambridge Workshop on Cool Stars, Stellar Systems, and the Sun (CS20.5). Virtually anywhere; March 2021.
1. **Stellar atmospheric parameters of CARMENES GTO M dwarfs with spectral synthesis and StePar Syn**
   E. Marfil, H. M. Tabernero, D. Montes, et al. (including **C. Duque-Arribas**)
   The 20.5th Cambridge Workshop on Cool Stars, Stellar Systems, and the Sun (CS20.5). Virtually anywhere; March 2021.

Bibliography

Abia, C., Tabernero, H. M., Korotin, S. A., et al. 2020, A&A, 642, A227

Abolfathi, B., Aguado, D. S., Aguilar, G., et al. 2018, ApJS, 235, 42

Abt, A. 1952, ApJ, 115, 199

Adams, F. C. & Laughlin, G. 1997, Reviews of Modern Physics, 69, 337

Adibekyan, V., Deal, M., Dorn, C., et al. 2024, A&A, 692, A67

Adibekyan, V., Dorn, C., Sousa, S. G., et al. 2021, Science, 374, 330

Adibekyan, V. Z., Santos, N. C., Sousa, S. G., et al. 2012a, A&A, 543, A89

Adibekyan, V. Z., Sousa, S. G., Santos, N. C., et al. 2012b, A&A, 545, A32

Alam, S., Albareti, F. D., Allende Prieto, C., et al. 2015, ApJS, 219, 12

Allard, F. 2014, in IAU Symposium, Vol. 299, Exploring the Formation and Evolution of Planetary Systems, ed. M. Booth, B. C. Matthews, & J. R. Graham, 271–272

Allard, F., Hauschildt, P. H., Alexander, D. R., & Starrfield, S. 1997, ARA&A, 35, 137

Allard, F., Hauschildt, P. H., & Schwenke, D. 2000, ApJ, 540, 1005

Alonso-Floriano, F. J., Morales, J. C., Caballero, J. A., et al. 2015, A&A, 577, A128

Alonso-Santiago, J., Negueruela, I., Marco, A., Tabernero, H. M., & Castro, N. 2020, A&A, 644, A136

Alonso-Santiago, J., Negueruela, I., Marco, A., et al. 2019, A&A, 631, A124

Alvarez, R. & Plez, B. 1998, A&A, 330, 1109

Amarsi, A. M., Asplund, M., Collet, R., & Leenaarts, J. 2015, MNRAS, 454, L11

Amarsi, A. M., Nissen, P. E., & Skúladóttir, Á. 2019, A&A, 630, A104

Anders, E. & Grevesse, N. 1989, Geochim. Cosmochim. Acta, 53, 197

Andreasen, D. T., Sousa, S. G., Tsantaki, M., et al. 2017, A&A, 600, A69

Andrews, J. J., Chanamé, J., & Agüeros, M. A. 2018, MNRAS, 473, 5393

Antoniadis-Karnavas, A., Sousa, S. G., Delgado-Mena, E., et al. 2020, A&A, 636, A9

Asplund, M., Amarsi, A. M., & Grevesse, N. 2021, A&A, 653, A141

Asplund, M., Grevesse, N., Sauval, A. J., & Scott, P. 2009, ARA&A, 47, 481

Bahcall, J. N. & Soneira, R. M. 1980, ApJS, 44, 73

Baraffe, I., Chabrier, G., Allard, F., & Hauschildt, P. H. 1998, A&A, 337, 403

Battistini, C. & Bensby, T. 2015, A&A, 577, A9

Bayo, A., Rodrigo, C., Barrado Y Navascués, D., et al. 2008, A&A, 492, 277

Bean, J. L., Sneden, C., Hauschildt, P. H., Johns-Krull, C. M., & Benedict, G. F. 2006, ApJ, 652, 1604

Beech, M. 2015, Alpha Centauri

Behmard, A., Brinkman, C. L., Hattori, S., Rubenzahl, R. A., & Bedell, M. 2025a, AJ, 170, 282

Behmard, A., Ness, M. K., Casey, A. R., et al. 2025b, ApJ, 982, 13

Bello-García, A., Passegger, V. M., Ordieres-Meré, J., et al. 2023, A&A, 673, A105

Bensby, T., Feltzing, S., & Lundström, I. 2003, A&A, 410, 527

Bensby, T., Feltzing, S., & Lundström, I. 2004, A&A, 415, 155

Bensby, T., Feltzing, S., Lundström, I., & Ilyin, I. 2005, A&A, 433, 185

Bensby, T., Feltzing, S., & Oey, M. S. 2014, A&A, 562, A71

Bensby, T., Gould, A., Asplund, M., et al. 2021, A&A, 655, A117

Bergemann, M., Collet, R., Schönrich, R., et al. 2017, ApJ, 847, 16

Bergemann, M., Gallagher, A. J., Eitner, P., et al. 2019, A&A, 631, A80

Bergemann, M., Hoppe, R., Semenova, E., et al. 2021, MNRAS, 508, 2236

Bergemann, M., Pickering, J. C., & Gehren, T. 2010, MNRAS, 401, 1334

Berger, D. H., Gies, D. R., McAlister, H. A., et al. 2006, ApJ, 644, 475

Bertran de Lis, S., Delgado Mena, E., Adibekyan, V. Z., Santos, N. C., & Sousa, S. G. 2015, A&A, 576, A89

Biazzo, K., D'Orazi, V., Desidera, S., et al. 2022, A&A, 664, A161

Biazzo, K., Gratton, R., Desidera, S., et al. 2015, A&A, 583, A135

Birky, J., Hogg, D. W., Mann, A. W., & Burgasser, A. 2020, ApJ, 892, 31

Blanco-Cuaresma, S. 2019, MNRAS, 486, 2075

Blanco-Cuaresma, S., Soubiran, C., Heiter, U., & Jofré, P. 2014, A&A, 569, A111

Blundell, C., Cornebise, J., Kavukcuoglu, K., & Wierstra, D. 2015, arXiv e-prints, arXiv:1505.05424

Bodaghee, A., Santos, N. C., Israelian, G., & Mayor, M. 2003, A&A, 404, 715

Boeshaar, P. C. 1976, The Spectral Classification of M-Dwarf Stars., PhD thesis, The Ohio State University

Boeshaar, P. C. & Tyson, J. A. 1985, AJ, 90, 817

Bond, J. C., O'Brien, D. P., & Lauretta, D. S. 2010, ApJ, 715, 1050

Bonfils, X., Delfosse, X., Udry, S., et al. 2005, A&A, 442, 635

Bonnarel, F., Fernique, P., Bienaymé, O., et al. 2000, A&AS, 143, 33

Borsa, F., Allart, R., Casasayas-Barris, N., et al. 2021, A&A, 645, A24

Bouchy, F., Doyon, R., Artigau, É., et al. 2017, The Messenger, 169, 21

Boyajian, T. S., von Braun, K., van Belle, G., et al. 2012, ApJ, 757, 112

Brewer, J. M., Fischer, D. A., Valenti, J. A., & Piskunov, N. 2016, ApJS, 225, 32

Brewer, M.-M. & Carney, B. W. 2006, AJ, 131, 431

Brooks, S. P. & Gelman, A. 1998, Journal of Computational and Graphical Statistics, 7, 434

Buchhave, L. A., Latham, D. W., Johansen, A., et al. 2012, Nature, 486, 375

Buder, S., Lind, K., Ness, M. K., et al. 2019, A&A, 624, A19

Burgasser, A. J., Geballe, T. R., Leggett, S. K., Kirkpatrick, J. D., & Golimowski, D. A. 2006, ApJ, 637, 1067

Burgasser, A. J., Kirkpatrick, J. D., Reid, I. N., et al. 2003, ApJ, 586, 512

Burgasser, A. J., Reid, I. N., Siegler, N., et al. 2007, in Protostars and Planets V, ed. B. Reipurth, D. Jewitt, & K. Keil, 427

Burrows, A., Marley, M., Hubbard, W. B., et al. 1997, ApJ, 491, 856

Bürkner, P.-C. 2017, Journal of Statistical Software, 80, 1–28

Caballero, J. A. 2009, A&A, 507, 251

Caballero, J. A., Seifert, W., Quirrenbach, A., et al. 2025, arXiv e-prints, arXiv:2503.05501

Carpenter, B., Gelman, A., Hoffman, M. D., et al. 2017, Journal of Statistical Software, 76, 1

Carter-Bond, J. C., O'Brien, D. P., & Raymond, S. N. 2012, ApJ, 760, 44

Casagrande, L. & VandenBerg, D. A. 2014, MNRAS, 444, 392

Castelli, F. & Kurucz, R. L. 2003, in IAU Symposium, Vol. 210, Modelling of Stellar Atmospheres, ed. N. Piskunov, W. W. Weiss, & D. F. Gray, A20

Cenarro, A. J., Moles, M., Cristóbal-Hornillos, D., et al. 2019, A&A, 622, A176

Chabrier, G. 2003, PASP, 115, 763

Cifuentes, C., Caballero, J. A., Cortés-Contreras, M., et al. 2020, A&A, 642, A115

Cifuentes, C., Caballero, J. A., González-Payo, J., et al. 2025, A&A, 693, A228

Clark, C. A., van Belle, G. T., Horch, E. P., et al. 2024, AJ, 167, 174

Claudi, R., Benatti, S., Carleo, I., et al. 2018, in Society of Photo-Optical Instrumentation Engineers (SPIE) Conference Series, Vol. 10702, Ground-based and Airborne Instrumentation for Astronomy VII, ed. C. J. Evans, L. Simard, & H. Takami, 107020Z

Cortés-Contreras, M., Béjar, V. J. S., Caballero, J. A., et al. 2017, A&A, 597, A47

Cortés-Contreras, M., Caballero, J. A., Montes, D., et al. 2024, A&A, 692, A206

Cosentino, R., Lovis, C., Pepe, F., et al. 2012, in Society of Photo-Optical Instrumentation Engineers (SPIE) Conference Series, Vol. 8446, Ground-based and Airborne Instrumentation for Astronomy IV, ed. I. S. McLean, S. K. Ramsay, & H. Takami, 84461V

Cristofari, P. I., Donati, J. F., Masseron, T., et al. 2022, MNRAS, 511, 1893

Croswell, K. 2002, S&T, 104, 38

Cui, X.-Q., Zhao, Y.-H., Chu, Y.-Q., et al. 2012, Research in Astronomy and Astrophysics, 12, 1197

Cushing, M. C., Kirkpatrick, J. D., Gelino, C. R., et al. 2011, ApJ, 743, 50

Cutri, R. M., Wright, E. L., Conrow, T., et al. 2021, VizieR Online Data Catalog, II/328

da Silva, R., Milone, A. d. C., & Rocha-Pinto, H. J. 2015, A&A, 580, A24

Davenport, J. R. A. & Dorn-Wallenstein, T. Z. 2019, Research Notes of the American Astronomical Society, 3, 54

Dawson, K. S., Schlegel, D. J., Ahn, C. P., et al. 2013, AJ, 145, 10

de Laverny, P., Recio-Blanco, A., Worley, C. C., & Plez, B. 2012, A&A, 544, A126

Delgado Mena, E., Adibekyan, V., Santos, N. C., et al. 2021, A&A, 655, A99

Delgado Mena, E., Israelian, G., González Hernández, J. I., et al. 2010, ApJ, 725, 2349

Demangeon, O. D. S., Zapatero Osorio, M. R., Alibert, Y., et al. 2021, A&A, 653, A41

Des Marais, D. J., Harwit, M. O., Jucks, K. W., et al. 2002, Astrobiology, 2, 153

Desidera, S., Gratton, R. G., Lucatello, S., & Claudi, R. U. 2006, A&A, 454, 581

Desidera, S., Gratton, R. G., Scuderi, S., et al. 2004, A&A, 420, 683

Díez Alonso, E., Caballero, J. A., Montes, D., et al. 2019, A&A, 621, A126

Dittmann, J. A., Irwin, J. M., Charbonneau, D., & Newton, E. R. 2016, ApJ, 818, 153

Donati, J. F., Kouach, D., Moutou, C., et al. 2020, MNRAS, 498, 5684

Dotter, A., Conroy, C., Cargile, P., & Asplund, M. 2017, ApJ, 840, 99

Draine, B. T. & Li, A. 2007, ApJ, 657, 810

Dressing, C. D. & Charbonneau, D. 2013, ApJ, 767, 95

Dupuis, J. A. & Robert, C. P. 2003, Journal of Statistical Planning and Inference, 111, 77

Duque-Arribas, C. 2022, METaMorPHosis: METallicity for M dwarfs using PHotometry

Duque-Arribas, C., Montes, D., Tabernero, H. M., et al. 2023, ApJ, 944, 106

Duque-Arribas, C., Tabernero, H. M., Montes, D., & Caballero, J. A. 2024, MNRAS, 528, 3028

Duque-Arribas, C., Tabernero, H. M., Montes, D., Caballero, J. A., & Galceran, E. 2025, A&A, 698, L12

Eker, Z., Bakış, V., Bilir, S., et al. 2018, MNRAS, 479, 5491

Endl, M., Cochran, W. D., Kürster, M., et al. 2006, ApJ, 649, 436

Engle, S. G. & Guinan, E. F. 2011, in Astronomical Society of the Pacific Conference Series, Vol. 451, 9th Pacific Rim Conference on Stellar Astrophysics, ed. S. Qain, K. Leung, L. Zhu, & S. Kwok, 285

Ercolano, B. & Clarke, C. J. 2010, MNRAS, 402, 2735

Espada, A. 2019, M.Sc. thesis, Universidad Complutense de Madrid, Spain

Fabbro, S., Venn, K. A., O'Briain, T., et al. 2018, MNRAS, 475, 2978

Fallows, C. P. & Sanders, J. L. 2022, MNRAS, 516, 5521

Faria, J. P., Suárez Mascareño, A., Figueira, P., et al. 2022, A&A, 658, A115

Feltzing, S., Fohlman, M., & Bensby, T. 2007, A&A, 467, 665

Feng, F., Butler, R. P., Vogt, S. S., et al. 2022, ApJS, 262, 21

Ferguson, D., Gardner, S., & Yanny, B. 2017, ApJ, 843, 141

Ferguson, J. W., Alexander, D. R., Allard, F., et al. 2005, ApJ, 623, 585

Ferreira Lopes, C. E., Gutiérrez-Soto, L. A., Ferreira Alberice, V. S., et al. 2025, A&A, 693, A306

Fischer, D. A. & Valenti, J. 2005, ApJ, 622, 1102

Fontanive, C., Biller, B., Bonavita, M., & Allers, K. 2018, MNRAS, 479, 2702

Fouesneau, M., Frémat, Y., Andrae, R., et al. 2023, A&A, 674, A28

Franchini, M., Morossi, C., Di Marcantonio, P., et al. 2021, AJ, 161, 9

Franchini, M., Morossi, C., Di Marcantonio, P., et al. 2020, ApJ, 888, 55

Gaia Collaboration, Babusiaux, C., van Leeuwen, F., et al. 2018a, A&A, 616, A10

Gaia Collaboration, Brown, A. G. A., Vallenari, A., et al. 2018b, A&A, 616, A1

Gaia Collaboration, Brown, A. G. A., Vallenari, A., et al. 2021a, A&A, 649, A1

Gaia Collaboration, Prusti, T., de Bruijne, J. H. J., et al. 2016, A&A, 595, A1

Gaia Collaboration, Smart, R. L., Sarro, L. M., et al. 2021b, A&A, 649, A6

Gaia Collaboration, Vallenari, A., Brown, A. G. A., et al. 2023, A&A, 674, A1

Gal, Y. & Ghahramani, Z. 2016, in Proceedings of Machine Learning Research, Vol. 48, Proceedings of The 33rd International Conference on Machine Learning, ed. M. F. Balcan & K. Q. Weinberger (New York, New York, USA: PMLR), 1050–1059

García Pérez, A. E., Allende Prieto, C., Holtzman, J. A., et al. 2016, AJ, 151, 144

Gelman, A., Hwang, J., & Vehtari, A. 2014, Stat Comput, 24, 997

Gelman, A. & Rubin, D. B. 1992, Statistical Science, 7, 457

Geraldía-González, S., Orell-Miquel, J., Pallé, E., et al. 2025, arXiv e-prints, arXiv:2507.15763

Gillon, M., Triaud, A. H. M. J., Demory, B.-O., et al. 2017, Nature, 542, 456

Goan, E. & Fookes, C. 2020, arXiv e-prints, arXiv:2006.12024

Goffo, E., Chaturvedi, P., Murgas, F., et al. 2024, A&A, 685, A147

Goldberg, L., Muller, E. A., & Aller, L. H. 1960, ApJS, 5, 1

Gonzalez, G. 1997, MNRAS, 285, 403

González Hernández, J. I., Delgado-Mena, E., Sousa, S. G., et al. 2013, A&A, 552, A6

González Hernández, J. I., Israelian, G., Santos, N. C., et al. 2010, ApJ, 720, 1592

González Hernández, J. I., Suárez Mascareño, A., Silva, A. M., et al. 2024, A&A, 690, A79

Goutis, C. & Robert, C. P. 1998, Biometrika, 85, 29

Gratton, R. G. 1989, A&A, 208, 171

Gray, D. F. 2022, The observation and analysis of stellar photospheres

Grevesse, N., Asplund, M., & Sauval, A. J. 2007, Space Sci. Rev., 130, 105

Grevesse, N. & Sauval, A. J. 1998, Space Sci. Rev., 85, 161

Grimm, S. L., Demory, B.-O., Gillon, M., et al. 2018, A&A, 613, A68

Grupp, F. 2004, A&A, 420, 289

Gustafsson, B., Edvardsson, B., Eriksson, K., et al. 2008, A&A, 486, 951

Gustafsson, B., Karlsson, T., Olsson, E., Edvardsson, B., & Ryde, N. 1999, A&A, 342, 426

Harre, J.-V. & Heller, R. 2021, Astronomische Nachrichten, 342, 578

Hauschildt, P. H., Barman, T., Baron, E., Aufdenberg, J. P., & Schweitzer, A. 2025, A&A, 698, A47

Hauschildt, P. H., Baron, E., & Allard, F. 1997, ApJ, 483, 390

Hawley, S. L., Covey, K. R., Knapp, G. R., et al. 2002, AJ, 123, 3409

Heiter, U., Lind, K., Bergemann, M., et al. 2021, A&A, 645, A106

Hejazi, N., Crossfield, I. J. M., Souto, D., et al. 2024, ApJ, 973, 31

Hejazi, N., De Robertis, M. M., & Dawson, P. C. 2015, AJ, 149, 140

Henry, T. J. & Jao, W.-C. 2024, ARA&A, 62, 593

Henry, T. J., Jao, W.-C., Subasavage, J. P., et al. 2006, AJ, 132, 2360

Hertzsprung, E. 1911, Publikationen des Astrophysikalischen Observatoriums zu Potsdam, 22, A1

Hinton, G. E., Srivastava, N., Krizhevsky, A., Sutskever, I., & Salakhutdinov, R. R. 2012, arXiv e-prints, arXiv:1207.0580

Hobson, M. J., Jofré, E., García, L., Petrucci, R., & Gómez, M. 2018, Rev. Mexicana Astron. Astrofis., 54, 65

Hon, M., Stello, D., & Yu, J. 2017, MNRAS, 469, 4578

Husser, T. O., Wende-von Berg, S., Dreizler, S., et al. 2013, A&A, 553, A6

Ida, S. & Lin, D. N. C. 2004, ApJ, 616, 567

Ioffe, S. & Szegedy, C. 2015, arXiv e-prints, arXiv:1502.03167

Irwin, J. M., Quinn, S. N., Berta, Z. K., et al. 2011, ApJ, 742, 123

Ishikawa, H. T., Aoki, W., Hirano, T., et al. 2022, AJ, 163, 72

Ishikawa, H. T., Aoki, W., Kotani, T., et al. 2020, PASJ, 72, 102

Jeffers, S. V., Schöfer, P., Lamert, A., et al. 2018, A&A, 614, A76

Jofré, P., Heiter, U., & Soubiran, C. 2019, ARA&A, 57, 571

Jofré, P., Heiter, U., Worley, C. C., et al. 2017, A&A, 601, A38

John, T. L. 1988, A&A, 193, 189

Johnson, J. A. & Apps, K. 2009, ApJ, 699, 933

Johnson, J. A., Butler, R. P., Marcy, G. W., et al. 2007, ApJ, 670, 833

Johnson, J. A., Gazak, J. Z., Apps, K., et al. 2012, AJ, 143, 111

Jones, H. R. A., Pavlenko, Y., Viti, S., et al. 2005, MNRAS, 358, 105

Jönsson, H., Holtzman, J. A., Allende Prieto, C., et al. 2020, AJ, 160, 120

Jontof-Hutter, D., Rowe, J. F., Lissauer, J. J., Fabrycky, D. C., & Ford, E. B. 2015, Nature, 522, 321

Kaminski, A., Sabotta, S., Kemmer, J., et al. 2025, A&A, 696, A101

Kang, W. & Lee, S.-G. 2012, MNRAS, 425, 3162

Kang, W., Lee, S.-G., & Kim, K.-M. 2011, ApJ, 736, 87

Kasting, J. F., Whitmire, D. P., & Reynolds, R. T. 1993, Icarus, 101, 108

Kausch, W., Noll, S., Smette, A., et al. 2015, A&A, 576, A78

Kheirdastan, S. & Bazarghan, M. 2016, Ap&SS, 361, 304

Kim, E. J. & Brunner, R. J. 2017, MNRAS, 464, 4463

Kiman, R., Faherty, J. K., Cruz, K. L., et al. 2021, AJ, 161, 277

Kingma, D. P. & Ba, J. 2017, Adam: A Method for Stochastic Optimization

Kirkpatrick, J. D., Henry, T. J., & McCarthy, Donald W., J. 1991, ApJS, 77, 417

Kirkpatrick, J. D., Henry, T. J., & Simons, D. A. 1995, AJ, 109, 797

Kirkpatrick, J. D., Marocco, F., Gelino, C. R., et al. 2024, ApJS, 271, 55

Kirkpatrick, J. D., Reid, I. N., Liebert, J., et al. 1999, ApJ, 519, 802

Kiselman, D. 1993, A&A, 275, 269

Kobayashi, C. 2016, Nature, 540, 205

Kobayashi, C., Karakas, A. I., & Lugaro, M. 2020, ApJ, 900, 179

Kobayashi, C., Karakas, A. I., & Umeda, H. 2011, MNRAS, 414, 3231

Kollmeier, J. A., Rix, H.-W., Aerts, C., et al. 2025, arXiv e-prints, arXiv:2507.06989

Kollmeier, J. A., Zasowski, G., Rix, H.-W., et al. 2017, arXiv e-prints, arXiv:1711.03234

Kopparapu, R. K., Ramirez, R. M., SchottelKotte, J., et al. 2014, ApJ, 787, L29

Kotani, T., Tamura, M., Nishikawa, J., et al. 2018, in Society of Photo-Optical Instrumentation Engineers (SPIE) Conference Series, Vol. 10702, Ground-based and Airborne Instrumentation for Astronomy VII, ed. C. J. Evans, L. Simard, & H. Takami, 1070211

Kruschke, J. K. 2014, Doing Bayesian Data Analysis: A Tutorial with R, JAGS, and Stan (2nd edition), ISBN 978-0-12-405888-0

Kurucz, R. L. 1993, Physica Scripta Volume T, 47, 110

Lada, C. J. 2006, ApJ, 640, L63

Larimer, J. W. 1975, Geochim. Cosmochim. Acta, 39, 389

Latham, D. W., Stefanik, R. P., Torres, G., et al. 2002, AJ, 124, 1144

Laureijs, R., Amiaux, J., Arduini, S., et al. 2011, arXiv e-prints, arXiv:1110.3193

Leger, A. & Puget, J. L. 1984, A&A, 137, L5

Lépine, S., Rich, R. M., & Shara, M. M. 2003, AJ, 125, 1598

Lillo-Box, J., Faria, J. P., Suárez Mascareño, A., et al. 2021, A&A, 654, A60

Lindegren, L., Klioner, S. A., Hernández, J., et al. 2021, A&A, 649, A2

Lohr, M. E., Negueruela, I., Tabernero, H. M., et al. 2018, MNRAS, 478, 3825

López-Morales, M. 2007, ApJ, 660, 732

López-Morales, M. & Ribas, I. 2005, ApJ, 631, 1120

Luck, R. E. 2017, AJ, 153, 21

Maddox, W., Garipov, T., Izmailov, P., Vetrov, D., & Wilson, A. G. 2019, arXiv e-prints, arXiv:1902.02476

Magg, E., Bergemann, M., Serenelli, A., et al. 2022, A&A, 661, A140

Magrini, L., Randich, S., Friel, E., et al. 2013, A&A, 558, A38

Mahadevan, S., Ramsey, L., Bender, C., et al. 2012, in Society of Photo-Optical Instrumentation Engineers (SPIE) Conference Series, Vol. 8446, Ground-based and Airborne Instrumentation for Astronomy IV, ed. I. S. McLean, S. K. Ramsay, & H. Takami, 84461S

Majewski, S. R., Schiavon, R. P., Frinchaboy, P. M., et al. 2017, AJ, 154, 94

Maldonado, J., Eiroa, C., Villaver, E., Montesinos, B., & Mora, A. 2015, A&A, 579, A20

Maldonado, J., Micela, G., Baratella, M., et al. 2020, A&A, 644, A68

Mallorquín, M., Goffo, E., Pallé, E., et al. 2023, A&A, 680, A76

Mann, A. W., Brewer, J. M., Gaidos, E., Lépine, S., & Hilton, E. J. 2013, AJ, 145, 52

Mann, A. W., Deacon, N. R., Gaidos, E., et al. 2014, AJ, 147, 160

Mann, A. W., Dupuy, T., Kraus, A. L., et al. 2019, ApJ, 871, 63

Mann, A. W., Feiden, G. A., Gaidos, E., Boyajian, T., & von Braun, K. 2015, ApJ, 804, 64

Manteiga, M., Santoveña, R., Álvarez, M. A., et al. 2025, A&A, 694, A326

Marboeuf, U., Thiabaud, A., Alibert, Y., Cabral, N., & Benz, W. 2014, A&A, 570, A36

Marconi, A., Abreu, M., Adibekyan, V., et al. 2020, in Society of Photo-Optical Instrumentation Engineers (SPIE) Conference Series, Vol. 11447, Ground-based and Airborne Instrumentation for Astronomy VIII, ed. C. J. Evans, J. J. Bryant, & K. Motohara, 1144726

Marfil, E., Tabernero, H. M., Montes, D., et al. 2021, A&A, 656, A162

Marocco, F., Eisenhardt, P. R. M., Fowler, J. W., et al. 2021, ApJS, 253, 8

Martín, E. L., Delfosse, X., Basri, G., et al. 1999, AJ, 118, 2466

Martín, E. L. & Kun, M. 1996, A&AS, 116, 467

Martin, E. L., Rebolo, R., & Zapatero-Osorio, M. R. 1996, ApJ, 469, 706

Martínez-Rodríguez, H., Caballero, J. A., Cifuentes, C., Piro, A. L., & Barnes, R. 2019, ApJ, 887, 261

Mas-Buitrago, P., González-Marcos, A., Solano, E., et al. 2024, A&A, 687, A205

Mason, B. D., Hartkopf, W. I., Gies, D. R., Henry, T. J., & Helsel, J. W. 2009, AJ, 137, 3358

Mason, B. D., Wycoff, G. L., Hartkopf, W. I., Douglass, G. G., & Worley, C. E. 2001, AJ, 122, 3466

Mayor, M., Pepe, F., Queloz, D., et al. 2003, The Messenger, 114, 20

Medan, I., Lépine, S., & Hartman, Z. 2021, AJ, 161, 234

Mendes de Oliveira, C., Ribeiro, T., Schoenell, W., et al. 2019, MNRAS, 489, 241

Mészáros, S., Jofré, P., Johnson, J. A., et al. 2025, AJ, 170, 96

Meynet, G. & Maeder, A. 2002, A&A, 390, 561

Michaud, G., Alecian, G., & Richer, J. 2015, Atomic Diffusion in Stars

Moedas, N., Deal, M., Bossini, D., & Campilho, B. 2022, A&A, 666, A43

Molina-Jorquera, F., Damke, G., Fernández-Olivares, D., et al. 2024, A&A, 691, A144

Montes, D., Fernández-Figueroa, M. J., De Castro, E., et al. 2000, A&AS, 146, 103

Montes, D., González-Peinado, R., Tabernero, H. M., et al. 2018, MNRAS, 479, 1332

Montes, D., López-Santiago, J., Gálvez, M. C., et al. 2001, MNRAS, 328, 45

Morgan, W. W. 1938, ApJ, 87, 589

Morton, D. C. 2000, ApJS, 130, 403

Moustakas, J., Kennicutt, Robert C., J., Tremonti, C. A., et al. 2010, ApJS, 190, 233

Moutou, C., Delfosse, X., Petit, A. C., et al. 2023, A&A, 678, A207

Mucciarelli, A., Pancino, E., Lovisi, L., Ferraro, F. R., & Lapenna, E. 2013, ApJ, 766, 78

Murgas, F., Pallé, E., Orell-Miquel, J., et al. 2024, A&A, 684, A83

Nagel, E., Czesla, S., Kaminski, A., et al. 2023, A&A, 680, A73

Negueruela, I., Chené, A. N., Tabernero, H. M., et al. 2021, MNRAS, 505, 1618

Negueruela, I., Monguió, M., Marco, A., et al. 2018, MNRAS, 477, 2976

Ness, M., Hogg, D. W., Rix, H. W., Ho, A. Y. Q., & Zasowski, G. 2015, ApJ, 808, 16

Neves, V., Bonfils, X., Santos, N. C., et al. 2012, A&A, 538, A25

Neves, V., Santos, N. C., Sousa, S. G., Correia, A. C. M., & Israelian, G. 2009, A&A, 497, 563

Newton, E. R., Charbonneau, D., Irwin, J., et al. 2014, AJ, 147, 20

Nissen, P. E., Chen, Y. Q., Carigi, L., Schuster, W. J., & Zhao, G. 2014, A&A, 568, A25

Nissen, P. E., Chen, Y. Q., Schuster, W. J., & Zhao, G. 2000, A&A, 353, 722

Nissen, P. E. & Schuster, W. J. 2010, A&A, 511, L10

Nutzman, P. & Charbonneau, D. 2008, PASP, 120, 317

Olander, T., Heiter, U., & Kochukhov, O. 2021, A&A, 649, A103

Origlia, L., Oliva, E., Baffa, C., et al. 2014, in Society of Photo-Optical Instrumentation Engineers (SPIE) Conference Series, Vol. 9147, Ground-based and Airborne Instrumentation for Astronomy V, ed. S. K. Ramsay, I. S. McLean, & H. Takami, 91471E

Parker, R. J. & Meyer, M. R. 2014, MNRAS, 442, 3722

Passegger, V. M., Bello-García, A., Ordieres-Meré, J., et al. 2022, A&A, 658, A194

Passegger, V. M., Bello-García, A., Ordieres-Meré, J., et al. 2020, A&A, 642, A22

Passegger, V. M., Reiners, A., Jeffers, S. V., et al. 2018, A&A, 615, A6

Passegger, V. M., Schweitzer, A., Shulyak, D., et al. 2019, A&A, 627, A161

Passegger, V. M., Wende-von Berg, S., & Reiners, A. 2016, A&A, 587, A19

Pavlenko, Y. V., Kaminsky, B. M., Jenkins, J. S., et al. 2019, A&A, 621, A112

Payne, C. H. 1925, Stellar Atmospheres; a Contribution to the Observational Study of High Temperature in the Reversing Layers of Stars., PhD thesis, RADCLIFFE COLLEGE.

Pepe, F., Cristiani, S., Rebolo, R., et al. 2021, A&A, 645, A96

Pepe, F. A., Cristiani, S., Rebolo Lopez, R., et al. 2010, in Society of Photo-Optical Instrumentation Engineers (SPIE) Conference Series, Vol. 7735, Ground-based and Airborne Instrumentation for Astronomy III, ed. I. S. McLean, S. K. Ramsay, & H. Takami, 77350F

Perdelwitz, V., Mittag, M., Tal-Or, L., et al. 2021, A&A, 652, A116

Petigura, E. A. & Marcy, G. W. 2011, ApJ, 735, 41

Piironen, J., Paasiniemi, M., & Vehtari, A. 2018, arXiv e-prints, arXiv:1810.02406

Piironen, J. & Vehtari, A. 2017, arXiv e-prints, arXiv:1707.01694

Piskunov, N. & Valenti, J. A. 2017, A&A, 597, A16

Plez, B. 2012, Turbospectrum: Code for spectral synthesis, Astrophysics Source Code Library, record ascl:1205.004

Popper, D. M. 1980, ARA&A, 18, 115

Qiu, D., Li, J., Zhang, B., et al. 2024, MNRAS, 527, 11866

Quirrenbach, A., CARMENES Consortium, Amado, P. J., et al. 2020, in Society of Photo-Optical Instrumentation Engineers (SPIE) Conference Series, Vol. 11447, Society of Photo-Optical Instrumentation Engineers (SPIE) Conference Series, 114473C

Rains, A. D., Žerjal, M., Ireland, M. J., et al. 2021, MNRAS, 504, 5788

Rajpurohit, A. S., Reylé, C., Allard, F., et al. 2014, A&A, 564, A90

Ramírez, I., Allende Prieto, C., & Lambert, D. L. 2007, A&A, 465, 271

Ramírez, I., Allende Prieto, C., & Lambert, D. L. 2013, ApJ, 764, 78

Raskin, G., van Winckel, H., Hensberge, H., et al. 2011, A&A, 526, A69

Reddy, B. E., Lambert, D. L., & Allende Prieto, C. 2006, MNRAS, 367, 1329

Reid, I. N., Gizis, J. E., Cohen, J. G., et al. 1997, PASP, 109, 559

Reid, I. N., Hawley, S. L., & Gizis, J. E. 1995, AJ, 110, 1838

Reiners, A., Zechmeister, M., Caballero, J. A., et al. 2018, A&A, 612, A49

Reylé, C., Jardine, K., Fouqué, P., et al. 2021, A&A, 650, A201

Ribas, I., Bolmont, E., Selsis, F., et al. 2016, A&A, 596, A111

Ribas, I., Reiners, A., Zechmeister, M., et al. 2023, A&A, 670, A139

Riello, M., De Angeli, F., Evans, D. W., et al. 2021, A&A, 649, A3

Rodrigo, C., Solano, E., & Bayo, A. 2012, SVO Filter Profile Service Version 1.0, IVOA Working Draft 15 October 2012

Rodríguez-López, C. 2019, Frontiers in Astronomy and Space Sciences, 6, 76

Rojas-Ayala, B., Covey, K. R., Muirhead, P. S., & Lloyd, J. P. 2010, ApJ, 720, L113

Rojas-Ayala, B., Covey, K. R., Muirhead, P. S., & Lloyd, J. P. 2012, ApJ, 748, 93

Rosenberg, H. 1910, Astronomische Nachrichten, 186, 71

Russell, H. N. 1914a, Popular Astronomy, 22, 331

Russell, H. N. 1914b, Science, 39, 791

Russell, H. N. 1929, ApJ, 70, 11

Rutten, R. J. 1988, in Astrophysics and Space Science Library, Vol. 138, IAU Colloq. 94: Physics of Formation of FE II Lines Outside LTE, ed. R. Viotti, A. Vittone, & M. Friedjung, 185–210

Ryabchikova, T., Piskunov, N., Kurucz, R. L., et al. 2015, Phys. Scr, 90, 054005

Sabotta, S., Schlecker, M., Chaturvedi, P., et al. 2021, A&A, 653, A114

Saha, M. N. 1920, Nature, 105, 232

Saha, M. N. 1921, Proceedings of the Royal Society of London Series A, 99, 135

Sana, H., de Mink, S. E., de Koter, A., et al. 2012, Science, 337, 444

Santos, N. C., Adibekyan, V., Dorn, C., et al. 2017, A&A, 608, A94

Santos, N. C., Adibekyan, V., Mordasini, C., et al. 2015, A&A, 580, L13

Sarmento, P., Delgado Mena, E., Rojas-Ayala, B., & Blanco-Cuaresma, S. 2020, A&A, 636, A85

Sarro, L. M., Ordieres-Meré, J., Bello-García, A., González-Marcos, A., & Solano, E. 2018, MNRAS, 476, 1120

Scalo, J., Kaltenegger, L., Segura, A. G., et al. 2007, Astrobiology, 7, 85

Schlaufman, K. C. & Laughlin, G. 2010, A&A, 519, A105

Schmidt, S. J., Wagoner, E. L., Johnson, J. A., et al. 2016, MNRAS, 460, 2611

Schöfer, P., Jeffers, S. V., Reiners, A., et al. 2019, A&A, 623, A44

Schweitzer, A., Passegger, V. M., Cifuentes, C., et al. 2019, A&A, 625, A68

Seager, S. & Deming, D. 2010, ARA&A, 48, 631

Seifahrt, A., Bean, J. L., Stürmer, J., et al. 2020, in Society of Photo-Optical Instrumentation Engineers (SPIE) Conference Series, Vol. 11447, Society of Photo-Optical Instrumentation Engineers (SPIE) Conference Series, 114471F

Seitenzahl, I. R., Cescutti, G., Röpke, F. K., Ruiter, A. J., & Pakmor, R. 2013, A&A, 559, L5

Shan, Y., Reiners, A., Fabbian, D., et al. 2021, A&A, 654, A118

Shan, Y., Revilla, D., Skrzypinski, S. L., et al. 2024, A&A, 684, A9

Shatsky, N. & Tokovinin, A. 2002, A&A, 382, 92

Shetrone, M., Bizyaev, D., Lawler, J. E., et al. 2015, ApJS, 221, 24

Shields, A. L., Ballard, S., & Johnson, J. A. 2016, Phys. Rep., 663, 1

Shkolnik, E., Liu, M. C., & Reid, I. N. 2009, ApJ, 699, 649

Silverstein, M. L. 2019, Sizing up red dwarfs in the solar neighborhood, PhD thesis, Georgia State University

Skrutskie, M. F., Cutri, R. M., Stiening, R., et al. 2006, AJ, 131, 1163

Smette, A., Sana, H., Noll, S., et al. 2015, A&A, 576, A77

Sneden, C., Cowan, J. J., Kobayashi, C., et al. 2016, ApJ, 817, 53

Sneden, C. A. 1973, Carbon and Nitrogen Abundances in Metal-Poor Stars., PhD thesis, University of Texas, Austin

Sobel, D. 2016, The Glass Universe: How the Ladies of the Harvard Observatory Took the Measure of the Stars

Somers, G., Cao, L., & Pinsonneault, M. H. 2020, ApJ, 891, 29

Soto, M. G. & Jenkins, J. S. 2018, A&A, 615, A76

Sousa, S. G., Santos, N. C., Adibekyan, V., Delgado-Mena, E., & Israelian, G. 2015, A&A, 577, A67

Sousa, S. G., Santos, N. C., Israelian, G., Mayor, M., & Monteiro, M. J. P. F. G. 2007, A&A, 469, 783

Sousa, S. G., Santos, N. C., Israelian, G., Mayor, M., & Udry, S. 2011, A&A, 533, A141

Sousa, S. G., Santos, N. C., Mayor, M., et al. 2008, A&A, 487, 373

Souto, D., Cunha, K., García-Hernández, D. A., et al. 2017, ApJ, 835, 239

Souto, D., Cunha, K., Smith, V. V., et al. 2020, ApJ, 890, 133

Souto, D., Cunha, K., Smith, V. V., et al. 2022, ApJ, 927, 123

Souto, D., Unterborn, C. T., Smith, V. V., et al. 2018, ApJ, 860, L15

Srivastava, N., Hinton, G., Krizhevsky, A., Sutskever, I., & Salakhutdinov, R. 2014, Journal of Machine Learning Research, 15, 1929

Stan Development Team. 2022, Stan Modeling Language Users Guide and Reference Manual, version 2.32

Stauffer, J. R. & Hartmann, L. W. 1986, ApJS, 61, 531

Steenbock, W. & Holweger, H. 1984, A&A, 130, 319

Stonkutė, E., Chorniy, Y., Tautvaišienė, G., et al. 2020, AJ, 159, 90

Suárez-Andrés, L., Israelian, G., González Hernández, J. I., et al. 2018, A&A, 614, A84

Tabernero, H. M., Dorda, R., Negueruela, I., & González-Fernández, C. 2018, MNRAS, 476, 3106

Tabernero, H. M., Dorda, R., Negueruela, I., & Marfil, E. 2021a, A&A, 646, A98

Tabernero, H. M., Marfil, E., Montes, D., & González Hernández, J. I. 2019, A&A, 628, A131

Tabernero, H. M., Marfil, E., Montes, D., & González Hernández, J. I. 2022, A&A, 657, A66

Tabernero, H. M., Montes, D., & González Hernández, J. I. 2012, A&A, 547, A13

Tabernero, H. M., Montes, D., González Hernández, J. I., & Ammler-von Eiff, M. 2017, A&A, 597, A33

Tabernero, H. M., Shan, Y., Caballero, J. A., et al. 2024, A&A, 689, A223

Tabernero, H. M., Zapatero Osorio, M. R., Allart, R., et al. 2021b, A&A, 646, A158

Takeda, Y. & Honda, S. 2005, PASJ, 57, 65

Tamura, M., Suto, H., Nishikawa, J., et al. 2012, in Society of Photo-Optical Instrumentation Engineers (SPIE) Conference Series, Vol. 8446, Ground-based and Airborne Instrumentation for Astronomy IV, ed. I. S. McLean, S. K. Ramsay, & H. Takami, 84461T

Tarter, J. C., Backus, P. R., Mancinelli, R. L., et al. 2007, Astrobiology, 7, 30

Taylor, M. B. 2005, in Astronomical Society of the Pacific Conference Series, Vol. 347, Astronomical Data Analysis Software and Systems XIV, ed. P. Shopbell, M. Britton, & R. Ebert, 29

Terrien, R. C., Mahadevan, S., Bender, C. F., et al. 2012, ApJ, 747, L38

Thévenin, F. & Idiart, T. P. 1999, ApJ, 521, 753

Thiabaud, A., Marboeuf, U., Alibert, Y., Leya, I., & Mezger, K. 2015, A&A, 580, A30

Ting, Y.-S. 2024, arXiv e-prints, arXiv:2412.05806

Tody, D. 1986, in Society of Photo-Optical Instrumentation Engineers (SPIE) Conference Series, Vol. 627, Instrumentation in astronomy VI, ed. D. L. Crawford, 733

Tolstoy, E., Hill, V., & Tosi, M. 2009, ARA&A, 47, 371

Torres, G., Andersen, J., & Giménez, A. 2010, A&A Rev., 18, 67

Tsantaki, M., Andreasen, D., & Teixeira, G. 2020, The Journal of Open Source Software, 5, 2048

Tsuji, T. & Nakajima, T. 2014, PASJ, 66, 98

Tsujimoto, T. & Shigeyama, T. 1998, ApJ, 508, L151

Unsöld, A. 1948, ZAp, 24, 306

Valenti, J. A. & Piskunov, N. 1996, A&AS, 118, 595

Van Eck, S., Neyskens, P., Jorissen, A., et al. 2017, A&A, 601, A10

Vehtari, A., Gelman, A., & Gabry, J. 2017, Stat Comput, 27, 1413–1432

Vehtari, A., Simpson, D., Gelman, A., Yao, Y., & Gabry, J. 2015, arXiv e-prints, arXiv:1507.02646

Voronov, Y. V., Yakovleva, S. A., & Belyaev, A. K. 2022, ApJ, 926, 173

Wanderley, F., Cunha, K., Souto, D., et al. 2023, ApJ, 951, 90

Wang, H. & Yeung, D.-Y. 2016, arXiv e-prints, arXiv:1604.01662

Weingartner, J. C. & Draine, B. T. 2001, ApJ, 548, 296

West, A. A., Hawley, S. L., Bochanski, J. J., et al. 2008, AJ, 135, 785

Whitten, D. D., Placco, V. M., Beers, T. C., et al. 2019, A&A, 622, A182

Wildi, F., Blind, N., Reshetov, V., et al. 2017, in Society of Photo-Optical Instrumentation Engineers (SPIE) Conference Series, Vol. 10400, Society of Photo-Optical Instrumentation Engineers (SPIE) Conference Series, ed. S. Shaklan, 1040018

Wilking, B. A., Meyer, M. R., Robinson, J. G., & Greene, T. P. 2005, AJ, 130, 1733

Winters, J. G., Henry, T. J., Jao, W.-C., et al. 2019, AJ, 157, 216

Winters, J. G., Henry, T. J., Lurie, J. C., et al. 2015, AJ, 149, 5

Woolf, V. M. & Wallerstein, G. 2006, PASP, 118, 218

Woosley, S. E. & Weaver, T. A. 1995, ApJS, 101, 181

Wright, E. L., Eisenhardt, P. R. M., Mainzer, A. K., et al. 2010, AJ, 140, 1868

Zhao, G., Chen, Y. Q., Qiu, H. M., & Li, Z. W. 2002, AJ, 124, 2224

Zhao, G., Mashonkina, L., Yan, H. L., et al. 2016, ApJ, 833, 225

CHAPTER A

Appendix of Chapter 2

This appendix contains the figures and tables referenced in Chapter 2:

- Fig. A.1 shows the color-color diagrams investigated, with the respective calibrations.
- Fig. A.2 is the same that Fig. A.1, but for the color-magnitude diagrams.
- Table A.1 compiles the M-dwarf secondaries with the espectroscopic metallicities from Montes et al. (2018) and the photometric metallicities from this work.

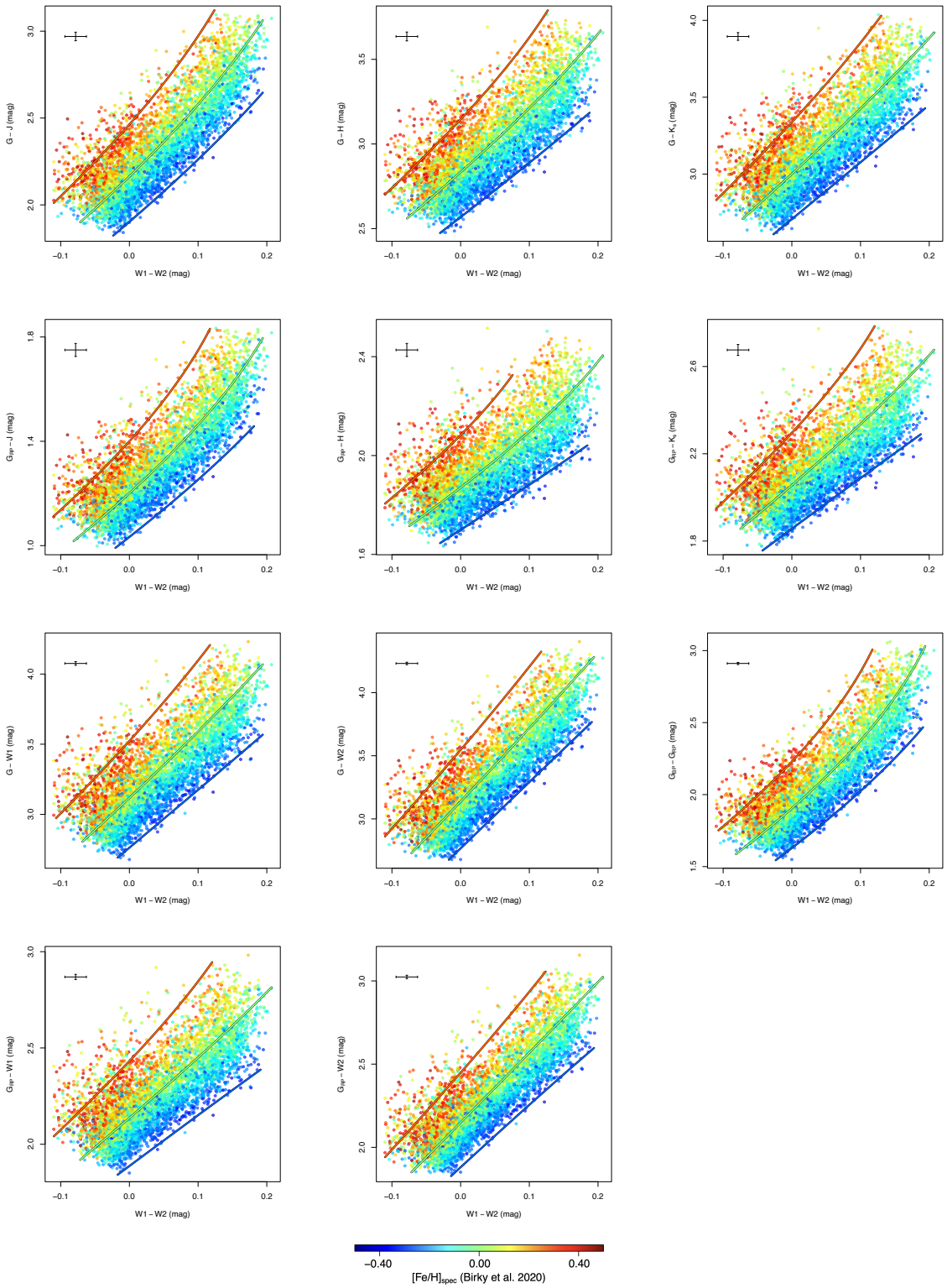

Figure A.1: Color–color diagrams of the stars from Birky et al. (2020), color-coded by $[\mathrm{Fe/H}]_{\mathrm{spec}}$, with the respective calibrations given by this work (red: $[\mathrm{Fe/H}] = +0.3$, green: $[\mathrm{Fe/H}] = 0.0$, blue: $[\mathrm{Fe/H}] = -0.3$). The mean uncertainties of the color indices involved are also shown in black in the top left corner of the panels.

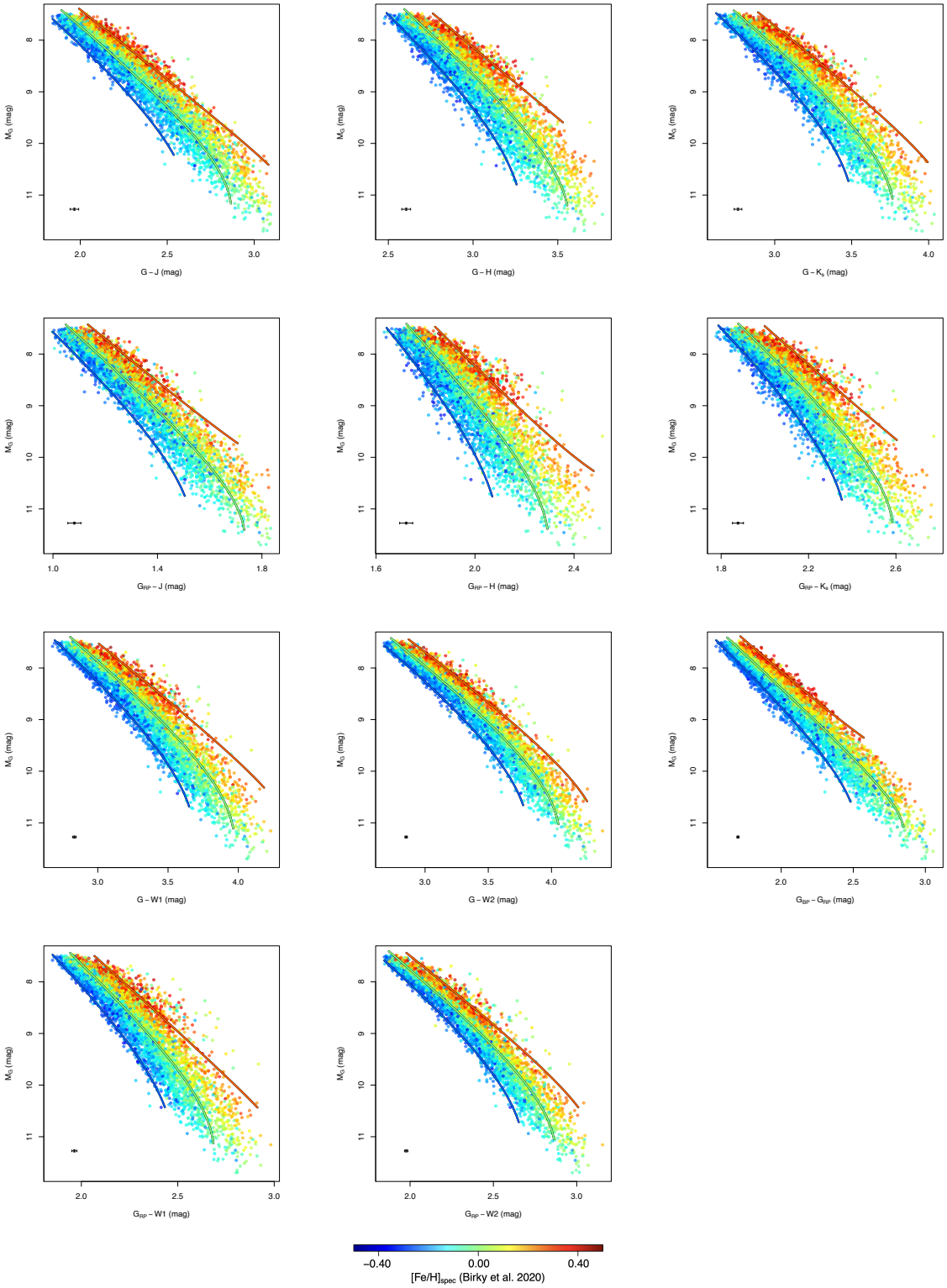

Figure A.2: Same as Fig. A.2 but for color–magnitude diagrams.

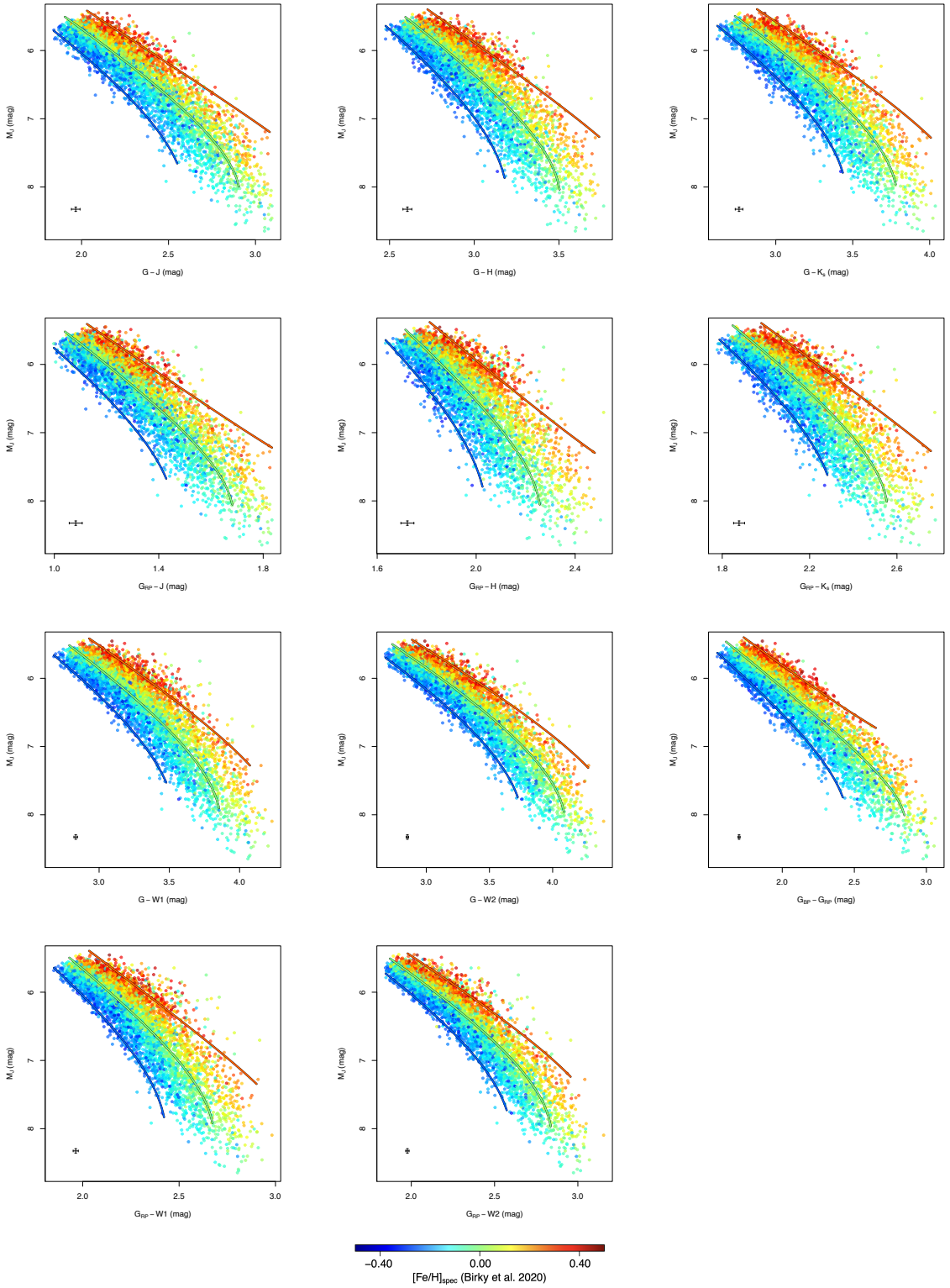

Figure A.2: *Continued*

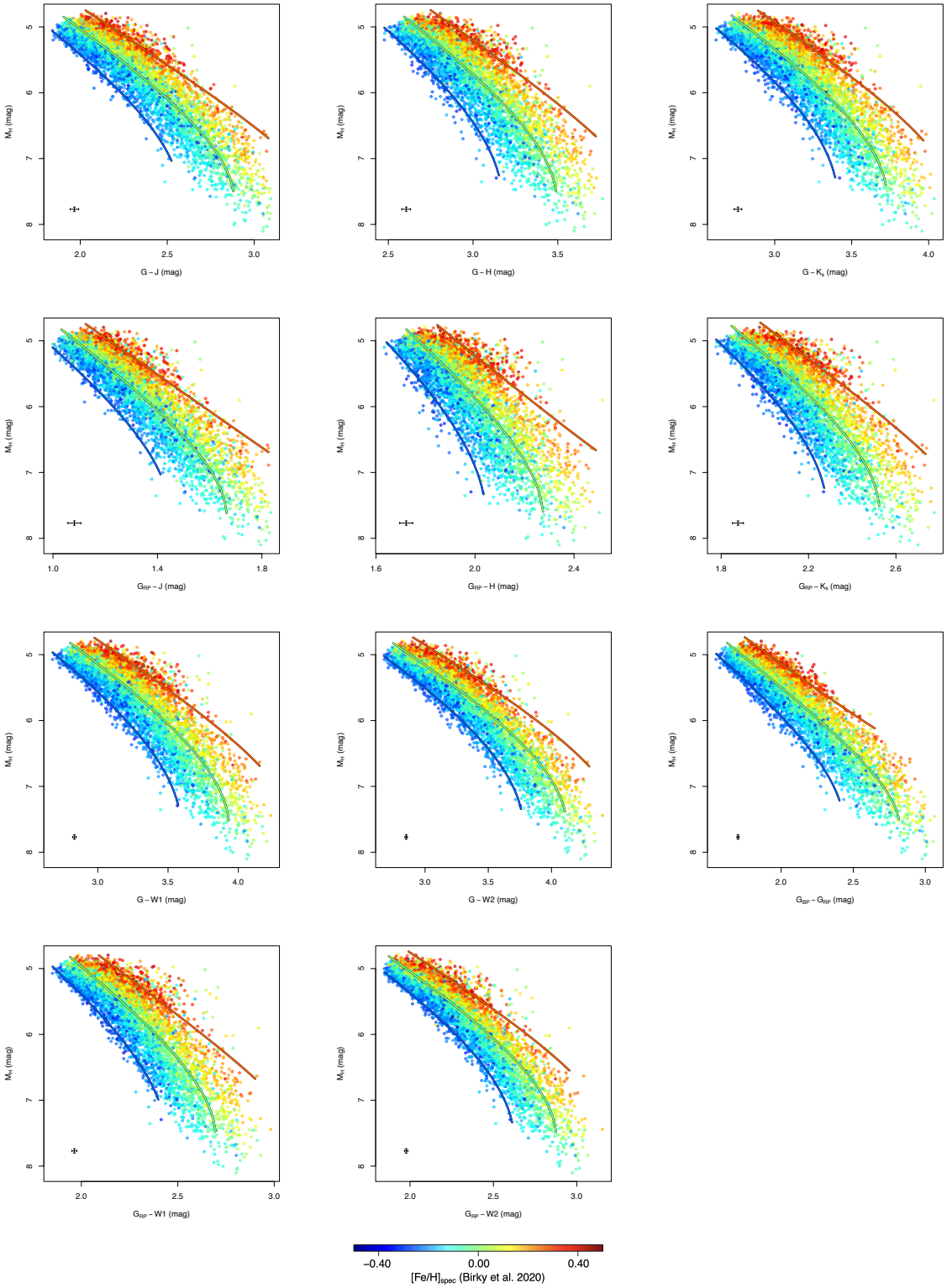

Figure A.2: *Continued*

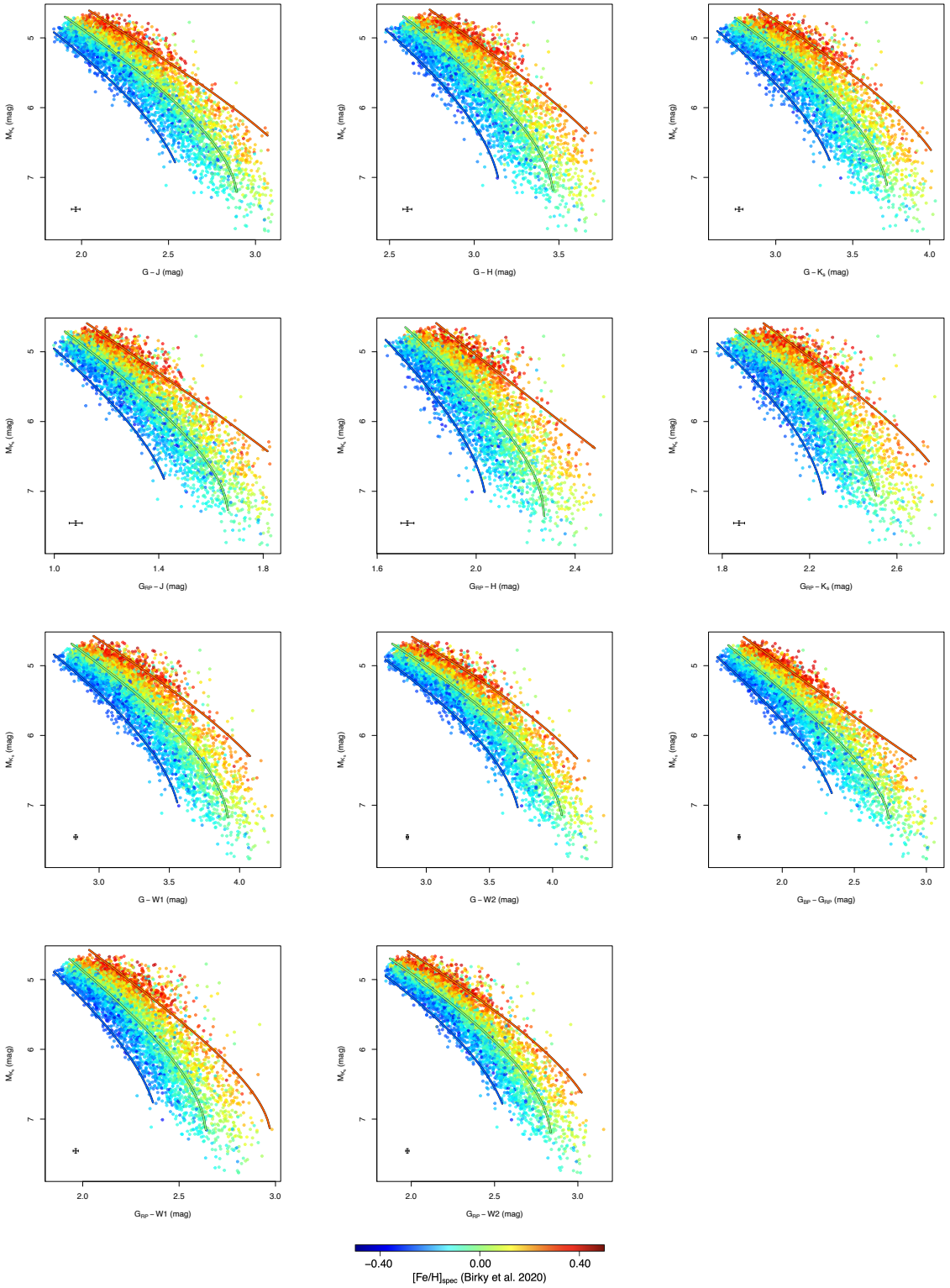

Figure A.2: *Continued*

Table A.1: Estimated metallicities of M-dwarf secondaries in FGK+M systems.

WDS	Name	α	δ	Sp. type	$[Fe/H]_{spec}$ Montes+18	$[Fe/H]_{phot}$ This work
J00467-0426	LP 646-9	00:46:43.4	−04:24:46	M4.0 V	-0.10 ± 0.07	0.09 ± 0.08
J01450-0104	LP 588-44	01:44:57.0	−01:03:04	M2.0	-0.37 ± 0.03	-0.33 ± 0.08
J02556+2652	HD 18143 C	02:55:35.8	+26:52:21	M4.0 V	0.18 ± 0.05	0.16 ± 0.08
J03078+2533	HD 19381B	03:07:58.3	+25:32:02	M3.5 V	0.11 ± 0.02	0.11 ± 0.08
J03203+0902	HD 20727B	03:20:42.5	+09:02:10	M4.0 V	-0.24 ± 0.02	-0.03 ± 0.08
J03356+4253	Wolf 191	03:35:28.5	+42:53:35	M0.5 V	-0.37 ± 0.03	-0.43 ± 0.08
J03520+3947	TYC 2868-639-1	03:51:58.1	+39:46:57	M0.0 V	-0.13 ± 0.05	-0.03 ± 0.08
J03556+5214	LSPM J0355+5214	03:55:36.9	+52:14:29	M2.5 V	-0.32 ± 0.02	-0.32 ± 0.08
J05003+2508	HD 31867B	05:00:19.5	+25:07:51	M1.0 V	-0.01 ± 0.02	-0.02 ± 0.08
J05264+0351	2MASS J05262029+0351111	05:26:20.3	+03:51:11	M1.5 V	0.01 ± 0.03	-0.09 ± 0.08
J05466+0110	HD 38529 B	05:46:19.4	+01:12:47	M2.5 V	0.32 ± 0.02	0.23 ± 0.08
J06319+0039	G 106-52	06:31:23.7	+00:36:45	M1.5 V	-0.29 ± 0.02	-0.30 ± 0.08
J06332+0528	HD 46375 B	06:33:12.1	+05:27:53	M2.0 V	0.23 ± 0.06	0.23 ± 0.08
J06461+3233	HD 263175 B	06:46:07.5	+32:33:15	M1.0 V	-0.38 ± 0.03	-0.41 ± 0.08
J07041+7514	LP 16-395	07:04:09.5	+75:14:37	M4.0 V	0.18 ± 0.02	0.10 ± 0.08
J08138+6306	NLTT 19115	08:14:19.0	+63:04:40	M1.5 V	-0.09 ± 0.01	-0.19 ± 0.08
J08484+2042	2MASS J08482492+2042188	08:48:24.9	+20:42:18	M1.5 V	-0.03 ± 0.02	-0.14 ± 0.08
J08492+0329	LEP 33	08:49:02.3	+03:29:47	M4	0.05 ± 0.02	0.04 ± 0.08
J09008+2347	HD 77052 B	09:00:53.2	+23:46:59	M2.5 V	0.04 ± 0.02	-0.02 ± 0.08
J09029+0600	2MASS J09025320+0602095	09:02:53.2	+06:02:10	M1.5 V	-0.12 ± 0.02	-0.09 ± 0.08
J09058+5532	NLTT 20915	09:05:51.2	+55:32:18	M3.5 V	0.03 ± 0.02	-0.02 ± 0.08
J09152+2323	BD+23 2063B	09:15:10.1	+23:21:33	M0.0 V	0.21 ± 0.02	0.19 ± 0.08
J11403+0931	LP 493-31	11:40:20.8	+09:30:45	M1.5 V	-0.28 ± 0.03	-0.25 ± 0.08
J11455+4740	G 122-46	11:47:21.7	+47:45:57	M2.5	-0.45 ± 0.02	-0.31 ± 0.08
J11523+0957	LP 493-64	11:52:17.9	+10:00:39	M4.0 V	0.22 ± 0.06	0.16 ± 0.08
J12051+1933	BD+20 2678B	12:05:11.9	+19:31:41	M2	-0.07 ± 0.03	0.02 ± 0.08
J12372+3545	2MASS J12371547+3549176	12:37:15.5	+35:49:18	M1.5 V	-0.05 ± 0.02	-0.03 ± 0.08
J13315-0800	HD 117579B	13:31:29.8	−07:59:59	M0.0 V	-0.18 ± 0.02	-0.09 ± 0.08
J14050+0157	NLTT 36190	14:04:55.8	+01:57:23	M2	-0.01 ± 0.02	0.00 ± 0.08
J14336+0920	HD 127871B	14:33:39.9	+09:20:10	M3.5 V	-0.11 ± 0.03	-0.09 ± 0.08
J14415+1336	HD 129290B	14:41:30.3	+13:37:36	M1.0 V	-0.12 ± 0.02	-0.08 ± 0.08
J15123+3939	LP 222-50	15:11:51.5	+39:33:02	M2.5 V	-0.21 ± 0.03	-0.21 ± 0.08
J15353+6005	LP 99-392	15:35:25.7	+60:05:08	M3.5 V	-0.13 ± 0.06	-0.02 ± 0.08
J16239+0315	G 17-23	16:33:02.8	+03:11:37	M3.0 V	0.01 ± 0.04	0.00 ± 0.08
J17428+1646	2MASS J17425203+1643476	17:42:52.0	+16:43:48	M1.5 V	-0.23 ± 0.03	-0.21 ± 0.08
J17477+2748	G 182-27	17:47:44.3	+27:47:07	M1.5 V	-0.06 ± 0.02	0.00 ± 0.08
J18006+6833	LDS 1460B	18:00:37.0	+68:32:54	K7 V	-0.02 ± 0.02	0.00 ± 0.12
J18006+2934	HD 164595B	18:00:45.4	+29:33:57	M2.0 V	-0.08 ± 0.01	-0.09 ± 0.08
J18090+2409	2MASS J18090192+2409041	18:09:01.9	+24:09:04	M1.0 V	-0.13 ± 0.02	-0.11 ± 0.08
J18292+1142	2MASS 18291369+1141271	18:29:13.7	+11:41:27	K5.0 V	0.28 ± 0.02	0.21 ± 0.08
J19321-1116	HD 183870B	19:32:08.1	−11:19:57	M3.5 V	-0.10 ± 0.06	-0.02 ± 0.08
J21324-2058	LP 873-74	21:32:21.0	−20:58:10	M0.5 V	-0.19 ± 0.03	-0.15 ± 0.08
J21575+2856	2MASS J21572970+2854494	21:57:29.7	+28:54:50	M1.5 V	0.15 ± 0.02	0.10 ± 0.08
J22090-1754	LP 819-37	22:08:54.2	−17:47:52	M2.5 V	-0.42 ± 0.02	-0.28 ± 0.08
J22159+5440	HD 211472B	22:16:02.6	+54:40:00	M4.0 V	-0.05 ± 0.02	0.00 ± 0.08
J22311+4509	HD 213519B	22:31:06.5	+45:09:44	M3	0.00 ± 0.01	-0.06 ± 0.08

CHAPTER B

Appendix of Chapter 4

This appendix contains the tables referenced in Chapter 4:

- Table B.1 comprises the abundances of C, O, Sc, V, Mn, and Co of the FGK primary stars in wide binary systems.
- Tables B.2–B.5 provide the HFS components for the Sc, V, Mn, and Co lines.

Table B.1: Abundances [X/H] with respect to the Sun for C, O, Sc, V, Mn, and Co.

WDS	Primary	RA (J2000)	DEC (J2000)	Spectral type	[C/H] (dex)	$[O/H]^{LTE}$ (dex)	$[O/H]^{NLTE}$ (dex)	[Sc/H] (dex)	[V/H] (dex)	$[Mn/H]^{LTE}$ (dex)	$[Mn/H]^{NLTE}$ (dex)	$[Co/H]^{LTE}$ (dex)	$[Co/H]^{NLTE}$ (dex)	Notes[a]
00153+5304	G 217-41	00:15:14.8	+53:04:27	K3 V	-0.32 ± 0.09	0.06 ± 0.14	0.10 ± 0.13	0.00 ± 0.07	0.13 ± 0.11	0.07 ± 0.10	0.06 ± 0.10	0.02 ± 0.09	-0.05 ± 0.11	
00385+4300	BD+42 126	00:38:29.2	+43:00:00	G5 V	-0.76 ± 0.08	-0.52 ± 0.11	-0.45 ± 0.10	-0.51 ± 0.09	-0.38 ± 0.13	-0.83 ± 0.08	-0.83 ± 0.07	-0.56 ± 0.06	-0.60 ± 0.06	
00452+0015	HD 4271 Aa,Ab	00:45:11.0	+00:15:12	F8 V	0.11 ± 0.06	0.21 ± 0.12	0.15 ± 0.10	0.10 ± 0.10	0.28 ± 0.21	0.00 ± 0.11	0.01 ± 0.11	0.01 ± 0.05	0.02 ± 0.04	
00467-0426	HD 4449	00:46:40.5	−04:25:37	G5 V	-0.05 ± 0.10	-0.23 ± 0.17	-0.19 ± 0.15	-0.09 ± 0.20	0.16 ± 0.11	0.13 ± 0.14	0.12 ± 0.14	0.04 ± 0.06	0.02 ± 0.06	
00491+5749	Achird Aa,Ab	00:49:06.2	+57:48:55	G0 V	-0.20 ± 0.02	-0.01 ± 0.05	0.00 ± 0.04	-0.24 ± 0.07	-0.30 ± 0.06	-0.36 ± 0.07	-0.35 ± 0.07	-0.30 ± 0.06	-0.26 ± 0.06	
01055+1523	HD 6440 A	01:05:29.9	+15:23:24	K3.5 V	...	-0.14 ± 0.16	-0.08 ± 0.15	-0.24 ± 0.17	-0.03 ± 0.11	-0.35 ± 0.18	-0.41 ± 0.18	-0.18 ± 0.12	-0.28 ± 0.10	
01076+2257	HD 6660 A	01:07:37.9	+22:57:19	K4 V	...	-0.17 ± 0.34	-0.03 ± 0.30	0.05 ± 0.26	0.45 ± 0.27	0.10 ± 0.13	0.05 ± 0.13	0.15 ± 0.16	0.15 ± 0.12	
01187-0052	HD 7895	01:18:41.1	−00:52:03	K0 V+	-0.18 ± 0.05	-0.09 ± 0.06	-0.04 ± 0.05	-0.16 ± 0.10	-0.04 ± 0.05	-0.18 ± 0.06	-0.20 ± 0.07	-0.16 ± 0.05	-0.20 ± 0.05	
01215+3120	EN Psc	01:21:28.2	+31:20:29	K2 V	-0.04 ± 0.06	0.04 ± 0.09	0.09 ± 0.08	-0.09 ± 0.08	0.14 ± 0.08	0.00 ± 0.05	-0.03 ± 0.05	0.01 ± 0.06	-0.06 ± 0.08	
01226+1245	BD+12 168 A	01:22:36.6	+12:45:04	K3 V	0.19 ± 0.18	-0.03 ± 0.26	0.02 ± 0.25	-0.03 ± 0.14	0.21 ± 0.21	-0.01 ± 0.11	-0.04 ± 0.11	-0.02 ± 0.14	-0.05 ± 0.11	
01230-1258	HD 8389 A	01:23:02.6	−12:57:58	K0 V	0.31 ± 0.10	0.33 ± 0.20	0.34 ± 0.17	0.40 ± 0.11	0.54 ± 0.12	0.49 ± 0.08	0.48 ± 0.08	0.46 ± 0.09	0.41 ± 0.10	
01340-0141	BD-02 247	01:34:02.1	−01:41:10	G5 V	-0.53 ± 0.05	-0.06 ± 0.05	-0.02 ± 0.04	-0.60 ± 0.11	-0.72 ± 0.15	-0.99 ± 0.19	-0.94 ± 0.18	-0.64 ± 0.12	-0.59 ± 0.09	
01450-0104	BD-01 237	01:44:59.1	−01:03:31	K0 V	-0.32 ± 0.05	0.13 ± 0.28	0.18 ± 0.22	-0.30 ± 0.12	-0.25 ± 0.08	-0.46 ± 0.05	-0.47 ± 0.04	-0.34 ± 0.04	-0.37 ± 0.04	
01572-1015	HD 11964 A	01:57:09.6	−10:14:33	G8 IV	-0.03 ± 0.05	0.17 ± 0.09	0.16 ± 0.07	0.03 ± 0.06	0.07 ± 0.06	0.01 ± 0.04	0.00 ± 0.04	0.00 ± 0.08	0.00 ± 0.07	
02290-1959	HD 15468	02:29:01.7	−19:58:45	K4 V+	-0.19 ± 0.39	-0.77 ± 0.14	-0.71 ± 0.14	-0.33 ± 0.33	0.20 ± 0.14	-0.45 ± 0.16	-0.52 ± 0.13	-0.30 ± 0.14	-0.32 ± 0.15	
02291+2252	BD+22 353 Aa,Ab	02:29:07.3	+22:52:05	K0 V	-0.12 ± 0.08	0.06 ± 0.09	0.10 ± 0.08	-0.01 ± 0.09	0.15 ± 0.09	-0.11 ± 0.07	-0.12 ± 0.07	0.01 ± 0.06	-0.04 ± 0.05	
02361+0653	HD 16160 A	02:36:04.9	+06:53:13	K0 V+	0.12 ± 0.09	-0.04 ± 0.11	0.01 ± 0.11	-0.11 ± 0.16	0.15 ± 0.10	-0.24 ± 0.06	-0.28 ± 0.06	-0.11 ± 0.10	-0.16 ± 0.09	
02442+4914	θ Per A	02:44:12.0	+49:13:42	F7 V	0.05 ± 0.06	0.25 ± 0.14	0.19 ± 0.12	0.02 ± 0.08	0.26 ± 0.33	-0.02 ± 0.10	0.00 ± 0.12	-0.05 ± 0.08	-0.02 ± 0.08	
02482+2704	BC Ari Aa,Ab	02:48:09.1	+27:04:07	K1 V	-0.04 ± 0.15	0.11 ± 0.11	0.14 ± 0.09	-0.09 ± 0.10	0.09 ± 0.06	0.00 ± 0.06	-0.02 ± 0.07	-0.05 ± 0.06	-0.10 ± 0.08	
02556+2652	HD 18143 A	02:55:39.1	+26:52:24	K2 IV	-0.04 ± 0.18	0.17 ± 0.15	0.20 ± 0.14	0.19 ± 0.09	0.33 ± 0.10	0.18 ± 0.07	0.15 ± 0.07	0.20 ± 0.08	0.16 ± 0.10	
03042+6142	HD 18757	03:04:09.6	+61:42:21	G4 V	-0.09 ± 0.07	0.14 ± 0.05	0.17 ± 0.04	-0.11 ± 0.08	-0.19 ± 0.06	-0.41 ± 0.16	-0.45 ± 0.11	-0.20 ± 0.04	-0.19 ± 0.02	
03078+2533	HD 19381 A	03:07:50.5	+25:33:07	F8 V	0.07 ± 0.07	0.23 ± 0.11	0.19 ± 0.10	0.13 ± 0.11	0.05 ± 0.13	0.07 ± 0.06	0.09 ± 0.06	-0.01 ± 0.07	0.00 ± 0.09	
03150+0101	BD+00 549 A	03:15:04.8	+01:02:15	G5 V	-0.69 ± 0.06	-0.40 ± 0.11	-0.34 ± 0.09	-0.65 ± 0.12	-0.68 ± 0.21	-1.19 ± 0.27	-1.20 ± 0.27	-0.67 ± 0.10	-0.64 ± 0.12	
03206+0902	HD 20727 Aa,Ab	03:20:37.0	+09:02:01	G0 V	-0.06 ± 0.12	0.07 ± 0.05	0.10 ± 0.04	-0.01 ± 0.07	-0.10 ± 0.09	-0.39 ± 0.07	-0.37 ± 0.07	-0.10 ± 0.06	-0.09 ± 0.06	
03321+4340	HD 21727 A	03:32:05.1	+43:40:12	G5 V	-0.04 ± 0.08	0.09 ± 0.06	0.10 ± 0.05	0.02 ± 0.06	0.00 ± 0.07	-0.10 ± 0.05	-0.10 ± 0.06	-0.02 ± 0.09	-0.07 ± 0.03	
03332+4615	V577 Per	03:33:13.5	+46:15:27	G5 V	0.03 ± 0.05	0.20 ± 0.07	0.24 ± 0.07	-0.08 ± 0.10	0.12 ± 0.07	-0.07 ± 0.13	-0.09 ± 0.15	-0.13 ± 0.12	-0.18 ± 0.12	
03356+4253	HD 22122	03:35:35.8	+42:53:15	F8 V	-0.19 ± 0.05	-0.02 ± 0.09	-0.04 ± 0.08	-0.29 ± 0.10	-0.31 ± 0.22	-0.42 ± 0.11	-0.36 ± 0.12	-0.34 ± 0.08	-0.22 ± 0.11	
03396+1823	V1082 Tau Aa,Ab	03:39:33.6	+18:23:06	G5+	...	...	...	...	...	...	...	...	...	SB2
03398+3328	HD 278874 Aa,Ab	03:39:49.0	+33:28:24	K2	...	...	...	...	...	...	...	...	...	SB2
03480+4032	HD 23596	03:48:00.4	+40:31:50	F8 V	0.22 ± 0.04	0.45 ± 0.20	0.36 ± 0.17	0.34 ± 0.09	0.26 ± 0.10	0.27 ± 0.06	0.28 ± 0.07	0.28 ± 0.07	0.29 ± 0.09	
03520+3947	HD 275867	03:52:00.3	+39:47:44	K2 V	...	-0.34 ± 0.17	-0.28 ± 0.17	-0.16 ± 0.21	0.19 ± 0.16	-0.15 ± 0.10	-0.19 ± 0.09	-0.15 ± 0.09	-0.20 ± 0.10	
03556+5214	HD 24421	03:55:37.1	+52:13:37	F8 V	-0.31 ± 0.02	-0.04 ± 0.07	-0.05 ± 0.06	-0.23 ± 0.08	-0.30 ± 0.08	-0.43 ± 0.12	-0.40 ± 0.13	-0.33 ± 0.05	-0.23 ± 0.08	
03566+5042	43 Per Aa,Ab	03:56:36.5	+50:41:43	F5 V	...	...	...	...	...	...	...	...	...	SB2
03575-0110	HD 24916 A	03:57:28.7	−01:09:34	K4 V	...	-0.10 ± 0.21	-0.04 ± 0.19	-0.13 ± 0.20	0.20 ± 0.16	-0.25 ± 0.20	-0.32 ± 0.18	-0.08 ± 0.13	-0.12 ± 0.13	
04153-0739	o^{02} Eri A	04:15:16.3	−07:39:10	K0.5 V	-0.25 ± 0.21	0.02 ± 0.06	0.08 ± 0.05	-0.17 ± 0.08	-0.08 ± 0.06	-0.45 ± 0.05	-0.47 ± 0.05	-0.20 ± 0.05	-0.24 ± 0.05	
04252+2545	HD 27887 A	04:25:10.8	+25:44:57	F5	...	...	...	...	...	...	...	...	...	Hot
04359+1631	Aldebaran	04:35:55.2	+16:30:33	K5 III	...	...	...	...	...	...	...	...	...	Cool
04397+0952	HD 286955	04:39:42.6	+09:52:19	K2 V+	...	-0.15 ± 0.13	-0.09 ± 0.13	-0.23 ± 0.22	0.03 ± 0.12	-0.38 ± 0.09	-0.42 ± 0.09	-0.24 ± 0.08	-0.28 ± 0.09	
04429+1843	HD 29836	04:42:51.7	+18:43:14	G2 V	0.17 ± 0.03	0.32 ± 0.18	0.27 ± 0.15	0.33 ± 0.04	0.25 ± 0.06	0.16 ± 0.06	0.16 ± 0.07	0.29 ± 0.05	0.27 ± 0.03	
04559+0440	HD 31412	04:55:55.9	+04:40:14	F9.5 V+	0.05 ± 0.05	0.20 ± 0.10	0.16 ± 0.09	0.11 ± 0.08	0.15 ± 0.11	0.06 ± 0.08	0.08 ± 0.08	0.03 ± 0.04	0.06 ± 0.05	
05003+2508	HD 31867 A	05:00:17.5	+25:08:11	G2 V	0.00 ± 0.12	0.02 ± 0.12	0.03 ± 0.10	0.02 ± 0.08	-0.01 ± 0.07	-0.07 ± 0.11	-0.07 ± 0.12	-0.03 ± 0.05	-0.04 ± 0.04	
05067+5136	9 Aur Aa,Ab	05:06:40.6	+51:35:52	F2 V+M2	...	...	...	...	...	...	...	...	...	Hot
05189-2124	HD 34751 A	05:18:47.2	−21:23:38	K6 V	0.54 ± 0.21	-0.35 ± 0.28	-0.28 ± 0.26	-0.03 ± 0.38	0.31 ± 0.23	-0.34 ± 0.29	-0.44 ± 0.27	0.00 ± 0.19	-0.04 ± 0.16	
05264+0351	HD 35638	05:26:23.1	+03:51:24	F5 V	0.01 ± 0.07	0.24 ± 0.13	0.18 ± 0.12	0.03 ± 0.08	0.34 ± 0.36	-0.10 ± 0.08	-0.07 ± 0.09	-0.04 ± 0.08	0.03 ± 0.08	
05289+1233	HD 35956 Aa,Ab	05:28:51.6	+12:33:03	G0 V	-0.07 ± 0.05	0.07 ± 0.08	0.06 ± 0.07	-0.02 ± 0.08	-0.02 ± 0.14	-0.14 ± 0.07	-0.13 ± 0.08	-0.15 ± 0.06	-0.12 ± 0.04	
05413+5329	V538 Aur	05:41:20.3	+53:28:52	K1 V	-0.10 ± 0.07	-0.01 ± 0.08	0.03 ± 0.07	-0.02 ± 0.09	0.14 ± 0.05	0.02 ± 0.04	-0.01 ± 0.04	-0.04 ± 0.05	-0.07 ± 0.06	
05427+0241	HD 38014	05:42:45.8	+02:40:45	K1 V	-0.17 ± 0.06	0.06 ± 0.14	0.10 ± 0.12	-0.03 ± 0.11	0.16 ± 0.09	-0.04 ± 0.15	-0.06 ± 0.16	0.00 ± 0.06	-0.05 ± 0.07	
05445-2227	γ Lep	05:44:27.8	−22:26:54	F6 V	-0.01 ± 0.06	0.16 ± 0.11	0.12 ± 0.09	0.01 ± 0.13	0.17 ± 0.20	-0.14 ± 0.06	-0.12 ± 0.06	-0.11 ± 0.08	-0.05 ± 0.11	
	AK Lep	05:44:26.5	−22:25:19	K2 V	0.03 ± 0.08	-0.15 ± 0.12	-0.10 ± 0.11	-0.15 ± 0.12	0.08 ± 0.10	-0.20 ± 0.11	-0.24 ± 0.11	-0.14 ± 0.07	-0.20 ± 0.08	

Table B.1: *Continued*

WDS	Primary	RA (J2000)	DEC (J2000)	Spectral type	[C/H] (dex)	[O/H]$^{\rm LTE}$ (dex)	[O/H]$^{\rm NLTE}$ (dex)	[Sc/H] (dex)	[V/H] (dex)	[Mn/H]$^{\rm LTE}$ (dex)	[Mn/H]$^{\rm NLTE}$ (dex)	[Co/H]$^{\rm LTE}$ (dex)	[Co/H]$^{\rm NLTE}$ (dex)	Notes[a]
05466+0110	HD 38529 A	05:46:34.9	+01:10:05	G4 IV	0.21 ± 0.05	0.44 ± 0.27	0.34 ± 0.23	0.32 ± 0.08	0.32 ± 0.07	0.37 ± 0.08	0.38 ± 0.09	0.31 ± 0.05	0.31 ± 0.05	
05584-0439	HD 40397 A	05:58:21.5	−04:39:02	G7 V	−0.02 ± 0.07	0.09 ± 0.05	0.12 ± 0.04	0.00 ± 0.09	−0.09 ± 0.05	−0.19 ± 0.09	−0.19 ± 0.09	−0.10 ± 0.03	−0.11 ± 0.03	
06066+0431	Ross 413	06:06:30.0	+04:30:41	K4 V	−0.46 ± 0.13	−0.11 ± 0.17	−0.04 ± 0.16	−0.32 ± 0.33	0.10 ± 0.16	−0.57 ± 0.08	−0.62 ± 0.07	−0.30 ± 0.06	−0.38 ± 0.05	
06173+0506	HD 43587	06:17:16.1	+05:06:00	F9 V	−0.01 ± 0.02	0.16 ± 0.09	0.14 ± 0.08	−0.02 ± 0.08	−0.04 ± 0.07	−0.05 ± 0.09	−0.04 ± 0.10	−0.09 ± 0.04	−0.06 ± 0.04	
06314-0134	HD 291763	06:31:23.1	−01:34:14	K2 V	...	−0.19 ± 0.09	−0.13 ± 0.09	−0.43 ± 0.10	−0.26 ± 0.08	−0.79 ± 0.15	−0.83 ± 0.16	−0.47 ± 0.06	−0.51 ± 0.06	
06319+0039	HD 291725	06:31:51.4	+00:38:59	G7 V	−0.38 ± 0.05	−0.09 ± 0.05	−0.06 ± 0.05	−0.19 ± 0.05	−0.22 ± 0.07	−0.47 ± 0.07	−0.46 ± 0.08	−0.29 ± 0.09	−0.32 ± 0.08	
06332+0528	HD 46375 A	06:33:12.6	+05:27:47	K1 V	−0.03 ± 0.14	0.23 ± 0.16	0.26 ± 0.14	0.27 ± 0.06	0.35 ± 0.10	0.25 ± 0.13	0.22 ± 0.14	0.29 ± 0.07	0.24 ± 0.09	
06368+3751	BD+37 1545	06:36:46.4	+37:51:07	G5 V	0.00 ± 0.05	0.11 ± 0.11	0.13 ± 0.09	0.08 ± 0.05	0.09 ± 0.07	0.11 ± 0.10	0.10 ± 0.11	0.08 ± 0.05	0.05 ± 0.06	
06461+3233	HD 263175 A	06:46:05.1	+32:33:20	K3 V	...	−0.42 ± 0.26	−0.36 ± 0.23	−0.38 ± 0.10	−0.20 ± 0.10	−0.43 ± 0.06	−0.47 ± 0.05	−0.36 ± 0.07	−0.41 ± 0.08	
06523-0510	HD 50281 A	06:52:18.1	−05:10:25	K3.5 V	...	−0.15 ± 0.19	−0.09 ± 0.18	−0.18 ± 0.22	0.17 ± 0.16	−0.16 ± 0.11	−0.21 ± 0.11	−0.14 ± 0.10	−0.18 ± 0.08	
07041+7514	HD 51067 A	07:04:03.9	+75:13:39	G0 V	0.03 ± 0.05	0.27 ± 0.12	0.23 ± 0.10	0.17 ± 0.07	0.18 ± 0.09	0.13 ± 0.07	0.14 ± 0.08	0.07 ± 0.04	0.07 ± 0.04	
	HD 51067 B	07:04:05.7	+75:13:50	G5	−0.08 ± 0.06	0.08 ± 0.06	0.11 ± 0.05	0.05 ± 0.07	0.15 ± 0.05	0.05 ± 0.07	0.02 ± 0.07	0.04 ± 0.06	0.03 ± 0.05	
07058+8337	HD 48974	07:05:49.9	+83:36:44	G5 V	−0.22 ± 0.08	−0.06 ± 0.07	−0.03 ± 0.06	−0.16 ± 0.10	−0.15 ± 0.07	−0.21 ± 0.05	−0.21 ± 0.05	−0.16 ± 0.06	−0.19 ± 0.05	
07191+6644	HD 55745 A	07:19:08.3	+66:44:23	F8 V	0.06 ± 0.05	0.28 ± 0.13	0.22 ± 0.11	0.21 ± 0.12	0.23 ± 0.11	0.21 ± 0.07	0.23 ± 0.07	0.11 ± 0.07	0.14 ± 0.07	
07321-0853	HD 59984	07:32:05.8	−08:52:53	G0 V	−0.61 ± 0.13	−0.22 ± 0.07	−0.20 ± 0.06	−0.50 ± 0.10	−0.62 ± 0.06	−0.81 ± 0.18	−0.74 ± 0.20	−0.67 ± 0.12	−0.50 ± 0.15	
07400-0336	V869 Mon	07:39:59.3	−03:35:51	K2 V	−0.02 ± 0.11	−0.12 ± 0.10	−0.06 ± 0.10	−0.17 ± 0.10	0.03 ± 0.04	−0.16 ± 0.06	−0.18 ± 0.06	−0.13 ± 0.07	−0.21 ± 0.06	
08082+7155	HD 66171	08:08:10.5	+71:55:28	G2 V	−0.33 ± 0.12	0.02 ± 0.10	0.04 ± 0.08	−0.23 ± 0.09	−0.34 ± 0.09	−0.40 ± 0.09	−0.39 ± 0.10	−0.28 ± 0.11	−0.28 ± 0.05	
08082+2106	BD+21 1764 A	08:08:13.2	+21:06:18	K7 V	0.41 ± 0.37	−0.55 ± 0.42	−0.50 ± 0.42	−0.15 ± 0.43	0.29 ± 0.38	−0.47 ± 0.24	−0.55 ± 0.21	−0.31 ± 0.21	−0.33 ± 0.18	
08107-1348	18 Pup A	08:10:39.8	−13:47:57	F6.5 V	0.05 ± 0.05	0.19 ± 0.10	0.15 ± 0.09	0.06 ± 0.08	−0.02 ± 0.11	−0.03 ± 0.11	−0.01 ± 0.12	−0.01 ± 0.10	0.01 ± 0.06	
08110+7955	BD+80 245	08:11:06.2	+79:54:30	G0 IV	...	−1.39 ± 0.08	−1.33 ± 0.05	−2.09 ± 0.17	...	−1.91 ± 0.30	−1.82 ± 0.28	...	...	
08138+6306	HD 67850	08:13:45.8	+63:06:14	G0 V	−0.32 ± 0.16	−0.01 ± 0.05	0.01 ± 0.04	−0.08 ± 0.06	−0.11 ± 0.04	−0.18 ± 0.05	−0.19 ± 0.05	−0.17 ± 0.06	−0.14 ± 0.05	
08161+5706	HD 68638	08:16:06.3	+57:05:39	G8 V	−0.24 ± 0.18	−0.13 ± 0.06	−0.08 ± 0.05	−0.24 ± 0.07	−0.21 ± 0.04	−0.30 ± 0.06	−0.31 ± 0.07	−0.30 ± 0.06	−0.32 ± 0.04	
08484+2042	HD 75076	08:48:24.0	+20:41:47	F8 V	−0.15 ± 0.03	0.16 ± 0.09	0.13 ± 0.08	0.01 ± 0.11	0.04 ± 0.15	−0.16 ± 0.11	−0.14 ± 0.12	−0.10 ± 0.06	−0.06 ± 0.04	
08492+0329	HD 75302	08:49:12.5	+03:29:05	G5 V	−0.07 ± 0.03	0.07 ± 0.08	0.08 ± 0.07	0.04 ± 0.07	0.03 ± 0.05	−0.03 ± 0.07	−0.05 ± 0.07	−0.01 ± 0.05	−0.02 ± 0.05	
08526+2820	ρ^{01} Cnc A	08:52:35.8	+28:19:51	G8 V	0.18 ± 0.08	0.25 ± 0.18	0.27 ± 0.15	0.34 ± 0.08	0.43 ± 0.09	0.36 ± 0.06	0.34 ± 0.07	0.36 ± 0.07	0.32 ± 0.08	
09008+2347	HD 77052	09:00:49.3	+23:46:48	G2 V	0.02 ± 0.06	0.11 ± 0.09	0.11 ± 0.08	0.05 ± 0.06	0.04 ± 0.10	0.00 ± 0.06	0.00 ± 0.07	0.02 ± 0.03	0.02 ± 0.04	
09029+0600	BD+06 2091	09:02:51.3	+06:00:28	G0 V	0.04 ± 0.33	0.10 ± 0.07	0.12 ± 0.06	−0.07 ± 0.13	0.02 ± 0.15	−0.17 ± 0.11	−0.17 ± 0.13	−0.08 ± 0.06	−0.09 ± 0.05	
09058+5532	HD 77599	09:05:45.9	+55:31:44	G0 V	−0.16 ± 0.03	0.11 ± 0.08	0.09 ± 0.07	0.01 ± 0.08	0.01 ± 0.10	−0.04 ± 0.09	−0.03 ± 0.10	−0.06 ± 0.06	−0.02 ± 0.05	
09152+2323	HD 79498	09:15:09.4	+23:22:32	G5 V	0.19 ± 0.07	0.23 ± 0.11	0.21 ± 0.09	0.25 ± 0.07	0.21 ± 0.07	0.27 ± 0.10	0.27 ± 0.11	0.21 ± 0.04	0.19 ± 0.05	
09211+6024	BD+61 1116	09:21:06.8	+60:24:11	K0 V	−0.27 ± 0.46	−0.13 ± 0.06	−0.09 ± 0.05	−0.20 ± 0.10	−0.07 ± 0.07	−0.24 ± 0.06	−0.26 ± 0.06	−0.19 ± 0.07	−0.24 ± 0.08	
09245+0621	HD 81212 AB	09:24:28.6	+06:21:00	F5	...	...	...	...	...	...	...	...	...	SB2
09327+2659	DX Leo	09:32:43.8	+26:59:19	G9 V	−0.06 ± 0.12	0.06 ± 0.05	0.10 ± 0.04	−0.15 ± 0.07	−0.02 ± 0.06	−0.10 ± 0.07	−0.11 ± 0.07	−0.19 ± 0.08	−0.26 ± 0.07	
09353-1019	HD 83008	09:35:17.9	−10:18:51	K0 V	−0.12 ± 0.15	−0.30 ± 0.20	−0.25 ± 0.16	−0.16 ± 0.12	0.05 ± 0.06	−0.14 ± 0.16	−0.16 ± 0.17	−0.12 ± 0.07	−0.15 ± 0.05	
09361+3733	HD 82939	09:36:04.3	+37:33:10	G5 V	0.03 ± 0.07	0.07 ± 0.05	0.09 ± 0.04	0.00 ± 0.07	0.09 ± 0.05	0.05 ± 0.04	0.04 ± 0.04	0.02 ± 0.03	−0.02 ± 0.04	
09393+1319	HD 83509 Aa,Ab	09:39:17.2	+13:18:45	F7 V	...	...	...	...	...	...	...	...	...	SB2
10010+3155	20 LMi A	10:01:00.7	+31:55:25	G3 V	0.09 ± 0.04	0.22 ± 0.10	0.19 ± 0.09	0.25 ± 0.05	0.20 ± 0.05	0.20 ± 0.05	0.20 ± 0.05	0.21 ± 0.04	0.20 ± 0.04	
10172+2306	39 Leo A	10:17:14.6	+23:06:23	F8 V	−0.32 ± 0.04	−0.02 ± 0.09	−0.03 ± 0.08	−0.26 ± 0.13	−0.27 ± 0.33	−0.45 ± 0.13	−0.42 ± 0.14	0.34 ± 0.13	−0.32 ± 0.08	
10306+5559	36 UMa A	10:30:37.6	+55:58:50	F8 V	−0.15 ± 0.02	0.08 ± 0.10	0.05 ± 0.08	−0.07 ± 0.08	0.03 ± 0.12	−0.17 ± 0.08	−0.16 ± 0.08	−0.20 ± 0.08	−0.16 ± 0.05	
10504-1326	BD-12 3277	10:50:22.4	−13:26:07	G3 V	−0.12 ± 0.09	0.00 ± 0.09	0.02 ± 0.09	−0.06 ± 0.05	−0.12 ± 0.07	−0.23 ± 0.09	−0.23 ± 0.10	−0.12 ± 0.05	−0.12 ± 0.04	
10507+5148	LZ UMa	10:50:40.3	+51:47:59	G5 V	−0.10 ± 0.05	−0.03 ± 0.07	0.03 ± 0.07	−0.10 ± 0.08	0.04 ± 0.08	−0.11 ± 0.05	−0.15 ± 0.05	−0.13 ± 0.10	−0.23 ± 0.06	
11047-0413	HH Leo	11:04:41.5	−04:13:16	G8 V	−0.10 ± 0.15	0.04 ± 0.04	0.07 ± 0.04	−0.07 ± 0.08	0.02 ± 0.08	−0.01 ± 0.06	−0.01 ± 0.06	−0.14 ± 0.05	−0.16 ± 0.04	
11152+7329	HD 97584 A	11:15:11.9	+73:28:31	K4 V	...	−0.18 ± 0.13	−0.12 ± 0.13	−0.14 ± 0.13	0.13 ± 0.12	−0.21 ± 0.09	−0.25 ± 0.09	−0.15 ± 0.08	−0.21 ± 0.08	
11214-2027	SZ Crt	11:21:26.6	−20:27:13	K7 V	...	...	...	...	...	...	...	...	...	Cool
11218+1811	HD 98736	11:21:49.3	+18:11:24	K0 V	0.21 ± 0.09	0.26 ± 0.14	0.28 ± 0.13	0.32 ± 0.10	0.41 ± 0.10	0.47 ± 0.17	0.47 ± 0.16	0.38 ± 0.07	0.33 ± 0.08	
11378+4150	BD+42 2230 A	11:37:50.8	+41:49:32	G6 V	−0.19 ± 0.08	0.09 ± 0.12	0.12 ± 0.10	−0.11 ± 0.07	−0.07 ± 0.07	−0.17 ± 0.07	−0.17 ± 0.08	−0.08 ± 0.10	−0.15 ± 0.04	
11403+0931	BD+10 2321	11:40:16.6	+09:30:44	K0 V	−0.47 ± 0.07	−0.17 ± 0.16	−0.11 ± 0.14	−0.36 ± 0.08	−0.25 ± 0.09	−0.37 ± 0.12	−0.41 ± 0.13	−0.35 ± 0.05	−0.43 ± 0.05	
11455+4740	HD 102158	11:45:30.5	+47:40:01	G2 V	−0.23 ± 0.05	0.10 ± 0.05	0.14 ± 0.04	−0.29 ± 0.11	−0.32 ± 0.13	−0.65 ± 0.11	−0.63 ± 0.12	−0.38 ± 0.06	−0.35 ± 0.05	
11475+7702	HD 102326	11:47:30.3	+77:02:24	G8 IV	0.23 ± 0.14	0.29 ± 0.11	0.30 ± 0.10	0.22 ± 0.07	0.18 ± 0.06	0.15 ± 0.03	0.14 ± 0.03	0.18 ± 0.05	0.14 ± 0.06	
11523+0957	HD 103112	11:52:20.9	+09:56:53	K0 IV	0.06 ± 0.23	0.25 ± 0.19	0.26 ± 0.17	0.22 ± 0.16	0.45 ± 0.12	0.21 ± 0.18	0.26 ± 0.11	0.29 ± 0.08	0.24 ± 0.08	

Table B.1: *Continued*

WDS	Primary	RA (J2000)	DEC (J2000)	Spectral type	[C/H] (dex)	[O/H]^{LTE} (dex)	[O/H]^{NLTE} (dex)	[Sc/H] (dex)	[V/H] (dex)	[Mn/H]^{LTE} (dex)	[Mn/H]^{NLTE} (dex)	[Co/H]^{LTE} (dex)	[Co/H]^{NLTE} (dex)	Notes[a]
12049+1729	HD 104923	12:04:57.0	+17:28:36	K0 V	−0.18 ± 0.11	−0.08 ± 0.06	−0.03 ± 0.05	−0.20 ± 0.06	−0.12 ± 0.06	−0.22 ± 0.10	−0.23 ± 0.11	−0.23 ± 0.06	−0.26 ± 0.06	
12051+1933	BD+20 2678 A	12:05:07.0	+19:33:16	G5 V	−0.09 ± 0.10	0.09 ± 0.06	0.11 ± 0.05	−0.13 ± 0.07	−0.10 ± 0.08	−0.15 ± 0.05	−0.15 ± 0.05	−0.14 ± 0.07	−0.13 ± 0.08	
12069+0548	HD 105219	12:06:56.5	+05:48:12	K0 V	−0.18 ± 0.19	−0.11 ± 0.06	−0.08 ± 0.05	−0.17 ± 0.04	−0.13 ± 0.05	−0.25 ± 0.06	−0.26 ± 0.07	−0.20 ± 0.05	−0.21 ± 0.06	
12089+2147	BD+22 2442	12:08:54.7	+21:47:19	G2 V+	−0.37 ± 0.05	−0.22 ± 0.10	−0.17 ± 0.08	−0.56 ± 0.13	−0.31 ± 0.10	−0.97 ± 0.11	−0.98 ± 0.12	−0.71 ± 0.10	−0.66 ± 0.13	
12372+3545	BD+36 2288	12:37:13.7	+35:44:46	G5 V	−0.15 ± 0.09	0.05 ± 0.10	0.05 ± 0.09	−0.06 ± 0.09	−0.02 ± 0.13	−0.09 ± 0.10	−0.08 ± 0.11	−0.11 ± 0.07	−0.14 ± 0.07	
12406+4017	HD 110279	12:40:37.4	+40:17:17	F8 V	−0.09 ± 0.07	0.03 ± 0.10	0.03 ± 0.08	0.05 ± 0.06	0.11 ± 0.08	−0.13 ± 0.17	−0.13 ± 0.19	−0.07 ± 0.06	−0.06 ± 0.06	
12482-2448	HD 111261 A	12:48:10.7	−24:48:24	K4 V	...	...	...	−0.32 ± 0.36	0.13 ± 0.16	−0.46 ± 0.15	−0.50 ± 0.16	−0.33 ± 0.14	−0.35 ± 0.13	
12489+1206	HD 111398	12:48:52.4	+12:05:47	G5 V	0.06 ± 0.04	0.24 ± 0.07	0.22 ± 0.06	0.10 ± 0.06	0.05 ± 0.06	0.00 ± 0.13	0.00 ± 0.14	0.05 ± 0.02	0.05 ± 0.03	
12549-0620	BD-05 3596	12:54:56.0	−06:20:19	K5 V	−0.37 ± 0.18	−0.70 ± 0.26	−0.62 ± 0.24	−0.20 ± 0.24	0.16 ± 0.20	−0.32 ± 0.14	−0.38 ± 0.13	−0.18 ± 0.12	−0.23 ± 0.13	
13018+6337	HD 113337 A	13:01:46.9	+63:36:37	F5 V	0.12 ± 0.04	0.54 ± 0.18	0.41 ± 0.15	0.21 ± 0.11	0.15 ± 0.42	0.16 ± 0.19	0.20 ± 0.21	0.05 ± 0.13	0.06 ± 0.16	
13077-1411	HD 114001	13:07:39.2	−14:11:17	F5 V	...	...	...	...	...	...	...	...	...	Fast
13114+0938	HD 114606 A	13:11:21.4	+09:37:34	G1 V	−0.34 ± 0.05	0.07 ± 0.04	0.11 ± 0.04	−0.33 ± 0.07	−0.37 ± 0.09	−0.69 ± 0.10	−0.67 ± 0.11	−0.48 ± 0.09	−0.39 ± 0.03	
13169+1701	HD 115404 A	13:16:51.0	+17:01:02	K2 V	−0.17 ± 0.06	−0.09 ± 0.11	−0.04 ± 0.09	−0.27 ± 0.06	−0.17 ± 0.08	−0.35 ± 0.10	−0.39 ± 0.10	−0.29 ± 0.07	−0.34 ± 0.06	
13253+4242	BD+43 2328	13:25:17.4	+42:41:58	K1 V	−0.20 ± 0.23	−0.18 ± 0.09	−0.13 ± 0.07	−0.36 ± 0.06	−0.31 ± 0.09	−0.43 ± 0.08	−0.45 ± 0.09	−0.36 ± 0.04	−0.37 ± 0.04	
13274-2138	HD 116963	13:27:24.9	−21:39:19	K4 V	−0.68 ± 0.19	−0.13 ± 0.35	−0.08 ± 0.31	−0.09 ± 0.21	0.26 ± 0.22	−0.10 ± 0.14	−0.14 ± 0.14	−0.11 ± 0.14	−0.14 ± 0.11	
13315-0800	HD 117579 A	13:31:28.7	−08:00:26	G5 V	−0.05 ± 0.20	0.02 ± 0.10	0.05 ± 0.08	−0.17 ± 0.08	−0.17 ± 0.06	−0.28 ± 0.08	−0.29 ± 0.08	−0.21 ± 0.04	−0.23 ± 0.03	
13316+5857	HD 117845	13:31:33.8	+58:57:10	G2 V	−0.22 ± 0.06	−0.02 ± 0.05	−0.02 ± 0.05	−0.15 ± 0.11	−0.09 ± 0.13	−0.29 ± 0.11	−0.27 ± 0.12	−0.27 ± 0.08	−0.22 ± 0.09	
13321-1115	HD 117676	13:32:04.7	−11:15:23	G8 V+	−0.26 ± 0.08	−0.06 ± 0.06	−0.03 ± 0.05	−0.18 ± 0.08	−0.20 ± 0.10	−0.28 ± 0.02	−0.29 ± 0.02	−0.21 ± 0.03	−0.23 ± 0.03	
13470+0621	HD 120066	13:46:57.1	+06:21:01	G0 V	−0.07 ± 0.04	0.21 ± 0.11	0.17 ± 0.09	0.23 ± 0.07	0.15 ± 0.08	−0.06 ± 0.05	−0.04 ± 0.06	0.08 ± 0.03	0.09 ± 0.02	
14050+0157	HD 122972	14:04:58.7	+01:56:59	G6 V	−0.12 ± 0.03	−0.02 ± 0.06	0.00 ± 0.05	−0.05 ± 0.09	−0.05 ± 0.05	−0.05 ± 0.05	−0.07 ± 0.03	−0.05 ± 0.04	−0.07 ± 0.05	
14196-0509	HD 125455 A	14:19:34.9	−05:09:04	K1 V	−0.34 ± 0.05	−0.14 ± 0.09	−0.09 ± 0.08	−0.16 ± 0.06	−0.05 ± 0.07	−0.22 ± 0.06	−0.24 ± 0.06	−0.17 ± 0.06	−0.20 ± 0.05	
14245+6015	BD+60 1536	14:24:26.9	+60:15:25	K5 V	−0.03 ± 0.13	−0.16 ± 0.21	−0.11 ± 0.20	−0.09 ± 0.17	0.22 ± 0.14	−0.05 ± 0.11	−0.10 ± 0.10	−0.01 ± 0.12	−0.03 ± 0.12	
14252+5151	θ Boo A	14:25:11.8	+51:51:03	F7 V	...	...	...	...	...	...	...	...	...	Fast
14255+2035	HD 126512	14:25:30.1	+20:35:25	F9 V	−0.40 ± 0.06	0.02 ± 0.06	0.05 ± 0.05	−0.39 ± 0.14	−0.52 ± 0.08	−0.85 ± 0.10	−0.82 ± 0.11	−0.51 ± 0.08	−0.42 ± 0.08	
14260+3422	BD+35 2558	14:25:59.9	+34:22:15	K0 V	0.14 ± 0.09	−0.63 ± 0.20	−0.57 ± 0.18	−0.62 ± 0.16	−0.46 ± 0.10	−0.96 ± 0.15	−0.97 ± 0.16	−0.72 ± 0.07	−0.76 ± 0.08	
14336+0920	HD 127871 A	14:33:34.9	+09:20:04	K2 V	−0.03 ± 0.09	−0.05 ± 0.13	0.00 ± 0.12	−0.14 ± 0.07	0.03 ± 0.08	−0.15 ± 0.08	−0.18 ± 0.08	−0.11 ± 0.09	−0.18 ± 0.11	
14415+1336	HD 129290 A	14:41:28.7	+13:36:05	G2 V	−0.13 ± 0.05	0.05 ± 0.06	0.04 ± 0.05	−0.10 ± 0.09	−0.20 ± 0.14	−0.22 ± 0.10	−0.21 ± 0.11	−0.19 ± 0.03	−0.16 ± 0.04	
14446-2215	HD 129715	14:44:35.5	−22:15:11	K2 V	...	−0.16 ± 0.31	−0.11 ± 0.28	0.25 ± 0.33	0.67 ± 0.21	0.22 ± 0.11	0.16 ± 0.09	0.31 ± 0.16	0.28 ± 0.16	
14493+4950	HD 130986 A	14:49:18.1	+49:50:16	F8 V+	−0.01 ± 0.04	0.20 ± 0.10	0.16 ± 0.09	0.03 ± 0.12	0.17 ± 0.09	0.03 ± 0.16	0.05 ± 0.18	−0.05 ± 0.08	0.00 ± 0.10	
14575-2125	HD 131977	14:57:28.0	−21:24:56	K4 V	−0.07 ± 0.11	...	...	−0.14 ± 0.13	0.25 ± 0.05	−0.08 ± 0.08	−0.11 ± 0.08	−0.03 ± 0.09	−0.08 ± 0.09	
14595+4528	HD 132830	14:59:32.9	+45:27:51	K0 V	−0.21 ± 0.11	−0.04 ± 0.08	0.00 ± 0.08	−0.11 ± 0.08	0.04 ± 0.07	−0.11 ± 0.09	−0.13 ± 0.10	−0.13 ± 0.05	−0.17 ± 0.06	
15123+3939	HD 135144	15:12:17.8	+39:39:21	K3 V	−0.13 ± 0.06	−0.19 ± 0.09	−0.14 ± 0.09	−0.22 ± 0.07	−0.08 ± 0.08	−0.23 ± 0.05	−0.25 ± 0.05	−0.18 ± 0.13	−0.26 ± 0.05	
15131+1808	BD+18 2985	15:13:06.9	+18:08:09	K0 V	−0.31 ± 0.05	−0.15 ± 0.08	−0.10 ± 0.08	−0.20 ± 0.10	−0.04 ± 0.07	−0.22 ± 0.06	−0.25 ± 0.05	−0.16 ± 0.08	−0.22 ± 0.07	
15164+1648	HD 135792 A	15:16:25.6	+16:47:39	G0 V	−0.28 ± 0.03	−0.01 ± 0.04	0.00 ± 0.04	−0.23 ± 0.07	−0.30 ± 0.15	−0.42 ± 0.13	−0.39 ± 0.14	−0.36 ± 0.05	−0.28 ± 0.06	
15204+0015	HD 136378	15:20:26.1	+00:14:41	K1 V	−0.42 ± 0.32	−0.32 ± 0.07	−0.26 ± 0.07	−0.42 ± 0.04	−0.40 ± 0.10	−0.51 ± 0.07	−0.53 ± 0.07	−0.45 ± 0.04	−0.49 ± 0.04	
15211+2534	HD 136655	15:21:09.3	+25:34:02	K2 V	0.16 ± 0.10	0.09 ± 0.19	0.13 ± 0.17	0.19 ± 0.14	0.38 ± 0.11	0.23 ± 0.13	0.20 ± 0.14	0.24 ± 0.07	0.19 ± 0.08	
15282-0921	HD 137763	15:28:09.6	−09:20:53	G9 V	0.08 ± 0.09	0.06 ± 0.08	0.08 ± 0.07	0.06 ± 0.07	0.19 ± 0.07	0.13 ± 0.05	0.11 ± 0.05	0.11 ± 0.06	0.06 ± 0.07	
	HD 137778	15:28:12.2	−09:21:28	K2 V	−0.11 ± 0.06	0.11 ± 0.14	0.15 ± 0.12	0.05 ± 0.12	0.28 ± 0.08	0.18 ± 0.15	0.15 ± 0.16	0.10 ± 0.06	0.04 ± 0.06	
15289+5727	HD 138367	15:28:51.9	+57:26:43	F7 V	−0.02 ± 0.07	0.06 ± 0.11	0.05 ± 0.10	0.05 ± 0.17	0.19 ± 0.12	−0.13 ± 0.12	−0.11 ± 0.14	−0.08 ± 0.08	−0.05 ± 0.08	
15353+6005	HD 139477	15:35:20.0	+60:05:13	K3 V	...	−0.11 ± 0.24	−0.05 ± 0.23	−0.19 ± 0.17	0.09 ± 0.18	−0.16 ± 0.12	−0.19 ± 0.11	−0.17 ± 0.09	−0.23 ± 0.11	
15431-1303	HD 140269	15:43:08.7	−13:03:23	G1 V	−0.03 ± 0.04	0.19 ± 0.13	0.14 ± 0.12	0.00 ± 0.14	0.01 ± 0.05	−0.22 ± 0.11	−0.19 ± 0.13	−0.18 ± 0.14	−0.21 ± 0.10	
15482+0134	V382 Ser	15:48:09.5	+01:34:18	G8 V	−0.21 ± 0.16	−0.03 ± 0.06	0.01 ± 0.06	−0.14 ± 0.07	−0.06 ± 0.06	−0.07 ± 0.15	−0.09 ± 0.16	−0.18 ± 0.05	−0.23 ± 0.06	
16024+0339	HD 143809	16:02:22.4	+03:39:07	G0 V+	...	...	...	...	...	...	...	...	...	Fast
16048+3910	HD 144579 A	16:04:56.8	+39:09:23	G8 V	−0.51 ± 0.03	−0.15 ± 0.05	−0.09 ± 0.05	−0.49 ± 0.14	−0.52 ± 0.11	−0.89 ± 0.13	−0.90 ± 0.14	−0.59 ± 0.08	−0.59 ± 0.04	
16147+3352	σ CrB B	16:14:40.4	+33:51:27	G1 V	−0.13 ± 0.07	0.07 ± 0.05	0.07 ± 0.04	−0.07 ± 0.10	−0.09 ± 0.09	−0.11 ± 0.05	−0.11 ± 0.05	−0.14 ± 0.04	−0.13 ± 0.05	
16150+6040	HD 146868	16:14:57.1	+60:40:11	G5 V	−0.23 ± 0.08	−0.12 ± 0.05	−0.09 ± 0.04	−0.28 ± 0.07	−0.30 ± 0.08	−0.39 ± 0.07	−0.40 ± 0.08	−0.36 ± 0.04	−0.34 ± 0.03	
16175+7545	η UMi A	16:17:30.3	+75:45:19	F5 V	...	...	...	...	...	...	...	...	...	Fast
16329+0315	HD 149162	16:32:51.6	+03:14:46	K1 V+	−0.08 ± 0.14	−0.08 ± 0.09	−0.04 ± 0.09	0.01 ± 0.13	0.06 ± 0.10	−0.03 ± 0.08	−0.06 ± 0.08	0.01 ± 0.10	−0.04 ± 0.13	
16348-0412	HD 149414 Aa,Ab	16:34:42.4	−04:13:45	G8 V	−0.58 ± 0.15	−0.51 ± 0.13	−0.44 ± 0.13	−1.04 ± 0.19	−0.90 ± 0.13	−1.40 ± 0.16	−1.36 ± 0.14	−1.03 ± 0.15	−0.98 ± 0.18	

Table B.1: *Continued*

WDS	Primary	RA (J2000)	DEC (J2000)	Spectral type	[C/H] (dex)	[O/H]$^{\rm LTE}$ (dex)	[O/H]$^{\rm NLTE}$ (dex)	[Sc/H] (dex)	[V/H] (dex)	[Mn/H]$^{\rm LTE}$ (dex)	[Mn/H]$^{\rm NLTE}$ (dex)	[Co/H]$^{\rm LTE}$ (dex)	[Co/H]$^{\rm NLTE}$ (dex)	Notes[a]
17050-0504	HD 154363 A	17:05:03.4	−05:03:59	K5 V	0.01 ± 0.19	...	...	−0.60 ± 0.15	0.17 ± 0.20	−0.69 ± 0.16	−0.77 ± 0.10	−0.37 ± 0.21	−0.38 ± 0.19	
17178+5227	HD 156985	17:17:50.4	+52:26:50	K2 V	−0.14 ± 0.08	−0.29 ± 0.11	−0.24 ± 0.10	−0.16 ± 0.13	0.07 ± 0.10	−0.27 ± 0.12	−0.32 ± 0.11	−0.16 ± 0.08	−0.20 ± 0.08	
17272+4213	HD 158415	17:27:13.9	+42:13:05	G5 V	−0.14 ± 0.06	0.11 ± 0.07	0.11 ± 0.06	0.09 ± 0.10	0.14 ± 0.07	0.08 ± 0.06	0.08 ± 0.06	0.03 ± 0.05	0.01 ± 0.07	
17411+7225	HD 161897	17:41:06.7	+72:25:13	G6 V	−0.09 ± 0.04	−0.04 ± 0.04	−0.02 ± 0.04	−0.01 ± 0.08	0.02 ± 0.05	−0.07 ± 0.05	−0.08 ± 0.05	−0.02 ± 0.09	−0.05 ± 0.08	
17428+1646	BD+16 3263	17:42:50.5	+16:45:54	K0 V	−0.20 ± 0.12	−0.05 ± 0.09	−0.01 ± 0.08	−0.24 ± 0.09	−0.15 ± 0.08	−0.33 ± 0.06	−0.34 ± 0.07	−0.30 ± 0.07	−0.32 ± 0.07	
17465+2743	μ^{01} Her A	17:46:27.5	+27:43:14	G5 IV+	0.24 ± 0.05	0.37 ± 0.15	0.32 ± 0.13	0.30 ± 0.08	0.27 ± 0.04	0.26 ± 0.06	0.26 ± 0.07	0.27 ± 0.04	0.25 ± 0.05	
17477+2748	BD+27 2891	17:47:39.2	+27:47:40	G0 V	−0.08 ± 0.23	0.08 ± 0.06	0.08 ± 0.05	0.03 ± 0.14	−0.08 ± 0.05	−0.18 ± 0.10	−0.16 ± 0.11	−0.12 ± 0.08	−0.14 ± 0.06	
18006+6833	BD+68 971	18:00:36.1	+68:33:24	K2 V	−0.20 ± 0.20	−0.03 ± 0.05	0.01 ± 0.05	−0.09 ± 0.16	0.03 ± 0.06	−0.05 ± 0.05	−0.08 ± 0.05	−0.07 ± 0.05	−0.11 ± 0.05	
18006+2934	HD 164595 A	18:00:38.9	+29:34:19	G2 V	−0.10 ± 0.07	0.05 ± 0.06	0.06 ± 0.05	−0.05 ± 0.06	−0.15 ± 0.06	−0.14 ± 0.09	−0.13 ± 0.10	−0.12 ± 0.03	−0.12 ± 0.04	
18090+2409	HD 166301	18:08:58.7	+24:09:30	G0 V	−0.08 ± 0.02	0.01 ± 0.07	0.02 ± 0.06	−0.09 ± 0.09	−0.11 ± 0.09	−0.19 ± 0.03	−0.19 ± 0.04	−0.17 ± 0.07	−0.12 ± 0.04	
18131+4129	HD 167389	18:13:07.2	+41:28:31	F8 V	−0.09 ± 0.06	0.04 ± 0.09	0.03 ± 0.07	0.03 ± 0.12	0.05 ± 0.06	−0.04 ± 0.07	−0.03 ± 0.08	−0.04 ± 0.03	−0.04 ± 0.03	
18161+6839	BD+68 986	18:16:04.0	+68:38:55	G8 V	−0.48 ± 0.24	−0.28 ± 0.05	−0.22 ± 0.05	−0.63 ± 0.10	−0.69 ± 0.10	−0.94 ± 0.11	−0.95 ± 0.12	−0.67 ± 0.12	−0.64 ± 0.10	
18292+1142	HD 170469	18:29:11.0	+11:41:44	G5 V	0.25 ± 0.03	0.39 ± 0.13	0.35 ± 0.11	0.37 ± 0.08	0.26 ± 0.07	0.33 ± 0.07	0.33 ± 0.08	0.31 ± 0.04	0.29 ± 0.05	
18333+2219	HD 171314 A	18:33:17.8	+22:18:51	K4 V	...	−0.33 ± 0.20	−0.27 ± 0.20	0.03 ± 0.22	0.35 ± 0.17	−0.06 ± 0.08	−0.11 ± 0.06	0.04 ± 0.15	0.00 ± 0.14	
18409+3132	BD+31 3330 A	18:40:54.9	+31:31:59	K2.5 V	...	−0.41 ± 0.11	−0.35 ± 0.10	−0.42 ± 0.11	−0.22 ± 0.08	−0.52 ± 0.11	−0.57 ± 0.11	−0.41 ± 0.07	−0.45 ± 0.06	
19321-1116	HD 183870 A	19:32:06.7	−11:16:30	K2 V	...	−0.07 ± 0.09	−0.02 ± 0.09	−0.14 ± 0.09	−0.01 ± 0.09	−0.14 ± 0.14	−0.18 ± 0.15	−0.16 ± 0.06	−0.23 ± 0.07	
19510+1025	o Aql A	19:51:01.6	+10:24:57	F8 V	0.04 ± 0.06	0.34 ± 0.16	0.25 ± 0.13	0.18 ± 0.09	0.17 ± 0.13	0.08 ± 0.07	0.10 ± 0.07	0.04 ± 0.05	0.05 ± 0.03	
19553+0624	β Aql A	19:55:18.8	+06:24:24	G9.5 IV	−0.29 ± 0.11	−0.08 ± 0.13	−0.07 ± 0.11	−0.13 ± 0.04	−0.09 ± 0.07	−0.25 ± 0.10	−0.25 ± 0.11	−0.12 ± 0.11	−0.17 ± 0.03	
20007+2243	V452 Vul	20:00:43.7	+22:42:39	K0 V	−0.10 ± 0.06	−0.01 ± 0.1	0.04 ± 0.10	−0.12 ± 0.14	0.07 ± 0.08	−0.05 ± 0.20	−0.05 ± 0.21	−0.12 ± 0.10	−0.15 ± 0.04	
20036+2954	HD 190360 A	20:03:37.4	+29:53:48	G7 V	0.20 ± 0.05	0.34 ± 0.10	0.33 ± 0.09	0.26 ± 0.09	0.27 ± 0.06	0.25 ± 0.13	0.25 ± 0.13	0.25 ± 0.05	0.23 ± 0.07	
20111+1611	HD 191785	20:11:06.1	+16:11:17	K0 V	−0.07 ± 0.05	0.14 ± 0.07	0.19 ± 0.06	−0.07 ± 0.09	0.06 ± 0.07	−0.24 ± 0.04	−0.26 ± 0.05	−0.05 ± 0.05	−0.09 ± 0.05	
20124-1237	ξ Cap	20:12:25.9	−12:37:03	F7 V	−0.21 ± 0.05	0.07 ± 0.10	0.04 ± 0.09	−0.09 ± 0.11	...	−0.32 ± 0.18	−0.30 ± 0.18	−0.20 ± 0.10	−0.13 ± 0.06	
20169+5017	HD 193216 Aa,Ab	20:16:54.5	+50:16:43	G5 V	−0.01 ± 0.06	0.26 ± 0.06	0.29 ± 0.05	0.04 ± 0.14	0.04 ± 0.06	−0.03 ± 0.04	−0.04 ± 0.04	0.03 ± 0.05	0.00 ± 0.06	
20408+1956	HD 197076 A	20:40:45.1	+19:56:08	G1 V	−0.18 ± 0.02	0.04 ± 0.05	0.05 ± 0.04	−0.02 ± 0.12	−0.19 ± 0.09	−0.22 ± 0.06	−0.22 ± 0.07	−0.17 ± 0.04	−0.15 ± 0.05	
20462+3358	ϵ Cyg A	20:46:12.7	+33:58:13	K0 III+	−0.35 ± 0.06	0.07 ± 0.20	0.04 ± 0.17	−0.10 ± 0.07	−0.03 ± 0.07	−0.19 ± 0.06	−0.18 ± 0.07	−0.09 ± 0.09	−0.10 ± 0.07	
20473+1052	BD+10 4379	20:47:16.8	+10:51:37	K2 V	−0.429 ± 0.11	...	...	−0.52 ± 0.11	0.10 ± 0.05	−0.66 ± 0.11	−0.69 ± 0.12	−0.42 ± 0.15	−0.45 ± 0.10	
20599+4016	HD 200077	20:59:55.3	+40:15:32	F8 V+	−0.26 ± 0.09	−0.20 ± 0.08	−0.24 ± 0.07	−0.10 ± 0.11	−0.09 ± 0.10	−0.20 ± 0.09	−0.16 ± 0.09	−0.29 ± 0.09	−0.26 ± 0.04	SB2
21324-2058	HD 204941	21:32:23.5	−20:57:27	K2 V	−0.37 ± 0.05	−0.09 ± 0.07	−0.04 ± 0.07	−0.16 ± 0.06	−0.10 ± 0.08	−0.23 ± 0.06	−0.26 ± 0.06	−0.20 ± 0.09	−0.23 ± 0.08	
21519+4221	HD 207966 A	21:51:52.9	+42:20:38	G8 V	−0.11 ± 0.06	−0.02 ± 0.08	0.01 ± 0.07	−0.10 ± 0.08	0.01 ± 0.06	−0.10 ± 0.05	−0.12 ± 0.05	−0.08 ± 0.05	−0.10 ± 0.05	
21546-0318	HD 208177	21:54:35.9	−03:18:05	F6 V	...	...	...	...	...	...	...	...	...	Fast
21575+2856	BD+28 4248	21:57:30.8	+28:56:13	G5 V	0.03 ± 0.04	0.23 ± 0.08	0.21 ± 0.07	0.12 ± 0.09	0.12 ± 0.11	0.10 ± 0.07	0.09 ± 0.08	0.08 ± 0.06	0.08 ± 0.06	
22066+4323	BD+42 4301	22:06:36.6	+43:22:33	G3V	0.20 ± 0.04	0.17 ± 0.08	0.16 ± 0.08	0.28 ± 0.05	0.26 ± 0.04	0.27 ± 0.09	0.26 ± 0.10	0.25 ± 0.05	0.23 ± 0.06	
22090-1754	HD 210190	22:08:58.7	−17:53:40	K0 V	−0.35 ± 0.47	−0.19 ± 0.11	−0.14 ± 0.08	−0.34 ± 0.13	−0.35 ± 0.07	−0.46 ± 0.06	−0.48 ± 0.06	−0.41 ± 0.04	−0.43 ± 0.04	
22159+5440	V447 Lac	22:15:54.1	+54:40:22	K1 V	−0.17 ± 0.17	0.01 ± 0.05	0.05 ± 0.05	−0.12 ± 0.07	0.01 ± 0.07	−0.05 ± 0.11	−0.06 ± 0.12	−0.14 ± 0.05	−0.18 ± 0.06	
22311+4509	HD 213519 A	22:31:05.7	+45:08:42	G5	0.01 ± 0.06	0.09 ± 0.09	0.09 ± 0.08	−0.03 ± 0.09	−0.09 ± 0.07	−0.05 ± 0.05	−0.05 ± 0.05	−0.03 ± 0.06	−0.02 ± 0.06	
22467+1210	ξ Peg A	22:46:41.6	+12:10:22	F6 V	−0.19 ± 0.04	0.07 ± 0.10	0.02 ± 0.09	−0.14 ± 0.08	...	−0.32 ± 0.12	−0.26 ± 0.12	−0.20 ± 0.16	−0.07 ± 0.16	
22524+0950	σ Peg A	22:52:24.1	+09:50:08	F6 V	−0.12 ± 0.05	0.22 ± 0.12	0.14 ± 0.11	−0.10 ± 0.06	−0.17 ± 0.36	−0.23 ± 0.16	−0.16 ± 0.17	−0.14 ± 0.14	−0.05 ± 0.11	
22589+6902	BD+68 1345 A	22:58:53.8	+69:01:50	K0 V	−0.12 ± 0.12	−0.04 ± 0.09	0.00 ± 0.07	−0.08 ± 0.05	−0.04 ± 0.07	−0.12 ± 0.05	−0.13 ± 0.05	−0.08 ± 0.05	−0.13 ± 0.06	
23026+2948	BD+29 4841 Aa,Ab	23:02:34.6	+29:48:18	K0 V	...	...	...	...	...	...	...	...	...	SB2
23104+4901	HD 218790	23:10:21.3	+49:01:06	G0 V	0.22 ± 0.02	0.38 ± 0.12	0.32 ± 0.10	0.33 ± 0.11	0.26 ± 0.06	0.26 ± 0.07	0.26 ± 0.08	0.28 ± 0.03	0.29 ± 0.03	
23194+7900	V368 Cep	23:19:26.6	+79:00:13	G9 V	...	...	...	...	...	...	...	...	...	Fast
23235+4548	HD 220445	23:23:28.8	+45:47:36	K0 V	...	−0.03 ± 0.14	0.02 ± 0.13	0.04 ± 0.11	0.24 ± 0.12	0.05 ± 0.06	0.02 ± 0.06	0.03 ± 0.07	−0.02 ± 0.08	
23266+4520	HD 220821	23:26:40.6	+45:20:17	G0 V+	−0.16 ± 0.11	−0.02 ± 0.06	−0.02 ± 0.05	−0.17 ± 0.08	−0.08 ± 0.07	−0.19 ± 0.15	−0.17 ± 0.16	−0.24 ± 0.05	−0.21 ± 0.06	
23355+3101	HD 221830 A	23:35:28.9	+31:01:02	F9 V	−0.24 ± 0.04	0.10 ± 0.05	0.12 ± 0.04	−0.15 ± 0.10	−0.24 ± 0.10	−0.58 ± 0.15	−0.56 ± 0.16	−0.30 ± 0.06	−0.25 ± 0.07	
23419-0559	HD 222582 A	23:41:51.5	−05:59:09	G5 V	−0.01 ± 0.06	0.12 ± 0.08	0.12 ± 0.07	0.03 ± 0.07	−0.03 ± 0.07	−0.08 ± 0.05	−0.08 ± 0.06	−0.01 ± 0.04	0.00 ± 0.03	
23536+1207	MCC 870	23:53:35.5	+12:06:22	K4 V	...	...	...	−0.52 ± 0.38	0.42 ± 0.32	−0.47 ± 0.27	−0.55 ± 0.26	−0.37 ± 0.22	−0.36 ± 0.20	
23556+0042	HD 224157	23:55:36.0	+00:41:45	K0 V	−0.05 ± 0.17	0.08 ± 0.15	0.11 ± 0.12	−0.02 ± 0.09	0.13 ± 0.06	0.07 ± 0.06	0.05 ± 0.06	0.03 ± 0.05	−0.01 ± 0.06	
23581+2420	HD 224459 Aa,Ab	23:58:03.9	+24:20:28	G2	...	...	...	...	...	...	...	...	...	SB2
	BD+23 4830 B	23:58:03.4	+24:20:33	K0 V	−0.09 ± 0.05	−0.02 ± 0.08	0.02 ± 0.07	−0.14 ± 0.09	−0.05 ± 0.06	−0.11 ± 0.03	−0.12 ± 0.04	−0.14 ± 0.06	−0.17 ± 0.06	

[a] SB2: Double-line spectroscopic binary; Hot: Spectral type $\leq$ F6 V; Cool: Spectral type $\geq$ K4 V; Fast: $v \sin i \geq 10$ km s^{-1}

Table B.2: HFS components for the Sc lines.

Sc I 5520.519		Sc I 5671.860		Sc II 5526.789		Sc II 5657.886		Sc II 5667.135		Sc II 5684.190		Sc II 6245.621		Sc II 6320.832	
λ (Å)	$\log(gf)$	λ (Å)	$\log(gf)$	λ (Å)	$\log(gf)$	λ (Å)	$\log(gf)$	λ (Å)	$\log(gf)$	λ (Å)	$\log(gf)$	λ (Å)	$\log(gf)$	λ (Å)	$\log(gf)$
5520.482	−0.339	5671.773	−0.926	5526.770	−2.805	5657.886	−1.166	5667.135	−1.804	5684.190	−1.553	6245.621	−1.624	6320.832	−2.410
5520.494	−0.339	5671.778	−0.808	5526.775	−2.402	5657.887	−1.736	5667.141	−2.000	5684.192	−2.042	6245.629	−2.364	6320.839	−2.606
5520.508	−0.339	5671.779	−1.378	5526.779	−1.592	5657.892	−1.736	5667.148	−2.000	5684.193	−2.741	6245.631	−1.795	6320.850	−2.606
5520.519	−0.339	5671.785	−0.690	5526.779	−2.190	5657.894	−1.564	5667.153	−3.185	5684.204	−1.846	6245.636	−3.364	6320.857	−3.791
		5671.787	−1.167	5526.782	−1.387	5657.895	−1.578	5667.157	−2.004	5684.206	−1.926	6245.638	−2.181	6320.862	−2.610
		5671.788	−2.378	5526.783	−2.080	5657.899	−1.578	5667.162	−2.004	5684.207	−2.301	6245.640	−2.002	6320.871	−2.610
		5671.795	−0.578	5526.785	−1.321	5657.900	−2.260	5667.166	−2.259	5684.215	−2.301	6245.644	−2.946	6320.876	−2.865
		5671.797	−1.071	5526.786	−2.059	5657.901	−1.589			5684.216	−2.046	6245.645	−2.148		
		5671.799	−2.171	5526.788	−1.325	5657.904	−1.589			5684.217	−2.030	6245.647	−2.273		
		5671.807	−0.474	5526.789	−0.663	5657.905	−3.686					6245.650	−2.712		
		5671.810	−1.035	5526.789	−2.168	5657.906	−1.762					6245.651	−2.207		
		5671.813	−2.143	5526.790	−1.386	5657.908	−1.762					6245.652	−2.691		
		5671.822	−0.378	5526.791	−0.784	5657.909	−1.938					6245.654	−2.566		
		5671.826	−1.051	5526.791	−1.508							6245.655	−2.390		
		5671.829	−2.223	5526.792	−1.691							6245.657	−2.469		
		5671.840	−0.288	5526.793	−0.920										
		5671.844	−1.133	5526.794	−1.076										
		5671.847	−2.415	5526.794	−1.837										
		5671.860	−0.204	5526.795	−1.261										
		5671.864	−1.351	5526.795	−1.495										
		5671.868	−2.804												

Table B.3: HFS components for the V lines.

V I 5670.831		V I 5737.027		V I 6081.461		V I 6224.520		V I 6251.802		V I 6274.659		V I 6285.162	
λ (Å)	$\log(gf)$	λ (Å)	$\log(gf)$	λ (Å)	$\log(gf)$	λ (Å)	$\log(gf)$	λ (Å)	$\log(gf)$	λ (Å)	$\log(gf)$	λ (Å)	$\log(gf)$
5670.811	−1.103	5737.027	−1.386	6081.418	−1.814	6224.486	−3.594	6251.767	−2.954	6274.611	−2.962	6285.108	−3.598
5670.819	−2.111	5737.037	−2.085	6081.418	−1.638	6224.495	−3.390	6251.784	−2.750	6274.632	−2.485	6285.128	−3.170
5670.826	−3.412	5737.041	−2.085	6081.428	−1.638	6224.504	−3.325	6251.799	−2.685	6274.644	−2.506	6285.133	−2.733
5670.831	−1.208	5737.051	−1.678	6081.429	−2.610	6224.513	−3.332	6251.802	−2.051	6274.659	−2.164	6285.144	−2.920
5670.838	−1.900	5737.059	−1.904	6081.429	−1.513	6224.520	−2.691	6251.813	−2.692	6274.660	−2.485	6285.147	−2.572
5670.844	−3.014	5737.063	−1.904	6081.443	−1.513	6224.521	−3.398	6251.814	−2.238	6274.682	−2.631	6285.158	−2.744
5670.848	−1.324	5737.070	−2.084	6081.443	−1.832	6224.525	−2.878	6251.824	−2.457			6285.159	−2.580
5670.855	−1.827	5737.077	−1.873	6081.444	−1.627	6224.528	−3.536	6251.825	−2.758			6285.162	−2.107
5670.860	−2.810	5737.080	−1.873	6081.461	−1.627	6224.529	−3.097	6251.833	−2.720			6285.168	−2.744
5670.863	−1.453	5737.086	−2.801	6081.461	−1.216	6224.533	−3.360	6251.835	−2.896			6285.172	−2.323
5670.868	−1.821	5737.091	−1.937			6224.534	−3.816	6251.840	−3.051			6285.179	−2.606
5670.872	−2.713	5737.093	−1.937			6224.535	−3.691	6251.844	−3.176			6285.182	−3.045
5670.875	−1.599	5737.098	−4.044			6224.537	−4.138	6251.845	−3.498				
5670.879	−1.868	5737.101	−2.136			6224.539	−4.837	6251.849	−4.197				
5670.882	−2.713	5737.103	−2.136			6224.544	−3.816	6251.849	−2.954				
5670.884	−1.769	5737.106	−2.391			6224.549	−3.536	6251.854	−2.750				
5670.887	−1.973					6224.552	−3.398	6251.855	−3.176				
5670.890	−2.868					6224.555	−3.332	6251.858	−2.685				
5670.891	−1.973					6224.557	−3.325	6251.858	−2.896				
5670.893	−2.169					6224.559	−3.390	6251.860	−2.692				
5670.895	−2.236					6224.560	−3.594	6251.860	−2.758				

Table B.4: HFS components for the Mn lines.

Mn I 4502.204		Mn I 4671.647		Mn I 4739.072		Mn I 5377.626		Mn I 5399.500		Mn I 5413.697	
λ (Å)	log(gf)	λ (Å)	log(gf)	λ (Å)	log(gf)	λ (Å)	log(gf)	λ (Å)	log(gf)	λ (Å)	log(gf)
4502.204	−0.912	4671.647	−2.242	4739.070	−1.635	5377.564	−1.576	5399.423	−1.403	5413.593	−1.981
4502.207	−1.830	4671.654	−3.160	4739.072	−1.158	5377.576	−1.166	5399.429	−1.271	5413.628	−1.550
4502.208	−3.047	4671.660	−4.377	4739.090	−1.533	5377.576	−1.400	5399.439	−1.771	5413.638	−1.437
4502.211	−1.052	4671.664	−2.382	4739.091	−1.707	5377.582	−1.722	5399.441	−1.373	5413.658	−1.437
4502.213	−1.654	4671.670	−2.984	4739.093	−1.635	5377.594	−1.245	5399.453	−2.980	5413.697	−1.073
4502.213	−2.695	4671.675	−4.025	4739.105	−1.665	5377.596	−0.893	5399.468	−1.403	5413.702	−1.534
4502.216	−1.210	4671.678	−2.540	4739.106	−3.242	5377.606	−1.768	5399.473	−1.445		
4502.217	−1.628	4671.683	−2.958	4739.107	−1.533	5377.620	−1.224	5399.497	−1.271		
4502.217	−2.570	4671.687	−3.900	4739.115	−2.033	5377.626	−0.681	5399.500	−0.896		
4502.220	−1.394	4671.689	−2.724	4739.116	−1.665	5377.637	−1.944	5399.532	−1.373		
4502.220	−1.695	4671.693	−3.025			5377.655	−1.370				
4502.220	−2.649	4671.695	−3.979			5377.678	−2.324				
4502.222	−1.616	4671.697	−2.946								
4502.222	−1.871	4671.699	−3.201								
4502.223	−1.901	4671.701	−3.231								

Table B.5: HFS components for the Co lines.

Co I 4594.669		Co I 4792.854		Co I 4813.471		Co I 5301.017		Co I 5342.706		Co I 5352.020		Co I 5359.188		Co I 5647.207		Co I 6814.958	
λ (Å)	log(gf)	λ (Å)	log(gf)	λ (Å)	log(gf)	λ (Å)	log(gf)	λ (Å)	log(gf)	λ (Å)	log(gf)	λ (Å)	log(gf)	λ (Å)	log(gf)	λ (Å)	log(gf)
4594.582	−1.848	4792.799	−2.583	4813.398	−2.862	5301.008	−3.345	5342.693	−0.459	5351.893	−3.244	5359.188	−0.429	5647.207	−2.127	6814.889	−2.917
4594.583	−1.568	4792.814	−2.173	4813.416	−2.464	5301.017	−2.646	5342.693	−0.542	5351.925	−2.855	5359.191	−0.534	5647.220	−2.343	6814.915	−2.803
4594.587	−1.430	4792.824	−1.469	4813.432	−1.561	5301.026	−3.164	5342.693	−0.373	5351.953	−1.791	5359.194	−0.650	5647.232	−2.626	6814.924	−2.506
4594.588	−2.869	4792.827	−1.951	4813.432	−2.260	5301.034	−2.938	5342.694	−0.289	5351.976	−1.573	5359.197	−0.779	5647.238	−2.753	6814.936	−2.928
4594.590	−1.848	4792.834	−1.273	4813.445	−1.350	5301.040	−3.133	5342.696	−0.208	5351.978	−2.583	5359.200	−0.925	5647.243	−3.065	6814.943	−3.122
4594.593	−1.364	4792.838	−1.826	4813.447	−2.163	5301.043	−3.345	5342.699	−0.130	5351.997	−1.491	5359.203	−1.095	5647.246	−2.592	6814.958	−2.190
4594.594	−2.170	4792.843	−1.219	4813.456	−1.277	5301.047	−3.344	5342.701	−1.267	5352.000	−2.611	5359.207	−1.299	5647.253	−2.600	6814.969	−3.104
4594.598	−1.568	4792.848	−1.775	4813.459	−2.163	5301.052	−3.197	5342.702	−0.056	5352.014	−1.475	5359.210	−1.562	5647.259	−2.764	6814.978	−2.917
4594.603	−1.723	4792.850	−1.241	4813.466	−1.271	5301.056	−3.164	5342.704	−1.049	5352.019	−2.818	5359.214	−1.495	5647.264	−3.618	6814.987	−2.803
4594.603	−1.357	4792.854	−0.629	4813.470	−2.318	5301.058	−4.061	5342.706	+0.014	5352.020	−0.644	5359.214	−1.299	5647.267	−3.190	6814.991	−2.928
4594.610	−1.430	4792.855	−1.805	4813.471	−0.553	5301.062	−3.396	5342.707	−0.955	5352.029	−1.511	5359.215	−1.194	5647.269	−2.940		
4594.615	−1.392	4792.856	−1.332	4813.473	−1.318	5301.065	−3.133	5342.711	−0.923	5352.036	−0.728	5359.215	−1.147	5647.269	−2.764		
4594.616	−1.422	4792.860	−1.520	4813.478	−0.658	5301.065	−5.304	5342.713	−2.480	5352.041	−1.607	5359.216	−1.153				
4594.624	−1.364	4792.860	−0.770	4813.479	−1.423	5301.070	−3.651	5342.716	−0.943	5352.048	−0.818	5359.216	−1.226				
4594.630	−1.129	4792.864	−0.934	4813.483	−1.619	5301.071	−3.197	5342.718	−2.246	5352.050	−1.818	5359.217	−1.437				
4594.631	−1.626	4792.867	−1.132	4813.485	−0.774	5301.074	−3.396	5342.722	−1.030	5352.059	−0.914	5359.221	−2.194				
4594.641	−1.357	4792.868	−1.775	4813.489	−0.903			5342.725	−2.200	5352.066	−1.018	5359.225	−2.039				
4594.648	−0.910	4792.868	−1.387	4813.490	−1.686			5342.728	−1.253	5352.070	−1.130	5359.229	−2.039				
4594.661	−1.422			4813.492	−1.049			5342.731	−2.267	5352.070	−1.366	5359.234	−2.136				
4594.669	−0.723			4813.493	−1.423			5342.739	−2.450	5352.072	−1.248	5359.238	−2.340				
4594.685	−1.626			4813.493	−1.219			5342.747	−2.832			5359.242	−2.738				

CHAPTER C

Appendix of Chapter 5

This appendix contains the example using projective inference, and the figures and tables referenced in Chapter 5:

- The first three pages show an example of the methodology based on the Stefan-Boltzmann law.
- Figs. C.4 and C.5 represent the [X/Fe] versus [Fe/H] trends for the CAFOS sample compared to the FGK primaries from Montes et al. (2018) and Duque-Arribas et al. (2024).
- Table C.2 lists the predictors and their coefficients for the calibrations of each abundance.
- Table C.3 presents the CAFOS sample.
- Table C.4 lists the abundances obtained with the calibrations for the CAFOS sample.

A projective inference example: the Stefan-Boltzmann law

The predictive projection is a two-stage approach: first, we construct the reference model, and then we select a minimal subset of predictors to characterise the predictions of the target variable. As an example, we predicted the luminosity L of a star relying on the Stefan-Boltzmann law:

$$L = 4\pi R^2 \sigma_B T_{\rm eff}^4 \tag{C.1}$$

where R denotes de radius of the star, $T_{\rm eff}$ its effective temperature and $\sigma_B \approx 5.670{\cdot}10^{-8}\,\mathrm{W\,m^{-2}K^{-4}}$ the Stefan–Boltzmann constant. We can simplify the equation using solar units:

$$\frac{L}{L_\odot} = \left(\frac{R}{R_\odot}\right)^2 \left(\frac{T}{T_\odot}\right)^4 \tag{C.2}$$

Or in logaritmic scale:

$$\log\left(\frac{L}{L_\odot}\right) = 2\log\left(\frac{R}{R_\odot}\right) + 4\log\left(\frac{T}{T_\odot}\right) \tag{C.3}$$

This is a linear expression with intercept 0, and coefficients 2 and 4. So, in order to predict the stellar luminosity, we only need its radius and effective temperature.

We can imagine we do not know this relation, and to estimate the luminosity we have a data sample with several predictors. In particular, we downloaded a sample of stars from the Gaia Archive[1] within 25 pc with determined astrophysical parameters (Gaia Collaboration et al., 2016, 2023; Fouesneau et al., 2023). These data provide values for the luminosity L, the distance d, the monochromatic extinction A_0 at 547.7 nm, the chromospheric activity index $A_{\rm Ca}$ measured on the calcium triplet using RVS spectra, the age t, the radius R, the effective temperature $T_{\rm eff}$, and the iron abundance [Fe/H] for 443 stars. We show a Hertzsprung–Russell diagram of these stars, color-coded by their radii, in Fig. C.1.

First, we construct the reference model using all the information available:

$$\log(L) \sim d + A_0 + A_{\rm Ca} + t + \log(R) + \log(T_{\rm eff}) + [\mathrm{Fe/H}] \tag{C.4}$$

[1] https://gea.esac.esa.int/archive/

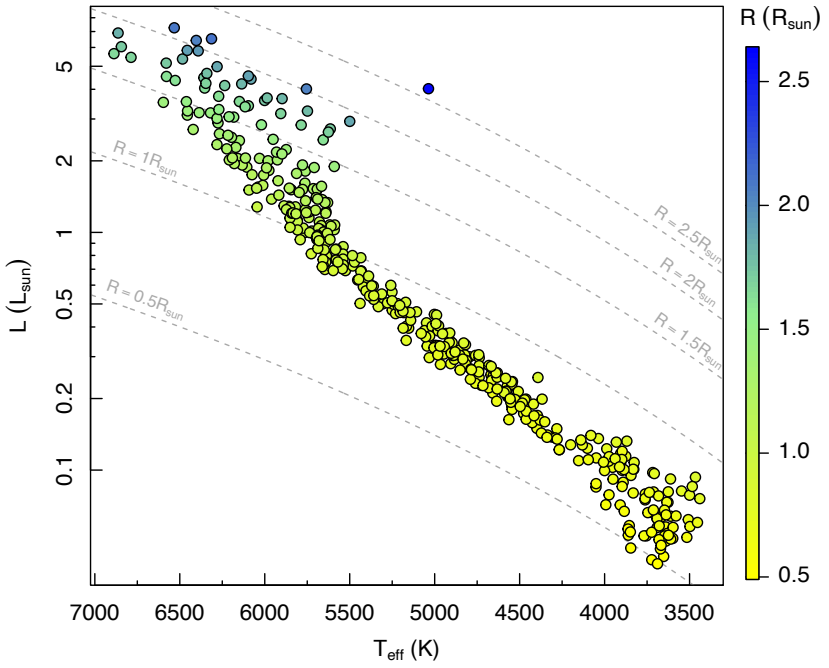

Figure C.1: HR diagram of the stars retrieved from the Gaia Archive, color-coded by stellar radius. The dashed lines represent constant radius.

We fitted this model with `brms` running 4 chains, each of them with 2000 iterations and 1000 of warmup, and assigned a regularised horseshoe prior on each coefficient. The results can be found in Table C.1.

Now we perform the projection predictive variable selection using the `projpred` package. We show the elpd and RMSE vs. the submodel size in Fig. C.2. Based on these results, we select a submodel size of 2, since adding more predictors does not enhance the predictive performance. Inspecting the solution path, we saw that the first two included predictors were $\log(T)$ and $\log(R)$. Then we project the reference model onto this final submodel. These results, shown in Table C.1 and Fig. C.3, are the expected ones from the Stefan-Boltzmann law. It is important to keep in mind that we do not only obtain point estimates for the parameters, but the whole posterior distribution as usual in Bayesian inference. Finally, we can generate draws from predictive distributions using the final submodel.

Table C.1: Results for the reference and proyected models

β	Reference model	Submodel size=2
Intercept	-0.0037 ± 0.0029	0.00084 ± 0.00085
d	0.00006 ± 0.000013	
A_0	-0.55 ± 0.13	
$A_{\rm Ca}$	0.013 ± 0.025	
t	0.00029 ± 0.00019	
$\log(R)$	1.9967 ± 0.0085	2.0024 ± 0.0077
$\log(T_{\rm eff})$	4.028 ± 0.016	4.016 ± 0.014
[Fe/H]	-0.0045 ± 0.0020	
σ	0.01201 ± 0.00041	0.01253 ± 0.00019

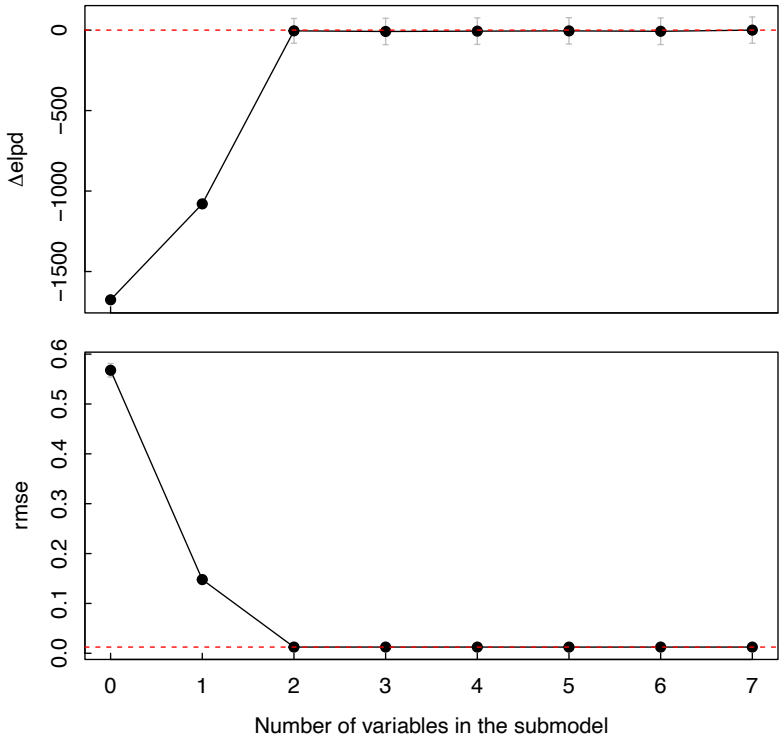

Figure C.2: elpd and rmse as function of the submodel size. The horizontal red dashed lines denote the corresponding value of the reference model.

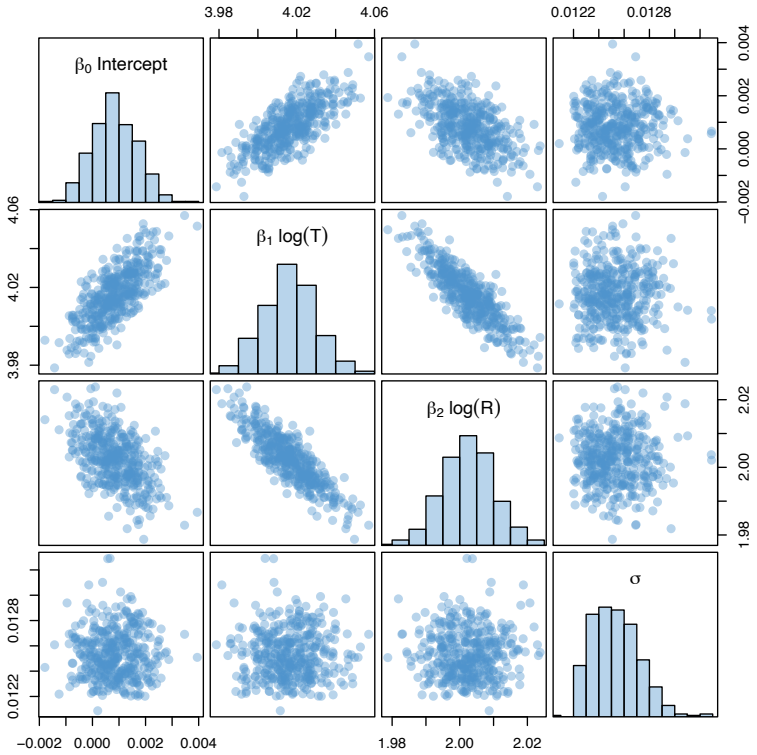

Figure C.3: Pairsplot of the results of the submodel.

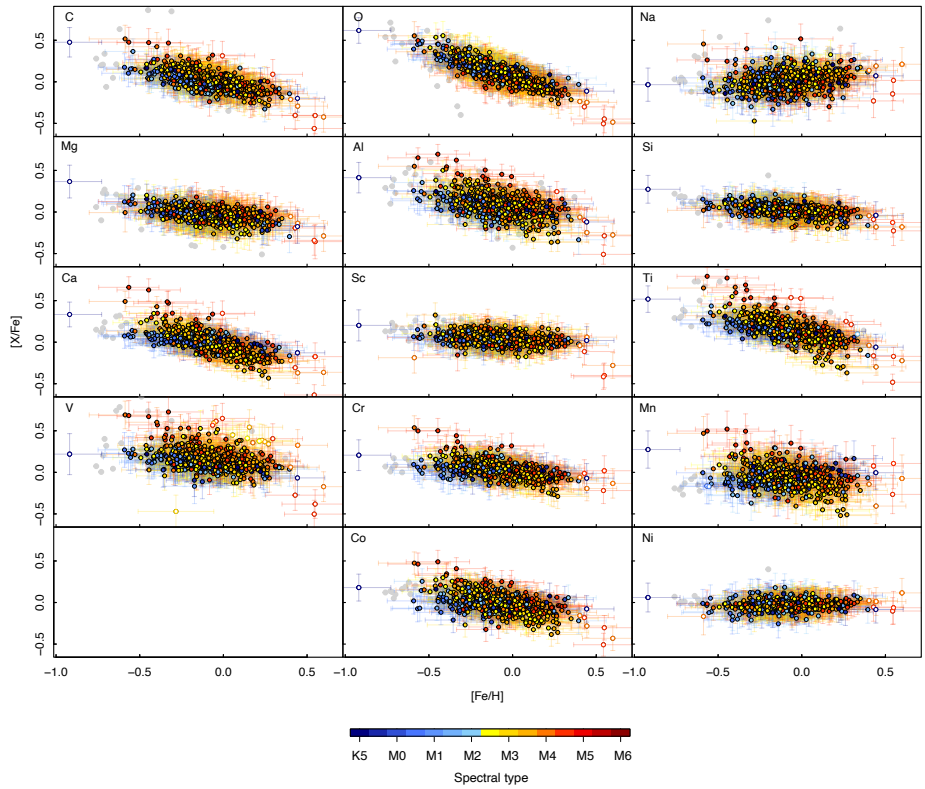

Figure C.4: Abundance ratios [X/Fe] versus [Fe/H] for the CAFOS sample using our predicted values, color-coded by spectral type. Open circles denote stars with predictions outside the range of application of the calibrations. In gray we represent the trends for the FGK primary stars from Montes et al. (2018) and Duque-Arribas et al. (2024). See also Fig. C.5.

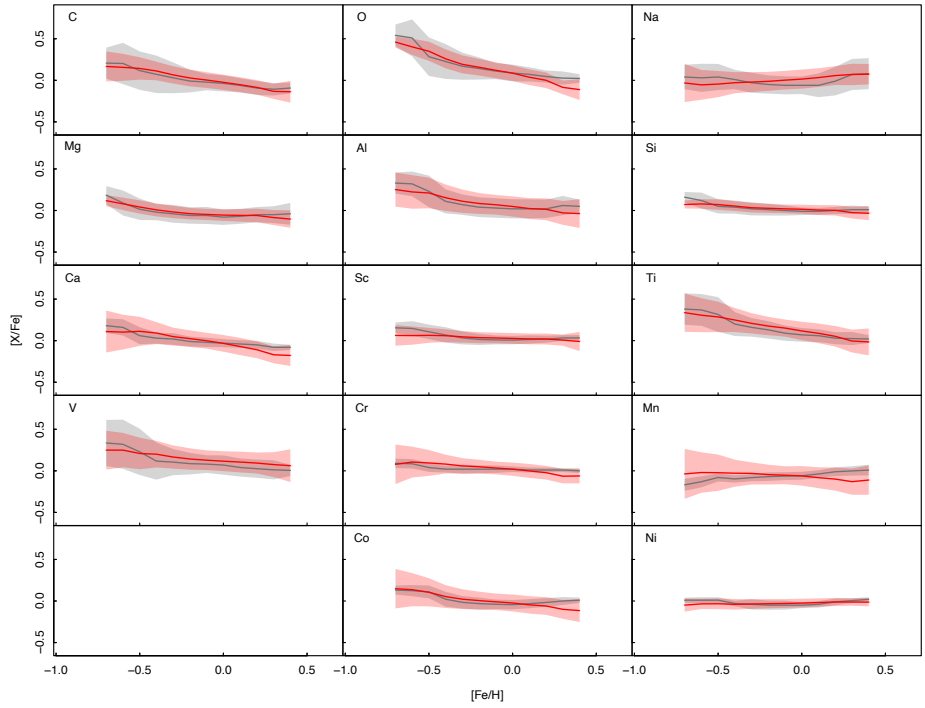

Figure C.5: Mean and standard deviation of the trends for the FGK primaries from Montes et al. 2018 and Duque-Arribas et al. 2024 (grey) and the M dwarfs of the CAFOS sample (red) shown in Fig. C.4.

Table C.2: Calibrations for each abundance.

[C/H]					
All		Early		Late	
Intercept	-1.77 ± 1.87	Intercept	-5.55 ± 2.94	Intercept	-1.55 ± 0.68
Ratio B	2.54 ± 0.86	F07	-4.10 ± 1.52	F05	1.31 ± 0.61
CaH 1	1.90 ± 0.50	CaH 1	2.73 ± 0.50		
F07	-2.31 ± 1.16	Ratio B	4.39 ± 1.14		
F03	-0.06 ± 0.51	Na-8190	1.84 ± 0.79		
VO 2	-2.27 ± 0.64	VO-7912	1.89 ± 0.91		
I3 (TiO)	-1.85 ± 0.57	F01	-1.60 ± 0.84		
F06	4.03 ± 1.36				
TiO 5	-2.42 ± 0.74				
TiO 4	1.50 ± 0.93				
[O/H]					
All		Early		Late	
Intercept	1.09 ± 1.28	Intercept	-6.33 ± 2.33	Intercept	1.34 ± 0.48
CaH 1	0.54 ± 0.37	F07	-2.03 ± 1.22	Ratio A	-1.50 ± 0.54
F05	0.07 ± 0.39	CaH 1	2.05 ± 0.65	TiO-7053	0.41 ± 0.24
I2 (CaH)	-0.34 ± 0.44	VO-7912	5.38 ± 1.07		
TiO 5	-1.08 ± 0.47	Ratio B	2.36 ± 0.88		
PC3	0.48 ± 0.36	I2 (CaH)	-0.45 ± 0.64		
Ratio A	-2.09 ± 1.28	CaH Narr	2.13 ± 0.63		
CaH Narr	0.46 ± 0.50	Ratio A	-3.13 ± 1.32		
Ratio B	0.68 ± 0.68	Na-8190	1.22 ± 0.68		
		TiO 1	-1.21 ± 0.56		
[Na/H]					
All		Early		Late	
Intercept	6.16 ± 2.43	Intercept	-1.95 ± 3.69	Intercept	4.51 ± 2.77
Ratio B	1.77 ± 0.77	F07	-11.3 ± 2.0	F05	2.01 ± 0.67
CaH 1	0.50 ± 0.47	CaH 1	-0.18 ± 0.73	I2 (CaH)	-2.22 ± 0.49
I2 (CaH)	0.23 ± 0.43	Ratio B	6.36 ± 1.37	F07	-3.10 ± 1.63
F07	-8.32 ± 1.57	VO 1	9.46 ± 1.83	CaH 3	-3.44 ± 1.18
CaH 2	0.67 ± 0.45	Hα	-2.19 ± 0.43	Na-8190	2.50 ± 0.94
PC1	3.11 ± 0.62	CaOH	6.96 ± 1.01	I3 (TiO)	-0.79 ± 0.40
TiO-7140	-0.70 ± 0.38	TiO 5	-5.33 ± 0.93	PC2	1.20 ± 0.43
TiO 5	-5.92 ± 0.96	F01	-3.12 ± 0.81	CaH Narr	-0.83 ± 0.48
TiO 4	1.56 ± 0.98				
I3 (TiO)	-1.46 ± 0.69				
Ratio A	-4.52 ± 1.08				
F06	8.49 ± 1.63				
VO 2	-4.37 ± 0.87				
TiO 6	-1.92 ± 0.63				
CaOH	0.91 ± 0.68				
CaH Narr	1.14 ± 0.49				
Ratio C	1.10 ± 0.45				
F02	-1.16 ± 0.68				
F04	1.41 ± 0.75				
[Mg/H]					
All		Early		Late	
Intercept	-0.17 ± 3.08	Intercept	-11.0 ± 4.0	Intercept	-2.41 ± 0.52
Ratio B	0.29 ± 0.76	F07	-5.94 ± 1.63	F05	2.04 ± 0.47
CaH 1	0.91 ± 0.51	CaH 1	2.48 ± 0.74		
F07	-2.12 ± 1.18	Ratio B	5.89 ± 1.50		
I2 (CaH)	-0.79 ± 0.44	Hα	-1.14 ± 0.44		
PC1	1.03 ± 0.56	CaH Narr	3.24 ± 0.94		
VO-a	-3.65 ± 1.15	CaH 3	3.72 ± 1.22		
Na-8190	2.94 ± 0.78	VO-7912	2.53 ± 1.39		
TiO-7053	-0.11 ± 0.58				
F06	2.10 ± 1.14				
PC3	0.48 ± 0.48				
TiO 5	-1.72 ± 0.56				
TiO 1	1.91 ± 0.72				
TiO-7140	0.00 ± 0.30				
TiO 4	0.84 ± 0.68				
Hα	-0.48 ± 0.19				
CaH Narr	1.69 ± 0.63				
Ratio A	-1.93 ± 1.02				
I3 (TiO)	-0.88 ± 0.55				
VO 1	2.42 ± 1.36				

Table C.2: *Continued*

[Al/H]					
All		Early		Late	
Intercept	3.25 ± 2.92	Intercept	2.44 ± 2.33	Intercept	-0.47 ± 0.74
Ratio B	2.02 ± 0.88	F07	-10.1 ± 1.7	F05	0.86 ± 0.41
CaH 1	-0.10 ± 0.35	CaH 1	2.03 ± 0.27	F04	1.41 ± 0.49
F07	-5.99 ± 1.22	Ratio B	6.22 ± 1.31	TiO 5	-1.80 ± 0.58
I2 (CaH)	-0.83 ± 0.39	Hα	-1.47 ± 0.36	I2 (CaH)	-1.00 ± 0.23
F05	0.35 ± 0.48			PC2	0.97 ± 0.26
CaH Narr	1.53 ± 0.49				
Hα	-0.24 ± 0.15				
TiO 1	1.62 ± 0.60				
TiO 5	-3.07 ± 0.88				
Ratio A	-2.27 ± 0.95				
TiO 4	1.11 ± 0.72				
CaH 2	1.04 ± 0.52				
I3 (TiO)	-0.60 ± 0.43				
PC1	1.90 ± 0.59				
TiO 3	0.54 ± 0.41				
F06	4.13 ± 1.44				
VO 2	-2.01 ± 0.69				
TiO 6	-0.98 ± 0.55				
VO-a	-1.17 ± 0.81				

[Si/H]					
All		Early		Late	
Intercept	1.46 ± 2.35	Intercept	-6.69 ± 2.92	Intercept	-2.28 ± 0.45
Ratio B	1.44 ± 0.69	F07	-7.99 ± 1.64	F05	2.28 ± 0.42
CaH 1	1.50 ± 0.50	CaH 1	0.74 ± 0.60	I2 (CaH)	-0.21 ± 0.14
I2 (CaH)	-0.15 ± 0.41	Ratio B	5.01 ± 1.18		
F07	-5.63 ± 1.26	Hα	-1.69 ± 0.39		
PC1	1.67 ± 0.51	CaH Narr	2.32 ± 0.58		
TiO-7053	-0.89 ± 0.58	CaOH	2.36 ± 0.42		
TiO 5	-2.94 ± 0.55	VO-7912	5.30 ± 1.32		
TiO 4	1.45 ± 0.70				
Ratio A	-3.51 ± 1.10				
CaH Narr	2.25 ± 0.49				
TiO 1	1.83 ± 0.62				
F06	4.04 ± 1.02				
VO 2	-1.54 ± 0.57				
Hα	-0.55 ± 0.18				
I3 (TiO)	-1.46 ± 0.46				

[Ca/H]					
All		Early		Late	
Intercept	3.31 ± 2.91	Intercept	-10.9 ± 2.8	Intercept	-0.17 ± 0.69
Ratio B	0.18 ± 0.58	F07	-5.77 ± 1.38	F05	0.77 ± 0.34
CaH 1	0.82 ± 0.51	CaH 1	1.90 ± 0.62	F04	1.12 ± 0.44
F07	-4.57 ± 1.06	CaH Narr	2.46 ± 0.53	TiO 5	-1.86 ± 0.69
I2 (CaH)	-0.62 ± 0.37	Hα	-1.56 ± 0.35	I3 (TiO)	-1.85 ± 0.57
CaH 3	-0.63 ± 0.87	Ratio B	4.37 ± 0.98	TiO-7053	1.58 ± 0.46
PC1	0.62 ± 0.48	CaOH	1.96 ± 0.35		
I3 (TiO)	-1.66 ± 0.51	VO 1	3.59 ± 1.39		
TiO 5	-2.66 ± 0.76	VO-7912	3.45 ± 1.07		
CaH 2	0.43 ± 0.37				
TiO 4	1.28 ± 0.76				
TiO 1	1.58 ± 0.61				
VO 1	3.56 ± 1.22				
Hα	-0.35 ± 0.15				
VO 2	-2.74 ± 0.72				
F06	4.94 ± 1.45				
CaH Narr	1.22 ± 0.48				
TiO 6	-0.81 ± 0.56				
VO-a	-1.76 ± 0.82				
Ratio A	-1.03 ± 0.84				

Table C.2: *Continued*

[Sc/H]					
All		Early		Late	
Intercept	9.39 ± 2.89	Intercept	-12.0 ± 4.6	Intercept	-2.42 ± 0.41
F07	-6.60 ± 1.09	F07	-4.95 ± 1.47	F05	2.12 ± 0.37
I2 (CaH)	-1.58 ± 0.34	CaH 1	1.77 ± 0.69		
F05	0.58 ± 0.36	CaH Narr	3.19 ± 0.75		
CaH 3	-1.68 ± 0.69	Hα	-1.63 ± 0.38		
TiO 1	2.51 ± 0.53	F04	0.04 ± 0.98		
Hα	-0.86 ± 0.16	VO-7912	4.57 ± 1.35		
CaH Narr	1.45 ± 0.49	Ratio B	3.07 ± 1.14		
VO-a	-4.17 ± 0.91	Na-8190	2.59 ± 0.80		
VO 2	-4.00 ± 0.72	CaOH	1.90 ± 0.98		
I3 (TiO)	-0.71 ± 0.37	Ratio A	-1.98 ± 1.30		
F06	5.58 ± 1.33	VO 1	4.02 ± 1.72		
VO 1	5.14 ± 1.12	VO-a	-4.62 ± 1.72		
TiO 6	-1.44 ± 0.54	VO	7.76 ± 4.66		
[Ti/H]					
All		Early		Late	
Intercept	3.97 ± 2.60	Intercept	-1.29 ± 2.40	Intercept	-1.13 ± 0.47
Ratio B	0.61 ± 0.74	F07	-7.56 ± 1.49	F05	0.86 ± 0.29
CaH 1	0.59 ± 0.31	CaH 1	3.44 ± 0.63	F04	1.55 ± 0.35
F07	-5.09 ± 1.30	Ratio B	4.44 ± 1.18	TiO 6	1.08 ± 0.22
F03	-0.30 ± 0.37	Hα	-1.21 ± 0.36	I3 (TiO)	-1.01 ± 0.31
VO 1	3.20 ± 1.02	CaH Narr	1.60 ± 0.46	TiO 5	-1.36 ± 0.51
I2 (CaH)	-0.99 ± 0.26				
TiO 5	-2.24 ± 0.53				
TiO 4	1.17 ± 0.74				
F02	0.64 ± 0.30				
TiO 1	0.60 ± 0.41				
VO-a	-2.60 ± 1.18				
VO	2.41 ± 2.27				
Ratio C	-0.26 ± 0.37				
F06	2.43 ± 0.88				
I3 (TiO)	-1.03 ± 0.32				
VO 2	-1.26 ± 0.47				
[V/H]					
All		Early		Late	
Intercept	-1.74 ± 5.47	Intercept	-4.38 ± 4.00	Intercept	-2.73 ± 0.38
F07	-4.92 ± 2.05	F07	-5.48 ± 2.18	F05	0.57 ± 0.40
I2 (CaH)	-1.89 ± 0.43	CaH 1	1.87 ± 0.89	F04	3.27 ± 0.70
F05	0.63 ± 0.43	Ratio B	3.84 ± 1.59	TiO 6	1.07 ± 0.18
CaH 3	-2.49 ± 0.84	CaH Narr	1.46 ± 0.83	CaH 2	-1.84 ± 0.63
VO 2	-3.86 ± 1.03	Hα	-1.11 ± 0.54		
TiO 4	0.90 ± 0.56	CaOH	2.14 ± 0.93		
F06	9.92 ± 2.46	TiO 5	-3.69 ± 1.32		
TiO 6	-1.44 ± 0.55	TiO 4	3.01 ± 1.35		
PC2	1.06 ± 0.51	Na-8190	1.29 ± 1.00		
PC3	1.74 ± 0.99				
F03	0.84 ± 0.53				
Na-8190	0.97 ± 1.00				
[Cr/H]					
All		Early		Late	
Intercept	5.42 ± 2.40	Intercept	-9.01 ± 3.42	Intercept	7.77 ± 2.33
F07	-5.83 ± 1.46	F07	-7.93 ± 1.68	F05	0.58 ± 0.53
I2 (CaH)	-0.85 ± 0.48	CaH 1	2.44 ± 0.71	CaOH	0.07 ± 0.51
CaH 3	-1.11 ± 1.05	CaH Narr	3.29 ± 0.81	F07	-3.77 ± 1.44
PC1	2.02 ± 0.59	Ratio A	-0.70 ± 1.13	I3 (TiO)	-2.43 ± 0.55
TiO-7053	-0.38 ± 0.53	Hα	-1.68 ± 0.42	TiO 2	-1.90 ± 0.67
F06	6.63 ± 1.58	Ratio B	4.83 ± 1.24	CaH 1	1.06 ± 0.47
VO 2	-3.81 ± 0.75	CaOH	1.79 ± 0.49	Ratio A	-1.92 ± 0.55
TiO 6	-1.37 ± 0.61	VO 1	5.80 ± 1.66	PC1	1.46 ± 0.54
Ratio C	1.00 ± 0.41			TiO 5	-1.37 ± 0.73
Ratio A	-3.20 ± 1.11				
TiO 1	1.36 ± 0.64				
CaH Narr	2.19 ± 0.55				
TiO 5	-2.58 ± 0.69				
CaOH	0.64 ± 0.50				
I3 (TiO)	-1.82 ± 0.62				
Hα	-0.32 ± 0.18				
CaH 1	1.30 ± 0.69				

Table C.2: *Continued*

[Mn/H]					
All		Early		Late	
Intercept	-4.87 ± 5.07	Intercept	-3.17 ± 4.12	Intercept	4.10 ± 2.56
F07	-7.21 ± 2.00	F07	-10.8 ± 2.27	F05	0.01 ± 0.63
I2 (CaH)	-1.15 ± 0.51	TiO 1	1.43 ± 0.99	CaOH	0.96 ± 0.61
CaH 3	0.49 ± 1.29	VO 1	9.68 ± 1.99	VO-7434	-1.84 ± 1.63
PC1	3.71 ± 0.72	F01	-2.90 ± 0.92	I3 (TiO)	-1.67 ± 0.68
TiO-7053	-1.21 ± 0.74	Ratio C	0.31 ± 0.64	TiO 5	-2.55 ± 1.06
F06	10.7 ± 2.01	Hα	-1.76 ± 0.53	Color-M	0.17 ± 0.27
VO 2	-2.21 ± 0.94	Ratio B	5.92 ± 1.60	I2 (CaH)	-1.21 ± 0.42
TiO 6	-1.21 ± 0.76	CaOH	3.60 ± 0.69	PC1	2.07 ± 1.12
Na-8190	2.68 ± 1.14	TiO 2	-3.44 ± 1.00		
PC3	1.63 ± 0.77				
Ratio A	-3.13 ± 1.37				
TiO 1	1.77 ± 0.75				
TiO 5	-4.65 ± 0.95				
CaH Narr	2.23 ± 0.71				
CaOH	1.58 ± 0.61				
TiO 4	1.79 ± 1.04				
Hα	-0.52 ± 0.21				
I3 (TiO)	-1.36 ± 0.62				

[Fe/H]					
All		Early		Late	
Intercept	3.76 ± 2.43	Intercept	-17.2 ± 6.0	Intercept	3.46 ± 2.37
F07	-5.31 ± 1.54	F07	-5.97 ± 1.75	F05	1.36 ± 0.47
I2 (CaH)	-0.73 ± 0.47	CaH 1	2.60 ± 0.72	CaOH	0.69 ± 0.55
CaH 3	-1.10 ± 1.10	CaH Narr	2.50 ± 0.68	VO-7434	-3.06 ± 1.57
PC1	1.86 ± 0.60	TiO 4	3.54 ± 0.60	I3 (TiO)	-2.40 ± 1.07
TiO-7053	-0.41 ± 0.63	Hα	-1.70 ± 0.43	TiO 5	-2.06 ± 1.10
F06	6.25 ± 1.62	Ratio B	5.24 ± 1.18	TiO-7140	0.52 ± 0.27
VO 2	-3.78 ± 0.79	VO 1	3.23 ± 1.64	CaH 1	1.13 ± 0.57
TiO 6	-1.01 ± 0.61	Na-8190	2.46 ± 0.82		
Hα	-0.53 ± 0.18	VO-7912	4.50 ± 1.25		
CaH Narr	2.69 ± 0.60				
TiO 1	2.31 ± 0.70				
Ratio A	-3.44 ± 1.15				
Ratio C	1.25 ± 0.44				
TiO 5	-2.19 ± 0.62				
I3 (TiO)	-2.10 ± 0.61				
CaH 1	1.72 ± 0.62				

[Co/H]					
All		Early		Late	
Intercept	7.14 ± 1.57	Intercept	2.73 ± 2.26	Intercept	3.59 ± 1.75
F07	-9.60 ± 0.88	F07	-12.2 ± 1.43	F05	0.28 ± 0.51
I2 (CaH)	-2.02 ± 0.19	CaH 1	4.14 ± 0.51	I2 (CaH)	-1.62 ± 0.34
TiO 5	-2.69 ± 0.48	CaH Narr	1.83 ± 0.39	PC1	1.35 ± 0.39
TiO 4	2.46 ± 0.76	Hα	-1.48 ± 0.29	CaH 2	-0.74 ± 0.33
PC1	3.02 ± 0.36	Ratio B	4.08 ± 0.95	F07	-2.95 ± 1.26
TiO-7053	-1.55 ± 0.42				
F06	7.27 ± 1.15				
VO 2	-3.24 ± 0.59				
TiO 6	-1.44 ± 0.39				

[Ni/H]					
All		Early		Late	
Intercept	2.66 ± 3.35	Intercept	-5.80 ± 3.36	Intercept	2.79 ± 2.06
F07	-6.79 ± 1.50	F07	-9.48 ± 1.74	F05	0.17 ± 0.54
I2 (CaH)	-0.66 ± 0.43	CaH 1	1.65 ± 0.72	CaOH	0.01 ± 0.76
CaH 3	0.25 ± 1.09	CaH Narr	2.70 ± 0.67	TiO 5	-1.66 ± 0.82
PC1	1.65 ± 0.67	Hα	-2.45 ± 0.39	F04	0.05 ± 0.88
TiO-7053	0.12 ± 0.60	F04	2.22 ± 1.07	I3 (TiO)	-1.47 ± 0.55
F06	5.94 ± 1.58	Ratio B	4.11 ± 1.26	Color-M	0.05 ± 0.23
VO 2	-2.16 ± 0.90	VO 1	6.25 ± 1.61	I2 (CaH)	-1.37 ± 0.36
TiO 6	-1.30 ± 0.65	TiO 5	-2.98 ± 0.88	F07	-1.41 ± 1.23
Ratio A	-2.26 ± 1.11	CaOH	2.77 ± 0.99	PC1	1.83 ± 0.88
CaH Narr	2.36 ± 0.57			TiO 1	0.77 ± 0.73
CaH 1	0.83 ± 0.62			Ratio C	0.59 ± 0.42
Ratio C	-0.01 ± 0.39			VO 2	-0.63 ± 0.56
Hα	-0.70 ± 0.19				
TiO 1	1.95 ± 0.76				
TiO 5	-3.98 ± 0.84				
I3 (TiO)	-1.99 ± 0.62				
TiO 4	1.73 ± 1.01				
VO-a	-2.42 ± 0.95				
VO 1	4.30 ± 1.36				
CaOH	0.97 ± 0.55				
Na-8190	1.00 ± 0.78				

Table C.3: CAFOS sample.

Karmn	RA	DEC	Jmag	SpT	Ref.[a]	Notes
J00051+457	00:05:10.80	+45:47:11.6	6.704	M1.0 V	This work	
J00066−070AB	00:06:39.26	−07:05:35.4	9.831	M4.5 V	AF15	
J00067−075	00:06:43.26	−07:32:14.7	8.323	M5.5 V	This work	
J00077+603AB	00:07:42.64	+60:22:54.3	8.911	M4.0 V	AF15	
J00115+591	00:11:31.83	+59:08:40.0	9.945	M5.5 V	AF15	
J00118+229	00:11:53.03	+22:59:04.8	8.862	M3.5 V	AF15	
J00119+330	00:11:56.54	+33:03:17.8	9.066	M3.5 V	AF15	
J00122+304	00:12:13.41	+30:28:44.3	10.242	M4.5 V	AF15	
J00133+275	00:13:19.52	+27:33:31.1	10.431	M4.5 V	AF15	
J00136+806	00:13:38.81	+80:39:56.9	7.756	M1.5 V	AF15	
J00146+202	00:14:36.15	+20:12:24.1	1.757	MIII	AF15	Giant
J00152+530	00:15:14.53	+53:04:45.7	10.823	M2.5 V	AF15	
J00162+198W	00:16:14.56	+19:51:38.6	7.875	M4.0 V	AF15	
J00162+198E	00:16:16.08	+19:51:51.5	8.893	M4.0 V	AF15	
J00183+440	00:18:22.57	+44:01:22.2	5.252	M1.0 V	AF15	
J00228−164	00:22:50.18	−16:27:44.4	10.248	M4.0 V	AF15	
J00240+264	00:24:03.77	+26:26:30.0	10.222	M4.0 V	AF15	
J00253+235	00:25:19.59	+23:32:51.8	9.789	M1.5 V	AF15	
J00286−066	00:28:39.48	−06:39:48.1	8.038	M3.5 V	This work	
J00297+012	00:29:43.22	+01:12:38.5	9.145	M1.0 V	AF15	
J00313+336	00:31:20.06	+33:37:37.5	8.750	M0.0 V	AF15	
J00313+001	00:31:21.57	+00:09:29.5	9.755	M3.0 V	AF15	
J00322+544	00:32:15.74	+54:29:02.8	9.387	M4.5 V	AF15	
J00328−045AB	00:32:53.14	−04:34:06.8	9.276	M4.5 V	AF15	
J00358+526	00:35:53.22	+52:41:12.4	8.932	M2.5 V	AF15	
J00367+444	00:36:46.45	+44:29:18.9	2.257	KIII	AF15	Giant
J00380+169	00:38:03.86	+16:56:02.9	9.380	M3.0 V	AF15	
J00385+429	00:38:33.17	+42:59:29.8	10.489	M0.5 V	M18	
J00389+306	00:38:58.79	+30:36:58.4	7.453	M2.5 V	AF15	
J00395+149S	00:39:33.49	+14:54:18.9	9.964	M4.0 V	AF15	
J00395+149N	00:39:33.74	+14:54:34.8	9.826	M4.5 V	AF15	
J00428+355	00:42:48.21	+35:32:55.4	7.164	M1.0 V	This work	SB
J00452+002AB	00:45:13.59	+00:15:51.0	10.114	M4.0 V	AF15	
J00464+506	00:46:29.90	+50:38:39.0	9.964	M4.0 V	AF15	
J00467−044	00:46:43.36	−04:24:45.5	11.198	M4.0 V	AF15	
J00484+753	00:48:29.71	+75:18:48.0	9.469	M3.0 V	AF15	
J00490+657	00:49:04.77	+65:44:37.8	9.304	M2.5 V	AF15	
J00490+578	00:49:05.17	+57:49:03.8	4.840	K7 V	AF15	
J00502+601	00:50:16.46	+60:07:55.7	5.496	KIII	AF15	Giant
J00502+086	00:50:17.53	+08:37:34.1	9.745	M4.5 V	AF15	Young
J00540+691	00:54:00.50	+69:11:01.3	9.462	M2.0 V	AF15	
J00548+275	00:54:48.03	+27:31:03.6	10.34	M4.5 V	AF15	
J00570+450	00:57:02.61	+45:05:09.9	8.101	M3.0 V	This work	
J00580+393	00:58:01.16	+39:19:11.2	9.561	M4.5 V	AF15	
J01009−044	01:00:56.44	−04:26:56.1	9.042	M4.0 V	AF15	
J01012+571	01:01:13.46	+57:08:44.4	10.05	MIII	AF15	Giant
J01013+613	01:01:20.07	+61:21:56.1	7.272	M2.0 V	This work	
J01014−010	01:01:24.66	−01:05:58.6	9.268	M3.5 V	AF15	
J01014+188	01:01:26.79	+18:53:10.5	9.625	M2.0 V	AF15	
J01025+716	01:02:32.13	+71:40:47.6	6.301	M2.5 V	This work	
J01026+623	01:02:38.96	+62:20:42.2	6.230	M1.5 V	AF15	
J01028+189	01:02:50.98	+18:56:54.4	9.514	M4.0 V	AF15	Young
J01028+470	01:02:53.43	+47:03:03.2	9.351	M1.5 V	AF15	

Table C.3: *Continued*

Karmn	RA	DEC	Jmag	SpT	Ref.[a]	Notes
J01032+712	01:03:14.43	+71:13:12.7	9.689	M4.0 V	AF15	
J01033+623	01:03:19.72	+62:21:55.7	8.611	M5.0 V	AF15	
J01048−181	01:04:53.69	−18:07:29.3	9.387	M5.0 V	This work	
J01055+153	01:05:29.75	+15:23:19.1	7.147	K7 V	AF15	
J01056+284	01:05:37.32	+28:29:34.0	9.486	M5.0 V	This work	
J01069+804	01:06:54.75	+80:27:34.4	9.350	M4.5 V	AF15	
J01074−025	01:07:27.51	−02:33:26.4	10.376	K5 V	AF15	
J01076+229E	01:07:38.52	+22:57:21.9	9.533	M3.5 V	AF15	
J01097+356	01:09:43.91	+35:37:13.8	−0.957	MIII	AF15	Giant
J01125−169	01:12:30.53	−16:59:57.0	7.258	M4.5 V	This work	
J01186−008	01:18:40.18	−00:52:27.6	8.012	K7 V	AF15	
J01214+313	01:21:27.40	+31:20:32.7	9.975	M3.5 V	AF15	
J01221+221	01:22:10.28	+22:09:03.2	8.412	M4.0 V	This work	Double or multiple
J01226+127	01:22:36.56	+12:45:03.5	7.855	K7 V	M18	
J01230−129	01:23:00.56	−12:57:29.9	7.485	M0.0 V	M18	
J01256+097	01:25:36.66	+09:45:24.4	8.952	M3.5 V	This work	
J01339−176	01:33:58.00	−17:38:23.5	8.842	M3.5 V	This work	
J01342−015	01:34:12.35	−01:34:26.0	11.722	M1.0 V	AF15	
J01356−200AB	01:35:39.84	−20:03:42.6	8.988	M2.5 V	AF15	
J01390−179AB	01:39:01.20	−17:57:02.7	6.283	M5.0 V	AF15	
J01406−081	01:40:39.60	−08:08:54.4	10.371	K5 V	AF15	
J01431+210	01:43:11.87	+21:01:10.6	9.249	M4.0 V	AF15	Double or multiple
J01433+043	01:43:20.16	+04:19:17.3	7.370	M2.5 V	This work	
J01449−010	01:44:57.00	−01:03:03.8	11.027	M2.0 V	M18	
J01466−086	01:46:36.81	−08:38:57.9	8.832	M3.5 V	This work	
J01518+644	01:51:51.08	+64:26:06.1	7.838	M2.5 V	This work	
J01541−156	01:54:07.96	−15:36:21.9	9.807	M4.0 V	AF15	
J01551−162	01:55:06.62	−16:15:52.2	9.939	K7 V	AF15	
J01562+001	01:56:14.92	+00:06:08.8	9.494	M3.0 V	AF15	
J01567+305	01:56:45.71	+30:33:28.8	10.323	M4.5 V	AF15	
J01571−102	01:57:11.10	−10:14:52.9	8.413	M0.0 V	AF15	
J01593+585	01:59:23.50	+58:31:16.2	7.790	M4.0 V	This work	Eruptive variable
J02000+135AB	02:00:02.25	+13:34:50.8	9.311	M3.5 V	AF15	
J02002+130	02:00:12.79	+13:03:11.2	7.514	M3.5 V	AF15	
J02015+637	02:01:35.33	+63:46:11.9	7.265	M2.5 V	This work	
J02019+342	02:01:58.65	+34:13:45.1	9.510	M0.5 V	AF15	
J02022+103	02:02:16.21	+10:20:13.7	9.842	M5.5 V	AF15	
J02023+012	02:02:22.38	+01:15:42.9	9.807	M2.5 V	AF15	
J02070+496	02:07:03.83	+49:38:44.1	8.366	M3.0 V	This work	
J02088+494	02:08:53.60	+49:26:56.6	8.423	M3.5 V	This work	Eruptive variable
J02100−088	02:10:03.64	−08:52:59.9	8.946	M3.0 V	AF15	
J02123+035	02:12:20.91	+03:34:31.1	6.830	M1.5 V	This work	
J02133+368AB	02:13:20.63	+36:48:50.7	9.367	M4.5 V	AF15	
J02142−039	02:14:12.51	−03:57:43.4	10.481	M5.5 V	AF15	
J02159−094ABC	02:15:58.93	−09:29:12.1	8.431	M2.5 V	AF15	Double or multiple
J02204+377	02:20:25.24	+37:47:30.7	8.952	M2.5 V	This work	
J02222+478	02:22:14.63	+47:52:48.1	6.377	M0.5 V	This work	
J02274+031	02:27:27.56	+03:10:54.8	9.978	M4.0 V	AF15	
J02285−200	02:28:31.89	−20:02:26.5	9.181	M2.5 V	AF15	
J02291+228	02:29:06.99	+22:52:01.9	8.726	K7 V	AF15	
J02336+249	02:33:37.17	+24:55:39.2	8.472	M4.0 V	This work	
J02358+202	02:35:53.28	+20:13:11.9	7.208	M2.0 V	This work	
J02362+068	02:36:15.36	+06:52:19.1	7.333	M4.0 V	AF15	
J02367+226	02:36:44.13	+22:40:26.5	10.081	M5.0 V	AF15	

Table C.3: *Continued*

Karmn	RA	DEC	Jmag	SpT	Ref.[a]	Notes
J02412−045	02:41:15.11	−04:32:17.7	9.199	M4.5 V	AF15	
J02441+492	02:44:10.25	+49:13:54.1	6.688	M1.5 V	AF15	
J02442+255	02:44:15.38	+25:31:25.0	6.752	M2.5 V	This work	Young / Eruptive variable
J02456+449	02:45:39.64	+44:56:55.7	7.818	M0.5 V	AF15	
J02479−124	02:47:55.92	−12:27:38.2	1.586	MIII	AF15	Giant
J02502+628	02:50:16.44	+62:51:19.8	9.368	M2.5 V	AF15	
J02530+168	02:53:00.85	+16:52:53.3	8.394	M7.0 V	AF15	
J02555+268	02:55:35.73	+26:52:20.9	9.561	M4.0 V	AF15	
J02558+183	02:55:48.46	+18:19:53.9	0.230	MIII	AF15	Giant
J02562+239	02:56:13.96	+23:59:10.5	9.977	M5.0 V	AF15	
J02565+554W	02:56:34.35	+55:26:14.5	7.425	M0.5 V	This work	
J02565+554E	02:56:35.07	+55:26:30.2	8.006	M2.5 V	This work	
J03026−181	03:02:38.01	−18:09:58.8	8.208	M2.5 V	AF15	
J03033−080	03:03:21.32	−08:05:15.4	9.122	M3.0 V	AF15	
J03047+617	03:04:43.35	+61:44:09.7	8.877	M3.0 V	AF15	
J03079+255	03:07:58.29	+25:32:01.3	11.25	M3.5 V	M18	
J03110−046	03:11:04.89	−04:36:35.8	9.406	M3.0 V	AF15	
J03133+047	03:13:23.00	+04:46:29.4	8.775	M5.0 V	This work	
J03147+114	03:14:47.20	+11:27:27.2	9.352	M2.0 V	AF15	Young
J03150+010	03:15:00.94	+01:03:08.4	11.622	M0.5 V	M18	
J03154+578	03:15:29.44	+57:51:33.0	11.121	M3.5 V	AF15	
J03162+581S	03:16:13.82	+58:10:02.4	7.344	M2.0 V	AF15	
J03162+581N	03:16:13.90	+58:10:07.3	7.501	M2.0 V	AF15	
J03167+389	03:16:46.13	+38:55:27.4	9.157	M3.5 V	AF15	
J03174−011	03:17:28.15	−01:07:26.5	9.730	M0.5 V	AF15	
J03179−010	03:17:55.37	−01:05:40.9	10.814	M2.0 V	AF15	
J03181+426	03:18:07.01	+42:40:09.1	9.254	M3.5 V	AF15	
J03181+382	03:18:07.42	+38:15:08.2	7.023	M1.0 V	This work	
J03194+619	03:19:28.73	+61:56:04.6	9.511	M4.0 V	AF15	
J03207+090	03:20:42.50	+09:02:09.9	11.079	M4.0 V	M18	
J03213+799	03:21:21.77	+79:58:02.2	7.704	M2.0 V	This work	
J03217−066	03:21:46.90	−06:40:24.2	7.857	M2.0 V	This work	
J03236+476	03:23:37.74	+47:37:26.5	9.483	M0.5 V	AF15	
J03236+056	03:23:39.16	+05:41:15.3	9.867	M4.5 V	AF15	
J03263+171	03:26:23.62	+17:09:31.0	9.774	M4.0 V	AF15	Double or multiple
J03275+222	03:27:30.84	+22:12:38.3	10.044	M4.5 V	AF15	
J03294+117	03:29:25.23	+11:42:11.2	9.335	M2.5 V	AF15	
J03303+346	03:30:23.32	+34:40:32.6	9.995	M4.0 V	AF15	
J03309+706	03:30:54.74	+70:41:14.6	9.487	M3.5 V	AF15	
J03319+492	03:31:56.98	+49:12:58.5	8.996	KIII	AF15	Giant
J03320+436	03:32:05.99	+43:40:01.0	9.239	K7 V	AF15	
J03325+287ABC	03:32:35.79	+28:43:55.5	9.357	M4.5 V	AF15	Young / Double or multiple
J03332+462	03:33:14.04	+46:15:19.4	8.382	M0.0 V	AF15	Young
J03354+428	03:35:28.52	+42:53:35.0	10.831	M0.5 V	AF15	
J03356−084	03:35:38.50	−08:29:22.4	10.377	M5.5 V	AF15	
J03361+313	03:36:08.68	+31:18:39.8	9.187	M4.5 V	AF15	
J03375+288	03:37:30.34	+28:52:28.3	9.471	M0.0 V	AF15	
J03375+178NAB	03:37:33.32	+17:51:14.6	9.100	M2.5 V	AF15	
J03375+178SAB	03:37:33.87	+17:51:00.5	9.186	M3.5 V	AF15	Young / Eruptive variable
J03392+565AB	03:39:15.33	+56:32:05.9	9.988	M2.5 V	AF15	
J03395+183	03:39:34.92	+18:18:51.8	9.331	M1.5 V	M18	
J03397+334	03:39:47.84	+33:28:30.7	8.967	M3.5 V	M18	
J03430+459	03:43:02.07	+45:54:18.2	9.668	M4.0 V	AF15	
J03463+262	03:46:20.12	+26:12:56.0	6.689	M0.0 V	This work	

Table C.3: *Continued*

Karmn	RA	DEC	Jmag	SpT	Ref.[a]	Notes
J03466+243AB	03:46:37.27	+24:20:36.7	10.123	K5 V	AF15	Young
J03473−019	03:47:23.33	−01:58:19.5	7.804	M3.0 V	AF15	Young
J03480+405	03:48:05.88	+40:32:22.6	9.354	M1.5 V	AF15	
J03510+142	03:51:00.79	+14:13:39.9	9.436	M4.5 V	AF15	
J03519+397	03:51:58.15	+39:46:56.8	8.277	M0.0 V	AF15	
J03531+625	03:53:10.42	+62:34:08.2	7.782	M2.5 V	This work	
J03548+163AB	03:54:53.20	+16:18:56.4	9.960	M4.0 V	AF15	Young
J03556+522	03:55:36.89	+52:14:29.1	10.885	M2.5 V	AF15	
J03565+319	03:56:33.08	+31:57:24.8	9.795	M3.5 V	AF15	Young
J03566+507	03:56:40.57	+50:42:48.2	8.145	K7 V	AF15	
J03574−011AB	03:57:28.92	−01:09:23.2	7.773	M2.5 V	AF15	
J03588+125	03:58:49.06	+12:30:24.2	9.757	M4.0 V	AF15	
J04041+307	04:04:06.16	+30:42:45.5	9.264	M1.5 V	AF15	
J04061−055	04:06:06.88	−05:34:44.4	9.128	M3.5 V	AF15	
J04079+142	04:07:54.80	+14:13:00.7	9.215	M2.5 V	AF15	
J04081+743	04:08:11.01	+74:23:01.8	9.247	M3.5 V	AF15	
J04083+691	04:08:23.72	+69:10:59.3	10.263	M4.5 V	AF15	
J04123+162AB	04:12:21.73	+16:15:03.3	9.736	M4.0 V	AF15	Young
J04153−076	04:15:21.73	−07:39:17.4	6.747	M4.5 V	AF15	Eruptive variable
J04177+410	04:17:44.31	+41:03:13.8	9.238	M3.5 V	AF15	
J04177+136AB	04:17:47.68	+13:39:42.3	9.405	M1.5 V	AF15	Young
J04191−074	04:19:06.60	−07:27:44.8	9.968	M3.5 V	AF15	
J04191+097	04:19:08.09	+09:44:48.2	9.990	M3.0 V	AF15	
J04205+815	04:20:35.05	+81:31:55.6	9.482	M3.0 V	AF15	
J04206+272	04:20:39.18	+27:17:31.7	10.497	M4.5 V	AF15	Young
J04206−168	04:20:41.34	−16:49:48.0	2.987	MIII	AF15	Giant
J04207+152AB	04:20:47.96	+15:14:09.2	9.490	M4.0 V	AF15	Young
J04224+036	04:22:25.04	+03:37:08.2	9.857	M3.5 V	AF15	Young
J04225+105	04:22:31.99	+10:31:18.8	8.471	M3.5 V	This work	
J04227+205	04:22:42.84	+20:34:12.5	10.458	M4.0 V	AF15	Young
J04229+259	04:22:59.26	+25:59:14.8	9.645	M4.5 V	AF15	
J04234+809	04:23:29.05	+80:55:10.2	9.412	M4.0 V	AF15	
J04238+149AB	04:23:50.33	+14:55:17.4	9.293	M3.5 V	AF15	Young
J04238+092AB	04:23:50.70	+09:12:19.4	9.117	M3.0 V	AF15	Young
J04247−067ABC	04:24:42.61	−06:47:31.4	9.566	M4.0 V	AF15	Young / SB
J04251+257	04:25:07.64	+25:44:57.9	11.505	M2.0 V	M18	
J04252+172ABC	04:25:13.53	+17:16:05.6	9.149	M3.5 V	AF15	Young
J04290+186	04:29:01.00	+18:40:25.5	9.571	M2.5 V	AF15	Young
J04308−088	04:30:52.03	−08:49:19.3	9.853	M4.0 V	AF15	
J04310+367	04:31:00.01	+36:47:54.8	9.445	M3.0 V	AF15	
J04311+589	04:31:11.48	+58:58:37.6	6.622	M4.0 V	This work	
J04313+241AB	04:31:23.82	+24:10:52.9	9.729	M4.5 V	AF15	Young
J04329+001S	04:32:56.24	+00:06:15.9	8.421	M0.5 V	AF15	
J04347−004	04:34:45.33	−00:26:46.4	9.307	M4.0 V	AF15	
J04359+165	04:35:57.45	+16:30:21.3		M3.0 V	M18	
J04360+188	04:36:04.17	+18:53:19.0	9.772	M2.5 V	AF15	Young
J04366+186	04:36:38.93	+18:36:56.8	9.777	M2.0 V	AF15	Young
J04373+193	04:37:21.89	+19:21:17.5	10.182	M4.0 V	AF15	Young
J04376−110	04:37:41.89	−11:02:19.8	6.943	M1.5 V	This work	
J04386−115	04:38:37.18	−11:30:14.5	8.672	M3.5 V	AF15	
J04388+217	04:38:53.53	+21:47:54.9	9.552	M3.5 V	AF15	
J04393+335	04:39:23.20	+33:31:49.4	9.919	M4.0 V	AF15	Young
J04397+098	04:39:43.26	+09:51:46.8	10.263	M3.0 V	M18	
J04398+251	04:39:48.98	+25:09:26.2	9.642	M3.5 V	AF15	

Table C.3: *Continued*

Karmn	RA	DEC	Jmag	SpT	Ref.[a]	Notes
J04413+327	04:41:23.89	+32:42:22.8	9.463	M4.0 V	AF15	
J04425+204AB	04:42:30.29	+20:27:11.5	9.396	M3.0 V	AF15	Young / SB
J04429+189	04:42:55.81	+18:57:28.6	6.462	M2.0 V	This work	
J04429+214	04:42:55.86	+21:28:23.1	7.958	M3.0 V	This work	
J04430+187AB	04:43:01.43	+18:42:41.9	7.751	K5 V	AF15	Young
J04458−144	04:45:52.73	−14:26:26.0	9.088	M4.0 V	AF15	
J04468−112AB	04:46:51.75	−11:16:47.6	8.144	M3.0 V	AF15	
J04472+206	04:47:12.25	+20:38:10.9	9.380	M5.0 V	AF15	
J04488+100	04:48:47.39	+10:03:02.6	8.127	M3.0 V	This work	
J04494+484AB	04:49:29.47	+48:28:45.9	9.059	M4.0 V	AF15	
J04496−153	04:49:36.98	−15:22:52.5	10.322	K5 V	AF15	
J04499+711	04:49:55.70	+71:09:47.0	9.633	M3.5 V	AF15	
J04520+064	04:52:05.73	+06:28:35.6	7.814	M2.5 V	This work	
J04536+623	04:53:40.12	+62:19:03.9	9.226	M3.5 V	AF15	
J04538−177	04:53:49.96	−17:46:23.6	7.413	M2.0 V	This work	
J04538+158	04:53:50.05	+15:49:15.6	9.432	M2.5 V	AF15	
J04544+650	04:54:29.82	+65:04:41.1	9.668	M4.0 V	AF15	
J04559+046	04:55:54.46	+04:40:16.4	8.501	M2.0 V	AF15	SB
J04560+432	04:56:03.54	+43:13:55.6	9.304	M4.0 V	AF15	
J04588+498	04:58:50.58	+49:50:57.3	6.925	M0.5 V	This work	
J05003+251AB	05:00:19.52	+25:07:51.0	9.410	M1.0 V	AF15	
J05019+011	05:01:56.66	+01:08:42.9	8.526	M4.0 V	AF15	Young
J05019−069	05:01:57.47	−06:56:45.9	7.617	M4.0 V	This work	
J05030+213AB	05:03:05.63	+21:22:36.2	9.750	M5.0 V	AF15	
J05032+213	05:03:16.08	+21:23:56.4	7.451	M1.5 V	AF15	SB
J05033−173	05:03:20.10	−17:22:24.5	7.819	M3.0 V	This work	
J05050+442	05:05:05.92	+44:14:03.8	9.829	M5.0 V	AF15	
J05062+046	05:06:12.93	+04:39:27.2	8.909	M4.0 V	AF15	Young
J05068+516	05:06:49.18	+51:36:34.8	7.338	K5 V	AF15	
J05072+375	05:07:14.50	+37:30:42.1	10.284	M5.0 V	AF15	
J05078+179	05:07:49.24	+17:58:58.4	8.023	M2.5 V	This work	
J05083+756	05:08:18.41	+75:38:15.5	9.391	M4.5 V	AF15	
J05127+196	05:12:42.24	+19:39:56.7	7.299	M2.0 V	This work	
J05151−073	05:15:08.05	−07:20:48.6	8.355	M1.0 V	AF15	
J05152+236	05:15:17.54	+23:36:26.1	10.186	M5.0 V	AF15	
J05173+321	05:17:19.96	+32:07:35.0	9.236	M3.5 V	AF15	
J05175+487	05:17:33.57	+48:46:14.6	9.965	M0.0 V	AF15	
J05187+464	05:18:44.55	+46:29:59.7	9.957	M4.5 V	AF15	
J05187−213	05:18:47.53	−21:23:36.5	7.850	M3.5 V	AF15	
J05195+649	05:19:31.18	+64:54:33.7	8.950	M3.5 V	AF15	
J05200−229	05:20:03.49	−22:57:03.3	9.173	M2.0 V	AF15	
J05223+305	05:22:20.53	+30:31:09.7	9.406	M3.0 V	AF15	
J05244+193	05:24:25.73	+19:22:07.0	9.464	M5.0 V	This work	
J05256−091AB	05:25:41.67	−09:09:12.3	8.454	M3.5 V	AF15	Young
J05263+038	05:26:20.30	+03:51:11.2	10.932	M1.5 V	M18	
J05280+096	05:28:00.15	+09:38:38.3	8.311	M3.5 V	This work	
J05289+125	05:28:56.50	+12:31:53.9	9.649	M4.0 V	AF15	
J05294+155E	05:29:27.04	+15:34:38.4	7.557	M0.5 V	AF15	
J05295−113	05:29:32.85	−11:19:57.3	10.130	M3.5 V	AF15	
J05300+121W	05:30:01.66	+12:07:26.6	9.653	K5 V	AF15	
J05300+121E	05:30:02.25	+12:07:34.9	10.253	M0.5 V	AF15	
J05314−036	05:31:27.35	−03:40:35.7	4.999	M1.5 V	AF15	
J05320−030AB	05:32:04.50	−03:05:29.2	7.879	M2.0 V	AF15	Young
J05322+098	05:32:14.67	+09:49:15.0	7.423	M3.5 V	This work	

Table C.3: *Continued*

Karmn	RA	DEC	Jmag	SpT	Ref.[a]	Notes
J05324−072	05:32:26.86	−07:14:19.0	7.947	M0.5 V	AF15	
J05328+338	05:32:51.95	+33:49:47.5	9.391	M3.5 V	AF15	
J05333+448	05:33:19.13	+44:48:58.8	8.197	M3.0 V	This work	
J05337+019	05:33:44.81	+01:56:43.4	7.764	M2.5 V	This work	
J05342+103S	05:34:15.08	+10:19:09.2	9.186	M4.5 V	AF15	
J05342+103N	05:34:15.14	+10:19:14.2	8.561	M3.0 V	AF15	
J05348+138	05:34:52.12	+13:52:47.2	7.781	M3.5 V	This work	
J05360−076	05:36:00.08	−07:38:58.1	8.464	M4.0 V	This work	
J05365+113	05:36:30.99	+11:19:40.2	6.126	K7−M0V	This work	
J05366+112	05:36:38.47	+11:17:48.8	8.266	M3.5 V	This work	
J05394+747	05:39:25.41	+74:46:04.9	9.330	M3.5 V	AF15	
J05415+534	05:41:30.73	+53:29:23.9	6.586	M1.0 V	AF15	Young
J05421+124	05:42:08.98	+12:29:25.3	7.124	M4.0 V	AF15	
J05424+506	05:42:25.02	+50:38:41.4	9.906	M3.0 V	AF15	
J05425+154	05:42:31.78	+15:25:01.6	9.443	M3.5 V	AF15	
J05427+026	05:42:45.50	+02:41:41.5	9.448	M3.0 V	AF15	
J05455−119	05:45:31.98	−11:58:03.5	9.590	M4.5 V	AF15	
J05456+729	05:45:38.80	+72:55:12.7	9.395	M3.0 V	AF15	
J05456+111	05:45:41.59	+11:07:48.5	9.902	M0.0 V	AF15	
J05457−223	05:45:43.22	−22:20:03.5	11.126	M3.5 V	AF15	Young
J05458+729	05:45:49.74	+72:54:07.2	9.338	M2.5 V	AF15	
J05463+012	05:46:19.38	+01:12:47.2	9.717	M2.5 V	AF15	
J05466+441	05:46:38.45	+44:07:19.8	8.459	M4.0 V	This work	
J05501+051	05:50:08.59	+05:11:53.7	9.369	M1.5 V	AF15	
J05511+122	05:51:10.40	+12:16:10.2	9.453	M4.0 V	AF15	
J05532+242	05:53:14.04	+24:15:32.9	7.485	M1.5 V		SB
J05566−103	05:56:40.66	−10:18:37.9	9.067	M3.5 V	AF15	
J05582−046	05:58:17.17	−04:38:01.3	11.113	M4.5 V	AF15	
J05588+213	05:58:53.33	+21:21:01.1	9.968	M5.0 V	AF15	
J05596+585	05:59:37.75	+58:35:35.1	7.068	M0.5 V	AF15	
J05599+585	05:59:55.69	+58:34:15.6	9.028	M4.0 V	This work	Eruptive variable
J06000+027	06:00:03.51	+02:42:23.6	6.905	M4.0 V	This work	
J06011+595	06:01:11.07	+59:35:50.8	7.465	M3.5 V	This work	
J06024+663	06:02:25.54	+66:20:40.4	9.855	M4.5 V	AF15	
J06024+498	06:02:29.18	+49:51:56.2	9.35	M5.0 V	AF15	
J06035+168	06:03:34.62	+16:51:45.7	9.387	M4.0 V	AF15	
J06035+155	06:03:34.82	+15:31:31.1	8.203	M0.0 V	AF15	
J06054+608	06:05:29.36	+60:49:23.2	9.096	M4.5 V	AF15	
J06065+045	06:06:30.57	+04:30:32.7	11.156	M3.0 V	AF15	
J06066+465	06:06:37.90	+46:33:46.3	9.231	M3.0 V	AF15	
J06075+472	06:07:31.86	+47:12:26.6	9.723	M4.5 V	AF15	Young
J06102+225	06:10:17.76	+22:34:19.9	9.876	M4.0 V	AF15	
J06103+722	06:10:18.26	+72:12:00.6	9.272	M2.5 V	AF15	
J06103+821	06:10:19.78	+82:06:25.7	6.869	M2.5 V	This work	
J06145+025	06:14:34.91	+02:30:27.4	9.296	M3.0 V	AF15	
J06151−164	06:15:11.99	−16:26:15.2	9.283	M4.0 V	AF15	
J06171+051AB	06:17:10.65	+05:07:02.4	9.088	M3.5 V	AF15	
J06185+250	06:18:34.81	+25:03:06.4	9.954	M4.0 V	AF15	
J06236−096AB	06:23:38.47	−09:38:51.7	9.819	M3.5 V	AF15	
J06238+456	06:23:51.24	+45:40:05.1	10.348	M5.0 V	AF15	
J06246+234	06:24:41.32	+23:25:58.6	8.662	M4.0 V	AF15	Young
J06298−027AB	06:29:50.28	−02:47:45.5	9.468	M4.0 V	AF15	SB
J06307+397	06:30:47.24	+39:47:37.1	9.405	M2.0 V	AF15	
J06313+006	06:31:23.74	+00:36:44.5	11.077	M1.5 V	AF15	

Table C.3: *Continued*

Karmn	RA	DEC	Jmag	SpT	Ref.[a]	Notes
J06314−016	06:31:28.52	−01:41:20.8	10.551	M1.5 V	AF15	
J06323−097	06:32:20.29	−09:43:29.0	9.848	M4.5 V	AF15	
J06325+641	06:32:30.61	+64:06:20.7	9.811	M4.0 V	AF15	
J06332+054	06:33:12.10	+05:27:53.2	8.701	M2.0 V	AF15	
J06354−040AB	06:35:29.87	−04:03:18.5	9.272	M5.5 V	AF15	
J06361+201	06:36:11.93	+20:08:14.2	9.434	M2.5 V	AF15	
J06367+378	06:36:43.22	+37:51:31.7	11.435	M3.5 V	AF15	
J06371+175	06:37:10.92	+17:33:52.7	6.674	M0.0 V	This work	
J06401−164	06:40:08.61	−16:27:26.9	9.121	M2.5 V	AF15	
J06421+035	06:42:11.18	+03:34:52.7	8.166	M3.0 V	This work	
J06435+166	06:43:34.77	+16:41:35.0	9.776	M4.5 V	AF15	
J06461+325	06:46:07.50	+32:33:14.9	8.992	M1.0 V	AF15	
J06474+054	06:47:27.51	+05:24:28.2	9.453	M4.0 V	AF15	
J06489+211	06:48:55.23	+21:08:03.9	9.367	M2.5 V	AF15	
J06509−091	06:50:59.48	−09:10:50.6	9.400	M3.5 V	AF15	
J06522+627	06:52:16.60	+62:46:58.7	9.416	M3.5 V	AF15	
J06522+179	06:52:16.82	+17:56:19.3	9.682	M0.0 V	AF15	
J06523−051SAB	06:52:18.05	−05:11:24.2	6.579	M2.0 V	AF15	
J06523−051N	06:52:18.06	−05:10:25.3	5.013	K5 V	AF15	
J06548+332	06:54:49.03	+33:16:05.9	6.104	M3.0 V	AF15	
J06565+440	06:56:30.94	+44:01:56.8	9.923	M4.5 V	AF15	
J06574+740	06:57:26.16	+74:05:26.5	8.926	M3.5 V	This work	
J07001−190	07:00:06.83	−19:01:23.6	9.029	M5.0 V	AF15	
J07009−023	07:00:59.78	−02:21:33.0	9.301	M3.0 V	AF15	
J07031+836	07:03:10.98	+83:38:58.9	11.113	M3.5 V	AF15	
J07033+346	07:03:23.17	+34:41:51.0	8.773	M4.0 V	This work	
J07041+752	07:04:09.48	+75:14:36.6	11.175	M4.0 V	M18	
J07044+682	07:04:25.94	+68:17:19.6	8.170	M2.5 V	This work	
J07051−101	07:05:11.95	−10:07:52.8	10.196	M5.0 V	AF15	
J07105−087	07:10:31.47	−08:42:48.5	9.054	M3.5 V	AF15	
J07105+283	07:10:34.17	+28:22:42.1	8.917	M0.0 V	AF15	
J07111−035	07:11:08.96	−03:34:11.6	9.097	M0.5 V	AF15	
J07111+434AB	07:11:11.38	+43:29:59.0	9.979	M5.5 V	AF15	
J07172−050	07:17:17.06	−05:01:03.1	8.873	M3.5 V	AF15	
J07182+137	07:18:12.91	+13:42:16.7	9.361	M3.5 V	AF15	
J07191+667	07:19:09.18	+66:44:29.8	8.882	M0.0 V	AF15	
J07195+328	07:19:31.27	+32:49:48.3	7.184	M0.0 V	AF15	
J07219−222	07:21:57.47	−22:16:38.4	10.001	M3.5 V	AF15	
J07274+052	07:27:24.50	+05:13:32.9	5.714	M3.5 V	AF15	
J07287−032	07:28:45.41	−03:17:52.4	7.544	M3.0 V	This work	
J07310+460	07:31:01.29	+46:00:26.6	9.948	M4.0 V	AF15	Eruptive variable
J07319+362N	07:31:57.35	+36:13:47.8	7.571	M3.5 V	AF15	Young
J07319+362SAB	07:31:57.74	+36:13:10.2	6.771	M2.5 V	AF15	Young
J07321−088	07:32:07.26	−08:53:01.7	8.034	K5 V	AF15	
J07324−130	07:32:28.40	−13:04:09.0	9.893	M0.0 V	AF15	
J07349+147	07:34:56.33	+14:45:54.5	7.287	M3.0 V	This work	Double or multiple
J07353+548	07:35:21.88	+54:50:59.0	7.772	M2.0 V	This work	
J07359+785	07:35:58.15	+78:32:52.9	9.214	M3.0 V	AF15	
J07361−031	07:36:07.09	−03:06:38.5	6.791	M1.0 V	AF15	Young
J07365−006	07:36:30.28	−00:39:35.2	9.422	M3.5 V	AF15	
J07366+440	07:36:39.28	+44:04:48.9	9.961	M3.5 V	AF15	
J07393+021	07:39:23.04	+02:11:01.2	6.769	M0.0 V	This work	
J07420+142	07:42:03.23	+14:12:30.5	1.588	MIII	AF15	Giant

Table C.3: *Continued*

Karmn	RA	DEC	Jmag	SpT	Ref.[a]	Notes
J07429−107	07:42:55.66	−10:43:45.1	9.519	M2.5 V	AF15	
J07446+035	07:44:40.18	+03:33:09.0	6.581	M4.5 V	This work	
J07467+574	07:46:42.03	+57:26:53.4	9.699	M4.5 V	AF15	
J07470+760	07:47:05.83	+76:03:19.6	9.976	M4.0 V	AF15	
J07472+503	07:47:13.85	+50:20:38.7	8.855	M3.5 V	This work	
J07497−033	07:49:42.16	−03:20:33.8	8.891	M3.5 V	AF15	
J07498−032	07:49:50.88	−03:17:19.5	8.039	M3.5 V	AF15	
J07523+162	07:52:23.90	+16:12:15.7	10.879	M6.0 V	AF15	Young
J07545−096	07:54:32.73	−09:41:47.8	9.697	M3.5 V	AF15	
J07545+085	07:54:34.12	+08:32:25.3	8.538	M2.5 V	AF15	
J07558+833	07:55:53.97	+83:23:05.0	8.744	M4.5:V	AF15	Eruptive variable
J07582+413	07:58:12.70	+41:18:13.5	7.734	M3.5 V	This work	
J07591+173	07:59:07.19	+17:19:47.4	9.468	M4.0 V	AF15	
J08025−130	08:02:32.91	−13:05:29.1	9.421	M2.5 V	AF15	
J08031+203AB	08:03:10.18	+20:22:15.5	9.242	M3.5 V	AF15	
J08069+422	08:06:55.32	+42:17:33.4	9.724	M4.0 V	AF15	
J08080+719	08:08:00.30	+71:55:16.8	10.878	M2.0 V	M18	
J08082+211N	08:08:13.17	+21:06:18.3	6.860	K7 V	AF15	
J08082+211SAB	08:08:13.59	+21:06:09.4	7.336	M3.0 V	AF15	SB
J08104−111	08:10:26.45	−11:09:37.1	8.287	M1.0 V	AF15	
J08105−138AB	08:10:34.29	−13:48:51.5	8.276	M2.5 V	AF15	
J08107+798	08:10:46.23	+79:52:52.2	12.541	K5 V	M18	
J08117+531	08:11:47.60	+53:11:51.4	9.293	M2.5 V	AF15	
J08143+630	08:14:18.97	+63:04:39.8	9.910	M1.5 V	AF15	
J08161+013	08:16:07.98	+01:18:09.2	6.625	M2.0 V	AF15	
J08161+570	08:16:10.26	+57:04:48.3	10.562	M2.5 V	M18	
J08283+553	08:28:18.81	+55:22:42.4	9.235	M2.5 V	AF15	
J08286+660	08:28:41.22	+66:02:23.9	9.197	M4.0 V	AF15	
J08298+267	08:29:49.50	+26:46:34.8	8.235	M6.5 V	AF15	Young
J08315+730	08:31:30.12	+73:03:45.9	8.780	M4.0 V	This work	
J08353+141	08:35:19.93	+14:08:33.4	9.163	M4.5 V	AF15	
J08358+680	08:35:49.16	+68:04:09.7	7.861	M2.0 V	This work	
J08375+035	08:37:30.21	+03:33:45.8	9.853	M4.0 V	AF15	
J08386−028	08:38:37.29	−02:48:58.2	10.568	K5 V	AF15	
J08394−028	08:39:24.53	−02:49:09.9	12.142	M0.5 V	AF15	
J08402+314	08:40:15.97	+31:27:06.9	8.122	M3.5 V	This work	
J08423−048	08:42:23.21	−04:53:54.8	9.047	M3.0 V	AF15	
J08449−066AB	08:44:55.67	−06:37:25.9	9.325	M3.5 V	AF15	
J08484+207	08:48:24.92	+20:42:18.8	11.332	M1.5 V	M18	
J08526+283	08:52:40.85	+28:18:58.9	8.560	M4.5 V	AF15	
J08531−202	08:53:10.91	−20:17:17.3	9.323	M3.0 V	AF15	
J08563−044	08:56:18.80	−04:24:55.2	9.775	M1.0 V	AF15	
J08572+194	08:57:15.41	+19:24:17.8	9.447	M3.5 V	AF15	
J08590+364	08:59:05.48	+36:26:32.6	8.846	M0.5 V	AF15	
J08595+537	08:59:35.93	+53:43:50.6	9.014	M3.5 V	AF15	
J08599+042	08:59:57.55	+04:17:55.3	9.934	M1.0 V	AF15	
J09003+218	09:00:23.59	+21:50:05.4	9.436	M6.5 V	AF15	
J09005+465	09:00:32.54	+46:35:11.8	8.604	M4.5 V	This work	
J09008+237	09:00:53.22	+23:46:58.7	11.396	M2.5 V	AF15	
J09023+177	09:02:23.08	+17:46:32.6	9.645	M4.0 V	AF15	
J09028+680	09:02:52.85	+68:03:46.4	8.453	M3.5 V	This work	
J09028+060	09:02:53.20	+06:02:09.6	11.259	M1.5 V	AF15	
J09040−159	09:04:05.55	−15:55:18.4	9.156	M2.5 V	AF15	

Table C.3: *Continued*

Karmn	RA	DEC	Jmag	SpT	Ref.[a]	Notes
J09045+164AB	09:04:31.04	+16:25:01.2	9.097	K5 V	AF15	
J09058+555	09:05:51.18	+55:32:18.4	11.491	M3.5 V	AF15	
J09091+227	09:09:07.99	+22:47:41.3	10.474	M4.5 V	AF15	
J09115+126	09:11:31.95	+12:37:23.7	9.408	M2.5 V	AF15	
J09143+526	09:14:22.98	+52:41:12.5	4.889	M0.0 V	AF15	
J09144+526	09:14:24.86	+52:41:11.8	4.779	M0.0 V	AF15	
J09151+233	09:15:10.12	+23:21:33.1	9.144	M0.0 V	AF15	
J09156−105AB	09:15:36.43	−10:35:47.0	8.605	M5.0 V	AF15	
J09201+037	09:20:10.87	+03:47:25.8	9.310	M3.5 V	AF15	
J09206−169	09:20:39.99	−16:54:58.5	9.569	M0.0 V	AF15	
J09212+603	09:21:17.66	+60:21:46.6	9.132	M1.5 V	AF15	
J09218−023	09:21:48.13	−02:19:43.4	8.441	M2.5 V	AF15	
J09243+063	09:24:23.86	+06:22:41.8	10.603	M4.0 V	AF15	Double or multiple
J09248+306	09:24:50.83	+30:41:37.3	9.490	M3.5 V	AF15	Young
J09256+634	09:25:40.33	+63:29:19.7	9.818	M4.5 V	AF15	
J09301−009	09:30:08.61	−00:57:59.0	8.763	M0.5 V	AF15	
J09308+024	09:30:50.85	+02:27:20.2	9.415	M4.0 V	AF15	
J09328+269	09:32:48.27	+26:59:44.3	10.356	M5.5 V	AF15	Young
J09351−103	09:35:11.85	−10:18:33.8	9.081	K5 V	AF15	
J09362+375	09:36:15.93	+37:31:45.7	8.085	M0.0 V	AF15	Young / SB
J09394+146	09:39:29.94	+14:38:49.8	9.393	M3.5 V	AF15	
J09449−123	09:44:54.22	−12:20:54.4	8.496	M5.0 V	AF15	
J09488+156	09:48:50.20	+15:38:44.9	9.303	M3.0 V	AF15	
J09526−156	09:52:41.77	−15:36:13.8	9.320	M3.5 V	AF15	
J09538−073	09:53:51.71	−07:20:07.8	7.829	M0.5 V	AF15	
J09589+059	09:58:56.51	+05:58:00.1	9.937	M4.5 V	AF15	
J09597+721	09:59:45.35	+72:11:59.8	9.059	M3.5 V	AF15	
J10008+319	10:00:50.31	+31:55:46.0	10.261	M6.0 V	AF15	
J10020+697	10:02:05.80	+69:45:29.4	9.768	M4.0 V	AF15	
J10028+484	10:02:49.36	+48:27:33.4	9.963	M5.5 V	AF15	
J10063−064	10:06:20.57	−06:26:08.8	13.257	M4.5 V	AF15	
J10068−127	10:06:52.11	−12:46:54.3	9.749	M4.5 V	AF15	
J10098−007	10:09:51.22	−00:46:18.9	9.010	K5 V	AF15	
J10120−026AB	10:12:04.66	−02:41:04.5	7.021	M2.5 V	AF15	
J10130+233	10:13:00.26	+23:20:50.5	9.194	M3.5 V	AF15	
J10148+213	10:14:53.16	+21:23:46.4	9.725	M4.5 V	AF15	
J10155−164	10:15:35.40	−16:28:23.6	9.363	M4.0 V	AF15	
J10196+198AB	10:19:36.35	+19:52:12.2	5.449	M3.0 V	AF15	Young
J10200+289	10:20:00.88	+28:57:13.1	9.159	M3.0 V	AF15	
J10238+438	10:23:51.85	+43:53:33.2	10.039	M5.0 V	AF15	
J10240+366	10:24:05.07	+36:39:32.6	9.429	M3.5 V	AF15	
J10278+028	10:27:49.66	+02:51:37.0	9.438	M3.5 V	AF15	
J10304+559	10:30:25.31	+55:59:56.9	6.119	K7 V	AF15	
J10359+288	10:35:57.25	+28:53:31.7	9.245	M3.0 V	AF15	Young
J10368+509	10:36:48.12	+50:55:04.1	9.866	M4.5 V	AF15	
J10430−092AB	10:43:02.93	−09:12:41.1	9.667	M5.5 V	AF15	
J10443+124	10:44:18.83	+12:25:11.8	9.422	M3.5 V	AF15	
J10482−113	10:48:12.58	−11:20:08.2	8.857	M6.5 V	AF15	
J10508+068	10:50:52.01	+06:48:29.3	7.319	M4.0 V	AF15	Young
J10546−073	10:54:41.98	−07:18:32.7	8.877	M4.0 V	AF15	
J10560+061	10:56:01.47	+06:11:07.6	0.434	MIII	AF15	Giant
J10563+042	10:56:22.25	+04:15:46.0	9.179	M2.5 V	AF15	
J10564+070	10:56:28.86	+07:00:52.8	7.085	M6.0 V	AF15	
J10584−107	10:58:28.00	−10:46:30.5	9.512	M5.0 V	AF15	

Table C.3: *Continued*

Karmn	RA	DEC	Jmag	SpT	Ref.[a]	Notes
J11018−024	11:01:49.67	−02:29:04.4	1.781	MIII	AF15	Giant
J11030+037	11:03:04.27	+03:44:22.6	9.307	M2.5 V	AF15	
J11033+359	11:03:20.24	+35:58:11.8	4.203	M1.5 V	AF15	
J11046−042SAB	11:04:40.97	−04:13:24.7	7.272	M0.5 V	AF15	Young
J11054+435	11:05:29.03	+43:31:35.7	5.538	M1.0 V	AF15	
J11055+435	11:05:31.33	+43:31:17.1	8.742	M5.5 V	AF15	
J11075+437	11:07:32.08	+43:45:56.4	9.941	M3.0 V	AF15	
J11151+734N	11:15:11.06	+73:28:36.0	7.880	M2.5 V	AF15	
J11151+734S	11:15:11.98	+73:28:30.8	5.776	K5 V	AF15	
J11201−104AB	11:20:06.10	−10:29:46.8	7.814	M2.0 V	AF15	
J11201+301	11:20:11.19	+30:07:13.7	4.339	MIII	AF15	Giant
J11214−204S	11:21:26.56	−20:27:09.5	6.638	M2.5 V	AF15	
J11214−204N	11:21:26.63	−20:27:13.5	6.097	K7 V	AF15	
J11218+181	11:21:49.13	+18:11:28.0	7.653	M0.0 V	AF15	
J11240+381	11:24:04.35	+38:08:10.9	9.928	M4.5 V	AF15	
J11306−080	11:30:41.79	−08:05:42.6	8.033	M3.5 V	AF15	
J11312+631	11:31:13.07	+63:09:27.2	7.397	K7 V	AF15	
J11378+418	11:37:49.92	+41:49:59.5	11.040	M2.0 V	AF15	
J11403+095	11:40:20.84	+09:30:45.4	10.115	M1.5 V	AF15	
J11421+267	11:42:10.96	+26:42:25.1	6.900	M2.5 V	AF15	
J11451+183	11:45:11.92	+18:20:58.7	9.162	M4.0 V	AF15	
J11458+065	11:45:51.56	+06:31:45.6	1.176	MIII	AF15	Giant
J11472+770	11:47:12.64	+77:02:36.0	9.203	K7 V	AF15	
J11474+667	11:47:28.58	+66:44:02.6	9.684	M5.0 V	AF15	
J11485+076	11:48:35.49	+07:41:40.4	9.476	M3.5 V	AF15	
J11511+352	11:51:07.37	+35:16:18.9	6.419	M1.5 V	AF15	
J11522+100	11:52:17.93	+10:00:39.2	11.418	M4.0 V	AF15	
J11549−021	11:54:56.93	−02:06:09.2	9.547	M3.0 V	AF15	
J12025+084	12:02:33.65	+08:25:50.6	10.74	M1.5 V	AF15	
J12049+174	12:04:56.11	+17:28:11.9	9.793	M3.5 V	AF15	
J12069+058	12:06:56.94	+05:48:09.3	8.582	K5 V	AF15	
J12088+217	12:08:55.41	+21:47:31.6	11.153	M0.5 V	AF15	
J12093+210	12:09:21.82	+21:03:07.7	9.472	M2.5 V	AF15	
J12104−131	12:10:28.34	−13:10:23.5	9.292	M4.5 V	AF15	
J12124+121	12:12:26.06	+12:11:38.1	9.391	M2.0 V	AF15	
J12162+508	12:16:15.06	+50:53:37.7	9.291	M4.0 V	AF15	Double or multiple
J12228−040	12:22:50.62	−04:04:46.2	9.662	M4.5 V	AF15	
J12322+454	12:32:14.39	+45:29:50.4	4.809	MIII	AF15	Giant
J12349+322	12:34:54.01	+32:14:27.9	9.459	M3.5 V	AF15	
J12364+352	12:36:28.70	+35:12:00.8	9.113	M4.5 V	AF15	
J12368−019	12:36:52.15	−01:59:00.7	9.440	M3.5 V	AF15	
J12372+358	12:37:15.47	+35:49:17.7	11.353	M1.5 V	AF15	
J12417+567	12:41:47.37	+56:45:13.8	9.483	M3.5 V	AF15	
J12440−111	12:44:00.76	−11:10:30.2	9.516	M4.5 V	AF15	
J12456+271	12:45:37.00	+27:07:43.9	5.090	MIII	AF15	Giant
J12470+466	12:47:01.02	+46:37:33.4	8.104	M2.5 V	AF15	
J12488+120	12:48:53.45	+12:04:32.7	11.40	M4.5 V	AF15	
J12533−053	12:53:19.44	−05:19:52.3	8.919	M3.0 V	AF15	
J12533+466	12:53:20.03	+46:39:22.9	3.360	MIII	AF15	Giant
J12549−063	12:54:55.14	−06:20:03.8	11.383	M4.5 V	AF15	
J12593−001	12:59:18.25	−00:10:33.9	8.788	M4.0 V	AF15	
J13027+415	13:02:47.52	+41:31:09.9	9.033	M3.5 V	AF15	
J13088−015	13:08:51.24	−01:31:07.6	8.920	M3.0 V	AF15	
J13102+477	13:10:12.69	+47:45:19.0	9.584	M5.0 V	AF15	

Table C.3: *Continued*

Karmn	RA	DEC	Jmag	SpT	Ref.[a]	Notes
J13113+096	13:11:22.44	+09:36:13.2	9.676	M0.0 V	AF15	
J13143+133AB	13:14:20.39	+13:20:01.2	9.754	M6.0 V	AF15	Young
J13167−123	13:16:45.47	−12:20:20.4	9.489	M3.5 V	AF15	
J13168+170	13:16:51.56	+17:01:00.1	6.532	M0.5 V	AF15	
J13179+362	13:17:58.40	+36:17:57.4	8.112	M1.0 V	AF15	
J13182+733	13:18:13.52	+73:22:07.4	9.541	M3.5 V	AF15	
J13247−050	13:24:46.48	−05:04:19.4	9.465	M4.0 V	AF15	
J13251−114	13:25:11.72	−11:26:36.9	9.156	M3.0 V	AF15	
J13253+426	13:25:23.51	+42:41:29.6	9.081	K7 V	AF15	
J13260+275	13:26:02.68	+27:35:02.1	9.249	M3.0 V	AF15	
J13294−143	13:29:24.08	−14:22:12.3	9.061	M3.5 V	AF15	
J13312+589	13:31:12.51	+58:57:19.1	10.951	M2.5 V	AF15	
J13314−079	13:31:29.79	−07:59:59.4	9.595	M0.0 V	AF15	
J13321−112	13:32:06.89	−11:16:40.7	9.451	M0.0 V	AF15	
J13326+309	13:32:39.08	+30:59:06.5	9.620	M4.5 V	AF15	
J13335+704	13:33:33.72	+70:29:41.3	9.227	M3.5 V	AF15	
J13386−115	13:38:40.87	−11:32:07.8	9.714	M4.5 V	AF15	
J13394+461AB	13:39:24.11	+46:11:11.5	7.054	M1.5 V	AF15	
J13413−091	13:41:21.22	−09:07:17.1	9.444	M2.5 V	AF15	
J13414+489	13:41:27.66	+48:54:45.8	9.002	M3.5 V	AF15	
J13474+063	13:47:28.79	+06:18:56.4	7.764	K7 V	AF15	
J13503−216	13:50:23.77	−21:37:19.3	9.458	M3.5 V	AF15	
J13537+521AB	13:53:45.89	+52:10:29.9	9.128	M3.5 V	AF15	
J13551−079	13:55:10.84	−07:56:59.0	8.728	M0.0 V	AF15	
J13555−073	13:55:35.12	−07:23:16.5	8.813	M3.0 V	AF15	
J13582−120	13:58:16.22	−12:02:59.2	9.728	M4.5 V	AF15	
J13583−132	13:58:19.56	−13:16:24.8	9.488	M4.0 V	AF15	
J13587+465	13:58:45.70	+46:35:46.6	4.118	MIII	AF15	Giant
J14019+432	14:01:58.79	+43:16:42.7	9.281	M2.5 V	AF15	
J14102−180	14:10:12.69	−18:01:16.3	10.028	M2.5 V	AF15	
J14159−110	14:15:54.17	−11:02:44.6	9.000	M1.5 V	AF15	
J14171+088	14:17:07.31	+08:51:36.3	9.109	M4.5 V	AF15	
J14175+025	14:17:30.21	+02:33:43.6	9.274	M3.0 V	AF15	
J14194+029	14:19:29.58	+02:54:36.5	9.954	M5.0 V	AF15	
J14195−051	14:19:35.85	−05:09:08.0	10.486	M4.0 V	AF15	
J14215−079	14:21:34.06	−07:55:16.6	9.456	M4.0 V	AF15	
J14227+164	14:22:43.41	+16:24:46.4	10.303	M5.0 V	AF15	
J14244+602	14:24:27.44	+60:15:17.0	9.734	M2.0 V	AF15	
J14251+518	14:25:11.60	+51:49:53.6	7.883	M2.5 V	AF15	
J14255−118	14:25:34.13	−11:48:51.5	9.353	M4.0 V	AF15	
J14312+754	14:31:13.49	+75:26:42.4	9.792	M4.0 V	AF15	
J14336+093	14:33:39.86	+09:20:09.5	10.233	M3.5 V	AF15	
J14415+136	14:41:30.25	+13:37:36.2	10.348	M1.0 V	AF15	
J14446−222	14:44:40.13	−22:14:45.5	10.569	M4.5 V	AF15	
J14472+570	14:47:13.54	+57:01:55.1	9.914	M4.0 V	AF15	
J14480+384	14:48:01.43	+38:27:58.6	7.230	K7 V	AF15	
J14485+101	14:48:33.16	+10:06:57.4	9.475	M3.5 V	AF15	
J14492+498	14:49:14.77	+49:49:39.1	10.238	M1.5 V	AF15	
J14501+323	14:50:11.12	+32:18:17.3	9.144	M3.5 V	AF15	
J14544+161ABC	14:54:29.23	+16:06:04.0	6.633	M1.0 V	AF15	
J14595+454	14:59:30.59	+45:26:52.9	8.099	K7 V	AF15	
J15079+762	15:07:57.24	+76:13:59.1	9.235	M4.5 V	AF15	Young
J15081+623	15:08:11.93	+62:21:53.6	9.296	M4.0 V	AF15	
J15118+395	15:11:51.45	+39:33:02.4	9.873	M2.5 V	AF15	

Table C.3: *Continued*

Karmn	RA	DEC	Jmag	SpT	Ref.[a]	Notes
J15131+181	15:13:06.64	+18:08:43.9	11.016	M2.0 V	AF15	
J15142−099	15:14:16.90	−09:58:38.7	9.665	M4.0 V	AF15	
J15147+645	15:14:46.81	+64:33:44.0	9.785	M3.5 V	AF15	Double or multiple
J15151+333	15:15:07.06	+33:18:03.3	9.207	M2.0 V	AF15	
J15157−074	15:15:43.72	−07:25:20.8	8.566	M4.0 V	AF15	
J15164+167	15:16:25.29	+16:47:41.5	7.823	K5 V	AF15	
J15197+046	15:19:45.85	+04:39:34.5	9.546	M4.0 V	AF15	
J15204+001	15:20:28.30	+00:11:26.9	9.426	M0.0 V	AF15	
J15210+255	15:21:04.80	+25:33:30.4	8.458	K7 V	AF15	
J15238+584	15:23:51.44	+58:28:06.4	9.905	M4.0 V	AF15	
J15277−090	15:27:45.07	−09:01:31.9	10.552	M4.5 V	AF15	
J15290+467AB	15:29:02.97	+46:46:24.0	9.942	M4.5 V	AF15	
J15291+574	15:29:09.36	+57:24:41.8	8.826	M1.0 V	AF15	
J15305+094	15:30:30.33	+09:26:01.4	9.569	M5.5 V	AF15	
J15340+513	15:34:03.87	+51:22:02.4	9.370	M4.5 V	AF15	
J15354+600	15:35:25.67	+60:05:07.7	9.270	M3.5 V	M18	
J15386+371	15:38:37.08	+37:07:24.8	9.979	M3.5 V	AF15	
J15430−130	15:43:05.74	−13:02:52.5	10.244	M1.5 V	AF15	
J15474+451	15:47:27.44	+45:07:51.2	9.082	M4.0 V	AF15	Eruptive variable
J15476+226	15:47:40.71	+22:41:16.5	9.543	M4.5 V	AF15	
J15480+043	15:48:02.80	+04:21:39.4	9.058	M2.5 V	AF15	
J15481+015	15:48:09.30	+01:34:36.0	9.298	M2.5 V	AF15	
J15499+796	15:49:55.18	+79:39:51.7	9.721	M5.0 V	AF15	
J15552−101	15:55:14.47	−10:10:23.2	8.477	M2.5 V	AF15	
J15557−103	15:55:42.34	−10:20:01.6	9.395	M3.5 V	AF15	
J15558−118	15:55:52.19	−11:54:19.5	8.978	M3.0 V	AF15	
J15569+376	15:56:58.24	+37:38:13.8	9.417	M2.5 V	AF15	
J15578+090	15:57:48.27	+09:01:09.9	9.282	M4.0 V	AF15	
J16023+036	16:02:16.91	+03:38:41.2	10.347	M1.5 V	AF15	
J16042+235	16:04:13.22	+23:31:38.7	9.971	M5.0 V	AF15	
J16048+391	16:04:50.93	+39:09:36.0	9.903	M4.0 V	AF15	
J16120+033N	16:12:05.04	+03:18:53.3	9.957	M3.5 V	AF15	
J16139+337AB	16:13:56.31	+33:46:24.4	8.598	M2.5 V	AF15	
J16148+606AB	16:14:52.97	+60:38:27.8	9.818	M3.0 V	AF15	
J16157+586	16:16:42.21	+58:39:43.3	10.181	M5.0 V	AF15	
J16167+672S	16:16:42.80	+67:14:19.7	5.779	M0.0 V	AF15	
J16167+672N	16:16:45.37	+67:15:22.4	6.908	M2.5 V	This work	
J16183+757	16:18:20.95	+75:43:08.1	10.841	M4.0 V	AF15	
J16243+199	16:24:22.72	+19:59:22.6	9.321	M3.0 V	AF15	
J16254+543	16:25:24.59	+54:18:14.9	6.608	M1.5 V	AF15	
J16255+260	16:25:32.35	+26:01:37.9	8.403	M2.5 V	This work	
J16269+149	16:26:54.41	+14:57:50.3	9.745	M4.0 V	AF15	
J16276−035AB	16:27:39.16	−03:35:03.3	8.653	K5 V	AF15	
J16299+048	16:29:54.66	+04:53:25.4	9.150	M3.0 V	AF15	
J16313+408	16:31:18.79	+40:51:51.6	9.461	M5.0 V	This work	
J16314+471	16:31:28.06	+47:10:21.2	9.397	M3.5 V	AF15	
J16330+031	16:33:02.79	+03:11:37.2	10.625	M3.0 V	AF15	
J16354+350	16:35:27.41	+35:00:57.7	8.615	M4.0 V	This work	
J16354−039	16:35:29.03	−03:57:57.2	11.086	sdM0	AF15	
J16365+287	16:36:30.30	+28:46:42.2	9.452	M3.5 V	AF15	
J16459+609	16:45:55.03	+60:57:04.0	9.393	M3.5 V	AF15	
J16462+164	16:46:13.72	+16:28:40.7	7.951	M3.0 V	This work	
J16465+345	16:46:31.55	+34:34:55.5	10.533	M6.0 V	AF15	
J16480+453	16:48:04.54	+45:22:43.0	9.354	M4.0 V	AF15	

Table C.3: *Continued*

Karmn	RA	DEC	Jmag	SpT	Ref.[a]	Notes
J16528+610	16:52:49.48	+63:04:39.0	9.592	M4.5 V	AF15	
J16536+560	16:53:39.16	+56:03:27.3	9.859	M3.5 V	AF15	
J16543+256	16:54:19.13	+25:37:36.4	9.387	M3.0 V	AF15	
J16555−083	16:55:35.29	−08:23:40.1	9.776	M7.0 V	AF15	
J16570−043	16:57:05.71	−04:20:56.0	7.971	M3.5 V	This work	
J16581+257	16:58:08.85	+25:44:39.2	6.448	M1.0 V	This work	
J16591+209	16:59:09.63	+20:58:16.0	8.338	M3.0 V	This work	
J17011+555	17:01:11.54	+55:35:00.4	9.152	M2.5 V	AF15	
J17017+741	17:01:45.90	+74:11:51.3	9.435	M3.5 V	AF15	
J17052−050	17:05:13.84	−05:05:38.6	6.780	M1.5 V	AF15	
J17062+646	17:06:17.67	+64:38:08.8	9.381	M3.0 V	AF15	
J17071+215	17:07:07.52	+21:33:14.4	7.875	M2.5 V	This work	
J17094+391	17:09:26.01	+39:09:38.5	9.842	M3.0 V	AF15	
J17115+384	17:11:34.72	+38:26:34.1	7.630	M3.0 V	This work	
J17126−099	17:12:40.74	−09:54:12.1	6.192	MIII	AF15	Giant
J17140+176	17:14:01.46	+17:38:55.2	9.283	M2.5 V	AF15	
J17154+308	17:15:28.04	+30:52:22.3	9.454	M2.5 V	AF15	
J17163−053	17:16:20.64	−05:23:51.3	8.697	M4.0 V	AF15	
J17166+080	17:16:40.98	+08:03:30.3	7.933	M1.5 V	This work	
J17167+115	17:16:47.80	+11:33:52.4	9.799	M4.0 V	AF15	
J17176+524	17:17:38.57	+52:24:22.7	9.768	M3.5 V	AF15	
J17198+417	17:19:52.67	+41:42:51.1	7.712	M2.0 V	This work	
J17198+265	17:19:52.98	+26:30:02.6	8.229	M4.5 V	AF15	Young
J17199+265	17:19:54.22	+26:30:03.0	7.273	M3.5 V	AF15	Young
J17199+242	17:19:59.48	+24:12:05.5	9.747	M4.5 V	AF15	Eruptive variable
J17216−171	17:21:39.95	−17:11:28.8	6.153	MIII	AF15	Giant
J17239+136	17:23:56.78	+13:38:20.5	9.504	M4.0 V	AF15	
J17246+617	17:24:39.94	+61:47:50.8	9.449	M3.0 V	AF15	
J17265−227	17:26:35.35	−22:44:02.1	9.555	M2.5 V	AF15	
J17267−050	17:26:46.79	−05:00:35.6	9.480	M2.5 V	AF15	
J17270+422	17:27:03.10	+42:14:07.9	8.498	K5 V	AF15	
J17281−017	17:28:11.05	−01:43:56.9	9.889	M4.0 V	AF15	
J17299−209	17:29:58.62	−20:59:24.2	9.781	M3.0 V	AF15	
J17301+546	17:30:06.15	+54:39:31.9	9.044	M3.5 V	AF15	
J17303+055	17:30:22.73	+05:32:54.7	6.240	M0.5 V	This work	
J17304+337	17:30:26.73	+33:44:52.3	9.456	M3.5 V	AF15	
J17338+169	17:33:53.15	+16:55:12.9	8.895	M5.5 V	This work	
J17355+616	17:35:34.46	+61:40:54.0	6.884	M0.5 V	This work	
J17364+683	17:36:25.94	+68:20:22.0	5.335	M3.0 V	AF15	
J17378+185	17:37:53.30	+18:35:29.5	6.360	M0.5 V	This work	
J17386+612	17:38:40.92	+61:13:59.3	10.245	M4.5 V	This work	Eruptive variable
J17412+724	17:41:16.12	+72:26:32.0	10.275	M4.0 V	AF15	
J17426+756	17:42:41.48	+75:37:18.7	9.680	M4.5 V	AF15	
J17428+167	17:42:52.04	+16:43:47.6	10.401	M1.5 V	AF15	
J17439+433	17:43:55.95	+43:22:44.1	6.812	M1.5 V	This work	
J17464+277AB	17:46:25.08	+27:43:01.5	5.772	M3.5 V	AF15	
J17477+277	17:47:44.32	+27:47:07.4	11.42	M1.5 V	AF15	
J17520+566	17:52:02.94	+56:36:27.8	9.229	M3.5 V	AF15	
J17542+073	17:54:17.10	+07:22:44.7	8.772	M4.0 V	This work	
J17559+294	17:55:58.02	+29:26:09.8	9.759	M3.5 V	AF15	
J17578+046	17:57:48.49	+04:41:40.5	5.244	M3.5 V	AF15	
J17578+465	17:57:50.96	+46:35:18.2	7.847	M2.5 V	AF15	
J18006+685	18:00:36.96	+68:32:54.0	9.666	K7 V	AF15	
J18007+295	18:00:45.44	+29:33:56.7	9.058	M2.0 V	AF15	

Table C.3: *Continued*

Karmn	RA	DEC	Jmag	SpT	Ref.[a]	Notes
J18019+001	18:01:58.35	+00:07:50.2	10.134	M3.5 V	AF15	
J18022+642	18:02:16.60	+64:15:44.6	8.541	M5.0 V	AF15	
J18027+375	18:02:46.25	+37:31:04.9	9.720	M4.5 V	This work	
J18028−030	18:02:49.35	−03:00:02.5	9.440	M3.5 V	AF15	
J18036−189	18:03:36.05	−18:58:50.3	9.131	M5.0 V	AF15	
J18041+838	18:04:10.62	+83:50:28.1	9.023	M3.5 V	AF15	
J18046+139	18:04:38.71	+13:54:14.4	9.469	M2.5 V	AF15	
J18051−030	18:05:07.56	−03:01:52.4	6.161	M1.5 V	This work	
J18054+015	18:05:29.12	+01:32:36.0	9.107	M3.5 V	AF15	
J18057−143	18:05:44.70	−14:22:42.5	9.777	M5.5 V	AF15	
J18068+177	18:06:48.56	+17:20:47.2	9.490	M4.0 V	AF15	
J18075−159	18:07:32.93	−15:57:46.5	8.639	M4.5 V	This work	
J18090+241	18:09:01.93	+24:09:04.2	9.303	M1.0 V	AF15	
J18112−010	18:11:14.91	−01:01:11.6	10.193	M3.5 V	AF15	
J18130+414	18:13:00.02	+41:29:19.8	10.207	M3.5 V	AF15	
J18131+260AB	18:13:06.57	+26:01:51.9	8.899	M4.0 V	AF15	
J18135+055	18:13:33.16	+05:32:11.9	9.702	M4.0 V	AF15	
J18149+196	18:14:59.85	+19:39:26.0	9.435	M2.0 V	AF15	
J18162+686	18:16:14.75	+68:40:27.8	11.533	M1.5 V	AF15	
J18180+387W	18:18:03.46	+38:46:36.0	9.197	M4.0 V	This work	
J18189+661	18:18:57.26	+66:11:33.2	8.740	M4.5 V	This work	
J18221+063	18:22:06.71	+06:20:37.7	8.671	M3.5 V	This work	
J18224+620	18:22:27.19	+62:03:02.5	8.640	M4.0 V	AF15	
J18234+281	18:23:28.35	+28:10:04.1	8.306	M3.5 V	This work	
J18253+186	18:25:17.99	+18:39:09.2	9.574	M3.5 V	AF15	
J18292+116	18:29:13.69	+11:41:27.2	10.501	K5 V	M18	
J18306−039	18:30:39.47	−03:56:18.9	9.724	M4.5 V	AF15	
J18313+649	18:31:21.80	+64:54:13.3	9.360	M3.5 V	AF15	Young
J18319+406	18:31:58.40	+40:41:10.4	8.065	M3.5 V	This work	
J18332+223	18:33:14.76	+22:19:17.7	11.117	M4.5 V	M18	
J18338+194	18:33:50.05	+19:26:11.2	9.156	M3.0 V	AF15	Double or multiple
J18346+401	18:34:36.64	+40:07:26.7	7.184	M4.0 V	This work	
J18353+457	18:35:18.33	+45:44:37.9	6.881	M0.5 V	AF15	
J18354+457	18:35:27.23	+45:45:40.3	8.886	M2.5 V	AF15	
J18363+136	18:36:19.23	+13:36:26.2	8.186	M3.5 V	This work	
J18400+726	18:40:02.39	+72:40:54.0	10.974	M6.5 V	AF15	
J18409+315	18:40:55.19	+31:31:52.1	8.210	M1.0 V	M18	
J18416+397	18:41:37.42	+39:42:12.3	9.216	M4.0 V	This work	Eruptive variable
J18419+318	18:41:59.09	+31:49:49.8	7.523	M3.0 V	This work	
J18423−013	18:42:20.54	−01:20:15.2	6.184	MIII	AF15	Giant
J18427+139	18:42:44.99	+13:54:16.8	8.361	M4.0 V	This work	Eruptive variable
J18427+596N	18:42:46.66	+59:37:49.9	5.189	M3.0 V	AF15	
J18427+596S	18:42:46.88	+59:37:37.4	5.721	M3.5 V	AF15	
J18453+188	18:45:22.94	+18:51:58.5	9.273	M4.0 V	AF15	
J18467+007	18:46:46.76	+00:43:26.1	9.593	M4.0 V	AF15	
J18482+076	18:48:17.53	+07:41:21.0	8.853	M5.0 V	AF15	
J18491−032	18:49:06.39	−03:15:17.5	9.613	M4.5 V	AF15	
J18499+186	18:49:54.49	+18:40:29.5	9.380	M4.5 V	AF15	
J18542+109	18:54:17.12	+10:58:09.2	9.376	M4.0 V	AF15	
J18550+429	18:55:04.52	+42:59:51.0	9.780	M4.0 V	AF15	Eruptive variable
J18570+473	18:57:00.54	+47:20:29.5	9.421	M2.5 V	AF15	
J18580+059	18:58:00.14	+05:54:29.7	6.239	M0.5 V	This work	
J19052+387	19:05:13.35	+38:45:05.0	9.349	M3.5 V	AF15	
J19060−074	19:06:02.60	−07:29:41.1	9.503	M2.5 V	AF15	

Table C.3: *Continued*

Karmn	RA	DEC	Jmag	SpT	Ref.[a]	Notes
J19070+208	19:07:05.56	+20:53:16.9	7.295	M2.0 V	AF15	
J19072+442	19:07:12.70	+44:16:07.1	10.447	M4.5 V	AF15	
J19084+322	19:08:29.96	+32:16:52.0	7.905	M3.0 V	This work	
J19098+176	19:09:50.98	+17:40:07.4	8.819	M4.5 V	This work	
J19105−075	19:10:33.32	−07:34:04.2	9.883	M3.5 V	AF15	
J19164+842	19:16:24.83	+84:13:41.2	9.977	M5.0 V	AF15	
J19168+003	19:16:48.80	+00:23:32.1	9.960	M3.5 V	AF15	
J19169+051N	19:16:55.26	+05:10:08.6	5.583	M2.5 V	AF15	
J19169+051S	19:16:57.62	+05:09:02.2	9.908	M8.0 V	AF15	
J19216+208	19:21:38.68	+20:52:02.8	8.796	M4.5 V	This work	
J19243+426	19:24:21.00	+42:37:25.5	9.335	M3.5 V	AF15	
J19251+283	19:25:08.46	+28:21:13.2	8.442	M3.5 V	This work	
J19260+244	19:26:01.61	+24:26:17.1	9.625	M4.5 V	AF15	
J19271+770	19:27:09.05	+77:04:32.7	9.241	M2.5 V	AF15	
J19282−001	19:28:13.65	−00:09:51.8	9.723	M5.0 V	AF15	
J19312+361AB	19:31:12.57	+36:07:30.1	9.609	M4.5 V	AF15	SB
J19316−069	19:31:38.69	−06:58:25.3	9.484	M2.5 V	AF15	
J19321−113	19:32:08.10	−11:19:57.3	9.604	M3.5 V	M18	
J19327−068	19:32:46.34	−06:52:17.9	9.939	M3.5 V	AF15	
J19346+045	19:34:39.82	+04:34:57.2	6.714	sdM1	AF15	
J19354+377	19:35:29.23	+37:46:08.2	7.562	M3.5 V	This work	
J19390+338	19:39:05.59	+33:52:02.2	9.392	M3.5 V	AF15	
J19393+148	19:39:22.09	+14:48:16.1	9.937	M3.0 V	AF15	
J19421+656	19:42:10.00	+65:38:29.8	9.348	M3.0 V	AF15	
J19430+102	19:43:02.73	+10:12:39.5	9.249	M2.0 V	AF15	
J19439−057	19:43:54.33	−05:46:36.4	9.745	M3.5 V	AF15	
J19452+407	19:45:12.48	+40:43:18.4	8.964	M0.5 V	AF15	
J19510+104N	19:51:00.59	+10:24:48.8	10.310	M3.5 V	M18	
J19510+104S	19:51:00.68	+10:24:40.1	8.888	M0.0 V	M18	
J19511+464	19:51:09.31	+46:28:59.9	8.586	M3.5 V	This work	Eruptive variable
J19519+141	19:51:55.45	+14:08:23.6	9.422	M0.5 V	AF15	
J19524+603	19:52:24.50	+60:22:14.5	9.791	M3.0 V	AF15	
J19539+444WAB	19:53:54.43	+44:24:54.2	7.791	M5.5 V	AF15	
J19539+444E	19:53:55.09	+44:24:55.0	8.275	M5.5 V	AF15	
J19547+844	19:54:47.18	+84:29:29.6	9.514	M4.0 V	AF15	
J19553+064	19:55:18.83	+06:24:37.2		M2.5 V	M18	
J19564+591	19:56:24.90	+59:09:21.7	9.653	M3.5 V	AF15	
J19565+591	19:56:34.01	+59:09:42.2	7.423	K7 V	AF15	
J19578−108	19:57:52.00	−10:53:05.0	9.730	M4.5 V	AF15	
J20021+130AB	20:02:10.55	+13:00:31.6	9.732	M3.5 V	AF15	
J20033+672	20:03:23.24	+67:16:48.7	9.448	M3.0 V	AF15	
J20034+298	20:03:26.52	+29:52:00.1	9.554	M4.5 V	AF15	
J20039−081	20:03:58.92	−08:07:47.3	9.184	M4.0 V	This work	
J20047+512	20:04:47.44	+51:13:16.9	9.491	M3.0 V	AF15	
J20065+159	20:06:31.06	+15:59:17.2	9.742	M2.0 V	AF15	
J20077+189	20:07:42.66	+18:59:00.3	9.431	M3.5 V	AF15	
J20093−012	20:09:18.25	−01:13:37.7	9.403	M5.0 V	AF15	
J20108+772	20:10:52.43	+77:14:20.1	6.409	K7 V	AF15	
J20112+161	20:11:13.29	+16:11:07.5	9.627	M4.0 V	AF15	
J20123−126	20:12:19.95	−12:37:02.6		< K5 V	AF15	
J20149+397	20:15:30.44	+39:47:20.7	14.827	M4.5 V	This work	
J20167+502	20:16:43.96	+50:17:14.1	9.412	M2.5 V	M18	
J20177+059	20:17:43.33	+05:59:17.3	9.321	M2.5 V	AF15	
J20182−202	20:18:14.55	−20:12:47.5	9.458	M2.5 V	AF15	

Table C.3: *Continued*

Karmn	RA	DEC	Jmag	SpT	Ref.[a]	Notes
J20198+229	20:19:49.25	+22:56:36.7	8.166	M2.5 V	This work	
J20216−199	20:21:41.11	−19:57:17.7	9.473	M2.0 V	AF15	
J20254−198	20:25:27.15	−19:48:03.3	10.042	M5.0 V	AF15	
J20260+585	20:26:05.29	+58:34:22.5	9.029	M5.0 V	This work	
J20283+617	20:28:19.22	+61:43:47.9	9.322	M2.5 V	AF15	
J20283+342	20:28:22.03	+34:12:08.8	10.189	M4.0 V	This work	
J20287−114	20:28:43.62	−11:28:30.8	8.394	M3.5 V	This work	
J20300+003AB	20:30:01.92	+00:23:55.3	9.911	M4.5 V	AF15	
J20301+798	20:30:07.11	+79:50:46.8	8.480	M2.5 V	This work	
J20305+654	20:30:32.08	+65:26:58.6	6.735	M2.5 V	This work	
J20314+385	20:31:25.61	+38:33:43.2	9.193	M3.5 V	This work	
J20332+283	20:33:15.80	+28:23:44.4	9.963	M4.0 V	AF15	
J20336+617	20:33:40.31	+61:45:13.6	8.287	M4.0 V	This work	
J20336+365	20:33:41.73	+36:35:58.2	9.418	M3.5 V	AF15	
J20382+231	20:38:14.41	+23:07:52.4	9.204	M2.0 V	AF15	
J20405+154	20:40:33.64	+15:29:57.2	8.641	M4.5 V	AF15	
J20407+199AB	20:40:44.50	+19:54:02.3	8.160	M2.5 V	AF15	
J20439+231	20:43:54.10	+23:07:13.9	9.275	M3.5 V	AF15	
J20450+444	20:45:04.03	+44:29:56.3	7.329	M1.5 V	This work	
J20460+339	20:46:06.45	+33:58:06.1	14.040	M3.0 V	M18	
J20467−118	20:46:43.61	−11:48:13.2	9.349	M4.0 V	AF15	Young
J20472+108	20:47:16.69	+10:51:50.7	11.963	M4.5 V	M18	
J20488+197	20:48:52.46	+19:43:05.0	9.236	M3.5 V	This work	
J20510+399	20:51:01.52	+39:55:42.6	9.058	M3.0 V	AF15	
J20525−169	20:52:33.04	−16:58:29.0	7.090	M4.0 V	This work	
J20533+621	20:53:19.77	+62:09:15.7	5.429	M0.5 V	This work	
J20540+603	20:54:05.05	+60:18:04.1	10.098	M2.5 V	AF15	
J20556−140S	20:55:37.07	−14:03:54.6	9.717	M4.5 V	This work	
J20556−140N	20:55:37.72	−14:02:07.8	8.117	M4.0 V	This work	
J20567−104	20:56:46.59	−10:26:53.4	7.766	M2.5 V	This work	
J20568−048	20:56:48.46	−04:50:49.0	7.816	M3.5 V	This work	
J20581+401AB	20:58:11.48	+40:11:29.0	8.142	K7V	AF15	
J20583+425	20:58:23.14	+42:35:03.6	9.490	M2.5 V	AF15	
J20593+530AB	20:59:20.35	+53:03:04.9	9.910	M3.5 V	AF15	
J21009+510	21:00:59.78	+51:03:14.8	9.878	M2.5 V	AF15	SB
J21012+332	21:01:16.10	+33:14:32.8	8.439	M2.5 V	This work	
J21019−063	21:01:58.66	−06:19:07.1	7.563	M2.5 V	AF15	
J21027+349	21:02:46.06	+34:54:36.0	9.846	M4.5 V	AF15	
J21053+208	21:05:22.22	+20:51:34.2	9.421	M2.5 V	AF15	
J21057+502W	21:05:42.44	+50:15:57.7	9.965	M4.0 V	AF15	
J21057+502E	21:05:45.38	+50:15:43.6	9.543	M3.5 V	AF15	
J21068+387	21:06:53.42	+38:44:53.0	3.114	K5 V	AF15	
J21069+387	21:06:54.74	+38:44:26.6	3.546	K7 V	AF15	
J21074+198	21:07:24.44	+19:50:52.3	9.182	M1.0 V	AF15	
J21074+468	21:07:28.10	+46:51:53.8	9.488	M2.0 V	AF15	
J21109+469	21:10:58.81	+46:57:32.5	9.878	M3.5 V	AF15	
J21114+658	21:11:27.41	+65:53:26.5	9.476	M2.0 V	AF15	
J21127−073	21:12:45.60	−07:19:55.8	9.902	M3.5 V	AF15	
J21147+160	21:14:47.53	+16:04:49.8	9.219	M3.5 V	AF15	
J21152+257	21:15:12.59	+25:47:45.4	8.403	M3.0 V	This work	
J21164+025	21:16:27.29	+02:34:51.5	8.219	M2.5 V	This work	
J21221+229	21:22:06.27	+22:55:53.1	7.400	M1.0 V	This work	
J21245+400	21:24:32.34	+40:04:00.0	10.339	M5.5 V	AF15	
J21323−209	21:32:21.02	−20:58:10.1	8.470	M0.5 V	M18	

Table C.3: *Continued*

Karmn	RA	DEC	Jmag	SpT	Ref.[a]	Notes
J21348+515	21:34:50.36	+51:32:13.8	8.038	M2.5 V	This work	
J21376+016	21:37:40.19	+01:37:13.7	8.802	M4.5 V	AF15	Young
J21414+207	21:41:26.63	+20:43:10.7	9.428	M3.0 V	AF15	
J21442+066	21:44:12.98	+06:38:29.2	8.271	M3.0 V	This work	
J21463+382	21:46:22.06	+38:13:04.8	7.949	M4.0 V	This work	
J21466+668	21:46:40.22	+66:48:10.6	8.837	M4.0 V	AF15	
J21466−001	21:46:40.40	−00:10:23.4	8.364	M4.0 V	This work	
J21467−212	21:46:45.49	−21:17:46.8	9.291	M4.0 V	AF15	
J21472−047	21:47:17.44	−04:44:40.6	9.416	M4.5 V	AF15	Young
J21518+423	21:51:53.87	+42:20:39.1	8.506	M0.5 V	M18	
J21521+056	21:52:10.40	+05:37:35.7	8.248	M3.0 V	This work	Young
J21547−033	21:54:45.30	−03:18:34.3	11.512	M3.5 V	M18	
J21554+596AB	21:55:24.37	+59:38:37.2	9.178	M4.0 V	AF15	
J21574+289	21:57:29.70	+28:54:49.5	10.532	M1.5 V	M18	
J22012+283	22:01:13.11	+28:18:24.9	7.635	M4.0 V	This work	
J22020−194	22:02:00.70	−19:28:59.3	8.046	M3.0 V	This work	
J22021+014	22:02:10.26	+01:24:00.6	6.196	M0.5 V	AF15	
J22035+036AB	22:03:33.38	+03:40:23.6	9.742	M4.0 V	AF15	
J22065+433	22:06:34.83	+43:22:42.4	10.778	M3.5 V	M18	
J22088+117	22:08:50.35	+11:44:13.2	9.901	M4.5 V	AF15	
J22089−177	22:08:54.18	−17:47:52.2	11.968	M2.5 V	AF15	
J22095+118	22:09:31.68	+11:52:53.7	9.901	M3.0 V	AF15	
J22096−046	22:09:40.30	−04:38:26.8	6.510	M3.0 V	This work	
J22114+409	22:11:24.17	+40:59:58.7	9.725	M5.5 V	AF15	
J22115+184	22:11:30.08	+18:25:34.1	6.725	M2.0 V	This work	
J22125+085	22:12:35.96	+08:33:11.1	8.277	M2.5 V	This work	
J22137−176	22:13:42.78	−17:41:08.2	8.955	M4.5 V	This work	
J22160+546	22:16:02.59	+54:39:59.5	9.718	M4.0 V	AF15	Young
J22202+067	22:20:13.27	+06:43:32.1	9.500	M2.5 V	AF15	
J22231−176	22:23:06.97	−17:36:25.0	8.242	M5.0 V	This work	
J22234+324AB	22:23:29.05	+32:27:33.4	6.898	M3.0 V	AF15	Young
J22252+594	22:25:17.06	+59:24:49.6	8.745	M3.5 V	This work	
J22264+583	22:26:24.99	+58:23:05.1	9.461	M3.0 V	AF15	
J22298+414	22:29:48.86	+41:28:48.0	8.849	M4.0 V	This work	
J22300+488AB	22:30:04.19	+48:51:34.7	9.524	M4.5 V	AF15	
J22330+093	22:33:02.25	+09:22:41.1	7.208	M1.0 V	This work	
J22386+567	22:38:37.91	+56:47:44.3	1.087	MIII	AF15	Giant
J22387+252	22:38:44.26	+25:13:30.5	9.769	M3.5 V	AF15	
J22396−125	22:39:41.59	−12:35:20.4	10.568	M3.0 V	AF15	
J22415+260	22:41:35.78	+26:02:12.9	9.044	M3.5 V	AF15	
J22437+192	22:43:43.78	+19:16:54.5	9.242	M3.0 V	AF15	
J22476+184	22:47:38.85	+18:26:36.5	9.102	M2.5 V	AF15	
J22489+183	22:48:54.59	+18:19:59.3	9.957	M4.5 V	AF15	
J22509+499	22:50:55.05	+49:59:13.2	9.804	M4.0 V	AF15	
J22518+317	22:51:53.49	+31:45:15.3	7.697	M3.0 V	This work	
J22524+099AB	22:52:29.77	+09:54:04.3	9.657	M3.0 V	AF15	
J22526+750	22:52:39.64	+75:04:19.0	9.089	M4.5 V	AF15	
J22532−142	22:53:16.72	−14:15:48.9	5.934	M4.5 V	This work	Young
J22559+178	22:55:59.85	+17:48:39.9	7.319	M1.0 V	This work	
J22565+165	22:56:34.97	+16:33:13.0	5.360	M1.0 V	This work	
J22582−110	22:58:16.43	−11:04:17.1	9.071	M2.5 V	AF15	
J22588+690	22:58:50.60	+69:01:37.1	10.588	M3.0 V	AF15	
J23006+036	23:00:36.14	+03:38:17.0	9.592	M3.0 V	AF15	
J23025+298	23:02:31.34	+29:48:01.7	11.124	M3.0 V	M18	

Table C.3: *Continued*

Karmn	RA	DEC	Jmag	SpT	Ref.[a]	Notes
J23028+436	23:02:52.51	+43:38:15.7	9.316	M4.0 V	AF15	
J23036−072	23:03:36.41	−07:16:29.9	9.483	M2.5 V	AF15	
J23036+097	23:03:37.45	+09:42:58.5	9.992	M3.5 V	AF15	
J23051+519	23:05:06.32	+51:59:13.3	9.680	M3.5 V	AF15	
J23051+452	23:05:08.71	+45:17:31.8	9.297	M3.5 V	AF15	
J23070+094	23:07:00.27	+09:24:34.0	1.584	MIII	AF15	Giant
J23103+490	23:10:21.45	+49:01:02.6	6.609	K5 V	M18	
J23113+085	23:11:23.78	+08:31:01.4	8.466	M3.5 V	This work	Double or multiple
J23174+382	23:17:24.41	+38:12:42.0	7.761	K4−K5V	This work	SB
J23177+490	23:17:44.63	+49:00:54.9	1.615	MIII	AF15	Giant
J23182+795	23:18:17.06	+79:34:47.4	9.712	M3.0 V	AF15	
J23194+790	23:19:24.47	+79:00:03.7	8.036	M3.5 V	AF15	Young
J23209−017AB	23:20:57.66	−01:47:37.3	9.355	M4.0 V	AF15	Young
J23216+172	23:21:37.52	+17:17:28.5	7.391	M4.0 V	This work	
J23220+569	23:22:00.71	+56:59:19.9	9.473	M3.0 V	AF15	
J23228+787	23:22:53.85	+78:47:38.6	10.418	M5.0 V	AF15	Young
J23235+457	23:23:30.67	+45:47:18.9	7.383	K5 V	AF15	
J23245+578	23:24:30.49	+57:51:15.3	6.795	M1.5 V	This work	
J23261+170AB	23:26:11.82	+17:00:08.3	9.356	M4.0 V	AF15	
J23266+453	23:26:37.98	+45:21:05.5	5.933	MIII	AF15	Giant
J23266+453W	23:26:39.62	+45:21:14.2	8.203	M0.0 V	M18	
J23293+414N	23:29:23.46	+41:28:06.9	7.925	M3.5 V	This work	
J23306+466	23:30:41.71	+46:39:56.3	9.967	M2.0 V	AF15	
J23317−064	23:31:47.64	−06:25:50.2	9.844	M4.5 V	AF15	
J23340+001	23:34:03.28	+00:10:45.2	7.664	M2.5 V	This work	
J23351−023	23:35:10.50	−02:23:21.4	9.148	M5.5 V	This work	
J23354+310	23:35:29.46	+31:00:58.5	9.484	M2.5 V	M18	
J23376+163	23:37:36.01	+16:22:03.1	10.479	M5.5 V	AF15	
J23381−162	23:38:08.19	−16:14:10.0	7.813	M2.0 V	This work	
J23416−065	23:41:39.26	−06:35:50.3	10.323	M4.5 V	AF15	
J23417−059AB	23:41:45.15	−05:58:14.7	10.392	M3.5 V	AF15	
J23419+441	23:41:54.99	+44:10:40.8	6.884	M5.0 V	AF15	
J23423+349	23:42:22.11	+34:58:27.7	9.315	M4.0 V	AF15	
J23425+392	23:42:33.50	+39:14:23.4	9.642	M0.0 V	AF15	
J23431+365	23:43:06.29	+36:32:13.2	8.110	M4.5 V	This work	
J23438+610	23:43:53.31	+61:02:15.7	9.392	M3.0 V	AF15	
J23490−086	23:49:02.30	−08:24:30.7	9.497	M2.0 V	AF15	
J23492+024	23:49:12.56	+02:24:03.8	5.827	M1.0 V	This work	
J23505−095	23:50:31.59	−09:33:32.1	8.943	M4.0 V	This work	
J23535+121	23:53:35.63	+12:06:16.8	8.670	M2.0 V	M18	SB
J23548+385	23:54:51.47	+38:31:36.3	8.937	M3.5 V	This work	
J23555+006	23:55:35.22	+00:41:41.2	9.930	M1.5 V	M18	
J23556−061	23:55:39.81	−06:08:32.8	7.600	M2.5 V	This work	
J23559−133	23:55:55.13	−13:21:23.8	9.257	M3.5 V	AF15	
J23560+150	23:56:00.30	+15:01:41.0	9.382	M2.5 V	AF15	
J23569+230	23:56:55.11	+23:05:03.3	9.149	M1.5 V	AF15	
J23577+233	23:57:44.10	+23:18:17.0	7.800	M3.5 V	This work	
J23585+242W	23:58:29.28	+24:12:01.6	10.633	M3.0 V	M18	
J23585+242	23:58:30.23	+24:12:04.5	9.134	K7 V	AF15	
J23585+076	23:58:32.64	+07:39:30.4	7.907	M3.0 V	This work	
J23590+208	23:59:00.42	+20:51:38.8	9.072	M2.5 V	AF15	
J23593+326	23:59:19.86	+32:41:24.5	10.451	M4.5 V	This work	

[a] SpT reference – AF15: Alonso-Floriano et al. (2015); M18: Montes et al. (2018)

Table C.4: Abundances for the CAFOS sample.

Karmn	[C/H]	[O/H]	[Na/H]	[Mg/H]	[Al/H]	[Si/H]	[Ca/H]	[Sc/H]	[Ti/H]	[V/H]	[Cr/H]	[Mn/H]	[Fe/H]	[Co/H]	[Ni/H]
J00051+457	−0.20 ± 0.16	0.00 ± 0.13	−0.13 ± 0.19	−0.23 ± 0.18	−0.13 ± 0.18	−0.15 ± 0.15	−0.17 ± 0.14	−0.16 ± 0.16	−0.06 ± 0.14	−0.06 ± 0.19	−0.14 ± 0.17	−0.21 ± 0.20	−0.17 ± 0.17	−0.23 ± 0.15	−0.21 ± 0.16
J00066−070AB	−0.11 ± 0.17	−0.02 ± 0.18	−0.23 ± 0.17	−0.20 ± 0.18	−0.02 ± 0.12	−0.08 ± 0.16	−0.12 ± 0.12	−0.16 ± 0.15	0.08 ± 0.11	−0.08 ± 0.17	−0.06 ± 0.14	−0.17 ± 0.20	−0.06 ± 0.17	−0.19 ± 0.14	−0.18 ± 0.16
J00077+603AB	−0.22 ± 0.17	−0.20 ± 0.18	−0.49 ± 0.18	−0.36 ± 0.18	−0.25 ± 0.12	−0.40 ± 0.16	−0.22 ± 0.13	−0.25 ± 0.14	−0.09 ± 0.11	−0.12 ± 0.16	−0.32 ± 0.15	−0.42 ± 0.21	−0.38 ± 0.17	−0.37 ± 0.14	−0.41 ± 0.16
J00118+229	0.02 ± 0.17	0.14 ± 0.18	0.08 ± 0.15	0.04 ± 0.17	0.14 ± 0.11	0.08 ± 0.15	−0.01 ± 0.12	0.05 ± 0.15	0.15 ± 0.10	0.12 ± 0.17	0.09 ± 0.14	0.02 ± 0.19	0.04 ± 0.16	0.07 ± 0.13	0.01 ± 0.14
J00119+330	−0.06 ± 0.16	0.09 ± 0.16	0.00 ± 0.17	−0.03 ± 0.17	0.04 ± 0.11	0.03 ± 0.15	−0.07 ± 0.12	0.06 ± 0.14	0.08 ± 0.10	0.12 ± 0.16	0.01 ± 0.14	−0.09 ± 0.20	0.03 ± 0.16	−0.03 ± 0.13	0.02 ± 0.15
J00122+304	0.12 ± 0.18	0.07 ± 0.17	0.02 ± 0.18	−0.10 ± 0.19	0.23 ± 0.12	0.04 ± 0.17	0.09 ± 0.13	0.02 ± 0.16	0.33 ± 0.10	0.41 ± 0.18	0.08 ± 0.15	0.12 ± 0.20	0.02 ± 0.18	0.06 ± 0.13	−0.06 ± 0.17
J00133+275	0.04 ± 0.17	0.03 ± 0.17	0.24 ± 0.18	0.03 ± 0.17	0.18 ± 0.12	0.08 ± 0.15	0.06 ± 0.13	0.15 ± 0.14	0.28 ± 0.10	0.39 ± 0.16	0.07 ± 0.14	0.06 ± 0.21	0.14 ± 0.17	0.04 ± 0.13	0.13 ± 0.16
J00136+806	−0.10 ± 0.16	0.06 ± 0.13	0.18 ± 0.19	−0.11 ± 0.18	0.06 ± 0.17	0.03 ± 0.16	0.04 ± 0.14	−0.06 ± 0.16	0.17 ± 0.15	0.09 ± 0.19	0.08 ± 0.17	0.03 ± 0.21	−0.10 ± 0.17	0.06 ± 0.15	0.08 ± 0.16
J00152+530	−0.02 ± 0.15	0.02 ± 0.17	0.03 ± 0.17	−0.09 ± 0.17	−0.08 ± 0.12	0.01 ± 0.15	−0.11 ± 0.13	0.02 ± 0.15	0.04 ± 0.10	0.05 ± 0.16	−0.01 ± 0.14	−0.12 ± 0.20	0.05 ± 0.16	−0.09 ± 0.13	0.00 ± 0.15
J00162+198W	0.09 ± 0.17	0.09 ± 0.17	0.02 ± 0.18	−0.03 ± 0.17	0.24 ± 0.12	−0.07 ± 0.16	0.07 ± 0.12	0.11 ± 0.14	0.22 ± 0.10	0.31 ± 0.18	−0.02 ± 0.14	−0.01 ± 0.20	−0.15 ± 0.17	0.08 ± 0.13	−0.08 ± 0.16
J00162+198E	0.00 ± 0.16	0.17 ± 0.17	−0.05 ± 0.16	0.00 ± 0.17	0.23 ± 0.11	0.00 ± 0.16	−0.05 ± 0.13	0.08 ± 0.14	0.14 ± 0.10	0.21 ± 0.17	0.04 ± 0.14	0.04 ± 0.21	−0.05 ± 0.16	0.10 ± 0.13	−0.06 ± 0.15
J00183+440	−0.35 ± 0.15	−0.08 ± 0.13	−0.33 ± 0.19	−0.37 ± 0.19	−0.26 ± 0.17	−0.23 ± 0.15	−0.29 ± 0.14	−0.30 ± 0.16	−0.21 ± 0.15	−0.19 ± 0.19	−0.27 ± 0.17	−0.44 ± 0.21	−0.28 ± 0.17	−0.40 ± 0.15	−0.36 ± 0.16
J00228−164	−0.06 ± 0.16	−0.02 ± 0.17	−0.05 ± 0.17	−0.14 ± 0.17	0.00 ± 0.11	−0.09 ± 0.15	−0.09 ± 0.12	−0.06 ± 0.14	0.07 ± 0.10	0.06 ± 0.16	−0.04 ± 0.14	−0.09 ± 0.20	−0.05 ± 0.17	−0.12 ± 0.13	−0.10 ± 0.15
J00240+264	0.05 ± 0.17	0.07 ± 0.16	0.22 ± 0.18	0.08 ± 0.17	0.17 ± 0.11	0.07 ± 0.15	0.07 ± 0.13	0.08 ± 0.15	0.24 ± 0.10	0.25 ± 0.16	0.15 ± 0.14	0.05 ± 0.20	0.07 ± 0.16	0.06 ± 0.13	0.10 ± 0.15
J00253+235	−0.12 ± 0.16	0.03 ± 0.13	−0.11 ± 0.19	−0.18 ± 0.18	−0.10 ± 0.18	−0.08 ± 0.16	−0.09 ± 0.14	−0.07 ± 0.15	0.01 ± 0.15	−0.02 ± 0.18	−0.11 ± 0.17	−0.26 ± 0.20	−0.12 ± 0.16	−0.13 ± 0.15	−0.14 ± 0.16
J00286−066	−0.03 ± 0.16	0.13 ± 0.17	0.01 ± 0.16	0.00 ± 0.17	0.19 ± 0.11	0.04 ± 0.15	−0.01 ± 0.12	0.03 ± 0.14	0.20 ± 0.10	0.12 ± 0.17	0.06 ± 0.14	0.03 ± 0.21	−0.05 ± 0.16	0.04 ± 0.13	−0.02 ± 0.15
J00297+012	−0.18 ± 0.16	−0.00 ± 0.13	−0.21 ± 0.18	−0.18 ± 0.19	−0.14 ± 0.17	−0.11 ± 0.15	−0.11 ± 0.14	−0.11 ± 0.16	−0.00 ± 0.14	−0.04 ± 0.19	−0.10 ± 0.17	−0.32 ± 0.20	−0.15 ± 0.16	−0.18 ± 0.15	−0.16 ± 0.16
J00313+336	−0.05 ± 0.15	0.06 ± 0.13	0.03 ± 0.19	−0.04 ± 0.18	0.04 ± 0.18	0.08 ± 0.16	0.05 ± 0.14	0.08 ± 0.16	0.11 ± 0.14	0.11 ± 0.19	0.10 ± 0.17	0.01 ± 0.20	0.10 ± 0.17	0.00 ± 0.14	0.05 ± 0.16
J00313+001	−0.04 ± 0.16	0.04 ± 0.16	0.01 ± 0.17	−0.04 ± 0.17	−0.01 ± 0.12	−0.00 ± 0.15	−0.08 ± 0.12	0.09 ± 0.14	0.03 ± 0.10	0.09 ± 0.16	0.02 ± 0.14	−0.09 ± 0.19	0.01 ± 0.16	−0.04 ± 0.13	0.02 ± 0.15
J00322+544	0.09 ± 0.17	0.20 ± 0.17	0.26 ± 0.18	0.17 ± 0.17	0.27 ± 0.11	0.23 ± 0.15	0.04 ± 0.12	0.26 ± 0.15	0.26 ± 0.10	0.32 ± 0.17	0.17 ± 0.14	0.21 ± 0.21	0.23 ± 0.17	0.17 ± 0.13	0.20 ± 0.15
J00328−045AB	0.12 ± 0.17	0.10 ± 0.17	0.07 ± 0.17	0.10 ± 0.17	0.16 ± 0.12	0.18 ± 0.15	0.02 ± 0.12	0.16 ± 0.15	0.23 ± 0.11	0.23 ± 0.17	0.14 ± 0.14	0.10 ± 0.19	0.17 ± 0.17	0.10 ± 0.13	0.12 ± 0.16
J00358+526	−0.11 ± 0.17	0.06 ± 0.16	−0.14 ± 0.17	−0.20 ± 0.17	−0.02 ± 0.12	−0.11 ± 0.16	−0.11 ± 0.12	−0.16 ± 0.14	0.04 ± 0.10	−0.03 ± 0.16	−0.07 ± 0.13	−0.15 ± 0.20	−0.18 ± 0.16	−0.10 ± 0.13	−0.18 ± 0.15
J00380+169	−0.14 ± 0.17	0.01 ± 0.17	−0.27 ± 0.16	−0.22 ± 0.17	−0.14 ± 0.12	−0.11 ± 0.15	−0.18 ± 0.12	−0.08 ± 0.14	−0.03 ± 0.10	−0.06 ± 0.16	−0.15 ± 0.14	−0.24 ± 0.20	−0.14 ± 0.16	−0.18 ± 0.13	−0.20 ± 0.14
J00385+429	−0.46 ± 0.16	−0.12 ± 0.14	−0.67 ± 0.19	−0.45 ± 0.19	−0.41 ± 0.18	−0.46 ± 0.16	−0.48 ± 0.14	−0.42 ± 0.17	−0.35 ± 0.15	−0.34 ± 0.20	−0.51 ± 0.17	−0.73 ± 0.21	−0.57 ± 0.17	−0.64 ± 0.16	−0.60 ± 0.16
J00389+306	−0.11 ± 0.16	0.04 ± 0.16	−0.28 ± 0.17	−0.18 ± 0.17	−0.04 ± 0.12	−0.11 ± 0.15	−0.08 ± 0.12	−0.09 ± 0.15	0.05 ± 0.10	−0.02 ± 0.16	−0.12 ± 0.14	−0.19 ± 0.21	−0.21 ± 0.16	−0.11 ± 0.13	−0.20 ± 0.15
J00395+149S	−0.02 ± 0.16	0.05 ± 0.17	−0.01 ± 0.17	−0.05 ± 0.17	0.06 ± 0.12	0.01 ± 0.16	−0.10 ± 0.12	0.05 ± 0.14	0.12 ± 0.10	0.16 ± 0.17	0.02 ± 0.14	−0.04 ± 0.20	0.01 ± 0.16	−0.01 ± 0.13	−0.03 ± 0.14
J00395+149N	0.08 ± 0.17	0.03 ± 0.17	0.01 ± 0.17	0.04 ± 0.17	0.15 ± 0.12	0.03 ± 0.16	0.01 ± 0.13	0.07 ± 0.15	0.20 ± 0.10	0.29 ± 0.17	0.10 ± 0.14	0.03 ± 0.20	0.04 ± 0.16	0.06 ± 0.13	0.01 ± 0.15
J00452+002AB	−0.03 ± 0.16	0.05 ± 0.17	0.05 ± 0.17	−0.06 ± 0.17	0.10 ± 0.12	0.00 ± 0.15	−0.04 ± 0.13	−0.06 ± 0.15	0.15 ± 0.10	0.12 ± 0.16	0.03 ± 0.14	0.02 ± 0.21	0.01 ± 0.17	0.03 ± 0.13	−0.02 ± 0.15
J00464+506	0.13 ± 0.17	0.16 ± 0.16	0.30 ± 0.16	0.18 ± 0.17	0.31 ± 0.12	0.19 ± 0.16	0.13 ± 0.13	0.27 ± 0.14	0.33 ± 0.11	0.36 ± 0.17	0.18 ± 0.14	0.11 ± 0.21	0.19 ± 0.16	0.19 ± 0.14	0.18 ± 0.15
J00467−044	−0.02 ± 0.17	0.10 ± 0.16	0.07 ± 0.17	−0.04 ± 0.17	0.16 ± 0.12	0.02 ± 0.15	−0.06 ± 0.13	−0.02 ± 0.15	0.12 ± 0.10	0.25 ± 0.17	0.09 ± 0.14	0.01 ± 0.20	0.02 ± 0.17	0.09 ± 0.14	−0.00 ± 0.15
J00484+753	−0.04 ± 0.16	0.03 ± 0.16	0.01 ± 0.17	−0.12 ± 0.16	0.01 ± 0.11	−0.02 ± 0.15	−0.04 ± 0.12	0.03 ± 0.14	0.13 ± 0.10	0.13 ± 0.16	−0.02 ± 0.14	−0.13 ± 0.20	−0.01 ± 0.17	−0.07 ± 0.13	−0.03 ± 0.15
J00490+657	−0.07 ± 0.17	0.07 ± 0.17	−0.04 ± 0.17	−0.13 ± 0.16	0.00 ± 0.11	−0.05 ± 0.15	−0.04 ± 0.13	−0.04 ± 0.15	0.10 ± 0.10	0.05 ± 0.16	0.03 ± 0.14	−0.11 ± 0.20	−0.07 ± 0.16	−0.07 ± 0.14	−0.11 ± 0.15
J00490+578	−0.18 ± 0.17	−0.04 ± 0.13	−0.17 ± 0.18	−0.20 ± 0.17	−0.06 ± 0.17	−0.09 ± 0.15	−0.11 ± 0.14	−0.15 ± 0.15	−0.02 ± 0.14	−0.08 ± 0.19	−0.09 ± 0.17	−0.18 ± 0.20	−0.18 ± 0.17	−0.18 ± 0.15	−0.17 ± 0.16
J00540+691	−0.21 ± 0.16	−0.04 ± 0.14	−0.17 ± 0.18	−0.19 ± 0.19	−0.20 ± 0.18	−0.02 ± 0.16	−0.01 ± 0.14	−0.04 ± 0.16	0.01 ± 0.14	−0.07 ± 0.19	−0.01 ± 0.17	−0.26 ± 0.20	−0.08 ± 0.17	−0.16 ± 0.15	−0.11 ± 0.17
J00548+275	0.01 ± 0.17	0.02 ± 0.17	−0.07 ± 0.18	−0.12 ± 0.17	0.15 ± 0.12	−0.13 ± 0.15	0.01 ± 0.13	−0.05 ± 0.15	0.19 ± 0.10	0.17 ± 0.17	−0.03 ± 0.14	−0.04 ± 0.20	−0.16 ± 0.17	−0.03 ± 0.14	−0.16 ± 0.15
J00570+450	−0.16 ± 0.16	0.01 ± 0.16	−0.19 ± 0.16	−0.18 ± 0.16	−0.08 ± 0.12	−0.11 ± 0.15	−0.15 ± 0.12	−0.07 ± 0.14	0.01 ± 0.10	−0.04 ± 0.16	−0.12 ± 0.14	−0.19 ± 0.19	−0.13 ± 0.16	−0.15 ± 0.13	−0.16 ± 0.15
J00580+393	−0.09 ± 0.17	−0.04 ± 0.17	−0.30 ± 0.18	−0.10 ± 0.17	−0.02 ± 0.12	−0.11 ± 0.15	−0.17 ± 0.13	0.03 ± 0.14	0.04 ± 0.10	0.12 ± 0.17	−0.19 ± 0.14	−0.18 ± 0.20	−0.15 ± 0.16	−0.12 ± 0.14	−0.17 ± 0.16
J01009−044	−0.16 ± 0.17	−0.02 ± 0.16	−0.24 ± 0.17	−0.23 ± 0.17	−0.10 ± 0.11	−0.12 ± 0.15	−0.17 ± 0.13	−0.12 ± 0.15	−0.02 ± 0.10	−0.11 ± 0.16	−0.09 ± 0.14	−0.15 ± 0.20	−0.12 ± 0.17	−0.18 ± 0.13	−0.17 ± 0.16
J01013+613	−0.20 ± 0.16	0.07 ± 0.14	−0.24 ± 0.19	−0.21 ± 0.18	−0.13 ± 0.18	0.02 ± 0.16	−0.16 ± 0.15	−0.09 ± 0.16	−0.09 ± 0.14	−0.09 ± 0.20	−0.25 ± 0.18	−0.32 ± 0.21	−0.14 ± 0.18	−0.21 ± 0.16	−0.30 ± 0.18
J01014−010	−0.05 ± 0.16	0.03 ± 0.16	0.08 ± 0.16	−0.07 ± 0.17	0.08 ± 0.11	0.01 ± 0.15	−0.09 ± 0.12	0.05 ± 0.15	0.09 ± 0.10	0.13 ± 0.16	−0.00 ± 0.14	−0.02 ± 0.20	−0.00 ± 0.17	−0.01 ± 0.13	0.00 ± 0.15
J01014+188	0.11 ± 0.16	0.22 ± 0.13	0.26 ± 0.18	0.00 ± 0.19	0.07 ± 0.17	0.05 ± 0.16	0.08 ± 0.14	0.05 ± 0.16	0.25 ± 0.15	0.21 ± 0.20	0.08 ± 0.18	0.03 ± 0.21	0.03 ± 0.18	0.15 ± 0.15	0.14 ± 0.17
J01025+716	−0.19 ± 0.17	0.22 ± 0.19	0.07 ± 0.22	−0.32 ± 0.19	−0.04 ± 0.12	−0.20 ± 0.16	−0.07 ± 0.12	−0.01 ± 0.18	−0.13 ± 0.11	0.39 ± 0.22	−0.04 ± 0.14	−0.23 ± 0.21	−0.14 ± 0.20	−0.03 ± 0.14	−0.18 ± 0.22
J01026+623	−0.08 ± 0.16	0.10 ± 0.13	0.14 ± 0.18	−0.06 ± 0.18	−0.01 ± 0.17	0.04 ± 0.16	0.07 ± 0.14	0.02 ± 0.15	0.13 ± 0.14	0.06 ± 0.19	0.11 ± 0.16	0.05 ± 0.20	0.01 ± 0.17	−0.01 ± 0.15	0.06 ± 0.16
J01028+470	−0.13 ± 0.16	−0.02 ± 0.14	−0.05 ± 0.18	−0.15 ± 0.18	−0.02 ± 0.18	−0.06 ± 0.16	−0.09 ± 0.14	−0.17 ± 0.15	0.11 ± 0.15	−0.02 ± 0.19	−0.08 ± 0.16	−0.15 ± 0.20	−0.22 ± 0.17	−0.02 ± 0.15	−0.13 ± 0.16
J01032+712	−0.07 ± 0.16	0.05 ± 0.17	0.14 ± 0.19	0.00 ± 0.18	0.10 ± 0.12	0.14 ± 0.16	0.00 ± 0.13	0.06 ± 0.15	0.14 ± 0.10	0.07 ± 0.17	0.24 ± 0.16	0.22 ± 0.22	0.18 ± 0.16	0.07 ± 0.14	0.12 ± 0.15
J01055+153	−0.15 ± 0.16	−0.05 ± 0.13	−0.21 ± 0.18	−0.19 ± 0.18	−0.06 ± 0.17	−0.11 ± 0.16	−0.20 ± 0.14	−0.15 ± 0.16	−0.03 ± 0.14	−0.03 ± 0.19	−0.17 ± 0.17	−0.24 ± 0.20	−0.19 ± 0.18	−0.18 ± 0.15	−0.18 ± 0.16
J01069+804	−0.10 ± 0.17	−0.03 ± 0.17	−0.27 ± 0.17	−0.32 ± 0.18	0.14 ± 0.12	−0.28 ± 0.16	0.04 ± 0.12	−0.27 ± 0.15	0.23 ± 0.10	0.12 ± 0.17	0.00 ± 0.14	−0.03 ± 0.20	−0.31 ± 0.16	−0.04 ± 0.13	−0.38 ± 0.16
J01074−025	0.04 ± 0.16	0.22 ± 0.14	0.39 ± 0.19	0.10 ± 0.18	0.17 ± 0.18	0.20 ± 0.16	0.17 ± 0.14	0.21 ± 0.16	0.23 ± 0.15	0.26 ± 0.20	0.20 ± 0.17	0.23 ± 0.21	0.18 ± 0.17	0.15 ± 0.16	0.18 ± 0.17
J01076+229E	0.26 ± 0.17	0.12 ± 0.17	0.38 ± 0.18	0.14 ± 0.17	0.22 ± 0.12	0.20 ± 0.16	0.07 ± 0.13	0.21 ± 0.15	0.30 ± 0.11	0.38 ± 0.17	0.17 ± 0.14	0.08 ± 0.21	0.24 ± 0.17	0.09 ± 0.14	0.23 ± 0.17
J01125−169	−0.32 ± 0.17	−0.16 ± 0.18	−0.33 ± 0.17	−0.15 ± 0.19	−0.28 ± 0.12	−0.11 ± 0.16	−0.29 ± 0.13	−0.14 ± 0.15	−0.13 ± 0.10	−0.18 ± 0.17	−0.22 ± 0.15	−0.43 ± 0.21	−0.08 ± 0.18	−0.38 ± 0.14	−0.13 ± 0.17
J01186−008	−0.21 ± 0.16	−0.07 ± 0.14	−0.14 ± 0.18	−0.19 ± 0.18	−0.03 ± 0.17	−0.12 ± 0.16	−0.14 ± 0.14	−0.19 ± 0.16	0.01 ± 0.14	−0.10 ± 0.19	−0.07 ± 0.16	−0.19 ± 0.19	−0.26 ± 0.17	−0.13 ± 0.15	−0.14 ± 0.16
J01214+313	−0.04 ± 0.16	0.10 ± 0.17	0.11 ± 0.17	−0.03 ± 0.17	0.10 ± 0.12	−0.01 ± 0.15	−0.05 ± 0.13	0.04 ± 0.15	0.12 ± 0.10	0.12 ± 0.16	0.03 ± 0.13	−0.03 ± 0.20	−0.02 ± 0.17	−0.02 ± 0.13	0.02 ± 0.15
J01226+127	−0.10 ± 0.17	0.02 ± 0.13	−0.16 ± 0.19	−0.11 ± 0.19	0.02 ± 0.17	−0.03 ± 0.16	−0.13 ± 0.14	−0.09 ± 0.16	0.07 ± 0.15	0.08 ± 0.19	−0.10 ± 0.17	−0.24 ± 0.20	−0.10 ± 0.17	−0.06 ± 0.15	−0.15 ± 0.17
J01230−129	0.21 ± 0.17	0.23 ± 0.14	0.58 ± 0.20	0.18 ± 0.19	0.41 ± 0.18	0.33 ± 0.17	0.21 ± 0.14	0.34 ± 0.16	0.37 ± 0.15	0.38 ± 0.20	0.30 ± 0.17	0.48 ± 0.21	0.31 ± 0.17	0.35 ± 0.16	0.40 ± 0.17
J01256+097	−0.16 ± 0.16	−0.01 ± 0.17	−0.14 ± 0.17	−0.17 ± 0.16	−0.06 ± 0.11	−0.12 ± 0.15	−0.15 ± 0.12	−0.11 ± 0.14	0.01 ± 0.10	−0.02 ± 0.16	−0.07 ± 0.15	−0.13 ± 0.20	−0.13 ± 0.16	−0.15 ± 0.13	−0.14 ± 0.15
J01339−176	−0.01 ± 0.17	0.02 ± 0.17	0.33 ± 0.19	−0.01 ± 0.19	−0.13 ± 0.11	0.07 ± 0.16	−0.17 ± 0.13	0.33 ± 0.16	−0.08 ± 0.10	0.62 ± 0.19	−0.03 ± 0.15	−0.29 ± 0.21	0.23 ± 0.18	−0.15 ± 0.14	0.20 ± 0.18
J01342−015	−0.39 ± 0.16	−0.08 ± 0.13	−0.56 ± 0.18	−0.39 ± 0.18	−0.30 ± 0.18	−0.44 ± 0.16	−0.40 ± 0.15	−0.46 ± 0.16	−0.19 ± 0.14	−0.32 ± 0.20	−0.40 ± 0.17	−0.61 ± 0.20	−0.55 ± 0.17	−0.40 ± 0.15	−0.49 ± 0.16
J01356−200AB	−0.05 ± 0.16	0.10 ± 0.17	−0.07 ± 0.17	−0.14 ± 0.17	0.02 ± 0.11	−0.07 ± 0.15	−0.07 ± 0.12	−0.11 ± 0.14	0.08 ± 0.11	0.01 ± 0.16	−0.02 ± 0.14	−0.11 ± 0.20	−0.11 ± 0.16	−0.07 ± 0.14	−0.13 ± 0.15
J01406−081	−0.12 ± 0.16	0.07 ± 0.13	−0.12 ± 0.19	−0.11 ± 0.19	−0.08 ± 0.18	−0.04 ± 0.16	−0.02 ± 0.14	−0.02 ± 0.16	0.03 ± 0.14	0.00 ± 0.19	−0.02 ± 0.17	−0.11 ± 0.19	−0.08 ± 0.17	−0.14 ± 0.16	−0.08 ± 0.16
J01433+043	−0.06 ± 0.17	0.05 ± 0.17	0.20 ± 0.19	−0.11 ± 0.19	−0.16 ± 0.11	−0.04 ± 0.16	−0.15 ± 0.12	0.24 ± 0.17	−0.11 ± 0.11	0.45 ± 0.20	−0.03 ± 0.14	−0.28 ± 0.21	0.08 ± 0.18	−0.14 ± 0.14	0.08 ± 0.18
J01449−010	−0.24 ± 0.16	0.00 ± 0.13	−0.37 ± 0.19	−0.25 ± 0.18	−0.19 ± 0.17	−0.21 ± 0.16	−0.28 ± 0.14	−0.20 ± 0.15	−0.11 ± 0.14	−0.16 ± 0.20	−0.29 ± 0.17	−0.42 ± 0.20	−0.27 ± 0.17	−0.30 ± 0.15	−0.41 ± 0.16
J01466−086	−0.02 ± 0.17	0.08 ± 0.17	0.08 ± 0.16	−0.03 ± 0.17	0.12 ± 0.12	0.08 ± 0.15	−0.05 ± 0.13	0.09 ± 0.15	0.16 ± 0.11	0.15 ± 0.17	0.04 ± 0.15	−0.02 ± 0.20	0.05 ± 0.16	−0.00 ± 0.13	0.06 ± 0.15
J01518+644	0.01 ± 0.17	0.08 ± 0.17	0.32 ± 0.20	−0.09 ± 0.17	−0.07 ± 0.12	0.02 ± 0.16	−0.12 ± 0.13	0.24 ± 0.16	−0.07 ± 0.10	0.55 ± 0.20	0.00 ± 0.14	−0.21 ± 0.20	0.14 ± 0.18	−0.09 ± 0.13	0.13 ± 0.18
J01541−156	−0.09 ± 0.16	−0.05 ± 0.17	−0.14 ± 0.18	−0.09 ± 0.18	0.05 ± 0.12	−0.18 ± 0.16	−0.17 ± 0.13	−0.03 ± 0.15	0.03 ± 0.10	0.20 ± 0.17	−0.18 ± 0.14	−0.24 ± 0.21	−0.23 ± 0.17	−0.08 ± 0.13	−0.18 ± 0.15
J01551−162	0.02 ± 0.16	0.16 ± 0.13	0.05 ± 0.18	0.05 ± 0.18	0.14 ± 0.17	0.17 ± 0.16	0.11 ± 0.14	0.19 ± 0.16	0.21 ± 0.14	0.20 ± 0.20	0.13 ± 0.17	0.06 ± 0.20	0.16 ± 0.18	0.11 ± 0.15	0.13 ± 0.17
J01562+001	−0.03 ± 0.16	−0.05 ± 0.16	−0.09 ± 0.17	−0.23 ± 0.16	−0.06 ± 0.12	−0.13 ± 0.15	−0.11 ± 0.12	−0.10 ± 0.15	0.04 ± 0.10	0.12 ± 0.17	−0.07 ± 0.14	−0.22 ± 0.20	−0.15 ± 0.16	−0.17 ± 0.13	−0.16 ± 0.14

Table C.4: *Continued*

Karmn	[C/H]	[O/H]	[Na/H]	[Mg/H]	[Al/H]	[Si/H]	[Ca/H]	[Sc/H]	[Ti/H]	[V/H]	[Cr/H]	[Mn/H]	[Fe/H]	[Co/H]	[Ni/H]
J01567+305	0.14 ± 0.17	−0.08 ± 0.18	0.07 ± 0.19	−0.33 ± 0.22	0.13 ± 0.12	−0.37 ± 0.20	0.14 ± 0.15	−0.48 ± 0.19	0.30 ± 0.11	0.40 ± 0.19	0.04 ± 0.15	0.02 ± 0.21	−0.33 ± 0.21	−0.06 ± 0.13	−0.39 ± 0.20
J01571−102	−0.13 ± 0.16	0.04 ± 0.13	−0.11 ± 0.18	−0.11 ± 0.19	0.05 ± 0.17	−0.06 ± 0.16	−0.07 ± 0.13	−0.07 ± 0.15	0.10 ± 0.14	0.00 ± 0.19	0.00 ± 0.17	−0.13 ± 0.20	−0.08 ± 0.17	−0.05 ± 0.15	−0.06 ± 0.16
J02000+135AB	0.01 ± 0.17	0.11 ± 0.17	0.17 ± 0.17	0.01 ± 0.17	0.10 ± 0.11	0.05 ± 0.15	−0.03 ± 0.12	0.06 ± 0.15	0.14 ± 0.10	0.18 ± 0.16	0.08 ± 0.14	−0.03 ± 0.20	0.08 ± 0.16	0.04 ± 0.13	0.06 ± 0.15
J02002+130	−0.23 ± 0.17	−0.15 ± 0.17	−0.34 ± 0.17	−0.33 ± 0.17	−0.20 ± 0.12	−0.34 ± 0.16	−0.20 ± 0.13	−0.38 ± 0.15	−0.02 ± 0.10	−0.10 ± 0.17	−0.23 ± 0.14	−0.38 ± 0.20	−0.31 ± 0.17	−0.31 ± 0.14	−0.40 ± 0.15
J02015+637	−0.01 ± 0.17	0.11 ± 0.18	0.35 ± 0.19	0.07 ± 0.18	−0.05 ± 0.12	0.02 ± 0.16	−0.13 ± 0.12	0.37 ± 0.18	−0.08 ± 0.10	0.59 ± 0.21	−0.03 ± 0.14	−0.25 ± 0.21	0.21 ± 0.19	−0.09 ± 0.14	0.23 ± 0.18
J02019+342	−0.05 ± 0.15	0.09 ± 0.13	0.08 ± 0.19	−0.04 ± 0.18	0.06 ± 0.17	0.05 ± 0.16	0.03 ± 0.14	0.07 ± 0.15	0.14 ± 0.14	0.13 ± 0.19	0.09 ± 0.17	−0.03 ± 0.20	0.04 ± 0.17	0.03 ± 0.14	0.06 ± 0.16
J02023+012	−0.24 ± 0.16	0.00 ± 0.17	−0.36 ± 0.17	−0.27 ± 0.17	−0.15 ± 0.12	−0.20 ± 0.15	−0.14 ± 0.12	−0.20 ± 0.14	−0.01 ± 0.10	−0.18 ± 0.16	−0.09 ± 0.14	−0.19 ± 0.20	−0.22 ± 0.16	−0.19 ± 0.14	−0.28 ± 0.15
J02070+496	−0.09 ± 0.17	0.01 ± 0.17	0.16 ± 0.20	−0.24 ± 0.17	−0.20 ± 0.11	−0.05 ± 0.15	−0.22 ± 0.12	0.10 ± 0.16	−0.16 ± 0.10	0.43 ± 0.20	−0.07 ± 0.14	−0.28 ± 0.21	0.08 ± 0.18	−0.18 ± 0.13	−0.00 ± 0.17
J02100−088	0.16 ± 0.18	0.12 ± 0.17	0.25 ± 0.17	0.10 ± 0.17	0.17 ± 0.12	0.14 ± 0.15	−0.00 ± 0.13	0.15 ± 0.15	0.26 ± 0.10	0.37 ± 0.18	−0.01 ± 0.15	−0.19 ± 0.21	0.11 ± 0.17	0.07 ± 0.14	0.10 ± 0.15
J02123+035	−0.22 ± 0.16	0.11 ± 0.13	−0.57 ± 0.19	−0.25 ± 0.18	−0.15 ± 0.16	−0.30 ± 0.17	−0.41 ± 0.14	−0.41 ± 0.17	−0.11 ± 0.15	−0.20 ± 0.20	−0.46 ± 0.18	−0.66 ± 0.21	−0.38 ± 0.18	−0.25 ± 0.16	−0.58 ± 0.17
J02133+368AB	−0.20 ± 0.18	−0.17 ± 0.18	−0.47 ± 0.17	−0.26 ± 0.18	−0.21 ± 0.13	−0.26 ± 0.16	−0.20 ± 0.12	−0.18 ± 0.15	−0.06 ± 0.11	−0.07 ± 0.17	−0.28 ± 0.16	−0.38 ± 0.21	−0.28 ± 0.17	−0.33 ± 0.14	−0.28 ± 0.16
J02204+377	−0.08 ± 0.16	0.03 ± 0.17	−0.01 ± 0.16	−0.10 ± 0.17	−0.06 ± 0.11	−0.03 ± 0.14	−0.12 ± 0.12	−0.00 ± 0.14	0.03 ± 0.10	0.04 ± 0.16	−0.04 ± 0.14	−0.16 ± 0.19	−0.05 ± 0.16	−0.10 ± 0.13	−0.05 ± 0.14
J02222+478	−0.19 ± 0.16	0.08 ± 0.14	−0.41 ± 0.19	−0.22 ± 0.19	−0.09 ± 0.18	−0.15 ± 0.16	−0.29 ± 0.14	−0.12 ± 0.16	−0.07 ± 0.15	−0.08 ± 0.20	−0.30 ± 0.18	−0.45 ± 0.21	−0.14 ± 0.17	−0.15 ± 0.15	−0.40 ± 0.17
J02274+031	−0.11 ± 0.16	−0.05 ± 0.17	−0.26 ± 0.18	−0.20 ± 0.17	−0.07 ± 0.12	−0.14 ± 0.15	−0.16 ± 0.13	−0.10 ± 0.15	0.04 ± 0.10	−0.01 ± 0.16	−0.12 ± 0.14	−0.23 ± 0.20	−0.16 ± 0.17	−0.19 ± 0.13	−0.20 ± 0.15
J02285−200	−0.00 ± 0.18	−0.07 ± 0.16	−0.22 ± 0.18	−0.17 ± 0.17	−0.07 ± 0.12	−0.21 ± 0.16	−0.14 ± 0.13	−0.12 ± 0.14	0.09 ± 0.10	0.19 ± 0.17	−0.21 ± 0.15	−0.39 ± 0.21	−0.24 ± 0.16	−0.19 ± 0.14	−0.29 ± 0.15
J02291+228	−0.06 ± 0.16	0.12 ± 0.13	−0.15 ± 0.19	−0.04 ± 0.18	0.01 ± 0.17	−0.03 ± 0.16	−0.04 ± 0.14	0.04 ± 0.16	0.10 ± 0.14	0.02 ± 0.19	0.01 ± 0.16	−0.14 ± 0.20	−0.01 ± 0.17	−0.01 ± 0.15	−0.07 ± 0.16
J02336+249	−0.10 ± 0.17	−0.03 ± 0.17	−0.08 ± 0.17	−0.11 ± 0.17	−0.04 ± 0.12	−0.08 ± 0.15	−0.16 ± 0.12	−0.08 ± 0.15	0.04 ± 0.10	0.08 ± 0.17	−0.05 ± 0.14	−0.13 ± 0.21	−0.06 ± 0.16	−0.14 ± 0.13	−0.13 ± 0.15
J02358+202	−0.10 ± 0.16	0.14 ± 0.13	0.15 ± 0.19	−0.05 ± 0.19	0.01 ± 0.17	0.00 ± 0.16	−0.01 ± 0.14	−0.01 ± 0.15	0.09 ± 0.15	0.03 ± 0.19	0.04 ± 0.17	−0.01 ± 0.21	−0.06 ± 0.17	−0.08 ± 0.16	−0.01 ± 0.16
J02362+068	−0.06 ± 0.16	0.09 ± 0.17	−0.10 ± 0.18	−0.06 ± 0.17	0.09 ± 0.12	−0.02 ± 0.15	−0.12 ± 0.13	0.02 ± 0.14	0.13 ± 0.11	0.12 ± 0.16	−0.09 ± 0.15	−0.13 ± 0.19	−0.10 ± 0.16	−0.04 ± 0.13	−0.10 ± 0.15
J02412−045	−0.11 ± 0.17	−0.08 ± 0.17	−0.32 ± 0.17	−0.19 ± 0.18	−0.06 ± 0.12	−0.17 ± 0.15	−0.12 ± 0.12	−0.05 ± 0.14	0.04 ± 0.10	0.05 ± 0.17	−0.15 ± 0.15	−0.21 ± 0.21	−0.18 ± 0.16	−0.19 ± 0.14	−0.21 ± 0.15
J02441+492	−0.14 ± 0.16	0.05 ± 0.13	−0.00 ± 0.19	−0.18 ± 0.18	−0.08 ± 0.17	−0.11 ± 0.15	−0.10 ± 0.14	−0.12 ± 0.15	−0.02 ± 0.14	0.01 ± 0.18	−0.07 ± 0.17	−0.15 ± 0.20	−0.06 ± 0.17	−0.18 ± 0.15	−0.13 ± 0.16
J02456+449	0.04 ± 0.16	0.10 ± 0.13	0.07 ± 0.19	−0.09 ± 0.18	0.03 ± 0.17	−0.06 ± 0.16	−0.07 ± 0.15	0.00 ± 0.16	0.09 ± 0.15	0.06 ± 0.19	−0.03 ± 0.16	−0.12 ± 0.20	−0.01 ± 0.17	−0.06 ± 0.15	−0.12 ± 0.16
J02502+628	−0.06 ± 0.16	0.05 ± 0.17	−0.13 ± 0.18	−0.16 ± 0.16	−0.05 ± 0.11	−0.07 ± 0.15	−0.12 ± 0.12	−0.03 ± 0.15	0.02 ± 0.10	0.03 ± 0.15	−0.04 ± 0.14	−0.14 ± 0.20	−0.09 ± 0.16	−0.10 ± 0.13	−0.14 ± 0.15
J02555+268	0.12 ± 0.17	0.20 ± 0.18	0.28 ± 0.17	0.21 ± 0.17	0.24 ± 0.12	0.28 ± 0.15	0.03 ± 0.13	0.23 ± 0.14	0.22 ± 0.10	0.26 ± 0.18	0.20 ± 0.14	0.15 ± 0.20	0.23 ± 0.16	0.14 ± 0.14	0.22 ± 0.15
J02565+554W	−0.06 ± 0.16	0.11 ± 0.14	0.11 ± 0.19	−0.07 ± 0.20	0.13 ± 0.18	−0.12 ± 0.17	−0.12 ± 0.14	−0.14 ± 0.16	0.11 ± 0.15	0.01 ± 0.18	−0.05 ± 0.17	−0.03 ± 0.21	−0.18 ± 0.17	−0.04 ± 0.15	−0.08 ± 0.17
J02565+554E	0.00 ± 0.17	0.15 ± 0.17	0.05 ± 0.18	−0.08 ± 0.17	0.13 ± 0.12	−0.02 ± 0.16	−0.03 ± 0.12	−0.03 ± 0.14	0.14 ± 0.10	0.08 ± 0.16	0.00 ± 0.14	−0.13 ± 0.20	−0.14 ± 0.16	−0.02 ± 0.13	−0.08 ± 0.15
J03026−181	−0.08 ± 0.17	0.04 ± 0.17	−0.08 ± 0.18	−0.06 ± 0.18	−0.04 ± 0.11	0.05 ± 0.16	−0.11 ± 0.12	−0.03 ± 0.15	0.07 ± 0.10	−0.03 ± 0.18	0.05 ± 0.14	−0.12 ± 0.20	−0.01 ± 0.18	−0.00 ± 0.13	−0.01 ± 0.16
J03033−080	0.09 ± 0.16	0.17 ± 0.17	0.09 ± 0.17	0.01 ± 0.17	0.12 ± 0.11	0.05 ± 0.16	0.00 ± 0.12	0.12 ± 0.15	0.16 ± 0.10	0.20 ± 0.17	0.02 ± 0.14	−0.08 ± 0.20	−0.00 ± 0.16	0.03 ± 0.13	−0.01 ± 0.15
J03047+617	−0.13 ± 0.17	0.16 ± 0.17	−0.28 ± 0.17	−0.15 ± 0.17	0.08 ± 0.12	−0.14 ± 0.16	−0.10 ± 0.12	−0.08 ± 0.14	0.06 ± 0.10	−0.05 ± 0.16	−0.11 ± 0.14	−0.14 ± 0.20	−0.26 ± 0.17	−0.02 ± 0.13	−0.29 ± 0.15
J03079+255	−0.04 ± 0.17	−0.00 ± 0.17	0.02 ± 0.17	−0.02 ± 0.17	−0.05 ± 0.12	0.03 ± 0.15	−0.12 ± 0.12	0.02 ± 0.15	0.03 ± 0.10	0.06 ± 0.16	−0.01 ± 0.14	−0.13 ± 0.20	0.03 ± 0.16	−0.14 ± 0.13	0.01 ± 0.15
J03110−046	−0.09 ± 0.17	0.07 ± 0.16	−0.17 ± 0.18	−0.13 ± 0.17	−0.03 ± 0.11	−0.06 ± 0.15	−0.09 ± 0.12	−0.03 ± 0.14	0.05 ± 0.10	−0.04 ± 0.16	−0.06 ± 0.14	−0.11 ± 0.19	−0.10 ± 0.16	−0.09 ± 0.13	−0.14 ± 0.14
J03150+010	−0.42 ± 0.16	−0.20 ± 0.13	−0.54 ± 0.19	−0.47 ± 0.19	−0.33 ± 0.17	−0.44 ± 0.16	−0.52 ± 0.15	−0.53 ± 0.17	−0.32 ± 0.15	−0.32 ± 0.21	−0.50 ± 0.18	−0.60 ± 0.20	−0.59 ± 0.18	−0.57 ± 0.16	−0.60 ± 0.17
J03154+578	−0.30 ± 0.18	−0.10 ± 0.17	−0.52 ± 0.19	−0.44 ± 0.17	−0.25 ± 0.12	−0.33 ± 0.15	−0.34 ± 0.13	−0.14 ± 0.15	−0.16 ± 0.11	−0.14 ± 0.17	−0.30 ± 0.15	−0.48 ± 0.22	−0.46 ± 0.17	−0.26 ± 0.13	−0.48 ± 0.16
J03162+581S	−0.14 ± 0.16	0.02 ± 0.14	−0.05 ± 0.19	−0.12 ± 0.18	−0.02 ± 0.18	−0.02 ± 0.16	−0.01 ± 0.14	−0.15 ± 0.16	0.09 ± 0.14	−0.05 ± 0.19	−0.02 ± 0.16	−0.10 ± 0.20	−0.12 ± 0.17	−0.06 ± 0.15	−0.08 ± 0.16
J03162+581N	−0.13 ± 0.16	0.01 ± 0.13	0.06 ± 0.19	−0.11 ± 0.19	0.00 ± 0.18	−0.03 ± 0.16	0.02 ± 0.14	−0.09 ± 0.15	0.14 ± 0.14	0.01 ± 0.19	0.05 ± 0.17	−0.08 ± 0.19	−0.11 ± 0.18	−0.00 ± 0.15	0.01 ± 0.16
J03167+389	−0.00 ± 0.16	0.10 ± 0.17	0.12 ± 0.17	0.00 ± 0.16	0.07 ± 0.12	0.06 ± 0.15	−0.02 ± 0.13	0.12 ± 0.14	0.13 ± 0.10	0.25 ± 0.16	0.06 ± 0.14	−0.05 ± 0.20	0.06 ± 0.16	0.02 ± 0.13	0.05 ± 0.15
J03174−011	−0.28 ± 0.16	−0.09 ± 0.14	−0.44 ± 0.18	−0.38 ± 0.18	−0.27 ± 0.17	−0.30 ± 0.16	−0.33 ± 0.14	−0.28 ± 0.16	−0.17 ± 0.14	−0.15 ± 0.19	−0.35 ± 0.16	−0.49 ± 0.21	−0.36 ± 0.17	−0.37 ± 0.16	−0.38 ± 0.16
J03179−010	−0.16 ± 0.15	−0.07 ± 0.13	−0.22 ± 0.19	−0.28 ± 0.19	−0.27 ± 0.18	−0.17 ± 0.16	−0.17 ± 0.14	−0.18 ± 0.16	−0.04 ± 0.14	−0.09 ± 0.20	−0.18 ± 0.17	−0.41 ± 0.20	−0.21 ± 0.18	−0.22 ± 0.15	−0.26 ± 0.16
J03181+426	0.05 ± 0.17	0.15 ± 0.17	0.17 ± 0.17	0.14 ± 0.18	0.20 ± 0.12	0.12 ± 0.16	0.02 ± 0.13	0.23 ± 0.14	0.18 ± 0.10	0.29 ± 0.16	0.09 ± 0.14	0.03 ± 0.20	0.15 ± 0.17	0.11 ± 0.13	0.13 ± 0.15
J03181+382	0.01 ± 0.16	0.15 ± 0.13	0.25 ± 0.18	−0.02 ± 0.18	0.12 ± 0.18	0.06 ± 0.15	0.02 ± 0.14	0.07 ± 0.15	0.14 ± 0.14	0.14 ± 0.20	0.09 ± 0.17	0.10 ± 0.20	0.06 ± 0.17	0.03 ± 0.15	0.07 ± 0.17
J03194+619	−0.04 ± 0.16	−0.04 ± 0.17	−0.13 ± 0.17	−0.12 ± 0.17	−0.00 ± 0.12	−0.11 ± 0.16	−0.08 ± 0.12	−0.06 ± 0.14	0.10 ± 0.10	0.17 ± 0.16	−0.09 ± 0.14	−0.14 ± 0.20	−0.12 ± 0.16	−0.10 ± 0.13	−0.14 ± 0.15
J03207+090	−0.11 ± 0.17	0.11 ± 0.17	−0.16 ± 0.18	−0.09 ± 0.17	0.22 ± 0.12	−0.02 ± 0.15	−0.06 ± 0.13	0.00 ± 0.15	0.19 ± 0.10	0.02 ± 0.17	−0.01 ± 0.14	0.00 ± 0.20	−0.16 ± 0.17	0.03 ± 0.13	−0.17 ± 0.16
J03213+799	−0.22 ± 0.16	0.05 ± 0.13	−0.14 ± 0.18	−0.16 ± 0.18	−0.15 ± 0.17	−0.07 ± 0.16	−0.12 ± 0.14	−0.08 ± 0.16	−0.06 ± 0.14	−0.06 ± 0.20	−0.10 ± 0.16	−0.25 ± 0.19	−0.11 ± 0.17	−0.23 ± 0.15	−0.18 ± 0.17
J03217−066	−0.11 ± 0.16	0.09 ± 0.14	0.05 ± 0.19	−0.10 ± 0.18	−0.05 ± 0.17	−0.02 ± 0.16	−0.03 ± 0.14	−0.03 ± 0.16	0.03 ± 0.14	−0.00 ± 0.19	−0.00 ± 0.16	−0.06 ± 0.21	−0.05 ± 0.17	−0.13 ± 0.16	−0.06 ± 0.16
J03236+476	−0.03 ± 0.16	0.11 ± 0.13	0.09 ± 0.18	−0.03 ± 0.18	0.05 ± 0.17	0.09 ± 0.16	0.05 ± 0.14	0.10 ± 0.15	0.13 ± 0.14	0.11 ± 0.19	0.08 ± 0.17	−0.00 ± 0.20	0.08 ± 0.17	−0.01 ± 0.15	0.07 ± 0.16
J03236+056	0.07 ± 0.17	0.12 ± 0.17	−0.20 ± 0.18	−0.09 ± 0.18	0.34 ± 0.12	−0.05 ± 0.16	0.11 ± 0.12	−0.07 ± 0.15	0.37 ± 0.10	0.24 ± 0.18	0.07 ± 0.15	0.13 ± 0.20	−0.16 ± 0.18	0.12 ± 0.14	−0.20 ± 0.15
J03275+222	−0.02 ± 0.17	0.11 ± 0.16	−0.21 ± 0.16	−0.11 ± 0.17	0.25 ± 0.11	−0.09 ± 0.15	0.04 ± 0.13	−0.04 ± 0.15	0.24 ± 0.10	0.14 ± 0.17	0.01 ± 0.15	0.05 ± 0.20	−0.18 ± 0.17	0.06 ± 0.14	−0.21 ± 0.16
J03294+117	0.10 ± 0.17	0.11 ± 0.17	0.17 ± 0.16	0.12 ± 0.18	0.05 ± 0.11	0.07 ± 0.16	−0.04 ± 0.12	0.10 ± 0.15	0.11 ± 0.10	0.15 ± 0.17	−0.02 ± 0.15	−0.17 ± 0.19	0.09 ± 0.17	−0.03 ± 0.14	0.08 ± 0.15
J03303+346	0.19 ± 0.17	0.06 ± 0.17	0.08 ± 0.17	−0.14 ± 0.17	0.25 ± 0.12	−0.07 ± 0.16	0.20 ± 0.13	−0.08 ± 0.15	0.33 ± 0.10	0.37 ± 0.17	0.19 ± 0.15	0.15 ± 0.21	−0.09 ± 0.17	0.07 ± 0.13	−0.09 ± 0.15
J03309+706	−0.20 ± 0.17	−0.05 ± 0.17	−0.22 ± 0.17	−0.22 ± 0.17	−0.16 ± 0.11	−0.17 ± 0.15	−0.19 ± 0.12	−0.06 ± 0.14	−0.05 ± 0.10	−0.05 ± 0.16	−0.11 ± 0.14	−0.24 ± 0.20	−0.15 ± 0.16	−0.19 ± 0.13	−0.19 ± 0.15
J03320+436	−0.12 ± 0.16	0.02 ± 0.13	−0.06 ± 0.18	−0.09 ± 0.18	−0.00 ± 0.17	−0.03 ± 0.15	−0.03 ± 0.14	−0.02 ± 0.15	0.07 ± 0.14	0.04 ± 0.19	0.03 ± 0.17	−0.08 ± 0.20	−0.04 ± 0.16	−0.05 ± 0.15	−0.02 ± 0.16
J03354+428	−0.30 ± 0.16	−0.13 ± 0.13	−0.39 ± 0.19	−0.41 ± 0.19	−0.24 ± 0.17	−0.28 ± 0.16	−0.30 ± 0.14	−0.32 ± 0.16	−0.19 ± 0.15	−0.27 ± 0.20	−0.34 ± 0.16	−0.47 ± 0.21	−0.42 ± 0.17	−0.34 ± 0.15	−0.36 ± 0.17
J03361+313	−0.12 ± 0.16	−0.07 ± 0.17	−0.30 ± 0.17	−0.35 ± 0.18	0.04 ± 0.12	−0.31 ± 0.16	−0.03 ± 0.12	−0.28 ± 0.15	0.17 ± 0.10	0.10 ± 0.16	−0.06 ± 0.14	−0.09 ± 0.20	−0.34 ± 0.17	−0.10 ± 0.14	−0.40 ± 0.15
J03375+288	−0.18 ± 0.16	0.05 ± 0.13	−0.25 ± 0.18	−0.15 ± 0.19	−0.14 ± 0.17	−0.18 ± 0.15	−0.14 ± 0.13	−0.13 ± 0.16	−0.02 ± 0.14	−0.07 ± 0.19	−0.10 ± 0.17	−0.30 ± 0.20	−0.19 ± 0.17	−0.21 ± 0.15	−0.16 ± 0.16
J03375+178NAB	−0.00 ± 0.16	0.04 ± 0.17	0.01 ± 0.17	−0.21 ± 0.16	−0.02 ± 0.12	−0.05 ± 0.16	−0.07 ± 0.12	−0.04 ± 0.15	0.08 ± 0.11	0.15 ± 0.17	−0.04 ± 0.14	−0.09 ± 0.20	−0.02 ± 0.16	−0.11 ± 0.13	−0.07 ± 0.15
J03392+565AB	0.06 ± 0.17	0.17 ± 0.18	0.09 ± 0.17	0.02 ± 0.17	0.15 ± 0.12	0.08 ± 0.15	−0.01 ± 0.12	0.10 ± 0.14	0.15 ± 0.10	0.17 ± 0.16	0.03 ± 0.15	−0.05 ± 0.21	0.01 ± 0.16	0.04 ± 0.13	0.02 ± 0.15
J03395+183	−0.36 ± 0.16	−0.06 ± 0.13	−0.41 ± 0.19	−0.34 ± 0.18	−0.32 ± 0.18	−0.23 ± 0.16	−0.27 ± 0.14	−0.28 ± 0.16	−0.21 ± 0.15	−0.22 ± 0.20	−0.27 ± 0.17	−0.49 ± 0.20	−0.29 ± 0.17	−0.43 ± 0.15	−0.40 ± 0.17
J03397+334	0.02 ± 0.16	−0.01 ± 0.16	0.03 ± 0.17	−0.22 ± 0.18	0.07 ± 0.11	−0.22 ± 0.16	0.03 ± 0.13	−0.19 ± 0.15	0.15 ± 0.10	0.21 ± 0.16	−0.01 ± 0.14	−0.05 ± 0.19	−0.19 ± 0.17	−0.09 ± 0.13	−0.23 ± 0.16
J03430+459	−0.16 ± 0.16	−0.02 ± 0.16	−0.15 ± 0.17	−0.11 ± 0.17	−0.09 ± 0.11	−0.07 ± 0.15	−0.15 ± 0.13	0.03 ± 0.14	0.01 ± 0.10	0.06 ± 0.16	−0.10 ± 0.14	−0.20 ± 0.20	−0.06 ± 0.16	−0.14 ± 0.13	−0.08 ± 0.15
J03463+262	−0.14 ± 0.16	−0.02 ± 0.13	−0.03 ± 0.18	−0.19 ± 0.19	−0.03 ± 0.18	−0.09 ± 0.16	−0.15 ± 0.14	−0.11 ± 0.16	−0.02 ± 0.15	−0.01 ± 0.19	−0.07 ± 0.17	−0.11 ± 0.20	−0.10 ± 0.17	−0.15 ± 0.15	−0.11 ± 0.16
J03480+405	0.25 ± 0.17	0.36 ± 0.14	0.51 ± 0.19	0.10 ± 0.19	0.06 ± 0.18	0.23 ± 0.17	0.23 ± 0.15	0.37 ± 0.16	0.24 ± 0.15	0.43 ± 0.21	0.29 ± 0.17	0.33 ± 0.21	0.39 ± 0.18	0.18 ± 0.16	0.31 ± 0.16
J03510+142	0.03 ± 0.17	0.01 ± 0.18	−0.20 ± 0.18	−0.39 ± 0.20	0.25 ± 0.12	−0.40 ± 0.17	0.18 ± 0.13	−0.42 ± 0.17	0.33 ± 0.10	0.22 ± 0.17	0.05 ± 0.15	0.07 ± 0.22	−0.45 ± 0.19	0.04 ± 0.14	−0.49 ± 0.17
J03519+397	−0.13 ± 0.16	−0.02 ± 0.13	−0.06 ± 0.18	−0.19 ± 0.18	−0.07 ± 0.17	−0.06 ± 0.16	−0.07 ± 0.13	−0.07 ± 0.15	0.00 ± 0.15	0.02 ± 0.19	−0.02 ± 0.17	−0.09 ± 0.20	−0.03 ± 0.16	−0.14 ± 0.15	−0.05 ± 0.16
J03531+625	−0.25 ± 0.17	0.02 ± 0.17	−0.39 ± 0.17	−0.38 ± 0.17	−0.11 ± 0.12	−0.33 ± 0.15	−0.17 ± 0.13	−0.34 ± 0.15	−0.03 ± 0.10	−0.18 ± 0.17	−0.21 ± 0.14	−0.24 ± 0.20	−0.40 ± 0.16	−0.21 ± 0.13	−0.45 ± 0.15
J03556+522	−0.22 ± 0.16	−0.06 ± 0.17	−0.30 ± 0.17	−0.33 ± 0.16	−0.27 ± 0.11	−0.25 ± 0.15	−0.22 ± 0.12	−0.26 ± 0.14	−0.12 ± 0.10	−0.19 ± 0.17	−0.18 ± 0.14	−0.33 ± 0.20	−0.27 ± 0.16	−0.25 ± 0.13	−0.35 ± 0.15
J03566+507	0.00 ± 0.16	0.12 ± 0.13	0.14 ± 0.18	0.01 ± 0.19	0.11 ± 0.18	0.13 ± 0.16	0.08 ± 0.14	0.13 ± 0.16	0.16 ± 0.14	0.12 ± 0.19	0.15 ± 0.16	0.13 ± 0.20	0.11 ± 0.17	0.08 ± 0.15	0.08 ± 0.17

Table C.4: *Continued*

Karmn	[C/H]	[O/H]	[Na/H]	[Mg/H]	[Al/H]	[Si/H]	[Ca/H]	[Sc/H]	[Ti/H]	[V/H]	[Cr/H]	[Mn/H]	[Fe/H]	[Co/H]	[Ni/H]
J03574−011AB	−0.08 ± 0.16	−0.03 ± 0.16	−0.15 ± 0.16	−0.25 ± 0.17	−0.12 ± 0.11	−0.13 ± 0.15	−0.13 ± 0.12	−0.07 ± 0.14	0.02 ± 0.10	0.04 ± 0.16	−0.10 ± 0.14	−0.16 ± 0.20	−0.11 ± 0.16	−0.16 ± 0.13	−0.16 ± 0.14
J03588+125	0.13 ± 0.17	0.19 ± 0.17	0.24 ± 0.17	0.17 ± 0.17	0.38 ± 0.12	0.16 ± 0.15	0.18 ± 0.13	0.22 ± 0.14	0.38 ± 0.10	0.39 ± 0.17	0.23 ± 0.14	0.23 ± 0.20	0.14 ± 0.16	0.24 ± 0.13	0.15 ± 0.15
J04041+307	−0.32 ± 0.16	−0.09 ± 0.13	−0.26 ± 0.20	−0.30 ± 0.18	−0.28 ± 0.18	−0.09 ± 0.16	−0.14 ± 0.14	−0.14 ± 0.16	−0.12 ± 0.14	−0.12 ± 0.20	−0.13 ± 0.18	−0.37 ± 0.20	−0.18 ± 0.18	−0.27 ± 0.15	−0.20 ± 0.17
J04061−055	−0.19 ± 0.16	0.01 ± 0.16	−0.15 ± 0.17	−0.11 ± 0.17	−0.10 ± 0.12	−0.07 ± 0.14	−0.13 ± 0.12	−0.05 ± 0.14	−0.01 ± 0.10	0.02 ± 0.17	−0.05 ± 0.14	−0.16 ± 0.19	−0.03 ± 0.16	−0.12 ± 0.13	−0.09 ± 0.15
J04079+142	−0.01 ± 0.16	0.12 ± 0.17	0.08 ± 0.17	0.01 ± 0.17	0.09 ± 0.12	0.05 ± 0.15	−0.06 ± 0.12	0.10 ± 0.14	0.11 ± 0.10	0.18 ± 0.16	0.02 ± 0.14	−0.08 ± 0.20	0.02 ± 0.16	−0.00 ± 0.13	0.03 ± 0.15
J04081+743	−0.14 ± 0.16	0.02 ± 0.17	−0.18 ± 0.17	−0.08 ± 0.17	−0.12 ± 0.12	−0.01 ± 0.16	−0.21 ± 0.12	0.05 ± 0.14	−0.04 ± 0.10	−0.01 ± 0.17	−0.09 ± 0.14	−0.17 ± 0.20	0.02 ± 0.16	−0.16 ± 0.13	−0.07 ± 0.15
J04083+691	−0.21 ± 0.17	−0.03 ± 0.17	−0.29 ± 0.17	−0.13 ± 0.17	−0.13 ± 0.11	−0.08 ± 0.15	−0.27 ± 0.13	−0.11 ± 0.14	−0.06 ± 0.10	−0.05 ± 0.16	−0.16 ± 0.14	−0.27 ± 0.20	−0.10 ± 0.17	−0.19 ± 0.13	−0.19 ± 0.15
J04177+410	−0.00 ± 0.16	−0.03 ± 0.16	−0.06 ± 0.17	−0.20 ± 0.18	−0.06 ± 0.11	−0.07 ± 0.16	−0.06 ± 0.13	−0.13 ± 0.14	0.09 ± 0.10	0.05 ± 0.17	0.02 ± 0.14	−0.10 ± 0.20	−0.08 ± 0.16	−0.14 ± 0.13	−0.13 ± 0.15
J04191−074	0.18 ± 0.17	0.19 ± 0.18	0.20 ± 0.18	0.24 ± 0.17	0.27 ± 0.12	0.25 ± 0.16	0.02 ± 0.13	0.23 ± 0.15	0.30 ± 0.10	0.33 ± 0.17	0.04 ± 0.14	0.01 ± 0.20	0.18 ± 0.16	0.14 ± 0.14	0.18 ± 0.16
J04191+097	−0.20 ± 0.16	0.00 ± 0.16	−0.28 ± 0.17	−0.28 ± 0.17	−0.09 ± 0.12	−0.23 ± 0.15	−0.16 ± 0.13	−0.20 ± 0.14	−0.01 ± 0.10	−0.08 ± 0.16	−0.13 ± 0.14	−0.17 ± 0.20	−0.26 ± 0.16	−0.18 ± 0.13	−0.31 ± 0.15
J04205+815	−0.13 ± 0.16	0.02 ± 0.17	−0.13 ± 0.17	−0.15 ± 0.16	−0.10 ± 0.12	−0.03 ± 0.15	−0.15 ± 0.12	−0.06 ± 0.14	0.01 ± 0.10	−0.04 ± 0.17	−0.01 ± 0.14	−0.13 ± 0.21	−0.03 ± 0.16	−0.15 ± 0.13	−0.12 ± 0.15
J04225+105	0.05 ± 0.17	0.13 ± 0.16	0.33 ± 0.16	0.19 ± 0.17	0.17 ± 0.11	0.16 ± 0.15	0.04 ± 0.13	0.25 ± 0.14	0.20 ± 0.10	0.33 ± 0.17	0.12 ± 0.15	−0.00 ± 0.21	0.20 ± 0.16	0.09 ± 0.14	0.24 ± 0.15
J04229+259	−0.01 ± 0.16	0.10 ± 0.17	0.11 ± 0.17	0.15 ± 0.17	0.14 ± 0.12	0.16 ± 0.16	−0.04 ± 0.13	0.18 ± 0.15	0.15 ± 0.10	0.23 ± 0.16	0.07 ± 0.14	0.00 ± 0.20	0.19 ± 0.16	0.05 ± 0.13	0.15 ± 0.15
J04234+809	0.01 ± 0.17	−0.04 ± 0.16	−0.02 ± 0.17	−0.15 ± 0.17	0.00 ± 0.11	−0.07 ± 0.15	−0.01 ± 0.12	−0.09 ± 0.15	0.13 ± 0.10	0.11 ± 0.17	0.05 ± 0.14	−0.03 ± 0.20	−0.04 ± 0.16	−0.11 ± 0.13	−0.10 ± 0.15
J04251+257	−0.24 ± 0.16	−0.02 ± 0.13	−0.15 ± 0.19	−0.19 ± 0.19	−0.21 ± 0.18	0.00 ± 0.16	−0.06 ± 0.15	−0.06 ± 0.16	−0.07 ± 0.15	−0.08 ± 0.19	−0.05 ± 0.16	−0.25 ± 0.21	−0.03 ± 0.17	−0.25 ± 0.15	−0.14 ± 0.17
J04308−088	−0.07 ± 0.17	−0.01 ± 0.17	0.04 ± 0.18	0.02 ± 0.17	0.00 ± 0.11	0.05 ± 0.15	−0.09 ± 0.13	0.07 ± 0.15	0.06 ± 0.10	0.07 ± 0.16	0.06 ± 0.14	−0.03 ± 0.20	0.12 ± 0.16	−0.07 ± 0.14	0.07 ± 0.15
J04310+367	−0.09 ± 0.16	−0.01 ± 0.16	−0.18 ± 0.17	−0.25 ± 0.17	−0.08 ± 0.11	−0.21 ± 0.15	−0.09 ± 0.12	−0.13 ± 0.15	0.05 ± 0.10	0.04 ± 0.16	−0.08 ± 0.14	−0.15 ± 0.19	−0.22 ± 0.16	−0.16 ± 0.13	−0.24 ± 0.15
J04311+589	−0.27 ± 0.18	0.15 ± 0.18	−0.09 ± 0.19	−0.09 ± 0.18	0.08 ± 0.11	−0.11 ± 0.16	0.07 ± 0.13	−0.18 ± 0.16	0.07 ± 0.10	−0.10 ± 0.19	0.15 ± 0.14	0.10 ± 0.21	−0.13 ± 0.18	0.12 ± 0.13	−0.10 ± 0.18
J04329+001S	−0.19 ± 0.16	−0.01 ± 0.13	−0.19 ± 0.19	−0.18 ± 0.19	−0.07 ± 0.17	−0.13 ± 0.16	−0.18 ± 0.13	−0.19 ± 0.15	0.00 ± 0.15	−0.04 ± 0.19	−0.14 ± 0.17	−0.31 ± 0.19	−0.22 ± 0.17	−0.17 ± 0.16	−0.22 ± 0.16
J04347−004	−0.16 ± 0.17	−0.03 ± 0.17	−0.26 ± 0.17	−0.12 ± 0.16	−0.13 ± 0.11	−0.07 ± 0.16	−0.23 ± 0.13	−0.07 ± 0.14	−0.02 ± 0.10	−0.03 ± 0.16	−0.16 ± 0.14	−0.24 ± 0.20	−0.11 ± 0.16	−0.20 ± 0.13	−0.15 ± 0.16
J04359+165	−0.08 ± 0.19	0.05 ± 0.21	−0.76 ± 0.27	−0.10 ± 0.21	−0.43 ± 0.13	−0.13 ± 0.18	−0.24 ± 0.16	−0.42 ± 0.18	−0.22 ± 0.12	−0.75 ± 0.20	−0.01 ± 0.18	−0.51 ± 0.24	−0.28 ± 0.23	−0.55 ± 0.15	−0.41 ± 0.23
J04376−110	−0.16 ± 0.16	0.05 ± 0.13	−0.07 ± 0.19	−0.18 ± 0.18	−0.12 ± 0.17	−0.12 ± 0.16	−0.15 ± 0.14	−0.14 ± 0.15	−0.04 ± 0.14	−0.07 ± 0.18	−0.12 ± 0.16	−0.18 ± 0.19	−0.17 ± 0.17	−0.23 ± 0.15	−0.21 ± 0.17
J04386−115	0.05 ± 0.17	0.08 ± 0.17	0.21 ± 0.17	−0.02 ± 0.17	0.12 ± 0.12	0.08 ± 0.16	−0.00 ± 0.13	0.03 ± 0.14	0.17 ± 0.10	0.19 ± 0.16	0.05 ± 0.14	−0.06 ± 0.20	0.05 ± 0.17	0.01 ± 0.13	0.03 ± 0.16
J04388+217	0.04 ± 0.16	0.12 ± 0.17	0.01 ± 0.17	0.01 ± 0.17	0.14 ± 0.12	0.06 ± 0.15	0.01 ± 0.13	0.06 ± 0.14	0.20 ± 0.10	0.17 ± 0.16	0.00 ± 0.14	−0.01 ± 0.20	−0.02 ± 0.16	−0.00 ± 0.13	0.02 ± 0.16
J04397+098	−0.23 ± 0.16	−0.07 ± 0.17	−0.26 ± 0.17	−0.25 ± 0.17	−0.21 ± 0.12	−0.17 ± 0.16	−0.21 ± 0.12	−0.11 ± 0.14	−0.06 ± 0.10	−0.09 ± 0.16	−0.16 ± 0.14	−0.30 ± 0.21	−0.16 ± 0.16	−0.28 ± 0.13	−0.20 ± 0.15
J04398+251	−0.07 ± 0.17	0.01 ± 0.16	−0.06 ± 0.17	−0.14 ± 0.17	−0.07 ± 0.12	−0.02 ± 0.15	−0.18 ± 0.12	0.00 ± 0.14	−0.00 ± 0.10	0.09 ± 0.16	−0.10 ± 0.14	−0.22 ± 0.20	−0.03 ± 0.16	−0.12 ± 0.13	−0.07 ± 0.15
J04413+327	0.06 ± 0.17	0.18 ± 0.17	0.13 ± 0.16	0.09 ± 0.17	0.27 ± 0.11	0.16 ± 0.15	0.04 ± 0.13	0.15 ± 0.14	0.27 ± 0.10	0.21 ± 0.17	0.18 ± 0.15	0.11 ± 0.20	0.09 ± 0.16	0.11 ± 0.13	0.08 ± 0.14
J04429+189	−0.06 ± 0.16	0.16 ± 0.13	0.14 ± 0.19	−0.05 ± 0.19	−0.01 ± 0.17	0.05 ± 0.16	0.01 ± 0.14	0.06 ± 0.15	0.09 ± 0.14	0.07 ± 0.19	0.05 ± 0.16	0.03 ± 0.20	0.02 ± 0.17	−0.03 ± 0.16	0.03 ± 0.16
J04429+214	−0.08 ± 0.16	0.06 ± 0.16	−0.04 ± 0.17	−0.12 ± 0.17	−0.00 ± 0.12	−0.02 ± 0.14	−0.11 ± 0.13	−0.01 ± 0.14	0.07 ± 0.10	0.05 ± 0.16	−0.03 ± 0.13	−0.10 ± 0.20	−0.05 ± 0.17	−0.09 ± 0.13	−0.07 ± 0.15
J04458−144	0.19 ± 0.17	0.18 ± 0.16	0.48 ± 0.17	0.24 ± 0.17	0.37 ± 0.12	0.36 ± 0.15	0.10 ± 0.13	0.32 ± 0.15	0.34 ± 0.10	0.41 ± 0.16	0.24 ± 0.14	0.18 ± 0.21	0.33 ± 0.17	0.21 ± 0.14	0.34 ± 0.15
J04468−112AB	0.02 ± 0.17	−0.07 ± 0.17	−0.10 ± 0.17	−0.20 ± 0.17	−0.09 ± 0.12	−0.14 ± 0.15	−0.15 ± 0.13	−0.10 ± 0.14	0.05 ± 0.10	0.10 ± 0.17	−0.16 ± 0.15	−0.30 ± 0.20	−0.16 ± 0.17	−0.19 ± 0.13	−0.22 ± 0.15
J04488+100	−0.19 ± 0.16	−0.06 ± 0.17	−0.20 ± 0.17	−0.29 ± 0.17	−0.20 ± 0.12	−0.18 ± 0.15	−0.21 ± 0.12	−0.16 ± 0.15	−0.05 ± 0.10	−0.03 ± 0.17	−0.16 ± 0.14	−0.26 ± 0.20	−0.18 ± 0.16	−0.25 ± 0.14	−0.23 ± 0.14
J04494+484AB	−0.01 ± 0.16	−0.04 ± 0.16	−0.08 ± 0.17	−0.15 ± 0.18	0.01 ± 0.12	−0.14 ± 0.16	−0.06 ± 0.12	−0.05 ± 0.14	0.09 ± 0.10	0.16 ± 0.16	−0.03 ± 0.14	−0.13 ± 0.20	−0.14 ± 0.16	−0.06 ± 0.13	−0.15 ± 0.15
J04496−153	−0.11 ± 0.16	0.05 ± 0.13	−0.09 ± 0.19	−0.08 ± 0.18	−0.02 ± 0.17	−0.01 ± 0.15	−0.04 ± 0.14	−0.03 ± 0.15	0.05 ± 0.15	0.03 ± 0.20	−0.01 ± 0.17	−0.09 ± 0.20	−0.03 ± 0.17	−0.08 ± 0.15	−0.11 ± 0.16
J04499+711	0.01 ± 0.16	0.13 ± 0.16	0.06 ± 0.17	0.07 ± 0.17	0.11 ± 0.12	0.05 ± 0.15	−0.05 ± 0.12	0.12 ± 0.15	0.10 ± 0.10	0.23 ± 0.17	0.05 ± 0.14	−0.02 ± 0.20	0.03 ± 0.16	0.04 ± 0.13	0.03 ± 0.15
J04520+064	0.01 ± 0.17	−0.00 ± 0.18	0.07 ± 0.18	−0.18 ± 0.17	−0.01 ± 0.11	−0.10 ± 0.16	−0.06 ± 0.13	−0.15 ± 0.14	0.11 ± 0.11	0.12 ± 0.18	−0.02 ± 0.14	−0.16 ± 0.20	−0.11 ± 0.16	−0.14 ± 0.14	−0.12 ± 0.14
J04536+623	−0.15 ± 0.16	0.06 ± 0.16	−0.21 ± 0.17	−0.17 ± 0.16	0.00 ± 0.12	−0.13 ± 0.15	−0.12 ± 0.12	−0.07 ± 0.15	0.05 ± 0.10	−0.03 ± 0.17	−0.10 ± 0.14	−0.12 ± 0.20	−0.19 ± 0.16	−0.11 ± 0.13	−0.20 ± 0.15
J04538−177	−0.32 ± 0.17	0.02 ± 0.14	−0.67 ± 0.19	−0.33 ± 0.19	−0.27 ± 0.18	−0.27 ± 0.16	−0.37 ± 0.15	−0.29 ± 0.16	−0.16 ± 0.15	−0.29 ± 0.20	−0.43 ± 0.17	−0.68 ± 0.21	−0.41 ± 0.18	−0.31 ± 0.15	−0.58 ± 0.17
J04538+158	−0.15 ± 0.16	0.03 ± 0.17	−0.21 ± 0.17	−0.21 ± 0.16	−0.07 ± 0.12	−0.12 ± 0.15	−0.12 ± 0.13	−0.09 ± 0.14	0.01 ± 0.10	−0.06 ± 0.16	−0.07 ± 0.15	−0.19 ± 0.20	−0.14 ± 0.16	−0.11 ± 0.13	−0.21 ± 0.15
J04544+650	−0.07 ± 0.16	−0.03 ± 0.17	−0.13 ± 0.17	−0.59 ± 0.23	−0.04 ± 0.11	−0.57 ± 0.21	−0.10 ± 0.12	−0.77 ± 0.18	0.06 ± 0.10	0.10 ± 0.17	−0.05 ± 0.14	−0.12 ± 0.20	−0.59 ± 0.21	−0.11 ± 0.13	−0.75 ± 0.22
J04560+432	−0.12 ± 0.16	0.01 ± 0.17	−0.04 ± 0.17	−0.09 ± 0.17	0.02 ± 0.12	−0.04 ± 0.15	−0.13 ± 0.13	0.04 ± 0.15	0.06 ± 0.10	0.15 ± 0.17	−0.09 ± 0.14	−0.13 ± 0.20	−0.06 ± 0.16	−0.03 ± 0.13	−0.07 ± 0.15
J04588+498	−0.12 ± 0.16	0.08 ± 0.13	−0.21 ± 0.19	−0.22 ± 0.18	−0.03 ± 0.17	−0.10 ± 0.16	−0.22 ± 0.14	−0.12 ± 0.15	−0.03 ± 0.14	−0.05 ± 0.19	−0.22 ± 0.17	−0.32 ± 0.22	−0.15 ± 0.17	−0.14 ± 0.15	−0.27 ± 0.17
J05003+251AB	−0.09 ± 0.16	0.00 ± 0.13	−0.06 ± 0.18	−0.18 ± 0.18	−0.07 ± 0.17	−0.16 ± 0.16	−0.18 ± 0.14	−0.11 ± 0.15	−0.01 ± 0.15	−0.07 ± 0.19	−0.12 ± 0.16	−0.12 ± 0.19	−0.17 ± 0.16	−0.18 ± 0.15	−0.21 ± 0.16
J05019−069	−0.18 ± 0.17	−0.08 ± 0.17	−0.16 ± 0.17	−0.14 ± 0.17	−0.16 ± 0.12	−0.08 ± 0.15	−0.21 ± 0.12	−0.04 ± 0.15	−0.04 ± 0.10	0.01 ± 0.16	−0.16 ± 0.14	−0.31 ± 0.20	−0.06 ± 0.16	−0.25 ± 0.13	−0.09 ± 0.15
J05033−173	−0.12 ± 0.16	0.02 ± 0.17	0.16 ± 0.18	−0.14 ± 0.18	−0.20 ± 0.11	−0.00 ± 0.15	−0.22 ± 0.13	0.19 ± 0.16	−0.15 ± 0.10	0.42 ± 0.20	−0.06 ± 0.14	−0.33 ± 0.22	0.12 ± 0.18	−0.20 ± 0.13	0.07 ± 0.17
J05068+516	−0.08 ± 0.15	0.09 ± 0.14	−0.03 ± 0.18	−0.04 ± 0.18	−0.01 ± 0.17	−0.01 ± 0.16	−0.03 ± 0.14	0.03 ± 0.16	0.06 ± 0.15	0.03 ± 0.19	0.01 ± 0.17	−0.04 ± 0.20	−0.02 ± 0.17	−0.06 ± 0.15	−0.07 ± 0.17
J05078+179	−0.28 ± 0.17	−0.08 ± 0.17	−0.29 ± 0.17	−0.35 ± 0.17	−0.26 ± 0.12	−0.25 ± 0.15	−0.24 ± 0.13	−0.25 ± 0.15	−0.10 ± 0.10	−0.15 ± 0.17	−0.19 ± 0.15	−0.36 ± 0.20	−0.26 ± 0.17	−0.31 ± 0.13	−0.31 ± 0.15
J05083+756	−0.14 ± 0.17	0.03 ± 0.17	−0.12 ± 0.18	−0.06 ± 0.18	−0.02 ± 0.11	0.00 ± 0.16	−0.16 ± 0.12	−0.14 ± 0.15	0.05 ± 0.11	−0.01 ± 0.17	−0.01 ± 0.14	−0.18 ± 0.21	−0.08 ± 0.17	−0.07 ± 0.13	−0.13 ± 0.16
J05127+196	−0.31 ± 0.16	0.04 ± 0.14	−0.60 ± 0.19	−0.35 ± 0.19	−0.33 ± 0.17	−0.23 ± 0.16	−0.33 ± 0.14	−0.19 ± 0.17	−0.19 ± 0.14	−0.21 ± 0.20	−0.39 ± 0.17	−0.67 ± 0.21	−0.30 ± 0.17	−0.34 ± 0.15	−0.51 ± 0.17
J05151−073	−0.20 ± 0.16	−0.05 ± 0.14	−0.30 ± 0.19	−0.23 ± 0.19	−0.08 ± 0.17	−0.13 ± 0.15	−0.18 ± 0.14	−0.21 ± 0.15	−0.02 ± 0.14	−0.09 ± 0.19	−0.19 ± 0.16	−0.39 ± 0.20	−0.23 ± 0.17	−0.18 ± 0.15	−0.27 ± 0.16
J05173+321	−0.03 ± 0.16	0.10 ± 0.17	−0.04 ± 0.17	−0.11 ± 0.17	0.08 ± 0.12	−0.02 ± 0.15	−0.04 ± 0.12	0.04 ± 0.14	0.12 ± 0.10	0.14 ± 0.17	−0.04 ± 0.14	−0.09 ± 0.20	−0.05 ± 0.16	−0.03 ± 0.13	−0.07 ± 0.16
J05175+487	−0.15 ± 0.16	−0.00 ± 0.13	−0.30 ± 0.19	−0.17 ± 0.19	−0.07 ± 0.17	−0.12 ± 0.16	−0.14 ± 0.14	−0.11 ± 0.16	−0.02 ± 0.14	−0.10 ± 0.18	−0.12 ± 0.17	−0.33 ± 0.20	−0.13 ± 0.16	−0.17 ± 0.15	−0.18 ± 0.16
J05187+464	−0.09 ± 0.18	−0.07 ± 0.17	−0.30 ± 0.18	−0.44 ± 0.19	0.09 ± 0.12	−0.52 ± 0.17	0.09 ± 0.13	−0.51 ± 0.16	0.23 ± 0.11	0.12 ± 0.18	−0.07 ± 0.15	−0.07 ± 0.20	−0.57 ± 0.18	−0.10 ± 0.13	−0.58 ± 0.17
J05187−213	0.00 ± 0.17	−0.06 ± 0.17	−0.09 ± 0.16	−0.23 ± 0.17	−0.01 ± 0.12	−0.19 ± 0.15	−0.07 ± 0.12	−0.12 ± 0.14	0.09 ± 0.10	0.10 ± 0.17	−0.10 ± 0.14	−0.20 ± 0.20	−0.24 ± 0.16	−0.13 ± 0.13	−0.21 ± 0.15
J05195+649	−0.05 ± 0.16	−0.01 ± 0.17	−0.25 ± 0.17	−0.19 ± 0.17	−0.04 ± 0.12	−0.20 ± 0.15	−0.12 ± 0.12	−0.12 ± 0.15	0.05 ± 0.10	0.11 ± 0.16	−0.18 ± 0.14	−0.25 ± 0.20	−0.18 ± 0.17	−0.14 ± 0.13	−0.24 ± 0.15
J05200−229	−0.07 ± 0.17	−0.00 ± 0.14	0.25 ± 0.19	−0.08 ± 0.18	0.03 ± 0.17	0.06 ± 0.16	0.04 ± 0.15	−0.14 ± 0.17	0.19 ± 0.15	0.01 ± 0.21	0.07 ± 0.16	0.13 ± 0.21	−0.16 ± 0.17	0.07 ± 0.15	0.02 ± 0.17
J05223+305	−0.01 ± 0.16	0.10 ± 0.17	0.10 ± 0.16	−0.05 ± 0.17	0.06 ± 0.11	0.01 ± 0.15	−0.03 ± 0.12	0.00 ± 0.15	0.10 ± 0.10	0.11 ± 0.16	0.01 ± 0.14	−0.06 ± 0.20	0.01 ± 0.16	−0.03 ± 0.14	−0.00 ± 0.14
J05263+038	−0.23 ± 0.16	−0.00 ± 0.13	−0.23 ± 0.19	−0.22 ± 0.18	−0.21 ± 0.17	−0.13 ± 0.16	−0.19 ± 0.15	−0.14 ± 0.16	−0.06 ± 0.15	−0.08 ± 0.20	−0.15 ± 0.17	−0.28 ± 0.19	−0.20 ± 0.17	−0.21 ± 0.15	−0.23 ± 0.17
J05280+096	−0.20 ± 0.16	−0.00 ± 0.17	−0.22 ± 0.16	−0.21 ± 0.17	−0.14 ± 0.12	−0.09 ± 0.15	−0.22 ± 0.12	−0.13 ± 0.14	−0.04 ± 0.10	−0.13 ± 0.17	−0.17 ± 0.14	−0.27 ± 0.20	−0.17 ± 0.16	−0.22 ± 0.13	−0.18 ± 0.15
J05289+125	−0.12 ± 0.16	−0.04 ± 0.17	−0.07 ± 0.16	−0.17 ± 0.17	−0.09 ± 0.11	−0.10 ± 0.15	−0.14 ± 0.12	−0.04 ± 0.14	−0.01 ± 0.10	0.07 ± 0.16	−0.08 ± 0.14	−0.16 ± 0.20	−0.03 ± 0.17	−0.13 ± 0.13	−0.12 ± 0.16
J05294+155E	−0.28 ± 0.16	−0.10 ± 0.13	−0.44 ± 0.18	−0.34 ± 0.19	−0.23 ± 0.17	−0.31 ± 0.16	−0.37 ± 0.14	−0.36 ± 0.16	−0.19 ± 0.14	−0.23 ± 0.19	−0.38 ± 0.17	−0.49 ± 0.20	−0.41 ± 0.17	−0.40 ± 0.15	−0.47 ± 0.16
J05295−113	−0.06 ± 0.17	0.11 ± 0.16	−0.16 ± 0.17	−0.14 ± 0.17	0.14 ± 0.12	−0.06 ± 0.15	−0.03 ± 0.12	0.03 ± 0.14	0.18 ± 0.10	0.12 ± 0.16	−0.06 ± 0.14	−0.09 ± 0.20	−0.16 ± 0.16	0.02 ± 0.13	−0.17 ± 0.15
J05300+121W	−0.01 ± 0.16	0.14 ± 0.13	0.13 ± 0.19	0.07 ± 0.18	0.14 ± 0.17	0.16 ± 0.16	0.12 ± 0.14	0.18 ± 0.16	0.21 ± 0.15	0.18 ± 0.19	0.19 ± 0.17	0.13 ± 0.20	0.17 ± 0.17	0.15 ± 0.16	0.16 ± 0.16
J05300+121E	−0.04 ± 0.16	0.09 ± 0.13	0.09 ± 0.18	−0.04 ± 0.18	0.09 ± 0.17	0.05 ± 0.16	0.01 ± 0.13	0.03 ± 0.15	0.12 ± 0.14	0.11 ± 0.19	0.08 ± 0.17	0.01 ± 0.20	0.05 ± 0.17	0.02 ± 0.16	0.07 ± 0.16
J05314−036	0.13 ± 0.16	0.24 ± 0.14	0.24 ± 0.19	0.08 ± 0.18	0.16 ± 0.18	0.14 ± 0.16	0.11 ± 0.14	0.25 ± 0.15	0.24 ± 0.15	0.19 ± 0.20	0.17 ± 0.17	0.13 ± 0.21	0.24 ± 0.17	0.15 ± 0.15	0.13 ± 0.16
J05322+098	−0.12 ± 0.17	−0.04 ± 0.17	0.10 ± 0.19	−0.18 ± 0.18	−0.22 ± 0.11	−0.19 ± 0.16	−0.20 ± 0.13	0.10 ± 0.16	−0.15 ± 0.10	0.48 ± 0.19	−0.16 ± 0.15	−0.44 ± 0.21	−0.03 ± 0.18	−0.27 ± 0.13	−0.06 ± 0.18

Table C.4: *Continued*

Karmn	[C/H]	[O/H]	[Na/H]	[Mg/H]	[Al/H]	[Si/H]	[Ca/H]	[Sc/H]	[Ti/H]	[V/H]	[Cr/H]	[Mn/H]	[Fe/H]	[Co/H]	[Ni/H]
J05324−072	−0.15 ± 0.16	−0.04 ± 0.13	−0.28 ± 0.19	−0.27 ± 0.18	−0.17 ± 0.17	−0.21 ± 0.15	−0.28 ± 0.14	−0.23 ± 0.15	−0.11 ± 0.15	−0.07 ± 0.19	−0.26 ± 0.17	−0.37 ± 0.20	−0.28 ± 0.17	−0.29 ± 0.16	−0.34 ± 0.17
J05328+338	−0.28 ± 0.16	−0.07 ± 0.18	−0.32 ± 0.17	−0.26 ± 0.17	−0.25 ± 0.12	−0.19 ± 0.15	−0.25 ± 0.12	−0.15 ± 0.14	−0.10 ± 0.10	−0.15 ± 0.16	−0.18 ± 0.14	−0.31 ± 0.20	−0.19 ± 0.16	−0.26 ± 0.13	−0.24 ± 0.15
J05333+448	−0.14 ± 0.17	−0.04 ± 0.16	−0.18 ± 0.17	−0.26 ± 0.18	−0.12 ± 0.12	−0.17 ± 0.15	−0.17 ± 0.12	−0.14 ± 0.14	0.00 ± 0.10	0.02 ± 0.16	−0.16 ± 0.15	−0.28 ± 0.20	−0.19 ± 0.17	−0.23 ± 0.13	−0.22 ± 0.15
J05337+019	0.04 ± 0.17	−0.04 ± 0.17	0.29 ± 0.18	−0.16 ± 0.17	−0.10 ± 0.11	−0.07 ± 0.16	−0.03 ± 0.13	−0.14 ± 0.15	0.07 ± 0.11	0.20 ± 0.17	0.11 ± 0.16	−0.02 ± 0.22	0.03 ± 0.17	−0.11 ± 0.13	−0.02 ± 0.17
J05342+103S	0.03 ± 0.17	0.13 ± 0.17	0.20 ± 0.20	0.24 ± 0.18	0.33 ± 0.12	0.34 ± 0.17	0.12 ± 0.13	0.32 ± 0.16	0.26 ± 0.11	0.15 ± 0.18	0.42 ± 0.16	0.51 ± 0.24	0.43 ± 0.18	0.25 ± 0.14	0.37 ± 0.17
J05342+103N	−0.05 ± 0.16	0.14 ± 0.17	0.01 ± 0.17	−0.03 ± 0.17	0.15 ± 0.11	0.07 ± 0.15	−0.02 ± 0.13	−0.01 ± 0.14	0.15 ± 0.10	0.06 ± 0.17	0.07 ± 0.14	−0.05 ± 0.20	0.00 ± 0.16	0.03 ± 0.13	−0.03 ± 0.15
J05348+138	−0.05 ± 0.17	0.07 ± 0.18	0.09 ± 0.17	−0.06 ± 0.17	0.05 ± 0.11	0.01 ± 0.15	−0.06 ± 0.13	−0.01 ± 0.14	0.10 ± 0.10	0.14 ± 0.16	0.01 ± 0.14	−0.11 ± 0.20	−0.03 ± 0.16	−0.05 ± 0.13	0.01 ± 0.15
J05360−076	0.15 ± 0.17	0.20 ± 0.18	0.63 ± 0.19	0.31 ± 0.19	0.20 ± 0.12	0.26 ± 0.15	0.07 ± 0.13	0.50 ± 0.16	0.15 ± 0.10	0.77 ± 0.19	0.25 ± 0.15	0.04 ± 0.21	0.44 ± 0.18	0.16 ± 0.14	0.46 ± 0.17
J05365+113	−0.13 ± 0.16	0.02 ± 0.14	−0.30 ± 0.19	−0.32 ± 0.19	−0.08 ± 0.17	−0.13 ± 0.17	−0.31 ± 0.15	−0.17 ± 0.17	−0.09 ± 0.16	−0.08 ± 0.20	−0.32 ± 0.18	−0.36 ± 0.21	−0.24 ± 0.18	−0.17 ± 0.15	−0.37 ± 0.17
J05366+112	−0.08 ± 0.16	−0.03 ± 0.17	−0.03 ± 0.17	−0.22 ± 0.17	−0.07 ± 0.12	−0.11 ± 0.15	−0.15 ± 0.12	−0.08 ± 0.15	0.04 ± 0.10	0.12 ± 0.16	−0.07 ± 0.14	−0.17 ± 0.20	−0.07 ± 0.16	−0.17 ± 0.13	−0.13 ± 0.15
J05394+747	−0.12 ± 0.16	0.04 ± 0.17	−0.02 ± 0.17	−0.10 ± 0.17	−0.02 ± 0.12	−0.03 ± 0.14	−0.09 ± 0.13	0.01 ± 0.14	0.05 ± 0.10	0.09 ± 0.17	0.00 ± 0.14	−0.10 ± 0.20	−0.01 ± 0.16	−0.07 ± 0.13	−0.06 ± 0.15
J05421+124	−0.09 ± 0.16	0.11 ± 0.17	−0.12 ± 0.16	−0.07 ± 0.17	0.08 ± 0.12	0.00 ± 0.15	−0.15 ± 0.13	0.06 ± 0.15	0.07 ± 0.10	0.09 ± 0.17	−0.06 ± 0.14	−0.10 ± 0.19	−0.08 ± 0.17	0.00 ± 0.13	−0.11 ± 0.16
J05424+506	−0.15 ± 0.16	0.02 ± 0.17	−0.17 ± 0.17	−0.22 ± 0.17	−0.08 ± 0.12	−0.16 ± 0.15	−0.13 ± 0.12	−0.11 ± 0.14	0.02 ± 0.10	−0.02 ± 0.17	−0.12 ± 0.15	−0.21 ± 0.19	−0.16 ± 0.17	−0.14 ± 0.13	−0.22 ± 0.15
J05425+154	−0.13 ± 0.17	−0.06 ± 0.17	−0.27 ± 0.17	−0.27 ± 0.17	−0.13 ± 0.11	−0.20 ± 0.15	−0.19 ± 0.13	−0.11 ± 0.15	−0.02 ± 0.11	0.07 ± 0.17	−0.19 ± 0.14	−0.35 ± 0.20	−0.20 ± 0.16	−0.22 ± 0.13	−0.26 ± 0.15
J05427+026	−0.01 ± 0.16	0.13 ± 0.17	−0.06 ± 0.17	−0.14 ± 0.17	0.13 ± 0.11	−0.04 ± 0.15	−0.05 ± 0.12	−0.02 ± 0.14	0.12 ± 0.10	0.11 ± 0.16	−0.03 ± 0.15	−0.11 ± 0.20	−0.16 ± 0.16	0.02 ± 0.13	−0.17 ± 0.15
J05455−119	0.09 ± 0.16	0.18 ± 0.18	0.19 ± 0.18	0.08 ± 0.17	0.31 ± 0.12	0.14 ± 0.15	0.09 ± 0.13	0.14 ± 0.14	0.30 ± 0.10	0.27 ± 0.16	0.19 ± 0.15	0.20 ± 0.20	0.08 ± 0.17	0.20 ± 0.13	0.09 ± 0.15
J05456+729	−0.13 ± 0.17	0.06 ± 0.16	−0.14 ± 0.17	−0.19 ± 0.17	−0.02 ± 0.11	−0.11 ± 0.15	−0.08 ± 0.13	−0.08 ± 0.14	0.06 ± 0.10	−0.01 ± 0.16	−0.02 ± 0.14	−0.10 ± 0.19	−0.13 ± 0.15	−0.09 ± 0.14	−0.17 ± 0.15
J05456+111	−0.01 ± 0.16	0.11 ± 0.13	0.16 ± 0.19	−0.01 ± 0.18	0.07 ± 0.17	0.10 ± 0.15	0.06 ± 0.14	0.14 ± 0.15	0.15 ± 0.14	0.19 ± 0.20	0.12 ± 0.16	0.05 ± 0.20	0.10 ± 0.17	0.05 ± 0.15	0.09 ± 0.16
J05458+729	0.01 ± 0.16	0.05 ± 0.17	−0.04 ± 0.17	−0.10 ± 0.17	−0.03 ± 0.12	0.03 ± 0.15	−0.11 ± 0.13	−0.06 ± 0.14	0.09 ± 0.10	0.02 ± 0.17	−0.07 ± 0.14	−0.24 ± 0.20	−0.00 ± 0.16	−0.10 ± 0.13	−0.09 ± 0.15
J05463+012	0.04 ± 0.17	0.07 ± 0.17	0.14 ± 0.17	−0.03 ± 0.17	0.04 ± 0.11	0.02 ± 0.14	−0.04 ± 0.12	0.10 ± 0.15	0.10 ± 0.10	0.23 ± 0.16	0.04 ± 0.14	−0.06 ± 0.20	0.05 ± 0.16	0.01 ± 0.14	0.03 ± 0.15
J05466+441	0.11 ± 0.16	0.17 ± 0.18	0.23 ± 0.17	0.09 ± 0.16	0.26 ± 0.12	0.16 ± 0.15	0.06 ± 0.13	0.14 ± 0.14	0.29 ± 0.10	0.27 ± 0.17	0.12 ± 0.14	0.07 ± 0.19	0.07 ± 0.17	0.11 ± 0.13	0.12 ± 0.15
J05511+122	0.01 ± 0.17	0.08 ± 0.17	0.04 ± 0.18	0.06 ± 0.17	0.15 ± 0.11	−0.01 ± 0.15	0.02 ± 0.13	0.10 ± 0.14	0.14 ± 0.10	0.26 ± 0.17	0.04 ± 0.15	0.03 ± 0.20	−0.03 ± 0.17	0.09 ± 0.13	0.02 ± 0.15
J05566−103	−0.11 ± 0.17	−0.10 ± 0.16	−0.22 ± 0.17	−0.30 ± 0.17	−0.15 ± 0.11	−0.24 ± 0.15	−0.14 ± 0.12	−0.07 ± 0.14	−0.03 ± 0.10	0.09 ± 0.16	−0.15 ± 0.14	−0.23 ± 0.21	−0.21 ± 0.16	−0.22 ± 0.13	−0.24 ± 0.16
J05582−046	−0.10 ± 0.18	0.01 ± 0.17	−0.17 ± 0.17	−0.14 ± 0.18	0.03 ± 0.11	−0.07 ± 0.15	−0.12 ± 0.12	−0.09 ± 0.14	0.10 ± 0.10	−0.01 ± 0.17	−0.09 ± 0.15	−0.15 ± 0.21	−0.14 ± 0.17	−0.03 ± 0.14	−0.18 ± 0.16
J05596+585	−0.18 ± 0.15	0.02 ± 0.13	−0.08 ± 0.19	−0.21 ± 0.18	−0.07 ± 0.17	−0.09 ± 0.16	−0.14 ± 0.14	−0.14 ± 0.16	−0.00 ± 0.14	0.03 ± 0.19	−0.11 ± 0.17	−0.26 ± 0.20	−0.21 ± 0.17	−0.15 ± 0.15	−0.14 ± 0.16
J06000+027	−0.27 ± 0.17	−0.05 ± 0.16	−0.24 ± 0.17	−0.36 ± 0.17	−0.13 ± 0.12	−0.27 ± 0.15	−0.13 ± 0.12	−0.34 ± 0.14	−0.03 ± 0.10	−0.11 ± 0.16	−0.10 ± 0.15	−0.21 ± 0.20	−0.28 ± 0.17	−0.22 ± 0.13	−0.29 ± 0.16
J06011+595	−0.01 ± 0.17	0.06 ± 0.17	0.32 ± 0.19	0.05 ± 0.19	−0.09 ± 0.12	0.09 ± 0.16	−0.16 ± 0.13	0.42 ± 0.16	−0.10 ± 0.09	0.61 ± 0.20	−0.02 ± 0.15	−0.24 ± 0.21	0.27 ± 0.18	−0.09 ± 0.13	0.25 ± 0.17
J06024+663	0.14 ± 0.17	0.16 ± 0.17	0.34 ± 0.17	0.20 ± 0.18	0.32 ± 0.12	0.23 ± 0.15	0.07 ± 0.13	0.23 ± 0.14	0.26 ± 0.10	0.41 ± 0.17	0.23 ± 0.14	0.17 ± 0.21	0.27 ± 0.16	0.23 ± 0.13	0.22 ± 0.15
J06035+168	−0.18 ± 0.17	−0.17 ± 0.18	−0.31 ± 0.16	−0.32 ± 0.18	−0.21 ± 0.12	−0.26 ± 0.15	−0.19 ± 0.13	−0.17 ± 0.15	−0.06 ± 0.10	−0.03 ± 0.17	−0.16 ± 0.14	−0.29 ± 0.20	−0.22 ± 0.16	−0.29 ± 0.13	−0.28 ± 0.15
J06035+155	−0.06 ± 0.16	0.11 ± 0.14	−0.03 ± 0.19	−0.09 ± 0.18	−0.04 ± 0.17	0.06 ± 0.16	0.03 ± 0.13	0.06 ± 0.16	0.08 ± 0.14	0.10 ± 0.19	0.04 ± 0.17	−0.06 ± 0.20	0.04 ± 0.17	−0.05 ± 0.15	0.03 ± 0.17
J06054+608	0.31 ± 0.17	0.13 ± 0.18	0.51 ± 0.18	0.11 ± 0.19	0.42 ± 0.13	−0.02 ± 0.17	0.34 ± 0.15	−0.08 ± 0.17	0.52 ± 0.11	0.64 ± 0.18	0.31 ± 0.15	0.28 ± 0.21	−0.01 ± 0.19	0.23 ± 0.15	0.07 ± 0.17
J06065+045	−0.14 ± 0.16	0.05 ± 0.17	−0.29 ± 0.17	−0.20 ± 0.17	0.00 ± 0.12	−0.18 ± 0.15	−0.13 ± 0.12	−0.10 ± 0.15	0.06 ± 0.10	−0.08 ± 0.16	−0.21 ± 0.14	−0.25 ± 0.20	−0.25 ± 0.16	−0.11 ± 0.14	−0.28 ± 0.15
J06066+465	−0.16 ± 0.17	0.07 ± 0.17	−0.15 ± 0.18	−0.22 ± 0.17	−0.01 ± 0.11	−0.11 ± 0.15	−0.10 ± 0.12	−0.15 ± 0.14	0.06 ± 0.10	0.02 ± 0.16	−0.03 ± 0.14	−0.10 ± 0.20	−0.14 ± 0.16	−0.07 ± 0.14	−0.18 ± 0.15
J06102+225	0.08 ± 0.16	−0.03 ± 0.17	0.17 ± 0.18	−0.07 ± 0.18	0.17 ± 0.12	−0.02 ± 0.16	0.10 ± 0.13	0.14 ± 0.15	0.26 ± 0.11	0.35 ± 0.17	0.05 ± 0.15	0.06 ± 0.21	0.06 ± 0.17	0.03 ± 0.14	0.05 ± 0.16
J06103+722	−0.11 ± 0.16	0.12 ± 0.17	−0.24 ± 0.17	−0.20 ± 0.17	0.05 ± 0.12	−0.18 ± 0.15	−0.06 ± 0.12	−0.08 ± 0.15	0.09 ± 0.10	0.05 ± 0.17	−0.15 ± 0.15	−0.21 ± 0.20	−0.27 ± 0.16	−0.07 ± 0.13	−0.29 ± 0.15
J06103+821	−0.04 ± 0.17	0.07 ± 0.17	0.26 ± 0.18	−0.16 ± 0.17	−0.11 ± 0.12	0.01 ± 0.16	−0.12 ± 0.13	0.16 ± 0.16	−0.08 ± 0.11	0.49 ± 0.20	0.05 ± 0.15	−0.21 ± 0.21	0.11 ± 0.18	−0.09 ± 0.14	0.09 ± 0.18
J06145+025	0.03 ± 0.16	0.13 ± 0.17	0.06 ± 0.17	−0.02 ± 0.17	0.09 ± 0.12	0.05 ± 0.16	−0.06 ± 0.12	0.06 ± 0.14	0.11 ± 0.10	0.18 ± 0.16	−0.02 ± 0.15	−0.13 ± 0.20	0.03 ± 0.17	−0.01 ± 0.13	−0.01 ± 0.15
J06151−164	0.06 ± 0.17	0.01 ± 0.17	0.23 ± 0.17	0.11 ± 0.17	0.03 ± 0.12	0.18 ± 0.16	0.03 ± 0.13	0.23 ± 0.15	0.11 ± 0.10	0.21 ± 0.17	0.20 ± 0.15	0.10 ± 0.21	0.27 ± 0.17	0.02 ± 0.13	0.27 ± 0.15
J06171+051AB	−0.15 ± 0.17	0.00 ± 0.17	−0.17 ± 0.16	−0.23 ± 0.17	−0.02 ± 0.11	−0.13 ± 0.15	−0.11 ± 0.12	−0.15 ± 0.14	0.03 ± 0.10	−0.03 ± 0.16	−0.10 ± 0.15	−0.13 ± 0.20	−0.15 ± 0.16	−0.11 ± 0.13	−0.17 ± 0.16
J06185+250	0.11 ± 0.16	0.19 ± 0.18	0.12 ± 0.17	0.18 ± 0.17	0.29 ± 0.12	0.16 ± 0.15	0.05 ± 0.13	0.17 ± 0.14	0.28 ± 0.11	0.29 ± 0.16	0.14 ± 0.14	0.08 ± 0.20	0.09 ± 0.16	0.17 ± 0.13	0.10 ± 0.15
J06236−096AB	−0.14 ± 0.17	−0.01 ± 0.17	−0.21 ± 0.17	−0.14 ± 0.17	−0.12 ± 0.11	−0.05 ± 0.15	−0.21 ± 0.12	−0.02 ± 0.14	−0.02 ± 0.10	−0.00 ± 0.17	−0.11 ± 0.13	−0.23 ± 0.20	−0.05 ± 0.16	−0.16 ± 0.13	−0.12 ± 0.16
J06307+397	−0.25 ± 0.16	0.01 ± 0.13	−0.31 ± 0.18	−0.23 ± 0.18	−0.23 ± 0.17	−0.11 ± 0.16	−0.15 ± 0.14	−0.09 ± 0.15	−0.08 ± 0.14	−0.11 ± 0.19	−0.14 ± 0.17	−0.37 ± 0.20	−0.11 ± 0.17	−0.24 ± 0.15	−0.23 ± 0.17
J06313+006	−0.17 ± 0.16	0.06 ± 0.13	−0.33 ± 0.19	−0.17 ± 0.18	−0.12 ± 0.17	−0.15 ± 0.16	−0.19 ± 0.14	−0.20 ± 0.15	−0.03 ± 0.14	−0.16 ± 0.18	−0.19 ± 0.17	−0.38 ± 0.20	−0.19 ± 0.16	−0.19 ± 0.15	−0.32 ± 0.16
J06314−016	−0.18 ± 0.15	−0.05 ± 0.14	−0.59 ± 0.20	−0.34 ± 0.19	−0.19 ± 0.17	−0.46 ± 0.16	−0.47 ± 0.15	−0.48 ± 0.16	−0.11 ± 0.14	−0.26 ± 0.20	−0.55 ± 0.18	−0.68 ± 0.20	−0.54 ± 0.18	−0.29 ± 0.15	−0.65 ± 0.17
J06323−097	−0.00 ± 0.17	0.05 ± 0.17	0.09 ± 0.17	−0.01 ± 0.17	0.07 ± 0.12	0.05 ± 0.15	−0.04 ± 0.12	0.08 ± 0.15	0.11 ± 0.10	0.23 ± 0.17	0.09 ± 0.14	0.00 ± 0.20	0.05 ± 0.16	0.04 ± 0.13	0.04 ± 0.14
J06325+641	0.10 ± 0.16	0.17 ± 0.17	0.17 ± 0.17	0.09 ± 0.16	0.28 ± 0.12	0.11 ± 0.15	0.07 ± 0.12	0.19 ± 0.15	0.29 ± 0.10	0.31 ± 0.17	0.09 ± 0.14	0.09 ± 0.21	0.03 ± 0.16	0.15 ± 0.13	0.07 ± 0.15
J06332+054	−0.03 ± 0.16	0.11 ± 0.14	0.40 ± 0.19	−0.03 ± 0.18	0.08 ± 0.18	0.13 ± 0.16	0.04 ± 0.15	0.12 ± 0.16	0.07 ± 0.15	0.13 ± 0.21	0.06 ± 0.17	0.25 ± 0.21	0.06 ± 0.17	−0.04 ± 0.15	0.13 ± 0.16
J06361+201	−0.19 ± 0.16	0.03 ± 0.16	−0.31 ± 0.16	−0.32 ± 0.16	−0.14 ± 0.11	−0.22 ± 0.15	−0.17 ± 0.12	−0.21 ± 0.14	−0.02 ± 0.10	−0.10 ± 0.17	−0.16 ± 0.14	−0.27 ± 0.19	−0.28 ± 0.16	−0.19 ± 0.13	−0.34 ± 0.15
J06367+378	0.10 ± 0.17	−0.01 ± 0.16	0.21 ± 0.17	−0.13 ± 0.17	0.12 ± 0.12	−0.10 ± 0.15	0.07 ± 0.12	−0.04 ± 0.15	0.23 ± 0.10	0.29 ± 0.17	0.02 ± 0.14	−0.04 ± 0.20	−0.08 ± 0.16	0.01 ± 0.13	−0.05 ± 0.15
J06371+175	−0.37 ± 0.16	−0.14 ± 0.14	−0.56 ± 0.19	−0.44 ± 0.19	−0.34 ± 0.17	−0.33 ± 0.16	−0.37 ± 0.14	−0.35 ± 0.16	−0.31 ± 0.14	−0.32 ± 0.21	−0.39 ± 0.17	−0.52 ± 0.21	−0.35 ± 0.19	−0.57 ± 0.15	−0.48 ± 0.17
J06401−164	−0.13 ± 0.16	0.03 ± 0.17	−0.23 ± 0.17	−0.25 ± 0.16	−0.09 ± 0.12	−0.20 ± 0.14	−0.14 ± 0.12	−0.19 ± 0.15	0.03 ± 0.10	−0.02 ± 0.16	−0.17 ± 0.15	−0.33 ± 0.20	−0.24 ± 0.16	−0.18 ± 0.14	−0.29 ± 0.15
J06421+035	−0.02 ± 0.17	0.10 ± 0.17	0.23 ± 0.19	−0.19 ± 0.18	−0.05 ± 0.11	0.02 ± 0.15	−0.12 ± 0.13	0.19 ± 0.16	−0.05 ± 0.10	0.50 ± 0.19	−0.01 ± 0.14	−0.24 ± 0.20	0.06 ± 0.18	−0.07 ± 0.14	0.03 ± 0.19
J06435+166	−0.01 ± 0.17	0.11 ± 0.17	0.08 ± 0.17	0.05 ± 0.17	0.16 ± 0.12	0.07 ± 0.15	0.02 ± 0.12	0.09 ± 0.14	0.20 ± 0.11	0.23 ± 0.17	0.11 ± 0.14	0.04 ± 0.19	0.04 ± 0.16	0.07 ± 0.14	0.03 ± 0.15
J06461+325	−0.33 ± 0.16	−0.15 ± 0.14	−0.37 ± 0.18	−0.39 ± 0.18	−0.29 ± 0.18	−0.25 ± 0.16	−0.28 ± 0.14	−0.30 ± 0.16	−0.20 ± 0.14	−0.21 ± 0.19	−0.27 ± 0.17	−0.42 ± 0.20	−0.32 ± 0.18	−0.39 ± 0.15	−0.33 ± 0.16
J06474+054	0.12 ± 0.16	0.18 ± 0.17	0.46 ± 0.18	0.20 ± 0.18	0.32 ± 0.12	0.19 ± 0.15	0.11 ± 0.12	0.28 ± 0.15	0.29 ± 0.10	0.46 ± 0.17	0.21 ± 0.15	0.15 ± 0.20	0.22 ± 0.17	0.20 ± 0.13	0.24 ± 0.15
J06489+211	−0.01 ± 0.16	0.02 ± 0.16	−0.03 ± 0.17	−0.21 ± 0.16	−0.06 ± 0.11	−0.10 ± 0.15	−0.09 ± 0.12	−0.05 ± 0.14	0.08 ± 0.10	0.12 ± 0.17	−0.06 ± 0.15	−0.14 ± 0.20	−0.12 ± 0.16	−0.14 ± 0.13	−0.15 ± 0.15
J06509−091	−0.07 ± 0.16	0.08 ± 0.16	−0.01 ± 0.16	−0.13 ± 0.17	0.05 ± 0.11	−0.02 ± 0.15	−0.07 ± 0.12	−0.03 ± 0.14	0.09 ± 0.10	0.05 ± 0.16	0.02 ± 0.14	−0.06 ± 0.20	−0.04 ± 0.17	−0.03 ± 0.13	−0.09 ± 0.15
J06522+627	−0.15 ± 0.17	−0.05 ± 0.17	−0.18 ± 0.17	−0.23 ± 0.17	−0.09 ± 0.11	−0.14 ± 0.15	−0.12 ± 0.13	−0.11 ± 0.14	0.04 ± 0.10	−0.01 ± 0.17	−0.04 ± 0.15	−0.12 ± 0.20	−0.14 ± 0.17	−0.16 ± 0.13	−0.20 ± 0.15
J06522+179	−0.26 ± 0.16	−0.07 ± 0.13	−0.49 ± 0.19	−0.31 ± 0.17	−0.24 ± 0.17	−0.24 ± 0.16	−0.26 ± 0.14	−0.20 ± 0.15	−0.16 ± 0.14	−0.21 ± 0.19	−0.26 ± 0.17	−0.45 ± 0.21	−0.27 ± 0.17	−0.35 ± 0.15	−0.34 ± 0.17
J06523−051SAB	−0.12 ± 0.16	0.12 ± 0.13	−0.02 ± 0.18	−0.11 ± 0.18	−0.12 ± 0.17	−0.03 ± 0.15	−0.04 ± 0.14	−0.04 ± 0.15	0.02 ± 0.14	−0.02 ± 0.18	−0.03 ± 0.16	−0.14 ± 0.20	−0.02 ± 0.17	−0.17 ± 0.15	−0.11 ± 0.16
J06523−051N	−0.02 ± 0.16	0.13 ± 0.13	−0.11 ± 0.19	−0.05 ± 0.19	0.06 ± 0.18	−0.02 ± 0.16	−0.07 ± 0.14	−0.02 ± 0.16	0.11 ± 0.15	0.01 ± 0.20	−0.08 ± 0.17	−0.18 ± 0.20	−0.07 ± 0.17	0.03 ± 0.15	−0.09 ± 0.16
J06548+332	−0.09 ± 0.16	0.05 ± 0.17	−0.06 ± 0.17	−0.09 ± 0.16	−0.02 ± 0.11	−0.01 ± 0.15	−0.09 ± 0.12	0.04 ± 0.14	0.04 ± 0.10	0.07 ± 0.16	−0.01 ± 0.14	−0.09 ± 0.20	0.01 ± 0.16	−0.06 ± 0.13	−0.05 ± 0.15
J06565+440	0.07 ± 0.16	0.15 ± 0.17	0.04 ± 0.18	0.00 ± 0.17	0.30 ± 0.12	0.06 ± 0.16	0.13 ± 0.13	0.08 ± 0.14	0.34 ± 0.10	0.28 ± 0.17	0.14 ± 0.14	0.18 ± 0.21	−0.02 ± 0.17	0.19 ± 0.13	−0.00 ± 0.15
J06574+740	−0.12 ± 0.16	−0.11 ± 0.18	−0.20 ± 0.17	−0.35 ± 0.18	−0.16 ± 0.11	−0.30 ± 0.16	−0.16 ± 0.13	−0.30 ± 0.14	0.02 ± 0.10	0.00 ± 0.17	−0.21 ± 0.14	−0.35 ± 0.20	−0.32 ± 0.17	−0.29 ± 0.13	−0.35 ± 0.16
J07009−023	−0.09 ± 0.16	0.07 ± 0.17	−0.08 ± 0.17	−0.18 ± 0.17	−0.02 ± 0.12	−0.08 ± 0.15	−0.06 ± 0.13	−0.13 ± 0.14	0.06 ± 0.10	0.03 ± 0.16	0.03 ± 0.14	−0.08 ± 0.20	−0.13 ± 0.16	−0.06 ± 0.13	−0.15 ± 0.15
J07031+836	−0.19 ± 0.16	−0.08 ± 0.18	−0.22 ± 0.18	−0.21 ± 0.18	−0.17 ± 0.12	−0.16 ± 0.15	−0.17 ± 0.13	−0.12 ± 0.15	−0.02 ± 0.10	−0.10 ± 0.17	−0.15 ± 0.14	−0.30 ± 0.21	−0.13 ± 0.16	−0.24 ± 0.13	−0.20 ± 0.15

Table C.4: *Continued*

Karmn	[C/H]	[O/H]	[Na/H]	[Mg/H]	[Al/H]	[Si/H]	[Ca/H]	[Sc/H]	[Ti/H]	[V/H]	[Cr/H]	[Mn/H]	[Fe/H]	[Co/H]	[Ni/H]
J07033+346	−0.09 ± 0.17	0.01 ± 0.18	0.18 ± 0.19	−0.07 ± 0.18	−0.13 ± 0.12	−0.09 ± 0.16	−0.14 ± 0.13	0.15 ± 0.16	−0.08 ± 0.10	0.48 ± 0.19	−0.04 ± 0.14	−0.22 ± 0.22	0.10 ± 0.18	−0.18 ± 0.13	0.04 ± 0.16
J07041+752	−0.05 ± 0.16	−0.01 ± 0.17	−0.01 ± 0.17	−0.10 ± 0.17	−0.01 ± 0.12	−0.02 ± 0.15	−0.12 ± 0.12	0.02 ± 0.14	0.09 ± 0.10	0.16 ± 0.17	−0.07 ± 0.14	−0.15 ± 0.19	0.00 ± 0.16	−0.11 ± 0.13	−0.06 ± 0.15
J07044+682	−0.09 ± 0.17	0.07 ± 0.17	0.00 ± 0.16	−0.09 ± 0.17	0.02 ± 0.12	−0.07 ± 0.15	−0.06 ± 0.12	−0.08 ± 0.14	0.08 ± 0.10	0.03 ± 0.16	−0.03 ± 0.14	−0.11 ± 0.20	−0.09 ± 0.15	−0.09 ± 0.13	−0.08 ± 0.15
J07105−087	−0.08 ± 0.16	0.05 ± 0.16	−0.06 ± 0.16	−0.06 ± 0.17	0.00 ± 0.12	0.05 ± 0.15	−0.12 ± 0.13	0.02 ± 0.15	0.08 ± 0.10	0.06 ± 0.16	−0.01 ± 0.14	−0.09 ± 0.20	0.03 ± 0.16	−0.07 ± 0.13	−0.04 ± 0.15
J07105+283	0.08 ± 0.16	0.17 ± 0.14	0.31 ± 0.18	0.03 ± 0.19	0.20 ± 0.18	0.19 ± 0.16	0.10 ± 0.14	0.21 ± 0.16	0.19 ± 0.15	0.23 ± 0.19	0.19 ± 0.17	0.21 ± 0.20	0.24 ± 0.17	0.12 ± 0.15	0.19 ± 0.16
J07111−035	−0.18 ± 0.15	−0.02 ± 0.13	−0.28 ± 0.18	−0.27 ± 0.18	−0.15 ± 0.18	−0.15 ± 0.15	−0.20 ± 0.14	−0.18 ± 0.15	−0.12 ± 0.15	−0.12 ± 0.18	−0.20 ± 0.16	−0.30 ± 0.20	−0.17 ± 0.17	−0.29 ± 0.14	−0.28 ± 0.17
J07172−050	−0.13 ± 0.16	−0.13 ± 0.17	−0.44 ± 0.17	−0.31 ± 0.17	−0.28 ± 0.12	−0.25 ± 0.15	−0.27 ± 0.13	−0.17 ± 0.15	−0.09 ± 0.10	−0.08 ± 0.17	−0.29 ± 0.15	−0.53 ± 0.21	−0.26 ± 0.17	−0.32 ± 0.13	−0.38 ± 0.15
J07182+137	0.01 ± 0.16	0.10 ± 0.16	0.17 ± 0.17	0.05 ± 0.18	0.11 ± 0.11	0.10 ± 0.15	−0.01 ± 0.12	0.12 ± 0.14	0.15 ± 0.11	0.23 ± 0.17	0.15 ± 0.14	0.03 ± 0.20	0.08 ± 0.16	0.06 ± 0.13	0.11 ± 0.15
J07191+667	0.02 ± 0.16	0.13 ± 0.13	0.30 ± 0.18	0.02 ± 0.18	0.13 ± 0.17	0.18 ± 0.16	0.13 ± 0.13	0.19 ± 0.15	0.20 ± 0.15	0.20 ± 0.20	0.22 ± 0.17	0.21 ± 0.19	0.16 ± 0.16	0.12 ± 0.16	0.24 ± 0.17
J07195+328	−0.13 ± 0.16	−0.04 ± 0.13	−0.17 ± 0.19	−0.18 ± 0.18	−0.08 ± 0.18	−0.15 ± 0.16	−0.17 ± 0.14	−0.16 ± 0.15	−0.05 ± 0.14	−0.06 ± 0.19	−0.14 ± 0.17	−0.12 ± 0.20	−0.13 ± 0.17	−0.23 ± 0.15	−0.21 ± 0.16
J07219−222	−0.05 ± 0.17	0.11 ± 0.18	−0.10 ± 0.17	−0.10 ± 0.17	0.13 ± 0.12	0.05 ± 0.15	−0.06 ± 0.13	0.01 ± 0.15	0.15 ± 0.10	0.03 ± 0.16	0.00 ± 0.15	−0.02 ± 0.20	−0.02 ± 0.16	0.01 ± 0.13	−0.07 ± 0.15
J07274+052	−0.10 ± 0.16	0.08 ± 0.17	−0.12 ± 0.17	−0.08 ± 0.17	0.07 ± 0.12	−0.01 ± 0.15	−0.15 ± 0.12	0.01 ± 0.14	0.12 ± 0.10	0.06 ± 0.16	−0.09 ± 0.14	−0.14 ± 0.19	−0.09 ± 0.17	−0.07 ± 0.14	−0.12 ± 0.15
J07287−032	−0.09 ± 0.17	0.08 ± 0.17	0.11 ± 0.18	−0.07 ± 0.18	−0.06 ± 0.12	−0.08 ± 0.16	−0.12 ± 0.13	0.14 ± 0.16	−0.04 ± 0.10	0.35 ± 0.19	−0.02 ± 0.14	−0.26 ± 0.21	0.03 ± 0.17	−0.11 ± 0.13	−0.00 ± 0.16
J07321−088	−0.29 ± 0.16	−0.13 ± 0.14	−0.60 ± 0.19	−0.30 ± 0.18	−0.21 ± 0.18	−0.32 ± 0.16	−0.36 ± 0.14	−0.40 ± 0.16	−0.14 ± 0.15	−0.24 ± 0.20	−0.38 ± 0.18	−0.60 ± 0.21	−0.46 ± 0.18	−0.30 ± 0.16	−0.48 ± 0.17
J07324−130	−0.10 ± 0.15	0.02 ± 0.13	−0.02 ± 0.18	−0.12 ± 0.18	0.03 ± 0.17	−0.03 ± 0.15	−0.11 ± 0.14	−0.04 ± 0.16	0.04 ± 0.15	0.06 ± 0.19	−0.06 ± 0.16	−0.13 ± 0.20	−0.07 ± 0.17	−0.09 ± 0.15	−0.08 ± 0.16
J07353+548	−0.20 ± 0.16	0.06 ± 0.13	−0.15 ± 0.19	−0.18 ± 0.18	−0.17 ± 0.18	−0.09 ± 0.16	−0.13 ± 0.13	−0.12 ± 0.15	−0.06 ± 0.14	−0.10 ± 0.19	−0.13 ± 0.17	−0.28 ± 0.20	−0.16 ± 0.16	−0.24 ± 0.15	−0.23 ± 0.16
J07359+785	−0.03 ± 0.16	0.10 ± 0.17	0.04 ± 0.17	−0.09 ± 0.17	0.07 ± 0.11	−0.04 ± 0.15	−0.03 ± 0.13	0.00 ± 0.13	0.12 ± 0.10	0.12 ± 0.16	−0.01 ± 0.14	−0.09 ± 0.20	−0.09 ± 0.16	−0.03 ± 0.14	−0.07 ± 0.15
J07365−006	−0.05 ± 0.16	0.04 ± 0.17	0.00 ± 0.16	−0.05 ± 0.17	0.01 ± 0.11	0.02 ± 0.15	−0.10 ± 0.12	0.01 ± 0.14	0.09 ± 0.10	0.09 ± 0.17	0.03 ± 0.15	−0.06 ± 0.20	0.04 ± 0.17	−0.05 ± 0.13	−0.00 ± 0.15
J07366+440	0.01 ± 0.16	0.12 ± 0.17	0.12 ± 0.17	0.02 ± 0.17	0.13 ± 0.12	0.02 ± 0.15	0.03 ± 0.13	0.08 ± 0.14	0.17 ± 0.10	0.21 ± 0.17	0.08 ± 0.14	0.02 ± 0.20	0.04 ± 0.16	0.06 ± 0.13	0.02 ± 0.15
J07393+021	−0.04 ± 0.16	0.11 ± 0.14	−0.15 ± 0.20	−0.13 ± 0.19	0.12 ± 0.18	0.02 ± 0.16	−0.17 ± 0.14	−0.12 ± 0.16	0.07 ± 0.16	0.00 ± 0.20	−0.16 ± 0.17	−0.22 ± 0.21	−0.06 ± 0.18	−0.00 ± 0.15	−0.22 ± 0.17
J07429−107	0.02 ± 0.16	0.06 ± 0.16	0.02 ± 0.17	−0.06 ± 0.16	0.00 ± 0.11	0.02 ± 0.15	−0.08 ± 0.12	0.01 ± 0.14	0.10 ± 0.10	0.15 ± 0.17	−0.00 ± 0.14	−0.13 ± 0.20	0.01 ± 0.16	−0.08 ± 0.13	−0.03 ± 0.15
J07446+035	−0.02 ± 0.17	0.01 ± 0.17	0.20 ± 0.19	−0.08 ± 0.21	−0.01 ± 0.11	−0.22 ± 0.17	0.02 ± 0.13	0.04 ± 0.17	0.03 ± 0.10	0.57 ± 0.19	0.00 ± 0.15	−0.24 ± 0.22	−0.04 ± 0.19	−0.11 ± 0.13	−0.12 ± 0.19
J07467+574	−0.12 ± 0.18	0.03 ± 0.17	−0.28 ± 0.17	−0.28 ± 0.17	0.15 ± 0.12	−0.26 ± 0.17	−0.05 ± 0.13	−0.31 ± 0.15	0.20 ± 0.10	0.18 ± 0.18	−0.09 ± 0.15	−0.07 ± 0.20	−0.39 ± 0.17	−0.05 ± 0.13	−0.41 ± 0.16
J07470+760	−0.11 ± 0.17	0.08 ± 0.17	−0.12 ± 0.17	−0.09 ± 0.17	0.06 ± 0.11	−0.02 ± 0.14	−0.07 ± 0.12	0.01 ± 0.15	0.12 ± 0.10	0.05 ± 0.16	0.03 ± 0.14	−0.07 ± 0.20	−0.05 ± 0.16	−0.03 ± 0.13	−0.09 ± 0.15
J07472+503	−0.05 ± 0.18	−0.04 ± 0.17	0.14 ± 0.19	−0.32 ± 0.19	−0.20 ± 0.11	−0.25 ± 0.17	−0.22 ± 0.12	−0.05 ± 0.18	−0.14 ± 0.10	0.53 ± 0.21	−0.16 ± 0.14	−0.34 ± 0.21	−0.06 ± 0.19	−0.28 ± 0.13	−0.17 ± 0.19
J07497−033	−0.12 ± 0.16	−0.08 ± 0.17	−0.19 ± 0.17	−0.21 ± 0.16	−0.19 ± 0.12	−0.12 ± 0.15	−0.21 ± 0.12	−0.10 ± 0.15	−0.03 ± 0.10	−0.02 ± 0.17	−0.17 ± 0.13	−0.33 ± 0.20	−0.12 ± 0.16	−0.22 ± 0.14	−0.17 ± 0.15
J07498−032	−0.06 ± 0.16	−0.12 ± 0.18	−0.24 ± 0.18	−0.30 ± 0.18	−0.16 ± 0.12	−0.31 ± 0.15	−0.15 ± 0.13	−0.29 ± 0.15	0.03 ± 0.10	0.03 ± 0.16	−0.23 ± 0.15	−0.43 ± 0.21	−0.27 ± 0.17	−0.28 ± 0.13	−0.35 ± 0.16
J07545−096	0.02 ± 0.16	0.04 ± 0.17	0.17 ± 0.17	−0.01 ± 0.18	0.02 ± 0.11	0.07 ± 0.15	−0.03 ± 0.12	0.14 ± 0.14	0.09 ± 0.10	0.21 ± 0.16	0.06 ± 0.14	−0.03 ± 0.20	0.13 ± 0.16	−0.03 ± 0.13	0.11 ± 0.15
J07545+085	−0.19 ± 0.16	0.00 ± 0.16	−0.27 ± 0.17	−0.29 ± 0.17	−0.16 ± 0.12	−0.19 ± 0.15	−0.19 ± 0.12	−0.19 ± 0.14	−0.03 ± 0.10	−0.08 ± 0.17	−0.13 ± 0.14	−0.23 ± 0.19	−0.24 ± 0.15	−0.20 ± 0.13	−0.27 ± 0.15
J07582+413	−0.01 ± 0.16	0.11 ± 0.17	0.35 ± 0.19	0.05 ± 0.18	−0.01 ± 0.11	0.06 ± 0.15	−0.10 ± 0.13	0.33 ± 0.16	−0.05 ± 0.10	0.62 ± 0.20	−0.02 ± 0.15	−0.20 ± 0.20	0.25 ± 0.18	−0.07 ± 0.13	0.21 ± 0.17
J07591+173	0.04 ± 0.16	−0.10 ± 0.18	−0.10 ± 0.17	−0.18 ± 0.18	0.02 ± 0.12	−0.21 ± 0.16	−0.02 ± 0.12	0.01 ± 0.15	0.12 ± 0.10	0.23 ± 0.16	−0.11 ± 0.14	−0.20 ± 0.21	−0.19 ± 0.17	−0.11 ± 0.13	−0.15 ± 0.16
J08025−130	−0.11 ± 0.16	0.05 ± 0.17	−0.11 ± 0.17	−0.16 ± 0.16	−0.07 ± 0.11	−0.08 ± 0.15	−0.08 ± 0.13	−0.08 ± 0.15	0.04 ± 0.10	0.03 ± 0.17	−0.01 ± 0.14	−0.12 ± 0.20	−0.08 ± 0.16	−0.07 ± 0.13	−0.17 ± 0.15
J08031+203AB	−0.04 ± 0.16	−0.06 ± 0.17	−0.16 ± 0.17	−0.25 ± 0.17	−0.08 ± 0.12	−0.21 ± 0.15	−0.10 ± 0.12	−0.13 ± 0.14	0.06 ± 0.10	0.12 ± 0.17	−0.11 ± 0.14	−0.20 ± 0.21	−0.16 ± 0.17	−0.17 ± 0.13	−0.22 ± 0.15
J08069+422	0.01 ± 0.17	0.06 ± 0.17	0.01 ± 0.17	0.07 ± 0.17	0.06 ± 0.12	0.14 ± 0.16	−0.08 ± 0.13	0.18 ± 0.15	0.10 ± 0.10	0.22 ± 0.16	0.05 ± 0.14	−0.02 ± 0.20	0.17 ± 0.16	0.03 ± 0.13	0.09 ± 0.15
J08080+719	−0.15 ± 0.15	0.09 ± 0.14	−0.04 ± 0.19	−0.10 ± 0.18	−0.07 ± 0.18	−0.01 ± 0.16	−0.06 ± 0.14	−0.06 ± 0.15	0.04 ± 0.14	−0.00 ± 0.19	−0.04 ± 0.16	−0.12 ± 0.20	−0.10 ± 0.17	−0.09 ± 0.15	−0.11 ± 0.17
J08082+211N	−0.08 ± 0.16	0.06 ± 0.13	−0.04 ± 0.19	−0.05 ± 0.18	0.02 ± 0.18	0.04 ± 0.16	0.00 ± 0.14	0.03 ± 0.15	0.08 ± 0.15	0.05 ± 0.18	0.04 ± 0.17	−0.05 ± 0.20	0.02 ± 0.17	−0.06 ± 0.15	−0.01 ± 0.15
J08104−111	−0.05 ± 0.16	0.09 ± 0.13	−0.07 ± 0.20	−0.13 ± 0.18	−0.02 ± 0.17	−0.10 ± 0.16	−0.15 ± 0.14	−0.10 ± 0.16	0.10 ± 0.15	0.09 ± 0.20	−0.15 ± 0.17	−0.33 ± 0.20	−0.20 ± 0.17	−0.02 ± 0.15	−0.13 ± 0.17
J08105−138AB	−0.07 ± 0.16	0.03 ± 0.17	−0.04 ± 0.17	−0.17 ± 0.16	−0.06 ± 0.12	−0.05 ± 0.15	−0.07 ± 0.13	−0.01 ± 0.15	0.05 ± 0.10	0.06 ± 0.16	0.01 ± 0.14	−0.13 ± 0.20	−0.04 ± 0.16	−0.07 ± 0.13	−0.08 ± 0.15
J08107+798	−0.44 ± 0.18	−0.30 ± 0.15	−0.95 ± 0.20	−0.55 ± 0.20	−0.51 ± 0.18	−0.65 ± 0.17	−0.59 ± 0.15	−0.72 ± 0.19	−0.40 ± 0.16	−0.70 ± 0.25	−0.71 ± 0.18	−0.64 ± 0.22	−0.92 ± 0.19	−0.74 ± 0.16	−0.86 ± 0.17
J08117+531	−0.10 ± 0.17	0.16 ± 0.17	−0.24 ± 0.17	−0.17 ± 0.17	0.08 ± 0.11	−0.16 ± 0.15	−0.10 ± 0.13	−0.09 ± 0.14	0.09 ± 0.10	0.00 ± 0.16	−0.11 ± 0.14	−0.22 ± 0.21	−0.26 ± 0.17	−0.05 ± 0.13	−0.30 ± 0.15
J08143+630	−0.14 ± 0.15	−0.01 ± 0.13	−0.22 ± 0.18	−0.25 ± 0.18	−0.15 ± 0.17	−0.21 ± 0.15	−0.22 ± 0.14	−0.21 ± 0.15	−0.06 ± 0.14	−0.08 ± 0.19	−0.20 ± 0.17	−0.28 ± 0.20	−0.20 ± 0.16	−0.22 ± 0.15	−0.31 ± 0.16
J08161+013	−0.09 ± 0.16	−0.02 ± 0.13	−0.03 ± 0.18	−0.14 ± 0.18	0.03 ± 0.17	−0.07 ± 0.16	−0.08 ± 0.14	−0.13 ± 0.15	0.11 ± 0.14	0.01 ± 0.19	−0.08 ± 0.17	−0.13 ± 0.20	−0.13 ± 0.17	−0.02 ± 0.15	−0.12 ± 0.16
J08161+570	−0.19 ± 0.16	−0.05 ± 0.17	−0.24 ± 0.16	−0.22 ± 0.17	−0.23 ± 0.12	−0.14 ± 0.16	−0.21 ± 0.12	−0.09 ± 0.14	−0.07 ± 0.10	−0.13 ± 0.17	−0.19 ± 0.14	−0.29 ± 0.20	−0.16 ± 0.16	−0.27 ± 0.13	−0.19 ± 0.15
J08283+553	−0.09 ± 0.16	0.07 ± 0.17	−0.07 ± 0.17	−0.10 ± 0.17	0.03 ± 0.12	−0.06 ± 0.15	−0.11 ± 0.12	0.02 ± 0.14	0.04 ± 0.10	0.08 ± 0.16	−0.06 ± 0.14	−0.12 ± 0.20	−0.05 ± 0.16	−0.03 ± 0.13	−0.11 ± 0.15
J08286+660	−0.12 ± 0.16	−0.06 ± 0.17	−0.24 ± 0.18	−0.30 ± 0.17	−0.06 ± 0.12	−0.23 ± 0.16	−0.18 ± 0.12	−0.20 ± 0.15	0.03 ± 0.10	0.06 ± 0.17	−0.19 ± 0.14	−0.26 ± 0.21	−0.25 ± 0.16	−0.17 ± 0.13	−0.30 ± 0.16
J08315+730	−0.05 ± 0.17	0.11 ± 0.17	0.19 ± 0.20	0.07 ± 0.18	0.00 ± 0.11	0.04 ± 0.16	−0.14 ± 0.12	0.36 ± 0.17	−0.06 ± 0.10	0.53 ± 0.20	−0.05 ± 0.14	−0.17 ± 0.20	0.18 ± 0.18	−0.06 ± 0.13	0.16 ± 0.17
J08353+141	0.04 ± 0.16	0.10 ± 0.18	0.06 ± 0.17	0.08 ± 0.18	0.19 ± 0.11	0.00 ± 0.15	0.05 ± 0.13	0.01 ± 0.14	0.23 ± 0.10	0.29 ± 0.18	0.08 ± 0.14	−0.01 ± 0.20	0.02 ± 0.16	0.11 ± 0.13	−0.01 ± 0.15
J08358+680	−0.11 ± 0.16	0.24 ± 0.14	−0.19 ± 0.20	−0.06 ± 0.19	−0.08 ± 0.18	0.10 ± 0.17	−0.05 ± 0.14	0.09 ± 0.17	0.07 ± 0.15	0.03 ± 0.20	−0.07 ± 0.18	−0.27 ± 0.21	0.03 ± 0.18	0.00 ± 0.16	−0.18 ± 0.17
J08375+035	−0.09 ± 0.16	0.07 ± 0.17	0.10 ± 0.18	0.02 ± 0.17	0.07 ± 0.11	0.02 ± 0.15	−0.05 ± 0.12	0.04 ± 0.15	0.11 ± 0.10	0.20 ± 0.16	0.11 ± 0.15	−0.01 ± 0.20	0.01 ± 0.16	0.02 ± 0.12	0.02 ± 0.15
J08394−028	−0.14 ± 0.15	−0.01 ± 0.14	−0.53 ± 0.20	−0.29 ± 0.18	−0.23 ± 0.18	−0.46 ± 0.16	−0.46 ± 0.15	−0.44 ± 0.16	−0.15 ± 0.14	−0.24 ± 0.20	−0.48 ± 0.17	−0.63 ± 0.20	−0.42 ± 0.17	−0.39 ± 0.16	−0.63 ± 0.17
J08402+314	−0.10 ± 0.16	0.06 ± 0.17	−0.07 ± 0.17	−0.08 ± 0.17	−0.03 ± 0.11	−0.02 ± 0.15	−0.14 ± 0.12	0.02 ± 0.14	0.03 ± 0.10	0.07 ± 0.17	−0.10 ± 0.14	−0.22 ± 0.19	−0.05 ± 0.16	−0.12 ± 0.13	−0.06 ± 0.14
J08423−048	−0.20 ± 0.16	0.06 ± 0.17	−0.24 ± 0.18	−0.18 ± 0.16	−0.06 ± 0.11	−0.13 ± 0.15	−0.12 ± 0.12	−0.16 ± 0.14	0.04 ± 0.10	−0.14 ± 0.17	−0.06 ± 0.14	−0.16 ± 0.19	−0.22 ± 0.17	−0.12 ± 0.14	−0.22 ± 0.15
J08449−066AB	−0.23 ± 0.16	−0.03 ± 0.16	−0.26 ± 0.17	−0.23 ± 0.17	−0.16 ± 0.11	−0.10 ± 0.16	−0.21 ± 0.13	−0.08 ± 0.15	−0.05 ± 0.10	−0.05 ± 0.17	−0.17 ± 0.14	−0.22 ± 0.19	−0.04 ± 0.16	−0.22 ± 0.13	−0.16 ± 0.15
J08484+207	−0.33 ± 0.16	−0.01 ± 0.13	−0.29 ± 0.19	−0.33 ± 0.19	−0.28 ± 0.17	−0.23 ± 0.16	−0.25 ± 0.15	−0.20 ± 0.16	−0.12 ± 0.15	−0.09 ± 0.19	−0.22 ± 0.17	−0.39 ± 0.21	−0.31 ± 0.17	−0.29 ± 0.15	−0.25 ± 0.17
J08526+283	0.15 ± 0.16	0.17 ± 0.17	0.46 ± 0.17	0.25 ± 0.17	0.31 ± 0.12	0.28 ± 0.16	0.14 ± 0.13	0.31 ± 0.14	0.30 ± 0.11	0.48 ± 0.17	0.28 ± 0.14	0.23 ± 0.21	0.28 ± 0.17	0.24 ± 0.14	0.31 ± 0.15
J08531−202	−0.17 ± 0.16	0.03 ± 0.16	−0.23 ± 0.16	−0.24 ± 0.17	−0.08 ± 0.12	−0.12 ± 0.15	−0.12 ± 0.12	−0.11 ± 0.14	0.03 ± 0.10	−0.08 ± 0.16	−0.08 ± 0.14	−0.16 ± 0.20	−0.15 ± 0.17	−0.14 ± 0.13	−0.22 ± 0.15
J08563−044	−0.19 ± 0.15	−0.02 ± 0.13	−0.20 ± 0.19	−0.23 ± 0.18	−0.15 ± 0.17	−0.12 ± 0.15	−0.15 ± 0.14	−0.12 ± 0.15	−0.07 ± 0.14	−0.08 ± 0.19	−0.14 ± 0.17	−0.26 ± 0.20	−0.14 ± 0.17	−0.25 ± 0.15	−0.20 ± 0.16
J08572+194	0.01 ± 0.16	0.07 ± 0.16	−0.00 ± 0.16	−0.01 ± 0.16	0.08 ± 0.11	−0.00 ± 0.14	−0.03 ± 0.12	0.02 ± 0.14	0.10 ± 0.10	0.09 ± 0.17	−0.01 ± 0.14	−0.08 ± 0.19	−0.00 ± 0.16	−0.02 ± 0.13	−0.04 ± 0.14
J08590+364	0.08 ± 0.16	0.17 ± 0.13	0.10 ± 0.19	0.04 ± 0.17	0.15 ± 0.18	−0.02 ± 0.16	−0.03 ± 0.14	0.06 ± 0.16	0.20 ± 0.15	0.15 ± 0.19	0.04 ± 0.16	−0.04 ± 0.20	0.04 ± 0.17	0.13 ± 0.15	0.02 ± 0.17
J08595+537	−0.11 ± 0.16	−0.17 ± 0.17	−0.23 ± 0.17	−0.32 ± 0.17	−0.20 ± 0.12	−0.25 ± 0.15	−0.20 ± 0.13	−0.10 ± 0.14	−0.07 ± 0.10	0.04 ± 0.17	−0.18 ± 0.14	−0.28 ± 0.21	−0.22 ± 0.17	−0.25 ± 0.13	−0.25 ± 0.16
J08599+042	−0.24 ± 0.16	−0.04 ± 0.13	−0.29 ± 0.18	−0.24 ± 0.18	−0.20 ± 0.17	−0.18 ± 0.16	−0.22 ± 0.14	−0.21 ± 0.16	−0.11 ± 0.14	−0.14 ± 0.19	−0.21 ± 0.17	−0.39 ± 0.20	−0.24 ± 0.17	−0.29 ± 0.15	−0.27 ± 0.16
J09005+465	−0.03 ± 0.17	0.02 ± 0.17	0.08 ± 0.16	−0.02 ± 0.17	0.04 ± 0.12	0.03 ± 0.15	−0.07 ± 0.12	0.08 ± 0.15	0.11 ± 0.10	0.20 ± 0.17	−0.01 ± 0.14	−0.08 ± 0.19	0.05 ± 0.16	−0.05 ± 0.13	0.03 ± 0.15
J09008+237	−0.09 ± 0.17	0.04 ± 0.17	−0.09 ± 0.17	−0.12 ± 0.17	−0.02 ± 0.12	−0.09 ± 0.15	−0.09 ± 0.12	−0.05 ± 0.15	0.04 ± 0.10	−0.01 ± 0.16	−0.11 ± 0.14	−0.19 ± 0.19	−0.17 ± 0.16	−0.09 ± 0.13	−0.12 ± 0.15
J09023+177	−0.08 ± 0.16	0.07 ± 0.17	−0.05 ± 0.18	−0.05 ± 0.17	0.05 ± 0.12	−0.02 ± 0.15	−0.04 ± 0.13	0.00 ± 0.14	0.12 ± 0.10	0.12 ± 0.17	0.03 ± 0.14	−0.05 ± 0.20	−0.05 ± 0.16	−0.02 ± 0.13	−0.07 ± 0.14
J09028+680	−0.12 ± 0.17	0.07 ± 0.17	−0.17 ± 0.17	−0.09 ± 0.16	0.03 ± 0.11	−0.05 ± 0.15	−0.12 ± 0.13	−0.02 ± 0.14	0.10 ± 0.10	−0.01 ± 0.17	−0.10 ± 0.14	−0.14 ± 0.20	−0.10 ± 0.15	−0.08 ± 0.13	−0.14 ± 0.15
J09028+060	−0.10 ± 0.16	0.06 ± 0.14	−0.18 ± 0.19	−0.21 ± 0.19	−0.08 ± 0.18	−0.17 ± 0.16	−0.19 ± 0.14	−0.12 ± 0.15	0.02 ± 0.14	−0.03 ± 0.18	−0.18 ± 0.16	−0.30 ± 0.19	−0.21 ± 0.17	−0.14 ± 0.15	−0.22 ± 0.16

Table C.4: *Continued*

Karmn	[C/H]	[O/H]	[Na/H]	[Mg/H]	[Al/H]	[Si/H]	[Ca/H]	[Sc/H]	[Ti/H]	[V/H]	[Cr/H]	[Mn/H]	[Fe/H]	[Co/H]	[Ni/H]
J09040−159	−0.05 ± 0.16	−0.01 ± 0.17	−0.09 ± 0.16	−0.28 ± 0.17	−0.14 ± 0.11	−0.14 ± 0.14	−0.11 ± 0.13	−0.15 ± 0.14	0.03 ± 0.10	0.03 ± 0.16	−0.06 ± 0.14	−0.21 ± 0.20	−0.16 ± 0.16	−0.18 ± 0.13	−0.24 ± 0.15
J09045+164AB	−0.00 ± 0.16	0.13 ± 0.13	−0.01 ± 0.18	−0.02 ± 0.19	0.03 ± 0.17	0.02 ± 0.15	−0.02 ± 0.14	0.05 ± 0.15	0.12 ± 0.15	0.05 ± 0.18	−0.03 ± 0.16	−0.05 ± 0.20	0.01 ± 0.18	0.03 ± 0.15	−0.02 ± 0.16
J09058+555	−0.14 ± 0.16	−0.06 ± 0.17	−0.19 ± 0.17	−0.25 ± 0.17	−0.12 ± 0.12	−0.15 ± 0.15	−0.19 ± 0.12	−0.13 ± 0.14	−0.00 ± 0.10	−0.02 ± 0.17	−0.19 ± 0.14	−0.25 ± 0.20	−0.15 ± 0.16	−0.17 ± 0.13	−0.23 ± 0.16
J09091+227	−0.09 ± 0.18	0.06 ± 0.18	−0.14 ± 0.17	0.15 ± 0.18	0.01 ± 0.12	0.13 ± 0.16	−0.15 ± 0.13	0.13 ± 0.15	0.02 ± 0.10	0.08 ± 0.17	0.02 ± 0.15	−0.09 ± 0.20	0.16 ± 0.17	−0.01 ± 0.13	0.06 ± 0.16
J09115+126	0.07 ± 0.17	0.14 ± 0.17	0.15 ± 0.17	0.07 ± 0.17	0.08 ± 0.11	0.12 ± 0.15	−0.03 ± 0.12	0.14 ± 0.14	0.12 ± 0.10	0.12 ± 0.16	0.06 ± 0.14	−0.07 ± 0.20	0.12 ± 0.17	−0.02 ± 0.13	0.09 ± 0.15
J09143+526	−0.16 ± 0.15	−0.03 ± 0.13	−0.19 ± 0.18	−0.18 ± 0.18	−0.05 ± 0.17	−0.07 ± 0.15	−0.12 ± 0.14	−0.12 ± 0.15	−0.00 ± 0.14	−0.05 ± 0.19	−0.08 ± 0.17	−0.20 ± 0.21	−0.11 ± 0.17	−0.15 ± 0.15	−0.14 ± 0.16
J09144+526	−0.17 ± 0.16	−0.06 ± 0.13	−0.17 ± 0.19	−0.20 ± 0.18	−0.05 ± 0.17	−0.10 ± 0.15	−0.12 ± 0.13	−0.14 ± 0.15	0.01 ± 0.14	−0.05 ± 0.19	−0.09 ± 0.16	−0.19 ± 0.20	−0.13 ± 0.17	−0.15 ± 0.15	−0.14 ± 0.16
J09151+233	0.02 ± 0.17	0.08 ± 0.13	0.12 ± 0.18	0.01 ± 0.18	0.17 ± 0.18	0.08 ± 0.15	0.03 ± 0.14	0.11 ± 0.15	0.18 ± 0.15	0.13 ± 0.19	0.13 ± 0.17	0.08 ± 0.20	0.11 ± 0.17	0.09 ± 0.15	0.09 ± 0.16
J09201+037	−0.05 ± 0.16	0.04 ± 0.16	−0.13 ± 0.17	−0.07 ± 0.16	−0.01 ± 0.12	−0.00 ± 0.16	−0.13 ± 0.12	0.00 ± 0.15	0.04 ± 0.10	0.08 ± 0.16	−0.02 ± 0.14	−0.08 ± 0.20	0.02 ± 0.16	−0.06 ± 0.13	−0.07 ± 0.15
J09206−169	−0.06 ± 0.16	0.05 ± 0.14	−0.03 ± 0.19	−0.07 ± 0.18	0.03 ± 0.17	0.02 ± 0.16	−0.04 ± 0.15	0.01 ± 0.15	0.07 ± 0.15	0.02 ± 0.19	0.01 ± 0.17	−0.05 ± 0.20	−0.02 ± 0.17	−0.06 ± 0.15	−0.05 ± 0.16
J09212+603	−0.13 ± 0.16	0.06 ± 0.13	−0.20 ± 0.18	−0.14 ± 0.17	−0.09 ± 0.17	−0.13 ± 0.15	−0.14 ± 0.14	−0.09 ± 0.15	0.01 ± 0.15	−0.04 ± 0.19	−0.12 ± 0.16	−0.27 ± 0.20	−0.13 ± 0.16	−0.17 ± 0.15	−0.18 ± 0.16
J09218−023	−0.38 ± 0.16	−0.08 ± 0.18	−0.59 ± 0.17	−0.49 ± 0.16	−0.31 ± 0.11	−0.44 ± 0.15	−0.26 ± 0.12	−0.39 ± 0.15	−0.13 ± 0.10	−0.32 ± 0.17	−0.30 ± 0.14	−0.40 ± 0.20	−0.49 ± 0.17	−0.36 ± 0.13	−0.55 ± 0.15
J09256+634	−0.13 ± 0.18	−0.05 ± 0.17	−0.23 ± 0.17	−0.14 ± 0.17	−0.05 ± 0.12	−0.19 ± 0.16	−0.12 ± 0.12	−0.18 ± 0.14	0.05 ± 0.10	0.08 ± 0.17	−0.10 ± 0.14	−0.16 ± 0.21	−0.21 ± 0.16	−0.11 ± 0.13	−0.24 ± 0.15
J09301−009	−0.13 ± 0.16	0.09 ± 0.13	−0.24 ± 0.18	−0.15 ± 0.17	−0.07 ± 0.17	−0.20 ± 0.15	−0.19 ± 0.14	−0.15 ± 0.16	−0.01 ± 0.14	−0.10 ± 0.19	−0.18 ± 0.17	−0.31 ± 0.20	−0.19 ± 0.17	−0.17 ± 0.15	−0.23 ± 0.16
J09308+024	−0.16 ± 0.16	−0.03 ± 0.16	−0.21 ± 0.17	−0.25 ± 0.18	−0.09 ± 0.11	−0.19 ± 0.15	−0.14 ± 0.12	−0.16 ± 0.13	0.02 ± 0.10	0.03 ± 0.17	−0.07 ± 0.14	−0.15 ± 0.21	−0.18 ± 0.16	−0.15 ± 0.13	−0.26 ± 0.15
J09351−103	−0.09 ± 0.16	−0.04 ± 0.13	−0.11 ± 0.19	−0.18 ± 0.18	−0.02 ± 0.17	−0.15 ± 0.16	−0.22 ± 0.14	−0.17 ± 0.16	0.03 ± 0.14	0.11 ± 0.19	−0.19 ± 0.16	−0.22 ± 0.20	−0.20 ± 0.17	−0.10 ± 0.15	−0.15 ± 0.16
J09394+146	−0.22 ± 0.16	−0.08 ± 0.17	−0.33 ± 0.17	−0.32 ± 0.17	−0.20 ± 0.11	−0.29 ± 0.15	−0.17 ± 0.12	−0.17 ± 0.14	−0.05 ± 0.10	−0.05 ± 0.16	−0.17 ± 0.14	−0.27 ± 0.20	−0.28 ± 0.16	−0.24 ± 0.13	−0.31 ± 0.15
J09488+156	−0.25 ± 0.17	−0.12 ± 0.17	−0.43 ± 0.17	−0.42 ± 0.17	−0.29 ± 0.12	−0.34 ± 0.15	−0.26 ± 0.12	−0.28 ± 0.15	−0.12 ± 0.10	−0.15 ± 0.17	−0.25 ± 0.14	−0.38 ± 0.20	−0.35 ± 0.16	−0.35 ± 0.14	−0.43 ± 0.15
J09526−156	−0.08 ± 0.16	0.03 ± 0.17	−0.25 ± 0.17	−0.18 ± 0.17	−0.06 ± 0.12	−0.14 ± 0.16	−0.18 ± 0.13	−0.11 ± 0.14	−0.03 ± 0.10	−0.02 ± 0.16	−0.19 ± 0.14	−0.27 ± 0.21	−0.20 ± 0.17	−0.14 ± 0.13	−0.24 ± 0.15
J09538−073	−0.14 ± 0.16	−0.09 ± 0.13	−0.16 ± 0.19	−0.34 ± 0.18	−0.16 ± 0.17	−0.15 ± 0.16	−0.19 ± 0.14	−0.20 ± 0.16	−0.07 ± 0.14	−0.05 ± 0.19	−0.18 ± 0.16	−0.29 ± 0.20	−0.21 ± 0.17	−0.21 ± 0.15	−0.20 ± 0.16
J09589+059	−0.05 ± 0.17	−0.12 ± 0.18	−0.14 ± 0.17	−0.14 ± 0.17	−0.08 ± 0.12	−0.06 ± 0.16	−0.11 ± 0.12	−0.01 ± 0.15	0.04 ± 0.10	0.08 ± 0.16	−0.07 ± 0.14	−0.18 ± 0.21	−0.01 ± 0.17	−0.17 ± 0.14	−0.08 ± 0.16
J09597+721	−0.13 ± 0.16	0.04 ± 0.17	−0.16 ± 0.16	−0.14 ± 0.17	−0.00 ± 0.11	−0.06 ± 0.15	−0.10 ± 0.13	−0.03 ± 0.14	0.05 ± 0.10	0.05 ± 0.16	−0.01 ± 0.14	−0.06 ± 0.20	−0.07 ± 0.17	−0.05 ± 0.13	−0.12 ± 0.15
J10020+697	−0.11 ± 0.17	0.03 ± 0.17	−0.07 ± 0.17	−0.06 ± 0.17	0.00 ± 0.11	−0.04 ± 0.15	−0.10 ± 0.12	0.01 ± 0.14	0.07 ± 0.10	0.13 ± 0.17	−0.00 ± 0.14	−0.10 ± 0.20	−0.04 ± 0.16	−0.05 ± 0.13	−0.07 ± 0.16
J10063−064	0.14 ± 0.22	0.10 ± 0.17	0.56 ± 0.24	0.19 ± 0.21	0.26 ± 0.12	0.32 ± 0.18	0.37 ± 0.17	0.15 ± 0.15	0.38 ± 0.11	0.17 ± 0.17	0.57 ± 0.18	0.65 ± 0.30	0.55 ± 0.20	0.25 ± 0.15	0.49 ± 0.20
J10068−127	−0.20 ± 0.18	−0.12 ± 0.17	−0.39 ± 0.17	−0.19 ± 0.18	−0.13 ± 0.12	−0.16 ± 0.17	−0.20 ± 0.13	−0.12 ± 0.15	0.00 ± 0.10	−0.03 ± 0.17	−0.22 ± 0.15	−0.30 ± 0.21	−0.18 ± 0.17	−0.25 ± 0.14	−0.23 ± 0.16
J10098−007	0.24 ± 0.17	0.33 ± 0.14	0.51 ± 0.19	0.27 ± 0.20	0.32 ± 0.17	0.40 ± 0.16	0.31 ± 0.14	0.46 ± 0.17	0.38 ± 0.15	0.38 ± 0.20	0.37 ± 0.18	0.44 ± 0.21	0.44 ± 0.17	0.37 ± 0.16	0.36 ± 0.16
J10120−026AB	−0.22 ± 0.16	0.00 ± 0.16	−0.24 ± 0.17	−0.26 ± 0.17	−0.12 ± 0.12	−0.18 ± 0.15	−0.12 ± 0.13	−0.20 ± 0.14	0.01 ± 0.10	−0.13 ± 0.16	−0.05 ± 0.15	−0.17 ± 0.19	−0.21 ± 0.16	−0.17 ± 0.13	−0.26 ± 0.15
J10130+233	−0.10 ± 0.17	0.12 ± 0.17	−0.26 ± 0.17	−0.18 ± 0.16	0.11 ± 0.11	−0.17 ± 0.15	−0.02 ± 0.12	−0.10 ± 0.14	0.14 ± 0.09	0.04 ± 0.17	−0.07 ± 0.14	−0.10 ± 0.19	−0.28 ± 0.16	−0.03 ± 0.13	−0.27 ± 0.15
J10148+213	−0.14 ± 0.17	−0.07 ± 0.17	−0.31 ± 0.18	−0.17 ± 0.17	−0.11 ± 0.11	−0.19 ± 0.16	−0.17 ± 0.13	−0.19 ± 0.15	0.01 ± 0.10	0.01 ± 0.18	−0.12 ± 0.15	−0.25 ± 0.20	−0.20 ± 0.17	−0.20 ± 0.14	−0.25 ± 0.16
J10155−164	0.11 ± 0.16	0.17 ± 0.17	0.10 ± 0.17	0.02 ± 0.16	0.23 ± 0.11	0.08 ± 0.15	−0.00 ± 0.12	0.08 ± 0.15	0.23 ± 0.10	0.22 ± 0.16	0.07 ± 0.14	0.01 ± 0.19	0.01 ± 0.16	0.09 ± 0.13	−0.02 ± 0.15
J10200+289	−0.25 ± 0.16	−0.04 ± 0.17	−0.31 ± 0.17	−0.29 ± 0.17	−0.19 ± 0.11	−0.23 ± 0.15	−0.18 ± 0.12	−0.14 ± 0.14	−0.06 ± 0.10	−0.09 ± 0.16	−0.14 ± 0.14	−0.25 ± 0.20	−0.26 ± 0.16	−0.20 ± 0.13	−0.29 ± 0.15
J10240+366	−0.05 ± 0.16	0.05 ± 0.17	−0.07 ± 0.16	−0.09 ± 0.16	0.02 ± 0.11	−0.02 ± 0.16	−0.09 ± 0.12	0.08 ± 0.14	0.07 ± 0.10	0.15 ± 0.17	−0.05 ± 0.14	−0.10 ± 0.20	0.01 ± 0.16	−0.06 ± 0.13	−0.04 ± 0.15
J10278+028	0.04 ± 0.16	0.16 ± 0.17	0.09 ± 0.17	0.04 ± 0.17	0.19 ± 0.12	0.10 ± 0.15	−0.02 ± 0.12	0.13 ± 0.14	0.18 ± 0.11	0.19 ± 0.16	0.06 ± 0.14	0.02 ± 0.20	0.03 ± 0.16	0.10 ± 0.13	0.05 ± 0.15
J10304+559	−0.25 ± 0.16	−0.08 ± 0.13	−0.32 ± 0.20	−0.24 ± 0.19	−0.13 ± 0.17	−0.11 ± 0.16	−0.14 ± 0.14	−0.14 ± 0.15	−0.05 ± 0.15	−0.10 ± 0.20	−0.10 ± 0.17	−0.21 ± 0.21	−0.13 ± 0.17	−0.15 ± 0.15	−0.18 ± 0.16
J10368+509	−0.19 ± 0.17	−0.06 ± 0.17	−0.39 ± 0.17	−0.24 ± 0.17	−0.04 ± 0.12	−0.32 ± 0.16	−0.09 ± 0.12	−0.21 ± 0.15	0.07 ± 0.10	0.04 ± 0.16	−0.13 ± 0.15	−0.18 ± 0.20	−0.35 ± 0.17	−0.15 ± 0.13	−0.36 ± 0.16
J10443+124	0.08 ± 0.16	0.19 ± 0.18	0.27 ± 0.17	0.21 ± 0.18	0.22 ± 0.12	0.21 ± 0.16	0.03 ± 0.13	0.20 ± 0.14	0.23 ± 0.11	0.25 ± 0.16	0.14 ± 0.14	0.07 ± 0.21	0.18 ± 0.16	0.13 ± 0.14	0.18 ± 0.15
J10546−073	0.16 ± 0.16	0.08 ± 0.17	0.37 ± 0.17	0.22 ± 0.17	0.19 ± 0.12	0.21 ± 0.15	0.07 ± 0.12	0.26 ± 0.14	0.21 ± 0.10	0.26 ± 0.17	0.13 ± 0.15	0.03 ± 0.20	0.22 ± 0.17	0.10 ± 0.14	0.23 ± 0.16
J10563+042	−0.07 ± 0.17	0.05 ± 0.17	−0.15 ± 0.16	−0.16 ± 0.17	−0.05 ± 0.12	−0.02 ± 0.15	−0.12 ± 0.12	−0.02 ± 0.14	0.04 ± 0.10	0.03 ± 0.16	−0.07 ± 0.14	−0.14 ± 0.19	−0.05 ± 0.16	−0.13 ± 0.14	−0.09 ± 0.15
J11030+037	−0.06 ± 0.16	0.05 ± 0.17	−0.06 ± 0.16	−0.13 ± 0.16	−0.07 ± 0.12	−0.01 ± 0.15	−0.14 ± 0.12	−0.00 ± 0.14	0.03 ± 0.10	0.04 ± 0.16	−0.05 ± 0.14	−0.15 ± 0.20	−0.00 ± 0.15	−0.12 ± 0.14	−0.07 ± 0.15
J11033+359	−0.19 ± 0.16	−0.14 ± 0.14	−0.41 ± 0.19	−0.41 ± 0.20	−0.23 ± 0.17	−0.43 ± 0.16	−0.38 ± 0.14	−0.42 ± 0.16	−0.14 ± 0.15	−0.17 ± 0.20	−0.46 ± 0.17	−0.50 ± 0.20	−0.37 ± 0.18	−0.37 ± 0.15	−0.52 ± 0.16
J11054+435	−0.33 ± 0.16	−0.16 ± 0.14	−0.47 ± 0.19	−0.42 ± 0.19	−0.33 ± 0.17	−0.31 ± 0.16	−0.34 ± 0.13	−0.35 ± 0.15	−0.21 ± 0.15	−0.22 ± 0.20	−0.34 ± 0.17	−0.54 ± 0.20	−0.37 ± 0.17	−0.42 ± 0.15	−0.43 ± 0.15
J11075+437	−0.15 ± 0.16	−0.06 ± 0.17	−0.31 ± 0.16	−0.25 ± 0.17	−0.20 ± 0.12	−0.18 ± 0.15	−0.23 ± 0.12	−0.08 ± 0.14	−0.08 ± 0.10	−0.05 ± 0.16	−0.18 ± 0.14	−0.27 ± 0.19	−0.18 ± 0.17	−0.23 ± 0.13	−0.24 ± 0.14
J11151+734N	−0.14 ± 0.16	0.05 ± 0.16	−0.14 ± 0.17	−0.19 ± 0.17	−0.07 ± 0.12	−0.06 ± 0.15	−0.13 ± 0.13	−0.08 ± 0.14	0.03 ± 0.10	−0.04 ± 0.16	−0.05 ± 0.14	−0.15 ± 0.20	−0.09 ± 0.16	−0.13 ± 0.13	−0.13 ± 0.14
J11151+734S	0.11 ± 0.16	0.20 ± 0.14	0.26 ± 0.19	0.07 ± 0.19	0.16 ± 0.17	0.15 ± 0.17	0.06 ± 0.14	0.17 ± 0.17	0.13 ± 0.15	0.07 ± 0.19	−0.01 ± 0.17	0.09 ± 0.21	0.02 ± 0.18	0.02 ± 0.16	−0.05 ± 0.17
J11201−104AB	0.26 ± 0.17	0.19 ± 0.14	0.11 ± 0.20	0.01 ± 0.20	0.18 ± 0.19	0.07 ± 0.16	0.03 ± 0.15	−0.02 ± 0.17	0.28 ± 0.16	0.26 ± 0.22	0.05 ± 0.18	−0.04 ± 0.22	0.10 ± 0.18	0.13 ± 0.16	−0.06 ± 0.17
J11214−204S	−0.10 ± 0.17	0.04 ± 0.16	−0.13 ± 0.16	−0.22 ± 0.17	−0.04 ± 0.12	−0.11 ± 0.15	−0.11 ± 0.12	−0.15 ± 0.15	0.04 ± 0.10	0.03 ± 0.17	0.00 ± 0.14	−0.02 ± 0.21	−0.11 ± 0.16	−0.11 ± 0.13	−0.18 ± 0.15
J11214−204N	−0.03 ± 0.16	0.04 ± 0.13	−0.03 ± 0.19	−0.08 ± 0.18	0.02 ± 0.17	−0.02 ± 0.16	−0.05 ± 0.14	−0.01 ± 0.16	0.06 ± 0.15	−0.02 ± 0.19	−0.01 ± 0.17	−0.01 ± 0.21	−0.04 ± 0.17	−0.08 ± 0.15	−0.09 ± 0.17
J11218+181	0.10 ± 0.16	0.14 ± 0.14	0.38 ± 0.19	0.01 ± 0.18	0.20 ± 0.17	0.16 ± 0.16	0.11 ± 0.14	0.20 ± 0.16	0.21 ± 0.15	0.27 ± 0.20	0.17 ± 0.17	0.25 ± 0.20	0.23 ± 0.17	0.15 ± 0.15	0.19 ± 0.17
J11240+381	−0.20 ± 0.17	−0.12 ± 0.17	−0.37 ± 0.17	−0.39 ± 0.18	−0.12 ± 0.12	−0.41 ± 0.15	−0.14 ± 0.12	−0.37 ± 0.15	0.03 ± 0.10	−0.02 ± 0.17	−0.18 ± 0.14	−0.24 ± 0.21	−0.43 ± 0.17	−0.22 ± 0.14	−0.46 ± 0.15
J11306−080	−0.05 ± 0.16	0.03 ± 0.16	0.01 ± 0.17	−0.05 ± 0.17	0.02 ± 0.12	0.00 ± 0.15	−0.05 ± 0.12	−0.01 ± 0.14	0.09 ± 0.10	0.06 ± 0.16	−0.01 ± 0.15	−0.12 ± 0.20	0.01 ± 0.16	−0.07 ± 0.13	−0.01 ± 0.15
J11312+631	−0.05 ± 0.15	−0.01 ± 0.13	−0.08 ± 0.19	−0.09 ± 0.18	−0.01 ± 0.17	−0.02 ± 0.16	−0.07 ± 0.14	−0.02 ± 0.15	0.03 ± 0.14	0.02 ± 0.18	−0.05 ± 0.16	−0.05 ± 0.20	−0.02 ± 0.17	−0.13 ± 0.16	−0.10 ± 0.16
J11378+418	−0.18 ± 0.16	0.07 ± 0.14	−0.28 ± 0.18	−0.25 ± 0.18	−0.27 ± 0.18	−0.31 ± 0.17	−0.26 ± 0.14	−0.29 ± 0.16	−0.09 ± 0.14	−0.15 ± 0.19	−0.26 ± 0.17	−0.40 ± 0.21	−0.26 ± 0.17	−0.25 ± 0.16	−0.31 ± 0.17
J11403+095	−0.23 ± 0.16	−0.07 ± 0.13	−0.46 ± 0.19	−0.34 ± 0.18	−0.27 ± 0.17	−0.23 ± 0.16	−0.28 ± 0.14	−0.29 ± 0.15	−0.13 ± 0.14	−0.17 ± 0.19	−0.33 ± 0.17	−0.55 ± 0.20	−0.28 ± 0.17	−0.29 ± 0.15	−0.41 ± 0.17
J11421+267	−0.14 ± 0.16	0.08 ± 0.17	−0.19 ± 0.17	−0.23 ± 0.17	−0.05 ± 0.11	−0.16 ± 0.15	−0.10 ± 0.13	−0.17 ± 0.15	0.05 ± 0.10	−0.07 ± 0.16	−0.08 ± 0.14	−0.17 ± 0.20	−0.21 ± 0.16	−0.13 ± 0.13	−0.24 ± 0.15
J11451+183	0.12 ± 0.17	0.20 ± 0.17	0.27 ± 0.17	0.21 ± 0.17	0.31 ± 0.12	0.28 ± 0.15	0.08 ± 0.12	0.24 ± 0.15	0.33 ± 0.10	0.28 ± 0.17	0.21 ± 0.14	0.15 ± 0.20	0.24 ± 0.17	0.18 ± 0.13	0.21 ± 0.15
J11472+770	0.06 ± 0.16	0.11 ± 0.13	0.14 ± 0.18	−0.04 ± 0.18	0.08 ± 0.18	−0.01 ± 0.15	−0.02 ± 0.14	0.10 ± 0.15	0.14 ± 0.14	0.14 ± 0.19	0.06 ± 0.16	0.04 ± 0.20	0.06 ± 0.17	0.03 ± 0.15	0.04 ± 0.16
J11485+076	−0.15 ± 0.16	−0.13 ± 0.17	−0.29 ± 0.18	−0.31 ± 0.17	−0.20 ± 0.12	−0.25 ± 0.15	−0.19 ± 0.13	−0.18 ± 0.15	−0.02 ± 0.10	−0.01 ± 0.17	−0.21 ± 0.15	−0.34 ± 0.21	−0.25 ± 0.16	−0.32 ± 0.13	−0.26 ± 0.16
J11511+352	−0.19 ± 0.16	−0.07 ± 0.13	−0.26 ± 0.19	−0.26 ± 0.18	−0.19 ± 0.17	−0.18 ± 0.16	−0.18 ± 0.14	−0.22 ± 0.16	−0.05 ± 0.15	−0.08 ± 0.18	−0.18 ± 0.17	−0.34 ± 0.20	−0.19 ± 0.17	−0.22 ± 0.16	−0.27 ± 0.17
J11522+100	0.24 ± 0.17	0.20 ± 0.17	0.37 ± 0.17	0.18 ± 0.17	0.35 ± 0.12	0.30 ± 0.15	0.15 ± 0.13	0.28 ± 0.14	0.34 ± 0.10	0.42 ± 0.16	0.24 ± 0.14	0.22 ± 0.21	0.29 ± 0.17	0.20 ± 0.14	0.26 ± 0.16
J11549−021	−0.11 ± 0.16	0.04 ± 0.17	−0.11 ± 0.17	−0.15 ± 0.17	−0.06 ± 0.12	−0.03 ± 0.15	−0.16 ± 0.12	−0.02 ± 0.14	0.02 ± 0.10	0.02 ± 0.17	−0.05 ± 0.14	−0.14 ± 0.20	−0.05 ± 0.16	−0.12 ± 0.13	−0.08 ± 0.15
J12025+084	−0.41 ± 0.17	−0.18 ± 0.13	−0.52 ± 0.18	−0.45 ± 0.18	−0.41 ± 0.18	−0.33 ± 0.16	−0.36 ± 0.14	−0.43 ± 0.16	−0.28 ± 0.14	−0.33 ± 0.20	−0.39 ± 0.17	−0.57 ± 0.19	−0.45 ± 0.17	−0.52 ± 0.15	−0.52 ± 0.16
J12049+174	−0.09 ± 0.16	−0.09 ± 0.17	−0.22 ± 0.17	−0.33 ± 0.17	−0.13 ± 0.12	−0.28 ± 0.16	−0.14 ± 0.12	−0.21 ± 0.15	−0.00 ± 0.10	0.07 ± 0.16	−0.18 ± 0.14	−0.29 ± 0.20	−0.27 ± 0.16	−0.25 ± 0.13	−0.29 ± 0.15
J12069+058	−0.14 ± 0.16	0.03 ± 0.13	−0.13 ± 0.19	−0.16 ± 0.18	−0.11 ± 0.17	−0.08 ± 0.16	−0.09 ± 0.14	−0.02 ± 0.15	−0.01 ± 0.15	−0.03 ± 0.19	−0.05 ± 0.17	−0.16 ± 0.20	−0.09 ± 0.17	−0.14 ± 0.15	−0.09 ± 0.17
J12088+217	−0.32 ± 0.16	−0.09 ± 0.14	−0.55 ± 0.19	−0.47 ± 0.19	−0.41 ± 0.17	−0.42 ± 0.16	−0.40 ± 0.14	−0.39 ± 0.16	−0.30 ± 0.15	−0.32 ± 0.19	−0.47 ± 0.17	−0.59 ± 0.20	−0.43 ± 0.17	−0.55 ± 0.15	−0.56 ± 0.17
J12093+210	−0.09 ± 0.17	0.06 ± 0.17	−0.10 ± 0.17	−0.13 ± 0.17	0.00 ± 0.11	−0.06 ± 0.15	−0.06 ± 0.12	0.02 ± 0.14	0.09 ± 0.10	0.04 ± 0.16	−0.01 ± 0.14	−0.08 ± 0.20	−0.08 ± 0.16	−0.07 ± 0.13	−0.10 ± 0.15
J12104−131	−0.11 ± 0.17	0.01 ± 0.18	−0.14 ± 0.18	0.03 ± 0.18	0.01 ± 0.12	0.01 ± 0.16	−0.09 ± 0.12	0.05 ± 0.15	0.06 ± 0.10	0.10 ± 0.16	−0.07 ± 0.14	−0.21 ± 0.20	−0.01 ± 0.17	−0.07 ± 0.13	−0.01 ± 0.15

Table C.4: *Continued*

Karmn	[C/H]	[O/H]	[Na/H]	[Mg/H]	[Al/H]	[Si/H]	[Ca/H]	[Sc/H]	[Ti/H]	[V/H]	[Cr/H]	[Mn/H]	[Fe/H]	[Co/H]	[Ni/H]
J12124+121	0.02 ± 0.16	0.17 ± 0.13	0.24 ± 0.19	−0.00 ± 0.19	0.02 ± 0.18	0.08 ± 0.15	0.09 ± 0.15	0.15 ± 0.16	0.19 ± 0.15	0.17 ± 0.20	0.14 ± 0.17	0.06 ± 0.20	0.08 ± 0.16	0.06 ± 0.15	0.14 ± 0.17
J12228−040	−0.11 ± 0.16	−0.06 ± 0.17	−0.21 ± 0.17	−0.19 ± 0.17	−0.03 ± 0.12	−0.20 ± 0.16	−0.12 ± 0.13	−0.19 ± 0.15	0.09 ± 0.10	0.04 ± 0.17	−0.11 ± 0.14	−0.21 ± 0.21	−0.21 ± 0.17	−0.19 ± 0.13	−0.23 ± 0.16
J12349+322	−0.11 ± 0.17	0.03 ± 0.17	−0.10 ± 0.16	−0.17 ± 0.17	−0.04 ± 0.12	−0.09 ± 0.15	−0.10 ± 0.12	−0.03 ± 0.14	0.05 ± 0.10	0.06 ± 0.17	−0.07 ± 0.14	−0.12 ± 0.20	−0.08 ± 0.16	−0.10 ± 0.13	−0.13 ± 0.15
J12364+352	−0.08 ± 0.17	0.05 ± 0.17	−0.08 ± 0.18	0.04 ± 0.18	0.02 ± 0.11	0.10 ± 0.15	−0.15 ± 0.13	0.04 ± 0.14	0.05 ± 0.11	0.08 ± 0.16	0.01 ± 0.14	−0.08 ± 0.20	0.08 ± 0.17	−0.02 ± 0.13	0.00 ± 0.15
J12368−019	0.10 ± 0.16	0.18 ± 0.16	0.23 ± 0.16	0.21 ± 0.18	0.22 ± 0.12	0.24 ± 0.15	0.01 ± 0.13	0.26 ± 0.15	0.21 ± 0.10	0.30 ± 0.17	0.13 ± 0.14	0.07 ± 0.21	0.23 ± 0.16	0.13 ± 0.14	0.22 ± 0.15
J12372+358	−0.13 ± 0.16	0.05 ± 0.14	−0.09 ± 0.19	−0.16 ± 0.18	−0.08 ± 0.17	−0.09 ± 0.16	−0.06 ± 0.14	−0.05 ± 0.16	0.05 ± 0.14	0.03 ± 0.18	−0.05 ± 0.17	−0.17 ± 0.19	−0.05 ± 0.17	−0.11 ± 0.15	−0.09 ± 0.16
J12417+567	−0.13 ± 0.17	−0.07 ± 0.17	−0.28 ± 0.18	−0.35 ± 0.18	−0.12 ± 0.12	−0.27 ± 0.15	−0.13 ± 0.12	−0.22 ± 0.14	0.02 ± 0.10	0.02 ± 0.16	−0.15 ± 0.14	−0.22 ± 0.21	−0.28 ± 0.16	−0.22 ± 0.13	−0.34 ± 0.15
J12440−111	−0.08 ± 0.16	−0.03 ± 0.17	−0.19 ± 0.17	−0.11 ± 0.17	−0.05 ± 0.11	−0.06 ± 0.15	−0.19 ± 0.13	−0.07 ± 0.15	0.00 ± 0.11	0.14 ± 0.16	−0.10 ± 0.15	−0.22 ± 0.20	−0.04 ± 0.16	−0.11 ± 0.13	−0.15 ± 0.15
J12470+466	−0.02 ± 0.16	0.11 ± 0.17	0.03 ± 0.16	−0.02 ± 0.17	0.04 ± 0.12	0.04 ± 0.15	−0.03 ± 0.13	0.05 ± 0.14	0.10 ± 0.10	0.11 ± 0.16	0.04 ± 0.14	−0.05 ± 0.20	0.01 ± 0.16	−0.02 ± 0.13	0.01 ± 0.15
J12488+120	0.01 ± 0.17	0.09 ± 0.17	−0.02 ± 0.16	0.05 ± 0.17	0.13 ± 0.12	0.06 ± 0.15	−0.04 ± 0.12	0.11 ± 0.15	0.16 ± 0.10	0.17 ± 0.16	0.01 ± 0.14	−0.00 ± 0.20	0.02 ± 0.17	0.07 ± 0.13	0.04 ± 0.16
J12533−053	−0.07 ± 0.17	0.06 ± 0.17	−0.17 ± 0.17	−0.23 ± 0.17	0.03 ± 0.12	−0.15 ± 0.16	−0.11 ± 0.12	−0.20 ± 0.15	0.09 ± 0.11	−0.02 ± 0.16	−0.18 ± 0.14	−0.27 ± 0.21	−0.23 ± 0.16	−0.11 ± 0.14	−0.29 ± 0.15
J12549−063	−0.20 ± 0.17	−0.22 ± 0.20	−0.36 ± 0.18	−0.29 ± 0.17	−0.11 ± 0.12	−0.25 ± 0.16	−0.13 ± 0.13	−0.18 ± 0.15	0.02 ± 0.11	0.06 ± 0.17	−0.11 ± 0.15	−0.10 ± 0.21	−0.17 ± 0.17	−0.18 ± 0.14	−0.21 ± 0.16
J12593−001	0.02 ± 0.16	0.13 ± 0.17	0.00 ± 0.17	−0.04 ± 0.17	0.21 ± 0.12	0.01 ± 0.15	−0.02 ± 0.12	−0.01 ± 0.14	0.21 ± 0.10	0.12 ± 0.17	0.02 ± 0.14	0.02 ± 0.20	−0.07 ± 0.16	0.08 ± 0.14	−0.08 ± 0.15
J13027+415	0.02 ± 0.17	0.13 ± 0.17	−0.04 ± 0.17	0.02 ± 0.17	0.14 ± 0.12	0.05 ± 0.15	−0.05 ± 0.12	0.08 ± 0.14	0.16 ± 0.10	0.13 ± 0.17	−0.00 ± 0.14	−0.04 ± 0.20	−0.02 ± 0.16	0.03 ± 0.13	−0.03 ± 0.15
J13088−015	−0.02 ± 0.16	0.06 ± 0.17	−0.05 ± 0.17	−0.14 ± 0.17	0.01 ± 0.11	−0.05 ± 0.15	−0.06 ± 0.13	−0.09 ± 0.14	0.10 ± 0.10	0.04 ± 0.17	−0.01 ± 0.14	−0.12 ± 0.20	−0.08 ± 0.16	−0.08 ± 0.13	−0.11 ± 0.15
J13113+096	−0.21 ± 0.15	0.02 ± 0.13	−0.48 ± 0.19	−0.23 ± 0.18	−0.18 ± 0.17	−0.28 ± 0.16	−0.33 ± 0.14	−0.27 ± 0.16	−0.11 ± 0.14	−0.14 ± 0.19	−0.34 ± 0.17	−0.54 ± 0.20	−0.35 ± 0.17	−0.29 ± 0.15	−0.38 ± 0.17
J13167−123	−0.12 ± 0.16	−0.02 ± 0.17	−0.21 ± 0.17	−0.14 ± 0.17	−0.08 ± 0.12	−0.05 ± 0.15	−0.18 ± 0.13	−0.01 ± 0.14	0.02 ± 0.10	−0.04 ± 0.17	−0.13 ± 0.15	−0.19 ± 0.20	−0.06 ± 0.16	−0.15 ± 0.13	−0.10 ± 0.14
J13168+170	−0.19 ± 0.16	−0.06 ± 0.13	−0.23 ± 0.19	−0.28 ± 0.18	−0.16 ± 0.17	−0.21 ± 0.16	−0.24 ± 0.14	−0.23 ± 0.15	−0.08 ± 0.14	−0.09 ± 0.19	−0.22 ± 0.17	−0.33 ± 0.20	−0.25 ± 0.16	−0.25 ± 0.15	−0.27 ± 0.16
J13179+362	−0.12 ± 0.15	−0.01 ± 0.14	−0.29 ± 0.18	−0.27 ± 0.18	−0.10 ± 0.17	−0.34 ± 0.16	−0.32 ± 0.14	−0.33 ± 0.16	−0.05 ± 0.14	−0.07 ± 0.19	−0.34 ± 0.17	−0.41 ± 0.19	−0.29 ± 0.17	−0.23 ± 0.15	−0.38 ± 0.15
J13182+733	−0.03 ± 0.16	0.16 ± 0.17	−0.11 ± 0.17	−0.00 ± 0.17	0.16 ± 0.12	0.05 ± 0.15	−0.08 ± 0.12	0.09 ± 0.15	0.16 ± 0.10	0.08 ± 0.17	−0.06 ± 0.14	−0.08 ± 0.20	−0.01 ± 0.16	0.03 ± 0.13	−0.07 ± 0.16
J13247−050	−0.03 ± 0.16	0.05 ± 0.17	0.16 ± 0.17	0.07 ± 0.17	0.10 ± 0.12	0.04 ± 0.15	0.02 ± 0.12	0.11 ± 0.14	0.14 ± 0.10	0.21 ± 0.17	0.09 ± 0.14	−0.01 ± 0.21	0.06 ± 0.17	−0.00 ± 0.14	0.08 ± 0.15
J13251−114	−0.07 ± 0.16	0.04 ± 0.16	−0.14 ± 0.17	−0.16 ± 0.16	−0.04 ± 0.12	−0.07 ± 0.15	−0.18 ± 0.12	−0.06 ± 0.14	0.05 ± 0.10	0.04 ± 0.16	−0.12 ± 0.14	−0.22 ± 0.20	−0.10 ± 0.16	−0.14 ± 0.14	−0.19 ± 0.15
J13253+426	−0.11 ± 0.16	−0.00 ± 0.14	−0.15 ± 0.18	−0.17 ± 0.18	−0.07 ± 0.17	−0.12 ± 0.16	−0.15 ± 0.14	−0.07 ± 0.16	−0.05 ± 0.15	−0.09 ± 0.19	−0.12 ± 0.17	−0.16 ± 0.20	−0.15 ± 0.17	−0.21 ± 0.15	−0.16 ± 0.16
J13260+275	−0.10 ± 0.17	0.02 ± 0.16	−0.17 ± 0.17	−0.19 ± 0.17	−0.07 ± 0.11	−0.11 ± 0.15	−0.23 ± 0.12	−0.00 ± 0.14	−0.00 ± 0.10	0.17 ± 0.16	−0.16 ± 0.14	−0.32 ± 0.20	−0.12 ± 0.16	−0.14 ± 0.13	−0.18 ± 0.14
J13294−143	0.01 ± 0.16	−0.03 ± 0.17	0.02 ± 0.16	−0.20 ± 0.17	−0.05 ± 0.11	−0.06 ± 0.15	−0.07 ± 0.12	−0.11 ± 0.14	0.10 ± 0.10	0.13 ± 0.16	0.02 ± 0.15	−0.12 ± 0.21	−0.04 ± 0.17	−0.15 ± 0.13	−0.09 ± 0.15
J13312+589	−0.24 ± 0.16	−0.06 ± 0.17	−0.41 ± 0.16	−0.32 ± 0.16	−0.20 ± 0.12	−0.23 ± 0.15	−0.21 ± 0.12	−0.24 ± 0.14	−0.09 ± 0.10	−0.21 ± 0.16	−0.16 ± 0.14	−0.27 ± 0.19	−0.27 ± 0.17	−0.21 ± 0.13	−0.32 ± 0.15
J13314−079	−0.09 ± 0.16	−0.01 ± 0.13	−0.23 ± 0.18	−0.14 ± 0.18	−0.04 ± 0.17	−0.19 ± 0.16	−0.20 ± 0.14	−0.16 ± 0.15	0.00 ± 0.15	−0.07 ± 0.19	−0.16 ± 0.17	−0.25 ± 0.21	−0.16 ± 0.17	−0.15 ± 0.15	−0.25 ± 0.16
J13321−112	−0.12 ± 0.16	0.01 ± 0.13	−0.15 ± 0.19	−0.18 ± 0.19	−0.09 ± 0.17	−0.10 ± 0.16	−0.15 ± 0.14	−0.05 ± 0.15	−0.03 ± 0.14	−0.01 ± 0.20	−0.15 ± 0.17	−0.25 ± 0.19	−0.15 ± 0.17	−0.19 ± 0.14	−0.13 ± 0.16
J13326+309	−0.03 ± 0.17	−0.02 ± 0.17	−0.15 ± 0.17	−0.12 ± 0.17	−0.01 ± 0.12	−0.07 ± 0.15	−0.11 ± 0.12	−0.10 ± 0.14	0.11 ± 0.10	0.11 ± 0.16	−0.06 ± 0.14	−0.19 ± 0.20	−0.11 ± 0.17	−0.11 ± 0.14	−0.16 ± 0.15
J13335+704	−0.05 ± 0.17	0.11 ± 0.17	0.08 ± 0.17	0.10 ± 0.17	0.11 ± 0.11	0.10 ± 0.15	−0.06 ± 0.12	0.11 ± 0.14	0.12 ± 0.10	0.14 ± 0.17	0.07 ± 0.14	−0.00 ± 0.20	0.13 ± 0.16	0.05 ± 0.13	0.09 ± 0.15
J13386−115	−0.04 ± 0.17	−0.07 ± 0.17	−0.16 ± 0.17	−0.21 ± 0.18	−0.01 ± 0.12	−0.13 ± 0.15	−0.09 ± 0.12	−0.09 ± 0.14	0.11 ± 0.10	0.10 ± 0.16	−0.10 ± 0.15	−0.17 ± 0.21	−0.14 ± 0.17	−0.15 ± 0.13	−0.18 ± 0.15
J13394+461AB	−0.16 ± 0.16	0.03 ± 0.14	−0.34 ± 0.18	−0.24 ± 0.18	−0.21 ± 0.18	−0.35 ± 0.16	−0.29 ± 0.14	−0.27 ± 0.15	−0.09 ± 0.14	−0.17 ± 0.19	−0.30 ± 0.17	−0.38 ± 0.20	−0.31 ± 0.17	−0.32 ± 0.16	−0.41 ± 0.17
J13413−091	−0.16 ± 0.17	0.03 ± 0.16	−0.18 ± 0.16	−0.15 ± 0.16	−0.08 ± 0.11	−0.08 ± 0.15	−0.20 ± 0.13	−0.08 ± 0.15	−0.02 ± 0.10	−0.05 ± 0.16	−0.16 ± 0.14	−0.23 ± 0.20	−0.12 ± 0.16	−0.16 ± 0.13	−0.18 ± 0.15
J13414+489	−0.14 ± 0.17	−0.01 ± 0.18	−0.25 ± 0.17	−0.24 ± 0.17	−0.08 ± 0.11	−0.21 ± 0.15	−0.15 ± 0.12	−0.14 ± 0.14	−0.03 ± 0.10	−0.03 ± 0.17	−0.14 ± 0.15	−0.18 ± 0.20	−0.25 ± 0.16	−0.13 ± 0.13	−0.28 ± 0.15
J13474+063	−0.15 ± 0.16	0.02 ± 0.13	−0.29 ± 0.18	−0.12 ± 0.18	−0.08 ± 0.18	−0.08 ± 0.16	−0.10 ± 0.14	−0.05 ± 0.15	0.02 ± 0.14	−0.03 ± 0.20	−0.09 ± 0.17	−0.22 ± 0.20	−0.07 ± 0.17	−0.12 ± 0.16	−0.17 ± 0.16
J13503−216	−0.04 ± 0.16	0.08 ± 0.17	0.03 ± 0.17	−0.05 ± 0.17	0.06 ± 0.12	0.03 ± 0.15	−0.12 ± 0.13	0.09 ± 0.14	0.06 ± 0.10	0.17 ± 0.16	−0.06 ± 0.14	−0.12 ± 0.20	−0.00 ± 0.16	−0.04 ± 0.13	0.01 ± 0.15
J13537+521AB	0.10 ± 0.17	0.13 ± 0.17	0.18 ± 0.17	0.22 ± 0.18	0.13 ± 0.12	0.21 ± 0.15	−0.01 ± 0.12	0.31 ± 0.15	0.19 ± 0.10	0.27 ± 0.17	0.04 ± 0.14	−0.08 ± 0.20	0.24 ± 0.17	0.01 ± 0.13	0.22 ± 0.15
J13551−079	−0.05 ± 0.16	0.07 ± 0.13	−0.06 ± 0.18	−0.07 ± 0.19	0.03 ± 0.18	−0.01 ± 0.16	−0.06 ± 0.14	0.01 ± 0.15	0.09 ± 0.14	0.12 ± 0.19	0.00 ± 0.17	−0.15 ± 0.19	0.01 ± 0.17	−0.03 ± 0.15	−0.02 ± 0.16
J13555−073	−0.15 ± 0.16	0.03 ± 0.17	−0.26 ± 0.17	−0.26 ± 0.17	−0.09 ± 0.11	−0.17 ± 0.15	−0.12 ± 0.12	−0.22 ± 0.14	0.01 ± 0.10	−0.15 ± 0.16	−0.09 ± 0.14	−0.19 ± 0.19	−0.21 ± 0.16	−0.15 ± 0.14	−0.30 ± 0.15
J13582−120	−0.02 ± 0.17	0.10 ± 0.17	−0.04 ± 0.17	0.12 ± 0.16	0.16 ± 0.12	0.17 ± 0.15	−0.07 ± 0.13	0.17 ± 0.14	0.16 ± 0.10	0.17 ± 0.17	−0.01 ± 0.14	−0.03 ± 0.20	0.14 ± 0.16	0.07 ± 0.13	0.08 ± 0.15
J13583−132	−0.13 ± 0.17	−0.02 ± 0.17	−0.05 ± 0.16	−0.08 ± 0.17	−0.05 ± 0.12	−0.05 ± 0.15	−0.16 ± 0.13	0.00 ± 0.14	0.01 ± 0.10	0.14 ± 0.17	−0.06 ± 0.14	−0.18 ± 0.20	−0.02 ± 0.16	−0.12 ± 0.13	−0.08 ± 0.15
J14019+432	−0.14 ± 0.16	0.00 ± 0.17	−0.26 ± 0.17	−0.26 ± 0.17	−0.11 ± 0.12	−0.23 ± 0.15	−0.14 ± 0.12	−0.20 ± 0.14	0.01 ± 0.10	−0.06 ± 0.16	−0.17 ± 0.14	−0.26 ± 0.20	−0.28 ± 0.17	−0.15 ± 0.14	−0.29 ± 0.15
J14102−180	0.05 ± 0.16	0.16 ± 0.16	0.10 ± 0.17	−0.02 ± 0.17	0.09 ± 0.12	0.09 ± 0.15	0.01 ± 0.13	0.08 ± 0.15	0.16 ± 0.10	0.16 ± 0.17	0.06 ± 0.14	−0.02 ± 0.20	0.06 ± 0.16	0.02 ± 0.13	0.03 ± 0.15
J14159−110	−0.02 ± 0.15	0.03 ± 0.14	−0.03 ± 0.18	−0.22 ± 0.17	−0.09 ± 0.18	−0.10 ± 0.16	−0.10 ± 0.14	−0.17 ± 0.16	0.03 ± 0.15	0.05 ± 0.19	−0.10 ± 0.16	−0.09 ± 0.19	−0.14 ± 0.17	−0.11 ± 0.15	−0.15 ± 0.16
J14171+088	−0.02 ± 0.17	0.05 ± 0.16	0.07 ± 0.17	0.00 ± 0.16	0.06 ± 0.11	−0.02 ± 0.15	−0.04 ± 0.12	0.03 ± 0.14	0.13 ± 0.10	0.23 ± 0.17	0.00 ± 0.15	−0.17 ± 0.20	−0.04 ± 0.16	0.01 ± 0.14	−0.04 ± 0.15
J14175+025	−0.19 ± 0.17	−0.04 ± 0.16	−0.35 ± 0.17	−0.33 ± 0.17	−0.19 ± 0.12	−0.27 ± 0.15	−0.17 ± 0.13	−0.22 ± 0.14	−0.06 ± 0.10	−0.10 ± 0.16	−0.15 ± 0.14	−0.26 ± 0.19	−0.28 ± 0.16	−0.23 ± 0.13	−0.35 ± 0.15
J14195−051	−0.11 ± 0.17	−0.04 ± 0.17	−0.03 ± 0.17	−0.16 ± 0.17	−0.06 ± 0.12	−0.10 ± 0.16	−0.19 ± 0.12	−0.16 ± 0.14	0.01 ± 0.10	−0.01 ± 0.16	−0.15 ± 0.14	−0.24 ± 0.19	−0.16 ± 0.17	−0.16 ± 0.13	−0.15 ± 0.15
J14215−079	−0.06 ± 0.17	0.09 ± 0.16	−0.03 ± 0.18	−0.13 ± 0.17	0.10 ± 0.11	−0.04 ± 0.15	−0.06 ± 0.12	0.06 ± 0.15	0.11 ± 0.10	0.12 ± 0.17	−0.06 ± 0.14	−0.03 ± 0.19	−0.08 ± 0.17	0.02 ± 0.13	−0.11 ± 0.17
J14244+602	−0.06 ± 0.16	0.07 ± 0.13	−0.01 ± 0.18	−0.11 ± 0.18	0.00 ± 0.18	−0.07 ± 0.16	−0.05 ± 0.14	−0.07 ± 0.15	0.12 ± 0.14	0.05 ± 0.19	−0.04 ± 0.17	−0.11 ± 0.20	−0.07 ± 0.17	0.03 ± 0.15	−0.06 ± 0.16
J14251+518	−0.13 ± 0.16	0.03 ± 0.17	−0.17 ± 0.17	−0.23 ± 0.16	−0.11 ± 0.11	−0.13 ± 0.15	−0.13 ± 0.12	−0.10 ± 0.14	0.01 ± 0.10	−0.02 ± 0.16	−0.11 ± 0.15	−0.20 ± 0.20	−0.16 ± 0.16	−0.14 ± 0.13	−0.17 ± 0.14
J14255−118	0.03 ± 0.16	0.07 ± 0.16	0.17 ± 0.17	0.07 ± 0.17	0.12 ± 0.11	0.01 ± 0.15	0.01 ± 0.12	0.07 ± 0.15	0.15 ± 0.10	0.25 ± 0.16	0.06 ± 0.14	0.02 ± 0.21	0.03 ± 0.16	0.05 ± 0.13	0.05 ± 0.15
J14312+754	−0.29 ± 0.17	−0.26 ± 0.19	−0.51 ± 0.17	−0.39 ± 0.17	−0.37 ± 0.12	−0.37 ± 0.16	−0.28 ± 0.13	−0.25 ± 0.15	−0.16 ± 0.10	−0.21 ± 0.17	−0.32 ± 0.15	−0.49 ± 0.21	−0.33 ± 0.17	−0.44 ± 0.13	−0.39 ± 0.15
J14336+093	−0.02 ± 0.17	0.07 ± 0.17	0.09 ± 0.17	−0.05 ± 0.17	0.03 ± 0.12	0.07 ± 0.15	−0.11 ± 0.12	0.07 ± 0.14	0.03 ± 0.10	0.07 ± 0.16	−0.00 ± 0.15	−0.10 ± 0.21	0.06 ± 0.16	−0.01 ± 0.13	0.04 ± 0.16
J14415+136	−0.15 ± 0.16	0.01 ± 0.13	−0.19 ± 0.18	−0.21 ± 0.18	−0.11 ± 0.17	−0.12 ± 0.15	−0.12 ± 0.14	−0.17 ± 0.15	0.00 ± 0.15	−0.00 ± 0.19	−0.14 ± 0.16	−0.26 ± 0.21	−0.15 ± 0.17	−0.19 ± 0.15	−0.18 ± 0.16
J14446−222	0.39 ± 0.18	0.13 ± 0.17	0.55 ± 0.17	0.13 ± 0.18	0.45 ± 0.12	0.30 ± 0.16	0.25 ± 0.13	0.37 ± 0.16	0.51 ± 0.11	0.70 ± 0.18	0.23 ± 0.15	0.20 ± 0.21	0.29 ± 0.18	0.25 ± 0.14	0.30 ± 0.16
J14472+570	−0.10 ± 0.17	−0.14 ± 0.18	−0.36 ± 0.17	−0.38 ± 0.17	−0.15 ± 0.11	−0.35 ± 0.16	−0.12 ± 0.12	−0.22 ± 0.14	0.01 ± 0.10	0.07 ± 0.17	−0.24 ± 0.15	−0.32 ± 0.21	−0.35 ± 0.17	−0.25 ± 0.13	−0.36 ± 0.15
J14480+384	−0.06 ± 0.15	−0.03 ± 0.14	0.03 ± 0.18	−0.15 ± 0.18	0.03 ± 0.18	−0.00 ± 0.16	−0.06 ± 0.14	−0.01 ± 0.16	0.05 ± 0.15	0.10 ± 0.19	−0.04 ± 0.17	−0.03 ± 0.20	0.02 ± 0.17	−0.05 ± 0.15	−0.08 ± 0.16
J14485+101	0.07 ± 0.17	0.14 ± 0.18	0.25 ± 0.17	0.10 ± 0.17	0.19 ± 0.11	0.14 ± 0.15	0.05 ± 0.13	0.16 ± 0.14	0.21 ± 0.10	0.26 ± 0.16	0.15 ± 0.14	0.07 ± 0.20	0.12 ± 0.16	0.12 ± 0.13	0.13 ± 0.15
J14492+498	−0.06 ± 0.16	0.06 ± 0.13	0.14 ± 0.19	−0.14 ± 0.18	−0.04 ± 0.17	0.02 ± 0.16	0.02 ± 0.14	0.00 ± 0.15	0.12 ± 0.14	0.08 ± 0.20	0.01 ± 0.16	−0.02 ± 0.20	−0.05 ± 0.17	−0.01 ± 0.15	0.03 ± 0.17
J14501+323	0.03 ± 0.16	0.15 ± 0.17	0.13 ± 0.17	0.04 ± 0.17	0.20 ± 0.12	0.04 ± 0.15	0.03 ± 0.12	0.08 ± 0.14	0.20 ± 0.10	0.19 ± 0.17	0.04 ± 0.14	0.00 ± 0.20	0.00 ± 0.16	0.07 ± 0.13	0.03 ± 0.15
J14544+161ABC	−0.02 ± 0.15	0.00 ± 0.13	0.02 ± 0.19	−0.13 ± 0.19	−0.06 ± 0.17	−0.07 ± 0.15	−0.10 ± 0.14	−0.09 ± 0.16	0.08 ± 0.14	0.09 ± 0.19	−0.06 ± 0.17	−0.11 ± 0.20	−0.15 ± 0.16	−0.07 ± 0.15	−0.13 ± 0.16
J14595+454	−0.08 ± 0.16	−0.01 ± 0.13	−0.14 ± 0.19	−0.14 ± 0.19	−0.06 ± 0.17	−0.11 ± 0.16	−0.11 ± 0.14	−0.05 ± 0.15	0.02 ± 0.14	−0.01 ± 0.19	−0.05 ± 0.16	−0.07 ± 0.21	−0.04 ± 0.16	−0.11 ± 0.15	−0.11 ± 0.16
J15081+623	−0.02 ± 0.17	0.01 ± 0.17	−0.04 ± 0.17	−0.15 ± 0.17	0.03 ± 0.11	−0.08 ± 0.15	−0.02 ± 0.13	−0.03 ± 0.15	0.10 ± 0.10	0.06 ± 0.16	−0.00 ± 0.14	0.00 ± 0.20	−0.09 ± 0.16	−0.07 ± 0.13	−0.09 ± 0.16
J15118+395	−0.16 ± 0.16	−0.00 ± 0.17	−0.25 ± 0.16	−0.26 ± 0.17	−0.13 ± 0.11	−0.18 ± 0.15	−0.14 ± 0.12	−0.18 ± 0.14	−0.02 ± 0.10	−0.12 ± 0.16	−0.08 ± 0.14	−0.18 ± 0.19	−0.19 ± 0.15	−0.17 ± 0.14	−0.24 ± 0.15
J15131+181	−0.04 ± 0.16	0.04 ± 0.14	−0.01 ± 0.19	−0.08 ± 0.18	0.01 ± 0.17	−0.01 ± 0.16	0.02 ± 0.14	−0.05 ± 0.16	0.17 ± 0.15	0.04 ± 0.19	0.01 ± 0.17	−0.11 ± 0.20	−0.05 ± 0.17	0.03 ± 0.15	−0.04 ± 0.16
J15142−099	−0.06 ± 0.16	−0.09 ± 0.16	−0.07 ± 0.17	−0.24 ± 0.17	−0.05 ± 0.12	−0.16 ± 0.16	−0.10 ± 0.12	−0.14 ± 0.15	0.07 ± 0.10	0.12 ± 0.16	−0.11 ± 0.14	−0.26 ± 0.20	−0.16 ± 0.16	−0.14 ± 0.14	−0.20 ± 0.15

Table C.4: *Continued*

Karmn	[C/H]	[O/H]	[Na/H]	[Mg/H]	[Al/H]	[Si/H]	[Ca/H]	[Sc/H]	[Ti/H]	[V/H]	[Cr/H]	[Mn/H]	[Fe/H]	[Co/H]	[Ni/H]
J15151+333	−0.14 ± 0.15	−0.05 ± 0.14	−0.08 ± 0.19	−0.22 ± 0.18	−0.15 ± 0.17	−0.13 ± 0.15	−0.11 ± 0.14	−0.10 ± 0.16	0.03 ± 0.15	−0.06 ± 0.20	−0.10 ± 0.17	−0.23 ± 0.20	−0.21 ± 0.17	−0.12 ± 0.15	−0.16 ± 0.16
J15157−074	−0.13 ± 0.16	−0.01 ± 0.17	−0.21 ± 0.17	−0.20 ± 0.17	−0.03 ± 0.12	−0.16 ± 0.15	−0.15 ± 0.12	−0.16 ± 0.14	0.05 ± 0.10	0.02 ± 0.17	−0.14 ± 0.14	−0.26 ± 0.21	−0.19 ± 0.16	−0.14 ± 0.13	−0.28 ± 0.15
J15164+167	−0.16 ± 0.16	−0.03 ± 0.14	−0.25 ± 0.18	−0.25 ± 0.18	−0.18 ± 0.18	−0.24 ± 0.16	−0.24 ± 0.14	−0.16 ± 0.16	−0.10 ± 0.14	−0.11 ± 0.19	−0.23 ± 0.17	−0.27 ± 0.19	−0.25 ± 0.17	−0.30 ± 0.15	−0.29 ± 0.16
J15197+046	−0.13 ± 0.17	−0.08 ± 0.17	−0.22 ± 0.17	−0.17 ± 0.17	−0.12 ± 0.12	−0.12 ± 0.15	−0.19 ± 0.12	0.04 ± 0.14	−0.03 ± 0.10	0.08 ± 0.16	−0.09 ± 0.15	−0.18 ± 0.20	−0.10 ± 0.16	−0.16 ± 0.13	−0.12 ± 0.15
J15204+001	−0.27 ± 0.15	−0.13 ± 0.13	−0.44 ± 0.19	−0.35 ± 0.19	−0.28 ± 0.18	−0.27 ± 0.16	−0.32 ± 0.14	−0.29 ± 0.16	−0.22 ± 0.15	−0.20 ± 0.20	−0.34 ± 0.17	−0.46 ± 0.19	−0.32 ± 0.17	−0.44 ± 0.16	−0.40 ± 0.16
J15210+255	0.12 ± 0.16	0.15 ± 0.13	0.23 ± 0.18	0.04 ± 0.18	0.17 ± 0.18	0.13 ± 0.15	0.10 ± 0.14	0.21 ± 0.16	0.19 ± 0.14	0.22 ± 0.20	0.16 ± 0.17	0.22 ± 0.20	0.26 ± 0.18	0.12 ± 0.15	0.15 ± 0.16
J15238+584	−0.07 ± 0.17	−0.10 ± 0.17	−0.22 ± 0.17	−0.33 ± 0.18	−0.14 ± 0.11	−0.30 ± 0.16	−0.10 ± 0.12	−0.32 ± 0.15	0.05 ± 0.10	0.00 ± 0.17	−0.14 ± 0.14	−0.24 ± 0.20	−0.29 ± 0.17	−0.24 ± 0.13	−0.36 ± 0.16
J15277−090	0.03 ± 0.16	0.08 ± 0.17	0.20 ± 0.18	0.16 ± 0.18	0.20 ± 0.11	0.08 ± 0.15	0.04 ± 0.13	0.06 ± 0.14	0.22 ± 0.10	0.30 ± 0.17	0.17 ± 0.15	0.08 ± 0.20	0.11 ± 0.17	0.12 ± 0.13	0.10 ± 0.15
J15290+467AB	−0.15 ± 0.17	−0.14 ± 0.17	−0.30 ± 0.18	−0.25 ± 0.17	−0.12 ± 0.12	−0.26 ± 0.15	−0.13 ± 0.13	−0.18 ± 0.14	0.01 ± 0.11	0.04 ± 0.16	−0.15 ± 0.14	−0.23 ± 0.21	−0.27 ± 0.17	−0.21 ± 0.14	−0.27 ± 0.15
J15291+574	−0.17 ± 0.16	−0.01 ± 0.13	−0.33 ± 0.18	−0.22 ± 0.18	−0.15 ± 0.17	−0.19 ± 0.17	−0.20 ± 0.14	−0.18 ± 0.16	−0.05 ± 0.14	−0.07 ± 0.18	−0.17 ± 0.17	−0.37 ± 0.19	−0.18 ± 0.17	−0.23 ± 0.16	−0.27 ± 0.15
J15340+513	0.07 ± 0.17	0.14 ± 0.17	0.22 ± 0.17	0.15 ± 0.17	0.23 ± 0.12	0.18 ± 0.15	0.09 ± 0.12	0.10 ± 0.15	0.25 ± 0.10	0.23 ± 0.17	0.23 ± 0.15	0.18 ± 0.21	0.12 ± 0.17	0.16 ± 0.13	0.14 ± 0.15
J15354+600	−0.13 ± 0.16	−0.11 ± 0.17	−0.17 ± 0.17	−0.37 ± 0.18	−0.12 ± 0.12	−0.31 ± 0.16	−0.11 ± 0.13	−0.35 ± 0.15	0.07 ± 0.10	0.02 ± 0.16	−0.10 ± 0.14	−0.22 ± 0.21	−0.28 ± 0.17	−0.25 ± 0.13	−0.36 ± 0.16
J15386+371	−0.08 ± 0.16	0.09 ± 0.17	−0.08 ± 0.17	−0.18 ± 0.17	0.01 ± 0.11	−0.09 ± 0.15	−0.08 ± 0.13	−0.13 ± 0.14	0.07 ± 0.10	−0.01 ± 0.17	−0.03 ± 0.14	−0.10 ± 0.20	−0.14 ± 0.17	−0.06 ± 0.13	−0.18 ± 0.15
J15430−130	−0.17 ± 0.15	−0.01 ± 0.13	−0.14 ± 0.18	−0.23 ± 0.18	−0.16 ± 0.17	−0.11 ± 0.15	−0.10 ± 0.15	−0.13 ± 0.15	−0.02 ± 0.14	−0.09 ± 0.19	−0.14 ± 0.17	−0.25 ± 0.20	−0.20 ± 0.17	−0.20 ± 0.15	−0.18 ± 0.16
J15476+226	−0.08 ± 0.16	−0.03 ± 0.17	−0.09 ± 0.17	−0.11 ± 0.17	0.02 ± 0.11	−0.21 ± 0.15	−0.03 ± 0.12	−0.11 ± 0.14	0.12 ± 0.11	0.17 ± 0.17	−0.05 ± 0.14	−0.16 ± 0.20	−0.19 ± 0.17	−0.07 ± 0.13	−0.20 ± 0.15
J15480+043	−0.02 ± 0.16	0.01 ± 0.17	0.02 ± 0.17	−0.19 ± 0.16	−0.05 ± 0.11	−0.16 ± 0.15	−0.03 ± 0.13	−0.07 ± 0.15	0.08 ± 0.10	0.13 ± 0.16	0.01 ± 0.14	−0.13 ± 0.20	−0.13 ± 0.17	−0.12 ± 0.14	−0.15 ± 0.15
J15481+015	−0.15 ± 0.16	0.01 ± 0.17	−0.20 ± 0.17	−0.19 ± 0.17	−0.07 ± 0.11	−0.15 ± 0.14	−0.12 ± 0.12	−0.09 ± 0.14	0.01 ± 0.10	−0.09 ± 0.17	−0.06 ± 0.14	−0.10 ± 0.20	−0.17 ± 0.16	−0.14 ± 0.13	−0.18 ± 0.15
J15552−101	−0.05 ± 0.17	0.06 ± 0.17	−0.12 ± 0.17	−0.22 ± 0.17	0.04 ± 0.12	−0.13 ± 0.15	−0.06 ± 0.13	−0.12 ± 0.15	0.11 ± 0.10	0.00 ± 0.17	−0.10 ± 0.14	−0.23 ± 0.21	−0.21 ± 0.16	−0.06 ± 0.13	−0.22 ± 0.15
J15557−103	0.02 ± 0.16	−0.09 ± 0.17	−0.01 ± 0.17	−0.20 ± 0.16	−0.02 ± 0.12	−0.12 ± 0.15	−0.10 ± 0.11	−0.04 ± 0.14	0.10 ± 0.11	0.21 ± 0.17	−0.06 ± 0.14	−0.23 ± 0.20	−0.07 ± 0.16	−0.16 ± 0.13	−0.14 ± 0.15
J15558−118	−0.04 ± 0.16	0.01 ± 0.17	0.02 ± 0.17	−0.13 ± 0.17	0.04 ± 0.12	−0.07 ± 0.16	−0.04 ± 0.12	−0.04 ± 0.14	0.11 ± 0.10	0.09 ± 0.17	−0.05 ± 0.14	−0.15 ± 0.20	−0.10 ± 0.16	−0.02 ± 0.13	−0.09 ± 0.16
J15569+376	0.03 ± 0.16	−0.01 ± 0.17	−0.06 ± 0.17	−0.34 ± 0.17	−0.05 ± 0.12	−0.21 ± 0.16	−0.01 ± 0.13	−0.16 ± 0.15	0.12 ± 0.10	0.15 ± 0.17	−0.10 ± 0.14	−0.18 ± 0.20	−0.16 ± 0.17	−0.18 ± 0.13	−0.24 ± 0.15
J15578+090	0.01 ± 0.17	0.11 ± 0.17	−0.10 ± 0.17	−0.03 ± 0.17	0.14 ± 0.11	0.00 ± 0.15	−0.03 ± 0.13	−0.02 ± 0.15	0.14 ± 0.10	0.14 ± 0.16	0.03 ± 0.14	0.04 ± 0.19	−0.12 ± 0.16	0.07 ± 0.13	−0.10 ± 0.15
J16023+036	0.12 ± 0.15	0.23 ± 0.13	0.22 ± 0.20	−0.11 ± 0.20	−0.13 ± 0.17	0.07 ± 0.17	0.05 ± 0.15	0.08 ± 0.16	0.04 ± 0.15	0.18 ± 0.20	0.07 ± 0.17	0.11 ± 0.21	0.06 ± 0.18	−0.08 ± 0.15	0.01 ± 0.17
J16048+391	−0.38 ± 0.17	−0.17 ± 0.17	−0.66 ± 0.18	−0.43 ± 0.18	−0.31 ± 0.12	−0.46 ± 0.16	−0.40 ± 0.14	−0.33 ± 0.14	−0.21 ± 0.10	−0.31 ± 0.17	−0.47 ± 0.15	−0.49 ± 0.22	−0.53 ± 0.17	−0.38 ± 0.14	−0.59 ± 0.15
J16120+033N	−0.02 ± 0.16	−0.02 ± 0.18	−0.06 ± 0.17	−0.11 ± 0.18	0.07 ± 0.11	−0.07 ± 0.15	−0.11 ± 0.13	0.09 ± 0.15	0.07 ± 0.10	0.19 ± 0.17	−0.10 ± 0.15	−0.21 ± 0.20	−0.07 ± 0.16	−0.07 ± 0.13	−0.06 ± 0.16
J16139+337AB	−0.08 ± 0.17	0.03 ± 0.17	−0.10 ± 0.17	−0.19 ± 0.17	−0.02 ± 0.11	−0.09 ± 0.15	−0.08 ± 0.12	−0.10 ± 0.14	0.06 ± 0.10	0.00 ± 0.16	−0.03 ± 0.14	−0.09 ± 0.20	−0.09 ± 0.16	−0.10 ± 0.13	−0.14 ± 0.15
J16148+606AB	−0.21 ± 0.17	−0.12 ± 0.18	−0.39 ± 0.17	−0.35 ± 0.17	−0.25 ± 0.11	−0.32 ± 0.15	−0.23 ± 0.12	−0.26 ± 0.15	−0.11 ± 0.10	−0.15 ± 0.16	−0.26 ± 0.14	−0.39 ± 0.20	−0.34 ± 0.16	−0.31 ± 0.13	−0.36 ± 0.15
J16167+672S	−0.04 ± 0.16	0.03 ± 0.13	0.04 ± 0.19	−0.08 ± 0.18	0.06 ± 0.17	−0.01 ± 0.16	−0.04 ± 0.14	0.00 ± 0.15	0.11 ± 0.14	0.11 ± 0.18	0.01 ± 0.17	−0.04 ± 0.21	0.01 ± 0.17	−0.03 ± 0.15	−0.04 ± 0.16
J16167+672N	0.01 ± 0.17	0.08 ± 0.16	0.05 ± 0.16	−0.02 ± 0.18	0.04 ± 0.12	0.04 ± 0.15	−0.05 ± 0.13	−0.02 ± 0.15	0.15 ± 0.10	0.10 ± 0.17	−0.07 ± 0.14	−0.19 ± 0.21	−0.01 ± 0.17	−0.09 ± 0.13	−0.01 ± 0.15
J16183+757	−0.05 ± 0.16	0.03 ± 0.17	−0.01 ± 0.17	−0.06 ± 0.17	0.07 ± 0.11	0.03 ± 0.15	−0.10 ± 0.13	0.02 ± 0.15	0.07 ± 0.10	0.10 ± 0.17	0.01 ± 0.15	−0.04 ± 0.20	0.06 ± 0.15	−0.01 ± 0.13	−0.04 ± 0.15
J16243+199	−0.03 ± 0.17	−0.13 ± 0.18	−0.23 ± 0.18	−0.29 ± 0.18	−0.14 ± 0.11	−0.19 ± 0.16	−0.20 ± 0.13	−0.10 ± 0.15	−0.02 ± 0.11	0.10 ± 0.17	−0.28 ± 0.15	−0.36 ± 0.21	−0.25 ± 0.17	−0.19 ± 0.13	−0.19 ± 0.16
J16254+543	−0.23 ± 0.16	−0.07 ± 0.13	−0.05 ± 0.18	−0.19 ± 0.18	−0.06 ± 0.17	0.03 ± 0.16	−0.00 ± 0.14	−0.07 ± 0.16	0.06 ± 0.15	−0.00 ± 0.20	0.03 ± 0.17	−0.15 ± 0.19	−0.08 ± 0.18	−0.06 ± 0.15	−0.04 ± 0.17
J16255+260	−0.03 ± 0.18	0.02 ± 0.17	−0.01 ± 0.17	−0.10 ± 0.18	−0.01 ± 0.11	−0.02 ± 0.15	−0.08 ± 0.13	−0.12 ± 0.14	0.14 ± 0.10	0.07 ± 0.17	−0.10 ± 0.14	−0.26 ± 0.20	−0.05 ± 0.17	−0.16 ± 0.13	−0.08 ± 0.16
J16269+149	0.13 ± 0.17	−0.04 ± 0.18	0.02 ± 0.18	−0.13 ± 0.19	0.17 ± 0.12	−0.10 ± 0.16	0.07 ± 0.13	0.03 ± 0.15	0.23 ± 0.11	0.24 ± 0.17	0.09 ± 0.15	0.10 ± 0.23	−0.03 ± 0.18	0.01 ± 0.14	−0.03 ± 0.17
J16276−035AB	−0.15 ± 0.16	0.00 ± 0.14	−0.16 ± 0.18	−0.15 ± 0.19	−0.10 ± 0.18	−0.10 ± 0.16	−0.11 ± 0.15	−0.09 ± 0.16	−0.00 ± 0.14	−0.01 ± 0.19	−0.09 ± 0.18	−0.16 ± 0.20	−0.12 ± 0.17	−0.13 ± 0.15	−0.16 ± 0.16
J16299+048	−0.07 ± 0.16	0.02 ± 0.16	−0.22 ± 0.17	−0.19 ± 0.16	−0.06 ± 0.11	−0.17 ± 0.16	−0.15 ± 0.12	−0.13 ± 0.14	−0.00 ± 0.10	−0.02 ± 0.16	−0.11 ± 0.14	−0.15 ± 0.20	−0.17 ± 0.16	−0.14 ± 0.13	−0.21 ± 0.15
J16314+471	−0.07 ± 0.16	−0.06 ± 0.17	−0.26 ± 0.17	−0.14 ± 0.17	−0.07 ± 0.12	−0.12 ± 0.16	−0.21 ± 0.12	−0.00 ± 0.14	−0.01 ± 0.11	0.12 ± 0.16	−0.26 ± 0.15	−0.36 ± 0.21	−0.13 ± 0.16	−0.18 ± 0.13	−0.18 ± 0.15
J16330+031	−0.03 ± 0.17	0.08 ± 0.17	−0.06 ± 0.17	−0.00 ± 0.17	0.05 ± 0.11	−0.09 ± 0.14	−0.07 ± 0.12	−0.05 ± 0.14	0.05 ± 0.10	−0.01 ± 0.16	−0.03 ± 0.14	−0.07 ± 0.20	−0.09 ± 0.16	−0.04 ± 0.13	−0.09 ± 0.15
J16354+350	−0.09 ± 0.17	−0.15 ± 0.18	−0.07 ± 0.17	−0.22 ± 0.17	−0.12 ± 0.11	−0.13 ± 0.16	−0.13 ± 0.13	−0.18 ± 0.15	0.07 ± 0.10	0.05 ± 0.17	−0.09 ± 0.14	−0.24 ± 0.21	−0.09 ± 0.16	−0.26 ± 0.13	−0.16 ± 0.15
J16354−039	−0.39 ± 0.16	−0.17 ± 0.14	−0.55 ± 0.19	−0.38 ± 0.18	−0.31 ± 0.18	−0.19 ± 0.16	−0.24 ± 0.14	−0.36 ± 0.17	−0.22 ± 0.15	−0.33 ± 0.21	−0.28 ± 0.17	−0.51 ± 0.20	−0.36 ± 0.18	−0.44 ± 0.16	−0.39 ± 0.17
J16365+287	0.04 ± 0.17	0.14 ± 0.17	0.31 ± 0.18	0.15 ± 0.17	0.23 ± 0.11	0.12 ± 0.15	0.06 ± 0.13	0.14 ± 0.15	0.22 ± 0.10	0.28 ± 0.17	0.18 ± 0.14	0.09 ± 0.21	0.14 ± 0.16	0.16 ± 0.14	0.16 ± 0.16
J16459+609	−0.12 ± 0.17	0.05 ± 0.16	−0.18 ± 0.17	−0.26 ± 0.17	0.03 ± 0.11	−0.16 ± 0.15	−0.15 ± 0.12	−0.21 ± 0.15	0.05 ± 0.10	0.01 ± 0.17	−0.12 ± 0.14	−0.20 ± 0.20	−0.25 ± 0.16	−0.09 ± 0.14	−0.27 ± 0.15
J16462+164	0.01 ± 0.17	0.04 ± 0.17	0.13 ± 0.18	0.04 ± 0.19	0.08 ± 0.12	0.18 ± 0.17	0.02 ± 0.13	−0.02 ± 0.16	0.19 ± 0.10	0.01 ± 0.18	0.20 ± 0.15	−0.02 ± 0.21	0.10 ± 0.18	−0.04 ± 0.13	0.14 ± 0.16
J16480+453	0.04 ± 0.17	−0.07 ± 0.17	−0.15 ± 0.17	−0.22 ± 0.17	0.07 ± 0.12	−0.19 ± 0.16	−0.01 ± 0.13	−0.13 ± 0.15	0.16 ± 0.10	0.15 ± 0.17	−0.10 ± 0.14	−0.11 ± 0.20	−0.18 ± 0.17	−0.11 ± 0.13	−0.19 ± 0.14
J16528+610	0.08 ± 0.17	0.12 ± 0.17	0.09 ± 0.17	0.04 ± 0.17	0.25 ± 0.11	0.15 ± 0.15	−0.02 ± 0.13	0.07 ± 0.15	0.23 ± 0.10	0.20 ± 0.16	0.10 ± 0.15	0.08 ± 0.21	0.10 ± 0.17	0.09 ± 0.13	0.01 ± 0.15
J16536+560	−0.08 ± 0.17	0.11 ± 0.17	−0.10 ± 0.17	−0.13 ± 0.16	0.07 ± 0.11	−0.07 ± 0.16	−0.12 ± 0.13	−0.07 ± 0.14	0.10 ± 0.10	0.04 ± 0.17	−0.14 ± 0.15	−0.19 ± 0.20	−0.12 ± 0.17	−0.06 ± 0.13	−0.18 ± 0.16
J16543+256	−0.05 ± 0.17	0.12 ± 0.18	−0.13 ± 0.17	−0.15 ± 0.17	0.07 ± 0.11	−0.12 ± 0.16	−0.07 ± 0.12	−0.11 ± 0.15	0.08 ± 0.11	0.03 ± 0.16	−0.05 ± 0.14	−0.13 ± 0.20	−0.19 ± 0.16	−0.03 ± 0.13	−0.24 ± 0.15
J16570−043	−0.15 ± 0.17	−0.10 ± 0.17	−0.02 ± 0.18	−0.22 ± 0.18	−0.12 ± 0.12	−0.13 ± 0.16	−0.17 ± 0.12	−0.18 ± 0.15	0.03 ± 0.11	0.01 ± 0.17	−0.08 ± 0.15	−0.25 ± 0.20	−0.06 ± 0.17	−0.25 ± 0.13	−0.15 ± 0.16
J16581+257	−0.21 ± 0.16	−0.08 ± 0.13	−0.15 ± 0.18	−0.20 ± 0.18	−0.01 ± 0.17	−0.16 ± 0.16	−0.21 ± 0.14	−0.28 ± 0.16	0.02 ± 0.15	−0.08 ± 0.19	−0.13 ± 0.16	−0.21 ± 0.20	−0.31 ± 0.18	−0.14 ± 0.15	−0.19 ± 0.16
J16591+209	−0.01 ± 0.18	−0.09 ± 0.17	−0.07 ± 0.18	−0.22 ± 0.18	−0.09 ± 0.11	−0.14 ± 0.17	−0.12 ± 0.12	−0.22 ± 0.16	0.12 ± 0.10	0.11 ± 0.18	−0.16 ± 0.15	−0.39 ± 0.20	−0.16 ± 0.17	−0.24 ± 0.13	−0.21 ± 0.16
J17011+555	−0.16 ± 0.16	−0.02 ± 0.16	−0.22 ± 0.17	−0.28 ± 0.17	−0.13 ± 0.11	−0.16 ± 0.15	−0.14 ± 0.12	−0.10 ± 0.15	−0.04 ± 0.10	−0.09 ± 0.17	−0.10 ± 0.14	−0.18 ± 0.20	−0.15 ± 0.17	−0.16 ± 0.13	−0.17 ± 0.15
J17017+741	−0.16 ± 0.16	−0.02 ± 0.17	−0.13 ± 0.17	−0.16 ± 0.16	−0.12 ± 0.11	−0.10 ± 0.15	−0.21 ± 0.12	−0.12 ± 0.14	−0.05 ± 0.10	−0.03 ± 0.17	−0.17 ± 0.14	−0.28 ± 0.20	−0.12 ± 0.16	−0.19 ± 0.13	−0.16 ± 0.15
J17052−050	−0.10 ± 0.15	0.14 ± 0.14	−0.20 ± 0.19	−0.13 ± 0.18	−0.09 ± 0.17	−0.22 ± 0.16	−0.17 ± 0.14	−0.15 ± 0.16	0.07 ± 0.15	−0.07 ± 0.19	−0.17 ± 0.18	−0.35 ± 0.20	−0.26 ± 0.17	−0.12 ± 0.14	−0.23 ± 0.16
J17062+646	−0.30 ± 0.17	−0.00 ± 0.16	−0.50 ± 0.18	−0.32 ± 0.17	−0.13 ± 0.11	−0.30 ± 0.15	−0.14 ± 0.12	−0.38 ± 0.15	−0.02 ± 0.10	−0.39 ± 0.17	−0.09 ± 0.14	−0.20 ± 0.19	−0.35 ± 0.17	−0.23 ± 0.13	−0.44 ± 0.16
J17071+215	−0.13 ± 0.16	0.03 ± 0.17	−0.11 ± 0.16	−0.17 ± 0.16	−0.07 ± 0.12	−0.10 ± 0.15	−0.10 ± 0.13	−0.13 ± 0.14	0.05 ± 0.10	−0.03 ± 0.16	−0.04 ± 0.14	−0.18 ± 0.20	−0.11 ± 0.16	−0.14 ± 0.13	−0.16 ± 0.14
J17094+391	−0.07 ± 0.17	−0.07 ± 0.17	−0.20 ± 0.17	−0.24 ± 0.17	−0.15 ± 0.12	−0.21 ± 0.15	−0.22 ± 0.12	−0.11 ± 0.15	−0.09 ± 0.11	0.02 ± 0.17	−0.22 ± 0.14	−0.35 ± 0.20	−0.26 ± 0.17	−0.23 ± 0.14	−0.21 ± 0.15
J17115+384	−0.03 ± 0.16	0.09 ± 0.17	0.00 ± 0.17	−0.09 ± 0.17	0.05 ± 0.12	−0.03 ± 0.15	−0.05 ± 0.12	−0.01 ± 0.14	0.13 ± 0.10	0.11 ± 0.16	−0.06 ± 0.14	−0.15 ± 0.19	−0.07 ± 0.16	−0.06 ± 0.14	−0.07 ± 0.14
J17140+176	−0.06 ± 0.16	0.08 ± 0.16	−0.09 ± 0.17	−0.22 ± 0.17	−0.04 ± 0.12	−0.09 ± 0.15	−0.10 ± 0.12	−0.20 ± 0.14	0.04 ± 0.10	−0.02 ± 0.16	−0.02 ± 0.14	−0.13 ± 0.20	−0.12 ± 0.16	−0.09 ± 0.13	−0.19 ± 0.15
J17154+308	−0.10 ± 0.17	0.03 ± 0.17	−0.05 ± 0.16	−0.17 ± 0.17	−0.08 ± 0.11	−0.12 ± 0.15	−0.10 ± 0.12	−0.10 ± 0.15	−0.00 ± 0.10	−0.03 ± 0.17	0.00 ± 0.14	−0.11 ± 0.21	−0.09 ± 0.16	−0.11 ± 0.13	−0.12 ± 0.15
J17163−053	0.04 ± 0.17	−0.06 ± 0.17	0.01 ± 0.20	−0.04 ± 0.19	0.09 ± 0.12	−0.03 ± 0.16	0.11 ± 0.13	−0.05 ± 0.15	0.23 ± 0.11	0.07 ± 0.17	0.03 ± 0.15	0.02 ± 0.21	0.03 ± 0.16	−0.07 ± 0.14	0.01 ± 0.16
J17166+080	−0.18 ± 0.16	0.02 ± 0.13	−0.05 ± 0.18	−0.17 ± 0.17	−0.07 ± 0.17	−0.09 ± 0.16	−0.17 ± 0.14	−0.17 ± 0.16	0.02 ± 0.13	−0.01 ± 0.19	−0.14 ± 0.17	−0.26 ± 0.21	−0.29 ± 0.18	−0.12 ± 0.15	−0.18 ± 0.16
J17167+115	0.07 ± 0.17	0.12 ± 0.17	0.18 ± 0.16	0.07 ± 0.17	0.26 ± 0.12	0.16 ± 0.15	0.03 ± 0.12	0.14 ± 0.15	0.27 ± 0.10	0.29 ± 0.16	0.06 ± 0.15	0.08 ± 0.21	0.15 ± 0.16	0.12 ± 0.13	0.13 ± 0.15
J17176+524	−0.15 ± 0.16	−0.03 ± 0.16	−0.13 ± 0.17	−0.20 ± 0.16	−0.06 ± 0.11	−0.12 ± 0.15	−0.19 ± 0.12	−0.07 ± 0.14	−0.02 ± 0.10	0.04 ± 0.17	−0.14 ± 0.14	−0.17 ± 0.19	−0.11 ± 0.16	−0.13 ± 0.13	−0.16 ± 0.15
J17198+417	−0.13 ± 0.15	0.10 ± 0.14	−0.09 ± 0.18	−0.10 ± 0.19	−0.08 ± 0.17	−0.04 ± 0.16	−0.09 ± 0.14	−0.05 ± 0.15	0.04 ± 0.14	−0.00 ± 0.19	−0.07 ± 0.17	−0.22 ± 0.20	−0.10 ± 0.17	−0.09 ± 0.15	−0.13 ± 0.17
J17239+136	−0.14 ± 0.17	−0.04 ± 0.16	−0.12 ± 0.17	−0.18 ± 0.17	−0.04 ± 0.11	−0.10 ± 0.15	−0.12 ± 0.12	−0.09 ± 0.14	0.04 ± 0.10	−0.01 ± 0.17	−0.04 ± 0.15	−0.12 ± 0.20	−0.08 ± 0.17	−0.16 ± 0.13	−0.13 ± 0.15
J17246+617	0.02 ± 0.16	0.02 ± 0.17	0.03 ± 0.17	−0.12 ± 0.17	−0.02 ± 0.11	0.03 ± 0.15	−0.09 ± 0.13	−0.05 ± 0.15	0.11 ± 0.10	0.07 ± 0.17	0.05 ± 0.14	−0.08 ± 0.20	−0.00 ± 0.16	−0.05 ± 0.13	−0.05 ± 0.15

Table C.4: *Continued*

Karmn	[C/H]	[O/H]	[Na/H]	[Mg/H]	[Al/H]	[Si/H]	[Ca/H]	[Sc/H]	[Ti/H]	[V/H]	[Cr/H]	[Mn/H]	[Fe/H]	[Co/H]	[Ni/H]
J17265−227	0.06 ± 0.17	0.02 ± 0.16	−0.10 ± 0.17	−0.12 ± 0.17	−0.05 ± 0.12	−0.09 ± 0.16	−0.13 ± 0.13	−0.04 ± 0.14	0.06 ± 0.10	0.09 ± 0.16	−0.12 ± 0.15	−0.24 ± 0.20	−0.14 ± 0.17	−0.12 ± 0.13	−0.13 ± 0.15
J17267−050	0.00 ± 0.16	0.10 ± 0.17	0.11 ± 0.16	0.05 ± 0.17	0.04 ± 0.11	0.08 ± 0.15	−0.05 ± 0.12	0.05 ± 0.14	0.09 ± 0.10	0.08 ± 0.16	0.07 ± 0.14	−0.05 ± 0.20	0.09 ± 0.17	−0.03 ± 0.13	0.09 ± 0.15
J17270+422	−0.14 ± 0.16	0.07 ± 0.13	−0.14 ± 0.18	−0.11 ± 0.18	−0.13 ± 0.17	−0.06 ± 0.16	−0.07 ± 0.14	−0.02 ± 0.15	−0.01 ± 0.15	0.03 ± 0.20	−0.07 ± 0.17	−0.16 ± 0.20	−0.08 ± 0.17	−0.18 ± 0.15	−0.15 ± 0.17
J17281−017	0.10 ± 0.17	0.04 ± 0.17	0.11 ± 0.17	0.09 ± 0.17	0.10 ± 0.12	0.07 ± 0.15	−0.05 ± 0.13	0.15 ± 0.15	0.12 ± 0.11	0.28 ± 0.17	0.06 ± 0.14	−0.03 ± 0.20	0.12 ± 0.16	0.03 ± 0.14	0.08 ± 0.15
J17299−209	0.06 ± 0.17	0.18 ± 0.17	0.07 ± 0.18	−0.04 ± 0.17	0.20 ± 0.12	0.01 ± 0.15	−0.00 ± 0.12	0.03 ± 0.15	0.17 ± 0.10	0.13 ± 0.17	0.04 ± 0.15	−0.05 ± 0.21	−0.06 ± 0.17	0.04 ± 0.13	−0.06 ± 0.15
J17301+546	0.14 ± 0.16	0.15 ± 0.17	0.19 ± 0.18	0.07 ± 0.17	0.22 ± 0.11	0.09 ± 0.15	0.03 ± 0.12	0.08 ± 0.15	0.20 ± 0.11	0.30 ± 0.17	0.07 ± 0.15	0.10 ± 0.21	0.09 ± 0.16	0.11 ± 0.14	0.10 ± 0.15
J17303+055	−0.23 ± 0.16	−0.08 ± 0.13	−0.26 ± 0.19	−0.27 ± 0.18	−0.09 ± 0.17	−0.19 ± 0.16	−0.27 ± 0.14	−0.25 ± 0.16	−0.08 ± 0.15	−0.12 ± 0.19	−0.23 ± 0.17	−0.30 ± 0.20	−0.28 ± 0.17	−0.27 ± 0.15	−0.28 ± 0.16
J17304+337	−0.03 ± 0.16	−0.00 ± 0.17	−0.10 ± 0.17	−0.20 ± 0.17	−0.05 ± 0.12	−0.17 ± 0.15	−0.15 ± 0.12	−0.06 ± 0.14	0.02 ± 0.10	0.13 ± 0.16	−0.16 ± 0.15	−0.27 ± 0.20	−0.19 ± 0.16	−0.16 ± 0.13	−0.19 ± 0.16
J17355+616	−0.18 ± 0.16	−0.04 ± 0.13	−0.12 ± 0.18	−0.22 ± 0.18	−0.08 ± 0.18	−0.15 ± 0.16	−0.24 ± 0.14	−0.20 ± 0.16	−0.05 ± 0.15	−0.03 ± 0.19	−0.19 ± 0.17	−0.26 ± 0.19	−0.23 ± 0.17	−0.22 ± 0.15	−0.23 ± 0.16
J17364+683	−0.09 ± 0.16	0.12 ± 0.17	−0.14 ± 0.17	−0.16 ± 0.18	0.11 ± 0.12	−0.10 ± 0.15	−0.01 ± 0.13	−0.13 ± 0.14	0.15 ± 0.10	−0.01 ± 0.17	−0.02 ± 0.15	−0.09 ± 0.20	−0.18 ± 0.16	−0.04 ± 0.13	−0.18 ± 0.16
J17378+185	−0.34 ± 0.16	−0.14 ± 0.14	−0.43 ± 0.18	−0.37 ± 0.19	−0.22 ± 0.18	−0.29 ± 0.16	−0.39 ± 0.15	−0.41 ± 0.16	−0.19 ± 0.15	−0.16 ± 0.20	−0.39 ± 0.17	−0.56 ± 0.20	−0.44 ± 0.18	−0.37 ± 0.15	−0.45 ± 0.17
J17412+724	−0.09 ± 0.16	−0.04 ± 0.17	−0.17 ± 0.17	−0.13 ± 0.17	−0.08 ± 0.11	−0.12 ± 0.15	−0.21 ± 0.12	−0.07 ± 0.14	−0.03 ± 0.10	0.01 ± 0.17	−0.17 ± 0.15	−0.27 ± 0.20	−0.11 ± 0.16	−0.17 ± 0.13	−0.17 ± 0.15
J17426+756	0.11 ± 0.17	0.07 ± 0.17	0.13 ± 0.18	0.03 ± 0.17	0.10 ± 0.12	0.10 ± 0.15	−0.10 ± 0.13	0.07 ± 0.15	0.06 ± 0.10	0.28 ± 0.17	0.04 ± 0.14	−0.10 ± 0.20	0.13 ± 0.16	0.02 ± 0.13	0.03 ± 0.16
J17428+167	−0.19 ± 0.16	0.01 ± 0.13	−0.25 ± 0.19	−0.23 ± 0.18	−0.24 ± 0.17	−0.18 ± 0.16	−0.20 ± 0.14	−0.18 ± 0.15	−0.07 ± 0.15	−0.07 ± 0.19	−0.21 ± 0.17	−0.32 ± 0.19	−0.18 ± 0.16	−0.26 ± 0.15	−0.28 ± 0.17
J17439+433	−0.13 ± 0.15	0.11 ± 0.13	0.02 ± 0.18	−0.13 ± 0.18	−0.06 ± 0.17	−0.03 ± 0.16	−0.10 ± 0.14	−0.06 ± 0.16	0.04 ± 0.14	0.06 ± 0.19	−0.08 ± 0.17	−0.18 ± 0.20	−0.13 ± 0.17	−0.08 ± 0.15	−0.10 ± 0.16
J17464+277AB	0.11 ± 0.17	0.12 ± 0.17	0.25 ± 0.17	0.06 ± 0.17	0.22 ± 0.11	0.11 ± 0.15	0.01 ± 0.12	0.12 ± 0.14	0.18 ± 0.10	0.27 ± 0.18	0.09 ± 0.14	0.03 ± 0.19	0.07 ± 0.16	0.07 ± 0.13	0.10 ± 0.15
J17477+277	−0.24 ± 0.16	−0.04 ± 0.13	−0.41 ± 0.18	−0.29 ± 0.19	−0.23 ± 0.17	−0.32 ± 0.15	−0.29 ± 0.14	−0.25 ± 0.16	−0.13 ± 0.14	−0.22 ± 0.20	−0.30 ± 0.17	−0.47 ± 0.20	−0.37 ± 0.17	−0.36 ± 0.16	−0.39 ± 0.17
J17520+566	0.02 ± 0.17	−0.03 ± 0.17	−0.04 ± 0.17	−0.13 ± 0.17	0.05 ± 0.12	−0.07 ± 0.15	−0.01 ± 0.12	−0.07 ± 0.14	0.17 ± 0.10	0.16 ± 0.17	0.03 ± 0.15	−0.04 ± 0.21	−0.03 ± 0.17	−0.02 ± 0.13	−0.12 ± 0.16
J17542+073	0.06 ± 0.16	0.15 ± 0.17	0.05 ± 0.16	0.03 ± 0.17	0.20 ± 0.12	0.14 ± 0.15	−0.00 ± 0.13	0.14 ± 0.15	0.27 ± 0.10	0.22 ± 0.17	0.02 ± 0.14	−0.08 ± 0.20	0.06 ± 0.16	0.03 ± 0.13	0.03 ± 0.16
J17559+294	0.14 ± 0.17	0.07 ± 0.16	0.28 ± 0.17	0.05 ± 0.17	0.05 ± 0.11	0.15 ± 0.16	−0.02 ± 0.12	0.19 ± 0.15	0.14 ± 0.10	0.24 ± 0.17	0.14 ± 0.15	−0.06 ± 0.19	0.21 ± 0.16	0.01 ± 0.13	0.13 ± 0.16
J17578+046	−0.41 ± 0.17	−0.12 ± 0.17	−0.66 ± 0.18	−0.35 ± 0.17	−0.31 ± 0.11	−0.37 ± 0.15	−0.38 ± 0.13	−0.33 ± 0.15	−0.20 ± 0.11	−0.42 ± 0.18	−0.40 ± 0.14	−0.46 ± 0.21	−0.44 ± 0.16	−0.41 ± 0.14	−0.49 ± 0.16
J17578+465	−0.18 ± 0.17	0.05 ± 0.17	−0.34 ± 0.17	−0.45 ± 0.19	−0.04 ± 0.12	−0.31 ± 0.16	−0.08 ± 0.12	−0.33 ± 0.16	−0.00 ± 0.10	−0.11 ± 0.16	−0.15 ± 0.14	−0.13 ± 0.20	−0.36 ± 0.17	−0.10 ± 0.13	−0.42 ± 0.16
J18006+685	−0.12 ± 0.16	−0.02 ± 0.13	−0.23 ± 0.19	−0.10 ± 0.18	0.00 ± 0.17	−0.07 ± 0.15	−0.08 ± 0.13	−0.05 ± 0.16	0.07 ± 0.15	0.07 ± 0.19	−0.01 ± 0.16	−0.16 ± 0.20	0.04 ± 0.18	−0.08 ± 0.15	−0.08 ± 0.16
J18007+295	−0.11 ± 0.16	0.17 ± 0.14	−0.04 ± 0.18	−0.07 ± 0.19	−0.08 ± 0.18	0.03 ± 0.16	−0.00 ± 0.14	0.07 ± 0.15	0.05 ± 0.15	0.00 ± 0.19	0.02 ± 0.17	−0.08 ± 0.20	0.06 ± 0.17	−0.09 ± 0.15	−0.07 ± 0.17
J18019+001	−0.22 ± 0.17	−0.12 ± 0.17	−0.40 ± 0.17	−0.31 ± 0.17	−0.20 ± 0.11	−0.20 ± 0.15	−0.28 ± 0.12	−0.23 ± 0.14	−0.11 ± 0.10	−0.15 ± 0.17	−0.24 ± 0.14	−0.33 ± 0.21	−0.24 ± 0.17	−0.29 ± 0.13	−0.30 ± 0.15
J18027+375	−0.05 ± 0.18	0.08 ± 0.18	−0.21 ± 0.18	−0.16 ± 0.19	0.08 ± 0.12	−0.02 ± 0.15	−0.06 ± 0.13	−0.14 ± 0.16	0.19 ± 0.11	0.10 ± 0.18	−0.09 ± 0.15	−0.17 ± 0.21	−0.12 ± 0.18	−0.03 ± 0.14	−0.21 ± 0.16
J18028−030	0.12 ± 0.17	0.17 ± 0.18	0.15 ± 0.17	0.09 ± 0.17	0.27 ± 0.12	0.06 ± 0.15	0.06 ± 0.13	0.14 ± 0.14	0.22 ± 0.10	0.32 ± 0.17	0.04 ± 0.14	−0.01 ± 0.20	0.03 ± 0.16	0.10 ± 0.13	0.04 ± 0.16
J18041+838	0.05 ± 0.17	0.09 ± 0.16	0.13 ± 0.17	0.03 ± 0.17	0.19 ± 0.11	0.08 ± 0.14	0.01 ± 0.12	0.13 ± 0.14	0.19 ± 0.10	0.19 ± 0.16	0.11 ± 0.14	0.09 ± 0.21	0.09 ± 0.16	0.08 ± 0.13	0.06 ± 0.14
J18046+139	−0.20 ± 0.16	−0.04 ± 0.17	−0.37 ± 0.17	−0.27 ± 0.17	−0.20 ± 0.12	−0.22 ± 0.15	−0.24 ± 0.12	−0.15 ± 0.15	−0.11 ± 0.10	−0.14 ± 0.16	−0.19 ± 0.14	−0.32 ± 0.20	−0.23 ± 0.16	−0.24 ± 0.14	−0.29 ± 0.15
J18051−030	−0.28 ± 0.15	−0.11 ± 0.13	−0.37 ± 0.19	−0.26 ± 0.18	−0.14 ± 0.18	−0.19 ± 0.16	−0.22 ± 0.14	−0.27 ± 0.16	−0.09 ± 0.15	−0.20 ± 0.20	−0.16 ± 0.16	−0.31 ± 0.19	−0.23 ± 0.18	−0.26 ± 0.15	−0.28 ± 0.16
J18054+015	0.02 ± 0.16	0.11 ± 0.17	0.10 ± 0.16	0.02 ± 0.16	0.10 ± 0.11	0.05 ± 0.15	−0.06 ± 0.13	0.04 ± 0.14	0.08 ± 0.10	0.12 ± 0.17	0.03 ± 0.14	−0.04 ± 0.20	0.05 ± 0.16	0.02 ± 0.13	0.01 ± 0.15
J18068+177	−0.02 ± 0.16	−0.02 ± 0.17	0.02 ± 0.17	−0.03 ± 0.17	−0.06 ± 0.11	0.07 ± 0.15	−0.13 ± 0.13	0.11 ± 0.15	−0.01 ± 0.10	0.05 ± 0.16	−0.00 ± 0.14	−0.10 ± 0.20	0.12 ± 0.16	−0.13 ± 0.13	0.10 ± 0.15
J18075−159	−0.22 ± 0.18	−0.15 ± 0.17	−0.30 ± 0.18	−0.19 ± 0.17	−0.12 ± 0.12	−0.19 ± 0.16	−0.15 ± 0.13	−0.21 ± 0.15	0.02 ± 0.11	−0.05 ± 0.17	−0.15 ± 0.15	−0.28 ± 0.21	−0.18 ± 0.17	−0.28 ± 0.14	−0.22 ± 0.16
J18090+241	−0.08 ± 0.17	0.02 ± 0.13	−0.03 ± 0.19	−0.13 ± 0.19	−0.00 ± 0.17	−0.08 ± 0.16	−0.07 ± 0.14	−0.09 ± 0.16	0.10 ± 0.15	0.04 ± 0.20	−0.05 ± 0.17	−0.16 ± 0.20	−0.10 ± 0.16	−0.06 ± 0.15	−0.10 ± 0.16
J18112−010	−0.06 ± 0.17	−0.06 ± 0.17	−0.26 ± 0.17	−0.30 ± 0.17	−0.02 ± 0.12	−0.23 ± 0.15	−0.15 ± 0.12	−0.13 ± 0.15	0.02 ± 0.10	0.08 ± 0.16	−0.18 ± 0.14	−0.24 ± 0.20	−0.31 ± 0.16	−0.16 ± 0.13	−0.26 ± 0.16
J18130+414	−0.01 ± 0.17	−0.03 ± 0.17	−0.05 ± 0.17	−0.05 ± 0.17	−0.10 ± 0.11	0.02 ± 0.15	−0.12 ± 0.12	0.05 ± 0.14	−0.01 ± 0.10	0.05 ± 0.16	−0.01 ± 0.15	−0.14 ± 0.20	0.10 ± 0.16	−0.14 ± 0.13	0.02 ± 0.15
J18131+260AB	0.04 ± 0.17	−0.05 ± 0.18	−0.16 ± 0.18	−0.06 ± 0.17	0.08 ± 0.12	−0.08 ± 0.16	−0.05 ± 0.13	0.07 ± 0.14	0.12 ± 0.10	0.22 ± 0.17	−0.04 ± 0.15	−0.15 ± 0.21	−0.07 ± 0.17	−0.05 ± 0.13	−0.09 ± 0.16
J18135+055	0.10 ± 0.17	0.09 ± 0.17	0.18 ± 0.17	0.13 ± 0.17	0.23 ± 0.12	0.08 ± 0.15	0.07 ± 0.13	0.18 ± 0.15	0.22 ± 0.10	0.24 ± 0.17	0.17 ± 0.14	0.14 ± 0.21	0.07 ± 0.16	0.14 ± 0.13	0.11 ± 0.15
J18149+196	−0.17 ± 0.16	−0.09 ± 0.14	0.09 ± 0.19	−0.13 ± 0.19	0.04 ± 0.17	0.08 ± 0.15	0.07 ± 0.15	−0.13 ± 0.16	0.18 ± 0.14	0.04 ± 0.20	0.12 ± 0.17	−0.00 ± 0.19	−0.06 ± 0.17	0.07 ± 0.14	0.04 ± 0.18
J18162+686	−0.22 ± 0.16	−0.03 ± 0.13	−0.41 ± 0.19	−0.30 ± 0.19	−0.28 ± 0.17	−0.25 ± 0.16	−0.28 ± 0.14	−0.31 ± 0.16	−0.11 ± 0.15	−0.18 ± 0.18	−0.30 ± 0.17	−0.35 ± 0.21	−0.31 ± 0.17	−0.29 ± 0.15	−0.40 ± 0.17
J18180+387W	−0.26 ± 0.16	−0.08 ± 0.17	−0.29 ± 0.17	−0.18 ± 0.17	−0.20 ± 0.12	−0.11 ± 0.16	−0.26 ± 0.13	−0.14 ± 0.15	−0.08 ± 0.11	−0.13 ± 0.17	−0.16 ± 0.14	−0.31 ± 0.20	−0.13 ± 0.16	−0.27 ± 0.13	−0.17 ± 0.14
J18189+661	−0.29 ± 0.17	−0.24 ± 0.19	−0.38 ± 0.18	−0.27 ± 0.17	−0.36 ± 0.13	−0.22 ± 0.16	−0.27 ± 0.13	−0.17 ± 0.15	−0.13 ± 0.10	−0.19 ± 0.17	−0.24 ± 0.15	−0.47 ± 0.22	−0.16 ± 0.18	−0.48 ± 0.14	−0.23 ± 0.16
J18221+063	−0.22 ± 0.17	0.06 ± 0.17	−0.34 ± 0.16	−0.25 ± 0.16	−0.02 ± 0.12	−0.21 ± 0.15	−0.16 ± 0.12	−0.25 ± 0.14	0.03 ± 0.10	−0.20 ± 0.17	−0.16 ± 0.15	−0.18 ± 0.20	−0.33 ± 0.16	−0.14 ± 0.14	−0.35 ± 0.15
J18224+620	0.18 ± 0.18	0.11 ± 0.18	0.81 ± 0.20	0.31 ± 0.19	0.32 ± 0.14	0.42 ± 0.16	0.24 ± 0.16	0.32 ± 0.16	0.38 ± 0.12	0.43 ± 0.18	0.47 ± 0.18	0.53 ± 0.28	0.60 ± 0.18	0.17 ± 0.15	0.71 ± 0.17
J18234+281	−0.06 ± 0.16	0.07 ± 0.17	0.05 ± 0.17	−0.01 ± 0.16	0.02 ± 0.12	0.04 ± 0.15	−0.07 ± 0.12	0.05 ± 0.15	0.10 ± 0.10	0.12 ± 0.17	−0.01 ± 0.14	−0.19 ± 0.20	0.03 ± 0.16	−0.06 ± 0.13	0.02 ± 0.15
J18253+186	−0.01 ± 0.17	0.03 ± 0.16	0.07 ± 0.17	−0.01 ± 0.17	0.03 ± 0.11	0.07 ± 0.16	−0.13 ± 0.12	0.08 ± 0.15	0.04 ± 0.10	0.12 ± 0.17	0.03 ± 0.14	−0.11 ± 0.20	0.03 ± 0.16	−0.02 ± 0.13	0.05 ± 0.15
J18292+116	−0.15 ± 0.16	0.12 ± 0.14	−0.06 ± 0.19	−0.07 ± 0.19	−0.12 ± 0.18	0.05 ± 0.16	0.04 ± 0.14	0.09 ± 0.17	0.04 ± 0.15	0.00 ± 0.20	−0.04 ± 0.17	−0.10 ± 0.21	−0.02 ± 0.18	−0.13 ± 0.16	−0.02 ± 0.17
J18306−039	−0.02 ± 0.17	0.04 ± 0.17	0.40 ± 0.20	0.20 ± 0.18	0.03 ± 0.12	0.42 ± 0.18	−0.09 ± 0.12	0.13 ± 0.15	0.06 ± 0.10	0.04 ± 0.17	0.32 ± 0.16	0.28 ± 0.23	0.54 ± 0.18	0.03 ± 0.14	0.44 ± 0.16
J18319+406	−0.08 ± 0.17	0.04 ± 0.17	0.04 ± 0.17	−0.07 ± 0.17	0.00 ± 0.12	0.01 ± 0.15	−0.07 ± 0.13	0.02 ± 0.14	0.09 ± 0.10	0.08 ± 0.17	0.02 ± 0.15	−0.07 ± 0.20	0.01 ± 0.16	−0.09 ± 0.13	0.00 ± 0.15
J18332+223	−0.10 ± 0.17	0.02 ± 0.17	−0.05 ± 0.17	−0.04 ± 0.17	0.05 ± 0.12	0.02 ± 0.15	−0.10 ± 0.13	0.04 ± 0.14	0.09 ± 0.10	0.13 ± 0.17	−0.04 ± 0.14	−0.13 ± 0.20	0.00 ± 0.16	−0.04 ± 0.13	−0.02 ± 0.15
J18346+401	0.19 ± 0.17	0.17 ± 0.17	0.54 ± 0.16	0.35 ± 0.17	0.34 ± 0.12	0.36 ± 0.15	0.18 ± 0.13	0.36 ± 0.14	0.36 ± 0.11	0.46 ± 0.17	0.34 ± 0.15	0.26 ± 0.21	0.40 ± 0.17	0.24 ± 0.14	0.42 ± 0.14
J18353+457	−0.26 ± 0.16	−0.04 ± 0.13	−0.34 ± 0.19	−0.32 ± 0.18	−0.19 ± 0.17	−0.31 ± 0.15	−0.34 ± 0.14	−0.30 ± 0.16	−0.16 ± 0.14	−0.15 ± 0.19	−0.32 ± 0.17	−0.44 ± 0.20	−0.34 ± 0.17	−0.36 ± 0.15	−0.36 ± 0.16
J18354+457	−0.02 ± 0.17	0.09 ± 0.17	0.29 ± 0.18	−0.04 ± 0.17	0.19 ± 0.12	0.07 ± 0.15	0.04 ± 0.13	0.03 ± 0.15	0.26 ± 0.11	0.13 ± 0.17	0.06 ± 0.15	0.12 ± 0.22	0.07 ± 0.16	−0.03 ± 0.13	0.17 ± 0.17
J18363+136	−0.08 ± 0.16	−0.02 ± 0.17	−0.02 ± 0.17	−0.15 ± 0.16	−0.00 ± 0.12	−0.09 ± 0.15	−0.07 ± 0.13	−0.08 ± 0.14	0.10 ± 0.10	0.10 ± 0.16	−0.01 ± 0.14	−0.07 ± 0.20	−0.07 ± 0.16	−0.13 ± 0.13	−0.10 ± 0.15
J18409+315	−0.26 ± 0.17	−0.15 ± 0.13	−0.34 ± 0.19	−0.31 ± 0.18	−0.21 ± 0.17	−0.19 ± 0.16	−0.25 ± 0.14	−0.24 ± 0.16	−0.12 ± 0.15	−0.13 ± 0.19	−0.22 ± 0.16	−0.34 ± 0.20	−0.24 ± 0.17	−0.29 ± 0.16	−0.32 ± 0.16
J18419+318	−0.19 ± 0.16	0.01 ± 0.16	−0.19 ± 0.16	−0.23 ± 0.17	−0.09 ± 0.12	−0.13 ± 0.16	−0.12 ± 0.12	−0.19 ± 0.14	0.02 ± 0.10	−0.08 ± 0.17	−0.05 ± 0.15	−0.18 ± 0.20	−0.17 ± 0.16	−0.15 ± 0.13	−0.20 ± 0.15
J18427+596N	−0.22 ± 0.17	0.07 ± 0.17	−0.32 ± 0.17	−0.27 ± 0.17	−0.04 ± 0.12	−0.23 ± 0.15	−0.14 ± 0.12	−0.27 ± 0.14	0.02 ± 0.10	−0.16 ± 0.16	−0.10 ± 0.14	−0.18 ± 0.20	−0.33 ± 0.16	−0.15 ± 0.13	−0.35 ± 0.15
J18427+596S	−0.27 ± 0.16	0.04 ± 0.17	−0.33 ± 0.17	−0.23 ± 0.17	−0.09 ± 0.12	−0.19 ± 0.15	−0.19 ± 0.12	−0.21 ± 0.14	−0.01 ± 0.10	−0.17 ± 0.16	−0.13 ± 0.15	−0.23 ± 0.20	−0.30 ± 0.15	−0.17 ± 0.13	−0.31 ± 0.15
J18453+188	−0.06 ± 0.16	−0.10 ± 0.16	−0.06 ± 0.16	−0.29 ± 0.18	−0.08 ± 0.11	−0.20 ± 0.15	−0.11 ± 0.12	−0.24 ± 0.15	0.04 ± 0.10	0.07 ± 0.17	−0.00 ± 0.14	−0.16 ± 0.21	−0.16 ± 0.17	−0.17 ± 0.12	−0.24 ± 0.15
J18467+007	−0.04 ± 0.16	−0.11 ± 0.17	−0.17 ± 0.17	−0.30 ± 0.18	−0.05 ± 0.12	−0.23 ± 0.15	−0.07 ± 0.13	−0.20 ± 0.15	0.09 ± 0.11	0.07 ± 0.17	−0.12 ± 0.15	−0.21 ± 0.20	−0.20 ± 0.17	−0.21 ± 0.13	−0.24 ± 0.15
J18491−032	0.11 ± 0.16	0.14 ± 0.17	0.22 ± 0.17	0.18 ± 0.16	0.22 ± 0.12	0.24 ± 0.16	−0.02 ± 0.12	0.21 ± 0.15	0.19 ± 0.11	0.29 ± 0.16	0.10 ± 0.15	0.09 ± 0.21	0.22 ± 0.17	0.12 ± 0.14	0.21 ± 0.15
J18499+186	−0.14 ± 0.16	−0.05 ± 0.17	−0.10 ± 0.17	−0.08 ± 0.17	−0.05 ± 0.12	−0.09 ± 0.16	−0.26 ± 0.14	0.03 ± 0.14	−0.05 ± 0.11	0.11 ± 0.18	−0.19 ± 0.15	−0.26 ± 0.20	−0.13 ± 0.16	−0.12 ± 0.14	−0.10 ± 0.16
J18542+109	0.01 ± 0.16	0.15 ± 0.17	0.17 ± 0.17	0.08 ± 0.17	0.22 ± 0.12	0.15 ± 0.15	−0.01 ± 0.13	0.14 ± 0.14	0.21 ± 0.10	0.16 ± 0.16	0.07 ± 0.14	0.02 ± 0.20	0.11 ± 0.16	0.10 ± 0.13	0.08 ± 0.15
J18570+473	−0.09 ± 0.16	0.02 ± 0.17	−0.19 ± 0.17	−0.25 ± 0.17	−0.06 ± 0.12	−0.17 ± 0.16	−0.16 ± 0.12	−0.17 ± 0.14	0.01 ± 0.10	−0.04 ± 0.17	−0.15 ± 0.14	−0.29 ± 0.20	−0.30 ± 0.17	−0.14 ± 0.13	−0.27 ± 0.16
J18580+059	−0.11 ± 0.16	0.01 ± 0.14	−0.08 ± 0.19	−0.15 ± 0.18	0.05 ± 0.18	−0.11 ± 0.16	−0.20 ± 0.14	−0.15 ± 0.15	0.03 ± 0.15	0.02 ± 0.19	−0.13 ± 0.16	−0.18 ± 0.21	−0.17 ± 0.17	−0.10 ± 0.16	−0.16 ± 0.17
J19052+387	−0.07 ± 0.16	0.02 ± 0.17	−0.02 ± 0.18	−0.00 ± 0.17	0.02 ± 0.11	0.10 ± 0.16	−0.04 ± 0.13	0.11 ± 0.15	0.09 ± 0.10	0.03 ± 0.16	−0.00 ± 0.15	0.02 ± 0.20	0.18 ± 0.16	−0.06 ± 0.13	0.11 ± 0.15

Table C.4: *Continued*

Karmn	[C/H]	[O/H]	[Na/H]	[Mg/H]	[Al/H]	[Si/H]	[Ca/H]	[Sc/H]	[Ti/H]	[V/H]	[Cr/H]	[Mn/H]	[Fe/H]	[Co/H]	[Ni/H]
J19060−074	−0.05 ± 0.16	0.09 ± 0.17	0.12 ± 0.17	0.01 ± 0.18	0.04 ± 0.11	0.08 ± 0.15	−0.07 ± 0.12	0.05 ± 0.14	0.08 ± 0.10	0.08 ± 0.17	0.02 ± 0.14	−0.10 ± 0.20	0.06 ± 0.17	−0.03 ± 0.13	0.09 ± 0.16
J19070+208	−0.39 ± 0.17	−0.17 ± 0.13	−0.34 ± 0.19	−0.36 ± 0.19	−0.21 ± 0.18	−0.23 ± 0.16	−0.32 ± 0.14	−0.38 ± 0.16	−0.15 ± 0.15	−0.15 ± 0.20	−0.29 ± 0.17	−0.45 ± 0.20	−0.43 ± 0.18	−0.33 ± 0.15	−0.38 ± 0.17
J19072+442	0.02 ± 0.16	0.11 ± 0.16	0.06 ± 0.17	0.08 ± 0.17	0.19 ± 0.12	0.02 ± 0.15	−0.02 ± 0.12	−0.02 ± 0.15	0.17 ± 0.10	0.19 ± 0.16	0.07 ± 0.14	0.02 ± 0.20	−0.00 ± 0.16	0.09 ± 0.13	−0.04 ± 0.15
J19084+322	−0.14 ± 0.16	0.03 ± 0.16	−0.09 ± 0.17	−0.12 ± 0.17	−0.05 ± 0.12	−0.02 ± 0.15	−0.12 ± 0.12	−0.07 ± 0.15	0.04 ± 0.10	−0.02 ± 0.16	−0.05 ± 0.15	−0.18 ± 0.19	−0.05 ± 0.16	−0.13 ± 0.13	−0.08 ± 0.15
J19098+176	−0.03 ± 0.16	0.10 ± 0.17	0.08 ± 0.17	0.06 ± 0.17	0.17 ± 0.12	0.10 ± 0.15	−0.01 ± 0.13	0.09 ± 0.14	0.20 ± 0.10	0.17 ± 0.17	0.10 ± 0.14	0.07 ± 0.20	0.08 ± 0.17	0.06 ± 0.13	0.07 ± 0.15
J19105−075	−0.05 ± 0.17	0.07 ± 0.17	0.06 ± 0.18	−0.01 ± 0.16	0.09 ± 0.11	0.01 ± 0.16	−0.08 ± 0.12	0.09 ± 0.15	0.09 ± 0.10	0.11 ± 0.16	−0.03 ± 0.14	−0.14 ± 0.20	−0.06 ± 0.17	−0.01 ± 0.13	0.00 ± 0.15
J19168+003	−0.01 ± 0.16	−0.05 ± 0.18	−0.01 ± 0.18	−0.24 ± 0.17	−0.02 ± 0.12	−0.14 ± 0.15	−0.07 ± 0.12	−0.08 ± 0.15	0.08 ± 0.10	0.20 ± 0.16	−0.06 ± 0.14	−0.14 ± 0.20	−0.11 ± 0.17	−0.15 ± 0.13	−0.10 ± 0.16
J19169+051N	−0.06 ± 0.16	0.08 ± 0.16	−0.05 ± 0.17	−0.12 ± 0.17	0.04 ± 0.12	−0.05 ± 0.15	−0.06 ± 0.13	−0.03 ± 0.14	0.07 ± 0.10	0.07 ± 0.16	−0.00 ± 0.14	−0.11 ± 0.19	−0.12 ± 0.16	−0.04 ± 0.13	−0.09 ± 0.15
J19216+208	−0.07 ± 0.16	0.05 ± 0.17	0.06 ± 0.17	0.03 ± 0.16	0.09 ± 0.11	0.05 ± 0.15	−0.02 ± 0.13	0.04 ± 0.14	0.13 ± 0.10	0.15 ± 0.17	0.07 ± 0.15	−0.00 ± 0.20	0.06 ± 0.16	0.01 ± 0.14	0.05 ± 0.16
J19243+426	0.07 ± 0.16	0.13 ± 0.16	0.36 ± 0.17	0.14 ± 0.17	0.22 ± 0.12	0.20 ± 0.15	0.03 ± 0.12	0.17 ± 0.15	0.20 ± 0.10	0.34 ± 0.17	0.16 ± 0.15	0.06 ± 0.20	0.23 ± 0.17	0.10 ± 0.13	0.21 ± 0.15
J19251+283	−0.03 ± 0.16	0.07 ± 0.17	0.05 ± 0.16	−0.00 ± 0.17	0.07 ± 0.11	0.01 ± 0.15	−0.07 ± 0.12	0.04 ± 0.14	0.12 ± 0.10	0.14 ± 0.16	−0.04 ± 0.14	−0.15 ± 0.21	−0.01 ± 0.16	−0.05 ± 0.14	0.01 ± 0.15
J19260+244	−0.00 ± 0.16	0.02 ± 0.17	0.01 ± 0.17	−0.11 ± 0.17	0.18 ± 0.12	−0.14 ± 0.15	0.02 ± 0.12	−0.13 ± 0.15	0.22 ± 0.10	0.21 ± 0.17	0.05 ± 0.14	0.01 ± 0.20	−0.14 ± 0.16	0.00 ± 0.14	−0.18 ± 0.15
J19271+770	−0.19 ± 0.16	−0.03 ± 0.17	−0.43 ± 0.17	−0.28 ± 0.17	−0.20 ± 0.11	−0.25 ± 0.15	−0.26 ± 0.13	−0.28 ± 0.14	−0.09 ± 0.10	−0.22 ± 0.17	−0.26 ± 0.15	−0.43 ± 0.21	−0.33 ± 0.17	−0.28 ± 0.13	−0.35 ± 0.15
J19316−069	−0.00 ± 0.17	0.07 ± 0.17	0.06 ± 0.17	−0.12 ± 0.17	0.01 ± 0.11	0.00 ± 0.15	−0.09 ± 0.12	0.05 ± 0.15	0.06 ± 0.10	0.17 ± 0.17	−0.03 ± 0.14	−0.17 ± 0.19	−0.04 ± 0.16	−0.04 ± 0.13	−0.01 ± 0.15
J19321−113	−0.04 ± 0.17	−0.06 ± 0.17	−0.07 ± 0.17	−0.10 ± 0.18	−0.08 ± 0.12	−0.02 ± 0.16	−0.17 ± 0.12	−0.01 ± 0.15	0.05 ± 0.10	0.15 ± 0.17	−0.15 ± 0.14	−0.31 ± 0.20	0.00 ± 0.16	−0.19 ± 0.13	−0.04 ± 0.16
J19327−068	0.06 ± 0.16	0.15 ± 0.18	0.12 ± 0.17	0.07 ± 0.17	0.21 ± 0.12	0.17 ± 0.15	−0.00 ± 0.12	0.16 ± 0.15	0.21 ± 0.10	0.16 ± 0.17	0.07 ± 0.14	0.01 ± 0.20	0.06 ± 0.16	0.09 ± 0.13	0.08 ± 0.15
J19346+045	−0.21 ± 0.15	−0.08 ± 0.13	−0.50 ± 0.20	−0.28 ± 0.18	−0.19 ± 0.17	−0.27 ± 0.15	−0.22 ± 0.14	−0.26 ± 0.19	−0.14 ± 0.14	−0.34 ± 0.21	−0.20 ± 0.17	−0.30 ± 0.21	−0.17 ± 0.17	−0.37 ± 0.16	−0.28 ± 0.19
J19354+377	−0.04 ± 0.16	−0.01 ± 0.17	0.07 ± 0.17	−0.14 ± 0.17	−0.00 ± 0.11	−0.08 ± 0.15	−0.05 ± 0.12	−0.10 ± 0.14	0.12 ± 0.10	0.10 ± 0.16	0.03 ± 0.15	−0.11 ± 0.19	−0.07 ± 0.16	−0.13 ± 0.14	−0.08 ± 0.15
J19390+338	0.11 ± 0.16	0.19 ± 0.17	0.26 ± 0.18	0.13 ± 0.17	0.35 ± 0.12	0.16 ± 0.15	0.09 ± 0.13	0.23 ± 0.15	0.30 ± 0.11	0.30 ± 0.17	0.15 ± 0.14	0.19 ± 0.21	0.16 ± 0.17	0.18 ± 0.14	0.16 ± 0.15
J19393+148	−0.02 ± 0.17	0.08 ± 0.17	0.01 ± 0.17	−0.11 ± 0.16	0.04 ± 0.12	−0.01 ± 0.15	−0.07 ± 0.12	−0.08 ± 0.14	0.07 ± 0.10	0.06 ± 0.17	0.04 ± 0.14	−0.06 ± 0.20	−0.06 ± 0.16	−0.01 ± 0.13	−0.05 ± 0.15
J19421+656	−0.01 ± 0.17	0.01 ± 0.17	−0.11 ± 0.16	−0.13 ± 0.17	−0.02 ± 0.12	−0.07 ± 0.15	−0.16 ± 0.12	0.07 ± 0.14	−0.01 ± 0.10	0.08 ± 0.16	−0.10 ± 0.14	−0.17 ± 0.20	−0.09 ± 0.16	−0.10 ± 0.13	−0.10 ± 0.15
J19430+102	−0.01 ± 0.16	0.16 ± 0.14	0.31 ± 0.19	−0.05 ± 0.19	0.06 ± 0.17	0.09 ± 0.16	0.12 ± 0.14	0.01 ± 0.16	0.23 ± 0.15	0.15 ± 0.20	0.13 ± 0.18	0.13 ± 0.20	0.02 ± 0.17	0.13 ± 0.16	0.12 ± 0.17
J19439−057	0.03 ± 0.16	−0.03 ± 0.17	−0.05 ± 0.17	−0.08 ± 0.17	0.03 ± 0.11	−0.04 ± 0.16	−0.12 ± 0.13	0.11 ± 0.14	0.11 ± 0.10	0.22 ± 0.18	−0.14 ± 0.14	−0.18 ± 0.19	0.01 ± 0.17	−0.12 ± 0.13	−0.05 ± 0.16
J19452+407	−0.21 ± 0.16	−0.03 ± 0.13	−0.18 ± 0.18	−0.25 ± 0.18	−0.12 ± 0.17	−0.13 ± 0.15	−0.15 ± 0.14	−0.12 ± 0.15	−0.06 ± 0.14	−0.12 ± 0.19	−0.14 ± 0.16	−0.23 ± 0.19	−0.18 ± 0.16	−0.23 ± 0.15	−0.17 ± 0.16
J19510+104N	−0.06 ± 0.16	0.05 ± 0.17	0.05 ± 0.17	−0.05 ± 0.17	0.02 ± 0.12	0.05 ± 0.14	−0.09 ± 0.12	0.07 ± 0.14	0.09 ± 0.10	0.13 ± 0.16	0.02 ± 0.14	−0.06 ± 0.20	0.06 ± 0.16	−0.05 ± 0.13	0.03 ± 0.15
J19510+104S	−0.19 ± 0.17	0.09 ± 0.15	−0.32 ± 0.21	−0.14 ± 0.19	−0.29 ± 0.19	−0.20 ± 0.17	−0.06 ± 0.15	−0.02 ± 0.19	−0.09 ± 0.15	−0.24 ± 0.20	−0.09 ± 0.19	−0.25 ± 0.23	−0.13 ± 0.19	−0.36 ± 0.16	−0.10 ± 0.20
J19519+141	−0.23 ± 0.16	−0.07 ± 0.13	−0.41 ± 0.19	−0.27 ± 0.18	−0.12 ± 0.17	−0.24 ± 0.16	−0.23 ± 0.14	−0.24 ± 0.16	−0.03 ± 0.14	−0.05 ± 0.19	−0.23 ± 0.17	−0.41 ± 0.21	−0.20 ± 0.16	−0.23 ± 0.15	−0.32 ± 0.16
J19524+603	−0.20 ± 0.17	−0.02 ± 0.17	−0.22 ± 0.17	−0.23 ± 0.17	−0.13 ± 0.11	−0.18 ± 0.15	−0.20 ± 0.12	−0.15 ± 0.14	−0.07 ± 0.10	−0.07 ± 0.17	−0.13 ± 0.14	−0.19 ± 0.19	−0.16 ± 0.16	−0.15 ± 0.14	−0.23 ± 0.15
J19547+844	0.06 ± 0.16	−0.02 ± 0.17	−0.16 ± 0.17	−0.28 ± 0.18	0.14 ± 0.12	−0.27 ± 0.16	0.02 ± 0.12	−0.19 ± 0.15	0.19 ± 0.10	0.27 ± 0.16	−0.08 ± 0.14	−0.09 ± 0.20	−0.26 ± 0.17	−0.06 ± 0.13	−0.31 ± 0.17
J19553+064	−0.14 ± 0.16	−0.05 ± 0.17	−0.01 ± 0.17	−0.10 ± 0.17	−0.06 ± 0.12	−0.09 ± 0.15	−0.12 ± 0.12	−0.03 ± 0.14	0.04 ± 0.10	0.06 ± 0.16	−0.07 ± 0.14	−0.18 ± 0.19	−0.03 ± 0.17	−0.18 ± 0.13	−0.04 ± 0.15
J19564+591	−0.12 ± 0.17	0.10 ± 0.17	−0.21 ± 0.18	−0.19 ± 0.17	0.08 ± 0.11	−0.13 ± 0.16	−0.16 ± 0.13	−0.09 ± 0.14	0.07 ± 0.10	−0.04 ± 0.17	−0.19 ± 0.15	−0.17 ± 0.20	−0.28 ± 0.16	−0.05 ± 0.13	−0.27 ± 0.15
J19565+591	−0.08 ± 0.16	0.10 ± 0.14	0.11 ± 0.18	−0.12 ± 0.19	0.05 ± 0.17	−0.03 ± 0.16	−0.03 ± 0.15	−0.03 ± 0.16	0.08 ± 0.14	0.03 ± 0.19	−0.03 ± 0.16	0.05 ± 0.20	−0.11 ± 0.17	−0.07 ± 0.15	−0.01 ± 0.16
J19578−108	0.06 ± 0.16	−0.04 ± 0.17	−0.10 ± 0.18	−0.17 ± 0.18	0.13 ± 0.12	−0.16 ± 0.16	−0.03 ± 0.12	−0.04 ± 0.15	0.11 ± 0.10	0.32 ± 0.17	−0.08 ± 0.14	−0.09 ± 0.20	−0.21 ± 0.17	−0.01 ± 0.13	−0.14 ± 0.16
J20021+130AB	−0.06 ± 0.16	0.08 ± 0.17	0.04 ± 0.17	−0.12 ± 0.17	0.08 ± 0.12	−0.03 ± 0.15	−0.08 ± 0.13	−0.10 ± 0.14	0.08 ± 0.10	0.08 ± 0.16	0.03 ± 0.14	−0.10 ± 0.20	−0.09 ± 0.16	−0.02 ± 0.13	−0.08 ± 0.15
J20033+672	−0.17 ± 0.16	0.02 ± 0.16	−0.27 ± 0.16	−0.15 ± 0.17	−0.04 ± 0.11	−0.16 ± 0.15	−0.14 ± 0.12	−0.14 ± 0.14	0.02 ± 0.10	−0.12 ± 0.17	−0.09 ± 0.14	−0.22 ± 0.20	−0.23 ± 0.16	−0.11 ± 0.13	−0.27 ± 0.15
J20034+298	0.08 ± 0.16	0.14 ± 0.17	0.06 ± 0.17	0.10 ± 0.17	0.28 ± 0.12	0.19 ± 0.15	0.03 ± 0.13	0.17 ± 0.15	0.32 ± 0.11	0.34 ± 0.17	0.12 ± 0.14	0.11 ± 0.21	0.13 ± 0.17	0.14 ± 0.13	0.12 ± 0.15
J20039−081	0.08 ± 0.17	0.13 ± 0.17	0.30 ± 0.17	0.18 ± 0.17	0.25 ± 0.12	0.21 ± 0.15	0.05 ± 0.13	0.23 ± 0.15	0.26 ± 0.11	0.31 ± 0.17	0.22 ± 0.14	0.11 ± 0.21	0.23 ± 0.16	0.12 ± 0.14	0.23 ± 0.16
J20047+512	−0.09 ± 0.16	0.09 ± 0.16	−0.18 ± 0.17	−0.19 ± 0.17	0.10 ± 0.12	−0.17 ± 0.15	−0.08 ± 0.12	−0.24 ± 0.14	0.11 ± 0.10	0.01 ± 0.16	−0.11 ± 0.13	−0.14 ± 0.20	−0.27 ± 0.16	−0.05 ± 0.13	−0.31 ± 0.15
J20065+159	−0.23 ± 0.16	0.01 ± 0.14	−0.15 ± 0.19	−0.10 ± 0.18	−0.06 ± 0.18	−0.00 ± 0.16	0.04 ± 0.14	−0.04 ± 0.16	0.10 ± 0.15	−0.03 ± 0.20	0.09 ± 0.17	−0.25 ± 0.20	−0.09 ± 0.17	−0.06 ± 0.15	−0.03 ± 0.17
J20077+189	0.03 ± 0.17	0.15 ± 0.17	0.09 ± 0.17	0.03 ± 0.16	0.20 ± 0.12	0.04 ± 0.15	0.01 ± 0.12	0.06 ± 0.14	0.21 ± 0.10	0.16 ± 0.17	0.05 ± 0.14	0.03 ± 0.19	0.02 ± 0.17	0.04 ± 0.13	0.01 ± 0.15
J20108+772	0.06 ± 0.16	0.15 ± 0.14	0.36 ± 0.18	0.10 ± 0.19	0.27 ± 0.18	0.23 ± 0.16	0.18 ± 0.14	0.19 ± 0.16	0.28 ± 0.15	0.27 ± 0.20	0.27 ± 0.17	0.31 ± 0.21	0.20 ± 0.18	0.20 ± 0.15	0.23 ± 0.17
J20112+161	−0.10 ± 0.18	0.10 ± 0.17	−0.00 ± 0.17	−0.08 ± 0.17	0.16 ± 0.12	−0.05 ± 0.16	−0.06 ± 0.12	0.00 ± 0.15	0.21 ± 0.10	0.10 ± 0.17	−0.01 ± 0.15	−0.02 ± 0.20	−0.15 ± 0.16	0.01 ± 0.13	−0.13 ± 0.16
J20149+397	−0.16 ± 0.16	−0.15 ± 0.17	−0.25 ± 0.17	−0.27 ± 0.18	−0.13 ± 0.12	−0.18 ± 0.16	−0.12 ± 0.12	−0.17 ± 0.14	0.06 ± 0.10	−0.03 ± 0.16	−0.18 ± 0.14	−0.28 ± 0.20	−0.14 ± 0.17	−0.31 ± 0.14	−0.20 ± 0.16
J20167+502	−0.08 ± 0.16	0.11 ± 0.17	−0.09 ± 0.17	−0.07 ± 0.16	0.06 ± 0.11	−0.05 ± 0.15	−0.05 ± 0.13	0.00 ± 0.15	0.09 ± 0.10	0.04 ± 0.16	−0.03 ± 0.14	−0.13 ± 0.20	−0.11 ± 0.17	−0.05 ± 0.13	−0.08 ± 0.15
J20177+059	−0.06 ± 0.16	0.07 ± 0.16	0.05 ± 0.17	−0.09 ± 0.17	0.02 ± 0.11	0.01 ± 0.15	−0.06 ± 0.12	−0.07 ± 0.15	0.08 ± 0.10	0.04 ± 0.17	0.05 ± 0.14	−0.05 ± 0.20	−0.02 ± 0.17	−0.02 ± 0.14	−0.03 ± 0.15
J20182−202	0.08 ± 0.17	0.11 ± 0.17	0.29 ± 0.17	0.05 ± 0.17	0.11 ± 0.11	0.18 ± 0.15	−0.02 ± 0.12	0.10 ± 0.14	0.15 ± 0.10	0.19 ± 0.17	0.12 ± 0.14	−0.00 ± 0.21	0.16 ± 0.17	0.04 ± 0.13	0.18 ± 0.15
J20198+229	0.17 ± 0.17	0.06 ± 0.17	0.50 ± 0.17	0.03 ± 0.18	0.07 ± 0.12	0.10 ± 0.16	0.04 ± 0.13	0.06 ± 0.15	0.22 ± 0.11	0.38 ± 0.17	0.13 ± 0.15	−0.08 ± 0.21	0.17 ± 0.17	−0.05 ± 0.13	0.16 ± 0.16
J20216−199	−0.17 ± 0.16	0.05 ± 0.13	−0.03 ± 0.18	−0.02 ± 0.18	0.06 ± 0.17	0.01 ± 0.15	0.05 ± 0.14	−0.12 ± 0.16	0.20 ± 0.14	0.06 ± 0.19	0.14 ± 0.16	−0.13 ± 0.21	−0.07 ± 0.18	0.10 ± 0.15	0.03 ± 0.17
J20283+617	−0.15 ± 0.17	0.02 ± 0.16	−0.21 ± 0.17	−0.20 ± 0.16	−0.11 ± 0.12	−0.17 ± 0.15	−0.15 ± 0.12	−0.15 ± 0.14	−0.05 ± 0.10	−0.10 ± 0.17	−0.07 ± 0.14	−0.19 ± 0.19	−0.19 ± 0.16	−0.15 ± 0.13	−0.21 ± 0.15
J20283+342	−0.16 ± 0.16	−0.02 ± 0.17	−0.07 ± 0.17	−0.07 ± 0.17	−0.05 ± 0.11	−0.01 ± 0.15	−0.18 ± 0.12	−0.02 ± 0.15	0.04 ± 0.10	0.00 ± 0.16	−0.11 ± 0.14	−0.21 ± 0.20	−0.02 ± 0.16	−0.17 ± 0.14	−0.05 ± 0.16
J20287−114	0.09 ± 0.18	−0.04 ± 0.17	0.21 ± 0.18	−0.08 ± 0.19	0.02 ± 0.11	0.00 ± 0.17	−0.02 ± 0.13	−0.12 ± 0.16	0.20 ± 0.11	0.20 ± 0.17	0.03 ± 0.15	−0.19 ± 0.20	0.02 ± 0.18	−0.16 ± 0.13	−0.01 ± 0.16
J20300+003AB	−0.29 ± 0.17	−0.19 ± 0.17	−0.39 ± 0.18	−0.32 ± 0.17	−0.30 ± 0.11	−0.29 ± 0.15	−0.28 ± 0.13	−0.29 ± 0.15	−0.14 ± 0.11	−0.20 ± 0.17	−0.29 ± 0.15	−0.48 ± 0.21	−0.30 ± 0.17	−0.38 ± 0.14	−0.32 ± 0.16
J20301+798	0.02 ± 0.17	0.01 ± 0.17	0.09 ± 0.17	−0.18 ± 0.17	−0.00 ± 0.11	−0.10 ± 0.15	−0.05 ± 0.13	−0.08 ± 0.15	0.12 ± 0.10	0.23 ± 0.16	−0.03 ± 0.14	−0.13 ± 0.20	−0.07 ± 0.17	−0.13 ± 0.13	−0.12 ± 0.15
J20305+654	−0.15 ± 0.16	0.01 ± 0.16	−0.23 ± 0.16	−0.24 ± 0.17	−0.12 ± 0.12	−0.15 ± 0.15	−0.15 ± 0.12	−0.13 ± 0.14	0.00 ± 0.10	−0.05 ± 0.16	−0.14 ± 0.14	−0.23 ± 0.19	−0.18 ± 0.16	−0.18 ± 0.13	−0.22 ± 0.15
J20314+385	−0.28 ± 0.17	−0.11 ± 0.17	−0.31 ± 0.17	−0.23 ± 0.17	−0.30 ± 0.12	−0.15 ± 0.16	−0.30 ± 0.13	−0.17 ± 0.15	−0.15 ± 0.10	−0.21 ± 0.17	−0.20 ± 0.15	−0.35 ± 0.20	−0.16 ± 0.17	−0.33 ± 0.13	−0.22 ± 0.15
J20332+283	0.07 ± 0.17	0.17 ± 0.18	0.25 ± 0.17	0.18 ± 0.17	0.26 ± 0.11	0.17 ± 0.15	0.03 ± 0.13	0.04 ± 0.14	0.23 ± 0.10	0.28 ± 0.17	0.20 ± 0.14	0.16 ± 0.20	0.14 ± 0.16	0.19 ± 0.13	0.11 ± 0.15
J20336+617	0.08 ± 0.17	0.14 ± 0.17	0.13 ± 0.16	0.09 ± 0.16	0.27 ± 0.12	0.14 ± 0.15	0.06 ± 0.12	0.17 ± 0.14	0.27 ± 0.10	0.25 ± 0.17	0.11 ± 0.14	0.13 ± 0.20	0.06 ± 0.16	0.12 ± 0.13	0.11 ± 0.16
J20336+365	−0.07 ± 0.16	0.01 ± 0.16	−0.11 ± 0.17	−0.14 ± 0.16	−0.03 ± 0.12	−0.05 ± 0.15	−0.15 ± 0.12	−0.07 ± 0.14	0.03 ± 0.11	0.02 ± 0.17	−0.05 ± 0.14	−0.11 ± 0.20	−0.06 ± 0.16	−0.13 ± 0.13	−0.10 ± 0.15
J20382+231	−0.06 ± 0.16	0.02 ± 0.14	−0.13 ± 0.18	−0.16 ± 0.19	−0.17 ± 0.18	−0.04 ± 0.16	−0.03 ± 0.14	−0.16 ± 0.17	0.06 ± 0.15	−0.03 ± 0.20	−0.02 ± 0.17	−0.10 ± 0.21	−0.09 ± 0.18	−0.11 ± 0.15	−0.19 ± 0.17
J20405+154	0.09 ± 0.17	0.08 ± 0.16	0.22 ± 0.17	0.12 ± 0.17	0.21 ± 0.12	0.10 ± 0.15	0.04 ± 0.12	0.06 ± 0.14	0.19 ± 0.10	0.27 ± 0.17	0.14 ± 0.14	0.10 ± 0.20	0.11 ± 0.17	0.11 ± 0.13	0.11 ± 0.16
J20407+199AB	−0.25 ± 0.17	0.02 ± 0.17	−0.30 ± 0.17	−0.29 ± 0.17	−0.11 ± 0.11	−0.21 ± 0.15	−0.14 ± 0.12	−0.25 ± 0.14	0.01 ± 0.10	−0.16 ± 0.16	−0.10 ± 0.14	−0.21 ± 0.19	−0.26 ± 0.16	−0.18 ± 0.13	−0.29 ± 0.15
J20439+231	0.16 ± 0.17	0.13 ± 0.17	0.52 ± 0.17	0.27 ± 0.18	0.25 ± 0.12	0.29 ± 0.15	0.12 ± 0.13	0.36 ± 0.15	0.26 ± 0.10	0.41 ± 0.17	0.26 ± 0.15	0.13 ± 0.21	0.35 ± 0.16	0.16 ± 0.14	0.40 ± 0.15
J20450+444	−0.22 ± 0.16	0.03 ± 0.14	−0.24 ± 0.18	−0.21 ± 0.18	−0.20 ± 0.18	−0.14 ± 0.16	−0.17 ± 0.14	−0.13 ± 0.16	−0.08 ± 0.15	−0.13 ± 0.19	−0.14 ± 0.16	−0.30 ± 0.20	−0.14 ± 0.17	−0.27 ± 0.15	−0.24 ± 0.16
J20460+339	−0.30 ± 0.16	−0.01 ± 0.16	−0.21 ± 0.17	−0.25 ± 0.17	−0.12 ± 0.11	−0.19 ± 0.15	−0.20 ± 0.12	−0.14 ± 0.15	−0.05 ± 0.10	−0.11 ± 0.16	−0.16 ± 0.13	−0.27 ± 0.20	−0.21 ± 0.16	−0.23 ± 0.13	−0.23 ± 0.15
J20472+108	−0.15 ± 0.16	−0.06 ± 0.13	−0.32 ± 0.19	−0.24 ± 0.19	−0.10 ± 0.17	−0.26 ± 0.16	−0.25 ± 0.15	−0.27 ± 0.16	−0.10 ± 0.15	−0.24 ± 0.20	−0.26 ± 0.17	−0.22 ± 0.20	−0.29 ± 0.17	−0.24 ± 0.16	−0.31 ± 0.16
J20488+197	−0.00 ± 0.16	0.12 ± 0.17	0.17 ± 0.17	0.09 ± 0.17	0.17 ± 0.12	0.11 ± 0.15	0.03 ± 0.13	0.09 ± 0.15	0.19 ± 0.10	0.18 ± 0.16	0.14 ± 0.14	0.06 ± 0.20	0.10 ± 0.16	0.07 ± 0.13	0.14 ± 0.15

Table C.4: *Continued*

Karmn	[C/H]	[O/H]	[Na/H]	[Mg/H]	[Al/H]	[Si/H]	[Ca/H]	[Sc/H]	[Ti/H]	[V/H]	[Cr/H]	[Mn/H]	[Fe/H]	[Co/H]	[Ni/H]
J20510+399	−0.07 ± 0.17	0.15 ± 0.18	−0.13 ± 0.17	−0.19 ± 0.17	0.17 ± 0.12	−0.11 ± 0.15	−0.00 ± 0.12	−0.18 ± 0.14	0.15 ± 0.10	0.01 ± 0.17	0.01 ± 0.14	−0.00 ± 0.20	−0.21 ± 0.17	−0.01 ± 0.13	−0.23 ± 0.15
J20525−169	−0.01 ± 0.17	0.03 ± 0.17	0.18 ± 0.17	0.04 ± 0.17	0.06 ± 0.11	0.15 ± 0.16	−0.09 ± 0.13	0.16 ± 0.15	0.10 ± 0.10	0.20 ± 0.17	0.06 ± 0.14	−0.07 ± 0.20	0.16 ± 0.16	−0.02 ± 0.14	0.16 ± 0.16
J20533+621	−0.23 ± 0.16	−0.05 ± 0.14	−0.17 ± 0.18	−0.27 ± 0.18	−0.12 ± 0.17	−0.20 ± 0.15	−0.24 ± 0.14	−0.27 ± 0.16	−0.07 ± 0.14	−0.09 ± 0.19	−0.20 ± 0.17	−0.27 ± 0.20	−0.29 ± 0.16	−0.24 ± 0.15	−0.27 ± 0.16
J20540+603	−0.10 ± 0.16	0.01 ± 0.16	−0.15 ± 0.17	−0.24 ± 0.17	−0.03 ± 0.12	−0.15 ± 0.15	−0.09 ± 0.13	−0.18 ± 0.14	0.07 ± 0.10	−0.04 ± 0.16	−0.05 ± 0.14	−0.10 ± 0.21	−0.21 ± 0.16	−0.13 ± 0.13	−0.19 ± 0.15
J20556−140S	−0.20 ± 0.17	−0.01 ± 0.17	−0.30 ± 0.18	−0.08 ± 0.18	−0.05 ± 0.12	−0.09 ± 0.16	−0.20 ± 0.12	−0.17 ± 0.15	0.04 ± 0.10	−0.15 ± 0.17	−0.14 ± 0.15	−0.21 ± 0.21	−0.19 ± 0.16	−0.16 ± 0.14	−0.24 ± 0.16
J20556−140N	−0.17 ± 0.17	0.06 ± 0.17	−0.25 ± 0.18	−0.12 ± 0.17	0.03 ± 0.12	−0.12 ± 0.16	−0.13 ± 0.12	−0.13 ± 0.15	0.08 ± 0.10	−0.11 ± 0.17	−0.11 ± 0.15	−0.12 ± 0.20	−0.19 ± 0.15	−0.09 ± 0.13	−0.22 ± 0.15
J20567−104	−0.03 ± 0.17	0.07 ± 0.17	0.14 ± 0.17	−0.04 ± 0.18	0.05 ± 0.12	0.08 ± 0.15	−0.06 ± 0.12	0.06 ± 0.15	0.11 ± 0.10	0.12 ± 0.17	0.06 ± 0.14	−0.10 ± 0.20	0.01 ± 0.17	−0.02 ± 0.14	0.06 ± 0.15
J20568−048	−0.17 ± 0.17	0.02 ± 0.17	−0.34 ± 0.17	−0.22 ± 0.17	0.03 ± 0.12	−0.25 ± 0.15	−0.11 ± 0.12	−0.15 ± 0.15	0.07 ± 0.10	−0.03 ± 0.17	−0.17 ± 0.15	−0.23 ± 0.20	−0.35 ± 0.17	−0.15 ± 0.14	−0.32 ± 0.15
J20581+401AB	−0.14 ± 0.16	−0.01 ± 0.13	−0.05 ± 0.19	−0.10 ± 0.18	0.01 ± 0.17	−0.02 ± 0.15	−0.04 ± 0.14	−0.07 ± 0.16	0.06 ± 0.14	0.01 ± 0.19	−0.00 ± 0.17	−0.07 ± 0.20	−0.06 ± 0.16	−0.08 ± 0.15	−0.08 ± 0.17
J20583+425	−0.07 ± 0.17	0.09 ± 0.16	−0.15 ± 0.17	−0.21 ± 0.17	0.01 ± 0.11	−0.09 ± 0.16	−0.09 ± 0.13	−0.11 ± 0.14	0.06 ± 0.10	−0.09 ± 0.16	−0.03 ± 0.14	−0.08 ± 0.20	−0.16 ± 0.16	−0.09 ± 0.14	−0.18 ± 0.15
J20593+530AB	−0.09 ± 0.16	−0.03 ± 0.17	−0.16 ± 0.17	−0.15 ± 0.17	−0.00 ± 0.11	−0.17 ± 0.16	−0.09 ± 0.12	−0.06 ± 0.14	0.08 ± 0.10	0.02 ± 0.16	−0.09 ± 0.14	−0.17 ± 0.19	−0.16 ± 0.16	−0.15 ± 0.13	−0.19 ± 0.15
J21012+332	−0.05 ± 0.17	−0.03 ± 0.17	−0.09 ± 0.17	−0.16 ± 0.18	−0.08 ± 0.11	−0.09 ± 0.15	−0.12 ± 0.12	−0.11 ± 0.14	0.09 ± 0.10	0.02 ± 0.17	−0.09 ± 0.15	−0.28 ± 0.20	−0.10 ± 0.17	−0.21 ± 0.14	−0.12 ± 0.15
J21019−063	−0.06 ± 0.17	0.09 ± 0.17	−0.00 ± 0.17	−0.09 ± 0.17	0.06 ± 0.12	−0.01 ± 0.15	−0.05 ± 0.13	−0.06 ± 0.14	0.09 ± 0.10	0.05 ± 0.16	0.01 ± 0.14	−0.12 ± 0.19	−0.07 ± 0.16	−0.04 ± 0.13	−0.06 ± 0.15
J21027+349	0.07 ± 0.17	0.12 ± 0.17	−0.19 ± 0.18	0.02 ± 0.18	0.24 ± 0.12	−0.05 ± 0.16	0.03 ± 0.13	−0.00 ± 0.15	0.30 ± 0.10	0.25 ± 0.18	−0.07 ± 0.15	−0.14 ± 0.22	−0.16 ± 0.18	0.05 ± 0.13	−0.17 ± 0.17
J21053+208	−0.16 ± 0.16	−0.01 ± 0.16	−0.22 ± 0.17	−0.31 ± 0.17	−0.15 ± 0.11	−0.15 ± 0.15	−0.20 ± 0.12	−0.22 ± 0.14	−0.04 ± 0.10	−0.10 ± 0.16	−0.08 ± 0.14	−0.21 ± 0.21	−0.19 ± 0.16	−0.19 ± 0.12	−0.26 ± 0.15
J21057+502W	0.18 ± 0.17	0.19 ± 0.17	0.21 ± 0.18	0.06 ± 0.17	0.33 ± 0.11	0.15 ± 0.15	0.12 ± 0.13	0.12 ± 0.14	0.36 ± 0.10	0.29 ± 0.16	0.15 ± 0.14	0.15 ± 0.20	0.07 ± 0.16	0.14 ± 0.13	0.06 ± 0.15
J21057+502E	0.10 ± 0.17	0.21 ± 0.18	0.22 ± 0.17	0.17 ± 0.17	0.29 ± 0.12	0.21 ± 0.15	0.05 ± 0.13	0.28 ± 0.14	0.29 ± 0.10	0.30 ± 0.17	0.10 ± 0.14	0.06 ± 0.20	0.18 ± 0.18	0.15 ± 0.13	0.16 ± 0.15
J21068+387	−0.11 ± 0.16	−0.00 ± 0.13	−0.28 ± 0.18	−0.20 ± 0.19	−0.07 ± 0.17	−0.20 ± 0.16	−0.21 ± 0.15	−0.19 ± 0.15	−0.04 ± 0.14	−0.14 ± 0.19	−0.22 ± 0.17	−0.24 ± 0.20	−0.22 ± 0.16	−0.20 ± 0.16	−0.25 ± 0.16
J21069+387	−0.15 ± 0.16	−0.02 ± 0.14	−0.37 ± 0.20	−0.27 ± 0.18	−0.13 ± 0.16	−0.23 ± 0.16	−0.22 ± 0.14	−0.22 ± 0.16	−0.12 ± 0.14	−0.27 ± 0.20	−0.22 ± 0.16	−0.28 ± 0.21	−0.17 ± 0.17	−0.34 ± 0.15	−0.30 ± 0.17
J21074+198	−0.18 ± 0.16	0.05 ± 0.14	−0.16 ± 0.19	−0.14 ± 0.19	−0.11 ± 0.18	−0.13 ± 0.16	−0.13 ± 0.14	−0.12 ± 0.16	0.07 ± 0.15	0.03 ± 0.20	−0.11 ± 0.17	−0.38 ± 0.20	−0.26 ± 0.18	−0.08 ± 0.15	−0.14 ± 0.16
J21074+468	0.25 ± 0.17	0.38 ± 0.14	0.50 ± 0.19	0.18 ± 0.19	0.28 ± 0.18	0.27 ± 0.17	0.27 ± 0.15	0.38 ± 0.17	0.43 ± 0.15	0.39 ± 0.22	0.31 ± 0.18	0.29 ± 0.21	0.33 ± 0.18	0.39 ± 0.15	0.40 ± 0.17
J21109+469	0.03 ± 0.16	0.14 ± 0.17	0.06 ± 0.16	−0.04 ± 0.17	0.15 ± 0.12	0.01 ± 0.16	−0.02 ± 0.12	−0.00 ± 0.15	0.16 ± 0.10	0.13 ± 0.16	0.02 ± 0.14	0.00 ± 0.20	−0.06 ± 0.16	0.02 ± 0.13	−0.05 ± 0.15
J21114+658	−0.12 ± 0.15	0.01 ± 0.13	0.01 ± 0.19	−0.04 ± 0.19	0.03 ± 0.17	0.21 ± 0.16	0.13 ± 0.15	0.09 ± 0.16	0.20 ± 0.15	0.04 ± 0.20	0.13 ± 0.17	−0.09 ± 0.20	0.02 ± 0.17	0.11 ± 0.15	0.08 ± 0.17
J21127−073	0.16 ± 0.17	0.13 ± 0.16	0.32 ± 0.18	0.17 ± 0.18	0.21 ± 0.13	0.27 ± 0.15	0.06 ± 0.13	0.15 ± 0.15	0.31 ± 0.10	0.31 ± 0.17	0.16 ± 0.14	−0.05 ± 0.20	0.22 ± 0.17	0.10 ± 0.14	0.21 ± 0.15
J21147+160	0.00 ± 0.16	0.15 ± 0.17	0.04 ± 0.17	0.06 ± 0.17	0.22 ± 0.11	0.03 ± 0.15	−0.01 ± 0.12	0.13 ± 0.14	0.19 ± 0.10	0.19 ± 0.16	0.05 ± 0.15	0.04 ± 0.20	−0.00 ± 0.16	0.09 ± 0.13	0.03 ± 0.15
J21152+257	0.15 ± 0.18	0.13 ± 0.17	0.40 ± 0.17	0.20 ± 0.18	0.21 ± 0.12	0.28 ± 0.16	0.07 ± 0.13	0.21 ± 0.15	0.29 ± 0.10	0.25 ± 0.17	0.18 ± 0.15	−0.02 ± 0.21	0.26 ± 0.16	0.06 ± 0.13	0.29 ± 0.15
J21164+025	−0.03 ± 0.17	0.08 ± 0.17	0.19 ± 0.18	−0.08 ± 0.17	0.02 ± 0.11	0.11 ± 0.15	−0.08 ± 0.12	0.04 ± 0.15	0.09 ± 0.10	0.22 ± 0.17	0.06 ± 0.15	−0.13 ± 0.20	0.13 ± 0.16	−0.07 ± 0.13	0.08 ± 0.16
J21221+229	−0.27 ± 0.17	−0.13 ± 0.13	−0.13 ± 0.20	−0.39 ± 0.18	−0.27 ± 0.18	−0.27 ± 0.16	−0.31 ± 0.14	−0.32 ± 0.17	−0.20 ± 0.14	−0.19 ± 0.20	−0.30 ± 0.17	−0.21 ± 0.21	−0.40 ± 0.16	−0.34 ± 0.15	−0.31 ± 0.16
J21323−209	−0.21 ± 0.16	−0.05 ± 0.14	−0.27 ± 0.19	−0.21 ± 0.18	−0.04 ± 0.17	−0.18 ± 0.15	−0.22 ± 0.14	−0.23 ± 0.16	−0.04 ± 0.14	−0.14 ± 0.20	−0.19 ± 0.17	−0.22 ± 0.21	−0.22 ± 0.16	−0.22 ± 0.15	−0.27 ± 0.17
J21348+515	−0.19 ± 0.17	0.14 ± 0.17	−0.46 ± 0.17	−0.25 ± 0.17	0.09 ± 0.11	−0.26 ± 0.16	−0.07 ± 0.12	−0.32 ± 0.15	0.13 ± 0.10	−0.22 ± 0.17	−0.21 ± 0.15	−0.20 ± 0.20	−0.42 ± 0.16	−0.12 ± 0.14	−0.47 ± 0.15
J21414+207	−0.06 ± 0.16	−0.03 ± 0.17	−0.12 ± 0.17	−0.22 ± 0.17	−0.05 ± 0.12	−0.17 ± 0.15	−0.09 ± 0.13	−0.10 ± 0.15	0.05 ± 0.10	0.04 ± 0.17	−0.05 ± 0.14	−0.16 ± 0.19	−0.13 ± 0.16	−0.17 ± 0.13	−0.21 ± 0.16
J21442+066	−0.09 ± 0.16	0.04 ± 0.17	−0.01 ± 0.17	−0.14 ± 0.17	0.03 ± 0.12	−0.05 ± 0.15	−0.06 ± 0.12	−0.09 ± 0.14	0.13 ± 0.10	0.05 ± 0.17	−0.00 ± 0.14	−0.09 ± 0.20	−0.07 ± 0.16	−0.07 ± 0.13	−0.11 ± 0.15
J21463+382	−0.33 ± 0.17	−0.04 ± 0.17	−0.43 ± 0.17	−0.26 ± 0.18	−0.19 ± 0.12	−0.22 ± 0.15	−0.31 ± 0.13	−0.21 ± 0.14	−0.08 ± 0.10	−0.27 ± 0.17	−0.26 ± 0.15	−0.32 ± 0.20	−0.30 ± 0.17	−0.27 ± 0.13	−0.36 ± 0.15
J21466+668	−0.02 ± 0.17	0.14 ± 0.17	0.08 ± 0.18	−0.00 ± 0.17	0.18 ± 0.12	0.02 ± 0.15	−0.01 ± 0.12	0.06 ± 0.14	0.16 ± 0.10	0.19 ± 0.16	0.08 ± 0.14	0.05 ± 0.20	0.03 ± 0.17	0.08 ± 0.13	−0.00 ± 0.16
J21466−001	−0.01 ± 0.16	0.09 ± 0.16	0.07 ± 0.16	−0.00 ± 0.17	0.11 ± 0.12	0.05 ± 0.15	−0.03 ± 0.13	0.05 ± 0.14	0.15 ± 0.10	0.12 ± 0.17	0.03 ± 0.14	−0.01 ± 0.20	0.01 ± 0.17	−0.00 ± 0.13	0.01 ± 0.15
J21467−212	0.01 ± 0.17	−0.09 ± 0.17	0.05 ± 0.18	−0.14 ± 0.18	−0.06 ± 0.11	−0.03 ± 0.16	−0.14 ± 0.13	−0.03 ± 0.15	0.03 ± 0.10	0.16 ± 0.17	−0.03 ± 0.15	−0.12 ± 0.21	0.02 ± 0.17	−0.10 ± 0.14	−0.04 ± 0.15
J21518+423	−0.19 ± 0.16	0.01 ± 0.13	−0.25 ± 0.18	−0.23 ± 0.18	−0.11 ± 0.17	−0.16 ± 0.15	−0.21 ± 0.13	−0.19 ± 0.15	−0.08 ± 0.14	−0.10 ± 0.19	−0.19 ± 0.16	−0.32 ± 0.20	−0.19 ± 0.17	−0.25 ± 0.16	−0.25 ± 0.16
J21547−033	−0.02 ± 0.16	0.08 ± 0.16	0.13 ± 0.16	−0.00 ± 0.16	0.07 ± 0.12	0.06 ± 0.15	−0.05 ± 0.12	0.05 ± 0.14	0.15 ± 0.10	0.13 ± 0.17	0.02 ± 0.14	−0.09 ± 0.20	0.06 ± 0.17	−0.02 ± 0.13	0.04 ± 0.14
J21554+596AB	−0.14 ± 0.16	−0.10 ± 0.17	−0.25 ± 0.17	−0.41 ± 0.17	−0.13 ± 0.11	−0.36 ± 0.16	−0.14 ± 0.13	−0.39 ± 0.15	0.00 ± 0.10	−0.02 ± 0.16	−0.18 ± 0.15	−0.23 ± 0.20	−0.34 ± 0.17	−0.23 ± 0.14	−0.45 ± 0.16
J21574+289	−0.08 ± 0.15	0.22 ± 0.14	0.06 ± 0.19	0.12 ± 0.19	0.06 ± 0.17	0.22 ± 0.17	0.18 ± 0.14	0.20 ± 0.15	0.23 ± 0.15	0.17 ± 0.21	0.27 ± 0.17	0.01 ± 0.20	0.25 ± 0.18	0.14 ± 0.15	0.21 ± 0.17
J22012+283	−0.13 ± 0.16	−0.13 ± 0.18	−0.21 ± 0.18	−0.32 ± 0.18	−0.14 ± 0.11	−0.27 ± 0.16	−0.13 ± 0.12	−0.23 ± 0.15	0.05 ± 0.10	0.06 ± 0.17	−0.17 ± 0.14	−0.28 ± 0.20	−0.27 ± 0.17	−0.30 ± 0.13	−0.28 ± 0.15
J22020−194	−0.06 ± 0.17	0.06 ± 0.17	0.10 ± 0.17	0.01 ± 0.17	0.04 ± 0.11	0.09 ± 0.15	−0.08 ± 0.13	0.01 ± 0.15	0.08 ± 0.10	0.07 ± 0.17	0.05 ± 0.14	−0.10 ± 0.20	0.07 ± 0.16	−0.07 ± 0.13	0.08 ± 0.15
J22021+014	−0.12 ± 0.16	0.02 ± 0.13	−0.06 ± 0.19	−0.13 ± 0.18	0.02 ± 0.16	−0.05 ± 0.15	−0.06 ± 0.14	−0.09 ± 0.15	0.07 ± 0.15	−0.01 ± 0.19	0.00 ± 0.17	−0.09 ± 0.20	−0.09 ± 0.16	−0.07 ± 0.15	−0.09 ± 0.16
J22035+036AB	−0.13 ± 0.17	−0.18 ± 0.18	−0.33 ± 0.18	−0.31 ± 0.16	−0.14 ± 0.12	−0.22 ± 0.16	−0.07 ± 0.12	−0.19 ± 0.15	0.09 ± 0.10	0.01 ± 0.17	−0.15 ± 0.15	−0.29 ± 0.20	−0.22 ± 0.16	−0.25 ± 0.14	−0.26 ± 0.16
J22065+433	0.13 ± 0.17	0.11 ± 0.17	0.29 ± 0.17	0.14 ± 0.17	0.14 ± 0.11	0.24 ± 0.15	0.01 ± 0.13	0.24 ± 0.14	0.20 ± 0.10	0.29 ± 0.16	0.06 ± 0.14	−0.07 ± 0.21	0.26 ± 0.17	0.02 ± 0.13	0.26 ± 0.15
J22088+117	−0.03 ± 0.17	0.03 ± 0.17	−0.16 ± 0.18	−0.31 ± 0.19	0.29 ± 0.11	−0.26 ± 0.16	0.15 ± 0.13	−0.31 ± 0.16	0.35 ± 0.10	0.19 ± 0.17	0.10 ± 0.15	0.16 ± 0.21	−0.34 ± 0.17	0.07 ± 0.13	−0.36 ± 0.17
J22089−177	−0.23 ± 0.15	−0.14 ± 0.17	−0.33 ± 0.17	−0.34 ± 0.17	−0.33 ± 0.12	−0.19 ± 0.16	−0.31 ± 0.13	−0.14 ± 0.15	−0.18 ± 0.10	−0.13 ± 0.17	−0.25 ± 0.14	−0.34 ± 0.20	−0.16 ± 0.16	−0.31 ± 0.13	−0.22 ± 0.15
J22095+118	−0.03 ± 0.16	0.11 ± 0.17	0.02 ± 0.17	−0.03 ± 0.17	0.05 ± 0.11	0.09 ± 0.15	−0.04 ± 0.12	0.05 ± 0.14	0.12 ± 0.10	0.06 ± 0.17	0.06 ± 0.14	−0.07 ± 0.19	0.09 ± 0.16	−0.02 ± 0.13	0.01 ± 0.15
J22096−046	0.08 ± 0.17	0.11 ± 0.16	0.34 ± 0.18	0.15 ± 0.17	0.15 ± 0.12	0.21 ± 0.15	0.01 ± 0.13	0.18 ± 0.15	0.19 ± 0.10	0.24 ± 0.17	0.14 ± 0.14	−0.00 ± 0.21	0.21 ± 0.17	0.05 ± 0.13	0.25 ± 0.15
J22115+184	0.03 ± 0.17	0.23 ± 0.14	0.33 ± 0.18	0.02 ± 0.18	0.09 ± 0.17	0.12 ± 0.16	0.09 ± 0.15	0.14 ± 0.16	0.19 ± 0.14	0.15 ± 0.19	0.14 ± 0.16	0.20 ± 0.20	0.08 ± 0.17	0.06 ± 0.15	0.15 ± 0.17
J22125+085	−0.13 ± 0.16	0.02 ± 0.17	−0.07 ± 0.17	−0.16 ± 0.17	−0.07 ± 0.12	−0.05 ± 0.14	−0.11 ± 0.13	−0.09 ± 0.15	0.02 ± 0.10	−0.00 ± 0.17	−0.06 ± 0.14	−0.22 ± 0.20	−0.10 ± 0.16	−0.13 ± 0.13	−0.10 ± 0.15
J22137−176	−0.12 ± 0.17	0.02 ± 0.17	−0.13 ± 0.18	−0.06 ± 0.17	0.04 ± 0.12	0.02 ± 0.15	−0.14 ± 0.13	−0.01 ± 0.14	0.09 ± 0.10	0.02 ± 0.16	−0.06 ± 0.15	−0.09 ± 0.21	−0.04 ± 0.16	−0.06 ± 0.14	−0.07 ± 0.15
J22202+067	−0.24 ± 0.16	−0.07 ± 0.17	−0.39 ± 0.16	−0.36 ± 0.16	−0.21 ± 0.12	−0.22 ± 0.15	−0.21 ± 0.12	−0.27 ± 0.15	−0.07 ± 0.10	−0.22 ± 0.17	−0.16 ± 0.14	−0.32 ± 0.20	−0.25 ± 0.16	−0.26 ± 0.13	−0.34 ± 0.15
J22252+594	0.05 ± 0.16	0.14 ± 0.17	0.14 ± 0.17	0.03 ± 0.17	0.20 ± 0.11	0.12 ± 0.15	0.02 ± 0.13	0.14 ± 0.15	0.24 ± 0.10	0.21 ± 0.16	0.07 ± 0.15	0.06 ± 0.20	0.05 ± 0.16	0.06 ± 0.14	0.07 ± 0.15
J22264+583	−0.13 ± 0.16	0.05 ± 0.17	−0.10 ± 0.17	−0.15 ± 0.16	0.00 ± 0.12	−0.05 ± 0.15	−0.06 ± 0.12	−0.08 ± 0.14	0.10 ± 0.10	−0.02 ± 0.17	0.01 ± 0.15	−0.08 ± 0.20	−0.08 ± 0.16	−0.07 ± 0.13	−0.13 ± 0.15
J22298+414	−0.00 ± 0.17	0.12 ± 0.17	0.08 ± 0.17	−0.00 ± 0.16	0.17 ± 0.11	0.06 ± 0.16	−0.01 ± 0.12	0.10 ± 0.14	0.21 ± 0.10	0.21 ± 0.15	0.06 ± 0.14	0.00 ± 0.20	0.01 ± 0.16	0.05 ± 0.13	0.01 ± 0.15
J22300+488AB	−0.13 ± 0.16	−0.14 ± 0.18	−0.04 ± 0.18	−0.25 ± 0.18	−0.10 ± 0.12	−0.16 ± 0.16	−0.05 ± 0.12	−0.16 ± 0.15	0.06 ± 0.10	0.01 ± 0.16	0.07 ± 0.16	0.03 ± 0.22	−0.12 ± 0.18	−0.19 ± 0.14	−0.14 ± 0.16
J22330+093	−0.25 ± 0.16	−0.07 ± 0.13	−0.20 ± 0.19	−0.27 ± 0.18	−0.10 ± 0.17	−0.17 ± 0.15	−0.21 ± 0.14	−0.26 ± 0.16	−0.08 ± 0.14	−0.13 ± 0.19	−0.18 ± 0.17	−0.25 ± 0.19	−0.26 ± 0.17	−0.27 ± 0.15	−0.26 ± 0.16
J22387+252	−0.04 ± 0.17	0.10 ± 0.17	−0.03 ± 0.17	−0.03 ± 0.17	0.08 ± 0.12	0.06 ± 0.15	−0.05 ± 0.13	0.02 ± 0.14	0.12 ± 0.10	0.07 ± 0.17	0.04 ± 0.15	−0.02 ± 0.19	0.02 ± 0.16	−0.01 ± 0.13	−0.02 ± 0.15
J22396−125	0.08 ± 0.17	0.02 ± 0.17	0.04 ± 0.17	−0.06 ± 0.17	−0.10 ± 0.12	0.11 ± 0.15	−0.05 ± 0.13	0.04 ± 0.16	0.06 ± 0.11	−0.07 ± 0.17	0.11 ± 0.15	−0.06 ± 0.20	0.06 ± 0.17	−0.13 ± 0.13	0.08 ± 0.15
J22415+260	−0.02 ± 0.17	0.01 ± 0.17	−0.00 ± 0.17	−0.17 ± 0.18	−0.06 ± 0.11	−0.04 ± 0.15	−0.13 ± 0.12	−0.03 ± 0.15	0.04 ± 0.10	0.13 ± 0.16	−0.04 ± 0.14	−0.17 ± 0.20	−0.03 ± 0.17	−0.13 ± 0.13	−0.10 ± 0.15
J22437+192	0.01 ± 0.16	0.03 ± 0.17	−0.06 ± 0.16	−0.12 ± 0.17	−0.05 ± 0.11	0.01 ± 0.15	−0.09 ± 0.12	−0.00 ± 0.15	0.08 ± 0.10	0.08 ± 0.16	−0.06 ± 0.14	−0.20 ± 0.20	0.01 ± 0.16	−0.11 ± 0.13	−0.06 ± 0.15
J22476+184	−0.01 ± 0.17	0.07 ± 0.17	−0.00 ± 0.17	−0.00 ± 0.16	−0.02 ± 0.11	0.06 ± 0.15	−0.11 ± 0.13	0.07 ± 0.15	0.07 ± 0.10	0.10 ± 0.17	−0.06 ± 0.14	−0.24 ± 0.20	0.04 ± 0.16	−0.09 ± 0.13	0.03 ± 0.16
J22489+183	−0.06 ± 0.16	−0.10 ± 0.18	−0.18 ± 0.17	−0.15 ± 0.17	−0.10 ± 0.12	−0.04 ± 0.16	−0.13 ± 0.13	−0.05 ± 0.14	0.04 ± 0.10	0.06 ± 0.17	−0.04 ± 0.15	−0.20 ± 0.21	−0.02 ± 0.17	−0.18 ± 0.14	−0.09 ± 0.16
J22509+499	0.02 ± 0.17	−0.01 ± 0.17	−0.19 ± 0.17	−0.37 ± 0.19	0.12 ± 0.11	−0.32 ± 0.17	0.03 ± 0.12	−0.37 ± 0.16	0.26 ± 0.10	0.20 ± 0.18	−0.11 ± 0.15	−0.19 ± 0.21	−0.40 ± 0.19	−0.07 ± 0.14	−0.48 ± 0.17
J22518+317	0.00 ± 0.16	−0.01 ± 0.17	0.07 ± 0.17	−0.26 ± 0.18	−0.03 ± 0.11	−0.20 ± 0.16	−0.05 ± 0.13	−0.26 ± 0.15	0.09 ± 0.10	0.13 ± 0.16	−0.02 ± 0.14	−0.16 ± 0.19	−0.21 ± 0.18	−0.15 ± 0.13	−0.24 ± 0.16

Table C.4: *Continued*

Karmn	[C/H]	[O/H]	[Na/H]	[Mg/H]	[Al/H]	[Si/H]	[Ca/H]	[Sc/H]	[Ti/H]	[V/H]	[Cr/H]	[Mn/H]	[Fe/H]	[Co/H]	[Ni/H]
J22524+099AB	−0.28 ± 0.17	−0.05 ± 0.17	−0.27 ± 0.17	−0.29 ± 0.17	−0.22 ± 0.11	−0.20 ± 0.15	−0.27 ± 0.13	−0.24 ± 0.15	−0.11 ± 0.10	−0.14 ± 0.17	−0.21 ± 0.14	−0.33 ± 0.20	−0.23 ± 0.16	−0.25 ± 0.13	−0.27 ± 0.15
J22526+750	0.19 ± 0.16	0.21 ± 0.18	0.37 ± 0.17	0.33 ± 0.17	0.35 ± 0.12	0.32 ± 0.15	0.12 ± 0.12	0.27 ± 0.15	0.33 ± 0.10	0.39 ± 0.17	0.29 ± 0.15	0.24 ± 0.21	0.31 ± 0.16	0.27 ± 0.13	0.30 ± 0.16
J22559+178	−0.15 ± 0.16	0.02 ± 0.14	−0.10 ± 0.18	−0.17 ± 0.19	−0.05 ± 0.17	−0.13 ± 0.15	−0.17 ± 0.14	−0.16 ± 0.16	−0.02 ± 0.15	−0.07 ± 0.20	−0.12 ± 0.17	−0.13 ± 0.20	−0.17 ± 0.17	−0.18 ± 0.15	−0.22 ± 0.17
J22565+165	−0.35 ± 0.15	0.01 ± 0.14	−0.53 ± 0.19	−0.39 ± 0.18	−0.35 ± 0.17	−0.39 ± 0.17	−0.36 ± 0.14	−0.29 ± 0.16	−0.22 ± 0.14	−0.31 ± 0.19	−0.33 ± 0.17	−0.52 ± 0.20	−0.44 ± 0.17	−0.43 ± 0.15	−0.45 ± 0.16
J22582−110	0.08 ± 0.18	0.02 ± 0.16	0.05 ± 0.18	−0.08 ± 0.17	−0.06 ± 0.12	0.07 ± 0.17	−0.07 ± 0.13	−0.09 ± 0.15	0.08 ± 0.11	−0.05 ± 0.16	0.13 ± 0.15	−0.06 ± 0.22	0.08 ± 0.18	−0.16 ± 0.13	0.00 ± 0.16
J22588+690	−0.12 ± 0.16	0.07 ± 0.16	−0.17 ± 0.17	−0.19 ± 0.17	0.03 ± 0.12	−0.13 ± 0.15	−0.13 ± 0.12	−0.14 ± 0.14	0.04 ± 0.10	−0.04 ± 0.17	−0.06 ± 0.14	−0.11 ± 0.20	−0.17 ± 0.16	−0.07 ± 0.13	−0.20 ± 0.15
J23006+036	−0.04 ± 0.16	0.05 ± 0.17	−0.06 ± 0.17	−0.18 ± 0.16	−0.02 ± 0.12	−0.06 ± 0.15	−0.13 ± 0.12	−0.09 ± 0.14	0.01 ± 0.10	0.02 ± 0.16	−0.04 ± 0.15	−0.12 ± 0.20	−0.12 ± 0.16	−0.08 ± 0.14	−0.13 ± 0.15
J23025+298	−0.35 ± 0.17	−0.14 ± 0.17	−0.39 ± 0.17	−0.38 ± 0.17	−0.32 ± 0.11	−0.26 ± 0.16	−0.31 ± 0.12	−0.29 ± 0.14	−0.15 ± 0.10	−0.24 ± 0.17	−0.25 ± 0.14	−0.42 ± 0.21	−0.27 ± 0.16	−0.38 ± 0.13	−0.32 ± 0.15
J23028+436	−0.10 ± 0.16	−0.13 ± 0.17	−0.31 ± 0.17	−0.16 ± 0.18	−0.15 ± 0.12	−0.19 ± 0.16	−0.17 ± 0.12	−0.01 ± 0.15	−0.04 ± 0.11	0.06 ± 0.17	−0.20 ± 0.14	−0.30 ± 0.20	−0.17 ± 0.17	−0.22 ± 0.13	−0.17 ± 0.16
J23036−072	−0.09 ± 0.16	0.09 ± 0.17	0.08 ± 0.16	−0.03 ± 0.17	0.12 ± 0.12	−0.00 ± 0.15	−0.04 ± 0.12	−0.00 ± 0.15	0.12 ± 0.10	0.07 ± 0.17	0.05 ± 0.14	−0.01 ± 0.21	0.01 ± 0.16	0.04 ± 0.13	−0.02 ± 0.15
J23036+097	−0.03 ± 0.17	0.14 ± 0.17	0.02 ± 0.17	0.04 ± 0.17	0.17 ± 0.12	−0.01 ± 0.15	0.00 ± 0.12	0.08 ± 0.14	0.18 ± 0.10	0.15 ± 0.16	0.02 ± 0.14	−0.07 ± 0.20	−0.06 ± 0.17	0.09 ± 0.13	−0.05 ± 0.16
J23051+519	0.07 ± 0.16	0.15 ± 0.18	0.21 ± 0.17	0.18 ± 0.17	0.23 ± 0.12	0.14 ± 0.15	0.06 ± 0.13	0.24 ± 0.14	0.24 ± 0.10	0.30 ± 0.17	0.09 ± 0.14	0.03 ± 0.19	0.14 ± 0.16	0.13 ± 0.13	0.16 ± 0.15
J23051+452	0.05 ± 0.16	0.04 ± 0.17	0.03 ± 0.17	−0.15 ± 0.17	0.07 ± 0.11	−0.13 ± 0.16	0.03 ± 0.13	−0.14 ± 0.15	0.18 ± 0.10	0.17 ± 0.16	0.04 ± 0.14	−0.10 ± 0.20	−0.10 ± 0.17	−0.09 ± 0.13	−0.16 ± 0.15
J23103+490	0.23 ± 0.16	0.31 ± 0.14	0.21 ± 0.19	0.23 ± 0.19	0.36 ± 0.17	0.33 ± 0.16	0.18 ± 0.15	0.29 ± 0.17	0.35 ± 0.15	0.23 ± 0.19	0.14 ± 0.17	0.25 ± 0.21	0.22 ± 0.17	0.30 ± 0.16	0.15 ± 0.16
J23182+795	−0.03 ± 0.16	0.08 ± 0.16	−0.04 ± 0.17	−0.14 ± 0.17	0.05 ± 0.12	−0.05 ± 0.15	−0.04 ± 0.12	−0.03 ± 0.14	0.13 ± 0.11	0.14 ± 0.17	−0.06 ± 0.14	−0.20 ± 0.20	−0.10 ± 0.16	−0.06 ± 0.13	−0.12 ± 0.15
J23216+172	0.09 ± 0.16	0.16 ± 0.17	0.23 ± 0.16	0.13 ± 0.17	0.30 ± 0.12	0.21 ± 0.15	0.10 ± 0.12	0.20 ± 0.14	0.33 ± 0.10	0.27 ± 0.16	0.19 ± 0.14	0.17 ± 0.20	0.15 ± 0.16	0.14 ± 0.13	0.18 ± 0.16
J23220+569	−0.15 ± 0.17	0.16 ± 0.17	−0.25 ± 0.16	−0.12 ± 0.16	0.12 ± 0.12	−0.15 ± 0.15	−0.08 ± 0.12	−0.06 ± 0.15	0.10 ± 0.10	−0.00 ± 0.17	−0.07 ± 0.15	−0.14 ± 0.20	−0.22 ± 0.16	0.00 ± 0.13	−0.26 ± 0.15
J23235+457	−0.03 ± 0.16	0.14 ± 0.13	0.17 ± 0.18	0.04 ± 0.18	0.11 ± 0.17	0.11 ± 0.15	0.10 ± 0.14	0.12 ± 0.16	0.19 ± 0.15	0.15 ± 0.19	0.16 ± 0.17	0.14 ± 0.20	0.08 ± 0.17	0.12 ± 0.15	0.12 ± 0.16
J23245+578	−0.10 ± 0.16	0.13 ± 0.14	−0.22 ± 0.19	−0.17 ± 0.18	−0.04 ± 0.18	−0.06 ± 0.16	−0.19 ± 0.15	0.03 ± 0.16	0.00 ± 0.15	−0.03 ± 0.20	−0.18 ± 0.18	−0.27 ± 0.20	−0.03 ± 0.17	−0.07 ± 0.16	−0.22 ± 0.17
J23261+170AB	−0.03 ± 0.17	−0.04 ± 0.17	−0.11 ± 0.17	−0.09 ± 0.17	−0.04 ± 0.12	0.01 ± 0.15	−0.15 ± 0.13	0.01 ± 0.15	0.08 ± 0.10	0.08 ± 0.16	−0.11 ± 0.14	−0.24 ± 0.21	−0.06 ± 0.16	−0.14 ± 0.14	−0.07 ± 0.15
J23266+453W	−0.14 ± 0.15	0.02 ± 0.13	−0.10 ± 0.19	−0.18 ± 0.18	−0.06 ± 0.17	−0.07 ± 0.16	−0.11 ± 0.14	−0.05 ± 0.16	−0.02 ± 0.14	−0.05 ± 0.19	−0.10 ± 0.16	−0.12 ± 0.20	−0.11 ± 0.17	−0.18 ± 0.15	−0.09 ± 0.16
J23293+414N	0.06 ± 0.18	0.02 ± 0.17	0.38 ± 0.20	−0.12 ± 0.19	−0.07 ± 0.11	−0.05 ± 0.16	−0.10 ± 0.13	0.28 ± 0.18	−0.02 ± 0.10	0.70 ± 0.21	0.01 ± 0.14	−0.20 ± 0.21	0.16 ± 0.20	−0.13 ± 0.13	0.12 ± 0.20
J23306+466	−0.14 ± 0.16	0.06 ± 0.13	−0.17 ± 0.19	−0.11 ± 0.17	−0.08 ± 0.17	−0.05 ± 0.16	−0.04 ± 0.14	−0.05 ± 0.15	0.09 ± 0.14	0.01 ± 0.19	−0.03 ± 0.16	−0.22 ± 0.20	−0.07 ± 0.17	−0.04 ± 0.15	−0.09 ± 0.17
J23317−064	0.27 ± 0.17	0.24 ± 0.18	0.42 ± 0.17	0.33 ± 0.17	0.51 ± 0.12	0.31 ± 0.16	0.26 ± 0.13	0.33 ± 0.15	0.51 ± 0.11	0.42 ± 0.17	0.31 ± 0.15	0.42 ± 0.21	0.26 ± 0.17	0.33 ± 0.14	0.32 ± 0.16
J23340+001	−0.05 ± 0.17	0.11 ± 0.18	0.17 ± 0.19	−0.16 ± 0.18	−0.07 ± 0.12	−0.08 ± 0.16	−0.10 ± 0.13	0.15 ± 0.16	−0.06 ± 0.10	0.43 ± 0.20	−0.00 ± 0.14	−0.28 ± 0.21	−0.04 ± 0.18	−0.08 ± 0.14	−0.00 ± 0.19
J23354+310	−0.25 ± 0.17	0.08 ± 0.17	−0.43 ± 0.17	−0.26 ± 0.17	−0.08 ± 0.12	−0.36 ± 0.16	−0.19 ± 0.13	−0.25 ± 0.15	−0.03 ± 0.10	−0.18 ± 0.16	−0.30 ± 0.15	−0.40 ± 0.21	−0.46 ± 0.17	−0.19 ± 0.13	−0.47 ± 0.15
J23381−162	−0.32 ± 0.16	−0.01 ± 0.14	−0.27 ± 0.19	−0.21 ± 0.18	−0.16 ± 0.18	−0.10 ± 0.16	−0.14 ± 0.14	−0.19 ± 0.16	−0.05 ± 0.14	−0.10 ± 0.20	−0.09 ± 0.16	−0.30 ± 0.20	−0.19 ± 0.18	−0.20 ± 0.15	−0.20 ± 0.16
J23416−065	0.16 ± 0.17	0.10 ± 0.17	0.49 ± 0.18	0.19 ± 0.17	0.26 ± 0.12	0.22 ± 0.17	0.06 ± 0.13	0.16 ± 0.15	0.22 ± 0.10	0.45 ± 0.17	0.21 ± 0.15	0.10 ± 0.21	0.23 ± 0.17	0.17 ± 0.14	0.25 ± 0.16
J23417−059AB	−0.10 ± 0.16	0.07 ± 0.17	0.03 ± 0.17	−0.05 ± 0.17	−0.02 ± 0.12	0.06 ± 0.15	−0.19 ± 0.12	0.02 ± 0.15	−0.01 ± 0.10	0.08 ± 0.17	−0.07 ± 0.14	−0.12 ± 0.20	0.05 ± 0.16	−0.02 ± 0.14	−0.04 ± 0.15
J23423+349	−0.07 ± 0.16	0.05 ± 0.16	−0.05 ± 0.17	−0.07 ± 0.17	0.05 ± 0.12	−0.06 ± 0.15	−0.06 ± 0.12	0.01 ± 0.14	0.11 ± 0.10	0.16 ± 0.17	−0.03 ± 0.14	−0.12 ± 0.19	−0.11 ± 0.16	0.00 ± 0.13	−0.12 ± 0.14
J23425+392	−0.16 ± 0.16	−0.01 ± 0.13	−0.53 ± 0.18	−0.33 ± 0.19	−0.30 ± 0.18	−0.31 ± 0.16	−0.31 ± 0.15	−0.30 ± 0.16	−0.19 ± 0.15	−0.19 ± 0.20	−0.34 ± 0.18	−0.48 ± 0.20	−0.32 ± 0.17	−0.41 ± 0.16	−0.47 ± 0.17
J23431+365	−0.07 ± 0.16	0.01 ± 0.16	0.03 ± 0.17	−0.05 ± 0.17	0.04 ± 0.12	0.01 ± 0.15	−0.06 ± 0.12	0.02 ± 0.14	0.11 ± 0.10	0.17 ± 0.16	0.05 ± 0.14	−0.04 ± 0.20	0.02 ± 0.16	−0.06 ± 0.14	0.01 ± 0.15
J23438+610	−0.23 ± 0.17	−0.02 ± 0.16	−0.44 ± 0.17	−0.34 ± 0.18	−0.16 ± 0.11	−0.29 ± 0.16	−0.23 ± 0.13	−0.18 ± 0.15	−0.05 ± 0.10	−0.10 ± 0.16	−0.30 ± 0.14	−0.39 ± 0.20	−0.37 ± 0.16	−0.25 ± 0.13	−0.38 ± 0.15
J23490−086	−0.22 ± 0.16	−0.01 ± 0.13	−0.23 ± 0.19	−0.20 ± 0.18	−0.13 ± 0.17	−0.11 ± 0.16	−0.09 ± 0.14	−0.15 ± 0.15	0.02 ± 0.14	−0.10 ± 0.19	−0.09 ± 0.17	−0.33 ± 0.20	−0.19 ± 0.17	−0.16 ± 0.15	−0.20 ± 0.17
J23492+024	−0.40 ± 0.16	−0.10 ± 0.13	−0.67 ± 0.18	−0.46 ± 0.19	−0.42 ± 0.17	−0.51 ± 0.17	−0.49 ± 0.14	−0.51 ± 0.16	−0.33 ± 0.16	−0.38 ± 0.19	−0.53 ± 0.17	−0.73 ± 0.21	−0.55 ± 0.18	−0.62 ± 0.15	−0.68 ± 0.17
J23505−095	0.12 ± 0.17	0.12 ± 0.18	0.28 ± 0.17	0.21 ± 0.17	0.23 ± 0.11	0.23 ± 0.15	0.07 ± 0.12	0.25 ± 0.14	0.27 ± 0.10	0.33 ± 0.17	0.15 ± 0.14	0.06 ± 0.20	0.26 ± 0.16	0.10 ± 0.13	0.27 ± 0.15
J23548+385	−0.14 ± 0.16	−0.13 ± 0.17	−0.19 ± 0.17	−0.30 ± 0.17	−0.15 ± 0.12	−0.24 ± 0.15	−0.15 ± 0.13	−0.21 ± 0.15	0.01 ± 0.10	−0.00 ± 0.17	−0.19 ± 0.14	−0.29 ± 0.21	−0.20 ± 0.16	−0.27 ± 0.13	−0.26 ± 0.15
J23555+006	−0.13 ± 0.16	0.10 ± 0.14	−0.02 ± 0.18	−0.12 ± 0.19	−0.02 ± 0.17	−0.09 ± 0.16	−0.13 ± 0.13	−0.14 ± 0.16	0.05 ± 0.14	−0.01 ± 0.19	−0.10 ± 0.17	−0.17 ± 0.20	−0.19 ± 0.17	−0.11 ± 0.15	−0.13 ± 0.16
J23556−061	0.05 ± 0.16	0.09 ± 0.17	0.22 ± 0.17	−0.00 ± 0.17	0.04 ± 0.12	0.12 ± 0.15	−0.02 ± 0.12	0.12 ± 0.14	0.13 ± 0.10	0.21 ± 0.16	0.03 ± 0.14	−0.08 ± 0.21	0.10 ± 0.16	−0.05 ± 0.13	0.13 ± 0.14
J23559−133	−0.06 ± 0.17	−0.04 ± 0.17	−0.19 ± 0.17	−0.24 ± 0.17	0.03 ± 0.12	−0.22 ± 0.15	−0.10 ± 0.12	−0.14 ± 0.15	0.08 ± 0.10	0.12 ± 0.17	−0.07 ± 0.14	−0.15 ± 0.19	−0.21 ± 0.16	−0.12 ± 0.13	−0.25 ± 0.15
J23560+150	−0.09 ± 0.17	0.05 ± 0.17	−0.13 ± 0.17	−0.12 ± 0.17	−0.07 ± 0.11	−0.03 ± 0.15	−0.12 ± 0.12	−0.04 ± 0.14	0.03 ± 0.10	0.03 ± 0.17	−0.06 ± 0.14	−0.16 ± 0.20	−0.07 ± 0.16	−0.09 ± 0.13	−0.10 ± 0.14
J23569+230	−0.11 ± 0.16	0.09 ± 0.13	−0.18 ± 0.19	−0.12 ± 0.18	−0.10 ± 0.17	−0.11 ± 0.16	−0.09 ± 0.13	−0.07 ± 0.16	0.06 ± 0.15	0.02 ± 0.18	−0.06 ± 0.16	−0.29 ± 0.20	−0.08 ± 0.17	−0.08 ± 0.15	−0.12 ± 0.16
J23577+233	−0.23 ± 0.17	0.06 ± 0.17	−0.39 ± 0.16	−0.28 ± 0.17	−0.03 ± 0.11	−0.21 ± 0.15	−0.18 ± 0.12	−0.21 ± 0.15	0.03 ± 0.10	−0.17 ± 0.16	−0.21 ± 0.15	−0.24 ± 0.19	−0.32 ± 0.16	−0.15 ± 0.13	−0.38 ± 0.15
J23585+242W	−0.09 ± 0.17	−0.05 ± 0.17	−0.19 ± 0.17	−0.28 ± 0.17	−0.12 ± 0.12	−0.21 ± 0.16	−0.14 ± 0.12	−0.25 ± 0.14	0.03 ± 0.10	−0.03 ± 0.16	−0.14 ± 0.14	−0.25 ± 0.20	−0.21 ± 0.16	−0.24 ± 0.14	−0.30 ± 0.15
J23585+242	−0.08 ± 0.16	0.06 ± 0.13	−0.02 ± 0.19	−0.06 ± 0.18	0.07 ± 0.17	0.03 ± 0.16	−0.02 ± 0.14	−0.05 ± 0.16	0.10 ± 0.14	0.05 ± 0.20	0.01 ± 0.17	−0.06 ± 0.20	−0.02 ± 0.17	−0.01 ± 0.15	−0.02 ± 0.16
J23585+076	−0.09 ± 0.17	0.07 ± 0.16	−0.12 ± 0.17	−0.12 ± 0.17	0.05 ± 0.12	−0.04 ± 0.16	−0.08 ± 0.12	−0.05 ± 0.14	0.11 ± 0.10	0.02 ± 0.16	−0.04 ± 0.14	−0.10 ± 0.20	−0.09 ± 0.16	−0.08 ± 0.13	−0.11 ± 0.15
J23590+208	0.12 ± 0.17	0.13 ± 0.17	0.21 ± 0.17	0.02 ± 0.17	0.12 ± 0.11	0.05 ± 0.15	−0.03 ± 0.13	0.21 ± 0.15	0.16 ± 0.10	0.33 ± 0.17	−0.05 ± 0.15	−0.11 ± 0.20	0.04 ± 0.16	0.02 ± 0.13	0.09 ± 0.15
J23593+326	0.26 ± 0.17	0.12 ± 0.16	0.21 ± 0.18	−0.00 ± 0.19	0.39 ± 0.12	−0.06 ± 0.18	0.27 ± 0.14	−0.13 ± 0.17	0.47 ± 0.11	0.50 ± 0.18	0.25 ± 0.15	0.29 ± 0.21	−0.06 ± 0.19	0.19 ± 0.13	−0.09 ± 0.17